Transactions of the ASME®

# Journal of Fluids Engineering

Published Quarterly by The American Society of Mechanical Engineers

VOLUME 116 • NUMBER 3 • SEPTEMBER 1994



(Contents continued on inside back cover)



**Transactions of the ASME, Journal of Fluids Engineering** (ISSN 0098-2202) is published quarterly (Mar., June, Sept., Dec.) for $150.00 per year by The American Society of Mechanical Engineers, 345 East 47th Street, New York, NY 10017. Second class postage paid at New York, NY and additional mailing offices. POSTMASTER: Send address changes to Transactions of the ASME, Journal of Fluids Engineering, c/o THE AMERICAN SOCIETY OF MECHANICAL ENGINEERS, 22 Law Drive, Box 2300, Fairfield, NJ 07007-2300.
**CHANGES OF ADDRESS** must be received at Society headquarters seven weeks before they are to be effective. Please send old label and new address.
**PRICES:** To members, $40.00, annually; to nonmembers, $150.00. Add $30.00 for postage to countries outside the United States and Canada.
**STATEMENT** from By-Laws. The Society shall not be responsible for statements or opinions advanced in papers or . . . printed in its publications (B7.1, Par. 3).

**INDEXED** by Applied Mechanics Reviews and Engineering Information, Inc.
Canadian Goods & Services Tax Registration #126148048

Contents (continued)

Journal of Fluids Engineering

# Editorial

We are pleased to announce new services offered by the *Journal of Fluids Engineering* and the Fluids Engineering Division. This is an expansion of our electronic on-line information service. The steps outlined below are experimental. In fact, in some of the services proposed here, we only offer some views and initiate processes on a voluntary basis. We hope that with input from our readership and the members of the Division, we will be able to arrive in a few years to an acceptable and useful format.

## 1. Expansion of our Data Bank Scope

For over a year now, this Journal has operated an electronic data bank for the deposition of selected experimental data. During this period, members of the Fluids Engineering Division have been debating whether similar requests should be made to authors of computational papers. Deliberation among members of the Coordinating Group of CFD was coordinated by Drs. Pratap Vanka and Oktay Baysal, while the discussion among members of the Editorial Board was led by Dr. Owen Jones. These three individuals have prepared written reports which one of us (DT) has combined, edited and present here to our readership. It appears that more discussion is necessary before a formal policy can be formulated. The readership is invited to participate in this process. Ideas and suggestions can be contributed directly to the Editor. The readers of this Journal are also invited to participate in the discussion during the meeting of the Coordinating Group of CFD at the upcoming Winter Annual Meeting in Chicago. In the meantime, we will immediately begin accepting material to be deposited on a voluntary basis as we describe later in this section.

Technically it is possible to deposit in the JFE Data Bank, computer codes, computer-generated grids and numerical results. This practice has many advantages. The availability of data that can be obtained in an electronic form eliminates much tedious work in extracting the same from a journal paper. The extraction of data from the journal article can also lead to inaccuracies. In addition, since the computer code and the grid that generated the data are also available, it is possible to generate additional data that were not previously reported. Computer codes in the repository can be starting points for further developments by other researchers. However, we believe that there can be a number of operational difficulties in such a policy. Some of these are:

(*a*) Requiring a computer code could be offending to some as it might imply doubt in the researcher's claims. Therefore, a clear statement of the purpose in such a request must be made in an editorial. Moreover, authors may be uncomfortable to part with their codes for a variety of reasons, some of which are understandable: (i) proprietary nature of the code; (ii) loss of competitive ability in future proposals; (iii) uncertainties of performance in unknown flows and for parameters not considered; (iv) lack of maintenance and support capability; and (v) migration of principal authors (either graduation or work stoppage) etc.

(*b*) If the authors deposit their codes with ASME, distribution and maintenance will require manpower. Further, most academic codes are not written for generality and clarity. Also, they are not generally documented adequately, and the benefit to future researchers may be minimal. However, a disclaimer statement could be accepted from the authors and included with the code.

(*c*) Deposition of tabular data presented as graphs in the manuscript could be very valuable. For example, if line plots are presented, a table of numerical data with $x$-$y$ values will be very useful. Vector and contour plots can be supplemented with tables of field variables, properly annotated. These may be maintained, but it should be cautioned that soon the data base could become voluminous and difficult to support.

(*d*) Deposition of the grid should also be useful for a variety of reasons. First, any attempt to duplicate the results should be made on a similar, if not identical, grid. After all, there is no such thing as "grid independence" but only "insignificant grid dependence." Since grid generation remains a time-consuming component of CFD, this practice can save significant amounts of time for future users.

(*e*) Other operational difficulties may be (i) the format for the data base, (ii) the updating of the system as advances continue to emerge, (iii) the cost of service as well as who will pay for it, and (iv) the fact that a code may change over the duration of work being published.

On these issues, we invite input from readers and members of the Division but in the meantime we will proceed on a voluntary basis. Authors of computational papers are invited to contribute to the JFE Data Bank any or all of the following: (i) data of their tables, (ii) data of the graphs, (iii) the grid employed in their calculations and finally, (iv) the codes that generated their results. As in the case of contributions of experimental data, the review and acceptance of a paper will not be influenced by the authors' decision to deposit information in the Bank. The invitation to submit material to the JFE Data Bank will be issued only after the paper has been accepted for publication.

## 2. Color Frames and Video

Quite often, experimental data or numerical results are presented more clearly in terms of color frames. Although it is now possible to include color figures in the Journal, cost and space restrictions limit the volume of such material. It is now possible to deposit color figures in the Data Bank. These figures will be accessed by the readers electronically in a way similar to the access of experimental and numerical data. Moreover, we have also succeeded in storing and playing back a short video and this option should also be available to our readership.

Authors willing to deposit color frames or video to accompany their paper are invited to communicate directly with the Technical Editor.

### 3. The JFE Bulletin Board

This electronic board will allow readers to offer discussion on papers published in the Journal. This service is being launched with this issue. Readers can log on to the Electronic JFE and open the Bulletin Board. They will then be prompted to open the file of a paper. File names are simply the letters FN followed by the year (last two digits) and the first page of the paper. For example, a paper that appeared on page 57 in 1994 will have the file name FN94057. In each file, readers will find discussions of the paper of their interest. They can also add their own.

Readers logging on to the Electronic JFE will be prompted to provide their name and e-mail address. In case a reader offers a discussion for a paper, his or her contribution will bounce back to his/her e-mail address to provide an opportunity for a final check. It will then be automatically entered in the Bulletin Board. The Editor will monitor the process.

The material added to the Bulletin Board will be retained for a few years but the contributing discusser will always have the option to submit a discussion for publication in the Journal. Discussions and authors' responses contributed to the Bulletin Board will not be edited, but discussions submitted for publication in the Journal will be reviewed and edited by the Editorial Board according to a procedure established long ago.

### 4. Conference Schedule

The Division of Fluids Engineering organizes two major meetings per year. Calls for papers for these meetings are a regular feature of the Journal and always appear at the end of each issue. These calls are issued about 12 to 15 months before each meeting. However, tentative schedules are being made for meetings four to five years down the road. The topic of the symposia and forums to be held in these meetings are not all known in advance and some are tentative. As time progresses, each meeting crystallizes gradually to its final form. This information therefore is fluent and cannot appear in print. The electronic medium is much more appropriate, because it allows continuous updating. The Electronic JFE will provide a meetings' schedule which will be continuously updated as more information becomes available. This idea has been already implemented by the *Journal of Tribology*, which offers its readers electronically Calls for Papers for tribology and other relevant conferences.

Readers who want to log on to the Electronic JFE should follow the directions that appear in the last page of each issue. There they will find simple instructions on how to log on to the Electronic JFE and reach the Data Bank, the Bulletin Board, the Figure/Video Section or the Conference Schedule. To inspect color frames or video, it is necessary to have one of the following software: Mosaic, MacWeb, WinWeb or OmniWeb.

Readers are welcome to provide feedback to the Editorial Board by offering discussion to this editorial. Its file name will follow the basic rule.

**James Powell**
**Editorial Assistant**

**Demetri P. Telionis**
**Technical Editor**

Journal of Fluids Engineering

Technical Forum

# Questions in Fluid Mechanics: Opportunities and Challenges of Flow Experiments in Helium

by K. R. Sreenivasan[1] and Russell J. Donnelly[2]

One of the frontier areas in low temperature research is in the micro-Kelvin range. The other frontier, with which this note is concerned, lies in harnessing helium in place of air and water for flow research, model testing, and turbulence experiments at high Reynolds numbers. Above the so-called λ-transition (which occurs at about 2.2 K), helium is a classical Navier-Stokes fluid, and offers two advantages. First, its low kinematic viscosity (on the order of $2 \times 10^{-4}$ $cm^2 s^{-1}$ compared to $10^{-2}$ for water and 0.15 for air), makes it possible to create, for a fixed Reynolds number, a flow with an apparatus which is fifty times smaller than that using water and seven hundred and fifty times smaller than that using air; this reduced size diminishes both capital equipment and operating costs by orders of magnitude. Second, by varying the pressure of gaseous helium, many decades of Rayleigh numbers can be achieved in a convection cell of a fixed size; this flexibility is ideal for research purposes.

This much has been known for a long time. Why, then, has no concerted effort been made to take advantage of these features? The answer is partly the natural resistance to adopting something novel, partly the hassle of refrigeration and the cost of installation when a helium facility exceeds a modest scale, and partly the extra demands placed on instrumentation by the small-scale of the apparatus. For instance, at a Reynolds number of ten million, easily achieved on a 10 cm model, the viscous sublayer is on the order of 10 μm, not accessible to meaningful measurements with the instrumentation available today. While forces and moments can indeed be measured accurately in helium flows—in fact the splendid technology of superconductors becomes available in liquid helium—demands on aerodynamic smoothness of testing models and the like will become more stringent. These issues—both favorable and unfavorable—have been discussed in the book *High Reynolds Number Flows Using Liquid and Gaseous Helium*, edited by R. J. Donnelly, Springer-Verlag, 1991.

Some new developments may well have placed helium facilities above the threshold of uncertainty. As is well known, the Department of Energy (DOE) was engaged in a project on Superconducting Super Collider in Waxahachie, Texas. Among the achievements made there was the construction of a unique and massive refrigeration facility, originally intended for cooling various SSC components such as magnets. This facility, constructed at the cost of about $32 million, consists of three independent helium refrigeration systems, each with a 4 kW capacity at the temperature of 4.5 K, and is now available for other uses. This availability has created a unique opportunity for constructing and operating *much bigger* helium facilities at much less cost than was possible until now.

Quite early in the days of the SSC project, we had recognized the advantage of constructing an off-line facility at the SSC Laboratory for the study of heat transfer and turbulence in helium gas. This proposal, received with enthusiasm at the time, lay dormant when the status of the SSC was hanging in balance. Following its eventual termination by the Congress, DOE solicited expressions of interest for using the facilities already in place. Along with Professor Robert Behringer of Duke University and Dr. Michael McAshan, formerly the Head of the Cryogenics Department of SSCL, we re-expressed an interest and, with some support from DOE, are now engaged in a study of the precise scientific objectives, design and instrumentation, and prospects as well as problems associated with the facility.

A few details might be worth mentioning even at this preliminary stage. The proposal is to build a large helium cell (on the order of 10 m in height and about half the height in diameter) which could be used for several experiments forming a coherent program of research. The most obvious candidate is a convection experiment using helium gas; by scaling up the pioneering experiments of A. Libchaber and colleagues (see, for example, the 1991 Ph.D. thesis of X. Z. Wu of the Department of Physics at the University of Chicago), it is estimated that Rayleigh numbers in the vicinity of $10^{18}$ can be produced without significant non-Boussinesq effects. These Rayleigh numbers come close to those attained in solar convection, and allow both the testing of the scaling laws expected at high Rayleigh numbers and the elucidation of the mechanisms of turbulence convection. The refrigeration needs are estimated to be on the order of 1.5 kW, well within the capacity of a single refrigeration unit at SSCL. One can also use the facility to study grid turbulence at high Reynolds numbers (typical mesh Reynolds number of the order of 20 million) by sweeping the grid (with and without heating) across the cell and allowing the resulting turbulence to decay. In a 1988 Ph.D. thesis of the Department of Mechanics and Materials Science at Johns Hopkins University, M. D. Walker has demonstrated the advantages of this configuration for studying grid turbulence. It is thought that these studies will provide the much-needed high-Reynolds-number measurements of classical features of shear-free turbulence both as a testing ground for

[1]Mechanical Engineering Department, Yale University, New Haven, CT 06520
[2]Department of Physics, University of Oregon, Eugene, Oregon 97403

competing theories and as a point of departure for shear flow turbulence with attendant complexities and constraints. Other possibilities such as oscillating and pulsed grid experiments, towed spheres, and so forth, are being considered. We are also proposing to undertake a study for establishing, within the convection cell, a helium tunnel for very high-Reynolds-number model testing purposes.

The venture is not without some uncertainties. The velocity and temperature scales to be resolved in these experiments are estimated to be on the order of tens of microns, between one and two orders of magnitude smaller than those encountered *typically in moderately high Reynolds number facilities*. Thus, an issue that needs to be addressed is one of suitable instrumentation. Modern developments in micro-electro-mechanical systems seem to allow the measurement of fluctuating temperature, wall stress and wall pressure with Kolmogorov scale resolution; also possible are variants of shadowgraph and schlieren techniques. In liquid helium, the use of quartz microspheres and frozen hydrogen-deuterium mixtures has already been demonstrated for flow visualization, as well as for laser-Doppler velocity measurements. With good tracer particles comes the feasibility of using particle image velocimetry. In the presence of substantial mean flow, micron-sized hot-wires using superconducting and resistive thin films can be (and have been) used for turbulence velocity measurements. In spite of the progress already made in these various directions, it is clear that some nontrivial work will be needed before their potential and limitations can be established satisfactorily.

The turbulence community has been in constant search for ways to reach high Reynolds numbers. Helium offers a way to progress rapidly in this desired direction. When coupled with the tools of low temperature physics and the unique opportunity offered by the cryogenic facilities at the site of SSCL, *time seems ripe for moving ahead. Opportunities and challenges* often go together, and this particular opportunity comes with the challenge—quite realizable, it would seem—of extending instrumentation to increasingly finer scales of resolution.

In keeping with the spirit of this Column, it is useful, in addition to inviting comments on it, to end with two questions: (*a*) What other uses can the unique facility now sitting in Texas be used for fluid-dynamic research purposes? (*b*) What new developments in instrumentation can be brought to bear usefully on the helium experiments presently contemplated?

# Comments on the Policy Statement on Numerical Accuracy

by Joel H. Ferziger[1]

Although I did not participate in the writing of the Policy Statement on Numerical Accuracy (Freitas, 1993), I have urged such a policy for many years and have read it, the comments on it by Shyy and Sindir (1994) and the various responses to those comments (Vanka, 1994; Freitas, 1994, Roache, 1994) with great interest. I would like to make the following suggestions and comments.

There seems to be no question that reporting of numerical accuracy is central to assessment of the quality of work in computational fluid dynamics (CFD) and that any paper published in this (or any other) journal must contain an assessment not only of the numerically introduced errors, but those arising from other sources (modeling, for example) as well. I would leave the matter at that.

It should not be our business to specify what methods may or may not be used. The range of methods in use is so broad that trying to police this issue will become very difficult. While I personally regard first order upwind methods as passe, it is not my job to prevent others from committing what I regard as foolishness. If someone wishes to spend more than necessary to find a solution, that is his/her business. However, I want to be assured of its accuracy, and of course, I want to retain the right, as a reviewer, to comment on the effectiveness of the methods used.

The required accuracy is a function of the field in which the work is done. What is acceptable to one field may be completely unusable to another. The *Journal of Fluids Engineering* covers a wide enough range of subjects that no uniform criterion can or should be given. A requirement that accuracy estimates be given and their genesis be carefully explained should be the only absolute. On the other hand, a referee should be permitted (indeed, encouraged) to recommend rejection of a paper on the ground that the solutions it contains are not accurate enough.

The judgment as to what constitutes quality and ultimate responsibility for seeing that the intent of the policy is carried out must remain, as it always has, a matter of the judgment of editors and reviewers. It is this author's hope that they will remain firm and consistent in the face of complaints that may issue from authors. This behavior will go a long way to further improving the quality of this journal.

I would like to close with a few remarks on the perspective by Douglas and Ramshaw (1994). They write "these concepts (essentially the issues addressed by the policy statement) are largely irrelevant to large-scale practical engineering applications of CFD"; this is a statement that (with variations) is often made. I believe it is more correct to say some engineering problems are too difficult to treat routinely with sufficient accuracy using CFD at the present time. While it is possible to correctly predict trends from computations that are somewhat inaccurate, when the errors are too large, it may not be possible to predict even the trend correctly. Thus, there are engineering problems for which one may need to forego CFD altogether until methods and/or computers are up to the task or use other approaches in conjunction with CFD. Development of methods for these problems is needed but should not be used prematurely. One should take advantage of whatever CFD can provide, but to adopt the attitude that because computers exist, we must solve the problems using CFD, may be flirting with danger.

These authors also address the issue of robustness, one that will be with us for a long time to come. A code that could be easily installed and run on any computer and would always produce reliable answers is the ideal, but no such method exists at present. Although the authors recommend methods that are

[1]Department of Mechanical Engineering, Stanford University, Stanford, CA 94305-3030.

competing theories and as a point of departure for shear flow turbulence with attendant complexities and constraints. Other possibilities such as oscillating and pulsed grid experiments, towed spheres, and so forth, are being considered. We are also proposing to undertake a study for establishing, within the convection cell, a helium tunnel for very high-Reynolds-number model testing purposes.

The venture is not without some uncertainties. The velocity and temperature scales to be resolved in these experiments are estimated to be on the order of tens of microns, between one and two orders of magnitude smaller than those encountered *typically in moderately high Reynolds number facilities*. Thus, an issue that needs to be addressed is one of suitable instrumentation. Modern developments in micro-electro-mechanical systems seem to allow the measurement of fluctuating temperature, wall stress and wall pressure with Kolmogorov scale resolution; also possible are variants of shadowgraph and schlieren techniques. In liquid helium, the use of quartz microspheres and frozen hydrogen-deuterium mixtures has already been demonstrated for flow visualization, as well as for laser-Doppler velocity measurements. With good tracer particles comes the feasibility of using particle image velocimetry. In the presence of substantial mean flow, micron-sized hot-wires using superconducting and resistive thin films can be (and have been) used for turbulence velocity measurements. In spite of the progress already made in these various directions, it is clear that some nontrivial work will be needed before their potential and limitations can be established satisfactorily.

The turbulence community has been in constant search for ways to reach high Reynolds numbers. Helium offers a way to progress rapidly in this desired direction. When coupled with the tools of low temperature physics and the unique opportunity offered by the cryogenic facilities at the site of SSCL, *time seems ripe for moving ahead. Opportunities and challenges often go together*, and this particular opportunity comes with the challenge—quite realizable, it would seem—of extending instrumentation to increasingly finer scales of resolution.

In keeping with the spirit of this Column, it is useful, in addition to inviting comments on it, to end with two questions: (*a*) What other uses can the unique facility now sitting in Texas be used for fluid-dynamic research purposes? (*b*) What new developments in instrumentation can be brought to bear usefully on the helium experiments presently contemplated?

# Comments on the Policy Statement on Numerical Accuracy

by Joel H. Ferziger[1]

Although I did not participate in the writing of the Policy Statement on Numerical Accuracy (Freitas, 1993), I have urged such a policy for many years and have read it, the comments on it by Shyy and Sindir (1994) and the various responses to those comments (Vanka, 1994; Freitas, 1994, Roache, 1994) with great interest. I would like to make the following suggestions and comments.

There seems to be no question that reporting of numerical accuracy is central to assessment of the quality of work in computational fluid dynamics (CFD) and that any paper published in this (or any other) journal must contain an assessment not only of the numerically introduced errors, but those arising from other sources (modeling, for example) as well. I would leave the matter at that.

It should not be our business to specify what methods may or may not be used. The range of methods in use is so broad that trying to police this issue will become very difficult. While I personally regard first order upwind methods as passe, it is not my job to prevent others from committing what I regard as foolishness. If someone wishes to spend more than necessary to find a solution, that is his/her business. However, I want to be assured of its accuracy, and of course, I want to retain the right, as a reviewer, to comment on the effectiveness of the methods used.

The required accuracy is a function of the field in which the work is done. What is acceptable to one field may be completely unusable to another. The *Journal of Fluids Engineering* covers a wide enough range of subjects that no uniform criterion can or should be given. A requirement that accuracy estimates be given and their genesis be carefully explained should be the only absolute. On the other hand, a referee should be permitted (indeed, encouraged) to recommend rejection of a paper on the ground that the solutions it contains are not accurate enough.

The judgment as to what constitutes quality and ultimate responsibility for seeing that the intent of the policy is carried out must remain, as it always has, a matter of the judgment of editors and reviewers. It is this author's hope that they will remain firm and consistent in the face of complaints that may issue from authors. This behavior will go a long way to further improving the quality of this journal.

I would like to close with a few remarks on the perspective by Douglas and Ramshaw (1994). They write "these concepts (*essentially the issues addressed by the policy statement*) are largely irrelevant to large-scale practical engineering applications of CFD"; this is a statement that (with variations) is often made. I believe it is more correct to say some engineering problems are too difficult to treat routinely with sufficient accuracy using CFD at the present time. While it is possible to correctly predict trends from computations that are somewhat inaccurate, when the errors are too large, it may not be possible to predict even the trend correctly. Thus, there are engineering problems for which one may need to forego CFD altogether until methods and/or computers are up to the task *or use other approaches in conjunction with CFD*. Development of methods for these problems is needed but should not be used prematurely. One should take advantage of whatever CFD can provide, but to adopt the attitude that because computers exist, we must solve the problems using CFD, may be flirting with danger.

These authors also address the issue of robustness, one that will be with us for a long time to come. A code that could be easily installed and run on any computer and would always produce reliable answers is the ideal, but no such method exists at present. Although the authors recommend methods that are

[1]Department of Mechanical Engineering, Stanford University, Stanford, CA 94305-3030.

likely to improve the situation, it is doubtful that any absolutely trustworthy method will be developed in the near future. For the present, it is probably necessary for companies that rely heavily on CFD to have a resident expert who can deal with at least some of the problems. For companies lacking the size or demand, consulting companies may be able to fill the need.

## References


Douglas, R. W., and Ramshaw, J. D., 1994, "Perspective: Future Research Directions in Computational Fluid Dynamics," JOURNAL OF FLUIDS ENGINEERING, Vol. 116, pp. 212–215.

Freitas, C. J., 1993, "Policy Statement on Control of Numerical Accuracy," ASME JOURNAL OF FLUIDS ENGINEERING, Vol. 115, pp. 339–340.

Freitas, C. J., 1994, Response to the Comments by Drs. Shyy and Sindir, ASME JOURNAL OF FLUIDS ENGINEERING, Vol. 116, p. 198.

Roache, P. J., 1994, Response to the Comments by Drs. Shyy and Sindir, ASME JOURNAL OF FLUIDS ENGINEERING, Vol. 116, pp. 198–199.

Shyy, S., and Sindir, M., 1994, Comments on Policy Statement on Control of Numerical Accuracy, ASME JOURNAL OF FLUIDS ENGINEERING, Vol. 116, pp. 196–197.

Vanka, P., 1994, Response to the Comments by Drs. Shyy and Sindir, ASME JOURNAL OF FLUIDS ENGINEERING, Vol. 116, pp. 197–198.

**Julimae McEligot**
Idaho Falls, ID 83404

**Donald M. McEligot**
Principal Thermal Scientist,
Idaho National Engineering Laboratory/
EG&G Idaho,
Idaho Falls, Idaho 83415-3890
and
Professor Emeritus,
University of Arizona,
Tucson, AZ 85721
Fellow ASME

# Perspective: Some Research Needs in Convective Heat Transfer for Industry

## Introduction

Several presentations at the recent ASME Fluids Engineering Division *Symposium on Basic Research Needs in Fluid Mechanics* addressed convective heat transfer and topics within this area, e.g., see the contributions by Douglass and Ramshaw, Schrock, Peterson, Chen and Liu, Humphrey and Ortega, Ghia, Jones and Lahey (Jones et al., 1992). (By definition, convection can be considered to be energy transfer by fluid motion, so convective heat transfer is an important field in fluid mechanics and vice versa). There have also been surveys of research needs in heat transfer that include convective processes. However, although about a third of the group leaders in the recent survey by Jacobs and Hartnett (1991) were outside the academic community, there still seems to be a lack of communication between the academic community and industrial users; recent comments by Bell (1991) and McGee (1992) address this aspect. Consequently, the present contribution will attempt to concentrate on basic needs relating to convective heat transfer as perceived by industry; in a sense, we attempt to swing the pendulum in the other direction by emphasizing "users" interests.

Primarily, the present paper treats the results of an ad hoc survey of colleagues from industrial and national laboratories. After describing our approach and some related philosophy, we will describe a few examples of applications and their related research needs to give the flavor of the difficulties and will end with a summary of some of the recurring themes evident in our raw data.

## Ad Hoc Survey

The *goal* of the survey was to identify research needs in convective heat transfer for industry. Accordingly, we sent the following query to about one hundred colleagues in industry, in national laboratories and at a few agencies:

"I would appreciate your suggestions of basic research topics in convective heat transfer that need to be addressed for industrial purposes. That is, what fundamental studies do you feel should be done to help you and your colleagues?"

About a quarter responded in varying degrees of depth. Table 1 is a listing of these responses, given as the application or area of need and the perceived needs in basic research that are related to each. While the process may not have identified all of the important research areas for industry overall, it has shown a wide range of concerns. Industries represented in the responses included electronics, nuclear, commercial Computational Fluid Dynamics (CFD), heat exchangers, defense, automotive, waste and environment, fire safety, aerospace, medical and gas turbines. Each entry in the table represents a response by one person, although some individuals suggested several separate research needs. The table is loosely organized by collecting the responses together into general areas of application. Overall, about forty needs were cited with some overlap.

The responses serve *two purposes*. First is to identify some needs, i.e., to accomplish our goal. However, in scanning Table 1, one has the feeling that there already have been extensive fundamental studies published and presented on some of the needs mentioned. For example, the listings and our discussion on gas turbine heat transfer applications include many issues which have been studied in considerable detail over the past few decades. Yet the practitioners responding apparently still lack the basic results they feel they need, such as turbulence models and related measurements, effects of freestream turbulence and heat transfer at low Reynolds numbers.

In cases where the topic has been studied extensively, if the available work does in fact address the needs mentioned, then the survey has identified a *second need*, i.e., one of effective technology transfer in the particular area. However, in the experience of one of us (DMM), when faced with a "new" practical heat transfer problem, often a logical approach reveals that a need for new basic research is the case rather than merely incomplete technology transfer. Typically, an order-of-magnitude analysis (remember "back-of-the-envelope" instead of general purpose cfd codes?) identifies the dominant aspects of the problem; a survey of the available literature then

Contributed by the Fluids Engineering Division and presented at the Symposium on Basic Research Needs in Fluids Mechanics, Fluids Engineering Conference, Los Angeles, CA. June 1992 of THE AMERICAN SOCIETY OF MECHANICAL ENGINEERS. Manuscript received by the Fluids Engineering Division October 26, 1992; revised manuscript received April 8, 1994. Associate Technical Editor: D. P. Telionis.

**Table 1 Applications and related basic needs**

| | |
|---|---|
| *Aerospace* | |
| Aerospace | Bases for prediction methods for flow past maneuvering 3D vehicle shapes |
| Airbreathing propulsion | Multiphase, turbulent reacting flows |
| Rocket propulsion | Diagnostic techniques for analyzing surface reactions and flames |
| NASP (National AeroSpace Plane) | Fluid-thermal interactions related to cooling and material integrity |
| Hypersonic kinetic energy penetrators | Aerodynamic heating, shock heating, ionizing/ reacting flow fields |
| Spacecraft thermal management | Flow boiling |
| Active control of boundary layers | Actuators and sensors as they relate to the physics of the flow |
| *Computational fluid dynamics* | |
| CFD | Heat transfer with phase change<br>- liquid-vapor (condensation/evaporation/boiling)<br>- solid-liquid (with micro and macro segregation) |
| CFD | Non-Newtonian fluids and porous media |
| CFD | Radiation-convection interaction - scattering models, particulate radiation |
| Benchmarking | Experiments on heat transfer in turbulent flows<br>- separated flows<br>- transition<br>- turbulence/chemistry interaction |
| *Defense* | |
| Defense | Non-equilibrium boundary layers - riblets, rough walls, non-Newtonian flows, unsteady, w/ and w/o pressure gradients |
| Defense | Small, complex passages with high flow rates - boiling and single phase, cryogens |
| *Environmental* | |
| Automotive exhaust systems | Pulsating, highly turbulent flows with radiation plus slightly-augmented natural convection |
| Particle deposition in exhaust systems | Turbulence structure in favorable and unfavorable pressure gradients in complex geometries |
| Release of ammonia | Two-phase buoyant wall boundary type flows near the ground |
| Stratified flow | Turbulence model(s) |
| Trichloroethylene spills | Multiphase, multicomponent flow of fluids of different densities through porous media - fingering |
| *Gas turbines* | |
| Airfoils | Heat transfer for fully-turbulent flow at low $Re_\theta$ |
| Axial flow compressors and turbines | Rotating stall and surge; unsteady heat transfer phenomena; cooling with complex turbine blade passages |
| Blades | Effects of freestream scale of turbulence |
| Blades | Internal cooling with rotation, large "turbulators," entrance effects and buoyancy |
| Gas turbines | Turbulence models for scalar transport in free shear layers |
| Gas turbines | Combined and secondary effects (high freestream turbulence, strong rotation, strong pressure gradients, superposed forced/free convection in complex passages, cross-flow) |
| Gas turbines | Data to benchmark codes for heat transfer enhancement, film cooling and flow unsteadiness |
| Gas turbines | Heat transfer after boundary layer restart (e.g., from interruption by ring or bolt flange) |
| Turbomachinery | Film cooling with non-equilibrium, compressibility and turbulence effects, complex hole shapes, unsteady freestream, surface roughness |
| *Heat exchangers* | |
| Heat exchangers | Turbulence modeling for enhanced surfaces with $h^+ = O(25)$, i.e., in viscous layer |
| Flow-induced vibration of shell-and-tube geometries | Streamwise-periodic flow over segmental baffles |
| Multiphase flow | Heat transfer at reattachment point after separation |
| Waste heat recovery | Flow field characteristics for shell side of finned-tube bundles |
| *Miscellaneous* | |
| Gas metal arc welding | Transition from droplet detachment to jet flow |
| High heat transfer rates in turbulent flow | Combined effects of fluid property variation and _____(fill in)_____ |
| Personal computers | Low Reynolds number mixed convection |
| Photocopy equipment | Low Reynolds number turbulent flow in complex passages, cooling - turbulence modeling |
| Various | Experimental verification studies coordinated with model development |
| *Nuclear* | |
| Nuclear | Experiments/analyses to support optimum fin shape design for multiple (interacting) fins |
| Nuclear | Quiet personal computer ( = ?) |
| Nuclear reactor safety | Heat transfer from molten core debris to a surrounding liquid (possible steam explosion) |
| Nuclear reactor safety | Turbulent natural convection across an enclosure formed by a cylinder and irregularly-shaped surroundings |
| Passive safety of advanced reactors | Turbulence models for mixed convection with significant property variation and possible laminarization |
| Space nuclear power and propulsion | Turbulence structure in "pure" forced convection with large gas property variation |

often shows that the actual problem has not really been addressed. For example, the non-dimensional ranges are significantly different; nothing like the actual geometry has been treated; etc., etc. Thus, we anticipate that the list is likely to be more indicative of actual needs in fundamental research than of untransferred technology.

A wide range was covered by the respondents. One indicated "It has been some years since I needed any basic information on convective heat transfer beyond what Bill Kays taught me in the 60s" then went on to mention a few topics not covered by standard texts or courses. One from an experimentalist in convective heat transfer indicated that his basic need was a quiet personal computer. He was followed by an engineer with a computer manufacturer, noting that more data are needed

## Nomenclature

$c$ = speed of sound
$c_p$ = specific heat at constant pressure
$D$ = diameter; $D_h$, duct hydraulic diameter
$g$ = acceleration of gravity
$h^+$ = roughness height, $hu_\tau/\nu$
$i$ = electrical current
$J$ = rotational Reynolds number, $\omega D_h^2/\nu$
$M$ = Mach number, $V/c$
Pr = Prandtl number, $c_p\mu/k$
$R$ = radius from axis of rotation
Ra = Rayleigh number, $\omega^2 R D_h^2 \beta(T_h - T_c)/(\nu\alpha)$
Re = Reynolds number, $VD_h/\nu$; $Re_\Theta$, based on momentum thickness
Ro = Rossby number, $V/(D_h\omega)$
$T$ = temperature
$u_\tau$ = friction velocity, $(\tau_w/\rho)^{1/2}$
$V$ = velocity
We = Weber number, $\rho V^3 D/\sigma$
$y^+$ = distance from wall, $yu_\tau/\nu$
$\alpha$ = thermal diffusivity
$\beta$ = volumetric coefficient of expansion, 1/T
$\epsilon$ = thermal emissivity
$\mu$ = absolute viscosity
$\nu$ = kinematic viscosity
$\omega$ = angular velocity
$\rho$ = density
$\sigma$ = surface tension or interfacial tension
$\tau_w$ = wall shear stress

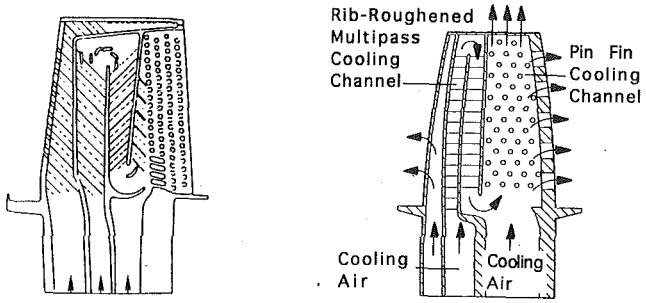


Fig. 1 Interior cross sections of typical turbine blades with internal cooling, (*a*) Johnson et al. (1992) and (*b*) Lau, Han and Kim (1989)

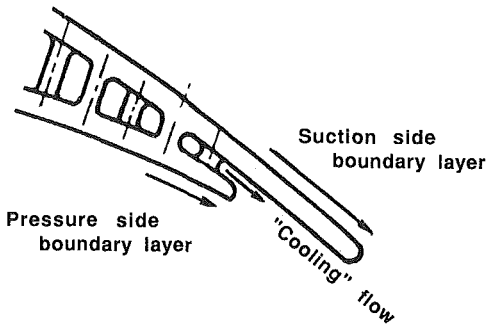


Fig. 2 Trailing edge geometry for turbine blade with internal cooling

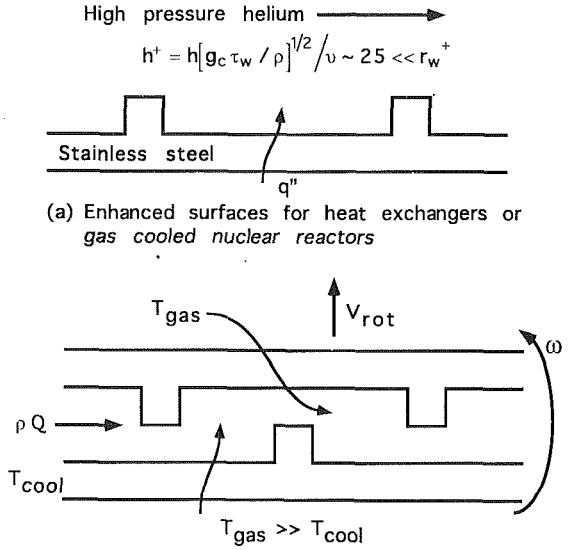


Fig. 3 Examples of enhanced heat transfer surfaces employing rectangular ribs

on mixed convection in order to reduce fan noise in personal computers (PCs). (Actually, PCs are becoming quieter by virtue of "convective cooling," meaning no fan = natural convection; six years ago disk drive targets were 60 db whereas now 45 db is being achieved, limited by track noise rather than the fan for forced convection (McEligot, 1992)). Some examples of application areas and their needs may provide insight into the complexities in convective heat transfer that concern the practicing engineer.

## Blades and Vanes in High Performance Gas Turbines

Designs for gas turbines typically achieve higher performance by increasing the turbine inlet temperature. Consequently, blades and vanes in the early stages of the high pressure turbine are cooled internally and film cooled externally to maintain structural integrity in a difficult external environment. Figure 1 shows examples of typical internal cooling schemes (Johnson et al., 1992; Lau et al., 1989). Sizes vary but many small aircraft gas turbine designs for the first stage have blade heights less than an inch (two cm)! Phenomena occurring in this rotating, micro-heat exchanger include film cooling by ejection of jets into a nonsteady cross stream, contractions and expansions giving favorable and unfavorable streamwise pressure gradients, short channels, flow around bends and various enhanced surfaces (more on that later), with significant spatial variation in gas temperatures and—therefore—properties all the while. Programs at the gas turbine manufacturers and various universities are attacking some aspects of these problems experimentally but much remains to be done. Coupled numerical and experimental studies probably offer the best chance of deriving predictive methods that are reliable across a reasonable range of phenomena; Mayle (1993) has presented comparable comments considering design methodology in his evaluation of the recent AGARD conference on heat transfer and cooling in gas turbines.

A practical trailing edge is sketched in Fig. 2. In contrast to the sharp, acute airfoil of our undergraduate texts, manufacturing and heat transfer constraints lead to blunt edges - and there is often an extra flow stream from the cooling air. One sees several thermal mixing layers (Marble, 1992) in the wake downstream of the blade that are formed as boundary layers, with different upstream histories and different curvatures and pressure gradients, interact with the cooling air flow which itself is initially a wall jet. Small recirculating flows and potential separation on the concave (pressure) surface are expected behind each of the blunt edges.

The short streamwise length of the blade leads to low chord-based Reynolds numbers, and one expects the location of transition to be well along the surface (and either stabilized or destabilized by the combined effects of the pressure gradients, curvature, mainstream turbulence intensity, time-unsteady wakes from upstream disturbances and—possibly—the transverse temperature gradient). Under actual engine conditions of high turbulence and wake-passing disturbances, transition is not as far downstream as one would expect from classical treatments. Useful transition and turbulence models are needed to handle the coupled, dominant phenomena—with the most significant phenomenon likely differing from design to design. Insight into the transition problem is provided by Mayle (1991). Several respondents identified "low Reynolds number; turbulent flow" as a concern; in the context of this perspective article, this term refers to flow with a turbulence intermittency factor (Schlichting, 1968; Mayle, 1991) near unity but with a Reynolds number too low for turbulence quantities to approach classical, asymptotic conditions.

A good review article has been published recently by Simoneau and Simon (1993) and further indications of needs for research in gas turbine heat transfer are given by Gaugler (1993) and Mayle (1991, 1993).

## Enhanced Surfaces

Gaseous convective heat transfer for forced flow can potentially benefit from the use of "enhanced" surface geometry. For example, Fig. 3 demonstrates a couple applications employing rectangular rib roughness elements. The first case is an outgrowth of proposals for a high-temperature, gas-cooled nuclear reactor. The use of helium at high pressure and high flow rates reduces the convective thermal resistance, while the low thermal conductivity of typical cladding materials increases the conductive thermal resistance. Turbulent flow is expected but optimization typically leads to non-dimensional roughness heights $h^+$ of about 25 (Webb, 1977). This height is the same

order as the viscous layer thickness ($y^+ = 30$ to 50) of a turbulent flow. Consequently, the convection problem and the conduction are intimately coupled as they would be in a laminar flow (Faas and McEligot, 1979), so they must be solved simultaneously (now referred to as a conjugate problem). Large temperature differences from the surface to the flowing gas cause significant gas property variation across the "linear" and viscous layers (terminology from Bradshaw, 1971). In this application, the heat flux to the solid from the nuclear fuel is likely to be the controlled variable which becomes the thermal boundary condition; instead, most laboratory experiments for rough surfaces use an isothermal wall, a different thermal boundary condition. What is the import for design predictions? Conceptually, one could solve the governing equations by a numerical approach. But in order to do so, one needs a turbulence model which (as a starter?) accounts for (1) recirculating flow in the viscous layer as well as (2) gas property variation and, possibly, (3) buoyancy forces. Are direct numerical simulations required? If so, periodic end conditions are not appropriate because gas properties vary in the streamwise direction was well.

Figure 3(*b*) relates to the internal cooling of turbine blades as in Fig. 1. Here the small sizes yield ribs (so-called "turbulators") that are large compared to the channel spacing. Despite the small size, Reynolds numbers imply turbulent flow. Channels are sometimes short with relatively few ribs; a fully developed situation is unlikely. Rotational fields can be as high as $2 \times 10^5$ g. For one recent design of a small high-performance gas turbine, the governing parameters could be estimated to be of the following orders of magnitude: $\mathrm{Re} \approx 30{,}000$, $\mathrm{M} \approx 0.1$, $\mathrm{Ro} \approx 3$, $\mathrm{Pr} \approx 0.7$, $\mathrm{Ra} \approx 10^9$, $\mathrm{Ra/Re}^2 \approx 1$, and rotational Reynolds number, $\mathrm{J} \approx 9000$. In this situation no one phenomenon can be expected to dominate. In a given design, do Coriolis effects stabilize one side and de-stabilize the other—or does the flow tend to one side with a slight transverse recirculation? The centrifugal force and temperature gradients induce buoyancy forces, which are significant if not dominant; mixed convection must be considered. Again gas property variation rears its ugly head. Further insight is available in the recent experiments of Johnson, Taslim, Han and their respective coworkers, e.g., Johnson et al., el Husayni et al. (1992) and Han et al. (1992). The current status of this work is probably best reported annually in the spring at the ASME's International Gas Turbine Conference.

Fabrication of turbine blades introduces another reality for the turbulators, again due to small size. The casting process leaves rounded corners and base fillets, which can be about ten per cent of the height. (Taslim and Spring, 1991 usefully describe this situation and related problems.) Data available on the effects are limited, since laboratory experiments are usually large enough that the corners are effectively sharp. Further, the casting process sometimes leaves individual ribs missing completely, yielding a coupled convection/conduction problem—as for an extended surface - to be solved along the wall for the maximum temperature (and minimum "strength") (Kreith, 1973). Dalle Donne and friends (1978) presented data from experiments with rounded trapezoidal elements but did not have comparisons to ones with sharp corners. Arman and Rabas (1992a, b, 1993) applied a two-layer turbulence model to predict thermohydraulic performance of enhanced circular tubes with transverse, periodic disruptions having sinusoidal-, semicircle-, arc-, and trapezoid-shaped cross sections; for these geometries in industrial heat exchangers, Rabas [1993] feels that CFD codes are well suited to address issues such as the effect of disruption shapes. In stationary experiments with a variety of shapes, Taslim and Spring demonstrated that the effects of rounding corners and that the heat transfer and friction factor sensitivities are dependent on a number of factors, including aspect ratio, spacing and channel blockage. For a rotating duct, one can conceive of general purpose CFD codes being applied to the geometry but it is doubtful that anyone would rely on the predictions without confirmatory data in the same ranges of the governing nondimensional parameters. But what turbulence models include combined effects of buoyancy, Coriolis forces and property variation adequately, particularly in the near wall region with complex geometry? Basic measurements are needed for the applications with realistic geometries and conditions before this question can be answered.

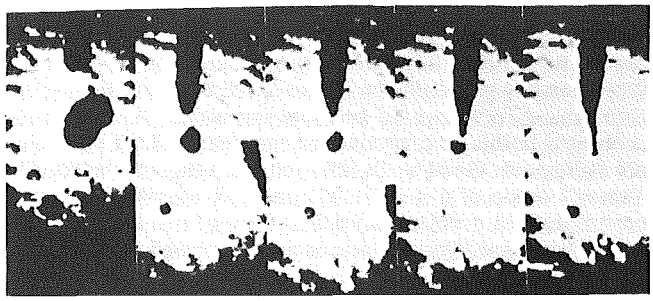


**Fig. 4 Observations of drop/jet formation from melting electrode in gas metal arc welding. Electrical current and wire feed speed increasing from left to right (Kim, 1989).**

Despite our skepticism, favorable reports are coming from the gas turbine industry. It is felt that significant progress on the validation of predictions for such combined phenomena is coming with $k$-$\epsilon$ turbulence models, and potentially Reynolds stress turbulence models for large vorticity flows. They are encouraged about recent validation of ability to predict complex surface heat transfer coefficients. Commercial CFD codes are rapidly moving into design tool utility. Complete 3-pass serpentine blade passages with turbulators have already been done with reasonable success (Abuaf and Kercher, 1992; Dawes and White, 1993). It is predicted that in about ten years most film cooling designs and analyses will be done via CFD.

## Droplet/Jet Formation

In gas metal arc welding the quality of the resulting joint is dependent on the "mode" of detachment of the molten drops which are formed (Cooksey and Miller, 1962). To protect the liquid metal from the surrounding atmosphere and to affect the detachment process, a mixture of inert gases (and oxygen in some cases!) flows coaxially with the melting wire. Convective heat transfer to this mixture is part of the overall thermal problem. But another fluid mechanics problem is perhaps more interesting in this case. The analysis of the drop behavior only requires the simultaneous solution of (1) the transient thermal energy equation, with possible Marangoni effects and thermal radiation and plasma boundary conditions, (2) Maxwell's equations for the electromagnetic body forces involved and (3) the transient fluid dynamics equations. Viscous effects are likely negligible unless Marangoni convection becomes important (Kim et al., 1991).

Figure 4 from Kim's thesis (1989) demonstrates the range of the fluids problem involved, which must be solved as a basis for treating the rest. This sequence of subfigures shows the effect of the electrical current on the typical size of molten drop or jet which is formed and is transported to the molten weld pool; the moving metal electrode wire appears vertically at the top of each subfigure. At low currents (and therefore low wire feed speeds), the drop grows quasi-hydrostatically until the weight of the drop overcomes the support of the surface tension forces at the neck (the "globular" drop at $i = 205$ amps). Many have solved this problem classically (Bashforth and Adams, 1883; Greene, 1960; Padday and Pitt, 1973; etc.) But poor quality welds result. The other extreme, at high

current, appears as a moving cylinder of liquid metal (the "streaming" mode at 310 amps)—a steady jet—which may break up later due to instabilities. Lienhard (1968) solved the corresponding problem of a jet in a vertical gravity field (electromagnetic forces would be more important in the present problem). In this case, production rates can be high but welds are again poor. Good welds fall in between these extremes (the "spray" mode of $i$ = 237, 253 and 281 amps). The corresponding fluid problem is vertical flow of a liquid from an orifice into a gas. Quasti-static drops are formed at low Weber numbers and steady jets at high values (and unsteady ones at higher values, etc.). How well can we predict the transient shape when the Weber number is of the order of one?

Only a few numerical techniques are available to predict the transient behavior of drops with surface deformations of large amplitude (Ryskin and Leal, 1984). Fromm (1984) handled drop formation for ink-jet printers (without gravity) and Asai (1992) treated the bubble jet printer. Marker-in-cell and related techniques from Los Alamos should apply (Daly, 1969; Hirt and Nichols, 1981; Kothe and Mjolsness, 1992). The examples manual for the FIDAP finite element code shows one of drop formation, but with a coarse grid and at low Weber number. These methods require extensive computer time and resources for "precise" results. (During the review/revision process for this perspective article, a promising one-dimensional analysis has appeared (Eggers and duPont, 1994).) Problems with significant surface tension forces fall in a mathematical class referred to as "Propagation of Surfaces under Curvature" (PSC) (Osher and Sethian, 1988). They tend to be sensitive and to require ad hoc techniques to reach a solution. As pointed out by Sethian (1990), the steps taken may yield solutions far from the desired one or, even worse, solutions to an unrelated problem. In order to solve the problem of droplet/jet formation confidently for application to gas metal arc welding, we should first demonstrate that solutions for the simpler case of the fluids problem alone agree with measurements over the range from low to "high" Weber numbers. Other applications involving droplet/jet formation and detachment include spray forming, controlled formation of sprays for fuel injection in internal combustion engines, prototyping via ink jet printing techniques, determination of interfacial tension for microbial enhanced oil recovery, jet cutting, molten metal entering liquid pools in severe accident scenarios, the liquid droplet radiator for space heat rejection, and nozzles in agricultural irrigation systems. Both experiments and useful predictive techniques for formation/detachment are needed for reliable practical application.

## Automotive Exhaust Systems (Provided by J. R. Mondt, GM AC Rochester Div.)

The automotive industry needs work related to advanced systems and technology for control of exhaust emissions and exhaust noise for automobiles and trucks, with catalytic converters as the primary technology for controlling emissions. Modeling and testing are combined to optimize exhaust systems for good emissions control, low pressure drop and reasonable cost. For a catalytic converter to function, the exhaust temperature must be heated quickly during a cold start, but cannot exceed upper temperature limits during warmed-up operation. Thus, thermal energy management is important to the design of modern exhaust systems. Minimum pressure drop is desired for the flow inside the exhaust system to minimize back pressure on the engine.

Modeling includes heat transfer for exhaust manifolds, crossover pipes, takedown pipes, and catalytic converters. The processes include heat transfer with combined radiation and high turbulence on the inside of these components, and radiation and slightly-augmented natural convection on the outside of these pipes. Exhaust flow inside the exhaust manifolds and downpipes is pulsating and highly turbulent. To model the heat transfer for exhaust components under an automobile requires knowledge of the flow field and the convective heat transfer processes between the moving automobile and the stationary road. For either heat transfer or pressure drop for these specific applications, very little technology has been reported in the archival journals.

## Natural Convection in Nuclear Reactors

A recent application, to one configuration of nuclear reactors, revealed a need for basic information on gaseous natural convection from one heated circular tube in a closely-packed array to surrounding tubes which are cooled. A number of reactor concepts utilize vertical fuel elements and cooling tubes surrounded by a liquid as moderator, such as the Advanced Thermal Reactor and the Steam Generating Heavy Water Reactor (Butcher et al., 1990; Leonard et al., 1990; Mochizuki and Ishii, 1992). In addition to fuel elements and cooling tubes, the control rods and safety rods typically are aligned vertically. Thus, tubes of several diameters are present and their spacings are of the same order as their diameters. One hypothetical accident scenario corresponds to gamma heating of a control/safety rod after a moderator tank has drained due to a loss of pumping power; energy dissipation from the rod then is constrained principally to natural convection and thermal radiation to the surrounding cooling tubes. The generic configuration cannot reasonably be considered to be an isolated single tube in infinite surroundings. Essentially, the heated cylinder and its surrounding array form an enclosure, possibly described as an annulus with an irregular and/or extended outer surface consisting of the other tubes.

For a typical nuclear reactor, tubes are of the order of two to ten cm in diameter and three to six meters in height. Therefore, the length-to-diameter ratios of individual tubes fall in the range of 30 to 300. If the potential temperature range is taken to be from room temperature to the melting point of aluminum, the length-based Rayleigh number will be greater than $10^{10}$ so that the induced flow can be expected to be turbulent above a meter or less from the bottom (Hama and Recesso, 1958).

Directly-related previous work is limited. A search of the literature revealed no work on the fundamental topic: turbulent natural convection from a vertical cylinder to a surrounding array. No published data were found for turbulent natural convection in an annular enclosure. However, Keyhani and Kulacki (1985) have presented data, nominally for the laminar boundary layer regime, that show evidence of transition at their highest Rayleigh numbers. Very few results are available for turbulent natural convection from isolated, slender, vertical cylinders of aspect ratios pertinent to the present study (e.g., Carne, 1937, Eigenson, 1940; Morgan, 1975, and Steimke, 1991). Lacking turbulent data for the geometry considered, the designer is forced to extrapolate from information for an isolated cylinder or for a rectangular enclosure.

One set of data is now available for this unique geometry (Fig. 5, McEligot et al., 1994). This study demonstrates that further fundamental measurements are needed on several topics. Only the heating rate was varied significantly in the experiment, so the effect of property variation was assumed rather than being tested by varying temperature ratio independently from Rayleigh number. Likewise, the geometric ratios (e.g., spacing) were not varied. Other geometric patterns for the surrounding array may change the behavior slightly and there is probably an infinite variety of "augmentation surfaces" which could be examined looking for optimization in some sense (Bergles, 1988). Measurements of mean turbulence structure are desirable, but meaningful data are difficult to obtain with the large temperature differences involved. And, since the reactors have large volumes with spatially varying

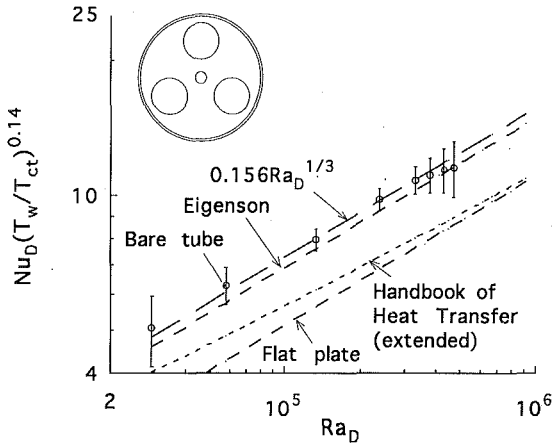


**Fig. 5 Turbulent natural convection from a smooth vertical tube to a triangular array of cooled tubes (McEligot et al., 1994)**

thermal conditions, large-scale recirculating flow patterns may be induced so that the local behavior for an individual tube and its immediate surroundings may be better described as mixed convection than as "pure" natural convection (and accompanying thermal radiation!).

## Concluding Remarks

In the cases of analytical/numerical techniques for problems in convection, the practicing engineer usually needs convincing demonstration that the wall heat transfer parameters and wall friction (or pressure drop) are predicted properly. Detailed measurements of the fine structure of the turbulence may be useful to the modeler developing the technique, but the end results must include these integral parameters to be of use. Comparison of mean profiles can be misleading, since they can often be presented graphically in a manner such that poor agreement appears good (McEligot, 1986).

It is clear that much basic work remains to be done on convective heat transfer problems for the benefit of our practicing community in industry. While a text, such as by Kays (1966), is still valuable for guidance on order-of-magnitude estimates for behavior of single-phase systems with classical geometries, the needs are more diverse and the industrial problems are more difficult. The survey of our colleagues in industry revealed a wide variety of perceived needs in fundamental research, as indicated in Table 1. Recurring themes in the responses included

- Unsteady or pulsating flows
- Turbulence
- Combined (coupled) effects
- Low Reynolds number flows (generally turbulent)
- Measurements/data for benchmarking computer predictions
- Turbulence modeling (still)
- Variation of transport properties due to temperature gradients
- Phase change, multiphase systems
- "Rough" or enhanced surfaces
- "Complications" beyond the "simple," classical cases in general

In addition to the basic studies required in these areas, it is suspected that more effective, reciprocal technology transfer is required between the practitioner and the 'engineering scientist" in order for the studies to benefit our industry and its international competitiveness.

The questions become: Where to now, particularly for academic colleagues? From where can the support come? Basic research is typically supported by government agencies, such as NSF, ONR, AFOSR, NASA, ARO-D, and DOE. Their program managers are becoming more sensitive to the idea that the work they support should be useful for some identified applications, perhaps those important for national competitiveness. Surveys such as this one can provide some "cannon fodder" on that score. However, some of these programs are being reduced in funding level while there are more and more fluid mechanics doctoral graduates competing for the pot. One is again hearing the traditional songs, "times are tight" and "no new starts," but there always seems to be a chance for the ideas that strike a program manager's fancy.

Some members of the academic community have developed good working relations and receive direct support from industry; Prof. J. H. Whitelaw and his colleagues studying automotive fluid mechanics at Imperial College are good examples. In Japan, faculty are being given strong encouragement to devote some of their research to industrial support; Prof. Y. Nagano's turbulence modeling has found application in design codes of torque converters in one of Toyota's operating divisions (Kondoh, 1993). But in the United States it is difficult to obtain direct support from industry for basic research. In recent years several companies have eliminated or reduced their own corporate research laboratories. Another inherent problem is that faculty members have strong desires to publish in the open literature while, if the work is worthwhile to industry, companies would prefer to keep results proprietary for competitive advantage. And, since there are federal laws that give universities and small businesses the right to patent their work regardless of source of funding, companies are reticent to pay their own dollars and lose any competitive benefit of the results.

This author (DDM) has no magic solution for the academic community. Improved interaction with industrial colleagues can give better appreciation for the real needs leading to lower costs, better reliability and more competitive products. The Fluids Engineering Division appears to have a better mix of industrial and academic members than some other ASME divisions. The FED meetings and committees give opportunities for informal direct discussions with industrial practitioners. Panel sessions given by industrial design engineers can help start a dialog. Cozy up to your industrial colleagues; they would like your work to be useful too. One route may be: learn their needs in your topical area; analyze/translate them to identify the key basic questions that still need resolution; calculate the parameter range involved; use this information as the basis for a collaborative proposal to the funding agencies (which should thereby be stronger than most of its competitors); in the resulting technical papers, include appendices that demonstrate the calculations necessary to apply your results to a specific industrial problem. We will all benefit.

## Acknowledgments

The study reported was partly supported through the EG&G Idaho Laboratory Directed Research and Development Program and the Long Term Research Initiative Program under DOE Idaho Field Office Contract DE-AC07-76ID01570. We are particularly grateful to J. Robert Mondt, Exhaust Systems Engineering, AC Rochester Div., General Motors Corp., to Bruce V. Johnson, United Technologies Research Center, John A. Weaver, GMC Allison Gas Turbine Div. and other members of the Gas Turbine Committee of the ASME Heat Transfer Division and to colleagues in the electronics, nuclear, commercial Computational Fluid Dynamics (CFD), heat exchanger, defense, waste and environment, fire safety, aerospace

and medical industries for their insight, responses and suggestions. For any misinterpretation of their input, we sincerely apologize. The views and opinions of the authors expressed herein do not necessarily state or reflect those of EG&G Idaho, Inc., or of the United States Government or any agency thereof.

## References

Abuaf, N., and D. M. Kercher, 1992, "Heat Transfer and Turbulence in a Turbulated Blade Cooling Circuit," ASME Paper 92-GT-187, International Gas Turbine Congress, Köln.

Arman, B., and Rabas, T. J., 1992a, " Influence of Prandtl Number and Effects of Disruption Shape on the Performance of Enhanced Tubes With the Separation and Reattachment Mechanism," Tech. Report, ANL/ESD-16, Argonne Nat. Lab.

Arman, B., and Rabas, T. J., 1992b, "Disruption Shape Effect on the Performance of Enhanced Tubes With the Separation and Reattachment Mechanism," *Enhanced Heat Transfer*, ASME HTD-Vol. 202, p. 67-76.

Arman, B., and Rabas, T. J., 1993, "Performance Comparisons of Enhanced Tubes With Discrete and Wavy Disruption Shapes," National Heat Transfer Conf., Atlanta.

Asai, A., 1992, "Three-Dimensional Calculation of Bubble Growth and Drop Ejection in a Bubble Jet Printer," ASME JOURNAL OF FLUIDS ENGINEERING, Vol. 114, pp. 638-641.

Bashforth, F., and Adams, J. C., 1883, *An Attempt to Test the Theory of Capillary Action*, Cambridge Univ. Press, Cambridge.

Bell, K. J., 1991, "The Research Game: Does Industry Want to Play? Will Academe Let It?" *Heat Transfer Engineering*, Vol. 12, No. 4, p. 5.

Bergles, A. E., 1988, "Some Perspectives on Enhanced Heat Transfer - Second - Generation Heat Transfer Technology," ASME *Journal of Heat Transfer*, Vol. 110, pp. 1082-1096.

Bradshaw, P., 1971, *An Introduction to Turbulence and Its Measurement*, Pergamon, London.

Butcher, P., Debenham, A. A., and Holloway, N. J., 1990, "PRA-Based Accident Management for the Winfrith Prototype Steam Generating Heavy Water Reactor," *Proc., Int. Topical Meeting on Safety, Status and Future of Noncommercial Reactors and Irradiation Facilities*, Amer. Nuclear Soc., Boise, pp. 273-277.

Carne, E. B., 1937, "Heat Loss by Natural Convection From Vertical Cylinders," *Phil. Mag.*, Vol. 24, pp. 635-653.

Cooksey, C. J., and Miller, D. R., 1962, "Metal Transfer in Gas Shielded Arc Welding," *Physics of the Welding Arc - A Symposium 1962*, pp. 123-132.

Dalle Donne, M., Hudina, M., Huggenberger, M., Meyer, L., and Rehme, K., 1978, "EIR, KfK Joint Heat Transfer Experiment on a Single Rod, Roughened With Trapezoidal Rounded Ribs and Cooled by Various Gases," Tech. Report KfK 2674, Kernforschungszentrum Karlsruhe.

Daly, B. J., 1969, "Numerical Study of the Effect of Surface Tension on Interfacial Stability," *Physic of Fluids*, Vol. 12, pp. 1340-1354.

Dawes, W. N., and White, A. J., 1993, "Fluid Flow and Heat Transfer Prediction in a Non-Rotating Axial Turbine Internal Coolant Passage and Comparison with Experiment," ASME Paper 93-GT-250, International Gas Turbine Congress, Cincinnati.

Eggers, J., and duPont, T. F., 1994, "Drop Formation in a One-Dimensional Approximation of the Navier-Stokes Equation," *Journal of Fluid Mechanics*, Vol. 262, pp. 205-221.

Eigenson, L. S., 1940, "Les Lois Gouvernant la Transmission de la Chaleur aux gaz Biatomique par les Parois des Cylindres Verticaux dans le cas de Convection Naturelle," *Dokl. Akad. Nauk SSSR*, Vol. 26, pp 440-444.

el Husayni, H. A., Taslim, M. E., and Kercher, D. M., 1992, "Experimental Heat Transfer Investigation of Stationary and Orthogonally Rotating Asymmetric and Symmetric Heated Smooth and Turbulated Channels," ASME Paper 92-GT-189.

Faas, S. E., and McEligot, D. M., 1979, "Convective Heat Transfer for Ship Propulsion," ONR 5th Ann. Summary Rpt., Univ. Arizona. Available from NTIS as AD-A094 249/0.

Fromm, J. E., 1984, "Numerical Calculation of the Fluid Mechanics of Drop-on-Demand Jets," *IBM Journal of Research Development*, Vol. 28, pp. 322-333.

Gaugler, R. E., 1993, "Basic Research Needs in Gas Turbine Heat Transfer," *Gas Turbine Heat Transfer - Atlanta 1993*, ASME Pub. No. HTD-Vol. 242 (abstract).

Greene, W. J., 1960, "An Analysis of Transfer in Gas Shielded Welding Arcs," *Trans., A.I.E.E.*, Vol. 7, pp. 194-203.

Hama, F. R., and Recesso, J. V., 1958, "The Axisymmetric Free-Convection Temperature Field Along a Vertical Thin Cylinder," Tech. Note BN-116, Inst. Fluid Dyn. Appl. Math., Univ. Maryland. Available from DTIC as ASTIA AD-148 064.

Han, J.-C., Zhang, Y. M., and Lee, C. P., 1992, "Influence of Surface Heating Condition on Local Heat Transfer in a Rotating Square Channel With Smooth Walls and Radial Outward Flow," ASME Paper 92-GT-188.

Hirt, C. W., and Nichols, B. D., 1981, 'Volume of Fluid (VOF) Method for the Dynamics of Free Boundaries," *Journal of Computational Physics*, Vol. 39, pp 201-225.

Jacobs, H. R., and Hartnett, J. P., 1991, "Thermal Engineering: Emerging Technologies and Critical Phenomena," Report, Mech. Engr., Pennsylvania State Univ.

Johnson, B. V., Wagner, J. H., Steuber, G. D., Yeh, F. C., 1992, "Heat Transfer in Rotating Serpentine Passages with Trips Skewed to the Flow," ASME Paper 92-GT-191.

Jones, O. C., Telionis, D., and Schultz, R. R., 1992, "Basic Research Needs in Fluid Mechanics," ASME Symposium FED-Vol. 134.

Kays, W. M., 1966, *Convective Heat and Mass Transfer*, McGraw-Hill, New York.

Keyhani, M., and Kulacki, F. A., 1985, "Natural Convection in Enclosures Containing Tube Bundles," *Natural Convection, Fundamentals and Applications*, S. Kakac, W. Aung and R. Viskanta, eds., Hemisphere, Washington, pp. 330-380.

Kothe, D. B., and Mjolness, R. C., 1992, "RIPPLE: A New Model For Incompressible Flows with Free Surfaces," *AIAA J.*, Vol. 30, pp. 2694-2700.

Kim, Y.-S., 1989, "Metal Transfer in Gas Metal Arc Welding," Ph.D. thesis, M.I.T.

Kondoh, T., 1993. Personal communication, Toyota Central Research and Development Labs.

Kreith, F., 1973, *Principles of Heat Transfer, 3rd ed.* Intext, Scranton.

Leonard, M. T., Williams, K. A., and Church, J. P., 1990, "Modifications to MELCOR for the Analysis of Heavy-Water Moderated, U-Al Fuel Reactors," *Proc., Int. Topical Meeting on Safety, Status and Future of Non-Commercial Reactors and Irradiation Facilities*, Amer. Nuclear Soc., Boise, pp. 104-111.

Lienhard, J. H., 1968, "Effects of Gravity and Surface Tension Upon Liquid Jets Leaving Poiseuille Tubes," ASME *Journal of Basic Engineering*, Vol. 90, pp. 262-268.

Lau, S. C., Han, J. C., and Kim, Y. S., 1989, "Turbulent Heat Transfer and Friction in Pin Fin Channels With Lateral Flow Ejection," ASME *Journal of Heat Transfer*, Vol. 111, pp. 51-58.

Marble, F. E., 1992, "Aerospace Propulsion Technology - A Fertile Source of Issues in Basic Fluid Mechanics," *Basic Research Needs in Fluids Mechanics*, ASME Symposium FED-Vol. 134.

Mayle, R. E., 1991, "The Role of Laminar-Turbulent Transition in Gas Turbine Engines," ASME *Journal of Turbomachinery*, Vol. 113, pp. 509-537.

Mayle, R. E., 1993, "Technical Evaluation Report," *Heat Transfer and Cooling in Gas Turbines*, AGARD CP-527, pp. T-1 to T-2.

McEligot, D. M., 1986, "Convective Heat Transfer in Internal Gas Flows With Temperature-Dependent Properties," *Adv. Transport Proc.*, Vol. IV, pp. 113-200.

McEligot, D. M., O'Brien, J. E., Stoots, C. M., Larson, T. K., Christenson, W. A., Mecham, D. C., and Lussie, W. G., 1994, "Natural Convection Between a Vertical Cylinder and a Surrounding Array," *Nuclear Engineering Design*, Vol. 146, pp. 267-276.

McEligot, S., 1992, Personal communication, Palo Alto, Calif., June.

McGee, H. A., 1992, "Support of Fluid Mechanics at NSF," Newsletter, Div. Fluid Dynamics, Amer. Physical Soc., Mar.

Mochizuki, H., and Ishii, Y., 1992, "Study of Thermalhydraulics Relevant to Natural Circulation in ATR," *Proc., 5th Int. Topical Meeting Reactor Thermal Hydraulics* (NURETH-5, Salt Lake City), Vol. I., pp. 127-134.

Morgan, V. T., 1975, "The Overall Convective Heat Transfer From Smooth Circular Cylinders," *Advances in Heat Transfer*, Vol. 11, pp. 199-264.

Osher, S., and Sethian, J. A., 1988, "Fronts Propagating with Curvature-Dependent Speed: Algorithms Based on Hamilton-Jacobi Formulations," *Journal of Computational Physics*, Vol. 79, pp. 12-49.

Padday, J. F., and Pitt, A. R., 1973, "The Stability of Axisymmetric Menisci," *Phil. Trans., Royal Society London*, Vol. 275, pp. 489-528.

Rabas, T. J., 1993, Personal communication, Energy Systems Div., Argonne National Laboratory.

Ryskin, G., and Leal, L. G., 1984, "Numerical Solution of Free Boundary Problems in Fluid Mechanics. Part 1. The Finite-Difference Technique," *Journal of Fluid Mechanics*, Vol. 148, pp. 1-17.

Schlichting, H., 1968, *Boundary-Layer Theory*, 6th Ed., McGraw-Hill, New York.

Sethian, J. A., 1990, "Numerical Algorithms for Propagating Interfaces: Hamilton-Jacobi Equations and Conservation Laws," *J. Diff. Geometry*, Vol. 31, pp. 131-161.

Simoneau, R. J., and Simon, F. F., 1993, "Progress Towards Understanding and Predicting Heat Transfer in the Turbine Gas Path," *International Journal of Heat Fluid Flow*, Vol. 14, No. 2, pp. 106-128.

Steimke, J. L., 1991, "Heat Transfer for Safety Rod and Thimble," Tech. Report WSRC-TR-91-600, Savannah River Lab.

Taslim, M. E., and Spring, S. D., 1991, "An Experimental Investigation Into the Effects Turbulator Profile and Spacing Have on Heat Transfer Coefficients and Friction Factors in Small Cooled Turbine Airfoils," Paper AIAA-91-2033, 27th Joint Propulsion Conf., Sacramento.

Webb, R. L., 1977. Personal communication, Pennsylvania State Univ.

# Perspective: A Method for Uniform Reporting of Grid Refinement Studies

**P. J. Roache**
Ecodynamics Research Associates, Inc.,
P.O. Box 9229,
Albuquerque, N.M. 87119

*This paper proposes the use of a Grid Convergence Index (GCI) for the uniform reporting of grid refinement studies in Computational Fluid Dynamics. The method provides an objective asymptotic approach to quantification of uncertainty of grid convergence. The basic idea is to approximately relate the results from any grid refinement test to the expected results from a grid doubling using a second-order method. The GCI is based upon a grid refinement error estimator derived from the theory of generalized Richardson Extrapolation. It is recommended for use whether or not Richardson Extrapolation is actually used to improve the accuracy, and in some cases even if the conditions for the theory do not strictly hold. A different form of the GCI applies to reporting coarse grid solutions when the GCI is evaluated from a "nearby" problem. The simple formulas may be applied a posteriori by editors and reviewers, even if authors are reluctant to do so.*

## Introduction

*"If you want a new idea, read an old book."* (Anon.)

The Computational Fluid Dynamics community is currently in the midst of a "reform movement" in regard to quantification of uncertainty (e.g., Mehta, 1991; Celik et al., 1993). Progressive journals are now explicit in their requirement for grid convergence studies or other uncertainty estimation (e.g., Roache et al., 1986; Freitas, 1993; AIAA, 1994). However, there is no uniformity in the performance of these studies, nor even more basically in the *reporting* of the results.

This paper proposes the use of a Grid Convergence Index (GCI) for the uniform reporting of grid refinement studies in Computational Fluid Dynamics and related disciplines. There are other possible techniques for the quantification of numerical uncertainty, but systematic grid refinement studies are the most common, most straightforward and arguably the most reliable. The motivation for the proposed uniform Grid Convergence Index is the inconsistent and confusing reporting of grid refinement studies in the engineering and scientific literature. The following hypothetical examples will suffice.

One paper states that the grid density was increased by 50 percent, resulting in a difference in some solution norm of 4 percent (of the fine grid solution) using a first-order accurate method. In another paper, grid density was doubled, resulting in a difference of 6 percent, using a second-order method. Which fine grid solution is more reliable?, i.e., better converged? More important, can the reader have any reasonable expectation that these numbers represent a "percent accuracy error band", i.e., that the fine-grid calculations are probably accurate to within 4 or 6 percent of the true solution of the continuum equations?

Note that we are concerned herein with verification of a particular calculation, i.e., estimating the grid convergence accuracy of a particular discretized solution. We assume that the code itself has already been verified for the same class of problems (so that coding errors are not an issue and, if done properly, the order of accuracy has been verified; e.g., see Steinberg and Roache, 1985; Blottner, 1990). Nor are we concerned with code validation, e.g., that a turbulence model is adequate. See Blottner (1990) for discussion of validation, or "solving right governing equations" versus verification, or "solving governing equations right." (In the present author's opinion, a code and a particular calculation can be verified, and not with excessive difficulty. However, a code cannot be validated in any general sense, i.e., by comparison with experimental values. Rather, only a particular calculation or narrow range of calculations can be validated.) Also, it is always worth noting that this paper and similar grid refinement studies address only "ordered" discretization errors, which by definition vanish as grid spacing $h \rightarrow 0$. Specifically, the errors introduced by the use of far-field computational boundaries must be assessed separately (e.g., see Roache, 1972). Further, I consider herein only *a posteriori* error estimation, being of the opinion that useful *a priori* estimation is not possible for fluids engineering problems.

## Richardson Extrapolation

Richardson Extrapolation, also known as "$h^2$ extrapolation" and "the deferred approach to the limit" and "iterated extrapolation," was first used by Richardson in 1910, and later embellished in 1927. The discrete solutions $f$ are assumed to have a series representation, in the grid spacing $h$, of

Contributed by the Fluids Engineering Division for publication in the JOURNAL OF FLUIDS ENGINEERING. Manuscript received by the Fluids Engineering Division September 11, 1993; revised manuscript received June 6, 1994. Associate Technical Editor: O. Baysal.

$$f = f[\text{exact}] + g_1 h + g_2 h^2 + g_3 h^3 + \ldots \quad (1)$$

The functions $g_1$, $g_2$, etc. are defined in the continuum and do not depend on any discretization. For infinitely differentiable solutions, they are related to all orders to the solution derivatives through the elementary Taylor series expansions, but this is not a necessary assumption for Richardson Extrapolation, nor is the infinite series indicated in Eq. (1). It is only necessary that Eq. (1) be a valid definition for the order of the discretization. Thus, the extrapolation may be valid for finite element solutions, etc..

For a second-order method, $g_1 = 0$. Then the idea is to combine two separate discrete solutions $f_1$ and $f_2$, on two different grids with (uniform) discrete spacings of $h_1$ (fine grid) and $h_2$ (coarse grid), so as to eliminate the leading order error terms in the assumed error expansion, i.e. to solve for $g_2$ at the grid points in Eq. (1), substitute this into Eq. (1) and obtain a more accurate estimate of $f[\text{exact}]$. The result is the original statement (Richardson, 1927) for $h^2$ extrapolation.

$$f[\text{exact}] = (h_2^2 f_1 - h_1^2 f_2)/(h_2^2 - h_1^2) + \text{H.O.T.} \quad (2)$$

where H.O.T. are higher-order terms. Using the grid refinement ratio $r = h_2/h_1$, this can be conveniently expressed in terms of a correction to the fine grid solution $f_1$, dropping H.O.T.

$$f[\text{exact}] \simeq f_1 + (f_1 - f_2)/(r^2 - 1) \quad (3)$$

The most common use of this method is with a grid doubling, or halving. (These are *identical*. Both use two grids, one twice as fine as the other, i.e., we have a coarse grid and a fine grid. Whether we "doubled" or "halved" just depends on which calculation came first!) With $r = 2$, Eq. (3) becomes

$$f[\text{exact}] \simeq 4/3 f_1 - 1/3 f_2. \quad (4)$$

It is often stated that Eq. (4) is fourth-order accurate if $f_1$ and $f_2$ are second-order accurate. Actually, as known by Richardson, this is true only if odd powers are absent in the expansion (1), which he achieved by assuming the exclusive use of second-order centered differences. If uncentered differences are used, e.g., upstream weighting of advection terms, even if these are second-order accurate (3-point upstream), the $h^2$ extrapolation is third-order accurate, not fourth. As a practical limitation, even extrapolations based on centered differences do not display the anticipated fourth-order accuracy until the cell Reynolds number Rc is reduced; for the 1-D advection-diffusion equation with Dirichlet boundary conditions, Rc $<$ 3 is required (Roache and Knupp, 1993).

Although Richardson Extrapolation is most commonly applied to grid doubling, and is often stated to be only applicable to integer grid refinement (e.g., Conte and DeBoor, 1965) this is not required. In order to use Eq. (3) it is necessary to have values of $f_1$ and $f_2$ at the same points, which would seem to require commonality of the discrete solutions, and therefore integer grid refinement ratios $r$ (grid doubling, tripling, etc.). However, even in his 1910 paper, Richardson looked forward to defining a continuum $f_2$ by higher-order interpolation, and in the 1927 paper had a specific approach worked out. Ferziger (1993) alludes to this approach with less detail but more generality. Similarly, Richardson Extrapolation is commonly applied only to obtaining a higher-order estimate on the coarse grid with $h_2 = 2h_1$, but Roache and Knupp (1993) show how to obtain fourth-order accuracy on all fine-grid points by simple second-order interpolation, not of the solution values $f_2$, but of the extrapolated *correction* from Eq. (4), i.e., by second-order interpolation of $1/3\ (f_1 - f_2)$. The use of simple second-order interpolation avoids complexities with nonuniform grids and near-boundary points.

Richardson (1910, 1927) also considered sixth-order extrapolation (using 3 grid solutions to eliminate $g_2$ and $g_4$), parabolic and elliptic equations, staggered grids (then called "interpenetrating lattices"), rapid oscillations and the $2h$ wavelength limit, *a priori* error estimates, singularities, integral equations, statistical problems, Fourier coefficients, and other noncalculus problems. For example, Richardson (1927) showed the power of the method in an elegant example of extrapolating two very crude approximations to a circle, namely an inscribed square and an inscribed hexagon, to get an estimate of $\pi$ with three-figure accuracy.

The usual assumptions of smoothness apply, as well as the assumption (often verified) that the local error order is indicative of the global error order. The extrapolation must be used with considerable caution, since it involves the additional assumption of monotone truncation error convergence in the mesh spacing $h$. This assumption may not be valid for coarse grids. Also, the extrapolation magnifies machine round-off errors and incomplete iteration errors (Roache, 1972). In spite of these caveats, the method is extremely convenient to use compared to forming and solving direct fourth-order discretizations, which involve more complicated stencils, wider bandwidth matrices, special considerations for near-boundary points and non-Dirichlet boundary conditions, additional stability analyses, etc., especially in nonorthogonal coordinates which generate cross-derivative terms and generally complicated equations. Such an application was given by the present author in Roache (1982).

The method is in fact oblivious to the equations being discretized and to the dimensionality of the problem, and can easily be applied as a postprocessor (Roache, 1982) to solutions on two grids with no reference to the codes, algorithms or governing equations which produced the solutions, as long as the original solutions are indeed second-order accurate.[1] The difference between the second-order solution and the extrapolated fourth-order solution is itself a useful diagnostic tool, obviously being an error estimator (although it does not provide a true *bound* on the error except possibly for certain trivial problems). It was used very carefully, with an experimental determination rather than an assumption of the *local* order of convergence, by de Vahl Davis (1983) in his classic benchmark study of a model free convection problem. See Nguyen and Maclaine-Cross (1988) for application to heat exchanger pressure drop coefficients. Zingg (1993) applied the Richardson error estimator to airfoil lift and drag calculations in body-fitted grids. (Zingg's work demonstrates the necessity of grid convergence testing even when experimental data are available. In 4 of 7 cases, experimental agreement was better with *coarse* grid calculations than with fine. Also, his data indicate that Richardson Extrapolation can be applied to the estimation of far-field boundary errors, with the error being first order in the inverse of distance to the boundary.) Blottner (1990) has used the same procedure to estimate effects of artificial dissipation terms in hypersonic flow calculations.

An important aspect of Richardson Extrapolation is that it applies not only to point-by-point solution values, but also to solution functionals, e.g., lift coefficient $C_L$ for an aerodynamics problem or integrated discharge for a groundwater flow problem, provided that consistent or higher-order methods are used in the evaluations (e.g., second or higher-order quadratures for lift) as well as the basic assumption that the "order" of the method applies globally as well as locally. If Richardson Extrapolation is applied to produce (say) fourth-order accurate grid values, one could in principle calculate a fourth-order accurate functional like $C_L$ from the grid values, but it would require careful implementation of fourth-order accurate quadratures. It is much simpler to apply the extrapolation directly to the $C_L$'s obtained in each grid, requiring only second-order

[1] I use the common but somewhat abusive terminology of "second-order accurate solution" to mean a solution obtained by a verified second-order accurate method applied in the asymptotic range of grid spacing.

quadratures. Indeed, this is a major attraction of Richardson Extrapolation compared to using fourth-order accurate stencils solved either directly or by deferred corrections. (Note, however, that the two approaches yield different answers, although both are fourth-order accurate if done properly.)

A very significant yet overlooked *disadvantage* of Richardson Extrapolation is that the extrapolated solution generally is not "conservative" in the sense of maintaining conservation properties (e.g., Roache, 1972). This could well dictate that Richardson Extrapolation not be used. For example, if it were used on the ground-water flow simulations for the Waste Isolation Pilot Plant (WIPP PA Dept., 1992), it would be "more accurate" in some norm, but would introduce additional nonconservative (i.e., lack of conservation property) source terms into the radionuclide transport equation. It is also noteworthy that Richardson (1927) pointed out that the accuracy of the extrapolation does not apply to arbitrarily high derivatives of the solution. The extrapolation can introduce noise to the solution which, although low level, may decrease the accuracy of the solution higher derivatives.

Thus, it is not advocated here that Richardson Extrapolation necessarily be used to improve the reported solution, since that decision involves these considerations and possibly others. What is advocated is that, regardless of whether Richardson Extrapolation is used to improve the solution, the proposed Grid Convergence Index (defined herein and based on the generalized theory of Richardson Extrapolation) be used to uniformly *report* grid convergence tests.

## A Generalization of Richardson Extrapolation

Without assuming the absence of odd powers in the expansion of Eq. (1), we can generalize Richardson Extrapolation to $p$th order methods and $r$-value of grid ratio, again eliminating the leading term in the error expansion, as follows.

$$f[\text{exact}] \simeq f_1 + (f_1 - f_2)/(r^p - 1). \tag{5}$$

If the next term in the series is zero, e.g., if centered differences were used, then the extrapolation is $(p + 2)$ order accurate. But generally, and notably if upstream-weighted methods for advection have been used, the extrapolation is $(p + 1)$ order accurate.

It may easily be verified that Eq. (5) is valid for multidimensions in any coordinates, including space and time, provided that the same grid refinement ratio $r$ is applied, and the order $p$ is uniform, in all space and time directions.

In Eq. (5), the correction to the fine grid solution $f_1$ is obviously an error estimator of the fine grid solution. Expressing this as an Estimated fractional error $E_1$ for the fine grid solution $f_1$, we have

$$E_1[\text{fine grid}] = \epsilon/(r^p - 1) \tag{6}$$

$$\epsilon = (f_2 - f_1)/f_1. \tag{7}$$

Defining the Actual fractional error $A_1$ of the fine-grid solution as usual,

$$A_1 = (f_1 - f[\text{exact}])/f[\text{exact}] \tag{8}$$

and using Eqs. (5)–(8) and the binomial expansion gives

$$A_1 = E_1 + 0(h^{p+l}, E_1^2) \tag{9}$$

where $l = 1$ generally or $l = 2$ if centered differences have been used. Thus, $E_1$ is an *ordered error estimator*, i.e., an ordered approximation to the actual fractional error of the fine grid solution. $E_1$ is a good approximation when the solution is of reasonable accuracy, i.e., when $E_1 \ll 1$.

This is generally *not* true of $\epsilon$ in Eq. (7), which is the quantity commonly reported in grid refinement studies. That is, $\epsilon$ is not always an error estimator since it does not take into account $r$ or $p$. For $r < 2$ and $p = 1$, $\epsilon$ alone is optimistic, underestimating the grid convergence error compared to $E_1$ (by a factor of 2 for $r = 1.5$). For $r = 2$ and $p = 2$, $\epsilon$ alone is conservative, over-estimating the grid convergence error compared to $E_1$ (by a factor of 3). Note that $\epsilon$ can be made (almost) arbitrarily small, just by choosing $r \simeq 1$. (The only qualification is that $r$ is limited by the integer character of the number of grid points, so the smallest $r = N/(N - 1)$ where $N$ is the number of grid points in each direction of the fine grid.) This is analogous to the situation wherein an arbitrarily small tolerance on *iterative* convergence can always be met by using an arbitrarily small relaxation factor, belying the adequacy of such an iterative convergence criterion (Roache, 1972; Ferziger, 1993).

$E_1$ may of course be expressed as a percent, and like any *relative* error indicator it will become meaningless when $f_1$ or $f$[exact] is zero or small relative to $(f_2 - f_1)$, in which case the denominator of Eq. (7) should be replaced with some suitable normalizing value for the problem at hand, as would the usual definition of actual relative error $A_1$ in Eq. (8).

As described earlier, one may choose to not use Richardson Extrapolation for good reasons, e.g., due to concern over the actual order of the method, or accumulation of round-off error, or incomplete iterative convergence error, or uncertainty that the asymptotic range has been reached, or lack of the conservation property in the extrapolated results, etc. But whether or not one chooses to use or report the results of the extrapolation, one can still use the theoretical basis to *consistently* report the results of the grid refinement study.

## Grid Convergence Index for the Fine Grid Solution

Although the error estimator $E_1$ of Eq. (6) is based on a rational and consistent theory, it is certainly not a *bound* on the error. (Nor is a reliable and practically tight bound on solution error for nonlinear problems likely to be forthcoming, in the author's opinion.) What is generally sought in engineering calculations is not a true "error bound" but just an "error band," i.e., a tolerance on the accuracy of the solution which may in fact be exceeded, but in which the reader/user can have some practical level of confidence. The error estimator $E_1$ itself does not provide a very good confidence interval. (One might expect that it is equally probable that $E_1$ be optimistic as conservative, i.e., it is just as likely that the actual error $A_1$ be greater than $E_1$ as less than $E_1$. This would correspond roughly to a 50 percent confidence band.) A well-founded probability statement on the error estimate, such as a statistician would prefer (e.g., a two-sigma limit) is not likely forthcoming for practical CFD problems. However, based on cumulative experience in the CFD community, at least a marginal confidence level exists for the $\epsilon$ of Eq. (7) obtained using a grid doubling and a verified second-order accuracy code.

That is, for a grid doubling with a second-order method, and some indication that the calculations are within the asymptotic range of convergence, most CFD practitioners would accept the $\epsilon$ of Eq. (7) as a reasonable error band, in the flavor of a statistician's 2-$\sigma$ range or an experimentalist's 20:1 odds (Kline and McClinstock, 1953). An $\epsilon$ of (say) 6 percent would be taken to indicate (not absolutely, but with reasonable confidence) that the fine grid solution was within 6 percent of the asymptotic answer. This confidence is well justified by the theory of Richardson Extrapolation, which shows, from Eqs. (6) and (7) with $r = 2$ and $p = 2$, that the error estimate $E_1$ is only 1/3 of this error band, or 2 percent.

The idea behind the proposed Grid Convergence Index is to approximately relate the $\epsilon$ of Eq. (7) obtained by whatever grid refinement study is performed (whatever $p$ and $r$) to the $\epsilon$ that would be expected from a grid refinement study of the same problem with the same fine grid using $p = 2$ and $r = 2$, i.e., a grid doubling with a second-order method. The relation is based on equality of the error estimates. Given an $\epsilon$ from an actual grid convergence test, the GCI is derived by calculating

the error estimate $E_1$ from Eqs. (6) and (7), then calculating an *equivalent* $\epsilon$ that would produce approximately the same $E_1$ with $p = 2$ and $r = 2$. The absolute value of that *equivalent* $\epsilon$ is the proposed Grid Convergence Index for the fine grid solution, which is conveniently expressed as

$$\text{GCI[fine grid]} = 3|\epsilon|/(r^p - 1) \tag{10}$$

where $\epsilon$ is defined in Eq. (7).

We note immediately that for a grid doubling ($r = 2$) with a second-order method ($p = 2$), we obtain GCI = $|\epsilon|$, as intended.

The purpose of the proposed GCI is not to preclude more convincing grid convergence tests (such as using Richardson Extrapolation over several grid refinements, e.g., Shirazi and Truman, 1989; Blottner, 1990). The modest purpose herein is just to get minimal two-calculation grid refinement exercises onto a uniform reporting basis.

The GCI, like the theory of Richardson Extrapolation on which it is based, is equally applicable not only to grid values, but also to solution functionals (e.g., $C_L$) and to plotted curves, wherein $\epsilon$ may be read visually or calculated from interpolated tabular values. Thus it may be used to produce plots of the estimated error band about a fine grid solution by post-processing the results of any two grid solutions. Nonphysical oscillations in the solutions ("wiggles", e.g., see Roache, 1972) are of course a cue that the solutions are not in the asymptotic range, Richardson Extrapolation is not accurate, $E_1$ of Eq. (6) is not a valid error estimator, and confidence in the GCI as an error band is not justifiable.

Applying Eq. (10) to the hypothetical cases in the second paragraph of the introduction, we see that a 4 percent difference from a grid refined by 50 percent using a first-order method gives a fine-grid GCI = 24 percent, whereas a 6 percent difference from a doubled grid using a second-order method gives a fine-grid GCI = 6 percent. Even though the first paper's reported raw deviation $\epsilon$ from coarse to fine grid calculations might appear at first glance to be better than that reported in the second paper (4 percent compared to 6 percent), it is in fact not nearly as well converged (24 percent compared to 6 percent), as indicated by the proposed Grid Convergence Index.

For a less hypothetical example, consider the grid convergence results reported by the present author (Roache, 1982) for benchmark calculations of weakly separated flows obtaining using Richardson Extrapolation applied with grid doubling. The reported quantification of convergence was the maximum fractional deviation $\epsilon_4$ between the fine-grid second-order and the extrapolated fourth-order solution $f_4$ from Eq. (4),

$$\epsilon_4 = (f_1 - f_4)/f_4 \tag{11}$$

The values reported were $\epsilon_4 = 0.17$ percent for wall vorticity and 0.13 percent for a velocity profile at a longitudinal station traversing the separation bubble. This $\epsilon_4$ is easily related to the $\epsilon$ of Eq. (7); combining Eqs. (4), (7), and (11) shows

$$\epsilon = 3 - 3/(1 + \epsilon_4) = 3\epsilon_4 + 0(\epsilon_4^2). \tag{12a}$$

$$\text{GCI[fine grid]} \simeq 9\epsilon_4 \tag{12b}$$

The reported grid convergence criteria (Roache, 1982) of 0.17 percent for wall vorticity and 0.13 percent for velocity would now be replaced by the much more conservative GCI[fine grid] = 1.53 and 1.17 percent.

In such cases wherein Richardson Extrapolation is actually used to produce a higher order accurate solution, rather than just to estimate the error of the fine grid solution, the GCI of Eq. (10) (or (12*b*)) appears to be unfairly conservative. The solution used is the (say) fourth-order accurate solution, but the reported GCI would be the same even if only the second-order accurate fine grid solution were used. That is, $E_1$ and GCI are respectively the error estimator and Grid Convergence Index for the fine grid second-order solution, not for the fourth-order solution. Although we expect the extrapolated solution to be more accurate than the fine grid solution, we would need additional information (a solution on a third grid) to estimate the error of the extrapolated solution itself. Such a third grid solution could be used in principle (possibly not in practice, for nonlinear fluids engineering problems) to extrapolate a sixth order accurate solution. That is, the error estimate (and therefore the GCI) will always lag the best solution estimate. This is quite conservative when the conditions for validity of Richardson Extrapolation have been convincingly demonstrated by numerical experiments (e.g., Roache, 1982; Shirazi and Truman, 1989; Blottner, 1990; Roache and Knupp, 1993). A heuristic extension for such situations is to report the GCI for the extrapolated solution based on Eq. (10) with $\epsilon$ replaced by $\epsilon_4$ from Eq. (11), giving GCI[ext. sol.] $\simeq |E_1$ [fine grid]$| = |\epsilon|/(r^p - 1)$.

On the other extreme, it is recognized that ostensibly second-order algorithms may fail to attain second-order performance in a particular calculation, due to coding quirks or errors, subtleties in nonlinear problems, overly strong grid stretching, failure to attain the asymptotic range, etc. (see, e.g., de Vahl Davis, 1983; Steinberg and Roache, 1985; Shirazi and Truman, 1989; Roache et al., 1990.) Unless the author has convincingly verified that the code actually attains the theoretical order, at least on a "nearby" problem, the more conservative value of $p = 1$ should be used in reporting the GCI in Eq. (10).

Two calculations of the same problem with the same value of GCI, say a first-order calculation on a finer grid and a second-order calculation on a coarser grid, are not quite indifferent as to the uncertainty of the calculations. The GCI of the first-order calculations is based on an only second-order accurate error estimator, whereas the GCI of the second-order calculations is based on a third or fourth-order accurate error estimator. Thus, even with the same GCI, the second-order calculations have less uncertainty (in their uncertainty estimates) than the first-order calculations.

## Grid Convergence Index for the Coarse Grid Solution

Ostensibly, if we have a fine grid and a coarse grid solution, we would be expected to use the fine grid solution, so reporting of the above fine-grid GCI of Eq. (10) would apply. However, a practical scenario occurs for which the contrary situation applies, i.e., we use the coarse grid solution.

Consider a parametric study in which hundreds of variations are to be run. (For example, consider a 3-D time-dependent study of dynamic stall, with perhaps 3 Mach numbers, 6 Reynolds numbers, 6 airfoil thickness ratios, 3 rotor tip designs, and 2 turbulence models: a total of 648 combinations.) A scrupulous approach would require a grid refinement study for each case, but most engineers would be satisfied with one or a few good grid refinement tests, expecting, e.g., that a grid adequate for a NACA 0012 airfoil could be assumed to be adequate for a NACA 0015 airfoil. (In fact, this is often not justified by experience, e.g., stall characteristics can be quite sensitive to thickness ratio.) So for the bulk of the stack of calculations, we would be using the coarse grid solution, and we want a Grid Convergence Index for it. That is, we derive a Grid Convergence Index from Eq. (5), not as the correction to the fine grid solution $f_1$, but as the correction to the coarse grid solution $f_2$. In this case, the error estimate changes and must be less optimistic.

$$f[\text{exact}] \simeq f_2 + (f_1 - f_2)r^p/r^p - 1). \tag{13}$$

The coarse-grid GCI is then

$$\text{GCI[coarse grid]} = 3|\epsilon|r^p/(r^p - 1). \tag{14}$$

$$\text{GCI[coarse grid]} = r^p \cdot \text{GCI[fine grid]}. \tag{15a}$$

$$\text{GCI[coarse grid]} = \text{GCI[fine grid]} + 3|\epsilon|. \tag{15b}$$

**Table 1 Grid convergence index (GCI) calculated from Eqs. (10) and (14) for common values of grid ratios ($r$) and orders of the basic numerical method ($p$), for both coarse grid solutions and fine grid solutions, normalized to $\epsilon = 1$ percent**

| | Fine grid GCI | | | | Coarse grid GCI | | |
|---|---|---|---|---|---|---|---|
| | $r = 2$ | 1.5 | 1.1 | | $r = 2$ | 1.5 | 1.1 |
| $p$ | | | | $p$ | | | |
| 1 | 3.00% | 6.00% | 30.00% | 1 | 6.00% | 9.00% | 33.00% |
| 2 | 1.00% | 2.40% | 14.29% | 2 | 4.00% | 5.40% | 17.29% |
| 3 | 0.43% | 1.26% | 9.06% | 3 | 3.43% | 4.26% | 12.06% |
| 4 | 0.20% | 0.74% | 6.46% | 4 | 3.20% | 3.74% | 9.46% |

Applying this equation to the hypothetical cases in the second paragraph, we see that a 4 percent difference from a grid refined by 50 percent using a first-order method gives a coarse-grid GCI = 36 percent, whereas a 6 percent difference from a doubled grid using a second-order method gives a coarse-grid GCI = 24 percent. Note that the higher-order method appears to be working against us here, because we are coarsening, rather than refining, the grid. In actuality, the $\epsilon$ for the higher order method will be smaller for the same grid refinement close to convergence.

GCI values for some common combinations of $r$ and $p$, normalized to $\epsilon = 1$ percent, are given in Table 1.

## Should the Coefficient be "1" or "3"?

The functional form of the definition of the GCI (Eqs. (10), (14), (15)) is rational and objective, but the coefficient "3" is a judgment call. It could arguably be "1", or conceivably "1.5" or "2" or something else between 1 and 3.

The value "3" is possibly too conservative. As the quality and rigor of the grid convergence study increases, so does the conservatism of using the coefficient "3" in the definition of the GCI. However, consider practical complications such as rapidly varying coefficients from turbulent eddy viscosities or strong grid stretching, nonlinear systems, nonuniform behavior of various error norms, experimental determination of spatially varying $p$ (e.g., see de Vahl Davis, 1983), nonmonotonic convergence (e.g., see Celik and Zhang, 1993). Such complications, while not contradicting the ultimate applicability of Richardson Extrapolation (i.e., in the asymptotic range) do increase the uncertainty associated with the error estimate for practical engineering fluid dynamics calculations. Likewise, if the grid convergence exercise is only performed for a representative "nearby" problem, uncertainty is increased. These considerations provide additional rationale for retaining "3" as the coefficient, in the sense of a "factor of safety".

As noted above, using the value "3" makes grid doubling with second-order methods into the standard of comparison. This is not intended to make second-order methods the goal, only the standard. (Like an IQ of 100, it is not meant to discourage genius.) It just means that for $p = 2$ and $r = 2$, we obtain GCI [fine grid] = $\epsilon$. That is, it does not change what authors who use grid doubling with a second-order method already have been reporting, namely $\epsilon$.

Using the value "1" would make the GCI equal the error estimator obtained from Richardson Extrapolation. As noted earlier, since this is the best estimate we can make given only the information from calculations on two grids, we can only expect equal probability that the true answer is inside or outside of this band. Also, simple tests on the steady-state Burgers equation will quickly demonstrate that "1" is *not* usually conservative. Is $<50$ percent probability acceptable for an error band? I think not. Perhaps most damning, the use of "1" makes grid doubling with first order methods into the standard of comparison, i.e., for $p = 1$ and $r = 2$, the GCI [fine grid] calculated using "1" would = $\epsilon$. Clearly, we do not want first order methods to be the standard of comparison! (See, e.g., Freitas, 1994.)

A 50 percent "factor of safety" over the Richardson error estimator would be achieved with the value "1.5", or the naieve value of "2" might prove to be a neat and reasonable compromise. But much experimentation would be required over an ensemble of problems to determine a near-optimum value and to establish the correspondence with statistical measures such as the 2-$\sigma$ band. Note that a true optimum would likely depend upon the family of numerical methods (e.g., medium-order FVM, high-order FDM or FEM, etc.) and upon the family of problems (e.g., turbulence, transonic, free surface, etc.)

All things considered, and after discussions solicited from many (on the order of 200) CFD practitioners, I recommend use of the value "3" in the definition of the GCI, even though it will be too conservative for high quality grid convergence studies. Of course, there is nothing to preclude an author from reporting *both* the GCI and the Richardson Error estimator $E_1$.

## Noninteger Grid Refinement

Although it is generally assumed that grid doubling is preferable, it is argued here that, especially for the computer limitations frequently encountered in practice for multidimensional problems, it may be better to use a smaller change in grid resolution, say 10 percent. Consider a base grid, and refine or coarsen. If engineering intuition or studies on related ("nearby") problems have led to a good (economical, yet adequately accurate) grid selection for the base grid, then we are likely in the asymptotic range, but perhaps just barely. If we can afford to double the grid, we will certainly get more accurate answers, but the cost can be large. With an optimal numerical solution method, e.g., a good multigrid method, in which the computing cost is merely proportional to the number of unknowns, doubling a grid in three space dimensions and time will increase the cost over the base grid calculation by a factor of 16; if suboptimal methods are used, the penalty is worse. If we coarsen the grid instead, the economics work for us, i.e., the coarse grid solution is only 1/16 as expensive as the base grid; however, the coarse grid solution may be out of the asymptotic range. This situation is especially evident in turbulent boundary layer calculations, wherein we need $y^+ < 1$ for the first grid point off the wall. See, e.g., Shirazi and Truman (1989) or Wilcox (1993). This applies only when the turbulence equations are integrated to the wall. Different requirements apply if wall functions are used; e.g., see Celik and Zhang (1993) or Wilcox (1993).

Since the theory of generalized Richardson Extrapolation is valid for noninteger $r$, it is easier to use a small value (unless the computor is confident that the coarse grid with $r = 2$ will still be in the asymptotic range). However, there are practical limits to small $r$. For example, increasing the number of grid points by one in a base grid calculation of a $100 \times 100$ grid gives $r = 1.01$, and the theory is still valid. (Indeed, it would still be better than no grid refinement study at all.) But the results will now be obscured by other error sources, e.g., the "noise" of incomplete iterative convergence and machine round-off error. That is, as we reduce the change in the discretization error by using $r \to 1$, the leading truncation error term may be swamped by noise. As an intuitive engineering guess, a minimum 10 percent change ($r = 1.1$) is recommended. Of course, provided that the coarse grid is within the asymptotic range, the estimates are more reliable for larger $r$, for grid *refinement*.

A reviewer has expressed skepticism that one really can learn anything about grid convergence by changing the resolution by only 10 percent. It is intuitively obvious that the error estimates are more reliable for larger $r$, *for grid refinement*. It is perhaps less obvious that the opposite is true for grid coarsening, i.e., when we keep the answers of the finer grid.

Then it should be clear that there is *more* additional information, and therefore sharper error estimates, available for $r \sim 1$ than for $r \gg 1$ (limited only by noise pollution from round-off and incomplete iteration errors). For example, consider a fine grid using 100 nodes. A coarse grid calculation using 90 nodes ($r = 1.1111 \ldots$) contains more information (and is more expensive) than a coarse grid calculation using 50 nodes ($r = 2$). A set of easily reproduced calculations was performed on the steady-state Burgers equation with $u(0) = 1$ and $u(1) = 0$ (suggestive of stagnation flow), Re = 10, and $p = 2$, with a fine grid of 100 interior nodes and coarse grids from 25 to 99 nodes. The error estimator for $f = du/dx$ at $x = 1$ obtained using the coarse grid of 90 nodes ($r = 1.1111$, or a factor of 0.9 coarsening) is 3.2 times *more* accurate than the error estimator obtained using the coarse grid of 50 nodes ($r = 2$, or a factor of 0.5 coarsening).

## Independent Coordinate Refinement and Mixed Order Methods

The simplest mode in which to apply the proposed Grid Convergence Index is to use a single parameter $r$ to refine/coarsen the grid in all coordinates, space and time. However, there are often good reasons for not doing this. In boundary layer calculations (whether using boundary layer equations, full Navier-Stokes equations, or something intermediate) it is often the case that grid convergence is easy to establish in the longitudinal direction (being essentially dictated by the free-stream flow, which is not sensitive to Reynolds number) but is more problematical in the transverse direction, being sensitive to Re. Also, in time-dependent problems, it is much easier to develop a code that is solution-adaptive in the time-step than in the spatial grid, so that time discretization errors might be independently controlled (e.g., see Roache, 1991, 1992A, 1993) and the systematic grid refinement test would be restricted to the spatial grid.

In such a case, the multidimensional theory indicates that the error estimates can be obtained orthogonally. (The functions $g_1$, $g_2$, etc. in Eq. (1) for the $x$ direction now depend on $\Delta y$, and a constant (in $x$) term appears, but it may be verified that these do not affect the algebra of solving for $g_1$, even with cross derivatives present from nonorthogonal grids, at least for $p = 1$ or 2.) In each coordinate direction, Eq. 10 or 14 is applied separately, with $r_t \neq r_x \neq r_y$, etc., and the resulting Grid Convergence Indexes are added.

$$\text{GCI} = \text{GCI}_t + \text{GCI}_x + \text{GCI}_y + \text{GCI}_z, \text{ etc.} \qquad (16)$$

The additional error made by this "alternating direction Richardson extrapolation," compared to refinement in all directions at once, is not merely heuristic but is ordered (it improves for fine grids and for $r \sim 1$) and small enough for the procedure to be practical. It is important to note that the procedure must be performed globally, i.e., with complete global solutions obtained for each refinement in independent coordinate directions; attempts to apply the extrapolation procedure by lines do not produce ordered or usable error estimates.

Consistent Richardson Extrapolation error estimators cannot be obtained from just two calculations (a coarse and a fine grid calculation) when different $r$ are used in different coordinate directions, because there is no basis for separating out the directional contributions. In this case, a conservative GCI should be used, based on the smallest directional $r$. For example, in a 2-D steady flow calculated in a fine grid of 100 $\times$ 100 cells and a coarse grid of 50 $\times$ 75 cells, unless other theoretical considerations apply, we would have to conservatively attribute the change in solution to the more modest grid refinement, and use $r = 4/3$ to calculate the fine-grid GCI from Eq. (10).

A similar situation occurs with mixed-order methods, e.g., the not uncommon situation of a method with first-order time accuracy, and second-order space accuracy. A conservative approach would be to use $p = 1$ in Eq. (10), but a better estimate would be obtained using separate grid convergence studies in space and time, using $p = 1$ for the time contribution and $p = 2$ for the space contribution from Eq. (10), and simply adding the results as in Eq. (16). For hybrid methods that shift locally to two-point upstream differencing for large cell Re, the conservative $p = 1$ must be used. For methods which use higher order stencils for advection than for diffusion, the error will be dominated asymptotically by the lower order term. For example, for solutions calculated by Leonard's ULTIMATE method (Leonard, 1991) which is third order for advection, the GCI would have to be reported conservatively using $p = 2$ in Eq. (10) or (14).

## Non-Cartesian Grids, Boundary Fitted Grids, Unstructured Grids, Adaptive Grids

The procedures for calculating GCI definitely apply to non-cartesian grids, with special considerations and caveats.

The Taylor series basis of Richardson Extrapolation applies to stretched orthogonal and nonorthogonal grids as long as the stretching is analytical. It is cleanest to apply in the transformed plane ($\xi$, $\eta$, $\zeta$) where $r$ is defined as above. The order of the extrapolation accuracy will now be affected by the order and iterative convergence of the grid generation equations. Shirazi and Truman (1989) found a surprising sensitivity of the error estimates to discretization of metrics and Jacobians, and to incomplete iterative convergence. For another example, if strong exponential source terms are used (e.g., near trailing edges of airfoils) which depend strongly on $h$ (e.g., see Thompson et al., 1985) then a refined-grid generation will pollute the Richardson Extrapolation.

However, even if the grid generation equations are not converged, making the actual Richardson Extrapolation less dependable, it is still recommended that the proposed uniform GCI be reported rather than the simple raw data of $\epsilon$.

Solution-adaptive grid generation codes may have their own internal *local* error estimators. More often, solution adaptive grid generation of the redistribution or enrichment types (Thompson et al., 1985; Knupp and Steinberg, 1993) is not based on any error estimator but on solution behavior (gradient, curvature, or simply resolution requirement) which is only loosely related to *local* error (which in turn is very loosely related to the *global* error of interest herein). In such a case, the GCI reporting procedure recommended herein can be applicable if the solution-adaptive procedure is used only to obtain the base grid solution. This grid can then be changed nonadaptively, perhaps refined by a higher-order interpolation or coarsened by simply removing every other point as in Zingg (1993) and the GCI of Eqs. (10) or (14) applied to this new grid. However, practical coding difficulties exist for time-dependent solution-adaptive grids, and it is not clear how to perform meaningful *global* error estimation nor uniform grid convergence reporting in this important situation. (See also remarks on unstructured grids below.)

Another difficulty occurs for unstructured grids. If the base grid is unstructured, the GCI procedure would still apply if one used a systematic method of grid refinement or coarsening, e.g., refining each base grid triangle into four new triangles gives $r = 2$ for use in Eq. (10). However, if the coarsening/refinement is also unstructured, as occurs in some algorithms and in user-interactive grid generation codes, there is no systematic and quantifiable grid refinement index like $r$ to use in Eq. (10). Such grid refinement FEM studies are customarily reported simply in terms of the total number of elements used in the coarse ($N_2$) and fine ($N_1$) grids. Use in Eq. (10) of an

$$\text{effective } r = (N1/N2)^{1/D}, \qquad (17)$$

where $D$ is the dimensionality of the problem, and reporting the GCI is clearly preferable to simply reporting $\epsilon$. But it does not have the firm basis of a structured grid refinement, and may significantly underestimate or overestimate the accuracy, depending on whether the grid refinement algorithm (or the intuition of the interactive user) refined the grid in the critical areas or not.

For unstructured grid refinement and (structured or unstructured) grid adaption, I suppose it should be the burden of the algorithm developer to convince the reader/user that the local grid adaptivity process (sometimes based on a *local* error estimator) can be usefully correlated with a meaningful engineering *global* error estimate, which is the real interest. This is very difficult to accomplish convincingly for any problem which a fluid dynamicist would consider non-trivial (mainly because local truncation errors are advected downstream) but it can be done; see Schonauer et al., 1981).

## Shocks, Discontinuities, Singularities

In both his 1910 and 1927 papers, Richardson already considered the effect of singularities on the extrapolation procedure. These cases must be considered individually. If the form of the singularity is known *a priori*, it may be removed analytically. If unknown, its presence may be detected by checking to see if the asymptotic range has been reached (see below). Shocks and other discontinuities (e.g., contact surfaces) invalidate the Taylor series basis of Richardson Extrapolation, but unless the flow contains large numbers of complex shock patterns, the GCI procedure herein would still seem to have validity and be recommended. As pointed out by Ferziger (1993), a more appropriate error measure here might be the shock position. (Further experience with complex shocked flows is needed.)

Note also that Blottner (1990) has shown how the concept of Richardson Extrapolation can be applied to systematically estimating the error due to artificial dissipation terms used in hypersonic shock calculations. The contribution of these terms to the proposed GCI must also be calculated orthogonally to the other terms. If these terms are not estimated separately, the grid convergence tests will be polluted, since the (nonlinear) shock dissipation terms depend on $h$, and therefore the continuum problem being approximated changes from grid to grid. See also Kuruvila and Anderson (1985). (This is the same difficulty that can appear with grid generation equations, noted above.)

Also, the theory of Richardson Extrapolation is not applicable to nonlinear flux limiters, but again we expect these to be local applications, and still recommend the reporting of GCI over simply reporting the raw data for $\epsilon$, but also recommend more detailed investigation, e.g., perhaps 3 grids (see below). The point is that the presence of shocks, other discontinuities or singularities can complicate grid convergence studies whether or not the proposed GCI is used for reporting the results, so these complications do not constitute a criticism of the proposed GCI.

## Achieving the Asymptotic Range

The theory of Richardson Extrapolation, and therefore of the proposed Grid Convergence Index, depends on the assumption that the Taylor series expansion (or at least, the definition of the order of the discretization implied by Eq. (4)) is valid asymptotically, and that the two grids are within the asymptotic range. For smooth elliptic problems, this is easy to achieve. (A second-order accurate discretization of a Laplace equation with smooth boundary values is well behaved over virtually all discretizations.) For Reynolds numbers $\gg 1$, it is more problematic, and more than two grid solutions are required. The methodology proposed herein does allow for detecting this situation in a straightforward manner, provided that the order of the method, $p$, is uniform.

If an exact solution is known to a model problem, we can monitor

$$E_p = \text{error}/h^p \tag{18}$$

as $h$ is refined. Then the (approximate) constancy of $E_p$ is a faithful verification of the order $p$ and an indication that the asymptotic range is achieved (e.g., see Richardson, 1927; Steinberg and Roache, 1985; Roache et al., 1990; Blottner, 1990; Roache and Knupp, 1993). In the practical case wherein the exact solution is not known, we perform at least three grid solutions and calculate two GCI, from fine grid to intermediate ($GCI_{12}$) and from intermediate to coarse grid ($GCI_{23}$). Then the (approximate) constancy of $E_p \simeq \text{GCI}/(3h^p)$, or

$$GCI_{23} \simeq r^p\, GCI_{13} \tag{19}$$

indicates that the asymptotic range is achieved.

This indication that the asymptotic range has been achieved is usually faithful, in the author's experience (Roache, 1982; Roache et al., 1990; Roache and Knupp, 1993). But an exception (and unfortunately, an important one) occurs in problems with multiple scales of solution variation wherein a finer scale of the problem variation has been completely missed in the grid refinements. For example, in dual-continuum models of transport in porous media (WIPP PA Dept., 1992) the time scale for diffusion and storage in the material matrix blocks may be orders of magnitude less than the time scale for essentially advective transport in the fracture system. Time-step refinement may indicate no substantial change in the results (i.e., a false indication of convergence) if the time step is of the order of the advective time scale. Similar situations occur in turbulent boundary layer studies where some minimal viscous sublayer resolution is required (see Wilcox, 1993; Shirazi and Truman, 1989) and in chemically reacting flows which can have more time scales than species. Adaptive ODE solvers are good at detecting multiple time scales, but in multidimensional flows, at present there seems to be no substitute for an independent estimate (from theory or experiment) of the physical scales of interest.

Since so many authors are reluctant to perform even the most minimal grid convergence tests with two grids (Roache, et al., 1986; Roache, 1990), it may seem scrupulous to recommend *three* grids as a matter of course. In fact, it is required to be sure that the calculations are in the asymptotic range, if this is not already inferred from experience with a "nearby" calculation as in, e.g., Nguyen and Maclaine-Cross (1988) or Blottner (1990). But the presently proposed GCI is an easier improvement over the simplistic reporting of raw data on $\epsilon$.

G. de Vahl Davis (1983), in his classic benchmark calculations of a buoyancy-driven cavity, indicated local convergence rates of *less* than first order for the relatively coarse grids used, even though the method was asymptotically second-order accurate. In the absence of such meticulous work as that of de Vahl Davis, the reporting of a GCI based on the assumed $p = 2$ would be preferable to simplistic reporting the raw data of $\epsilon$, but if there is any indication of less-than-theoretical convergence rates, the more conservative estimate with GCI evaluated from Eq. (10) or (14) using $p = 1$ should be reported.

## Method of Characteristics and Spectral Methods

It is not clear how or if the proposed GCI would be applicable to calculations obtained by the classic method of characteristics, as used in gas dynamics, because of the possibly discontinuous solutions and the irregular gridding. The various Modified Method of Characteristics (e.g., see references in Roache, 1992b) will produce more systematic grid refinement, but the concept of "order" is more tenuous for the Flux-Based

MMOC (as evidenced by the fact that the accuracy *improves* as the Courant number increases above 1), and the GCI may not be applicable. Similarly, for spectral and pseudo-spectral methods, and certainly for spectral elements, different extrapolation procedures would be required. It is not known at this time how well the GCI would apply or could be extended.

## Nonsmooth Property Variation

In aerodynamics problems, one typically deals with smooth property variations over modest ranges, if not with constant property problems. In groundwater flow and transport calculations, uncertainty is much greater, and sensitivity studies are often performed with Monte Carlo techniques used to generate property variations of orders of magnitude, even from one grid block (finite volume) to the next (WIPP PA Dept., 1992). Geologic layering produces discontinuous variations in properties of several orders of magnitude.

In these situations, it is not advisable to use noninteger grid refinement parameters $r$, because additional errors would be introduced by interpolation of properties. This confusion would be aggravated by the common use of harmonic averaging for properties (e.g., Roache, 1991, 1992A, 1993). Likewise, grid coarsening is not advisable if a coarsened grid would not resolve the scale of the property variations (often the case for expensive two-phase flow calculations, e.g., WIPP PA Dept., 1992). The only approach applicable is a brute-force grid refinement by a factor of 2, which avoids any necessity for interpolation of properties.

The GCI proposed herein still has two contributions to such problems, (*a*) in including the effect of the order of the method $p$ in Eq. (10), and (*b*) in economizing a consistent treatment of *further* grid refinement. That is, a third grid (second refinement) need not involve the expense of another grid doubling (to a quadrupling of the base grid resolution) but can be done on a tripled grid, and reported consistently with the proposed GCI. The difference in computer time between calculating the sequence (base $h_0$, $1/2h_0$, $1/4h_0$) and the sequence (base $h_0$, $1/2h_0$, $1/3h_0$) can be significant. Consider an *optimal* method with base-case computer time $= T_2$ in 2-D and $T_3$ in 3-D, and time-step resolution increased in proportion to the spatial grid resolution. The quadrupling sequence costs $73T_2$ in 2-D while the tripling sequence costs $36T_2$; in 3-D, the costs are $273T_3$ and $98T_3$, respectively. The savings of a factor of 2 in 2D and somewhat less than 3 in 3D will be greatly amplified if *suboptimal* direct solution methods are used (WIPP PA, 1992).

A more fundamental question arises when geostatistical methods are used to generate particular realizations of grid-block property variations with specified statistical parameters. Only the statistical results are of interest, not the solutions of the individual realizations. The question is then, should the grid refinement studies be performed separately from the geostatistical realizations? That is, should the solution of the partial differential equations be converged on finer grids with the assumed continuum property variation fixed at a geostatistically generated coarse-grid distribution, or should the geostatistical generation also change as the grid is refined? This is not a trivial question, and although definition of a fixed continuum problem for the grid refinement studies is conceptually easier, it is clear that substantial computer savings could accrue to the combined convergence approach. In either case, the grid increments should be less than (be able to partially resolve) the correlation length of the property variation.

## Example

A reviewer has requested a simple example of the calculation of a Grid Convergence Index. I choose the easily reproduced case of a steady-state Burger's equation

$$-uu_x + u_{xx}/\mathrm{Re} = 0, \quad u(0) = 1, \quad u(1) = 0 \tag{20}$$

for Re = 1000 solved with second-order centered differences on a uniform grid, and evaluate the quantity $f = du/dx$ at $x = 1$. Using a fine grid calculation with 2000 cells, we obtain $f_1 = -529.41$. Then we coarsen the grid to 1600 cells ($r = 1.25$) and obtain $f_2 = -544.48$. The quantity typically reported (from Eq. (7)) would be $|\epsilon| = 100$ percent $\cdot (f_2 - f_1)/f_1 = 2.85$ percent. The factor $(r^p - 1)$ is $(1.25^2 - 1) = 0.5625$. The magnitude of the Richardson Extrapolation error estimator for the fine grid solution from Eq. (6) is $|E_1| = |\epsilon|/(r^p - 1) = 2.85$ percent$/0.5625 = 5.07$ percent. The fine grid value of the Grid Convergence Index from Eq. (10) is GCI[fine grid] $= 3|\epsilon|/(r^p - 1) = 3 \cdot 2.85$ percent$/0.5625 = 15.20$ percent. Comparison with the exact solution $f_{\text{exact}} = -500.00$ indicates that the exact magnitude of the fine-grid error $A_1$ is 100 percent $\cdot |(f_2 - f_{\text{exact}})/f_{\text{exact}}| = 100$ percent $\cdot |-529.41 + 500.00|/500.00 = 5.88$ percent. As is typical, the Richardson Extrapolation error estimator $E_1$ is not conservative (5.07 $<$ 5.88 percent), whereas the GCI is conservative and quite so (15.20 $>$ 5.88 percent), in the spirit of a $2\sigma$ error band.

If the coarse grid solution (or the coarse grid solution to a nearby problem) were to be used, the Richardson Extrapolation error estimator would be increased to $|E_1| + |\epsilon| = 5.07 + 2.85$ percent $= 7.92$ percent. The GCI would be increased by $3|\epsilon|$ as in Eq. (15*b*) to GCI[coarse grid] $= 15.20 + 3 \cdot 2.85$ percent $= 23.75$ percent. The actual magnitude of the coarse grid error is 100 percent $\cdot |(f_2 - f_{\text{exact}})/f_{\text{exact}}| = 100$ percent $\cdot |-544.48 + 500.00|/500.00 = 8.90$ percent. Again, the Richardson Extrapolation error estimator E1 is not conservative for the coarse grid (7.92 $<$ 8.90 percent), whereas the GCI is conservative (23.75 $>$ 8.90 percent).

## Conclusion

The quantification of uncertainty in CFD publications has been noticeably improving, with minimal grid refinement studies becoming more common. Unfortunately, it has not always been possible to uniformly interpret these studies.

In this paper, it has been proposed that the results of systematic grid refinement studies be uniformly reported using the Grid Convergence Index of Eq. (10) or (14), which is based upon a grid refinement error estimator derived from the theory of the generalized Richardson Extrapolation. While not answering all questions involved with verification of a calculation, this proposed method at least enforces some uniformity in the reporting and is based upon an objective asymptotic estimate of the grid convergence error, although the GCI is not a true error bound.

Since the GCI will often be less optimistic than the simplistic $\epsilon$ of Eq. (7), especially for the all-too-popular first-order methods, some reluctance of authors may be anticipated. Fortunately, the formulas are simple enough to be applied *a posteriori* by editors and reviewers. It is urged that they do so in the review process to continue improving the quality of CFD papers. To quote Ferziger (1993), "... *the frequently heard argument 'any solution is better than none' can be dangerous in the extreme. The greatest disaster one can encounter in computation is not instability or lack of convergence but results that are simultaneously good enough to be believable but bad enough to cause trouble.*"


## Acknowledgments

This work was partially supported by Sandia National Laboratories and the United States Department of Energy under Contract DE-AC04-76DP00789, Dr. M. G. Marietta, Technical Monitor, and the United States Army Aviation Systems Command, Aeroflightdynamics Directorate under Contract NAS2-13618, Dr. W. J. McCroskey, Technical Monitor. The author appreciates the significant suggestions of Dr. F. G.

Blottner, Dr. M. Fewell, Dr. P. M. Gresho, Dr. P. M. Knupp, Dr. B. P. Leonard, Dr. S. L. Steinberg, Dr. C. R. Truman, Dr. D. C. Wilcox, and two anonymous reviewers, and the opening quotation from Dr. S. Piacsek.

## References

AIAA, 1994, "Editorial Policy Statement on Numerical Accuracy and Experimental Uncertainty," *AIAA Journal*, Vol. 32, No. 1, Jan., p. 3.

Blottner, F. G., 1990, "Accurate Navier-Stokes Results for the Hypersonic Flow over a Spherical Nosetip," *Journal Spacecraft and Rockets*, Vol. 27, No. 2, pp. 113–122.

Celik, I., Chen, C. J., Roache, P. J., and Scheuerer, G., 1993, *Symposium on Quantification of Uncertainty in Computational Fluid Dynamics*, FED Vol. 158, ASME Fluids Engineering Division Summer Meeting, Washington, DC, June 20–24.

Celik, I., and Zhang, W-M., 1993, "Application of Richardson Extrapolation to Some Simple Turbulent Flow Calculations," *FED Vol. 158, Symp. on Quantification of Uncertainty in Computational Fluid Dynamics*, ASME Fluids Engineering Division Summer Meeting, Washington, DC, June 20–24, pp. 29–38.

Conte, S. D., and de Boor, C., 1965, *Elementary Numerical Analysis: An Algorithmic Approach*, McGraw-Hill, New York, p. 313.

de Vahl Davis, G., 1983, "Natural Convection of Air in a Square Cavity: A Bench Mark Numerical Solution," *Int. J. for Numerical Methods in Fluids*, Vol. 3, No. 3, pp. 249–264.

Ferziger, J. H., 1981, *Numerical Methods for Engineering Application*, Wiley, New York, NY.

Ferziger, J. H., 1993, "Estimation and Reduction of Numerical Error," *FED Vol. 158, Symp. on Quantification of Uncertainty in Computational Fluid Dynamics*, ASME Fluid Engineering Division, Summer Meeting, Washington, D.C., June 20–24, pp. 1–8.

Freitas, C. J., 1993, "Editorial," ASME JOURNAL OF FLUIDS ENGINEERING, Vol. 115, No. 3, Sept., pp. 339–340.

Kline, S. J., and McClinstock, F. A., 1953, "Describing Uncertainties in Simple-Sample Experiments," *Mechanical Engineering*, Jan., pp. 3–8.

Knupp, P. M., and Steinberg, S. L., 1993, *Fundamentals of Grid Generation*, CRC Press, Boca Raton, FL.

Kuruvila, G., and Anderson, J. D., 1985, "A Study of the Effects of Numerical Dissipation on the Calculation of Supersonic Separated Flows," AIAA Paper 85-0301, Jan.

Leonard, B. P., 1991, "The ULTIMATE Conservative Difference Scheme Applied to Unsteady One-Dimensional Advection," *Computational Methods in Applied Mechanics and Engineering*, Vol. 88, pp. 17–74.

Mehta, U. B., 1991, "Some Aspects of Uncertainty in Computational Fluid Dynamics Results," ASME JOURNAL OF FLUIDS ENGINEERING, Vol. 113, No. 4, Dec., pp. 538–543.

Nguyen, T. V., and Maclaine-Cross, I. L., 1988, "Incremental Pressure Drop Number in Parallel-Plate Heat Exchangers," ASME JOURNAL OF FLUIDS ENGINEERING, Vol. 110, pp. 93–96, March 1988.

Richardson, L. F., 1910, "The Approximate Arithmetical Solution by Finite Differences of Physical Problems Involving Differential Equations, with an Application to the Stresses in a Masonry Dam," *Transactions of the Royal Society of London*, Series A, Vol. 210, pp. 307–357.

Richardson, L. F., 1927, "The Deferred Approach to the Limit," *Transactions of the Royal Society of London*, Series A, Vol. 226, pp. 299–361. "Part I. Single Lattice," "Part II. Interpenetrating Lattices" by J. A. Gaunt.

Roache, P. J., 1972, *Computational Fluid Dynamics*, Hermosa Publishers, Albuquerque, NM. First Edition.

Roache, P. J., 1982, "Scaling of High-Reynolds-Number Weakly Separated Channel Flows," *Numerical and Physical Aspects of Aerodynamic Flows*, T. Cebeci, ed., Chapter 6, Springer Verlag, NY, pp. 87–98.

Roache, P. J., Ghia, K. N., and White, F. M., 1986, "Editorial Policy Statement on the Control of Numerical Accuracy," ASME JOURNAL OF FLUIDS ENGINEERING, Vol. 108, No. 1, p. 2.

Roache, P. J., 1990, "Need for Control of Numerical Accuracy," *Journal of Spacecraft and Rockets*, Vol. 27, No. 2, pp. 98–102, Mar.–Apr.

Roache, P. J., Knupp, P. M., Steinberg, S., and Blaine, R. L., 1990, "Experience with Benchmark Test Cases for Groundwater Flow," ASME FED Vol. 93, *Benchmark Test Cases for Computational Fluid Dynamics*, I. Celik and C. J. Freitas, eds., Book No. H00598, pp. 49–56, June.

Roache, P. J., 1991, "Computational Fluid Dynamics Algorithms and Codes Developed for WIPP Site Simulations," in *Computational Mechanics*, Cheung, Y. K., Lee, J. H. W., and Leung, A. Y. T., eds., *Proc. Asian Pacific Conf. on Computational Mechanics*, A. A. Balkema, Rotterdam, Vol. 2, pp. 1325–1335, Hong Kong, 11–13 Dec.

Roache, P. J., 1992, "Computational Fluid Dynamics Algorithms Developed for WIPP Site Simulations," in Russell, T. F., et al., eds., *Proc. IX International Conference on Computational Methods in Water Resources*, Denver, CO, June 9–12, Elsevier Applied Science, New York, pp. 375–382.

Roache, P. J., 1992, "A Flux-Based Modified Method of Characteristics," *International Journal for Numerical Methods in Fluids*, Vol. 15, pp. 1259–1275.

Roache, P. J., and Knupp, P. M., 1993, "Completed Richardson Extrapolation," *Communications in Numerical Methods in Engineering*, Vol. 9, pp. 365–374.

Roache, P. J., 1993, "The SECO Suite of Codes for Site Performance Assessment," *Proc. 1993 Int. High-Level Radioactive Waste Management Conf.*, Las Vegas, NV, Apr. 26–30.

Schonauer, W., Raith, K., and Glotz, G., 1981, "The Principle of the Difference of Difference Quotients as a Key to the Self-Adaptive Solution of Nonlinear Partial Differential Equations," *Computer Methods in Applied Mechanics and Engineering*, Vol. 28, No. 3, pp. 327–359.

Shirazi, S. A., and Truman, C. R., 1989, "Evaluation of Algebraic Turbulence Models for PNS Predictions of Supersonic Flow Past a Sphere-Cone," *AIAA Journal*, Vol. 27, No. 5, pp. 560–568.

Steinberg, S. L., and Roache, P. J., 1985, "Symbolic Manipulation and Computational Fluid Dynamics," *J. of Computational Physics*, Vol. 57, pp. 251–284.

Thompson, J. F., Warsi, Z. U. A., and Mastin, C. W., 1985, *Numerical Grid Generation Foundations and Applications*, North-Holland, NY.

Wilcox, D. C., 1993, *Turbulence Modeling for CFD*, DCW Industries, Inc., La Canada, CA.

WIPP PA Dept. (1992), *Annual Performance Assessment for the Waste Isolation Pilot Plant, Dec. 1992, Vol. 1 Preliminary Comparison with 40 CFR 191, Subpart B Vol. 2: Technical Basis*, Performance Assessment Department, Sandia National Laboratories, Albuquerque, NM.

Zingg, D. W., 1993, "Grid Studies for Thin-Layer Navier-Stokes Computations of Airfoil Flowfields," *AIAA Journal*, Vol. 30, No. 10, pp. 2561–2564.

**Terukazu Ota**
Professor,
Department of Machine Intelligence
and Systems Engineering,
Tohoku University,
Aramaki, Aoba-ku, Sendai 980-77, Japan

**Yasunori Okamoto**
Engineer,
Mechanical Engineering Laboratory,
Daikin Kogyo Co. Ltd.,
Kanaoka, Sakai 591, Japan

**Hiroyuki Yoshikawa**
Research Associate,
Department of Machine Intelligence
and Systems Engineering,
Tohoku University,
Aramaki, Aoba-ku, Sendai 980-77, Japan

# A Correction Formula for Wall Effects on Unsteady Forces of Two-Dimensional Bluff Bodies

*In wind tunnel studies on the flow around bluff bodies accompanying a large separated wake, the walls of the test section severely effect the flow characteristics around them. Proposed in this paper is a correction formula for the wall effects upon two-dimensional (2-D) unsteady separated flow of incompressible fluid around bluff bodies. The proposed formula is derived from numerical results with the discrete vortex method on 2-D separated flows around an inclined flat plate, a square cylinder, and also an elliptic cylinder located between two parallel walls. It is found that the present correction formula estimates reasonably well the wall effects upon the mean and fluctuating force coefficients over a wide range of blockage ratio and angle of attack through comparing the present calculated results with numerous experimental ones by several authors.*

## Introduction

Extensive analytical and experimental investigations have been carried out on the flow around airfoils and other bodies in wind or water tunnels. Examples include not only airfoils, airplanes, and fluid machines, but also road vehicles such as automobiles, high speed trains, bridges, and buildings. In the development of compact and high-speed machines of light weight, their unsteady flow features are very important items requiring clarification.

Wind tunnel walls cause two effects upon the flow around bodies tested therein. The first is the confinement effect. That is, the tunnel walls prohibit the extension of streamlines around the body resulting in an increase of local flow velocity. Accordingly, the force coefficient and the Strouhal number become greater than those in an unbounded flow. The second is the displacement effect due to the boundary layers developing on the walls. In general, however, the displacement effect is assumed to be smaller than the confinement effect since the boundary layer is thin at high Reynolds number. In experiments at very low Reynolds number, on the other hand, the confinement effect is smaller than the displacement effect.

Regarding the separated flow around bluff bodies forming the vortex street downstream of them, it has been shown that the Strouhal number and the force acting on the bodies in confined flow are greater than those in an unbounded flow due to an increase of vorticity in the separated shear layer. The wall effects on the flow around bluff bodies are essentially greater and more significant than on streamlined bodies without flow separation. Accordingly, it is of great worth to propose a correction formula for the wall effects upon the unsteady separated flow around bluff bodies in the wind tunnel.

Contributed by the Fluids Engineering Division for publication in the JOURNAL OF FLUIDS ENGINEERING. Manuscript received by the Fluids Engineering Division August 27, 1992; revised manuscript received June 6, 1994. Associate Technical Editor: Ho, Chih-Ming.

There have been numerous theoretical and empirical correction formulae on the wall effects. Among others, Maskell (1963) proposed a correction formula upon the mean base pressure and drag coefficients by applying a free streamline theory. In addition, several correction equations have been reported based on Maskell's method. Modi and El-Sherbiny (1973), Ranga Raju and Singh (1976), and Courchesne and Laneville (1979) published different empirical correction formulas based on experimental data for a square cylinder and a circular cylinder, respectively, for the wall effects depend on both the model shape and the angle of attack. The previous correction formulas, however, have not considered the effects upon the unsteady flow characteristics originated from the vortex shedding behind the body; the Strouhal number is an exception.

We have proposed a discrete vortex method combined with an image method, and have applied it to the 2-D unsteady flow of incompressible fluid around an inclined flat plate, a square cylinder, and an elliptic cylinder located between two parallel walls (Ota and Okamoto, 1990a and 1990b; Ota et al., 1990). Numerical results obtained demonstrate that the mean and fluctuating pressure distributions and the force coefficients are in qualitatively good agreement with the existing experimental data. The purpose of the present study is to propose a correction formula of the 2-D wall effects upon not only the mean forces, but also the fluctuating forces and the Strouhal number based on the numerical results obtained in our previous theoretical works.

## Discrete Vortex Method

The discrete vortex method is well known (Sarpkaya, 1989) as an effective method for analyzing unsteady separated flow at high Reynolds numbers around bluff bodies by approxi-

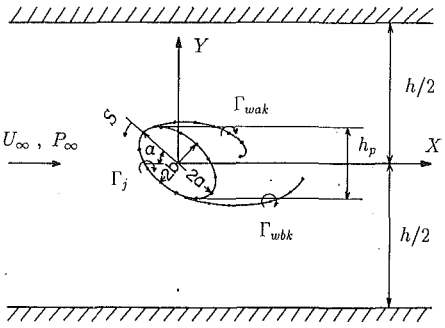


**Fig. 1 Flow configuration and physical parameters**

mating the separated shear layer by a discretized vortex filament. This method is suitable for simulating the unsteady flow accompanying the vortex shedding downstream of the body with a short calculation time, and has the capability of obtaining such characteristic data as the mean and fluctuating forces acting on the body and the pressure and velocity fields around it. Accordingly, this method has been applied to many flow configurations, and numerous papers have been published illustrating the results. Essentials of this method and extensive numbers of existing papers were comprehensively reviewed by Sarpkaya (1989).

A surface vorticity technique was presented to model the 2-D unsteady separated flow past bluff bodies of arbitrary shape by Lewis (1981) and Sakata et al. (1983). We have proposed a method to simulate the 2-D unsteady separated flow of incompressible fluid around bluff bodies of arbitrary shape located between two parallel walls by combining the surface vorticity technique with the image method (Ota and Okamoto, 1990a and 1990b; Ota et al., 1990). An inclined flat plate, a square cylinder, and an elliptic cylinder have been analyzed in their papers. Figure 1 shows the flow configuration treated and important physical parameters. Details of the analytical procedure have already been described therein. Accordingly, their details are deleted in this paper. Several points to be noticed are as follows:

- Body-surface and separated shear layers are discretized by vortex filaments.
- Image vortex filaments are introduced to simulate two parallel walls.
- A viscous core is introduced into the center of the vortex filament in order to eliminate an unreliable induced velocity when two vortices approach each other.
- After vortices move far downstream, they are replaced by one equivalent vortex.
- The vortex-shedding time interval under wall confinement is determined from

$$\Delta T = \Delta T_\infty (1 - h_p/h) \tag{1}$$

  where $\Delta T_\infty$ is the vortex-shedding interval in an unbounded flow. Such a time interval brings about no essential variation of the distance between two neighboring vortices shed from the body even under wall confinement.
- The force acting on the body is calculated from the Blasius formula extended to unsteady flow (Imai, 1974).

Detailed numerical procedures are described by Okamoto (1990). Numerical calculations were made on flows over various geometries of the body: an inclined flat plate (Ota and Okamoto, 1990a), a square cylinder (Ota and Okamoto, 1990b), and an elliptic cylinder (Ota et al., 1990). The angle of attack and the blockage ratio were varied over a wide range. It is clearly shown in those papers that the present method qualitatively simulates the instantaneous and time-averaged flow patterns around the bluff bodies, such as the formation of the vortex sheet and the mean and fluctuating pressure fields in the near wake.

## Correction Formula

Several correction formulae of the wall effects upon the flow around bodies have been proposed. Most of them, however, are mainly concerned with only the steady flow features. Among others, Maskell's theory (1963) is well known as the correction formula for the mean drag and base pressure coefficients of the separated flow around bluff bodies. In his theory, the walls of the wind tunnel are assumed to simply increase the oncoming flow velocity. The profile of surface pressure is considered not to vary with the blockage ratio. The following equation was obtained for the mean-drag coefficient by applying the momentum balance between the upstream uniform flow and the downstream wake:

$$\overline{C}_D/\overline{C}_{D\infty} = (1 - \overline{C}_{pb})/k_c^2 = 1 + (h_p/h)/(k_c^2 - 1) \tag{2}$$

It has been determined, however, in previous studies (West and Apelt, 1982; Ayukawa et al., 1985) that this correction formula may not be applicable to a blockage ratio greater than approximately 0.1. In addition, the factor $k_c$ varies with the body shape and the angle of attack. Several modified correction formulae have been reported (Fackrell, 1975; Modi and El-Sherbiny, 1977). Furthermore, there are numerous correction formulae based upon the experimental data. Among others, representative examples are summarized in the following.

The correction formula by Modi and El-Sherbiny (1973) is

$$\overline{C}_D/\overline{C}_{D\infty} = 1 + \sum_{i=1}^{n} A_i (\overline{C}_D h_p/h)^i \tag{3}$$

That by Ranga Raju and Singh (1976) is

$$\overline{C}_{D\infty}/\overline{C}_D = (1 - h_p/h)^N \tag{4}$$

Courchesne and Laneville (1979) proposed

$$\overline{C}_{D\infty}/\overline{C}_D = 1 - \xi h_p/h \tag{5}$$

$$\overline{C}_D/\overline{C}_{D\infty} = 1 + K h_p/h \tag{6}$$

In these equations, $A_i$, $N$, $\xi$, and $K$ are empirical constants, respectively. Equations (4) and (6) may be regarded as the same as Eq. (5) when the blockage ratio is small. It is found that Eq. (6) overestimates the correction in the case of a large blockage ratio (Courchesne and Laneville, 1979).

In this paper a new correction formula is proposed by analyzing minutely our previous numerical results on an inclined flat plate (Ota and Okamoto, 1990a), a square cylinder (Ota and Okamoto, 1990b), and an elliptic cylinder (Ota et al., 1990). In the present study, the correction formula Eq. (5) is employed as a base not only for the mean force coefficients,

## Nomenclature

$2a$, $2b$ = long and short axis lengths of elliptic cylinder
$C_D$, $C_L$ = drag and lift coefficients
$d$ = reference length in St
$h$ = tunnel height
$h_p$ = projected height of body
St = Strouhal number $= fd/U_\infty$
$\alpha$ = angle of attack
$\xi_F$ = correction factor

**Superscripts**

$\overline{\ }$ = mean value
$'$ = rms value of fluctuation

**Subscript**

$\infty$ = value in an unbounded flow ($h_p/h = 0$)

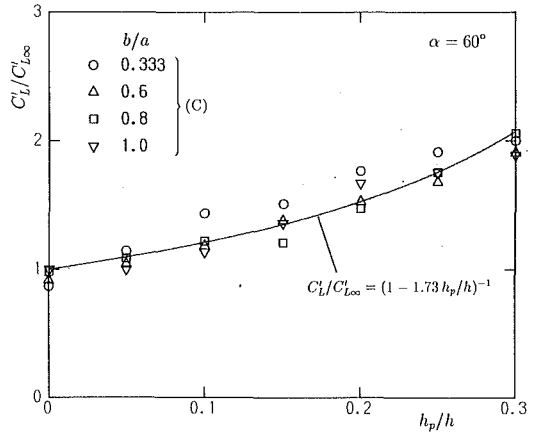


**Fig. 2 Comparison of correction formula with numerical results for $C_L'$ for an elliptic cylinder, $\alpha = 60$ deg**

but also for the Strouhal number and the fluctuating force coefficients. That is,

$$C_F = C_{F\infty}/(1 - \xi_F h_p/h) \tag{7}$$

where $C_F$ means the coefficient of $F$, $\xi_F$ the correction factor, and the subscript $\infty$ the value in an unbounded flow. The superscripts $^-$ and $'$ shown later define the time averaged and rms values of fluctuating force coefficients. $C_{F\infty}$ and $\xi_F$ are determined by applying the method of least squares to curve fit the numerical data obtained in the analyses.

A representative example of the results is shown in Fig. 2 for $C_L'$ of elliptic cylinders of various axis ratios at $\alpha = 60$ deg. Included in the figure is the correction formula for $C_L'$ obtained by the method of least squares. A difference of the cylinder axis ratio results in no essential variation, though some scatter, approximately 30 percent, can be detected. In the case of the elliptic cylinder, the numerical calculations were conducted on four cylinder axis ratios, say $b/a = 0.333$, 0.6, 0.8, and 1.0. The axis ratio 1.0 naturally means the circular cylinder. It is found that the mean and rms fluctuating force coefficients show no great change with the cylinder axis ratio. Accordingly, the correction formulae presented in this paper are applicable to the elliptic cylinder of axis ratio from 0.333 to 1.0.

Table 1 summarizes the correction factors of the mean and rms fluctuating force coefficients and the Strouhal number for the inclined flat plate, the square cylinder, and the elliptic cylinder. In the case of the inclined flat plate, the correction factor of $C_L'$ is found to depend upon $\alpha$. On the other hand, it is well known in the square cylinder that the force coefficients reach maxima around $\alpha = 15$ deg. Accordingly, two correction factors are separately determined in two regions of $\alpha$, $\alpha \leq 10$ deg and $\alpha \geq 20$ deg. A previous study (Okamoto, 1990) has determined that $\overline{C}_L$ of the square cylinder varies in a complicated way with $\alpha$ and $h_p/h$. In accordance with such facts, the present correction procedure was not applied to $\overline{C}_L$ of the square cylinder.

The uncertainty of the numerical results with the discrete vortex method depends on several factors such as the size of viscous-core vortices, the time interval and the position of vortex shedding. Through numerical calculations made under several situations, the uncertainty of the present results is estimated to be about $\pm 5$ percent in the mean force coefficients and about $\pm 15$ percent in the rms values of fluctuating force coefficients. The present correction formulas are derived from the numerical results with the discrete vortex method. Accordingly, its limitation of applicability is the same as that of the latter. Further, the experimental data shown in the following were almost all obtained in the subcritical Reynolds number range, where the general flow features exhibits no essential variation with Reynolds number. Therefore the effective Reynolds number range of the proposed correction formulae is in the subcritical one.

**Table 1 Correction factors for Eq. (7)**

| body shape | $\xi_{\overline{C}_D}$ | $\xi_{C_D'}$ | $\xi_{\overline{C}_L}$ | $\xi_{C_L'}$ | $\xi_{St}$ |
|---|---|---|---|---|---|
| inclined plate ($30° \leq \alpha \leq 90°$) | 1.52 | $2.2(1 - \alpha/\pi)$ | 1.52 | $2.2(1 - \alpha/\pi)$ | 0.82 |
| square cylinder | | | | | |
| ($\alpha \leq 10°$) | 1.44 | 1.44 | ... | 1.67 | 1.16 |
| ($\alpha \geq 20°$) | 1.45 | 1.33 | ... | 1.50 | 0.90 |
| elliptic cylinder ($0.333 \leq b/a \leq 1.0$) ($30° \leq \alpha \leq 90°$) | 1.80 | 1.80 | 1.88 | 1.73 | 0.44 |

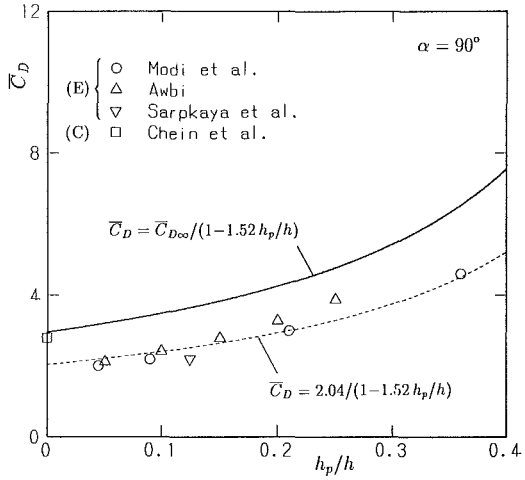


**Fig. 3 Comparison of $\overline{C}_D$ on a normal flat plate**

The standard deviation of the present numerical results from the correction formulae proposed in the paper is estimated to be within about 0.11. Further, that of the previous experimental and calculated data by several authors from the correction formulae is evaluated to be within about 0.17.

## Comparison of Proposed Correction Formula with Experimental Data for Various Shapes

In order to demonstrate the reliability of the proposed correction formulas, comparisons are made with numerous published experimental data for various shapes. A comprehensive survey was made on the experimental and the calculated results. Selected as the typical body shape in the present paper is the normal flat plate, the square cylinder at $\alpha = 0$ deg, and the circular cylinder. Comparisons are illustrated in Figs. 3 through 9, where the symbol (E) means the experimental data and (C) the calculated ones. Numerous data by several authors are included in the figures, but only representative papers are cited in the references. A solid line in the figure is the present correction formula, in which the value $C_{F\infty}$ in an unbounded flow ($h_p/h = 0$) is derived from the numerical results by the discrete vortex method. A dashed line in the figure is obtained by determining the value of $C_{F\infty}$ from the experimental ones at a blockage ratio of $h_p/h = 0.2$. The dashed lines are referred to as the semi-empirical formulae.

Figure 3 represents a comparison for the normal flat plate. The present correction formula overestimates the wall effects upon $\overline{C}_D$. It is clear, however, that the semi-empirical correction formula (dashed line) agrees reasonably well with the experimental data by several authors. A result by Chein and Chung (1988) for $h_p/h = 0$ is obtained with the discrete vortex method using the conformal mapping.

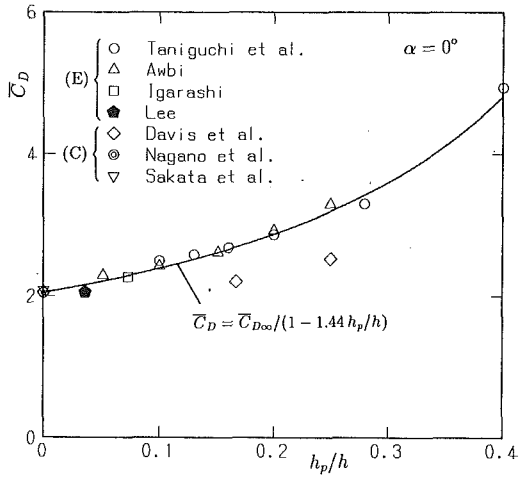


Fig. 4 Comparison of $\overline{C}_D$ on a square cylinder, $\alpha = 0$ deg

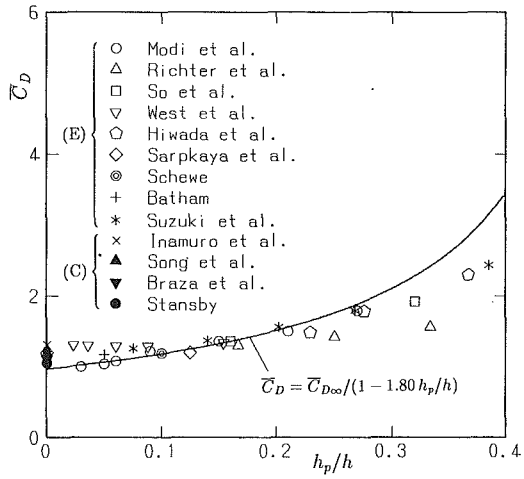


Fig. 7 Comparison of $\overline{C}_D$ on a circular cylinder

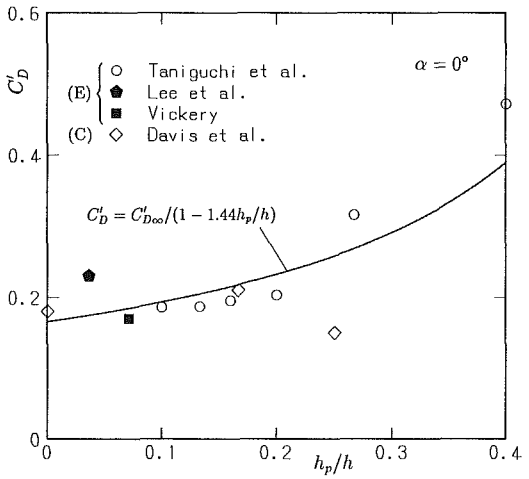


Fig. 5 Comparison of $C'_D$ on a square cylinder, $\alpha = 0$ deg

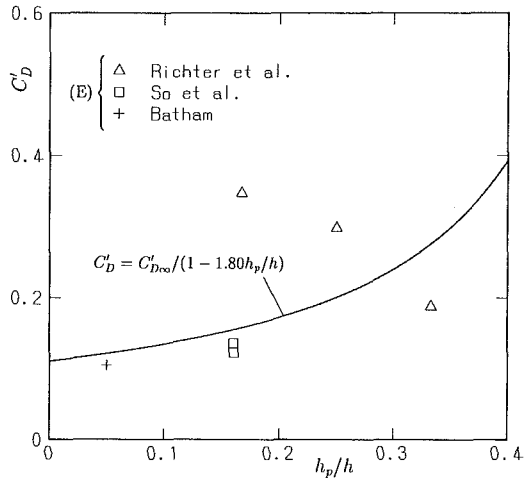


Fig. 8 Comparison of $C'_D$ on a circular cylinder

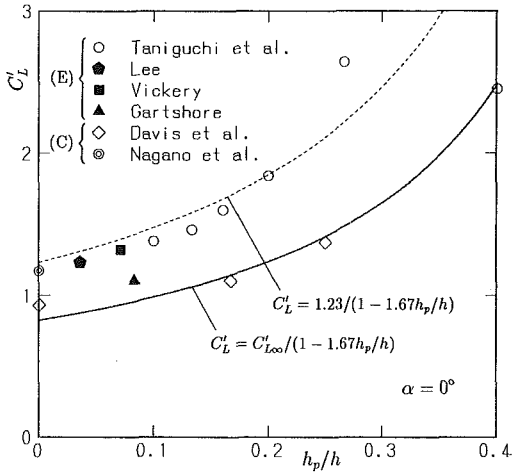


Fig. 6 Comparison of $C'_L$ on a square cylinder, $\alpha = 0$ deg

Shown in Figs. 4 through 6 are the results for the square cylinder at $\alpha = 0$ deg. It is found that the present correction formula estimates $\overline{C}_D$ very well over a wide range of blockage ratio. The present result in an unbounded flow agrees with those by Nagano et al. (1981), Sakata et al. (1983), and Davis and Moore (1982). Davis et al. (1984) calculated the blockage effect by solving the Navier-Stokes equation, but their results underestimate the effect, as shown in Fig. 4. The present correction formula can be used to estimate the blockage effect upon $C'_D$ with reasonable reliability, at least, in the range of blockage ratio smaller than about 0.2, as shown in Fig. 5. As for $C'_L$, the present results are in good agreement with numerical ones by Davis et al. (1984), but they seem to underestimate the wall effect. An increasing rate of the present correction formula with the blockage ratio is, however, almost equal to the experimental results. Accordingly, the semi-empirical formula (dashed line in Fig. 6) estimates reasonably well the wall effects and is in good agreement with the existing experimental data.

The results for the circular cylinder are compared n Figs. 7 through 9. Many papers have been published on the flow around the circular cylinder. Figure 7 shows a comparison of $\overline{C}_D$. Several data at $h_p/h = 0$ are obtained by using the discrete vortex method (Inamuro and Adachi, 1986; Stansby, 1981) and by solving the Navier-Stokes equation (Song and Yuan, 1990; Braza et al., 1990). The present correction formula is found to predict very well the wall effect upon $\overline{C}_D$ up to a blockage ratio 0.3.

On the other hand, there have been little data on $C'_D$. Three data points by Richter and Naudascher (1976) are shown in Fig. 8, and they exhibit a trend quite different from others. The present correction formula seems to have a capability for reasonably estimating $C'_D$, though many additional studies are expected. As for $C'_L$, the data scatter is not small in either the

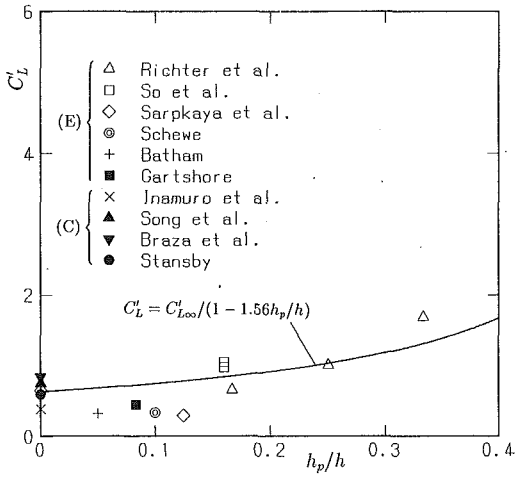


**Fig. 9 Comparison of $C'_L$ on a circular cylinder**

calculated results or the experimental ones, as shown in Fig. 9. The estimated results by the present correction formula seem to be reliable. Additional experimental data for $C'_L$ with high accuracy may be expected to be similar to $C'_D$.

The Strouhal number is also compared for those three body shapes, though their figures are omitted in this paper. The present correction formulae overestimates many calculated and experimental data, but an increasing rate of $St$ with the blockage ratio is almost equal in both. The semi-empirical correction formulae are in very good agreement with numerous experimental data for a blockage ratio smaller than about 0.3.

## Concluding Remarks

A new correction formula is proposed for correcting the wall effects upon 2-D unsteady separated flow of incompressible fluid around bluff bodies. The proposed formula is derived from numerous calculated results with the discrete vortex method combined with the image method. A distinctive feature of the proposed formula is the capability to estimate the wall effects upon the unsteady forces originated from the vortex shedding. Flow configurations treated in the paper are an inclined flat plate, a square cylinder, and an elliptic cylinder. The simple correction formula is determined by curve fitting with the method of least squares to numerous calculated results on the flow configurations noted above.

The predicted numerical results, including the wall effects, are compared in detail with the previous experimental ones. The selected body shapes are a normal flat plate, a square cylinder at $\alpha = 0$ deg, and a circular cylinder. It is found from detailed comparisons that the proposed formulae estimate qualitatively well the wall effects over a wide range of the body shape and the blockage ratio. The semi-empirical formulae, in which the reference values in an unbounded flow are determined from the experimental ones, estimate the wall effects quite accurately.

## References


Ayukawa, K., Kawasaki, N., Ohkura, M., and Asano, R., 1985, "Rectangular Cylinder in a Shear Flow," *Trans. JSME*, Vol. 51B, pp. 3887–3895.

Braza, M., Chassaing, P., and Ha Minh, H., 1990, "Prediction of Large-Scale Transition Features in the Wake of a Circular Cylinder," *Physics of Fluids A*, Vol. 2, pp. 1461–1471.

Chein, R., and Chung, J. N., 1988, "Discrete-Vortex Simulation of Flow over Inclined and Normal Plates," *Computers and Fluids*, Vol. 16, pp. 405–427.

Courchesne, J., and Laneville, A., 1979, "A Comparison of Correction Methods Used in the Evaluation of Drag Coefficient Measurements for Two-Dimensional Rectangular Cylinders," ASME JOURNAL OF FLUIDS ENGINEERING, Vol. 101, pp. 506–510.

Davis, R. W., and Moore, E. F., 1982, "A Numerical Study of Vortex Shedding from Rectangles," *Journal of Fluid Mechanics*, Vol. 116, pp. 475–506.

Davis, R. W., Moore, E. F., and Purtell, L. P., 1984, "A Numerical-Experimental Study of Confined Flow around Rectangular Cylinders," *Physics of Fluids*, Vol. 27, pp. 46–59.

Fackrell, J. E., 1975, "Blockage Effects of Two-Dimensional Bluff Body Flow," *Aeronautical Quarterly*, Vol. 26, pp. 243–253.

Imai, I., 1974, *Fluid Dynamics*, Vol. 1, Tokyo, Shokabo.

Inamuro, T., and Adachi, T., 1986, "A Numerical Analysis of Unsteady Separated Flow by Vortex Shedding Model—Flow around a Circular Cylinder," *Trans. JSME*, Vol. 52B, pp. 1600–1607.

Lewis, R. I., 1981, "Surface Vorticity Modelling of Separated Flows from Two-Dimensional Bluff Bodies of Arbitrary Shape," *Journal of Mechanical Engineering Science*, Vol. 23, pp. 1–12.

Maskell, E. C., 1963, "A Theory of the Blockage Effects on Bluff Bodies and Stalled Wings in a Closed Wind Tunnel," ARC R&M, No. 3400.

Modi, V. J., and El-Sherbiny, S., 1973, "On the Wall Confinement Effects in the Industrial Aerodynamic Studies," *Symp. on Vibration Problems in Industry*, Paper 116, Keswick, England.

Modi, V. J., and El-Sherbiny, S., 1977, "A Free-Streamline Model for Bluff Bodies in Confined Flow," ASME JOURNAL OF FLUIDS ENGINEERING, Vol. 99, pp. 585–592.

Nagano, S., Naito, M., and Takata, H., 1981, "A Numerical Analysis of Two-Dimensional Flow Past Rectangular Prisms by a Discrete Vortex Model," *Trans. JSME*, Vol. 47B, pp. 32–43.

Okamoto, Y., 1990, "Discrete Vortex Analysis of Wall Effects upon Separated Flow," Ph.D. thesis of Tohoku University.

Ota, T., and Okamoto, Y., 1990a, "Discrete Vortex Method Analysis of the Wall Effect on a Separated Flow Past an Inclined Flat Plate," *Trans. JSME*, Vol. 56B, pp. 21–28.

Ota, T., and Okamoto, Y., 1990b, "Discrete Vortex Method Analysis of the Wall Effect on a Separated Flow Past a Square Cylinder," *Trans. JSME*, Vol. 56B, pp. 958–964.

Ota, T., Okamoto, Y., and Asano, K., 1990, "Discrete Vortex Method Analysis of the Wall Effect on a Separated Flow Past an Elliptic Cylinder," *Trans. JSME*, Vol. 56B, pp. 2845–2851.

Ranga Raju, K. G., and Singh, V., 1976, "Blockage Effects on Drag of Sharp-Edged Bodies," *Journal of Industrial Aerodynamics*, Vol. 1, pp. 301–309.

Richter, A., and Naudascher, E., 1976, "Fluctuating Forces on a Rigid Circular Cylinder in Confined Flow," *Journal of Fluid Mechanics*, Vol. 78, pp. 561–576.

Sakata, H., Adachi, T., and Inamuro, T., 1983, "A Numerical Analysis of Unsteady Separated Flow by Discrete Vortex Model—Flow Around a Square Prism," *Trans. JSME*, Vol. 49B, pp. 801–808.

Sarpkaya, T., 1989, "Computational Methods with Vortices—The 1988 Freeman Scholar Lecture," ASME JOURNAL OF FLUIDS ENGINEERING, Vol. 111, pp. 5–52.

Song, C. C. S., and Yuan, M., 1990, "Simulation of Vortex-Shedding Flow about a Circular Cylinder at High Reynolds Numbers," ASME JOURNAL OF FLUIDS ENGINEERING, Vol. 112, pp. 155–163.

Stansby, P. K., 1981, "A Numerical Study of Vortex Shedding from One and Two Circular Cylinders," *Aeronautial Quarterly*, Vol. 32, pp. 48–71.

West, G. S., and Apelt, C. J., 1982, "The Effects of Tunnel Blockage and Aspect Ratio on the Mean Flow Past a Circular Cylinder with Reynolds Numbers between $10^4$ and $10^5$," *Journal of Fluid Mechanics*, Vol. 114, pp. 361–377.

# A Small Wind Tunnel Significantly Improved by a Multi-Purpose, Two-Flexible-Wall Test Section

P. Kankainen

E. Brundrett

J. A. Kaiser

Department of Mechanical Engineering,
University of Waterloo,
Waterloo, Ontario, Canada, N2L 3G1

*A small open-return wind tunnel has been renovated to include a longer test section with a flexible roof and floor and improved entrance flow quality. The flexible-wall test section allows models with up to 30 percent nominal blockage to be tested, resulting in a significant increase in the maximum attainable Reynolds numbers. Interchangeable rigid side-wall panels allow flexibility of application which is essential for a university wind tunnel facility. Configurations have been developed for automotive, aerodynamic and atmospheric-boundary-layer testing. Data acquisition and wall positioning are at an economical semi-automated level of operation. The flexible-wall concept has been well-documented previously, and provides interference-free data without flow pattern assumptions after a few iterations of the roof and floor shape. Representative data are presented for a circular cylinder and an airfoil.*

## The Original Wind Tunnel

This paper reviews the renovation of a thirty-year old, open-return wind tunnel improved by the installation of a new test section with a flexible roof and floor. The original wind tunnel, shown in Fig. 1(*a*), consisted of an entrance/contraction section, a constant-area test section and a diffuser/fan section. the tunnel's utility was greatly limited by the small size of the test section (610 mm wide by 910 mm high by 1828 mm long). In addition, flow quality in the test section was poor as a result of an inadequate entrance section which included a honeycomb flow-straightener, a single screen and a short (200 mm) settling chamber. At the inlet to the test section, the relative turbulence intensity was 0.8 percent while the mean velocity varied by ±2 percent across the test section. These conditions were not acceptable for reportable aerodynamic tests.

The inadequacy of the original test section geometry was clearly demonstrated by Kankainen (1988) in a study involving a NACA 64A215 airfoil with a 0.6 m chord. His project was the first comprehensive use of the wind tunnel in more than ten years and lead to the conclusion that useful aerodynamic results could not be obtained without replacement of the test section. It was therefore decided that a significantly-longer test section which could reduce blockage effects was required. The most promising concept appeared to be the design incorporating two flexible walls as defined by Goodyer (1975), and as refined by Wolf (1979, 1984, 1988) and by Wolf and Goodyer (1988). For testing of two-dimensional airfoil models, Wolf (1984) recommended minimum upstream and downstream distances (measured from the airfoil quarter chord point, based upon the airfoil chord length, $c$) of 3.64 $c$ and 5.64 $c$, respectively. For the 0.6 m airfoil used by Kankainen (1988), this recommendation corresponded to a required test section length of approximately 5.6 m.

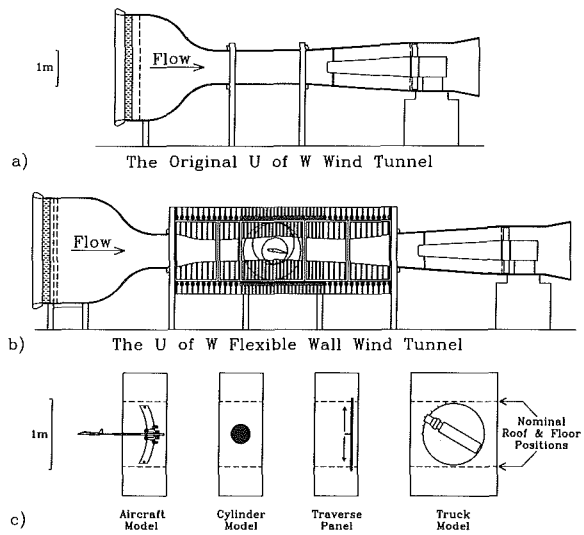


**Fig. 1 Schematic diagram showing; (*a*) the original wind tunnel, (*b*) the new University of Waterloo flexible-wall wind tunnel, and (c) interchangeable rigid side-wall panels (shown at twice the scale of *a* and *b*).**

## The Flexible-Wall Wind Tunnel

Complete descriptions of the selection, design, and construction of the new University of Waterloo flexible-wall wind tunnel (UWFWWT) are given by Brundrett and Kankainen (1991a, 1991b); however, a brief description is given here for

Contributed by the Fluids Engineering Division for publication in the JOURNAL OF FLUIDS ENGINEERING. Manuscript received by the Fluids Engineering Division March 4, 1993; revised manuscript received December 7, 1993. Associate Technical Editor: W. S. Saric.

completeness. An overall view of the UWFWWT is shown in Fig. 1(*b*). The original entrance/contraction section was retained with the addition of a second screen (Brundrett, 1993) and an additional 610 mm long settling chamber. These improvements have reduced the longitudinal turbulence intensity at the test entrance to $0.15 \leq u'/U \leq 0.25$ percent over the full range of velocity and the mean velocity variation across the test section to $\pm 0.5$ percent or less. The entrance to the test section remains 610 mm wide by 910 mm high with an extended length of 6.63 m. Downstream of the test section, the original diffuser/fan assembly was retained. With the new configuration, speeds of up to 55 m/s can be achieved when the flexible roof and floor are streamlined to eliminate blockage effects. Speeds of up to 80 m/s have been attained by reducing the effective test section area by using the flexible roof and floor to form a second contraction at the test section inlet and a diffuser at its outlet as shown in Fig. 1(*b*).

The flexible roof and floor are constructed from 610 mm wide flexible panels of shatter-proof Lexan polycarbonate plastic sheets which run the full length of the test section. The roof and floor are each manually positioned by 48 pairs of rack and pinion jacks which allow the floor to be positioned to within 0.1 mm at each jack location. The central 2.39 m of each has a thickness of 3.2 mm and 100 mm jack spacings to allow maximum practical control of panel flexure. The 2.12 m ends of the roof and floor have 150 mm jack spacings and a thickness of 4.8 mm to maintain constant stiffness. The roof and floor are each equipped with seventy 1 mm-diameter static pressure taps located along the center line at a spacing of 51 mm over the central portion and of 152 mm over each end. The edges of the roof and floor have inflatable rubber seals to prevent leakage during operation, yet allow easy movement of the surfaces during positioning. The ends of the roof and floor are mounted to full-width sliding plates to accommodate changes in length during wall positioning while maintaining tangency with the fixed contraction and fixed diffuser.

The rigid side-walls were designed to be interchangeable and were constructed in sections of either 610 mm, 1220 mm, or 1830 mm-width. These panels consist of 25.4 mm-thick Plexiglas or particle board mounted to steel frames to reduce deflection under suction loads. All of the panels can be reversed top to bottom and can be mounted in any location along either side of the test section. The panels range in weight from 120 kg to 200 kg and are bolted to full-length structural planks at the top and bottom of the test section. A hand-operated hydraulic crane is used to support the panels during installation, removal, and transport.

A number of different panel configurations have been constructed for typical applications (Fig. 1(*c*)). Two 610 mm panels are used to support a two-dimensional circular-cylinder. Another 610 mm panel has been equipped with a slot and moving seal to allow automated two-dimensional traverses of the test section at any streamwise location. A set of 1830 mm panels has been constructed for two-dimensional airfoil testing, which allows variable angle of attack and/or vertical and horizontal translation (shown in Fig. 1(*b*)). Vertical translation of the airfoil can be used to prevent wake-interaction with the floor boundary layer when testing at high angles of attack (Wolf, 1984). Another set of panels has been constructed to simulate an atmospheric boundary layer for testing of building models.

## The Adaptive Wall Concept

Adaptive wall wind tunnels control the flow near the test section walls so that the boundary conditions conform to those which would exist in an infinite flow field. Simulating the infinite flow field requires a test section with sufficient length to permit the formation of streamlines around the model which will not end abruptly at the test section inlet or exit (a length of at least 9.28 *c* as recommended by Wolf, 1984). The procedures used to adapt the walls do not require any knowledge of the model shape or the flow field around it. The wall adjustment strategy (WAS) selected for the UWFWWT is described in detail, along with complete listings of the software, by Wolf and Goodyer (1988), and for this application by Sumner and Kankainen (1993). The adaptive wall concept was first examined in the 1930s and again in the 1950s but was abandoned in each case due to the intensive computational task (Goodyer, 1975). Modern microcomputers have effectively eliminated this computational barrier.

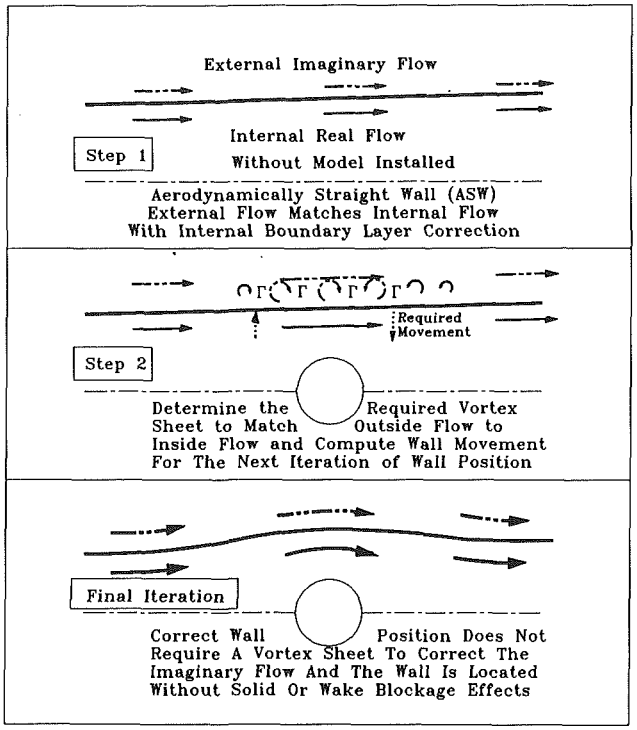


**Fig. 2 Schematic diagram illustrating the iterative wall adjustment strategy (WAS)**

Wall adjustment strategies calculate new wall positions by comparing two measured flow variables. For flexible-wall tunnels, these variables are usually static pressure and wall slope. Variables inside the walls are referred to as *real* (subscript *r*), while calculated variables outside the walls are referred to as *imaginary* (subscript *i*). The measured pressures along the roof and floor are used to obtain the real velocity field, $u_r(x)$, while the imaginary flow field, $u_i(x)$, is obtained from the previous iteration (Fig. 2). Typically, the initial case is aerodynamically-straight walls, corresponding to the condition which yields zero pressure gradient in the streamwise direction. If discrepancies occur at any point along the wall between the internal measured velocity and external calculated velocities, then the wall does not represent a streamline in an infinite flow field. The wall shape is then adjusted to eliminate the discrepancy; new wall pressure profiles are obtained, and the comparative process is repeated. The iterative wall movements are complete when the measured internal quantities agree with the calculated external values to within the range of experimental error (often determined by the precision to which the wall can be positioned).

## The Wall Adjustment Strategy (WAS)

A brief review of the wall adjustment strategy is outlined below. For a more comprehensive description the reader is referred to Wolf and Goodyer (1988). The strategy uses a vorticity distribution, $\Gamma$, at the wall to accommodate the velocity difference across it during the first unmatched flow

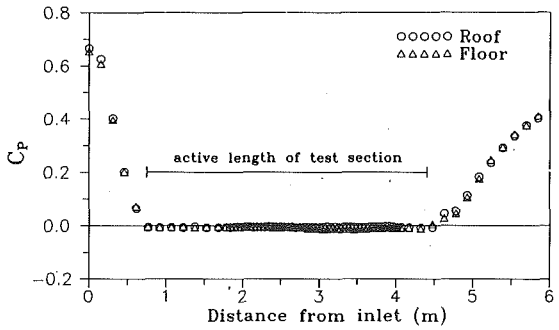


**Fig. 3 Empty-tunnel roof and floor pressure distributions for aerodynamically straight walls with the 2-D airfoil test configuration. The maximum combined uncertainty in $C_p$ is 0.042 with 95 percent confidence.**

iterations (Fig. 2). At each longitudinal jack station at streamwise location $x$, the velocity difference is represented by:

$$\Gamma(x) = u_r(x) - u_i(x) \tag{1}$$

The required distribution of vorticity induces a normal velocity component $\omega(\xi)$ at a longitudinal location $\xi$. This is approximately equal to the sum of the vorticity contributions at each $x$, and is given for small slopes by:

$$v_i(\xi) = \frac{1}{2\pi} \int_{-\infty}^{\infty} \frac{\Gamma(x)dx}{\xi - x} \tag{2}$$

The wall must be adjusted such that the change in the normal component of the freestream velocity $v_r$ offsets that due to vorticity $v_i$. For freestream velocity $U_o$, the required change in wall slope is then given by:

$$\Delta \frac{dy}{dx}(\xi) = \frac{-v(\xi)}{U_o} = \frac{1}{2\pi U_o} \int_{-\infty}^{\infty} \frac{\Gamma(x)dx}{(x-\xi)} \tag{3}$$

Integration of the above expression leads to the required wall deflection $\Delta y(\xi)$. Once the wall is set based on the above $\Delta$, the velocity on either side will change by half of the velocity difference from the previous iteration.

The difference between the real and imaginary pressure coefficients ($C_{Pr} - C_{Pi}$) is used as a measure of the quality of the streamlining process. The average error, $E$, is defined for the roof and floor by the magnitude of this difference averaged over all jack stations. Higher values of $E$ indicate higher loading on the respective panel and thus higher flow blockage. Lewis (1988) observed that the panels are streamlined and the flow can be assumed to be interference-free within experimental error when the value of $E$ is less than 0.01 on both roof and floor.

## Empty Tunnel Calibration

Aerodynamically straight walls (ASW) are obtained by diverging the flexible walls sufficiently to account for boundary layer growth on the test section walls and give zero longitudinal pressure gradient for a given velocity. The boundary layer displacement thickness, $\delta_x^*$, can be calculated from flat plate boundary layer theory by assuming a turbulent velocity profile with a 1/7th power law. Using iterative procedures, the roof and floor are positioned at some multiple of $\delta_x^*$ to compensate for boundary layer growth on the side-walls as well as the roof and floor. As an example, Fig. 3 shows ASW pressure profiles for the two-dimensional airfoil test configuration described later in this paper. For this specific case the flexible roof and floor were used to create a contraction at the test section inlet and a diffuser at the test section outlet in order to reduce the nominal test section dimensions, thereby increasing the maximum attainable Reynolds number (based on airfoil chord). Note that zero pressure gradient over the active length of the test section (as indicated in Fig. 3) was achieved by deflecting roof and floor by 1.91 $\delta_x^*$).

In the presence of a model, all four walls of the test section are subject to significantly different velocities and large pressure gradients. Although the pressure gradients can be very large on the side-walls, it is the gradients that exist on the roof and floor which affect the performance of WAS. In order for the assumption of aerodynamically-straight walls to be valid, the effect of the longitudinal pressure gradient on the roof and floor boundary layer must be accounted for. Hence, the difference $\Delta\delta_x^*$ between the empty test section $\delta_x^*$ and that with the model present is used to adjust the wall contours. Values for $\delta_x^*$ with the model present are satisfactorily predicted using the momentum integral equation from boundary layer theory (see Schlichting, 1960).

## Model Test Procedure

Currently, pressure readings for the roof, floor and model static pressure taps are measured using a single electronic differential pressure transducer connected to a series of Scanivalve fluid switch wafers. Output from the pressure transducer (and other transducers, such as thermocouples and strain gauges) is measured using a datalogger and stored on a microcomputer. Frequency response is limited by the transducer and the amount of connecting tubing. Using the existing arrangement, approximately 10 minutes are required in order to measure the static pressure distribution on the roof and floor for input to WAS.

For typical tests with a model installed in the UWFWWT, the first iteration from ASW requires approximately 40 minutes to manually position the roof and floor. Subsequent iterations require only about 15 minutes, since jack movements are only small corrections to the previous settings. Final wall positions are usually achieved in three iterations, resulting in a total required test time of under three hours. Automation of jack positioning and an updated pressure measurement system could significantly reduce this time, but at considerable expense.

## Representative Circular Cylinder Results

A circular cylinder with a diameter of 272 mm and a length of 610 mm spanning the test section was tested at a Reynolds number of 500,000 using various wall-positioning strategies. The deflection of the flexible walls is shown in Fig. 4 for each of three configurations.

The first configuration was with aerodynamically-straight roof and floor (Fig. 4, STRAIGHT). The dashed line indicates the correction required due to the effect of the pressure gradient imposed by the presence of the model on the test section boundary layer. The second configuration was defined by calculated ideal flow streamlines upstream of the cylinder, with an allowance for boundary layer growth downstream of the cylinder's mean streamwise location (Fig. 4, IDEAL). For the final configuration, roof and floor positions were determined using the wall adjustment strategy. The final streamlined wall shape yielded by WAS is shown in Figure 4 (WAS); again, the dashed line indicates the $\delta^*$ correction required due to pressure gradient.

The distribution of pressure coefficient, $C_p$, around the circular cylinder was obtained from an array of static pressure taps around the perimeter of the cylinder located at mid-span (Brundrett and Kankainen, 1991a, 1991b). The maximum combined uncertainty in $C_p$ was 0.042 with 95 percent certainty. This value was dominated by the bias errors associated with the calibration of the pressure drop across the wind tunnel contraction, which is used to determine the test section dynamic pressure.

Pressure distributions around the circular cylinder using the various wall adjustment techniques are shown in Fig. 5. The STRAIGHT data showed significant solid and wake blockage which persisted for the IDEAL data. Even when the IDEAL

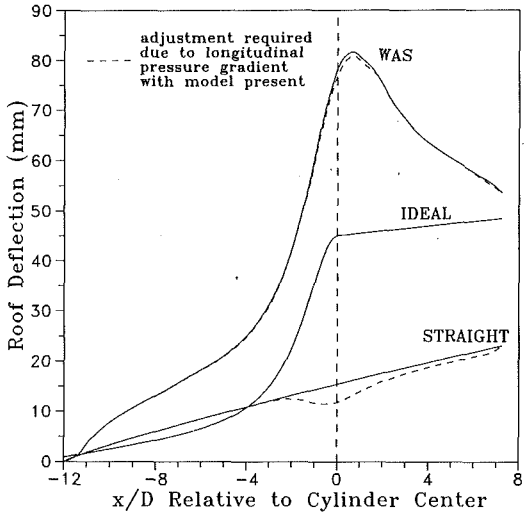


Fig. 4 Roof deflection for various wall adjustment techniques applied to flow about a circular cylinder (vertical scale exaggerated)

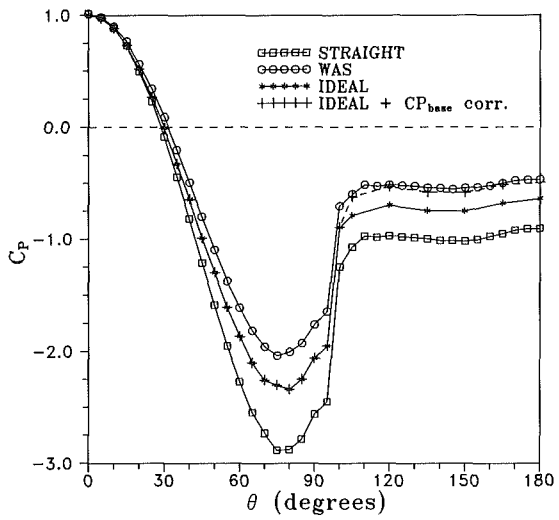


Fig. 5 Pressure distributions around a circular cylinder with various wall adjustment techniques. The maximum combined uncertainty in $C_p$ is 0.042 with 95 percent confidence.

data were base pressure-corrected in the wake region there was still a residual blockage effect from $\theta = 30$ to 100 deg ($\theta$ is defined as the angle measured from the stagnation point) that resulted in significant error in drag calculated by integrating the measured cylinder pressure profile. Only the WAS configuration yielded blockage-free results for the range of $\theta = 30$ to 110 deg. The base pressure coefficient (over the range of $\theta = 100$ to 180 deg) was in agreement with available literature (ibid.). The resulting profile-integrated drag coefficient of $C_D = 0.366$, which does not account for skin friction drag, was only 2.7 percent lower than the momentum balance value of $C_D = 0.376$ obtained from the wake velocity transverses. If the integrated drag coefficient is multiplied by 100/97 is account for the 3 percent contribution of skin friction (White, 1986), then the value is $C_D = 0.3746$ and is only 0.37 percent less than the momentum balance value. This is well within the expected experimental error range of $\pm 2$ percent for combined velocity and pressure measurements.

It is interesting to note that the nominal cylinder blockage rate of 29.9 percent was successfully accommodated by WAS with an 82 mm maximum deflection each of the roof and floor (Fig. 4). By comparison, the IDEAL roof and floor positions

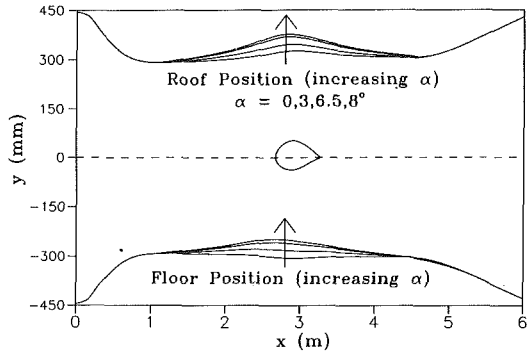


Fig. 6 Roof and floor deflections given by final iteration of the wall adjustment strategy for a two-dimensional NACA 64A215 airfoil model at several angles of attack (vertical scale exaggerated). Final wall shape was repeatable to within ±1 mm at each jack station.

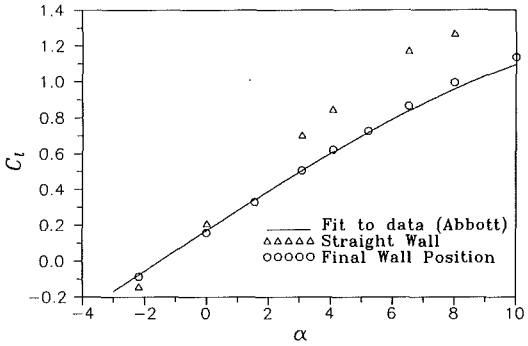


Fig. 7 Lift curve data obtained using aerodynamically-straight walls versus final adapted walls as compared to data reported by Abbott and von Doenhoff (1959). The maximum combined uncertainty in $C_l$ is 0.03 with 95 percent confidence.

were only moved outward a total of 45 mm each, thereby resulting in the observed residual blockage errors.

## Representative Airfoil Results

A NACA 64A215 profile airfoil was constructed with chord, $c$, and span, $b$, both equal to 600 mm (Kankainen 1988). In order to increase the maximum attainable Reynolds number, the nominal vertical dimension, $h$, of the test section was reduced to 581 mm. This was accomplished by using the flexible roof and floor to define a contraction at the test section inlet and a diffuser at the test section exit (Fig. 6). The effective test section length was 3750 mm as given by the region of zero longitudinal pressure gradient with aerodynamically straight walls (Fig. 3). The resulting ratio of $c/h$ was 1.03, which is much higher than the recommended solid-wall test section range of $0.3 \leq c/h \leq 0.4$ (Rae and Pope, 1984; and Van den Berg, 1971). However, a configuration with a $c/h$ of 0.9 has been used successfully by Wolf (1984) in a wind tunnel with a flexible wall test section.

The reported tests (Figs. 6, 7) were performed with a nominal velocity of 65 m/s and a Reynolds number based on airfoil chord of 2,500,000. Lift data was obtained by integration of the static pressure profiles at 40 stations around the centerline of the airfoil. The resulting lift coefficient curve is in excellent agreement with data reported by Abbott and von Doenhoff (1959) at approximately the same Reynolds number, up to $\alpha \approx 5$ deg. Deviation from the reported lift curve at $\alpha > 6$ deg was caused by increasing interaction of the airfoil wake with the floor boundary layer, invalidating the assumptions in the WAS correction procedures (Fig. 7). It is expected that it will be possible to obtain agreement with reported data over the full

range of $\alpha$ by translating the airfoil upwards (avoiding wake/boundary layer interaction).

The final iteration of the roof and floor positions are shown in Fig. 6 for several angles of attack (0, 3, 6.5, and 8 deg). For each case, final wall shape was repeatable to within $\pm 1$ mm at each jack station. It is interesting to note that, for $\alpha = 0$ deg both the roof and floor move outward moderately to compensate for the airfoil blockage (approximately 15.5 percent). However, for $\alpha \leq 3$ deg, both the roof and floor move upward significantly to accommodate for both blockage and circulation effects.

## Additional Applications

Perhaps the greatest strength of the UWFWWT is its capability of being easily modified for a wide variety of applications. In addition to the tests outlined above, studies have been performed on a 3-D aircraft model, tractor/trailer models, and a series of building models.

A six-component NASA-type sting balance assembly has been constructed (Fig. 1(*c*)) to allow testing of an X-29 aircraft model in the UWFWWT (Abramian et al., 1991). The objective of this test program was to modify the X-29 control surfaces and weight distribution sufficiently to obtain an aerodynamically-stable configuration for R/C model applications. For this study, the effects of blockage were small (model blockage was 3 percent) and were corrected using conventional fixed-wall techniques (Rae and Pope, 1984). In the future these results can be reexamined using the WAS correction procedures.

Studies of conventional and aerodynamic tractor/trailer models have been performed using a turntable panel instrumented with a drag balance (Fig. 1(*c*)). The frontal area of the models was approximately 7.5 percent of the nominal cross sectional area of the test section. Blockage effects were minimized using WAS without correcting for the 3-D nature of the flow. For the conventional tractor/trailer model, a drag coefficient (based on frontal area) of 0.80 was expected, while the measured drag coefficient was $0.796 \pm 0.015$ with 95 percent certainty. For comparison, uncorrected results with aerodynamically straight walls yielded a drag coefficient of 0.88.

Tests have been performed on a number of building models in a simulated atmospheric boundary layer (Tam et al., 1992). the thickened boundary layer was produced using a set of turbulence-generating spires and roughness elements installed on one of the rigid side-walls. Two such side-wall configurations, capable of developing boundary layers representative of rural and urban conditions, have been constructed based on recommendations reported by Irwin (1981).

## Conclusions

A small open-return wind tunnel has been renovated to include a test section with a flexible roof and floor which conforms to the recommendations of Wolf (1984). A number of different rigid side-wall panels have been developed which allow the wind tunnel to be easily adapted to a wide variety of applications. The operation of the wind tunnel is at a cost effective semi-automated level, consisting of automated data acquisition and reduction with manual adjustment of the roof and floor and wind tunnel speed. The wall adjustment strategy developed by Wolf and Goodyer (1988) has been substantiated by airfoil and circular cylinder data which have been shown to be essentially free of blockage effects; at present, up to a nominal blockage of 30 percent. This has permitted an order-of-magnitude increase in attainable Reynolds numbers (large wind tunnel results) without post-treatment of the data for blockage effects. The cost and effort required to modify an existing small test section need not be excessive and are well justified.

## Acknowledgments

Funding for the renovation and operation of UWFWWT has been provided in part by the Canadian Natural Sciences and Engineering Research Council (NSERC), the Canadian International Development Research Agency, the Faculty of Engineering of the University of Waterloo, and private sources.

## References

Abbott, I. H., and von Doenhoff, A. E., 1959, *Theory of Wing Sections: Including a Sumamry of Airfoil Sections*, Dover Publications.

Abramian, M., Kankainen, P., Brundrett, E., and Howard, J. H. G., 1991, "Wind-Tunnel Investigation of Aerodynamic And Stability Characteristics of a Forward Swept Wing X-29 Model," *Proceedings of the 3rd Canadian Symposium on Aerodynamics, Canadian Aeronautics and Space Institute*, Toronto, Canada.

Baines, W. D., 1963, "Effects of Velocity Distribution on Wind Loads and Flow Patterns on Buildings," *Proceedings 1st. Symposium on Wind Effects on Buildings and Structures, National Physics Laboratory*, Teddington, pp. 197–223.

Brundrett, E., 1992, "Prediction of Pressure Drop for Incompressible Flow Through Screens," ASME JOURNAL OF FLUIDS ENGINEERING, Vol. 115, pp. 239–242.

Brundrett, E., and Kankainen, P., 1991a, "The Construction and Passive Wall Testing of The U of W 610 by 910 mm Flexible Walled Wind Tunnel," Department of Mechanical Engineering, University of Waterloo, Technical Report FWWT 91-1.

Brundrett, E., and Kankainen, P., 1991b, "The Construction and Commissioning of a Flexible Walled Wind Tunnel," *Canadian Aeronautics and Space Journal*, Vol. 37, No. 3, pp. 108–119.

Goodyer, M. J., 1975, "A Low Speed Self Streamlining Wind Tunnel," AGARD CP-174 pp. 13.1-13.8.

Irwin, H. P. A. H., 1981, "The Design of Spires for Wind Simulation," *Journal of Wind Engineering and Industrial Aerodynamics*, Vol. 7, pp. 361–366.

Kankainen, P., 1988, "Automation of Wind Tunnels for Two Dimensional Testing of Large Scale Models," M.A.Sc. thesis, Department of Mechanical Engineering, University of Waterloo.

Lewis, M. C., 1988, "Aerofoil Testing in a Flexible Walled Wind Tunnel," NASA CR 4128.

Rae, W. H. Jr., and Pope, A., 1984, *Low Speed Wind Tunnel Testing*, Second Edition, Wiley Interscience.

Schlichting, H., 1960, *Boundary Layer Theory*, Forth Edition, McGraw-Hill.

Sumner, D., and Kankainen, P., 1993, "Wall Adjustment Strategy Codes for Two-Dimensional Testing in the UWFWWT," Department of Mechanical Engineering, University of Waterloo, Technical Report FWWT 93-1.

Tam, P. W. M., Handa, V. K., and Brundrett, E., 1992, "Wind Tunnel Analysis for Housing in the West Indies," Division of Construction Management, Department of Civil Engineering, University of Waterloo, Vols. 1-3, pp. 1–723.

Van den Berg, B., 1971, "Some Notes on Two-Dimensional High-Lift Tests in Wind Tunnels," AGARD LS-43, Paper No. 5.

White, F. M., 1986, *Fluid Mechanics*, Second Edition, McGraw-Hill.

Wolf, S. W. D., 1979, "Application of Data Acquisition Systems for On-Line Definition of Wind Tunnel Shape," Von Karman Institute for Fluid Mechanics, Lecture Series 1979 No. 5, pp. 1–61.

Wolf, S. W. D., 1984, "The Design and Operational Development of Self-Streamling Two-Dimensional Flexible Walled Test Section," NASA CR 172328.

Wolf, S. W. D., 1988, "Adaptive Wall Technology for Minimization of Wall Interferences in Transonic Wind Tunnels," NASA CR 4191.

Wolf, S. W. D., and Goodyer, M. J., 1988, "Predictive Wall Adjustment Strategy for Two-Dimensional Adaptive Wall Wind Tunnel—A Detailed Description of the First One Step Method," NACA CR 181635.

**Ming Zhu**
Department of Naval Architecture and Ocean Engineering, University of Tokyo, Tokyo, Japan

**Yuji Hanaoka**
Body Engineering Department, ISUZU Motors, Ltd., Kanagawa, Japan

**Hideaki Miyata**
Department of Naval Architecture and Ocean Engineering, University of Tokyo, Tokyo, Japan

# Numerical Study on the Mechanism of Wind Noise Generation About a Car-Like Body

*Three-dimensional flow separation about the sharp-edged front-pillar of a car-like body at high cruising speed is numerically studied. A time-dependent and full Navier-Stokes simulation is carried out for the understanding of mechanism of wind noise generation due to the vortical flow motions. The surface pressure fluctuations on the front-side window are examined in terms of wind noise, based on a simplified Lighthill-Curle's equation. The simulated results are validated regarding the numerical grid resolution and assessed by comparison with the conventional acoustic theory. The analyses of the simulated flow-field data indicate that there is a strong relationship between the vortical motions associated with the flow separation and the surface pressure fluctuations on the front-side window. The bifurcations of flow geometry, such as the breakdown of a separated vortex as well as the vortex-vortex interaction, seem to be most strongly related to the production of surface pressure fluctuations.*

## 1 Introduction

As engine, tire, and other automobile noises have been reduced in these days, the interior noise levels in many cars are significantly affected by the wind noise when the cruising speed exceeds 100 km/h. It is well known that the surface pressure fluctuations on the front-side window of a road vehicle are a major source of the wind noise (George, 1990). It is quite important to predict the wind noise as well as to understand the mechanism of wind noise generation from both an engineering and a scientific standpoint.

There are several methods to predict the spectrum of these pressure fluctuations empirically (Chou and George, 1987). There are also new techniques to measure the external aerodynamic noise such as the method using near-field acoustic holography (Maynard, 1985). Aside of the experimental techniques, there are very few prediction methods available today which provide information about the distribution of unsteady pressures on the body surface of a road vehicle.

Experimental measurements are very costly. They require the facility free of ambient noise and the instruments capable of coping with the high-frequency pressure fluctuations and the pure aerodynamic noise (George, 1990). It is also difficult to obtain the detailed external flow-field data simultaneously with the noise data by means of measurement. Without the simultaneous flow-field data and the surface pressure fluctuation data (or wind noise data), it is difficult to understand the mechanism of wind noise generation.

Watanabe et al. (1978) experimentally showed a conical flow separation structure around the front-pillar (A-pillar) of a relatively low inclination. They explained that the unsteady pressures on the front-side window surface are produced due to the existence of a separated vortex. Stapleford et al. (1970) showed that the surface pressure spectra about the separated vortex core have a much higher hump than those of the surroundings, in an experimental study of pressure fluctuations on a yawed rectangular-shaped box. Simpson et al. (1987) described that the effective pressure fluctuations may be along or near the locus of the maximum shear stress position in their experimental study of a separating turbulent boundary layer.

However, when the inclination angle of A-pillar (or the yaw angle in the case of rectangular box) becomes large, like in the case of large attack-angle of a wing, the flow geometry around A-pillar may not be so simple as is shown by Watanabe et al. (1987). In fact, Sadakata et al. (1988) showed a sudden increase in sound pressure when the inclination angle is over some critical angle in their measurement. Although they tried to relate the change in sound pressure to a flapping angle of the flow separation around the front-pillar, the flow phenomenon is not yet well explained.

The question here is, what is the mechanism of flow producing the surface pressure fluctuations. Simpson (1989) noted that the large-scale motions produced in the flow separation which leads to flapping shear layers around bluff bodies, do not contribute so much to the turbulent shear stresses but change the mean flow-field and produce the low-frequency pressure fluctuations. This kind of pressure fluctuations are considered as the dominant sources of aerodynamic noise when the Mach number is low enough, such as in the case of a road vehicle at high cruising speed.

The source of aerodynamic sound due to the vortical motion is evaluated on the basis of the fluctuation of div $(\mathbf{u} \times \omega)$ (Pow-

Contributed by the Fluids Engineering Division for publication in the JOURNAL OF FLUIDS ENGINEERING. Manuscript received by the Fluids Engineering Division April 3, 1993; revised manuscript received March 14, 1994. Associate Technical Editor: O. Baysal.

ell, 1964; Howe, 1976), a source term of the Poisson equation for the Bernoulli-field of incompressible flow. Laufer (1974) explained that the noise due to the vortical motion is generated by the vortex pairing. Hussain (1983, 1986) argued in his analysis of aerodynamic noise in a circular jet, that the coherent structure breakdown process, rather than the vortex sound by vortex pairing, is the dominant mechanism of noise generation.

Both of the vortex pairing and breakdown, as well as flow separation, can be considered as a kind of bifurcation or breakdown of flow geometry. For low-Mach-number flow, it can be assumed that the pressure fluctuations are generated through a kind of bifurcation or breakdown of flow geometry. For example, the first-order pressure fluctuations may be produced by the flow separation itself, a kind of bifurcation of flow geometry by the interaction between the mean flow and the A-pillar of an automobile. Thus, the drastic increase in SPL versus the inclination angle of the A-pillar indicates that there is some change in flow geometry. It is essential to elucidate this change in flow geometry to understand the aerodynamic noise about the A-pillar of a road vehicle. This understanding also may be directly of help to understand the mechanism of coherent structure in turbulence.

The objective of this study is to understand the relationship between the external flow structure and the surface pressure fluctuations with the help of time-dependent and full Navier-Stokes simulation. In order to simplify the problem, a car-like model is designed only employing the fore part with a sharp-edged front-pillar. The flow separation line is predetermined and then there is only one kind of leading-edge type laminar-flow separation about the A-pillar.

As discussed by George (1990), at low Mach numbers, the dipole source of sound is due to the unsteady pressure and the quadrupole is due to the turbulence. The quadrupole strength divided by the dipole strength is directly proportional to the Mach number squared. For the case of interest in this work, the Mach number of a 100km/h cruising speed is 0.0857. Then the quadrupole strength associated with turbulence is only about 0.735 percent of the dipole strength. This is why the unsteady pressure is considered as a major sound source of the wind noise about the A-pillar of an automobile. Therefore, it may be possible to employ a flow model of a incompressible Navier-Stokes system (without turbulence model) for the numerical simulation of this kind of low-frequency pressure-field dominant separating flow. It will be assessed throughout this study, that this consideration regarding numerical modeling of a separating flow about the front-pillar of a car-like body is correct.

In Section 2, at first, the numerical method used is briefly described. The theoretical considerations on the analysis of vortical motion related to the wind noise generation are presented. The conditions of simulation are given and the numerical grid resolutions are validated through numerical testing. In Section 3, the analysis of the numerical results are carried out. The surface pressure fluctuation intensity is predicted quantitatively by using a simplified formulation of Lighthill-Curle's equation. The simulated results are assessed by comparison with the acoustic theory. A sophisticated analysis is performed for elucidation of vortical structure related to the wind noise generation. The relationships between the coherent turbulence structure and the wind noise are discussed and clarified. Some concluding remarks are given in Section 4.

## 2 Numerical Prediction Method

**2.1 Numerical Method.** A well-documented commercial code called SCRYU$^{TM}$ (Manual of SCRYU, 1992) is used in this study. The incompressible Navier-Stokes equations are discretized in the generalized boundary-fitted coordinates system. A third-order upwind TVD (MUSCL-type) scheme is employed for the convection term. It is a time accurate method in a MAC-type algorithm. The details of the method are abbreviated here. The numerical uncertainties will be validated and assessed in the subsequent sections. It will be recognized that this numerical method is quite accurate and stable for the simulation of a separating flow about the sharp-edged front-pillar of a car-like body.

**2.2 Analysis Method.** Since the dipole source due to the unsteady pressure is a dominant source of wind noise in this study, a simplified Lighthill-Curle's equation (Lighthill, 1951; Curle, 1955) is employed as follows to evaluate the surface pressure fluctuation intensity.

$$p_f(\xi, t) = \frac{L_0}{4\pi c} \frac{\partial p(\xi, t)}{\partial t} \quad \text{(Pa)} \tag{1}$$

where

- $p_f$: surface pressure fluctuation intensity at every numerical point $\xi$ on the front-side window surface $\partial\Omega$;
- $p$: simulated unsteady pressure;
- $c$: speed of sound;
- $L_0$: characteristic length being set at 1.0.

Therefore, the pressure fluctuation level (PFL) analogous to the sound pressure level (SPL) is defined as follows:

$$\text{PFL} = 10 \log_{10}\left(\frac{p_f}{p_0}\right)^2 \quad \text{(dB)} \tag{2}$$

where $p_0$ is the base sound pressure set at $2\times10^{-5}$ (Pa). The total surface pressure fluctuation $p_{fa}$ over the front-side window surface is calculated by integrating Eq. (1) over the front-side window as follows:

$$p_{fa} = \frac{1}{L_0^2}\int_{\partial\Omega} p_f(\xi, t)dS(\xi) = \frac{1}{4\pi c L_0}\frac{\partial}{\partial t}\int_{\partial\Omega} p(\xi, t)dS(\xi) \quad \text{(Pa)} \tag{3}$$

In this study, "total" means the physical value of an integrated one over the front-side window surface while "overall" means the physical value level of integrated spectra over Fourier space.

The algorithm of analysis is as follows: Once the flow fields are solved about the car-like body, the time sequences of unsteady pressure at every numerical point on the front-side window are recorded as well as the near-field velocity data. The surface pressure fluctuation intensities are calculated from Eq. (1) and their PFLs from Eq. (2). By means of the fast Fourier transformation (FFT) technique, PFLs are transformed into frequency domain and calculated for frequencies corresponding to the preferred 1/3-octave band-center frequencies. The total surface pressure fluctuation is calculated from Eq. (3) and its 1/3-octave power spectrum is calculated by FFT. In order to extract the characteristic scale of flow structure, the frequency is nondimensionalized in a Strouhal scaling manner as follows:

$$\hat{f} = \frac{fL_0}{V_m} \tag{4}$$

where $V_m$ is the vehicle cruising speed.

In order to study the vortex structure related to the production of surface pressure fluctuations, in this paper, the vorticity is decomposed into the following two parts as shown in Fig. 1.

The helicity or Lamb scalar:

$$L_s = \boldsymbol{\omega}\cdot\mathbf{u} \tag{5}$$

the inertial vortex force or Lamb vector:

$$L_v = \boldsymbol{\omega}\times\mathbf{u} \tag{6}$$

where $\boldsymbol{\omega}$ is the vorticity vector and $\mathbf{u}$ is the velocity vector. The swirl angle $\Psi$ of the vortex is defined as the angle between the

velocity vector and the vorticity vector in order to study the evolution of the vortex structure in this study.

For the incompressible flow, the Poisson equation for the Bernoulli quantity can be written into the following form:

$$\text{div grad } B = -\text{div } L_v \tag{7}$$

where

$$B = \frac{1}{2}\rho \mathbf{u}^2 + p \tag{8}$$

where $\rho$ is the fluid density. On the body surface, the velocity is set at zero so that the pressure is determined by the local divergence of inertial vortex force or Lamb vector. The hypothesis raised in this study is that the bifurcation of flow geometry is represented by the generation of helical vortex (longitudinal vortex) which induces the fluctuations of the flow fields. This analysis is based on the fact, that when the flow over a flat plate with an infinite extension, the turbulence is starting to be accompanied by a kind of bifurcation of flow structure, i.e., the generation of the streamwise vortex streets over the plate. This kind of streamwise vortex streets (corresponding to the helicity, i.e., the shear flow corresponding to the inertial vortex force), is responsible for the fluctuations of the flow field. Therefore, the fluctuations of the flow field such as in the case of this study may have the similar mechanism.

**2.3 Condition of Simulation.** Figure 2 is the base car-like model and its grid. The full length of this model is 4 m and the height is 1.3 m. The front-pillar has a sharp edge, so that the separation line is predetermined. The streamwise inclinations of the front-pillar $\theta$ are set at 30, 45, 52.5, 60 and 75 deg. The cruising speeds $V_m$ are set at 75 km/h, 100 km/h and 150 km/h, which correspond to the Reynolds number at $5.34\times10^6$, $7.12\times10^6$ and $1.07\times10^7$, respectively, with the vehicle length used as the length scale. The non-slip boundary condition of velocity is imposed on the car-body. A uniform streamwise velocity of the cruising speed is set at the inflow boundary, and the pressure is set at zero at the outer boundary.

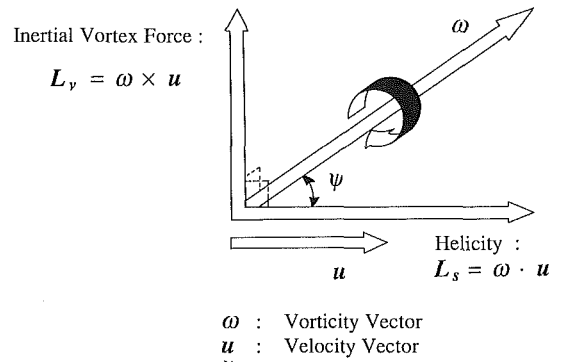


**Fig. 1 Decomposition of vorticity component**

Free slip condition is set at the centerline boundary and the ground boundary. Open conditions are set at the lateral boundary. Since the surface pressure fluctuations due to the flow separation are of the most interest and neither the near-field nor the far-field acoustic wave equations are being solved in this study, the boundary conditions are set only for the unsteady aerodynamic field and may be not so tremendous as in the case of direct computation of aerodynamic sound generation (Colonius et al., 1993).

The time step is updated when the maximum pressure residual is smaller than $\delta p = 10^{-5}$ Pa. The time increment is set at $\delta t = 1\times10^{-4}$ seconds so that the maximum Courant number in the calculation is smaller than 0.4. The sampling time is about 0.5 or 0.6 seconds for every case. This sampling time corresponds to more than 4 dimensionless times and seems to be enough for a separation flow about the A-pillar. The computation was carried out on CRAY-YMP supercomputer at ISUZU Motors, Ltd. Every case of computation took about 45 hours of CPU time. With the pressure residual criterion and time increment, the permissive error for the surface pressure fluctuation intensities at every numerical point can be calculated from Eqs. (1) and (2) in the following way,

$$\text{permissive error} = 10\log_{10}\left(\frac{L_0}{4\pi c p_0}\frac{\delta p}{\delta t}\right)^2 \cong 1.37 \quad \text{(dB)} \tag{9}$$

**2.4 Numerical Test.** It is very important to carry out the numerical validation to show the capability of numerical method and the accuracy of numerical solution. Grid resolution is one of the most important targets in the numerical validation. In this study, as shown in Table 1, four grid cases are considered regarding the physical case when the A-pillar inclination $\theta$ is 30 deg and the cruising speed $V_m$ is 100 km/h. Figure 3 shows the time sequences of the predicted total surface pressure fluctuation levels (PFLs) at four grid cases. It is obvious that Grid A and B are too coarse to reveal the surface pressure fluctuations in time. Figure 4 is the comparison of the 1/3-octave total PFL spectra between four grid cases. It can be said that the spectra of Grid C and D have almost the same behavior especially for the two dominant humps over the low-frequency region (for details of these humps see next section). The overall values of PFL $P_{OA}$ and the relative errors $\epsilon_{RE}$ between Grid D and others are calculated as shown in Table 1. The relative error between Grid D and C is about 2 percent and the absolute error is 1.095 dB. Compared with permissive error of Eq. (9), the absolute error is small. Therefore, Grid C and D may be the smallest grid resolution required for the problem of interest here. Hence, in this study, Grid D

**Table 1 Numerical grid resolution**

| Case | Grid | $P_{OA}$ (dB) | $P_{OA}^{D}$-$P_{OA}$ (dB) | $\epsilon_{RE}$ (%) |
|---|---|---|---|---|
| A | 50,430 | 32.880 | 12.032 | 26.79 |
| B | 91,200 | 38.803 | 6.109 | 13.60 |
| C | 114,608 | 43.817 | 1.095 | 2.44 |
| D | 144,652 | 44.912 | — | — |

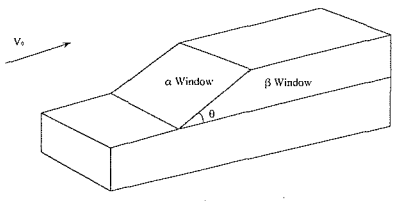


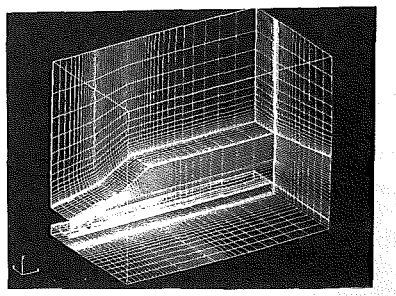

**Fig. 2 Base car model and grid**

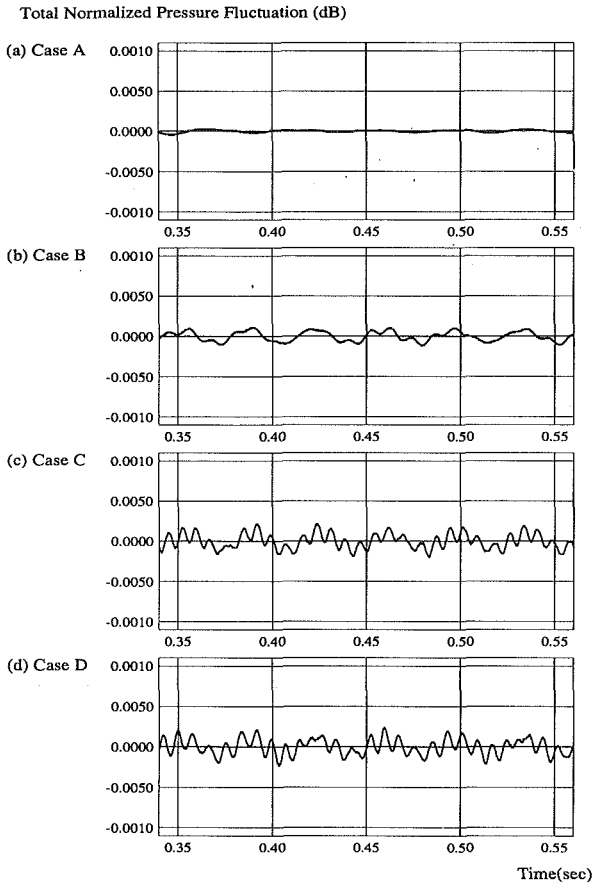


**Fig. 3 Numercial grid resolution (1): time sequence of total surface pressure fluctuations upon the front-side window of different grid ($\theta = 30$ deg)**

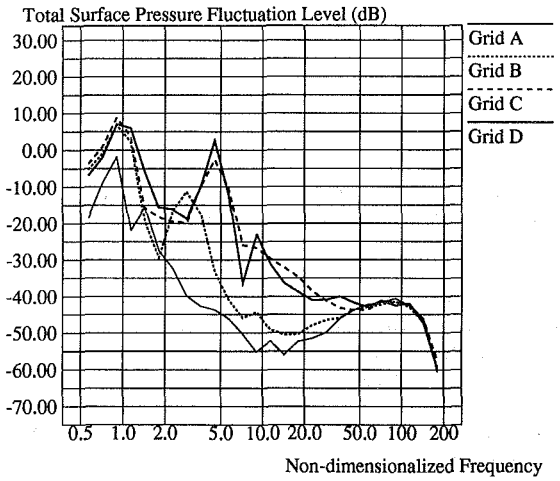


**Fig. 4 Numerical grid resolution (2): 1/3 octave spectra of predicted total surface PFL ($\theta = 30$ deg)**

with the resolution of 144,652 grid points is adopted in all of the simulation cases.

Therefore, for the problem of interest of this study, both the numerical method used and the simulation conditions including grid resolution seem to be well posed. As shown in the subsequent sections, the characteristic length-scale of the separated vortices behind the front-pillar, analogue to that of a delta-wing (George, 1990), is approximately in unit order compared with $L_0$ (Eq. (1)). The simulated results show that those separated vortices are resolved by employing Grid D which has

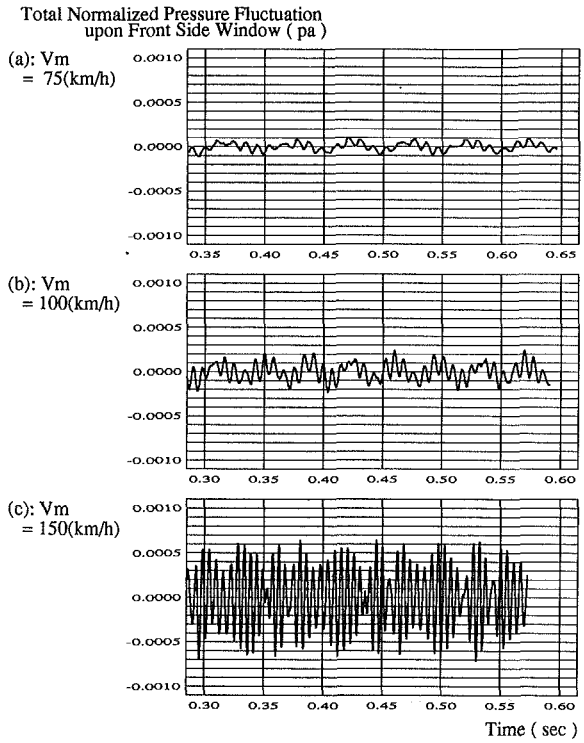


**Fig. 5 Time sequence of total surface pressure fluctuations upon the front-side window ($\theta = 30$ deg)**

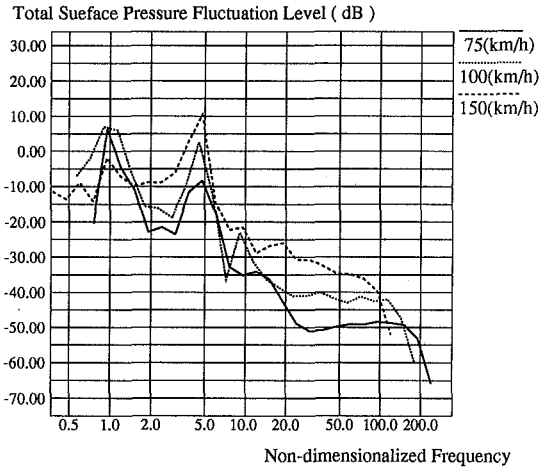


**Fig. 6 1/3 Octave spectra of predicted total surface PFL ($\theta = 30$ deg)**

been validated in the present section. Furthermore, the dimensionless frequencies of most energy-containing flow structures are in the relatively lower region of Fourier space (see next section). These frequencies are far smaller than those for the equilibrium-range of turbulence represented by the Kolmogorov microscale of time $\tau = (\nu/\epsilon)^{1/2}$ (Tennekes and Lumley, 1972), where $\epsilon$ is the turbulent dissipation rate and $\nu$ is the kinematic viscosity.

## 3 Analysis of Numerical Results

**3.1 For Vehicle Cruising Speed.** Figure 5 shows the time sequence of predicted total surface pressure fluctuation levels (PFLs) at three cruising speeds when the front-pillar inclination $\theta$ is 30 deg. It indicates that the pressure fluctuation levels over the panel increase as the cruising speed is increased. Figure 6 is the comparison of the 1/3-octave total PFL spectra between

Table 2 Frequency of coherent structure

| $\hat{f}$ | $V_m$ (km/h) | $f$ (Hz) | $\omega\ (=2\pi f)$ |
|---|---|---|---|
| 0.904 | 75 | 18.833 | 118.33 |
| | 100 | 25.111 | 157.78 |
| | 150 | 41.091 | 257.61 |
| 4.352 | 75 | 90.667 | 569.68 |
| | 100 | 120.889 | 759.57 |
| | 150 | 181.333 | 1139.35 |

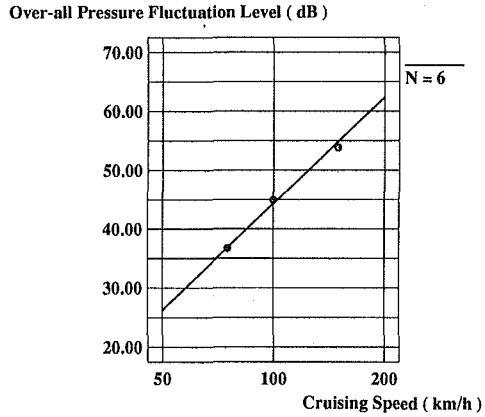


Fig. 7 Over-all predicted surface PFL versus vehicle cruising speed ($\theta = 30$ deg)

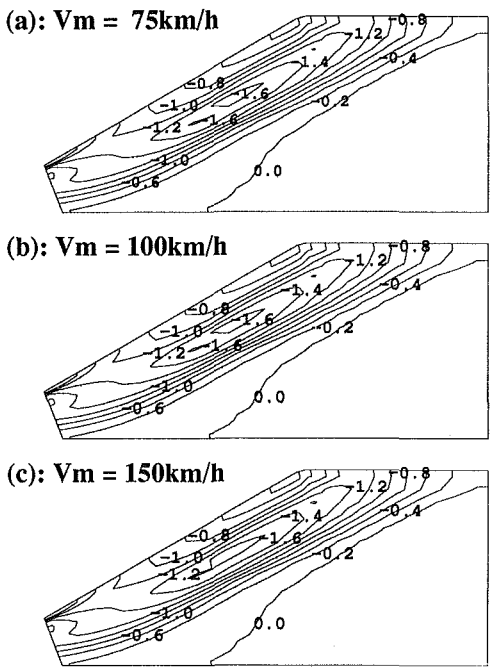


Fig. 8 Time-averaged surface pressure distribution upon the front-side window ($\theta = 30$ deg)

three cruising speeds. It is obvious that the spectra of these three cases have a similarity of phase coherence when the frequency is nondimensionalized in a Strouhal scaling manner, indicating that there are coherent structures when the front-pillar inclination $\theta$ is 30 deg. The humps of spectra correspond to the characteristic scales of flow structure about the front-pillar. The dimensionless frequencies of first two humps is 0.904 and 4.352. Table 2 shows the actual frequencies of these two humps at different cruising speeds, respectively. It is noted that the second hump seems to correspond mostly to the wind noise generation when the cruising speed exceeds 100 km/h in this case. It is also very interesting to note that the first hump

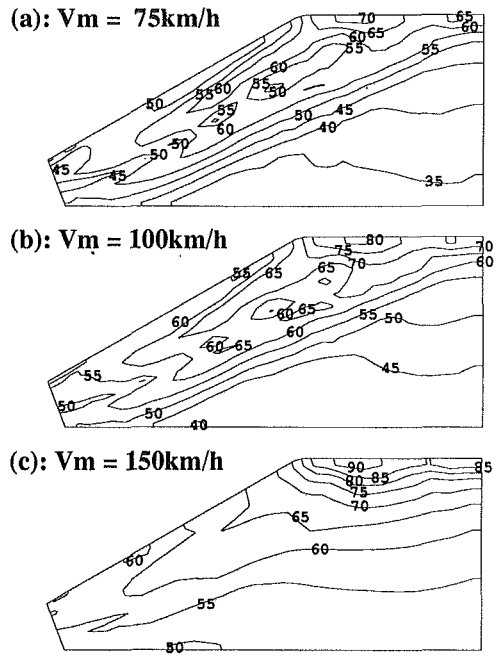


Fig. 9 Overall surface pressure fluctuation intensity upon the front-side window ($\theta = 30$ deg)

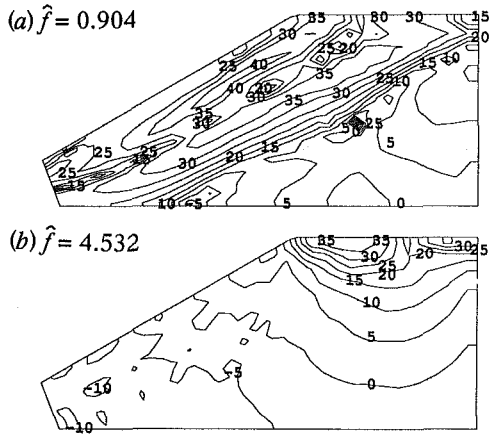


Fig. 10 Surface pressure fluctuations upon the front-side window at $\hat{f} = 0.904$ and $\hat{f} = 4.532$ ($V_m = 100$ km/h, $\theta = 30$ deg)

does not change much except when $V_m = 150$ (km/h). But the second hump increases with the increase of cruising speed. By integrating the spectra of Fig. 6, as shown in Fig. 7, one can find that the simulated results reveal fairly well the dependency of the over-all pressure fluctuation level upon the sixth power-law of vehicle cruising speed, i.e., the acoustic theory of dipole sound source. Therefore, the numerical results in this study can be used for the analysis of flow separation related to the wind noise generation.

The simulated time-averaged pressure contour maps on the panel at the three cruising speeds ($\theta = 30$ deg) are shown in Fig. 8. The pressure distribution has almost the same pattern for these three cases at different cruising speeds. The over-all PFL intensity distribution on the panel is shown in Fig. 9. One can find that the PFL intensities about the roof-side window junction increase much more significantly than those behind the front-pillar. The difference of strongest intensity at these two places is 5 dB at 75 km/h, 15 dB at 100 km/h and almost 30 dB at 150 km/h, while the maximum pressure fluctuation behind the front-pillar stays at about 60 dB to 65 dB. Therefore, these two kinds of sources show a different dependence on the

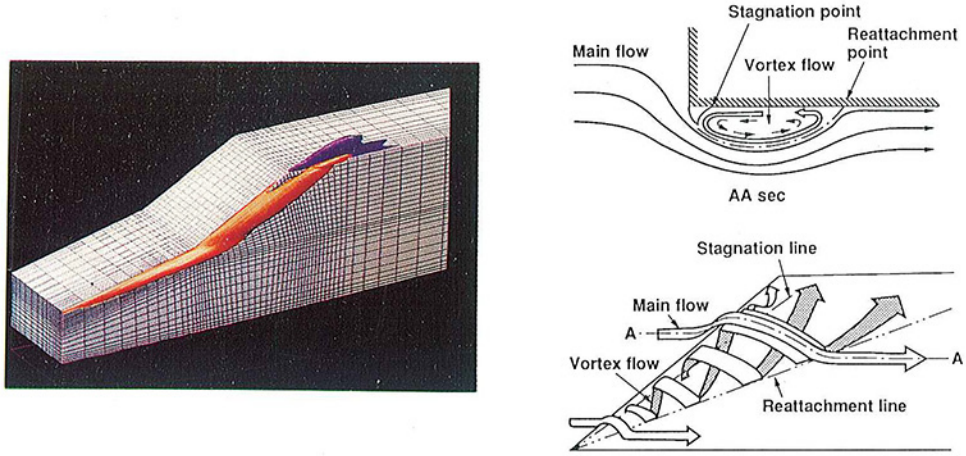


Fig. 11 Iso-helicity surface contour about the front-pillar ($\theta = 30$ deg) with the schematic of flow field behind A-pillar (Watanabe et al., 1978)

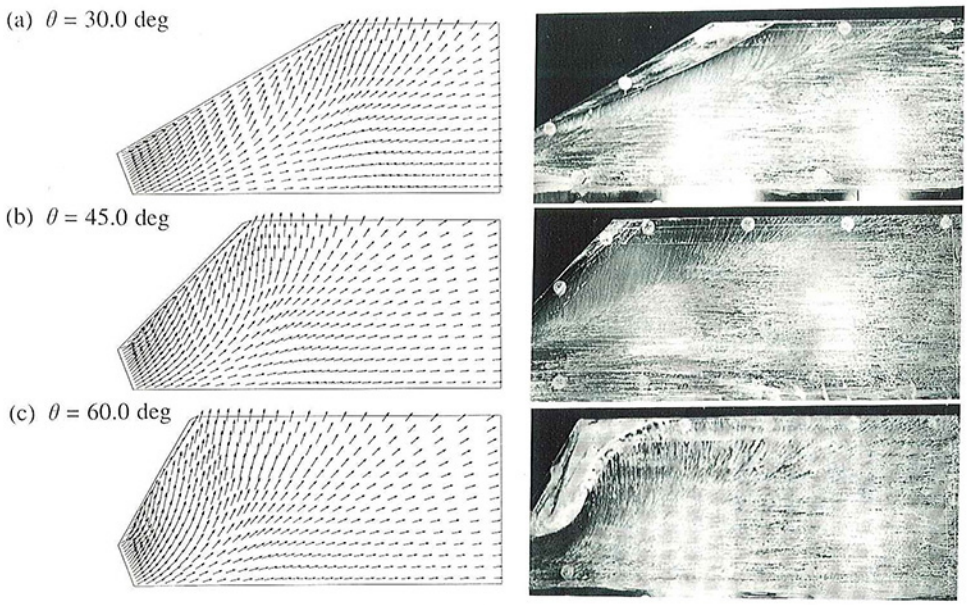


Fig. 12 Comparison of streamlines on the front-side window surface between the numerical simulation and the visualization experiment

cruising speed and hence may have resulted from a different kind of flow structure. Figure 10 is the pressure fluctuation intensity distribution over the panel at dimensionless frequency $\hat{f} = 0.904$ and at $\hat{f} = 4.352$, respectively. It can be found that there are different flow structures at the different frequency humps of the spectrum, that is, the first hump is related to the flow separation from the sharp-edged front-pillar and the flow reattachment on the panel while the second hump is related to the interaction of separated vortices at the roof-side window junction.

In order to clarify the flow structure about the front-pillar associated with the generation of pressure fluctuations, the iso-helicity contour surface about the front-pillar is shown in Fig. 11, where the red portion denotes the positive value and the blue denotes the negative one. The positive helicity corresponds to the separated vortex core and the negative one is generated by another flow separation of the growing-up flow at the roof-side window junction corner. It is very interesting to note that, when the proper values of the helicity contour are chosen, they exhibit a very distinct overlapping in the region where the pressure fluctuation levels are large. This means that the three-dimensional helicity contour shows a quite distinct conical vortex structure of separation from the sharp-edged front-pillar, similar to the case shown by Watanabe et al. (1978). Therefore, it is clear that the first hump is related to the flow separation while the second hump is related to the vortex-vortex interaction between the vortices with opposite signs, that is, a kind of vortex pairing at the roof-side window junction corner.

**3.2 For the Front-Pillar Inclination.** The comparisons of time-averaged velocity vector at the first grid points from the body surface and the visualization measurement by means of an oil film are shown in Fig. 12. Experiments are carried out by using 1/5 scale models of those in the computation for three inclination angles. The streamwise speed is 30 m/s (108 km/h) which corresponds to the Reynolds number of $1.54 \times 10^6$. Although the Reynolds number is different between the computation and the experiment, the directions of the simulated velocity vector show fairly good agreement with the experiment. This means that the reattachment line is quite well predicted in the computation, while the separation line is known to occur at the sharp edge of the front-pillar. There are stagnations of flow in the vicinity of the roof-side pillar corner especially in the case at 60 deg, indicating that there is a com-

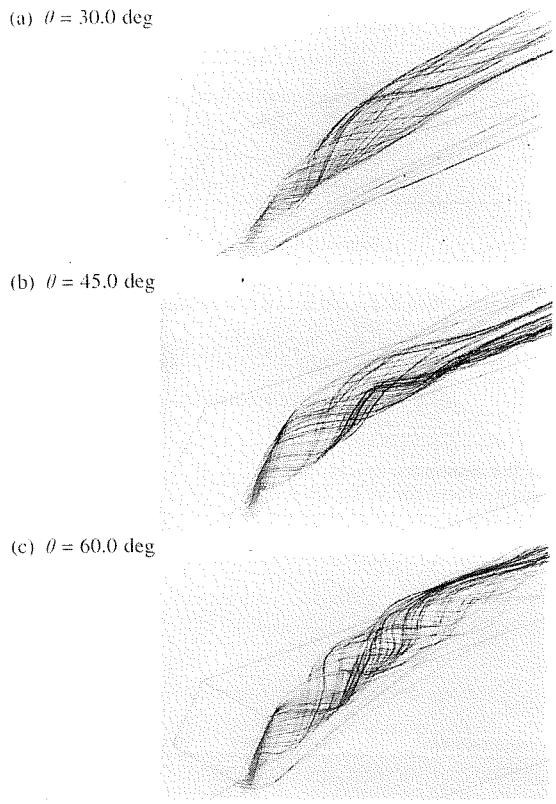


Fig. 13 Flow streamline about the front-pillar

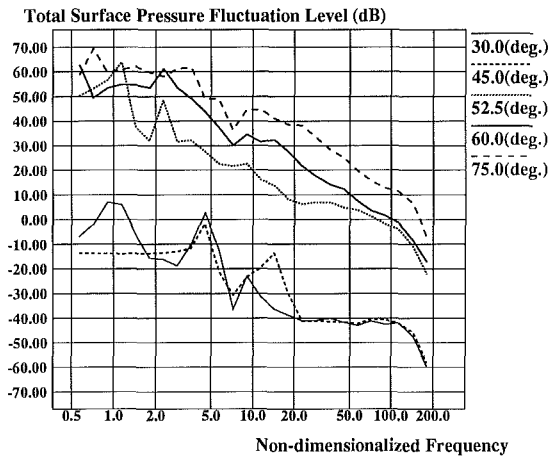


Fig. 14 1/3 octave spectra of predicted surface PFL ($V_m$ = 100 km/h)

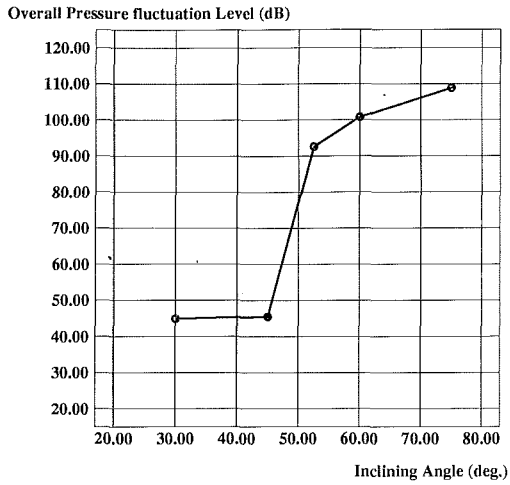


Fig. 15 Overall surface PFL versus the inclination of front-pillar

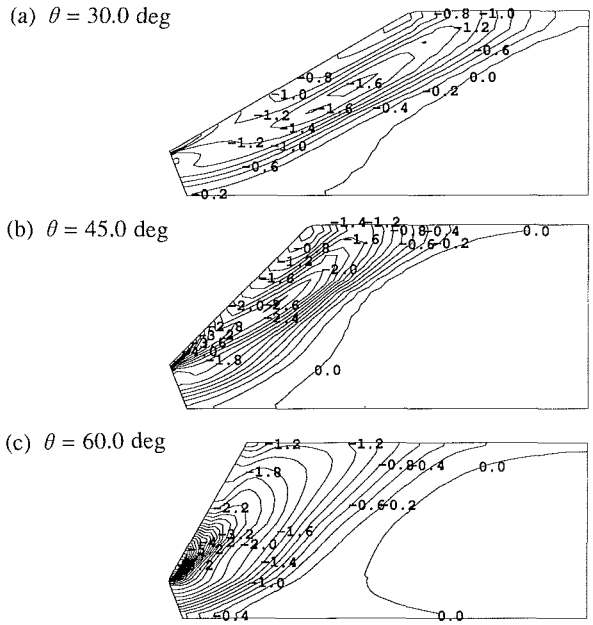


Fig. 16 Time-averaged surface pressure distribution upon the front-side window ($V_m$ = 100 km/h)

plicated flow structure associated with three-dimensional flow separation. The simulated streamlines about the front-pillar in three cases of inclination angle, 30 deg, 45 deg, and 60 degrees are shown in Fig. 13. It is worth mentioning that the streamlines at 60 deg show a much more divergence feature than the other two cases of smaller inclination.

The comparison of 1/3 octave total PFL spectra between five inclination angles of front-pillar when $V_m$ = 100 km/h is shown in Fig. 14. It is noted that there are quite different levels of spectra as well as the spectrum pattern between the two smaller-angle cases, i.e., 30 deg and 45 deg, and other three larger-angle cases. For 30 and 45 deg, the spectrum levels are small and have a relatively distinct coherent structure pattern. In contrast, the spectra of the three cases of larger angle show a higher level in magnitude and a continuous distribution over a broadband of frequency. It may be easy to recognize the distinct flow structure scale at a small inclination angle, such as those shown in the previous subsection when $\theta$ = 30 deg. However, for instance, when the inclination angle is 60 deg, one could not find that kind of distinct flow structure scale but could see the excited continuous flow spectra at almost every frequency, i.e., a distinct onset of turbulence.

The overall total PFL spectra versus inclination angles is shown in Fig. 15, indicating that there is a critical angle for PFL between 45 deg and 50 deg which was implied in the experimental investigation by Sadakata et al. (1988). Therefore, the sudden change before and after the critical angle is due to some change of flow structure. The time-averaged pressure distribution is shown in Fig. 16 at three inclination angles, i.e., 30 deg, 45 deg, and 60 deg. The time-averaged pressure distributions show the existence of a separated vortex core and a large gradient of unsteady pressure over the panel, especially for the case of 60 deg.

The time sequences of the iso-helicity surface contour about the 45-deg front-pillar are shown in Fig. 17(*a*), those at 52.5 deg in Fig. 17(*b*), and at 60 deg in Fig. 17(*c*). The most distinct differences between these three cases are as follows: For 45

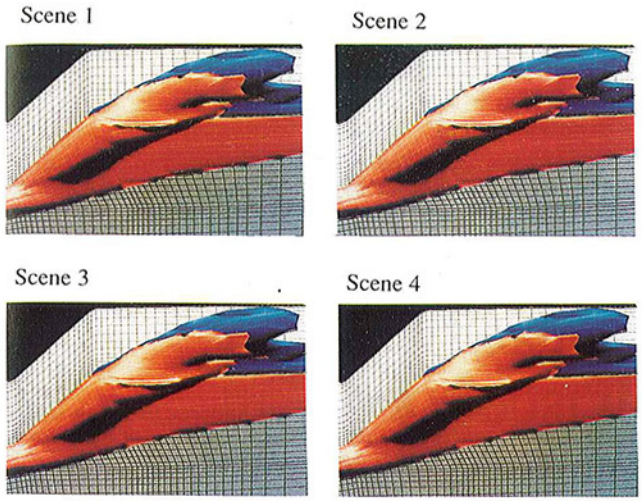


Fig. 17(*a*) Iso-helicity surface contour about the front-pillar ($\theta = 45$ deg)

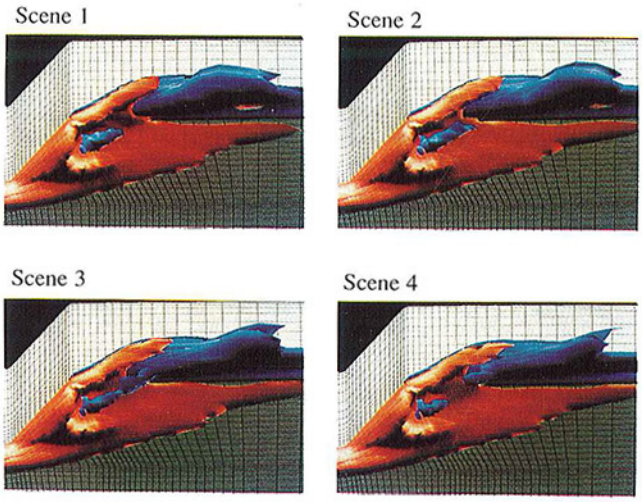


Fig. 17(*b*) Iso-helicity surface contour about the front-pillar ($\theta = 52.5$ deg)

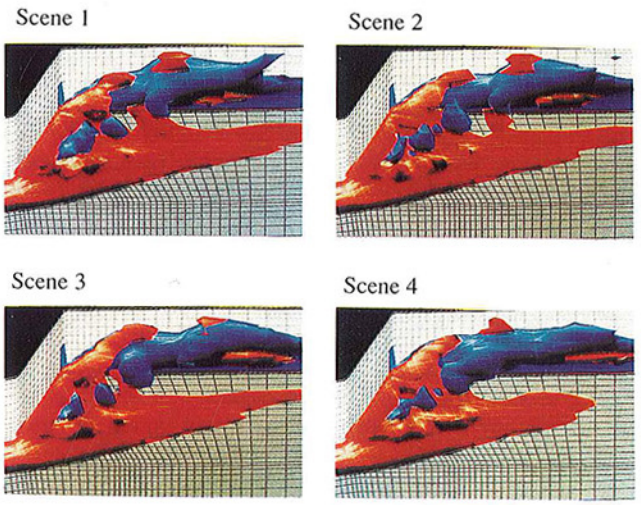


Fig. 17(*c*) Iso-helicity surface contour about the front-pillar ($\theta = 60$ deg)

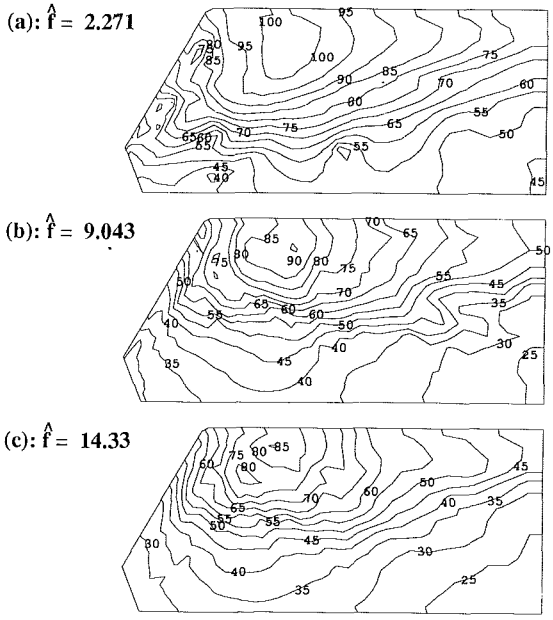


Fig. 18 Comparison of predicted pressured fluctuation intensity upon the front-side window at three frequencies ($\theta = 60$ deg)

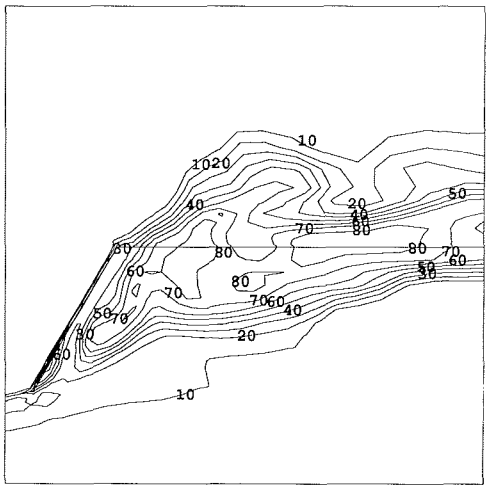

Fig. 19 Swirl angle distribution in the vicinity of front-side window ($\theta = 60$ deg)

deg, the helical vortex is almost steady in time, but for 52.5 deg and 60 deg, the helical vortices show an unsteady flow behavior over the front-side window, that is, the formation of an excessive amount of separated vortices, their burst and breakdown in time. Moreover the unsteadiness at 60 deg is much more significant than that at 52.5 deg. Therefore, it is supposed that the drastic change in overall PFL is due to the change in helical vortex behavior before and after the critical angle of front-pillar inclination.

The PFL intensity distributions of three frequencies on the front-side window surface with 60-deg inclination is shown in Fig. 18. One can observe that the portions of the strongest intensity correspond to those where the vortex is broken down as shown in Fig. 17(*c*). Therefore, it can be said that the vortex breakdown may make a significant contribution to the wind noise generation. Regarding the vortex breakdown problem, there are various opinions on its critical criterion (Leibovich, 1984, 1991). Hall (1972) used the following three conditions for the definition of vortex breakdown: 1) the critical swirl angle of the vortex tube is about 40 deg, 2) there is a positive or adverse gradient of pressure in the vortex axis direction and 3) a divergence of the streamline tubes in the vortex core. In this study, it is obvious that the last two conditions are satisfied, that is, from Fig. 16 for pressure gradient and Fig. 13 for divergence of streamline tube. In order to verify the first con-

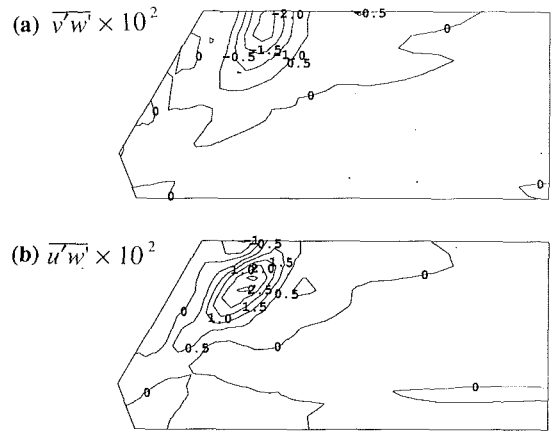


**Fig. 20 Reynolds shear stress distributions in the vicinity of front-side window ($\theta = 60$ deg)**

dition of critical swirl angle, the swirl angle about the vortex core in 60-deg inclination is shown in Fig. 19. All features of swirl angle are like those of a vortex "jet" spreading over the front-side window surface. The critical angle defined by Hall (1972) corresponds only to "the nozzle of jet" in this study which is the burst point of the vortex. The largest swirl angle almost exceeds 80 deg at the portion where the pressure fluctuation intensities are strongest.

The Reynolds shear stresses distributions in the vicinity of the front-side window are shown in Fig. 20. The shear stresses of maximum intensity are again distributed on the portion where the pressure fluctuations are strongest. This result is relevant to the analysis by Simpson et al. (1987) on the generation of effective pressure fluctuations, indicating an "occurrence of vortex breakdown—generation of maximum shear stresses—production of pressure fluctuations" mechanism of wind noise about the front-side window surface.

## 4 Concluding Remarks

This study showed that when the Mach number is low and the influence of boundary layer is small, the wind noise due to the laminar flow separation can be qualitatively predicted based on the time-dependent Navier-Stokes solution.

The bifurcating processes of flow geometry, such as flow separation and vortex breakdown, may correspond to the mechanism of wind noise generation. The bifurcation of flow geometry is represented by the generation of a helical vortex (longitudinal vortex) which induces the fluctuations of flow fields. This finding is relevant to the hypothesis that the flow cascade in turbulence requires a specific phase coherence of helicity-associated fluctuations (Tur and Levish, 1992).

The most interesting finding in this study is the issue of vortex breakdown responsible for the sudden noise increase at the inclined angles of front-pillar about 45–50 deg. This event is distinctly related to the onset of turbulence of the flow separating about the front-pillar, which is represented by the beginning of continuous spectra of the flow-fields fluctuations. Therefore the vortex breakdown may be considered as one of the most coherent structure in turbulence.

## Acknowledgment

This work is supported by ISUZU Motors, Ltd. The authors appreciate the assistance by Mr. K. Aoki, Mr. R. Ono and other colleagues at ISUZU. The authors are grateful for the valuable discussions by Prof. Albert R. George at Sibley School of Mechanical and Aerospacing Engineering, Cornell University, and for the helpful suggestions by the reviewers of this paper.

## References

Chou, S.-T., and George, A. R., 1987, "An Analytical Parametric Study of the Broadband Noise from Axial-Flow Fans," *Proceeding of Noise-Con 87*, Noise Control Foundation, New York, pp. 83–88.

Colonius, T., Lele, S. K., and Moin, P., 1993, "Boundary Conditions for Direct Computation of Aerodynamic Sound Generation," *AIAA Journal*, Vol. 31, No. 9, pp. 1574–1582.

Curle, N., 1955, "The Influence of Solid Boundaries Upon Aerodynamic Sound," *Proceeding of Royal Society of London*, Series A231, pp. 505–514.

George, A. R., 1990, "Automobile Aerodynamic Noise," SAE Paper 900315.

Hall, M. G., 1972, "Vortex Breakdown," *Annual Review of Fluid Mechanics*, Vol. 4, pp. 195–218.

Haruna, S., et al., 1990, "Estimation Method for Automobile Aerodynamic Noise," SAE paper 900316.

Howe, M. S., 1976, "Contributions to the Theory of Aerodynamic Sound, With Application to Excess Jet Noise and the Theory of the Flute," *Journal of Fluid Mechanics*, Vol. 71, Part 4, pp. 625–673.

Hussain, A. K. M. Fazle, 1983, "Coherent Structure—Reality and Myth," *Physics of Fluids*, Vol. 26, pp. 2816–2850.

Hussain, A. K. M. Fazle, 1986, "Coherent Structures and Turbulence," *Journal of Fluid Mechanics*, Vol. 173, pp. 303–356.

Laufer, J., 1974, "On the Mechanism of Noise Generation by Turbulence," University of South California, Aerospace Engineering 125.

Leibovich, S., 1984, "Vortex Stability and Breakdown: Survey and Extension," *AIAA Journal*, Vol. 22, No. 9, pp. 1192–1206.

Leibovich, S., 1991, "Vortex Breakdown: A Coherent Transition Trigger in Concentrated Vortices," M. Lesieur, O. Metais, eds., *Turbulence and Coherent Structure*, Dordrecht, Kluwer, pp. 285–302.

Lighthill, M. J., 1952, "On Sound Generated Aerodynamically Part I. General Theory," *Proceeding of Royal Society of London*, Series A211, pp. 564–587.

Manual of SCRYU, 1992; SCRYU-3D, A Thermal Fluid Analysis Program in Boundary-Fitted Coordinate System, CRADLE, Lt..

Maynard, J. D., et al., 1985, "Nearfield Acoustic Holography: Theory of Generalized Holography and the Development of NAH," *Journal of the Acoustical Society of America*, Vol. 78(4), pp. 2061–2068.

Powell, A., 1964, "Theory of Vortex Sound," *Journal of the Acoustical Society of America*, Vol. 33, pp. 177–195.

Sadakata, O., et al., 1988, "A Consideration of Wind Noise Reduction by Air Flow Control," SAE Paper 885115.

Simpson, R. L., Ghodbane, M., and McGrath, B. E., 1987, "Surface Pressure Fluctuations in a Separating Turbulent Boundary Layer," *Journal of Fluid Mechanics*, Vol. 177, pp. 167–186.

Simpson, R. L., 1989, "Turbulent Boundary-Layer Separation," *Annual Review of Fluid Mechanics*, Vol. 21, pp. 205–234.

Stapleford, W. R., and Carr, G. W., 1970, "Aerodynamic Noise in Road Vehicle, Part 1: The Relationship Between Aerodynamic Noise the Nature of Airflow," The Motor Industry Research Association, Report No. 1971/2.

Tennekes, H., and Lumley, J. L., 1972, *A First Course in Turbulence*, The MIT Press.

Tur, A. V., and Levich, E., 1992, "The Origin of Organized Motion in Turbulence," *Fluid Dynamics Research*, Vol. 10, pp. 75–90.

Watanabe, M., Harita, M., and Hayashi, E., 1978, "The Effect of Body Shapes on Wind Noise," SAE Paper 780268.

# Response of Two-Dimensional Separation to Three-Dimensional Disturbances

**Laura L. Pauley**
Associate Professor,
Department of Mechanical Engineering
The Pennsylvania State University
University Park, PA 16802.
Mem. ASME

*The present study investigates the development and structure of three-dimensionality due to a three-dimensional velocity perturbation applied to the inlet of an unsteady two-dimensional separation computation. A random noise perturbation and a sine-wave perturbation are considered separately. In both cases, the spanwise variations were amplified in the separation and within the shed vortices. The vortex shedding frequency observed in the two-dimensional computation was not altered by the three dimensionality of the flow field. No observable spanwise structure was produced by the random noise perturbation. The sine-wave perturbation, however, produced longitudinal Görtler vortices within the separation. Using a linear stability analysis, the presence of longitudinal vortices in a separated laminar boundary layer was predicted by Inger (1987). When the velocity field was averaged across the span, it was found that the sine-wave perturbation increased the separation length and reduced the strength of shed vortex. The span-averaged streamlines from the random noise perturbation, however, reproduced the unsteady separation of the two-dimensional computations.*

## Introduction

Separated flows at the tip and base of airfoils, turbine blades, and hydrofoils are three-dimensional and often complex. Along much of a high aspect ratio foil, however, the pressure gradient is primarily in the streamwise direction. Locally, spanwise variations in the pressure and velocity fields are often negligible. Studies of separation in two-dimensional geometries can therefore reveal many characteristics of boundary layer separation seen in applications. The present study is a numerical investigation of low Reynolds number separation. The applied adverse pressure gradient will be uniform across the span of the three-dimensional domain. Although the resulting separated region is primarily two-dimensional, boundary layer instability will produce three-dimensionality. By adding an inflow velocity perturbation, the growth and nature of three-dimensional instabilities will be examined.

Many experimental studies have investigated laminar boundary layer separation produced in a two-dimensional geometry. Flow visualization of Werlé (as reported by McCroskey, 1977) and Koromilas and Telionis (1980) show large-scale vortex shedding from the primary (fixed) separation. Several investigators including Brendel and Mueller (1988) and Zaman et al. (1989) have reported that vortex shedding occurred across the span of the airfoil and produced a two-dimensional unsteady separation (except near the tunnel side walls). The investigations found a clearly defined steady separation line extending across the span of the airfoil. Shedding of spanwise vortices occurred at an observable period. The reattachment point and shed vortex were nearly uniform across the span of the tunnel, however, some spanwise variation could be observed. Downstream of separation, velocity measurements also identified a low frequency velocity oscillation characteristic of vortex shedding. These investigations found that the large-scale laminar vortex shedding was the dominant mechanism causing the unsteadiness of the separated region. Of course, small-scale turbulence is also present and produces three-dimensionality. The large-scale unsteady vortex structures, however, are observed as primarily two-dimensional.

Mabey (1972) summarized those experiments which gathered low frequency surface pressure measurements and found that the amplitude of the fluctuations in a separation bubble increased gradually from the separation line, reached a maximum near reattachment, and then slowly decreased downstream of reattachment; but offered no hypothesis to describe the underlying structure that caused the fluctuations. These observations are consistent with vortex shedding from the separation where velocity fluctuations are reduced as the shed vortex dissipates downstream. McCroskey (1977) summarized studies which investigate unsteady boundary layer behavior including unsteady separated flows.

Oil film visualization can be used to identify the time-averaged surface topology of a separated region. Arena and Mueller (1978) and Winkelmann and Barlow (1980), have identified spanwise variations of the separation using oil film visualization. A scalloped reattachment line was visible, indicating that three-dimensional eddy formations were positioned at preferred locations across the span of the tunnel. It was not de-

Contributed by the Fluids Engineering Division for publication in the JOURNAL OF FLUIDS ENGINEERING. Manuscript received by the Fluids Engineering Division August 3, 1993; revised manuscript received February 16, 1994. Associate Technical Editor: W. S. Saric.

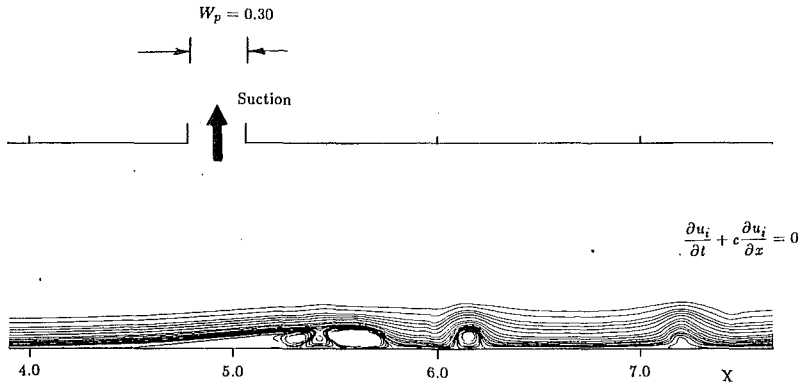


**Fig. 1 Computational domain**

termined if the structures were created by the inlet conditions, surface conditions, or hydrodynamic instabilities.

When a boundary layer separates from a surface, the path of the shear layer is turned and therefore has curvature. The curvature of the shear layer can produce streamwise vortices due to a Görtler instability. By considering the Reynolds number and separation angle of several experimental studies, Inger (1987) found that the Görtler instability will grow under many typical airfoil operating conditions which produce laminar boundary layer separation. An analysis of the eigenvalue problem showed that the longitudinal vortices will have a spanwise wavelength that is two to four times the boundary layer thickness. Previously, Inger (1977) had shown that the spanwise pressure variations in a separation experiment by Ginoux (1965) were due to Görtler vortices.

In the present paper, the source of the experimentally observed spanwise nonuniformities is investigated through numerical computations. A small three-dimensional velocity perturbation is added at the inlet of a previously two-dimensional boundary layer separation computation. Two forms of inlet perturbation are considered. In one case, random noise is added at the inlet of the computational domain. The second case considers the three-dimensionality produced by an inflow perturbation containing only one wavelength. The three-dimensional computations use periodic boundary conditions at the side walls which allow an investigation of various three-dimensional effects without the side wall influence found in experimental studies.

## Problem Definition

**Geometry.** The geometry of the computational study is shown in Fig. 1. The geometry is uniform in the spanwise direction ($Z$ direction). The geometry was designed to produce a localized separation using well described boundary conditions. The laminar boundary layer on one wall (the "test wall"), which developed under zero pressure gradient, was exposed to a local adverse pressure gradient by suction through a port on the opposite wall (the "control wall"). Throughout the entire computation of the two-dimensional separation, the freestream velocity upstream remained uniform and steady.

The flow variables are non-dimensionalized using the channel height $h$ and upstream approach velocity $u_0$. Lower-case symbols are dimensional quantities and capital letters denote nondimensional variables. For example, $X = x/h$, $Y = y/h$, $U = u/u_0$, $T = tu_0/h$. The upstream edge of the suction port is at $X = 4.77$ and the length of the suction port is 0.30. The computational domain extends from $X = 3.89$ to $X = 7.68$. The domain width is 1.1, approximately eight times the boundary layer thickness near separation.

The strength of the pressure gradient was set such that the test wall boundary layer would separate. The thickness of the separated region does not exceed 20 percent of the channel height, thus, effectively producing an external boundary layer flow with an imposed pressure gradient. Therefore, the response of the boundary layer is rather insensitive to the manner with which the adverse pressure gradient was imposed. To initiate the two-dimensional computations, the adverse pressure gradient was applied to a previously zero pressure gradient boundary layer. Shortly after the pressure gradient was applied, vortex shedding occurred from the separation. The two-dimensional computation was continued until limit cycle vortex shedding was reached. Details of the two-dimensional computations can be found in Pauley et al. (1990), herein denoted as PMR.

In order to examine the response of the two-dimensional separation to three-dimensional disturbances, spanwise noise was added at $T = 0$ to the inlet of an otherwise two-dimensional flow field. The initial condition across the channel span applied the two-dimensional limit cycle solution for $\mathrm{Re}_x = 120$, 544 and 22 percent of the throughflow removed at the suction port. The Reynolds number, $\mathrm{Re}_x$ is based on the inflow freestream velocity and the streamwise location of the upstream edge of the suction port. This location is also the approximate location of the separation point. The noise added at the inlet of the computational domain was held fixed in time. Two different types of noise were added to the solution at the inlet of the domain. In one case, random noise was added to approximate the effects of freestream turbulence found in an experiment. In another case a perturbation containing only one wavelength was applied, simulating a freestream perturbation which may be produced experimentally by upstream flow conditioning elements.

**Numerical Computation.** The fractional timestep method developed by Kim and Moin (1985) was used to solve the unsteady incompressible Navier-Stokes equations with constant viscosity. The method is second-order accurate in space and time. The present computational study is a direct numerical simulation of all resolvable structures. No turbulence modeling was applied.

The three-dimensional computations contained 256 points in the streamwise direction, 128 points in the normal direction, and 32 points in the spanwise direction. Half of the grid points were clustered in the boundary layer on the test wall using a hyperbolic tangent distribution. Uniform grid spacing was used in the streamwise and spanwise directions. The grid-independence of the solution was tested for a two-dimensional computation by doubling the number of points in the streamwise and normal directions independently; for both cases the changes in the flow velocity and shedding frequency were less than 0.5 percent (see PMR).

No-slip boundary conditions were applied on the test wall while no-stress conditions were used along the control wall to

reduce the required resolution in this region. To avoid strong local gradients, a parabolic variation of the suction velocity was applied in the streamwise direction to make the wall-normal velocity continuous along the control wall. Periodic boundary conditions were used in the spanwise direction.

For the two-dimensional computation, the inlet flow was prescribed as a Blasius boundary layer of the proper thickness under a steady uniform external flow. The inlet boundary was set at a location where the inviscid flow field, produced by transpiration from the suction port, varied by less than 2 percent from wall to wall across the channel. Various exit boundary conditions were tested by Pauley, et al. (1988), and it was found that the convective exit boundary conditions

$$\frac{\partial u}{\partial t}+c\frac{\partial u}{\partial x}=0,\quad \frac{\partial v}{\partial t}+c\frac{\partial v}{\partial x}=0,\ \text{and}\quad \frac{\partial w}{\partial t}+c\frac{\partial w}{\partial x}=0,\qquad (1a,b,c)$$

allowed the propagating vortices to exit the domain with little distortion. The propagation speed of the vortices within the computational domain gave the value for $c$. Virtually the same computational results were obtained when the average exit velocity was used for $c$, and hence the value of $c$ was not critical to the numerical solution. Other investigators, such as Bottaro (1990) and Nataf (1989), have also found the convective boundary condition to describe most accurately the vortex propagation from the computational domain.

To test the influence of the exit boundary location on the computational results, the length of the domain was extended in a two-dimensional separation study (see PMR). The computational domain was 50 percent larger and contained 50 percent more grid points in the streamwise direction, retaining the same grid spacing. Near the exit of the short domain, the results of the two computations differed by up to 3 percent, but the results differed by less than 0.2 percent at locations more than one channel height upstream of the exit plane. Thus, the results of interest were essentially independent of the domain truncation.

The timestep for the computations was $\Delta T=0.005$. To check the timestep independence of the solution, a computation of the two-dimensional geometry was run with $\Delta T=0.0025$. The flow velocities and shedding frequencies for the two step sizes differed by at most 0.5 percent.

**Two-Dimensional Computation.** The limit cycle solution from the two-dimensional computation of PMR was used as the initial flow condition for the present study. Figure 2 shows the instantaneous streamlines produced at six equally spaced intervals in the limit cycle oscillation. For each shedding cycle, the primary separation grows until a small counter-rotating vortex develops at the test surface. This counter-rotating vortex expands until it divides the main vortex into two distinct vortices. The downstream vortex is carried away from the main separation region by the freestream flow, and travels the length of the computational domain. The upstream separation remains in position, but continues to grow until another small counter-rotating vortex develops, thus repeating the cycle. Fluctuations in the height of the recirculating region indicate that boundary-layer fluid is entrained to allow the continuation of the shedding process. The upstream portion of the separation region remains largely unaffected by the downstream unsteady behavior. Throughout the cycle, the flow near the separation point remains steady.

The development of the shed vortex can be tracked from its inception to where it passes out of the computational domain. The streamlines suggest that the shed vortex initially has a rapid decay in strength. Pressure contours, shown in Fig. 3, can also be used to track the motion of the shed vortex since the vortex center is observed as a low pressure region. The pressure contours show that the apparent rapid decay in the vortex strength is due to the vortex motion away from the test

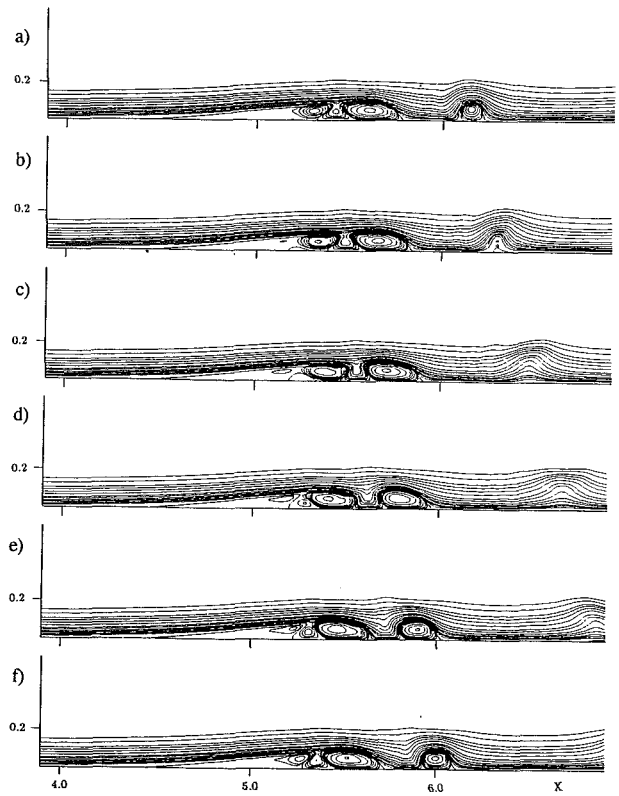


**Fig. 2 Streamlines for limit cycle shedding in the two-dimensional geometry. (*a*) $T=43.46$, (*b*) $T=43.72$, (*c*) $T=43.99$, (*d*) $T=44.25$, (*e*) $T=44.51$, (*f*) $T=44.78$.**

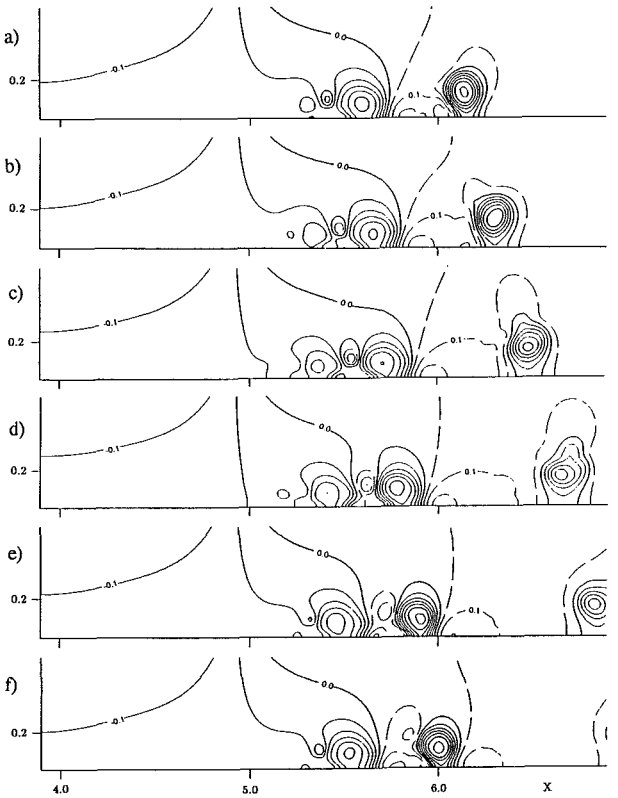


**Fig. 3 Pressure contours for limit cycle shedding in the two-dimensional geometry. Contour increment is 0.05. Solid contours are negative pressures. (*a*) $T=43.46$, (*b*) $T=43.72$, (*c*) $T=43.99$, (*d*) $T=44.25$, (*e*) $T=44.51$, (*f*) $T=44.78$.**

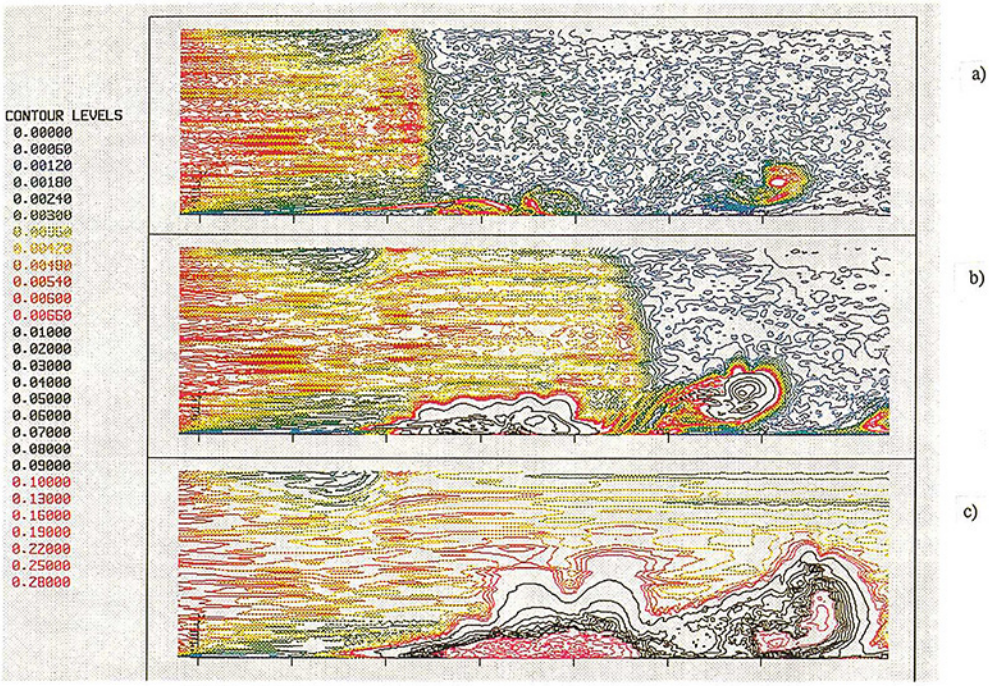


Fig. 4 Spanwise variation of the streamwise velocity due to a random noise perturbation. (*a*) $T = 1.1$, (*b*) $T = 2.5$, (*c*) $T = 4.3$.

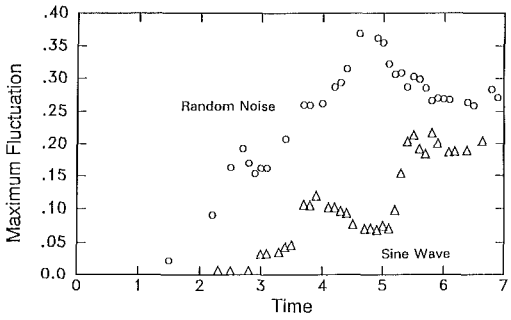


Fig. 5 Maximum spanwise variation of the streamwise velocity as a function of time

surface rather than an actual deterioration of the vortex strength.

## Random Noise Disturbance

To approximate the effects of random noise in the freestream of an experiment, a random noise with a peak noise amplitude of $\pm 1$ percent was added at $T = 0$ to the streamwise velocity at the inlet plane. The random noise produced a spatial RMS fluctuation of 0.58 percent at the inlet. The noise propagated downstream at the speed of the freestream velocity. The level of noise present at a given location in the channel was determined by calculating the spatial RMS fluctuation of the streamwise velocity across the span.

Contours of the RMS fluctuation across the channel are shown in Fig. 4 for three consecutive shedding periods. The amplitude of the noise decayed slightly as the noise front moved downstream until it reached the separated boundary layer. When the noise front passed across the stagnant leading portion of the separation (Fig. 4(*a*)) the noise accelerated through the separation and was amplified first in regions of high vorticity. High noise amplitudes occurred in the high vorticity regions of the separated shear layer and shed vortex. In the next period of oscillation shown in Fig. 4(*b*) the maximum cross-stream fluctuation rose above 10 percent as the noise front passed the separation. High noise amplitude could be seen in the "tails" of vorticity created by steep velocity gradients at the time of shedding. After the noise front had propagated through the entire computational domain (Fig. 4(*c*)), peak noise amplitudes in the separation were over 36 percent.

The growth of the maximum spanwise variation of the streamwise velocity is shown in Fig. 5. The peak spanwise variation was present near the unsteady reattachment point and increased when vortex shedding occurred. The shedding period of $T = 1.6$ can be seen as the time between maxima of the peak noise amplitude. After the spanwise noise had saturated the flow field, the peak noise in the channel varied between 27 to 36 percent during the vortex shedding process.

Initially the flow was two-dimensional. As the noise front passed over the separation, the location of the shed vortex varied across the span. The spanwise variation in vortex shedding can be identified using pressure contours. Figure 6 shows the pressure contours on the horizontal plane at $Y = 0.072$ after the noise perturbation had propagated through the domain. Low pressure regions are shown as blue in the figure. The low pressure regions mark shed vortices, separated flow, and the upstream boundary layer. The three-dimensionality due to the noise perturbation caused vortex shedding to be delayed in portions of the span. After shedding completely along the span, the vortex straightened, as seen by the shed vortex near the exit to the domain. The shedding frequency is constant across the span of the channel and a coherent spanwise vortex is produced. The shedding frequency and the spanwise-averaged streamlines compare favorably with the results of the two-dimensional computation. The favorable comparison indicates that a two-dimensional computation accurately describes the spanwise averaged flow and can therefore provide accurate information concerning the three-dimensional flow field.

Using the streamwise velocities across a span, spectra were computed at different heights and at several streamwise locations including the locations of separation, vortex production, vortex shedding, and vortex propagation. The energy in each wave number grew as the three-dimensionality developed, but no wave number showed prominence in energy content. The energy at all wavelengths increased at approximately the same rate. This indicates that the three-dimensional scalloped

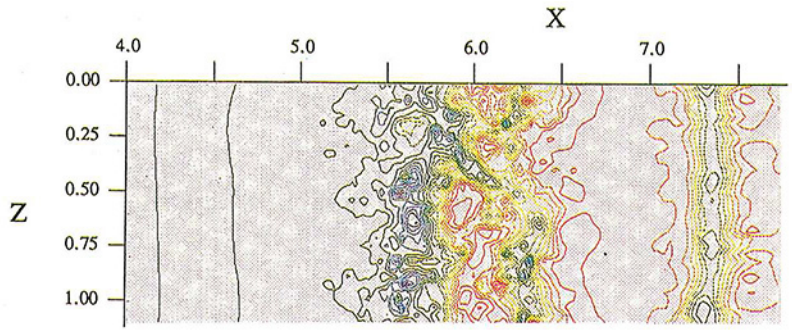


Fig. 6 Pressure contours in the horizontal plane at $Y=0.072$ due to a random noise perturbation

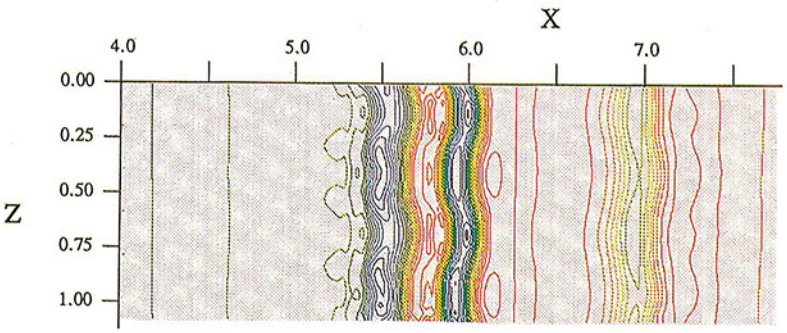


Fig. 7 Pressure contours in the horizontal plane at $Y=0.072$ due to a sine-wave noise perturbation

structure found by experimental oil film visualization was not caused by the amplification of one dominant wavelength from a random noise perturbation. Through a stability analysis of a separated boundary layer, Inger (1987) determined that Görtler vortices having a range of wavelengths will be amplified due to the shear layer curvature. The present computations confirm that spanwise perturbations having a range of wavelengths are unstable and one instability wavelength will not dominate.

## Sine Wave Disturbance

As a second test of the three-dimensionality found within the boundary layer separation, the inlet velocity profile was modified by superposing a periodic disturbance across the span. This upstream condition is similar to that occurring in an experimental apparatus with flow conditioning screens, honeycomb elements, or other upstream effects. In this test, a sine wave with an amplitude of 0.2 percent of the freestream velocity and a wavelength of half of the domain width was added across the inlet. A lower amplitude perturbation was selected in this test since all energy was injected at one wavelength. The author considered the addition of a higher amplitude fluctuation at a single wavelength to be severe forcing of the perturbation which would not convincingly test the findings from the stability analysis of Inger (1987). The imposed perturbation had a wavelength which was four times the boundary layer thickness near separation.

RMS fluctuation contours showed characteristics similar to the random noise case shown in Fig. 4 except that the RMS fluctuation in the freestream was 0.13 percent. The growth of the maximum spanwise fluctuation in the channel is shown in Fig. 5 for the sine-wave disturbance. Since the inlet perturbation had a lower amplitude than in the previous case, the instability took longer to grow. The maximum amplitude of the spanwise fluctuations in the flow field reached a level near 20 percent. As observed in the random noise case, the amplitude of the maximum spanwise variation increased when vortex shedding occurred. The maximum spanwise variation in the streamwise velocity was produced in the region of reattachment and vortex shedding. Spectra of the spanwise variations in the streamwise velocity were used to identify the modes with most energy. Initially, all energy was contained in the imposed wavenumber perturbation. At $T=3.7$, the fluctuation amplitude had increased by 100 times and the first harmonic of the imposed perturbation contained 30 percent of the energy. When the three-dimensional disturbances had reached a maximum amplitude, half of the energy was contained in the first harmonic. The energy spectra showed only low amplitude spanwise variations at higher wavenumbers. Therefore, the spanwise nonuniformity was primarily comprised of fluctuations at the imposed wavelength and its first harmonic.

To visualize the three-dimensional instability, pressure and velocity contours were considered. Figure 7 shows the pressure contours at $T=5.9$ along a horizontal plane at $Y=0.072$. Well-defined sinusoidal oscillations in the pressure contours extend across the span of the channel. Both the shed spanwise vortex and the primary, fixed separation have been altered. When the propagation of the shed vortex was monitored, it was found that the spanwise vortex straightened as it moved downstream. Spanwise variations in the pressure and velocity fields were, therefore, more significant near the location of vortex shedding. Figure 8 shows the velocity contours at a streamwise location near vortex shedding. In this spanwise plane, the Görtler vortex array is clearly seen. The inlet sine-wave perturbation has produced a preferred wavelength which results in a coherent spanwise structure. As observed by Inger (1987), typical conditions producing laminar boundary separation will also generate Görtler vortices.

The influence of three-dimensionality on the separation was examined by considering streamlines produced by the velocity field which was averaged across the span. The vortex shedding frequency of the two-dimensional separation was not altered

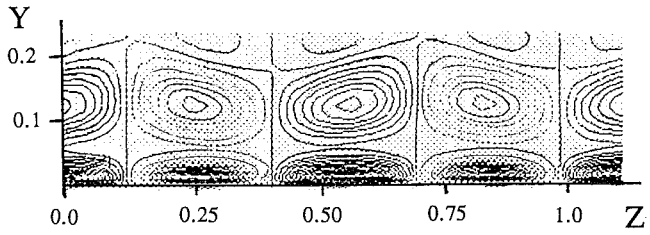


**Fig. 8 Spanwise velocity contours at $T = 5.9$ in a $Y - Z$ (cross-span) plane at $X = 5.785$ due to a sine-wave noise perturbation**

by the spanwise variation. The spanwise variations of the separation, however, increased the spanwise-averaged length of the separation and reduced the strength of the shed vortex. The coherent longitudinal vortices produced by the sine-wave perturbation enhanced mixing across the shear layer and delayed the shear layer rollup.

## Conclusions

A spanwise perturbation was added to a previously unsteady two-dimensional computation of boundary layer separation to investigate the development of spanwise velocity variations. The two-dimensional unsteady separation of Pauley et al. (1990) was used as the initial flow field in the present study. The two-dimensional flow field was characterized by unsteady periodic vortex shedding.

In one computation, a spanwise random noise perturbation was applied at the inlet of the domain. The noise front propagated through the domain at the freestream velocity. When the noise front reached the separation, the amplitude of the spanwise variations in the streamwise velocity increased rapidly to a maximum of 36 percent of the local streamwise velocity. The spanwise variations did not contain a dominant wavelength or coherent structure. The vortex shedding frequency was not altered by the spanwise velocity variations. When the velocity field was averaged across the span, it was found that the separation length and strength of the shed vortices were not modified by the three-dimensionality.

In a second computation, a spanwise sine-wave perturbation was applied at the inlet of the computational domain. The spanwise variations were amplified within the boundary layer separation and shed vortices. The spanwise perturbation contained energy at the imposed wavelength and its first harmonic. Velocity contours across the channel span showed the formation of Görtler vortices as predicted by Inger (1987) for many conditions producing laminar separation. The presence of the coherent spanwise structures did not change the vortex shedding frequency. The longitudinal vortices, however, increased the spanwise-averaged length of the separation and reduced the strength of the shed vortices.

## Acknowledgments

This research has been supported by the Office of Naval Research. Computer facilities were provided by the NAS facility at NASA Ames Research Center. These contributions are gratefully acknowledged.

## References

Arean, A. V., and Mueller, T. J., 1978, "Visualization of the Separation and Subsequent Transition Near the Leading Edge of Airfoils," NASA CP 2045, Paper 35.

Bottaro, A., 1990, "Note on Open Boundary Conditions for Elliptic Flows," *Numerical Heat Transfer*, Part B, Vol. 18, pp. 243–256.

Brendel, M., and Mueller, T. J., 1988, "Boundary Layer Measurements on an Airfoil at Low Reynolds Numbers," *Journal of Aircraft*, Vol. 25, pp. 612–617.

Inger, G. R., 1977, "Three-Dimensional Heat- and Mass-Transfer Effects across High-Speed Reattaching Flows," *AIAA Journal*, Vol. 15, No. 3, pp. 383–389.

Inger, G. R., 1987, "Spanwise-Periodic 3-D Disturbances in the Wake of a Slightly Stalled Wing," AIAA 25th Aerospace Sciences Meeting, Reno, NV, Paper AIAA-87-0456.

Ginoux, J. J., 1965, "Streamwise Vortices in Laminar Flow," AGARDograph 97, May, pp. 395–422.

Kim, J., Moin, P., 1985, "Application of a Fractional-Step Method to Incompressible Navier-Stokes Equations," *Journal of Computational Physics*, Vol. 59, pp. 308–323.

Koromilas, C. A., Telionis, D. P., 1980, "Unsteady Laminar Separation: An Experimental Study," *Journal of Fluid Mechanics*, Vol. 97, pp. 347–384.

Mabey, D. G., 1972, "Analysis and Correlations of Data on Pressure Fluctuations in Separated Flows," *Journal of Aircraft*, Vol. 9, p. 642–645.

McCroskey, W. J., 1977, "Some Current Research in Unsteady Fluid Dynamics," ASME JOURNAL OF FLUIDS ENGINEERING, Vol. 5, pp. 8–39.

Nataf, F., 1989, "An Open Boundary Condition for the Computation of the Steady Incompressible Navier-Stokes Equations," *Proceedings Fifth International Symposium Numerical Methods in Engineering*, Vol. 1, pp. 749–756.

Pauley, L. L., Moin, P., and Reynolds, W. C., 1988, "A Numerical Study of Unsteady Laminar Boundary Layer Separation," Report TF-34, Department of Mechanical Engineering, Stanford University, Stanford, CA.

Pauley, L. L., Moin, P., and Reynolds, W. C., 1990, "The Structure of Two-Dimensional Separation," *Journal of Fluid Mechanics*, Vol. 220, pp. 397–411.

Winkelmann, A. E., and Barlow, J. B., 1980, "Flowfield Model for a Rectangular Planform beyond Stall," *AIAA Journal*, Vol. 18, No. 8, pp. 1006–1008.

Zaman, K. B. M. Q., McKinzie, D. J., and Rumsey, C. L., 1989, "A Natural Low-Frequency Oscillation of the Flow over an Airfoil Near Stalling Conditions," *Journal of Fluid Mechanics*, Vol. 202, pp. 403–442.

# On the Unsteady and Turbulent Characteristics of the Three-Dimensional Shear-Driven Cavity Flow

**S. A. Jordan**
Naval Undersea Warfare Center,
Code 8322 Building 1246,
Newport, RI 02841

**S. A. Ragab**
Department of Engineering
Science and Mechanics,
Virginia Polytechnic Institute
and State University,
Blacksburg, VA 24061

*The three-dimensional shear-driven cavity flow is numerically investigated at Reynolds numbers of 5000 and 10000. This investigation focuses on the unsteadiness and turbulent characteristics of the flow. At the moderate Reynolds number (Re = 5000) where the cavity flow is fully laminar, a direct numerical simulation (DNS) is used whereas large-eddy simulation (LES) methodology is adopted to predict the cavity flow at the higher Reynolds number (Re = 10000). Establishing a suitable form for the subgrid scale (SGS) turbulence model in this complex flow is guided by the DNS results at Re = 5000. Additionally, the SGS model is verified against DNS results at Re = 7500 where the cavity flow is known through experimentation to be locally transitional. The LES results verify the published experimental evidence as well as uncover new flow features within the cavity.*

## Introduction

For more than three decades, the shear-driven cavity flow problem has served as an excellent test case for verifying new or improved numerical solution techniques of incompressible flows. Usually, the test case involves simulating a two-dimensional (2D) cavity flow at a low Reynolds number ($Re \leq 1000$). Under these conditions, the flow is strictly laminar and steady. The primary purpose of the simulations is to illustrate the rapid speed of convergence to steady state and the solution method's ability to capture the basic features of the flow. Some 2D simulations (for example, Ghia et al., 1982 and Gustafson and Halasi, 1986) include a discussion of the flow characteristics and have revealed important salient features of the steady flow at much higher Reynolds numbers ($Re \leq 10000$). The extensive results of Ghia et al., in particular, serve most often as a base for comparison of new 2D predictions because of the fine grid resolution they used at the corresponding Re. Only a few numerical studies have reported the turbulent characteristics of the shear-driven cavity flow (Gosman et al., 1968, Young, et al., 1976, Ideriah, 1978, and Gaskell and Lau, 1988, for instance). Each study simulated a 2D geometry with the turbulence fully modeled. Treatment of the results was focussed primarily on validating the particular numerical scheme or evaluating the particular turbulence model. Separate studies showing the flow evolution in the 2D cavity under an impulsively started lid and an oscillating lid were reported by Soh and Goodrich (1988). In both simulations, the flow was laminar ($Re = 400$) and the predictions continued until a periodic state was reached. Published results from three-dimensional simulations include those of Kim and Moin (1985), Freitas et al. (1985), and Prasad et al. (1988) where the Reynolds number was restricted to low to moderate values ($Re \leq 3200$). There, the flow was also laminar. The simulations showed the appearance of pairs of quasi-steady and unsteady spanwise Taylor-Görtler-like vortices along the cavity bottom. Besides validating the conservativeness of their particular solution technique, each group revealed this important three-dimensional characteristic which had been observed experimentally, but eluded numerically.

In addition to furnishing us with a classic problem for validating solution techniques of incompressible flows, the predominant features of the shear-driven cavity flow also have important physical significance in engineering design. For example, the main flow characteristics created by three-dimensional geometries such as recessed cavities, recurrent ribs for slots and curved ducts, for the purposes of mass and/or energy exchange, are similar to those of this model problem. Given this fact, the objective of the present work is to identify and characterize, through numerical simulation, the unsteadiness and turbulence in a three-dimensional shear-driven cavity flow. This numerical investigation is presented for Reynolds numbers of 5000 and 10000. Numerical results of the unsteady and laminar flow characteristics at much lower Reynolds numbers ($Re = 2000$ and $Re = 3200$) were presented by Jordan and Ragab (1993).

For the moderate Reynolds number test case ($Re = 5000$) where the flow is laminar but unsteady, the computation was a direct numerical simulation (DNS). At the higher Re, the prediction method was a large-eddy simulation (LES). Although extensive experimental results of the high-Re cavity

Contributed by the Fluids Engineering Division for publication in the JOURNAL OF FLUIDS ENGINEERING. Manuscript received by the Fluids Engineering Division March 3, 1993. Associate Technical Editor: G. Karniadakis.

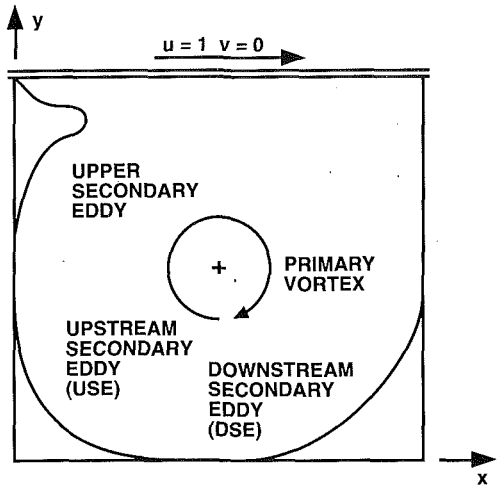


Fig. 1 Sketch of the basic features of recirculation in the two-dimensional shear-driven cavity flow problem

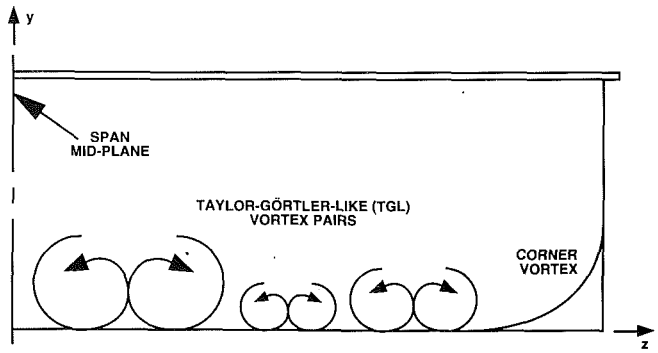


Fig. 2 Sketch of the Taylor-Görtler-Like (TGL) vortex pairs as observed in the flow visualization experiments

flow have been reported for just over ten years now, this LES investigation is a first attempt to study the turbulent flow characteristics numerically. Recently, Zang et al. (1993) performed an LES calculation of the shear-driven cavity flow, but they focussed the results on verification of their new dynamic turbulence model. They showed good agreement between the LES results and the experimental measurements in terms of the turbulent quantities through the cavity centerline at the spanwise mid-plane. Their investigation however did not include discussions of the time-dependent characteristics such as the spanwise vortices or the secondary eddies. In the present work, the numerical results are first scrutinized thoroughly against the experimental evidence, before discussing any new unsteady or turbulent flow characteristics. Thus, this LES computation verifies the published experimental data as well as reveal some new features about the flow.

## Basic Model Problem Including Experimental Observations

Geometrically, the classic 2D problem consists of a closed cavity of unit height (H) and unit width (W) with a lid moving horizontally at unit velocity ($U$). The Reynolds number is defined as $\mathrm{Re} = UW/\nu$, where $\nu$ is the kinematic viscosity. The associated recirculation flow is characterized basically by a primary vortex, a downstream secondary eddy, an upstream secondary eddy and an upper secondary eddy. These basic features are sketched in Fig. 1. The upper secondary eddy appears at $\mathrm{Re} \geq 3200$. At higher $\mathrm{Re}(\geq 5000)$ the 2D predictions show a tertiary eddy in each of the lower corners. However, these tertiary eddies are not supported by the experimental observations of Koseff and Street (1984c) of the three-dimensional (3D) cavity flow. Koseff and Street also reported that the horizontal and vertical centerline velocity profiles of the recirculation flow are similar in shape throughout the cavity span at high Reynolds numbers where the flow is locally transitional.

In the 3D cavity new vortical structures are formed. In a spanwise plane, there are several pairs of Taylor-Görtler-like (TGL) vortices and a lower corner vortex at the end-walls (see sketch in Fig. 2). According to Koseff and Street (1984b) and Prasad et al. (1988), the impetus manifesting the TGL vortices is the instability of the concave free shear layer that separates the primary vortex from the downstream secondary eddy. Generation of the vortices occurs just above the concave surface much like the experimental observations of Taylor (1923) for the flow between rotating cylinders and also the concave boundary layer investigated by Görtler (1954). The size and number of pairs of TGL vortices depends strongly on the Reynolds number and the cavity spanwise aspect ratio (SAR). In the flow visualization results reported by Rhee et al. (1984) for $\mathrm{Re} \leq 6000$ and $\mathrm{SAR} = 3.0$, the spanwise flow maintained symmetry about the midspan plane. Although the TGL vortices meander slowly along the cavity bottom at moderate Re, Koseff and Street (1984a) noted that their basic spanwise flow character still remains symmetric. The other important feature in the spanwise direction is the lower corner vortex. The origin of this flow structure was explained by Koseff and Street (1984b) after examining the experimental results of de Brederoede and Bradshaw (1972). Manifestation of this vortex is a consequence of the shear and pressure force adjustment in the streamwise recirculating flow caused by the no-slip condition along the spanwise end-wall. Like the TGL vortices, the corner vortex becomes unsteady at moderate Reynolds numbers ($\mathrm{Re} \geq 3200$). The size and extent of the corner vortex strongly influences the TGL vortices. Thus, the numerical simulations must provide sufficient resolution, spatially and temporally, to capture its characteristics accurately.

Experimental observations show the first sign of turbulence taking place within the free shear layer that lies between the primary vortex and downstream secondary eddy. This local transition to turbulence occurs at a Reynolds number somewhere between 6000 and 8000 (Koseff and Street, 1984a). The flow within that region is unsteady. If the Reynolds number is increased, turbulence diffuses the TGL vortices such that their deterministic structure becomes obscured. At $\mathrm{Re} = 10000$, frequency spectra of both the horizontal and vertical fluctuations within the region of the free shear layer display an inertial subrange. It should be noted that the visualization results show the flow within the free shear layer at $\mathrm{Re} = 10000$ as being still transitional.

## Governing Equations and Method of Solution

The governing LES equations of the resolvable field are the spatially filtered incompressible Navier-Stokes equations (Moin and Kim, 1980):

$$\frac{\partial \bar{u}_i}{\partial t} + \frac{\partial}{\partial x_j}(\bar{u}_i \bar{u}_j) = -\frac{\partial \bar{p}}{\partial x_i} + \frac{1}{\mathrm{Re}} \frac{\partial^2 \bar{u}_i}{\partial x_j \partial x_j} + \frac{\partial \tau_{ij}}{\partial x_j}, \tag{1}$$

$$\frac{\partial \bar{u}_j}{\partial x_i} = 0. \tag{2}$$

where $p$ the pressure, and $\tau_{ij}$ is the subgrid scale stress tensor which is defined as $\tau_{ij} = \overline{u_i u_j} - \bar{u}_i \bar{u}_j$. The overbar symbolizes the filtered field.

The system of equations is time-advanced according to a variant of the fractional-step method (Kim and Moin, 1985). The Crank-Nicolson scheme is applied to the viscous terms to eliminate the viscous stability restriction. An explicit three-

step, third-order accurate Runge-Kutta (R-K) scheme is used for the convective terms instead of the more popular Adams-Bashforth method (see Clark et al., 1977). This is because the Adams-Bashforth method is weakly unstable when applied to the linear convection equation. Also, the explicit form of the R-K scheme easily permits high-order spatial differences. In this application of the LES approach, the convective terms are spatially discretized by third-order upwind-biased finite differences while the diffusive terms are differenced by second-order central differences. At the points next to the wall boundaries, exterior points necessary to complete the upwind differencing are obtained through extrapolation of the interior field points. All terms in Poisson's equation for solution of the pressure variable are central differenced to the second order. Strong coupling between the pressure and velocity components is maintained through a fourth-order accurate compact differencing scheme for the pressure gradient in the velocity update equation. This discretization scheme provides an overall method which is second-order accurate in both space and time.

The velocity components are collocated with the grid points to permit easy development of a set of wall boundary conditions for the velocity field. Approximate-factorization (A-F) is applied for solution of the intermediate velocity components. Since the shear-driven cavity is fully enclosed, no boundary condition is needed for the pressure variable to solve the discretized pressure-Poisson equations. The pressure gradient normal to the boundary can be expressed in terms of the velocity field. Thus, the pressure-Poisson equation is solved with a Neumann type boundary condition. The pressure field is staggered from the velocity field to eliminate spurious oscillations in the flow solutions (Patankar, 1980). The staggered pressure field also facilitates the application of the Neumann boundary condition. The pressure-Poisson equation is recast into a residual form and solved by a variant of the modified strongly implicit procedure (Jordan, 1992). This procedure is implemented as an implicit elliptic solver of a planar surface that moves through the volume. After the initial time steps, only a few iterations on the pressure variable are necessary to satisfy the incompressibility constraint at each of the following time steps.

Extensive details of the numerical scheme, along with several test cases, were reported by Jordan and Ragab (1993). The temporal and spatial accuracy of the scheme were verified by systematically refining the grid in a simulation of an exact solution to the 2D Navier-Stokes equations. Also, the shear-driven cavity flow problem at $Re \leq 3200$ was computed and the results compared to the reported experimental data. In those DNS computations, the spatial resolution was sequentially refined until good quantitative agreement was reached between the predictions and the experimental measurements. The final grid sizes helped establish the proper spatial resolution for the present computations of the shear-driven cavity flow.

## Subgrid Turbulence Model

For the computations of the turbulent shear-driven cavity flow, the Smagorinsky eddy viscosity model (Smagorinsky, 1963) was implemented to represent the subgrid scale turbulence. In tensor notation the Smagorinsky model is:

$$\tau_{ij} - \frac{1}{3}\delta_{ij}\tau_{kk} = 2\nu_T \bar{S}_{ij}, \tag{3}$$

$$\bar{S}_{ij} = \frac{1}{2}(\bar{u}_{i,j} + \bar{u}_{j,i}), \tag{4}$$

$$\nu_T = l^2\sqrt{2\bar{S}_{ij}\bar{S}_{ij}} \tag{5}$$

In this model, $l$ is the turbulent characteristic length scale and is given by

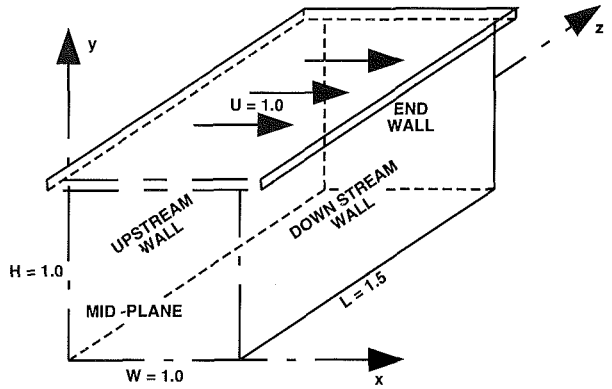


**Fig. 3 Model problem for present DNS and LES predictions of the shear-driven cavity flow**

$$l = C_S[1 - \exp(-y^+/A^+)^m]^n(\Delta_1\Delta_2\Delta_3)^{1/3} \tag{6}$$

The subscripts 1, 2 and 3 of the filter width $\Delta$ permit versatile filtering for modeling anisotropic flows (Deardorff, 1970). As a minimum $\Delta_i = 2h_i$, where $h_i$ is the grid spacing in the $i$-direction. Modification of the length scale by a form of Van Driest damping (Van Driest, 1956) was necessary to account for the effects of the solid wall boundaries. The length parameter $y^+$ is the minimum field value of $y\sqrt{\tau/\rho}/\nu$, where $\tau$ is the magnitude of the local shear stress. The exponents $m$ and $n$ in the damping function were estimated by analyzing DNS results and by qualitative comparisons to the published experimental measurements (Koseff and Street, 1984c). Smagorinsky's constant $C_S$ was set equal to 0.1 based on the recommendation by Piomelli et al. (1988). The importance of including damping in the Smagorinsky model became apparent after applying the model to the DNS results at $Re = 5000$ without the damping modification. The model repeatedly showed high levels of turbulent eddy viscosity near the upper half of the downstream wall. At times, these levels reached the same order of magnitude as the kinematic viscosity, marking the onset of turbulence. According to the experimental observations however, this is a false indication. As discussed earlier, the flow visualization results suggest that initial signs of turbulence occur within the free shear layer between the primary vortex and the downstream secondary eddy which is located near the lower half of the downstream wall. By damping the length scale according to a form of Van Driest, the near-wall turbulent eddy viscosity was reduced and the modified model agreed qualitatively with the experimental evidence. This issue is addressed further in the next section.

## Results and Discussion

We present in this section the unsteady and turbulent flow results from a numerical investigation of the 3D shear-driven cavity and include comparisons to the published experimental observations and measurements. The cavity geometry, shown in Fig. 3, was modeled with a cavity width $W = 1.0$ ($x$-direction), a height $H = 1.0$ ($y$-direction) and a span $L = 1.5$ ($z$-direction). One boundary of the span was modeled as a plane of symmetry ($z = 0.0$) and the other a solid end-wall ($z = 1.5$). The span boundaries were modeled in this way because the published flow visualization data for $Re \leq 6000$ (Koseff and Street, 1984a, 1984b and 1984c) and previous simulations for $Re \leq 3200$ (Freitas et al., 1985, Prasad et al., 1988 and Jordan and Ragab, 1993) report a symmetric flow about the mid-span. The spanwise aspect ratio of the cavity ($SAR \equiv 2L/W$) was therefore equal to 3.0. It is worth noting that in the recent LES computation by Zang et al. (1993), the cavity spanwise aspect ratio was 0.5. While all the TGL vortices display strong spanwise meandering activity in the cavity with a $SAR = 3.0$,

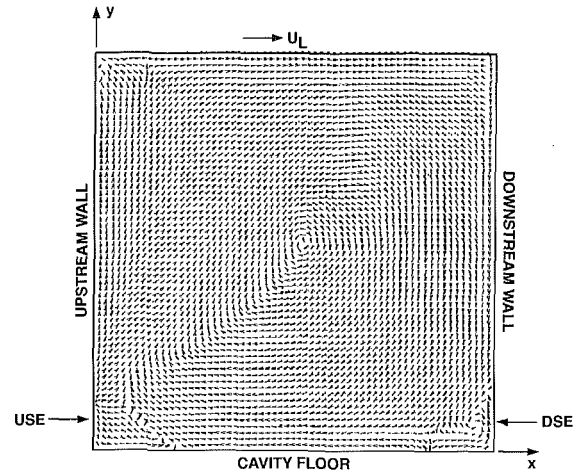


Fig. 4(*a*)

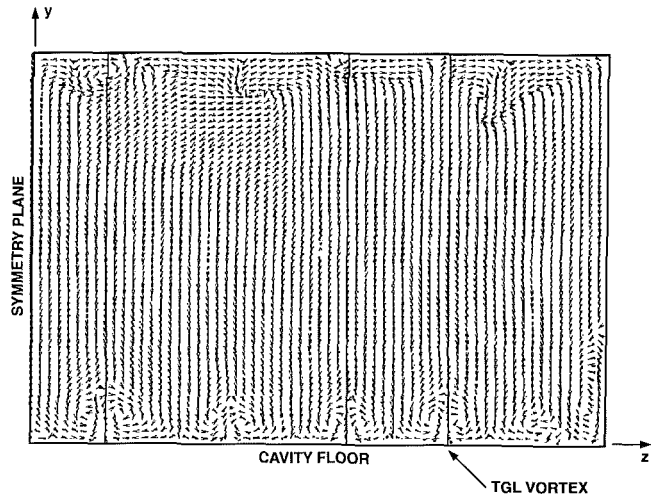


Fig. 4(*b*)

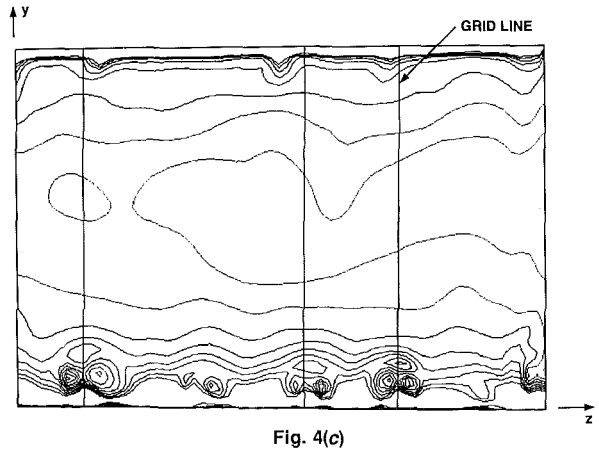


Fig. 4(*c*)

**Fig. 4 Snapshots of the unsteady velocity vectors in the shear-driven cavity flow at relative time $T_r = 15.0$; (*a*) recirculation at mid-span symmetry plane, (*b*) TGL vortices at plane $x = 0.77$ and (*c*) spanwise static pressure contours**

the single TGL vortex pair in the cavity with a SAR = 0.5 is locked in position at the mid-span (Prasad and Koseff, 1989). In the present work, the lid moved horizontally with unit velocity ($U = 1.0$). No-slip conditions were enforced along all boundaries except at the mid-span plane which was treated numerically as a plane of symmetry. We simulated Reynolds numbers of 5000 and 10000. For the Re = 10000 simulation, we will show a localized effect of the symmetry plane assumption on the numerical results. All grids selected had uniform point spacing and all times ($T$) were nondimensional; $T = tU/W$.

Each simulation was initialized by an impulsively started lid. Inasmuch as the convective terms are time-split by the Runge-Kutta technique, extremely small time increments were not necessary early in the simulation to maintain stability. For both simulations, a low CFL value of 0.5 was chosen to insure proper temporal resolution of the flow unsteadiness rather than control the numerical stability. It was found that CFL values near the stability limit distorted the TGL vortex structures. Herein, computational results which are labeled $T_r = 0.0$ represent solutions that had been time-advanced until the transient effects of the impulsively started lid on the flow evolution became negligible. In both simulations, this reference time was an actual nondimensional time of $T \cong 60$ since lid start-up.

In view of the experimental evidence, the cavity flow is entirely deterministic at low to moderate Reynolds numbers ($Re \leq 5000$). Therefore, the simulation results reported here at Re = 5000 are from a DNS prediction. For this computation, a $65 \times 65 \times 65$ ($x$, $y$, $z$-direction) uniform grid was used. Comparisons between the DNS results and the experimental data show that this spatial resolution captured the flow characteristics accurately. Further refinement of the grid did not alter the flow structure. The uniform grid selected for the LES computations at Re = 10000 was $101 \times 101 \times 81$. Based on the turbulent scales estimated by Koseff and Street (1984c) for the 3D cavity flow at Re = 10000, this grid provides a higher spatial resolution than that needed to resolve Taylor's microscale.

**DNS Results.** For the DNS computation of the shear-driven cavity flow, the Reynolds number was 5000. Figures 4(*a*) and 4(*b*) show a set of snapshots of the unsteady flow results at time $T_r = 15.0$. The velocity vectors in Fig. 4(*a*) represent the recirculation flow at the mid-span plane whereas those in Fig. 4(*b*) depict spanwise flow at plane $x \cong 0.77$. For clarity, all of the velocity vectors are normalized by their own respective magnitude. Although there seems to be three-dimensional effects in the upper half of the spanwise plane, their magnitudes are small and therefore have little significance on the flow structure. At this instant in time ($T_r = 15.0$), the basic characteristics of the recirculation flow which are common to the 2D simulations are distinctly visible. Likewise, the primary vortex core is positioned close to the cavity center. This agreement with the 2D simulations is due primarily to the minimal influence of the spanwise flow on the mid-span recirculation flow (see Fig. 4(*b*)). The spanwise flow vectors show four TGL vortices of nearly the same height that lie fully within the cavity span. Since the static pressure attains a minimum within the vortex core, contours of the pressure variable can verify the existence of each vortex. An example of this is portrayed in Fig. 4(*c*). A few grid lines are superimposed over the pressure contours and the corresponding velocity vectors to help identify each respective vortex.

At time $T_r = 181.0$, the snapshots paint a very different picture (see Figs. 5(*a*) and 5(*b*)). The three-dimensional effects on the basic recirculating flow features are clearly displayed. For example, the TGL vortex that straddles the mid-span plane severely distorts the basic structure of the downstream secondary eddy (DSE). Throughout most of the simulation, a TGL vortex structure straddled the mid-span plane which precluded development of the local DSE. According to the experimental results (Rhee et al., 1984), 8 pairs of TGL vortices were visualized at Re = 3200 and 11 vortex pairs at Re = 6000. At Re = 5000, we found 9 vortex pairs; one typically straddling the mid-span plane and four others spanning the cavity floor. This result is shown in Fig. 6 which is a plot of the $x$-vorticity

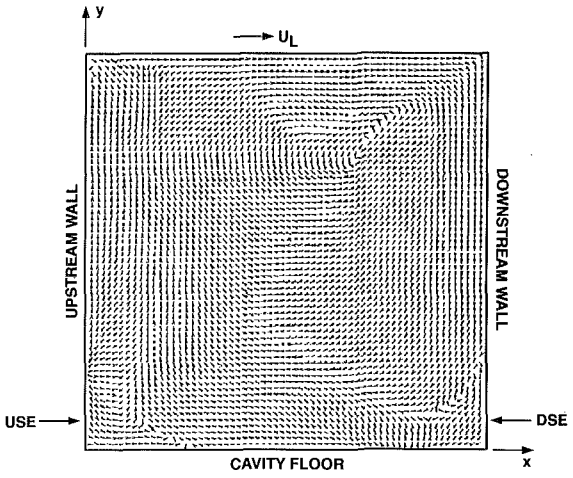

Fig. 5(*a*)

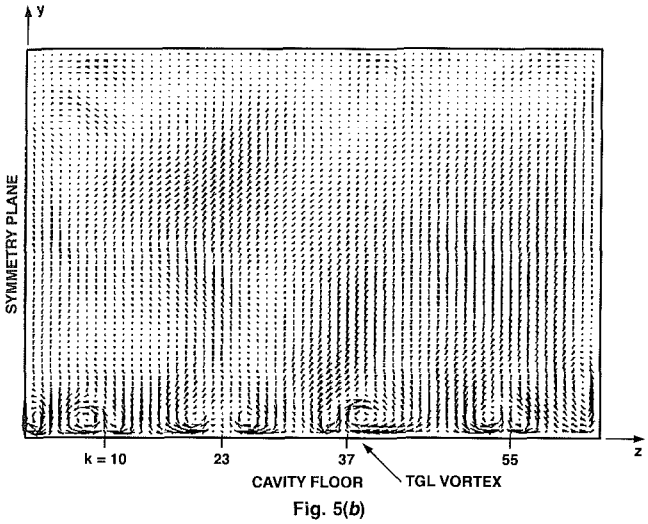

Fig. 5(*b*)

**Fig. 5 Snapshots of the unsteady velocity vectors in the shear-driven cavity flow at relative time $T_r = 181.0$; (*a*) recirculation at mid-span symmetry plane and (*b*) TGL vortices at plane $x = 0.77$**

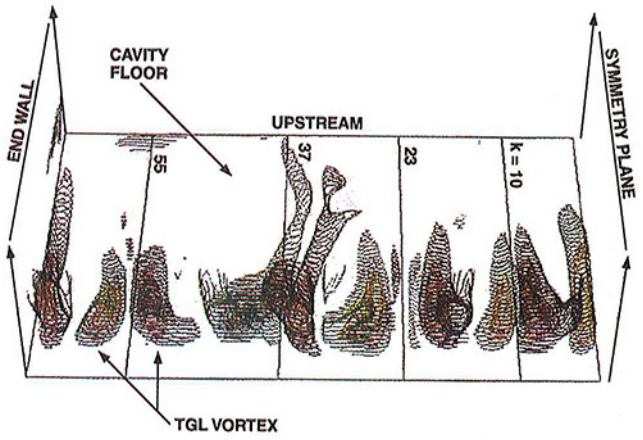

**Fig. 6 Spanwise distribution and streamwise extent of TGL vortex contours at completion of DNS computation ($T_r = 181.0$)**

contours at completion of the simulation ($T_r = 181.0$). Notice that the streamwise extent of each vortex pair does not strongly interact with the upstream secondary eddy (USE). This is because the flow process of fluid entrainment from the primary vortex to sustain the structural integrity of each TGL vortex is terminated once the primary vortex separates upstream. Particle traces which illustrate this flow process are presented in the next section.

In the literature, neither velocity time traces nor mean velocity experimental data appear for the 3D cavity flow at Re = 5000 and SAR = 3.0. Here, we show in Figs. 7(*a*) through 7(*d*) time traces of a vertical and horizontal velocity component and their power spectra for the Re = 5000 test case. The traces were extracted from recordings taken in the vicinity of the downstream free shear layer. For reference, the power spectra include Kolmogorov's slope of the inertial subrange. Both spectra show numerous amplified frequencies signifying an unsteady flow which is still deterministic. In Fig. 8, the computed mean horizontal velocity along the mid-span centerline is compared against the reported experimental data for SAR = 1:1 and SAR = 0.5:1 (Prasad and Koseff, 1989). The DNS profile illustrates a further weakening of the "energy-sink" effect of the spanwise end-walls on the primary recirculation vortex core when the cavity SAR is extended to three.

The importance of the present DNS results with respect to the LES methodology lies in attempting to estimate the turbulent length scale damping parameters. In particular, parametric studies were performed on the DNS results at intermittent time intervals to find values for the exponents ($m$ and $n$) in the Van Driest damping function. There is no strong fundamental basis for obtaining these parameters in this way. However, the LES results will show that the turbulent eddy viscosity magnitudes and distribution throughout the cavity were in good agreement with the experimental evidence. The procedure used here to determine the model damping parameters closely follows the SGS turbulence model development by Clark et al. (1977). The damping parameters were judged according to the best overall set of coefficients acquired from correlations between the exact (computed from the DNS data) and the model results in terms of the SGS stresses $\tau_{ij}$. The correlation coefficient ($c_{ij}$) is defined as

$$\langle c_{ij} \rangle = \langle e_{ij} m_{ij} \rangle / \langle e_{ij}^2 \rangle^{1/2} \langle m_{ij}^2 \rangle^{1/2} \tag{7}$$

where $\langle e_{ij} \rangle$ and $\langle m_{ij} \rangle$ are the spatially ensemble-averaged exact model $\tau_{ij}$ components, respectively. Inasmuch as the spanwise flow direction was assumed to be homogeneous, only the coefficients $c_{11}$, $c_{22}$, and $c_{12}$ were determined of which only positive values were considered. Furthermore, signs of transition first emerge within the downstream free shear layer (Koseff and Street, 1984a). By knowing this information a priori, it is also possible to perform quality checks on the model in terms of the turbulent eddy viscosity magnitudes and distribution. In the following figures, the turbulent eddy viscosity ($\nu_\tau^*$) is normalized by the kinematic viscosity. Since the TGL vortices severely disturbed the basic features of the recirculating flow, the model quality was inspected only on planes lying between the spanwise vortex pairs.

The best set of fully averaged correlation coefficients attained from a parametric study of the DNS results was $c_{11} = 0.30$, $c_{22} = 0.29$ and $c_{12} = 0.31$. The corresponding global model constants are $m = 8.0$, $n = 0.14$ and $C_S = 0.1$. Distribution of the $c_{12}$ coefficient, plotted in Fig. 9, shows pockets of nearly perfect correlation close to the cavity walls and near the region of downstream free shear layer. Notice that the poorest correlations occur primarily where the model $\nu_\tau^*$ levels are expected to be low. As an example, see Fig. 10a where the highest $\nu_\tau^*$ levels found in the individual recirculation planes are shown for the DNS results at completion of the simulation. This figure also reveals that the model predicts $\nu_\tau^*$ magnitudes and distributions in accordance with the experimental observations.

As a final note, the model constants as acquired from the Re = 5000 simulation were also checked against DNS results

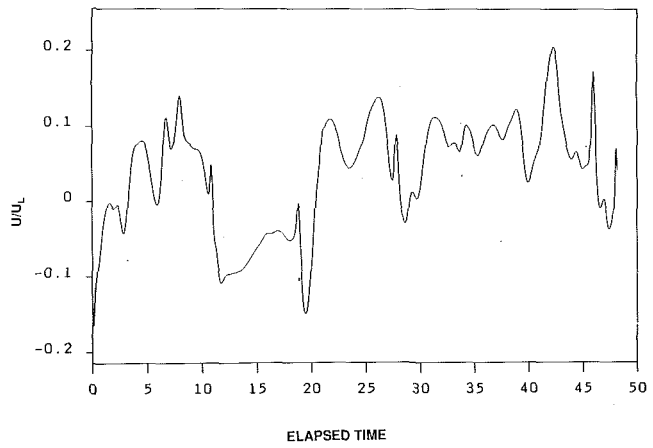


Fig. 7(a)

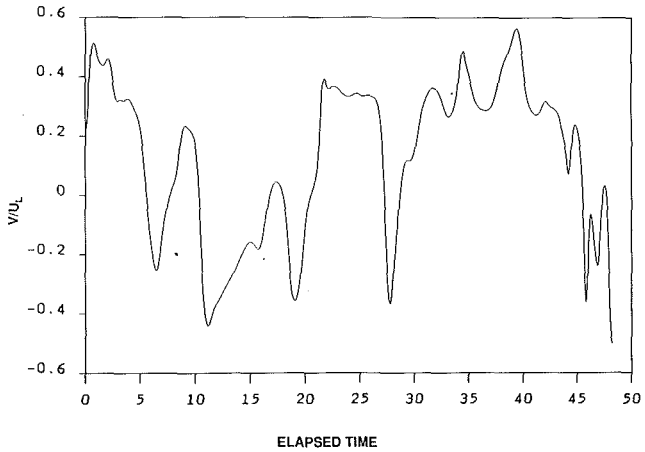


Fig. 7(c)

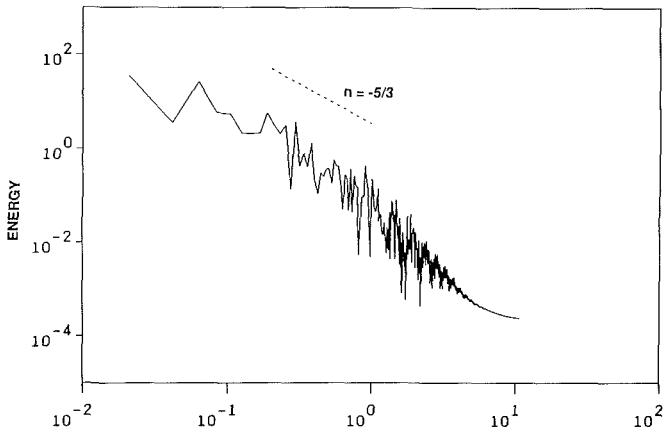


Fig. 7(b)

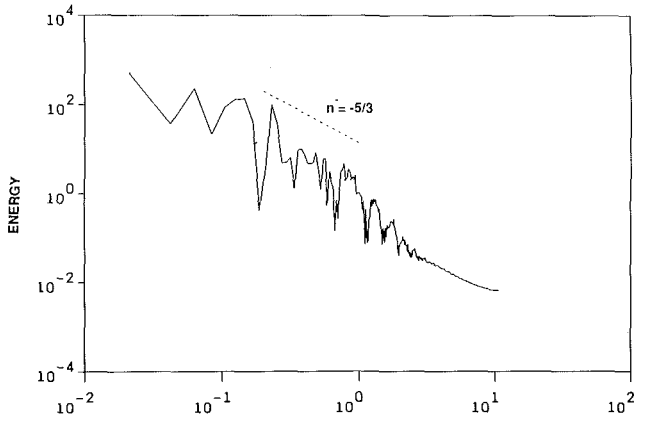


Fig. 7(d)

**Fig. 7 Time traces (*a*) and (*c*) and power spectra (*b*) and (*d*) of horizontal and vertical velocity components near the downstream free shear layer for test case Re = 5000**

from a higher Reynolds number test case (Re = 7500) where the flow is locally transitional (Koseff and Street, 1984a). The highest $\nu_\tau^*$ levels computed on the individual recirculation planes are shown in Fig. 10*b*. Indeed, the peak levels of $\nu_\tau^*$ are concentrated within the downstream free shear layer which is in agreement with the experimental data.

**LES Results.** For the LES computation of the cavity flow, the Reynolds number was 10000. Shown in Figs. 11(*a*) and 11(*b*) are snapshots of the velocity field at a sample time $T_r = 6.5$. The spanwise velocity vectors represent flow at the $x \cong 0.77$ plane while the DSE region is shown at various planes between the TGL vortices. Besides the corner vortex, the spanwise velocity vectors show five additional vortex structures that appear distorted when compared to the DNS results at the lower Reynolds number (Re = 5000). Breakdown of the TGL vortex structure is due to the onset of turbulence within the adjacent downstream free shear layers. Prasad and Koseff (1989) (SAR = 1.0) and Koseff and Street (1984a) (SAR = 3.0) also reported a loss of TGL vortex structure at this Re, but were unable to visualize the vortex flow patterns due to the rapid lateral dispersion of the dye streaks. The existence of the vortex structures and their streamwise extent is further illustrated in Figs. 12 and 13 in the form of stream function contours. In Fig. 12, these contours are computed on each recirculation plane (*x*-*y*) as if the flow were 2D and then stacked side-by-side from the spanwise end-wall to the symmetry plane. The stream function contours in Fig. 13 are computed similarly on the *z*-*y* planes and then stacked in the *x*-direction from the

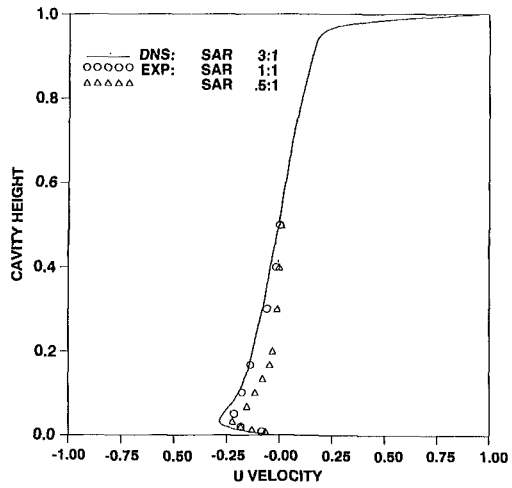


**Fig. 8 Quantitative comparisons between the DNS results and experimental data (Prasad and Koseff, 1989) in terms of the centerline mean velocities at the cavity mid-span plane**

downstream to the upstream walls. In both figures, only the stream function contours from the lower half of the cavity are shown. The marking of grid lines in Fig. 13 and in the velocity vectors (Fig. 11(*b*)) help quantify the intensity, spanwise size and streamwise extent of each vortex. The instability mechanism of TGL vortex generation still exists at this Re as evi-

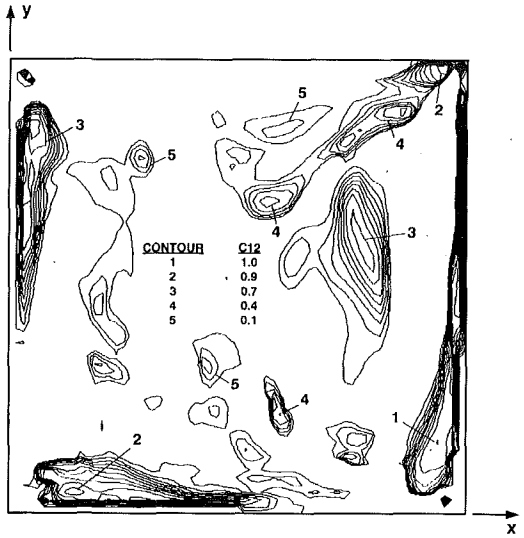


Fig. 9 Distribution of correlation coefficient $C_{12}$ in Eq. (7) using damping parameters $m = 8.0$ and $n = 0.14$ and Smagorinsky constant $C_S = 0.1$ in turbulence length scale definition of Eq. (6). Correlation computed from DNS data taken at completion of test case Re = 5000 ($T_r = 181.0$).

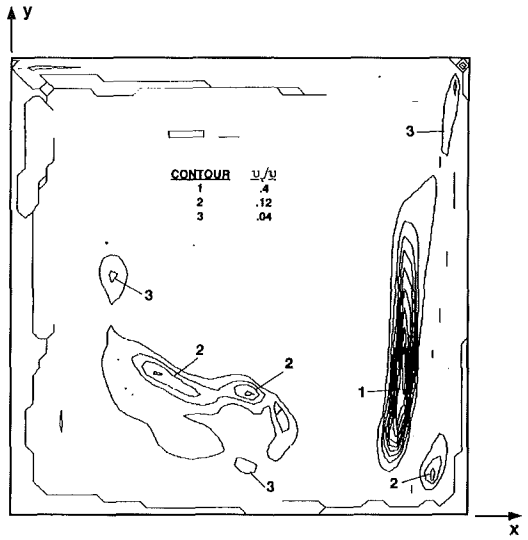


Fig. 10(*a*)

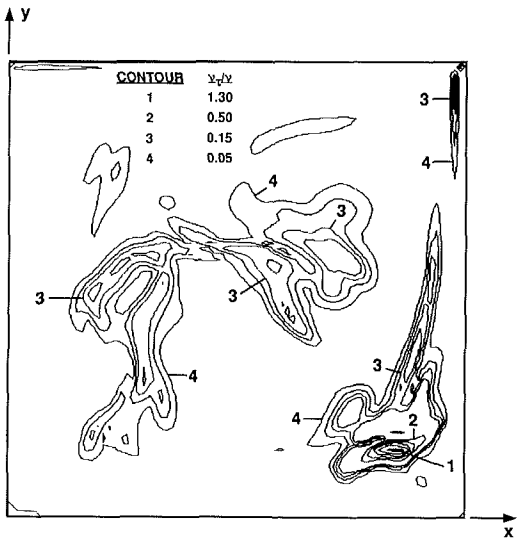


Fig. 10(*b*)

Fig. 10 Turbulent eddy viscosity levels (normalized by the kinematic viscosity) computed from DNS data taken at completion of simulation; (*a*) Re = 5000 and (*b*) Re = 7500

denced by the vortex structure created above the DSE between grid lines $k = 49$ and $k = 62$. Like the DNS results, neither the TGL vortices nor the corner vortex interact with the USE. Thus, the basic structure of the USE remains intact throughout the cavity span. On the other hand, the irregular development of the DSE in the spanwise direction suggests complex interactions between the unsteady effects of the primary recirculation vortex and the TGL vortices. As an example, Koseff and Street (1984b) and Prasad et al. (1988) reported appearances of spiraling spanwise motions within the DSE which they attributed to its interaction with the local vortices. Verification of their observation as well as uncovering other interactions are presented next.

Between the spanwise vortices shown in Fig. 13, the stream function contours form four surfaces that give a cave-like impression. Beneath these surfaces, the basic two-dimensional structure of the DSE develops due to separation of the primary recirculation vortex from the downstream wall (see Fig. 11(*a*)). The vortices adjacent to the DSE strongly influence its spanwise characteristics. An attempt to understand these complicated characteristics as well as the other flow features of the 3D cavity at Re = 10000 is illustrated in Fig. 14 at the sample time $T_r = 6.5$. There, five sets of particle traces were initiated either within the DSE region or the outer extremes of the primary recirculation vortex; in particular, the first computational point off the downstream wall ($x = 0.99$). Also, each set originated half way up the downstream wall ($y = 0.5$) except set number five which started at $y = 0.05$. Set number 1 contains three particle traces that were initiated directly over the center of the large TGL vortex (grid line $k = 10$). After release, all three particles were entrained by the downwash flow of the large vortex. Their spiraling path then transversed streamwise only a short distance before being entrained by the upwash region of the vortex as given by the mid-span recirculation flow. Particles from sets three and four had a similar fate. Set number three initiated above and to the left of the TGL vortex at grid line $k = 28$ while set four originated between the TGL vortices marked grid lines $k = 28$ and $k = 36$. Initially, each particle was convected by the primary recirculation vortex which traced a path that coincides with the streamline surface shown in Fig. 12. As the particles neared the cavity bottom, they were entrained by the respective vortex instead of the DSE. The reason for this is illustrated by particle sets two and five. Set two started above and to the right of the TGL vortex at grid line $k = 28$ while set five was centered just above the tiny flow structure that is positioned between grid line $k = 62$ and the end wall. As the particles of set two approached the cavity bottom they were entrained by the DSE. However, because the large adjacent vortex induced a dominant spanwise velocity component on the DSE, the particles traced a broad spanwise spiral which turned quickly streamwise once fully entrained by the vortex. This spanwise spiral within the DSE region is also traced by particle set number five. From these observations, we can conclude that the streamwise extent of the TGL vortex structures shown in Fig. 13 are sustained through two patterns of fluid entrainment. Close to the downstream wall, these vortices entrain fluid from the adjacent DSE regions which in turn extract fluid from the primary recirculation vortex. As mentioned earlier, this flow pattern was also observed locally in the 3D cavity in the flow visualization experiments. Upstream from the DSE region however, the TGL vortices entrain fluid from the primary vortex directly. Loss of the

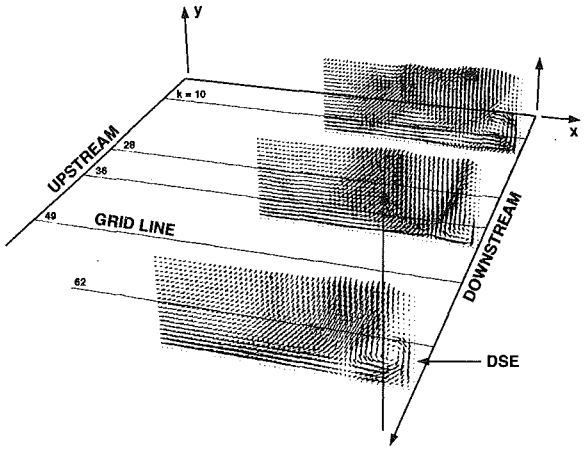


Fig. 11(*a*)

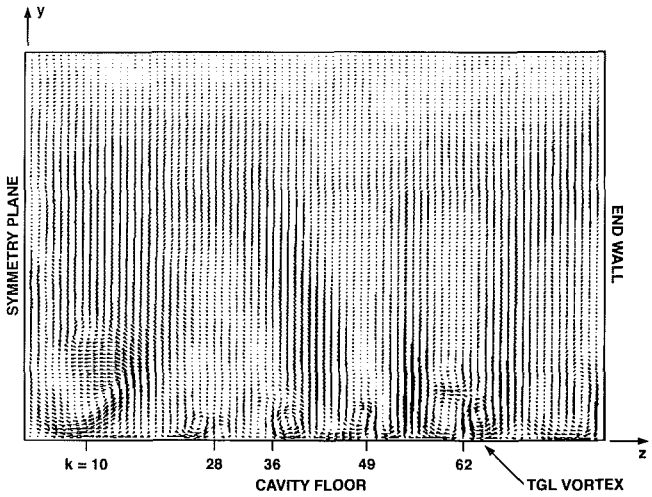


Fig. 11(*b*)

**Fig. 11 Velocity vectors illustrating (*a*) regions of the downstream secondary eddy and (*b*) TGL and corner vortices for LES test case Re = 10000 at relative time $T_r = 6.5$**

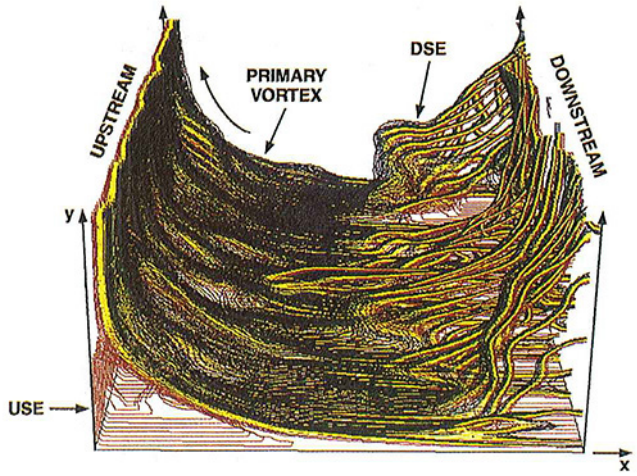


**Fig. 12 Stream function contours showing the downstream (DSE) and upstream (USE) secondary eddies in the LES computation of the shear-driven cavity flow at Re = 10000 and relative time $T_r = 6.5$**

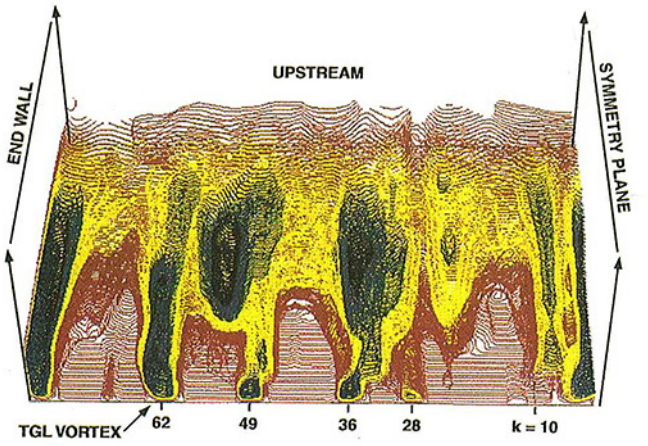


**Fig. 13 Stream function contours showing the TGL and corner vortices in the LES computation of the shear-driven cavity flow at Re = 10000 and relative time $T_r = 6.5$**

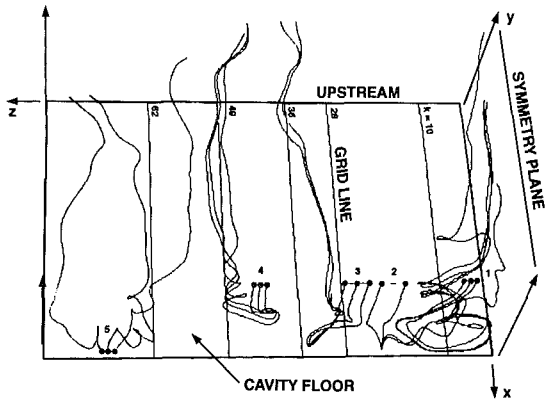


**Fig. 14 Five sets of particle traces illustrating the interaction among the primary recirculation vortex, downstream secondary eddy and TGL and corner vortices of the LES computation at relative time $T_r = 6.5$**

vortex structure occurs upstream once the primary vortex separates from the cavity bottom.

Having this understanding of the flow pattern within the DSE region, the tiny flow structure between grid line $k = 62$ and the span's end wall is another vortex pair. Creation of this secondary vortex pair is due to the opposing spanwise viscous interactions of the corner vortex, the adjacent TGL vortex and the no-slip condition along the cavity bottom. Above its center position lies an imaginary surface within the DSE region that demarcates fluid entrained by the corner vortex apart from that extracted by the adjacent TGL vortex. The existence of this flow surface is illustrated by the right and left particle traces in set number five. As shown in Fig. 14, the spanwise spiral trace of each particle is in opposite directions. Thus, these particles started on opposite sides of the flow surface. Because the adjacent TGL vortices change size and meander along the cavity floor over time, the flow surfaces and corresponding secondary vortices are not stationary. As a matter of fact, flow visualizations of the numerical results showed extremely complicated dynamics that governed these tiny structures. However, their impact on momentum and energy transfer throughout the cavity was never significant.

We will now discuss the effects of the symmetry plane assumption on these LES results. Koseff and Street (1984c) noted that the mean recirculation flow in the 3D cavity with SAR = 3.0 became similar when the Reynolds number was increased to 10000. By examining the comparisons between the computed center-line mean velocity profiles and the experimental results in Figs. 15(*a*) and 15(*b*), one can see that this is indeed the case. While the experimental data is at the mid-span plane, the computed profiles are shown along the center-line of recirculation plane $z = 0.28$; hereinafter called the K15 plane. In

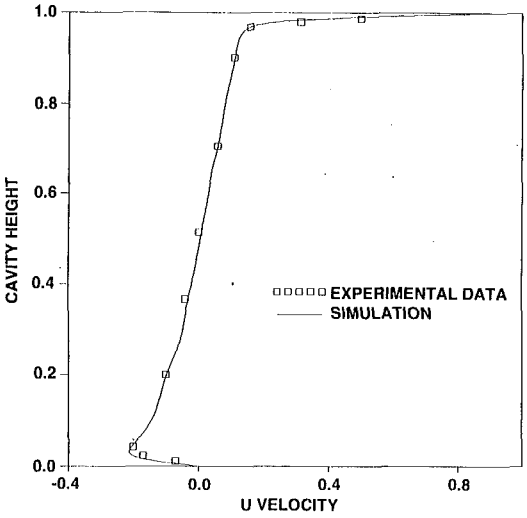


Fig. 15(*a*)

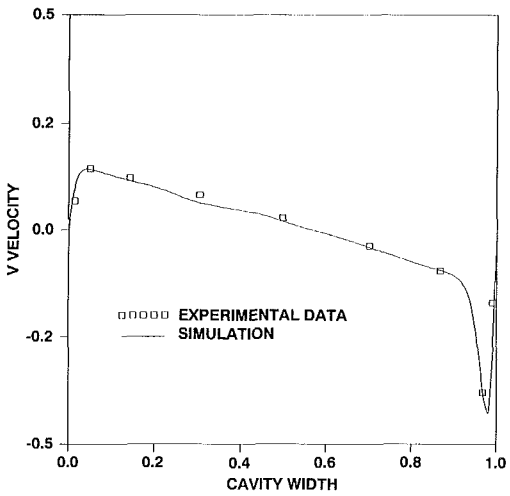


Fig. 15(*b*)

**Fig. 15 Comparison between LES and experimental (Koseff and Street, 1984c) results in terms of centerline mean velocity profiles: simulation profile at K15 plane ($z = 0.28$) and experimental data measured at mid-span plane; (*a*) *U*-velocity, (*b*) *V*-velocity**

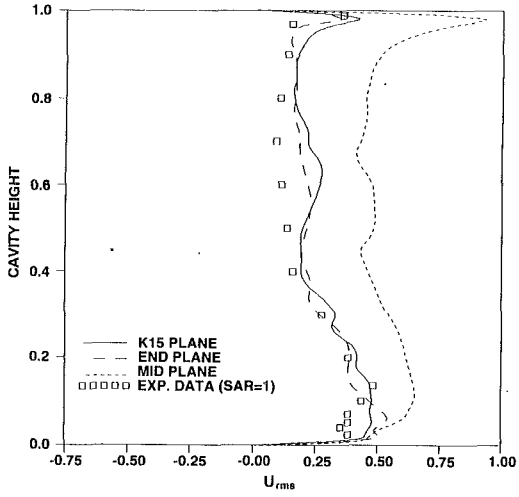


Fig. 16(*a*)

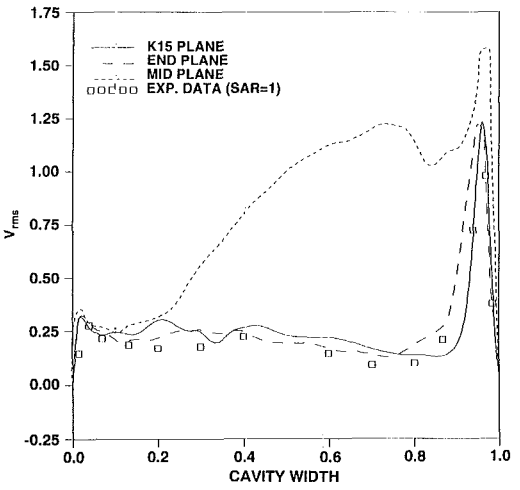


Fig. 16(*b*)

**Fig. 16 Profiles of centerline horizontal and vertical RMS velocity fluctuations; LES profiles are at the spanwise K15, end and mid-span planes while experimental data taken at the mid-span plane of cavity with spanwise aspect ratio equal to 1.0; (*a*) horizontal, (*b*) vertical**

both profiles, the averaged error (as compared to the data) is less than 2 percent. Thus, the symmetry plane assumption has a negligible effect on the mean recirculation at the K15 plane and throughout the remainder of the cavity span. Unfortunately, no center-line Reynolds stresses or turbulent velocity fluctuations were published of the 3D cavity flow with SAR = 3.0. However, data was reported by Prasad and Koseff (1989) at the mid-span plane for SAR = 1.0. Quantitative comparisons between that data and the LES results at the mid-span, K15 and end planes are shown in Figs. 16(*a*) and 16(*b*) in terms of the centerline root-mean-square (rms) velocity fluctuations. The end plane profile in each figure was computed at recirculation plane $z = 1.25$. Both figures clearly show large discrepancies between the computed and experimental mid-span plane rms results. Conversely, rms profiles at the K15 and end planes agree reasonably well with each other as well as with the experimental mid-span plane data. Furthermore, the computed profiles extend the overall observed trend that turbulent kinetic energy is lost near the cavity walls when the cavity SAR is reduced (Koseff and Street, 1984b and Prasad and Koseff, 1989). Hence for this test case, these observations along with the experimental agreement of the computed mean recirculation flow illustrated a localized effect of the spanwise symmetry plane assumption on the LES results.

Finally, we could pose the following questions. Do these LES computations support the explicit understanding that turbulence dominates the flow characteristics near the downstream free shear layer? And at this Reynolds number, what are the spatial distributions of the velocity fluctuations elsewhere in the cavity? Figures 17(*a*) and 17(*b*) show the energy spectrum of the velocity fluctuations calculated from a $T_r = 90$ sample record taken in the vicinity of the downstream free shear layer. Both spectral profiles display an inertial subrange with about an order of magnitude larger energy content within the vertical fluctuations. This result as well as the bandwidth over which the inertial subrange occurs agree with similar analyses conducted on the experimental data (Kaseff and Street, 1884c). In Figs. 18(*a*) and 18(*b*), distributions of the vertical rms fluctuations and shear stress component $u'v'$ at the K15 plane indeed disclose highest levels within the downstream free shear layer region. However, one should note that the rms levels of the vertical velocity fluctuation are also significant along the downstream wall.

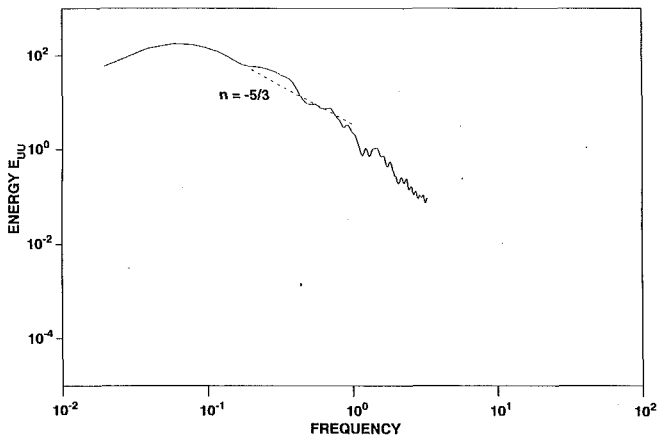


Fig. 17(*a*)

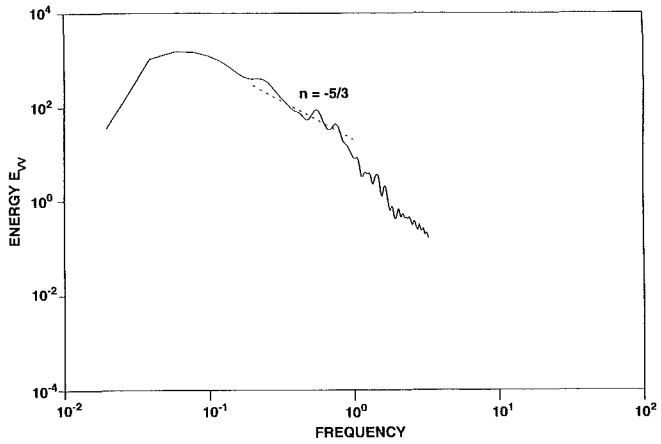


Fig. 17(*b*)

**Fig. 17 Power spectra of velocity components near the downstream free shear layer; (*a*) horizontal, (*b*) vertical**

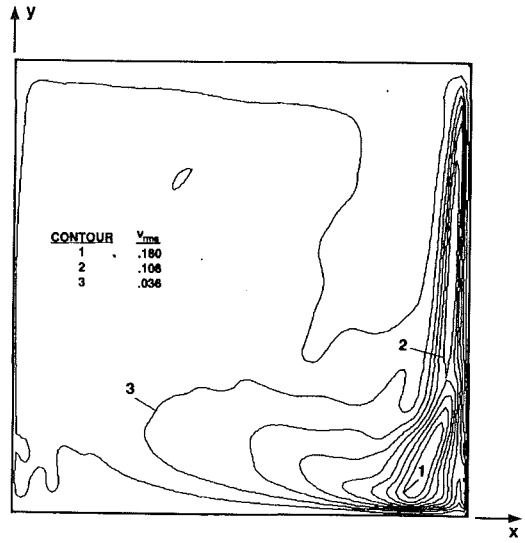


Fig. 18(*a*)

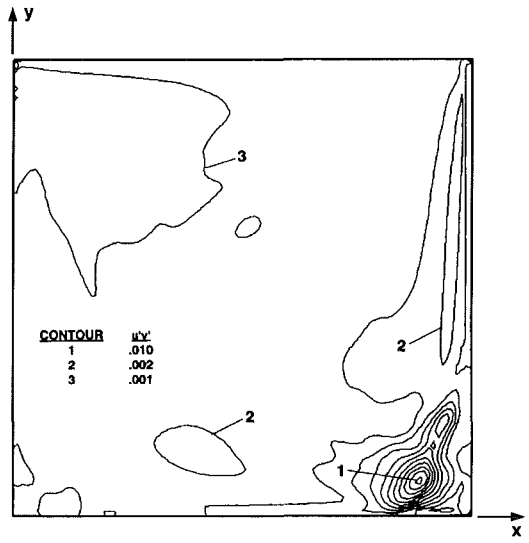


Fig. 18(*b*)

**Fig. 18 Distributions of the (*a*) vertical RMS fluctuations and (*b*) $\overline{u'v'}$ turbulent shear stress component at the K15 plane ($z = 0.28$)**

## Conclusions

The direct numerical simulation (DNS) and large eddy simulation (LES) methodologies are used to study the unsteady and turbulent characteristics of the three-dimensional shear-driven cavity flow at Reynolds numbers 5000 and 10000. Based on the numerical results, the following conclusions about this flow are offered:

At Re = 5000 (DNS results), the flow is laminar, but the three-dimensionality and unsteadiness severely disturbs the basic structure of the classic recirculation flow features. The Taylor-Gortler-like (TGL) vortices change rapidly in size and they meander only locally. We predicted 9 TGL vortex pairs spanning the cavity bottom with one straddling the mid-span plane. The flow remains fully deterministic.

At Re = 10000 (LES results) the instability mechanism for TGL vortex generation still exists, but the vortices themselves have now become distorted due to the onset of turbulence within the downstream free shear layer. Their physical characteristics throughout the 3D cavity vary randomly. The combined effects of the primary recirculation vortex and the TGL and corner vortices cause a complicated irregular development of the downstream secondary eddy (DSE). Near the downstream wall the TGL vortices extract fluid from the downstream eddy region which concurrently entrains fluid from the primary recirculation vortex. Upstream of the downstream eddy region, the TGL vortices entrains fluid directly from the primary vortex. Lastly, secondary vortex pairs are created intermittently within the DSE region due to the viscous interactions among the adjacent larger vortices and the cavity floor.

Although the constants of length scale damping function in the SGS turbulence model were estimated from a DNS computation of a deterministic flow, the spatial distributions of the vertical rms fluctuations and shear stress as given by the model for the turbulent flow agreed with the experimental data.

## Acknowledgments

The first author gratefully acknowledges the support of the Office of Naval Research (Dr. L. P. Purtell, Scientific Officer) and the Independent Research/Independent Engineering Development Program (Dr. K. Lima, Coordinator) at the Naval Undersea Warfare Center Division Newport. The second author has been supported by the Office of Naval Research, under grant No. N00014-91-J-1233. The authors wish to thank the JFE reviewers for their important comments to improve the content of this manuscript.

## References


Clark, R. A., Ferziger, J. H., and Reynolds, W. C., 1077, "Evaluation of Subgrid-Scale Turbulence Models Using an Accurately Simulated Turbulent Flow," *Journal of Fluid Mechanics*, Vol. 91, pp. 1–16.

Deardorff, J. W., 1970, "A Numerical Study of Three-Dimensional Channel Flow of Large Reynolds Numbers," *Journal of Fluid Mechanics*, Vol. 41, Part 2, pp. 453–480.

de Brederoede, V., and Bradshaw, P., 1972, "Three-Dimensional Flow in Nominally Two-Dimensional Separation Bubbles I. Flow Behind a Rearward Facing Step," I. C. Aeronautics Report 72-19.

Freitas, C. J., Street, R. L., Findikakis, A. N., and Koseff, J. R., 1985, "Numerical Simulation of Three-Dimensional Flow in a Cavity," *International Journal of Numerical Methods in Fluids*, Vol. 5, No. 6, pp. 561–576.

Gaskell, P. H., and Lau, A. K. C., 1988, "The Method of Curvature Compensation and its Use in the Prediction of Highly Recirculating Flows," AIAA/ASME/SIAM/APS 1st National Fluid Dynamics Congress, pp. 272–279.

Ghia, U., Ghia, K. N., and Shin, G. T., 1982, "High-Re Solutions of Incompressible Flow Using the Navier-Stokes Equations and a Multigrid Method," *Journal of Computational Physics*, Vol. 48, pp. 387–411.

Görtler, H., 1954, "On the Three-Dimensional Instability of Laminar Boundary Layers on Concave Walls," NACA Technical Memorandum, 1375.

Gosman, A. D., Pan, W. M., Runchal, W. M., Spalding, D. B., and Wofshtein, 1968, *Heat and Mass Transfer in Recirculating Flows*, Academic Press, London.

Gustafson, K., and Halasi, K., 1986, "Vortex Dynamics of Cavity Flows," *Journal of Computational Physics*, Vol. 64, No. 2, pp. 279–319.

Ideriah, F. J. K., 1978, "On Turbulent Forced Convection in a Square Cavity," *Numerical Methods in Laminar/Turbulent Flow*, Proceedings 1st International Conference, pp. 257–269.

Jordan, S. A., 1992, "An Iterative Scheme for Numerical Solution of Steady Incompressible Viscous Flows," *Computer and Fluids*, Vol. 21, No. 4, pp. 503–517.

Jordan, S. A., and Ragab, S. A., 1993, "An Efficient Fractional-Step Technique for Unsteady Three-Dimensional Flows," *Journal of Computational Physics* (in review).

Kim, J., and Moin, P., 1985, "Application of a Fractional-Step Method to Incompressible Navier-Stokes Equations," *Journal of Computational Physics*, Vol. 59, pp. 308–310.

Koseff, J. R., and Street, R. L., 1984a, "Visualization Studies of a Shear Three-Dimensional Recirculating Flow," ASME JOURNAL OF FLUIDS ENGINEERING, Vol. 106, No. 1, pp. 21–29.

Koseff, J. R., and Street, R. L., 1984b, "On End Wall Effects in a Lid-Driven Cavity Flow," ASME JOURNAL OF FLUIDS ENGINEERING, Vol. 106, No. 1, 1984, pp. 385–389.

Koseff, J. R., and Street, R. L., 1984c, "The Lid-Driven Cavity Flow: A Synthesis of Qualitative and Quantitative Observations," ASME JOURNAL OF FLUIDS ENGINEERING, Vol. 106, No. 1, pp. 390–398.

Moin, P., and Kim, J., 1980, "On the Numerical Solution of Time-Dependent Viscous Incompressible Fluid Flows Involving Solid Boundaries," *Journal of Computational Physics*, Vol. 35, pp. 381–392.

Patankar, S. V., 1980, *Numerical Heat Transfer and Fluid Flow*, Hemisphere, Washington, DC.

Piomelli, U., Ferziger, J. H., and Moin, P., 1988, "Model for Large Eddy Simulation of Turbulent Channel Flow Including Transpiration," Department of Mechanical Engineering Report, TF-32, Stanford U., Stanford, CA.

Prasad, A. K., and Koseff, J. R., 1989, "Reynolds Number and End-Wall Effects on a Lid-Driven Cavity Flow," *Physics of Fluids A*, Vol. 1, No. 2, pp. 208–218.

Prasad, A. K., Perng, C. Y., and Koseff, J. R., 1988, "Some Observations on the Influence of Longitudnal Vortices in a Lid-Driven Cavity Flow," AIAA/ASME/SIAM/APS 1st National Fluid Dynamics Congress, pp. 288–295.

Rhee, H. S., Koseff, J. R., and Street, R. L., 1984, "Flow Visualization of a Recirculating Flow by Rheoscopic Liquid and Liquid Crystal Techniques," *Experiments in Fluids*, Vol. 2, pp. 57–64.

Smagorinsky, J., 1963, "General Circulation Experiments with the Primitive Equations, I. The Basic Experiment," *Monthly Weather Review*, Vol. 91, pp. 99–164.

Soh, W. Y., and Goodrich, J. W., 1988, "Unsteady Solution of Incompressible Navier-Stokes Equations," *Journal of Computational Physics*, Vol. 79, pp. 113–134.

Taylor, G. I., 1923, "Stability of Viscous Liquid Contained Between Two Rotating Cylinders," *Philosophical Transaction of the Royal Society* (London), Vol. 223, pp. 289–343.

Van Driest, E. R., 1956, "On the Turbulent Flow Near a Wall," *Journal of Aeronautical Sciences*, No. 23, pp. 1007–1012.

Young, D. L., Liggett, J. A., and Gallagher, R. H., 1976, "Unsteady Stratified Circulation in a Cavity," *J. Eng. Mech. Div.*, ASCE 102, EM6, pp. 1009–1023.

Zang, Y., Street, R. L., and Koseff, J. R., 1993, "A Dynamic Mixed Subgrid-Scale Model and Its Application to Turbulent Recirculation Flows," *Physics of Fluids*, Vol. 5, No. 12, pp. 3186–3196.

**P. C. Chan**
Senior Scientist,
Applied Science and Engineering
Technology Division.
Mem. ASME

**H. H. Klein**
Program Manager,
Applied Science and Engineering
Technology Division.

JAYCOR,
P. O. Box 85154,
9775 Towne Centre Drive,
San Diego, CA 92138-5154

# A Study of Blast Effects Inside an Enclosure[1]

*A study of blast effects inside an enclosure was performed for a 1-lb C4 charge placed at the center of a rectangular bunker. The prediction based on the Euler equations shows good agreement with the test data. Predictions calculated by the method of images were also obtained to help illustrate the internal shock reflection effects. The results show that the confined blast loading is more complex than the free field loading due to internal shock reflections and interactions. Focusing of multiple reflections is possible and may cause significant late time loadings.*

## Introduction

A blast field is generated when a high energy explosive is detonated. A blast flow field is dominated by moving shock waves with significant destructive capabilities. Blast studies can be divided into two major categories, namely, free field blasts and confined blasts. Research efforts in studying blast effects usually focus on developing hardening technologies to protect military targets, such as tanks, vehicles and bunkers. However, human injuries can occur at blast levels much lower than those that cause equipment damage (Philips, 1986). There is an ongoing need to study the blast flow fields in detail at levels relevant to human effects. Recently, there is an increased interest in studying confined blasts for small charges to help design new aircraft luggage containers hardened against terrorist bombing up to the detectable level.

A confined blast field can be generated by the explosion of a penetrated shaped charge inside an armored personnel vehicle or the detonation of a small smuggled terrorist bomb inside a confinement. Due to multiple shock reflections, the blast field inside an enclosure is more complex than in the free field. The characterization of blast loading depends heavily on experimental scaling (Heap, 1987). Free field explosion scaling involves mainly the charge energy and the standoff distance. However, for confined blasts, there are several combinations of geometric parameters such as the size and shape of the enclosure, and the relative location of the explosive and the target to each other and to the surrounding walls. Scaling and semi-empirical modeling usually overlook the details of the shock reflection effects (Britt and Drake, 1987; Army Corps of Engineers, 1986). More accurate analytical studies are needed before a satisfactory data base can be established for confined blast effects. The application of computational fluid dynamics (CFD) technology can provide a comprehensive simulation of the multiple shock reflection effects inside an enclosure.

This paper presents a study of the blast effects inside a rectangular bunker. Results from Euler computations were compared against experimental data. Calculations were also obtained by the method of images (MOI) to illustrate the confined shock reflection effects.

## Experiment

A series of confined blast experiments was sponsored by the US Army Medical Research and Development Command and performed at the Los Alamos National Laboratory (Dodd, 1990). The two experiments selected for the present computational study consist of detonating 1 lb of C4 explosive at the center of a 10 × 8 × 8 ft rectangular steel bunker. Figure 1 shows the plan views of the two test configurations across the mid-horizontal plane of the bunker. The present study focuses on comparing the calculated results with the measured data for the front, left and corner free sensors. These are Susquehanna Model ST-2 gauges pointing vertically upwards and located on the same mid-horizontal plane as the charge. Their responses will reveal the shock reflection patterns inside the bunker. Data analyses show that the overall gauge measurements have an error margin of ±20 percent. Figure 1 shows that each test also collected loading data on a 12 × 30 in. steel cylinder and two small sheep that will not be addressed by the present study.

## Euler Simulation

The advantage of a full Euler simulation is the self-consistent capturing of the shock reflection and interaction that is important for predicting the blast effects in an enclosure. A time-dependent three-dimensional Euler simulation was performed using JAYCOR's Equation Independent Transient Analysis Computer Code, EITACC. The EITACC code solves the full time-dependent three-dimensional Navier-Stokes Equations by semi-implicit finite difference. It has been successfully applied to a wide range of gas dynamics problems, including combustion (Chan et al., 1988; Chan and Klein, 1989; Klein and

[1]This paper was presented at the 62nd Shock and Vibration Symposium sponsored by the Defense Nuclear Agency in Springfield, VA, October 29–31, 1991.

Contributed by the Fluids Engineering Division for publication in the JOURNAL OF FLUIDS ENGINEERING. Manuscript received by the Fluids Engineering Division April 27, 1993; revised manuscript received October 27, 1993. Associate Technical Editor: D. M. Bushnell.

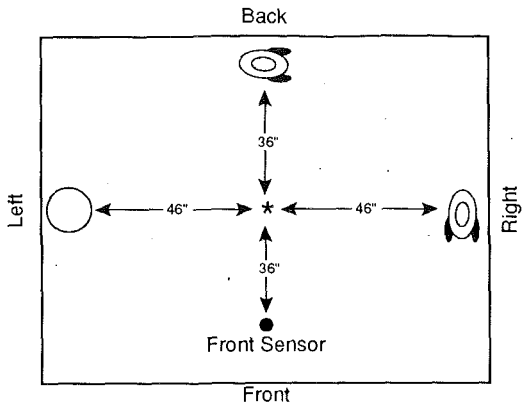


(a) Test A-2, front sensor location

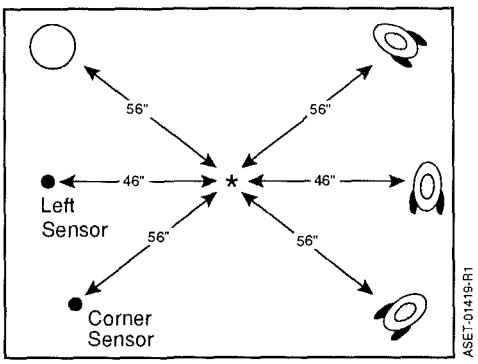


(b) Test A-5, left and corner sensor locations

● Sensor ○ Cylinder

Sheep ★ Charge

**Fig. 1 Test setup on mid-horizontal plane in 10 × 8 × 8 ft rectangular bunker**

Chan, 1989). The stress terms were suppressed for the present investigation.

The governing equations are presented in cartesian $x$-$y$-$z$ coordinates as follows.

The continuity equation is

$$\frac{\partial \rho}{\partial t}+\left[\frac{\partial}{\partial x}\rho u+\frac{\partial}{\partial y}\rho v+\frac{\partial}{\partial z}\rho w\right]=0 \tag{1}$$

The three momentum equations are

$$\frac{\partial}{\partial t}\rho u+\left[\frac{\partial}{\partial x}\rho uu+\frac{\partial}{\partial y}\rho uv+\frac{\partial}{\partial z}\rho uw\right]=-\frac{\partial P}{\partial x} \tag{2}$$

$$\frac{\partial}{\partial t}\rho v+\left[\frac{\partial}{\partial x}\rho vu+\frac{\partial}{\partial y}\rho vv+\frac{\partial}{\partial z}\rho vw\right]=-\frac{\partial P}{\partial y} \tag{3}$$

$$\frac{\partial}{\partial t}\rho w+\left[\frac{\partial}{\partial x}\rho wu+\frac{\partial}{\partial y}\rho wv+\frac{\partial}{\partial z}\rho ww\right]=-\frac{\partial P}{\partial z} \tag{4}$$

$t$ is the time coordinate. $u$, $v$, and $w$ are the velocity components in $x$, $y$, and $z$ directions, respectively. $\rho$ and $P$ are the density and pressure.

The conservation equation for the total specific enthalpy $H$ is

$$\frac{\partial}{\partial t}\rho H+\left[\frac{\partial}{\partial x}\rho uH+\frac{\partial}{\partial y}\rho uH+\frac{\partial}{\partial z}\rho uH\right]=\frac{\partial P}{\partial t} \tag{5}$$

Viscosity and heat conduction effects were assumed negligible for the present computation.

The equation of state is modeled by the ideal gas law as

$$P=\rho RT \tag{6}$$

where $R$ is the gas constant and $T$ is the temperature. The total specific enthalpy is

$$H=C_pT+\gamma\frac{P}{\rho}\frac{\mathrm{M}^2}{2} \tag{7}$$

where $C_p$ is the constant pressure specific heat. $\gamma$ and M are the ratio of specific heats and Mach number.

The numerical method used is similar to the semi-implicit method of Liles and Reed (1978), and Chan et al., (1986). The method was first developed for solving complex two-phase flow equations, but has also been successfully applied to subsonic-supersonic flow with combustion. It provides full coupling of the primitive variables to pressure and thermodynamics. The pressure is fully implicit, which is advantageous in solving coupled subsonic-supersonic problems. The integration of the advection and diffusion terms is explicit in time. The third order QUICK differencing scheme developed by Leonard (1979) was used for the advection terms. The EITACC code employs staggered grid convention by placing momentum variables on the computational cell faces and scalar variables at cell centers. Cell size dimensions can be nonuniform.

As the dependent variables of each computational cell at ($x$, $y$, $z$), with index referenced as ($i$, $j$, $k$), are advanced in time from level $n$ to $n$ + 1, they are coupled through a matrix representation as

$$[A][Q]=[S] \tag{8}$$

where the column matrix $Q$ contains the dependent variables,

## Nomenclature

$a_0$ = ambient sound speed
$C_p$ = constant pressure specific heat
$e$ = specific energy per unit mass of explosive
$H$ = specific total enthalpy per unit mass
M = Mach number
$P$ = pressure
$P_i$ = the peak value of the blast wave
$P_j$ = the individual reflected blast wave
$P_0$ = ambient pressure
$P_r$ = reflected overpressure
$P_s$ = side-on overpressure
$R$ = gas constant; or charge stand off distance
$\bar{R}$ = nondimensional scaled distance
$T$ = temperature
$t$ = time
$t'$ = time after the arrival of the blast wave
$\bar{t}$ = nondimensional scaled time
$t_d$ = positive duration of the Friedlander blast wave
$u$ = velocity in $x$-direction
$v$ = velocity in $y$-direction
$w$ = velocity in $z$-direction
$W$ = charge weight
$x$ = Cartesian coordinate in $x$-direction
$y$ = Cartesian coordinate in $y$-direction
$z$ = Cartesian coordinate in $z$-direction
$\gamma$ = ratio of specific heats
$\theta$ = angle of incidence between the incident blast wave and sensor orientation
$\rho$ = density

$$[Q] = \begin{vmatrix} \rho u_{i,j,k} \\ \rho v_{i,j,k} \\ \rho w_{i,j,k} \\ H_{i,j,k} \\ T_{i,j,k} \\ P_{i,j,k} \\ P_{i+1,j,k} \\ P_{i-1,j,k} \\ P_{i,j+1,k} \\ P_{i,j-1,k} \\ P_{i,j,k+1} \\ P_{i,j,k-1} \end{vmatrix}^{n+1} \tag{9}$$

The coefficients of the matrix A are formulated from Eqs. (1) to (7). The governing conservation equations (Eqs. (1) through (5)) are integrated over a cell by the finite volume approach, coupling the scalars in the cell center and momentum vectors across the cell faces. QUICK differencing is used for advection terms, and central differencing is used for diffusion terms. Equations (6) and (7) are linearized as

$$\rho^{n+1} = \rho^n + \left(\frac{\partial \rho}{\partial T}\right)^n (T^{n+1} - T^n) + \left(\frac{\partial \rho}{\partial P}\right)^n (P^{n+1} - P^n) \tag{10}$$

and

$$H^{n+1} = H^n + \left(\frac{\partial H}{\partial T}\right)^n (T^{n+1} - T^n) + \left(\frac{\partial H}{\partial P}\right)^n (P^{n+1} - P^n) \tag{11}$$

The source vector $S$ in Eq. (8) contains known information from the previous time level $n$. By a series of Gaussian eliminations of Eq. (8) for all the computational cells, a final system of linear equations for the pressure throughout the entire computational domain can be obtained as

$$[B] \begin{bmatrix} P_{i,j,k} \\ P_{i+1,j,k} \\ P_{i-1,j,k} \\ P_{i,j+1,k} \\ P_{i,j-1,k} \\ P_{i,j,k+1} \\ P_{i,j,k-1} \end{bmatrix}^{n+1} = [D] \tag{12}$$

Equation (12) is usually solved by an alternating direction line successive overrelaxation (LSOR) method. Once the pressure is known, all the other dependent variables can be back-solved from Eq. (8).

When solving problems involving the presence of shock waves, the fourth order MacCormack shock damping method is used (MacCormack and Baldwin, 1975).

The calculation modeled one octant of the empty bunker. The effects of the small obstacles were neglected. Significant savings in computation time was achieved by making use of the 1/8 symmetry. Uniform 1.1 in. computational cells were used that resulted in 105,600 computational cells. The charge was represented by a high pressure and temperature zone equivalent to the energy of the explosive at time zero. The calculation was performed on the HP Apollo 700 desktop workstation.

Figures 2 and 3 present some computed results on the mid-

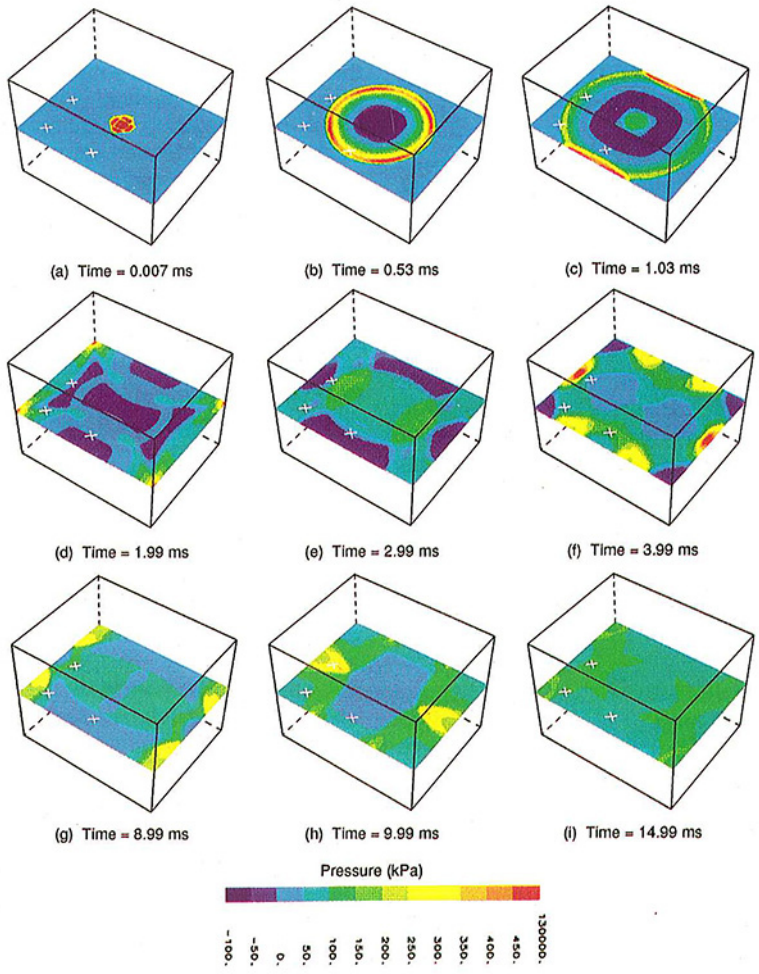


Fig. 2 Overpressure contours on the mid-horizontal plane

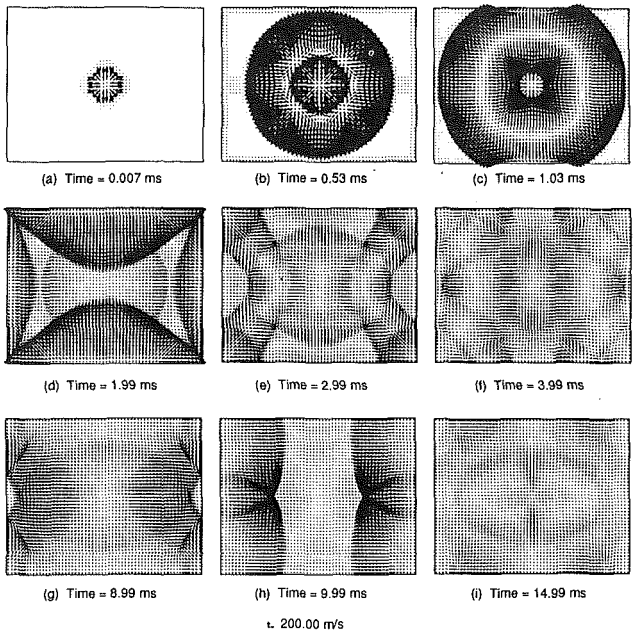


**Fig. 3 Vector plots on the mid-horizontal plane**

horizontal plane of the rectangular bunker. Figure 2 shows the overpressure contours in an isometric view, and Fig. 3 shows the corresponding vector plots in a plan view.

Figures 2(*a*) and 3(*a*) show the early concentrated explosive zone at 0.007 ms. Figures 2(*b*) and 3(*b*) show the expanding free shock at 0.53 ms that has just passed the front sensor and is about to reach the left sensor. Figure 2(*b*) also shows that the center region of the bunker is rarefied after the initial explosion, with the pressure dropping below the ambient value. This rarefaction is due to the overexpansion of the initial blast field. This rarefied center region will implode quickly and radiate a secondary pressure wave outwards, as shown in Figs. 2(*c*) and 3(*c*). Figure 2(*c*) also shows that the free shock is passing the corner sensor at about 1 ms, and part of the free shock is reflecting from the front and back walls. Since the bunker has a square cross-section, the shock is also reflecting from the top and bottom walls simultaneously.

Figures 2(*d*) and 3(*d*) show that the initial free shock has reached all the bunker walls, and the reflected shocks are converging at the bunker center and interacting with the outflowing secondary shock formed by the postblast center implosion. Figures 2(*e*) and 3(*e*) show that the converged shocks radiate outwards again and interact with the shocks reflecting off the four vertical bunker edges. Figures 2(*f*) and 3(*f*) show that the reflected shocks are reconverging to the bunker center the second time. Shock reflections and shock-shock interactions will continue and generate complex flow fields, as shown in Figs. 2(*g–i*) and 3(*g–i.*)

The Euler results show that shock patterns inside an enclosure are much more complex than in the free field. The loading on an object in the free field depends primarily on the standoff distance between the charge and the object, but an object inside an enclosure will receive repeated loadings from multiple shock reflections.

## Method of Images (MOI)

The blast effects inside an empty bunker can also be calculated by the method of images (MOI) analogous to optical ray tracing. A calculation of the internal blast waves was performed using JAYCOR's BWAVES code based on the method of images (Kan, 1991). The blast waves are produced by the explosive source and reflected images off the bunker walls. Figure 4 illustrates a third order reflected wave arriving at the

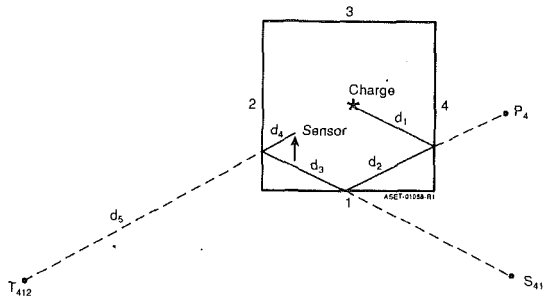


**Fig. 4 Illustration of a third order reflection**

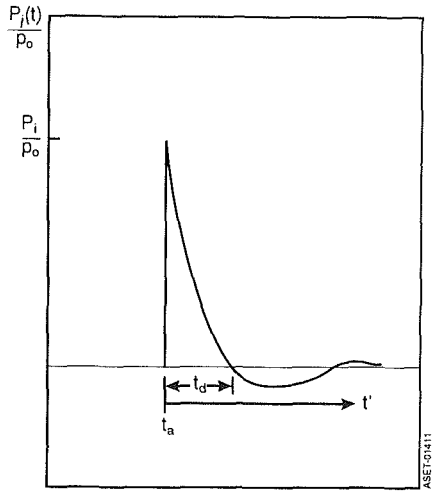


**Fig. 5 Illustration of a Friedlander wave**

sensor from the source charge at the bunker center. The tertiary image $T_{412}$ comes successively from the secondary and primary images $S_{41}$ and $P_4$, respectively.

The pressure-time history $P(t)$ is computed as the sum of all blast waves, $P_j(t)$, that can be viewed at the sensor location of interest,

$$P(t) = \sum_{j=1}^{N} P_j(t) \tag{13}$$

The total number of blast waves, $N$, is controlled by the order of reflection desired for each calculation. Each individual blast wave generated by the charge or an image is assumed to be a Friedlander wave expressed in the nondimensional form as

$$\frac{P_j(t)}{P_0} = \frac{P_i}{p_0}\left[1 - \frac{t'}{t_d}\right] e^{-b(t'/t_d)} \tag{14}$$

where the wave form is illustrated in Fig. 5. $P_i$ is the peak incident overpressure, and $P_0$ is the ambient pressure. $t'$ is the time measured from the wave arrival time $t_a$. $t_d$ is the positive duration, and $b$ is the exponential shape parameter. The parameters for the Friedlander wave were taken from the blast data compiled by Baker (1973).

The blast data compiled by Baker correlate the normalized peak reflected overpressure, $P_r/P_0$, and the peak side-on overpressure, $P_s/P_0$, with the nondimensional scaled distance $\overline{R}$,

$$\overline{R} = \frac{RP_0^{1/3}}{(We)^{1/3}} \tag{15}$$

where $R$ is the charge standoff distance, $W$ is the charge weight, and $e$ is the specific energy per unit charge weight. For C4 explosive, $e$ is $6.314 \times 10^6$ J/kg. Time is also scaled as

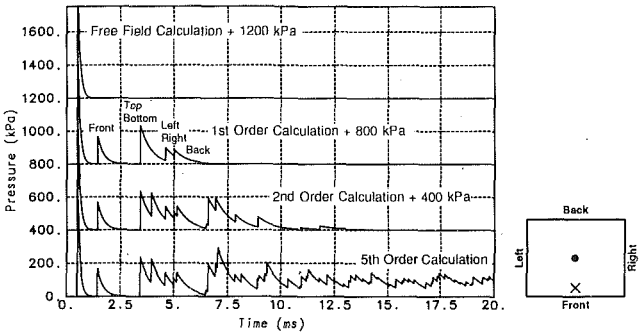


**Fig. 6 MOI results for the front sensor based on contribution from increasing orders of reflection**

$$\bar{t} = \frac{t a_0 P_0^{1/3}}{(We)^{1/3}} \tag{16}$$

where $a_0$ is the ambient sound speed.

The peak incident pressure, $P_i$, is expressed as

$$P_i = \begin{cases} \left[ \dfrac{P_r}{p_0} \cos(\theta) + \dfrac{P_s}{p_0} \sin(\theta) \right] S & (0 \le \theta \le \pi/2) \\ \dfrac{P_s}{p_0} [1 + 0.25 \cos(\theta)] S & (\pi/2 < \theta \le \pi) \end{cases} \tag{17}$$

where $\theta$ is the angle of incidence between the incident blast wave and the orientation of the sensor. $S$ is the wall surface reflectivity factor selected as 0.8.

The MOI algorithm is extremely efficient and provides detailed tracking of wave reflections. However, at higher charge weights and with the presence of complex blockages, the MOI is deficient in capturing nonlinear shock-shock interaction and wake effects.

A wave tracking analysis of the MOI results elucidates the effects of multiple reflections for a confined blast. Figure 6 shows the MOI results for the front sensor by comparing the calculated responses based on increasing orders of reflections. The curves in Figure 6 are each offset by 400 kPa. The top curve shows the response without any reflection, which is equivalent to the free field response without the bunker walls, where the loading is over in less than 1 ms. The second curve shows the first order results that indicate the effects of the primary reflections from the six walls from 1.5 to 6 ms. The first primary reflection is the immediate reflection from the front wall, followed by reflections from the top and bottom, the left and right, and the back walls. The third curve shows the effects of second order reflections dominating from 6 to 11 ms. The bottom curve shows the calculated sensor response up to the fifth order. Compared to the previous three curves, the fifth order results show that the third and higher order reflections are still well sustained between 10 to 20 ms.

## Data Comparison

Figure 7 shows the data comparison for the front sensor. The Euler results follow closely with the data in both magnitude and timing. The measured free shock side-on peak overpressure of about 600 kPa at 0.4 ms was well reproduced by the Euler and MOI calculations. The MOI results agree well with the data before 6 ms. Beyond 6 ms, the MOI results show a slight time lag error. This time lag error is due to the use of the constant ambient sound speed $a_0$ in Eq. (16) for time scaling that is inherent when using Baker's free field blast data. However, in reality the shocks travel through a highly heated medium with increased sound speed due to multiple shock reflections.

Both the computed results and the data in Fig. 7 show that shock reflections can continue at significant magnitudes even

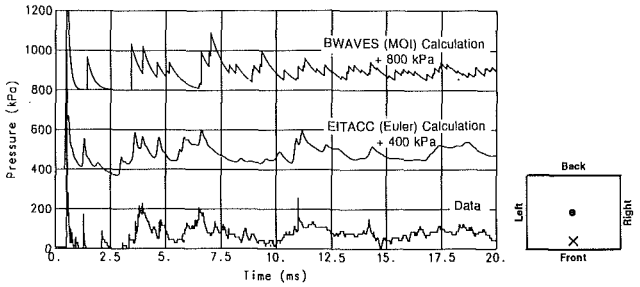


**Fig. 7 Comparison of predictions with data for the front sensor**

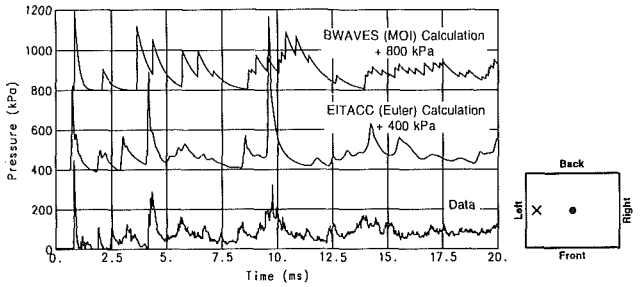


**Fig. 8 Comparison of predictions with data for the left sensor**

at 10 time scales beyond the passing of the initial free shock. From 2 to 12 ms, the resultant shock pressures at the front sensor location range from 1/3 to 1/2 of the first peak value.

Figure 8 shows the data comparison for the left sensor which is 46 in. from the charge. The initial free shock arrives at about 1 ms with a peak value of about 420 kPa which was well reproduced by the Euler and the MOI calculations. The MOI results show fair comparison with the data before 10 ms and suffer from time lag error due to the use of a constant sound speed for time scaling as discussed earlier for the front sensor.

Both the data and the Euler results in Fig. 8 show that the multiply reflected shocks arrive at the left sensor location in a more synchronized pattern than at the front sensor location (Fig. 7). This synchronized pattern produces pressure pulses at 4 and 9.5 ms comparable to the initial free shock strength. This must be due to the fact that the left sensor is located at the center of the square cross-section of the bunker. The square cross-section provides a symmetry that focuses the shock reflections more effectively onto its center line where the left sensor is located. The focused shock patterns at 4 and 9.5 ms can be observed in Figs. 2(*f*) and (*h*) and Figs. 3(*f*) and (*h*). The front sensor does not show such a synchronized reflection pattern, because it is located at the center of a rectangular cross-section with less symmetry.

The calculated Euler results in Fig. 8 show a general overprediction for the two focused spikes at 4 and 9.5 ms, although the timing comparison remains excellent. Since the calculation was performed for an octant of the bunker with perfect symmetry, it should produce the most perfect shock focusing effects. It is unlikely that the experiment would achieve such a perfect focusing. A slight misalignment between the charge and the probe can disrupt the perfect symmetry. Figure 9 compares the measured data with the calculated results at a location 3.5 in. off axis from the intended probe location. Figure 9 shows that the calculated peak values at 4 and 9.5 ms were reduced by 40 percent with excellent data agreement.

The results in Figs. 8 and 9 show that the late time shock focusing can be significant along lines of symmetry for a confined blast. Even though each reflected shock becomes weaker, the merging of a few reflected shocks together can be as strong as the initial shock. Shock focusing effects should be carefully studied when designing blast shielding for confined blasts.

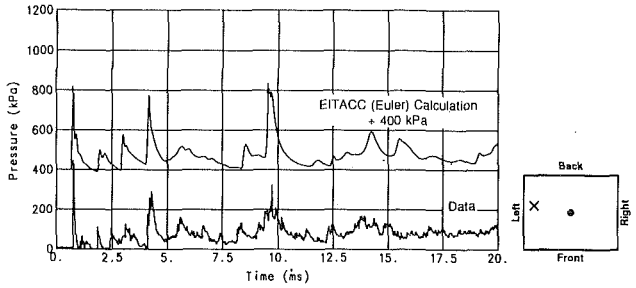


Fig. 9 Data comparison for the left sensor (3-1/2 in. offset)

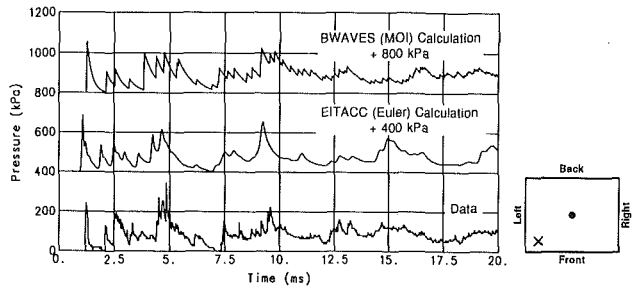


Fig. 10 Comparison of predictions with data for the corner sensor

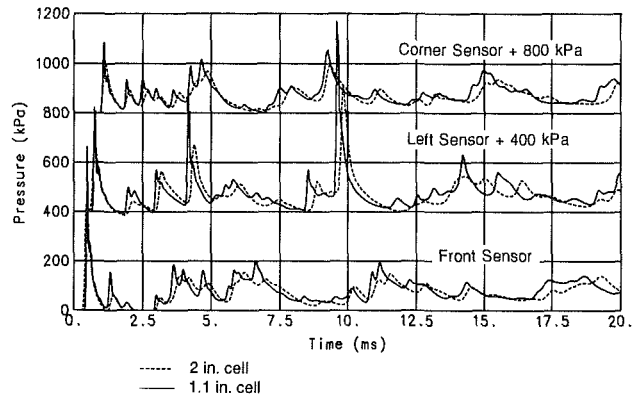


Fig. 11 Effects of resolution

Figure 10 shows the data comparison for the corner sensor which is 56 in. from the charge. This sensor measures the lowest initial shock peak pressure of about 100 kPa, because it is the farthest from the charge. Both the Euler and the MOI results show fair comparison with the data. The Euler results still agree with the data better, especially at late times beyond 10ms. Compared to the front and the left sensors (Figs. 7 and 8), the corner sensor shows the least synchronized reflection. This may be due to the fact that the sensor is located near a corner region without much geometric symmetry where wave reflections are more likely to be out of phase.

The calculated results presented based on 1.1 in. cell resolution (105,600 cells) were considered adequate for the estimation of biological tissue structural responses. A doubling of the resolution in each direction will require 844,800 computational cells and will far exceed the capacity of the available HP Apollo 700 desktop workstation. The typical structural response time for biological tissues is on the order of 5 ms. Although injuries are caused by shock loadings instead of quasistatic overpressure, injuries are usually not caused by high frequencies.

To quantify the effect of cell resolution, Fig. 11 compares the results based on a 1.1 in. cell size to those obtained from a 2 in. cell resolution. Both calculations generally follow each other, and the free shock response is not affected significantly by the resolution before 2 ms. Slight differences gradually develop as multiple reflections continue beyond 2.5 ms. The results based on 1.1 in. cells produce sharper peaks and higher order modes, with fluctuations within 1 ms clearly observable. Computer memory limitation prevented further grid refinement which would be expected to add higher order modes to the calculated responses.

The detailed comparison between calculation results and measured data has provided in-depth understanding of the confined blast effects. Since nonlinear shock reflection and shock-shock interaction is self-consistently modeled by the Euler method, it is more accurate than the MOI calculation. The MOI calculation will be deficient in modeling confined blasts with complex configurations, such as blockages and shields, since complex flows with wakes and recirculations are not analogous to optical reflections (Stuhmiller et al., 1991).

## Conclusion

A numerical study of the blast effects inside a rectangular bunker was successfully performed. The results show that multiple shock reflections can continue at significant magnitudes for a long period. Geometric symmetries can cause multiple reflected shocks to converge with strength comparable to the initial free shock. Euler code simulations can be a valuable analytic tool to help understand and extend the data base for confined blasts.

## Acknowledgment

The support of this work was provided under Contract No. DAMD17-89-C-9159 from the U.S. Army Medical Research and Development Command and the Walter Reed Army Institute for Research. Thanks to Dr. James H. Stuhmiller for his helpful discussion during the course of this investigation.

## References

Army Corps of Engineers, 1986, "Fundamentals of Protective Design for Conventional Weapons," *TM 5-855-1 Technical Manual*, Nov.

Baker, Wilfred E., 1973, "Explosions in Air," Univ. of Texas Press, Austin and London, pp. 150–167.

Britt, J. R., and Drake, J. L., 1987, "Blast Loads from Internal Explosions and Other Reflected Shock Waves," *International Symposium on the Interaction of Conventional Munitions with Protective Structures*, Mannheim, Germany, March 9–13.

Chan, P. C., Klein, H. H., and Chan, R. K.-C., 1988, "Computational Analyses of Subscale Space Shuttle Main Engine Nozzles at 3.2-sec Shutdown Condition," AIAA-88-3200, presented at the 24th Joint Propulsion Conference and Exhibit, Boston, MA, July 11–13.

Chan, P. C., and Klein, H. H., 1989, "Computational Studies of Venting Hydrogen Flame Impingement on the Space Shuttle External Tank," AIAA-89-0318, presented at the 27th Aerospace Sciences Meeting, Reno, Nevada, Jan 9–12.

Chan, R. K.-C., Masiello, P. J., and Srikantiah, G. S., 1986, "PORTHOS—A Computer Code for Solving General Three-Dimensional Time-Dependent Two-Fluid Equations," ASME Paper 86-WA/NE-3 presented at the Winter Annual Meeting, Anaheim, CA, Dec.

Heap, C. W., 1987, "Weapon Blast Scaling: Free Field and In Enclosure," Proceedings of the 3rd Workshop on Launch Blast Overpressure, June 9–10, 1986, Aberdeen Proving Ground, Maryland, U.S. Army Ballistic Research Lab. Special Publication BRL-SP-66, June.

Kan, Kit K., 1991, "Method of Image Treatment of Blast Waves in Enclosure with Arbitrary Geometry," Topical Report, Dept. of Respiratory Research, U.S. Army Division of Medicine, Walter Reed Army Institute of Research, Jan.

Klein, H. H., and Chan, P. C., 1989, "A Numerical Investigation of Scramjet Combustors," AIAA-89-2562, presented at the AIAA/ASME/SAE/ASEE 25th Joint Propulsion Conference, Monterey, California, July 10–12.

Leonard, B. P., 1979, "A Stable and Accurate Convective Modeling Procedure Based on Quadratic Upstream Interpolation," *Computer Methods in Applied Mech. and Engrg.*, Vol. 19, pp. 59–98.

Liles, D. R., and Reed, W. H., 1978, "A Semi-Implicit Method for Two-Phase Fluid Dynamics," *Journal of Computational Physics*, Vol. 26, No. 3, pp. 390–407.

MacCormack, R. W., and Baldwin, B. S., 1975, "A Numerical Method for Solving the Navier-Stokes Equations with Application to Shock Boundary Layer Interactions," AIAA Paper 75-1, Jan.

Phillips, Y. Y., 1986, "Primary Blast Injuries," *Annals of Emergency Medicine*, Dec., pp. 1446–1450.

Stuhmiller, J. H., Chan, P. C., Kan, K. K., and Klein, H. H., 1991, "Calculation of Blasts in Enclosures," 12th International Symposium on the Military Application of Blast Simulation, Perpignan, France, Sept. 22–25.

Sutherland, W., 1983, *Phil. Mag.*, Vol. 125, p. 507.

Dodd, K. T., 1990, Test Data Obtained from US Army Medical Research Command.

# The Minimum Drag Profile in Laminar Flow: A Numerical Way

**Ram K. Ganesh**
The University of Connecticut,
Mechanical Engineering Department,
Storrs, CT 06269-3139

*It would be of interest to engineers and scientists to know the shape of the body of a given volume that will have minimum drag when moving through a viscous fluid at constant speed. It would be extremely useful if one could devise an evolution procedure that can evolve the minimum drag body in a logical and an orderly manner. Such a procedure was suggested by Pironneau for laminar flow wherein optimality conditions derived using optimal control theory were used in a non-linear gradient algorithm. The literature cites an attempt of the procedure at high Reynolds number where for each iteration in the evolution process, the flow field required an outer and an inner solution and the calculation of the gradient optimality condition required the solution of the co-state equation, a type of boundary layer equation. This paper addresses the direct simulation of the governing elliptic partial differential equations, viz., the Navier-Stokes and the co-state equations. Even though the latter has no simple mechanical interpretation, capitalizing on its resemblance to the former, this paper shows how the solution to the co-state equation could be obtained by simply adapting an existing Navier-Stokes code. Solution of the flow field and the calculation of the necessary criteria required in the evolution process are also discussed. The novelty of this direct approach is to make the evolution process more general, arbitrary and less complex. The profile evolution is demonstrated for flows at different Reynolds numbers.*

## 1 Introduction

Nature experimented with myriad trial shapes by life and death process for periods over millions of years and using the mechanism of gene mutation and "the survival of the fittest" natural selection process evolved low drag profiles. A striking example is the profile of a trout which when viewed from above resembles a low drag airfoil designed by rational man. It is both challenging and interesting to see what engineers can do in relatively shorter periods of time about the evolution of such minimum drag profiles in laminar flows.

Recognizing the fact that the Helmholtz's functional is proportional to drag, Watson (1971) merged two variational principles (minimize the energy dissipated by the fluid with respect to the body shape and the velocity field) and with the aid of a numerical minimization procedure obtained an upper bound for the minimum possible drag on a body of given volume moving through a Stokes fluid. However, he did not try profiles with pointed ends.

The minimum drag problem in Stokes flow is also an optimal control problem for a distributed parameter system governed by a linear elliptic partial differential equation, the control being the geometric element of the system. Pironneau (1973) solved this problem using a variational method and derived, for a constant volume constraint of the body, the condition of uniform velocity gradient normal to the boundary of the body (optimality criterion) and outlined a numerical algorithm using the method of steepest descent. Sano and Sakai (1983) demonstrated that Pironneau's algorithm indeed works by obtaining the minimum drag profile in 2-D Stokes flow under an area constraint that has a fore-aft symmetry with pointed ends. Later, Pironneau (1974) derived a gradient optimality criterion for a minimum drag body in laminar flow. Glowinski and Pironneau (1975) attempted the complex evolution process numerically in 2-D laminar flow. A boundary layer splicing method, i.e., the inviscid/viscid patching at the outer edge of the boundary layer required a potential solution in the outer inviscid region and a solution to Prandtl's equations in the boundary layer. This combined with the calculation of the optimization criterion which required the solution of the co-state equations in the boundary layer made the algorithm more complex than it already was. It was also not clear how the optimum step size would be obtained, if it was used at all, in the steepest descent method employed in the gradient algorithm. After the tedious solution phase, the velocity gradients were evaluated and the evolution of the profile was carried out using the algorithm mentioned.

This type of evolution cannot be tried out for the intermediate Reynolds number range of $1\text{–}10^3$ due to the type of the method that was used to solve the velocity field and it is independent of the algorithm. This paper describes a suitable numerical technique that overcomes the disadvantages stated above using the algorithm suggested by Pironneau thereby making it more general by choosing to solve the velocity field directly. The governing Navier-Stokes equations and the co-

Contributed by the Fluids Engineering Division for publication in the JOURNAL OF FLUIDS ENGINEERING. Manuscript received by the Fluids Engineering Division April 13, 1992; revised manuscript received April 25, 1994. Associate Technical Editor: R. K. Agarwal.

state equations are elliptic in character and pose for solutions, boundary value problems with divergence free constraints. By specifying the appropriate boundary conditions, the solution can be obtained with the aid of a finite element code. The evaluation of the velocity gradient and the unique unit normals at the vortices of the approximated boundary of the body are also made simple by the method of finite elements.

In order to evaluate the gradient which is used to evolve profiles in laminar flow, the solution to the co-state equation is necessary in addition to the Navier-Stokes equation. This equation is linear in the co-state vector **w** (the Navier-Stokes equation is quasi-linear in the state vector **u**) and there is a way to solve this equation directly using the FEM if one is able to solve the Navier-Stokes equation. The method described here makes it possible to obtain a minimum drag body profile, for any arbitrary smooth starting profile, a task which is analytically rather cumbersome if not impossible. The pre-processing and the post-processing facilities available in the latest FEM codes also make it possible to portray the mesh, streamlines, contours of energy dissipation rate and the pressure. Hence, overall this work will also demonstrate that the choice of a more general and less complex, even though less elegant numerical process is indeed the right way when one is confronted with a complex optimization problem in fluid mechanics.

## 2 Theoretical Background

Assuming the flow velocity $U_\infty$ to be in the $x$-direction (with the associated unit vector $\hat{i}$), the component of the stress vector acting on a surface with unit normal $n$, in the $x$-direction is given by the Cauchy's formula (Fung, 1980)

$$T_i^n = \sigma_{xx} l + \sigma_{yx} m, \tag{2.1}$$

where $\sigma_{xx}$ and $\sigma_{yx}$ are the normal and shear stresses respectively and $l$ and $m$ are the direction cosines. The above formula gives the drag at a point on a boundary. The total drag force $D_b$, in the $x$-direction is obtained by integrating this expression along the boundary of the body.

$$\begin{aligned} D_b &= \int_\Gamma \{\sigma_{xx} l + \sigma_{xy} m\} d\Gamma \\ &= \int_\Gamma \left[ l\left\{ -p + 2\mu \frac{\partial u}{\partial x} \right\} + \mu m \left\{ \frac{\partial v}{\partial x} + \frac{\partial u}{\partial y} \right\} \right] d\Gamma. \end{aligned} \tag{2.2}$$

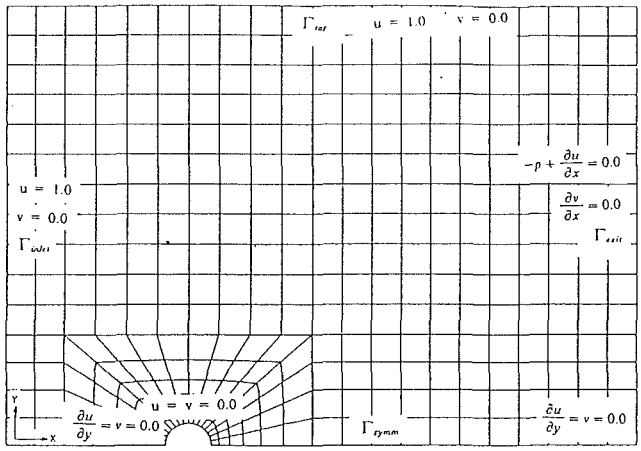


**Fig. 1 Mesh discretization of flow domain with boundary conditions**

The energy dissipation function in 2-D Cartesian coordinates is given by (Bird et al., 1960)

$$\phi = 2\left[ \left\{ \frac{\partial u}{\partial x} \right\}^2 + \left\{ \frac{\partial v}{\partial y} \right\}^2 + \frac{1}{2}\left\{ \frac{\partial u}{\partial y} + \frac{\partial v}{\partial x} \right\}^2 \right]. \tag{2.3}$$

The energy dissipation rate $\Phi$ is the product of dynamic viscosity $\mu$ and energy dissipation function $\phi$.

The field equations are the two-dimensional conservation of mass and the Navier-Stokes equations in their dimensionless form. Expressing the momentum equation in the stress-divergence form we get

$$\rho \mathbf{U} \cdot \nabla \mathbf{U} = \nabla \cdot (\mathbf{\Pi} - p\mathbf{I}), \tag{2.4}$$

where **I** is the unit tensor. Integrating this equation over the entire domain $\Omega$, we get

$$\int_\Omega \rho \mathbf{U} \cdot \nabla \mathbf{U}\, d\Omega = \int_\Omega \nabla \cdot (\mathbf{\Pi} - p\mathbf{I}) d\Omega. \tag{2.5}$$

Now (refer to Fig. 1), let $\Gamma_0$ be the boundary of the body over which the drag is to be obtained and $\Gamma_\infty$ be the complementary domain boundary (comprising $\Gamma_{\text{inlet}}$, $\Gamma_{\text{top}}$, $\Gamma_{\text{symm}}$ and $\Gamma_{\text{exit}}$) which encloses a large volume of fluid and theoretically perceived to extend up to infinity. With this definition of the

## Nomenclature

$a_q$ = a fraction of the deviation of the optimization criterion from the mean at the node
$b$ = parameter for maintaining the area constant
$B_i$ = element in right hand side flux vector
$d_q$ = deviation of optimization criterion from mean at the node
$D_b$ = drag evaluated on the boundary
$D_e$ = drag evaluated from energy
$D_m$ = drag evaluated from momentum equation
$E(S_i)$ = engineering criterion at the $i$th iteration
$E_t$ = total energy dissipation rate
$\mathbf{F}$ = generalized force
$F_i$ = element in right-hand side force vector
$\mathbf{I}$ = unit tensor
$K_i$ = mean value of optimization criterion
$l, m$ = direction cosines
$M_i$ = shape function in FEM
$n$ = normal direction coordinate
$n_q$ = unit normal at the node
$N_i$ = shape function in FEM
$O_q$ = optimization criterion
$p$ = pressure
$q$ = co-state equation variable similar to $p$
$S_0$ = initial shape
$\mathbf{T}$ = stress tensor
$T_i^v$ = traction vector component
$u$ = $x$-direction component of velocity
$\mathbf{U}$ = generalized velocity vector
$U_\infty$ = velocity at inlet
$v$ = $y$-direction component of velocity
$v_i$ = velocity component
$w_x$ = co-state equation variable similar to $u$
$w_y$ = co-state equation variable similar to $v$
$\mathbf{W}$ = generalized co-state velocity vector
$\epsilon$ = convergence limit
$\Gamma$ = boundary of fluid domain and body
$\Gamma_0$ = body boundary
$\Gamma_\infty$ = domain boundary
$\eta$ = local dimensionless variable in FEM
$\lambda$ = undetermined multiplier
$\mu$ = dynamic viscosity
$\nu$ = kinematic viscosity
$\xi$ = local dimensionless variable in FEM
$\mathbf{\Pi}$ = viscous part of stress tensor
$\rho$ = density
$\sigma_{xx}$ = normal stress
$\sigma_{xy}$ = shear stress
$\phi$ = energy dissipation function
$\Phi$ = energy dissipation rate
$\chi$ = solution vector
$\Omega$ = fluid domain

boundaries and using Gauss theorem it can be shown that (Ganesh, 1991)

$$\mathbf{F} = \int_{\Omega} \rho \mathbf{U} \cdot \nabla \mathbf{U} \, d\Omega - \int_{\Gamma_\infty} (\mathbf{\Pi} \cdot \mathbf{n} - p\mathbf{n}) d\Gamma. \tag{2.6}$$

where the total generalized force $\mathbf{F}$, exerted by the body on the fluid is

$$\mathbf{F} = \int_{\Gamma_0} (\mathbf{\Pi} \cdot \mathbf{n} - p\mathbf{n}) d\Gamma. \tag{2.7}$$

$D_m$ is the component of $\mathbf{F}$ in the direction of the relative approach velocity and can be obtained by the dot product of $\mathbf{F}$ and the unit vector in the direction of the relative approach velocity. Next, we form the scalar product of Navier-Stokes equation with the general velocity vector $\mathbf{U}$ to form the energy equation, as follows:

$$\mathbf{U} \cdot \rho(\mathbf{U} \cdot \nabla \mathbf{U}) = \mathbf{U} \cdot (\nabla \cdot \mathbf{\Pi}) - \mathbf{U} \cdot \nabla p. \tag{2.8}$$

Using vector calculus, Gauss theorem and invoking conservation of mass it can be shown that

$$-\mathbf{U}_\infty \cdot \mathbf{F} = \int_{\Omega} \Delta \mathbf{U} \cdot (\rho \mathbf{U} \cdot \nabla \mathbf{U}) d\Omega + \int_{\Omega} \Phi \, d\Omega. \tag{2.9}$$

where,

$$\Delta \mathbf{U} = (\mathbf{U} - \mathbf{U}_\infty), \tag{2.9a}$$

Equation (2.9) can be used to evaluate drag $D_e$, i.e., the $x$-component of $\mathbf{F}$ (assuming the free stream flow velocity to be in the $x$-direction) by specifying unit velocity. Note that the magnitude of the drag force which is a boundary quantity can be evaluated in term of domain integrals. This equation collapses to Stokes drag law equation

$$-U_\infty D_e = \int_{\Omega} \Phi \, d\Omega, \tag{2.10}$$

if the inertia integral term is neglected (Bird et al., 1960).

## 3 Numerical Experimentation

The finite element method is chosen because it is completely general with respect to geometry and material properties and is a result of the procedure being formulated in terms of areas rather than points. Furthermore, function and derivative boundary conditions are easily applied and the method can be shown to converge to the exact solution as the size of the elements decreases. We essentially shift our emphasis from relations that hold for any point in the system to relations that hold for the entire system.

The eight noded isoparametric quadrilateral serendipity elements were chosen with mixed order interpolation for velocity, pressure primitive variables. Since the flow is symmetric with respect to the mid-plane, only half the body and the associated flow domain is considered for solving the flow field. The inlet boundary is at a distance of five times the diameter of the semicircular body from the center of the body and the exit boundary is at a distance of ten times the diameter from the center of the body. The third boundary parallel to the symmetry boundary is at a distance of ten times the diameter from the center of the body. This selection of the boundaries simulate the far-field conditions fairly well (Taylor and Hood, 1973). Figure 1 shows the mesh discretization of the flow domain with the boundary conditions. As one can see near the body the size of the elements are smaller to resolve the sharp velocity and pressure gradients and the size of the elements become gradually bigger in the outward radial direction until they merge with the checker-board type elements.

## 4 The Evolution of Minimum Drag Profile

As shown in Section 2, the drag can be obtained by directly integrating the stresses on the boundary of the body, from force balance and from energy balance. These calculations possess complete arbitrariness with respect to the body shape and hence can be used to evaluate the drag in the actual evolution process, particularly when deciding on the optimum step size (to be explained). The Pironneau's algorithm is as follows: Step 1: Start with initial shape $S_0$; Step 2: Calculate flow field around $S_0$; Step 3: Calculate engineering criterion (or criteria), viz., the drag; $E\ (S_i)$; $i=0$; Step 4: Calculate optimization criterion on $S_i$; $O_q$ (at each node). This criterion is a function of the velocity gradients evaluated at the node point from the N-S equation solution and the co-state equation solution (refer Eq. (4.3)); Step 5: Calculate mean value of $O_q$, $K_i$ (average of the sum of the values at the nodes); Step 6: Calculate deviation at each node; $d_q = O_q - K_i$; Step 7: Define $a_q = \lambda d_q$ (to find optimum step size); Step 8: Calculate the shape and the flow field around it as a function of $\lambda$; $S(\lambda) = \{X | X_q = b(X_q - a_q n_q)\}$; $n_q$ = unit normal at the node; $b$ = a parameter for maintaining constant area; Step 9: Calculate $E(\lambda)$, i.e., calculate the engineering criterion (or criteria) as a function of $\lambda$; Step 10: Calculate optimum $\lambda_{opt}$ by one-dimensional unconstrained minimization. This step consumes lot of time, because for each value of $\lambda$, the meshing, the solution of flow field and the calculation of the engineering criterion (or criteria) have to be carried out; Step 11: Increment counter, $i = i+1$; Step 12: Retrieve body shape for $\lambda_{opt}$, from step 10; $S_{i+1}$; Step 13: Check for convergence, $E(S_{i-1}) - E(S_i) < \epsilon$; If yes, stop; if not, go back to step 4.

The above algorithm utilizes the principle of the steepest descent method (Johnson and Riess, 1980). This minimization process is mathematically modelled by answering two questions. At any given point, which direction represents the direction of steepest descent and how far should one go before changing directions. With the help of mean value theorem it can be shown that the direction of negative gradient makes the objective function decrease as much as possible (Step 8). To answer our second question, we know $E(\lambda)$ can be minimized by the familiar methods of single-variable calculus (Step 10).

The first order optimality criterion obtained by Pironneau, with the help of optimal control theory by the method of normal variations, with the area constraint for the profiles generated, is

$$\left| \frac{\partial \mathbf{U}}{\partial n} \right|^2 = \text{constant} \tag{4.1}$$

everywhere on the boundary of the body (Pironneau, 1973). This term, referred to as the absolute value of the norm is evaluated as follows:

$$\left| \frac{\partial \mathbf{U}}{\partial n} \right|^2 = \left[ \left\{ l \frac{\partial u}{\partial x} + m \frac{\partial u}{\partial y} \right\}^2 + \left\{ l \frac{\partial v}{\partial x} + m \frac{\partial v}{\partial y} \right\}^2 \right] \tag{4.2}$$

When the physical system is governed by the quasi-linear Navier-Stokes equation, the first order optimality criterion obtained by Pironneau with the area constraint, for the profiles generated is (Pironneau, 1984),

$$\left[ \left| \frac{\partial \mathbf{U}}{\partial n} \right|^2 + 2 \left( \frac{\partial \mathbf{U}}{\partial n} \cdot \frac{\partial \mathbf{W}}{\partial n} \right) \right] = \text{constant} \tag{4.3}$$

everywhere on the boundary of the body. The additional term appearing in the optimality criterion for the laminar flow is the contribution from the co-state equation.

The co-state equation has its origin in the optimal control theory which relies upon calculus of variations. The main objective in the calculus of variations problems is to find the extremals of functional or in other words to seek an optimum

of a previously defined cost function. When the problem at hand has a constraint, the method adopted for the solution is to find the extremal of the augmented functional by forcing its first variation to zero. When this is done, an auxiliary equation results and this is termed the co-state equation (Kirk, 1981). The equations given below do not have a simple mechanical interpretation, as they were obtained as the so called 'adjoint' or the 'co-state' equations, when the first order optimality criterion for the minimum drag profile was derived, using the method of normal variations, wherein the physical system is governed by the Navier-Stokes equations.

$$\frac{\partial w_x}{\partial x}+\frac{\partial w_y}{\partial y}=0, \tag{4.4}$$

$$\frac{\mu}{\rho}\left[\frac{\partial^2 w_x}{\partial x^2}+\frac{\partial^2 w_x}{\partial y^2}\right]-\left[\frac{\partial u}{\partial x}w_x+\frac{\partial v}{\partial x}w_y\right]+\left[u\frac{\partial w_x}{\partial x}+v\frac{\partial w_x}{\partial y}\right] =-\left[u\frac{\partial u}{\partial x}+v\frac{\partial u}{\partial y}\right]+\frac{\partial q}{\partial x}, \tag{4.5}$$

$$\frac{\mu}{\rho}\left[\frac{\partial^2 w_y}{\partial x^2}+\frac{\partial^2 w_y}{\partial y^2}\right]-\left[\frac{\partial u}{\partial y}w_x+\frac{\partial v}{\partial y}w_y\right]+\left[u\frac{\partial w_y}{\partial x}+v\frac{\partial w_y}{\partial y}\right] =-\left[u\frac{\partial v}{\partial x}+v\frac{\partial v}{\partial y}\right]+\frac{\partial q}{\partial y}. \tag{4.6}$$

These equations resemble the form of the Navier-Stokes equations in the sense that they also possess terms similar to convective, diffusive and the pressure gradient terms. By using the appropriate change of variables (Prandtl's approach) it can be shown that these equations could be reduced to boundary layer equations in laminar flow. The complexity of these equations, reflect the complexity of the optimal shape design problem in fluid mechanics.

Principal means of constructing a finite element model of the fluid flow are variational principles, method of weighted residuals and the Galerkin method. Here, the Galerkin method is used. The velocity components and the pressure are approximated in the mixed order formulation as

$$\hat{u}=\sum_{i=1}^{8}u_i N_i^u(\xi,\eta), \quad \hat{p}=\sum_{i=1}^{4}p_i M_i^p(\xi,\eta). \tag{4.7}$$

$N_i^u$, $N_i^v$, $N^{wx_i}$, and $N^{wy_i}$ are continuous serendipity quadratic shape functions in local nondimensional coordinates $\xi$ and $\eta$. $M^q{}_i$ and $M^p{}_i$ are the continuous serendipity linear shape functions of the same coordinates. Rearranging the co-state equation with all the convective, diffusive and the pressure gradient terms on one side, we get

$$-\left[u\frac{\partial w_x}{\partial x}+v\frac{\partial w_x}{\partial y}\right]+\left[\frac{\partial u}{\partial x}w_x+\frac{\partial v}{\partial x}w_y\right]+\frac{\partial q}{\partial x} -\left[u\frac{\partial u}{\partial x}+v\frac{\partial u}{\partial y}\right]-\nu\left[\frac{\partial^2 w_x}{\partial x^2}+\frac{\partial^2 w_x}{\partial y^2}\right]=0. \tag{4.8}$$

Employing the Galerkin weighted residual approach (Taylor and Hughes, 1981), the above equation becomes

$$\sum_{i_e=1}^{n_e}\int_{A_e}N_i\left[-\sum_{k=1}^{n}N_k u_k\sum_{j=1}^{n}\frac{\partial N_j}{\partial x}(w_x)_j\right]dA^e -\int_{A_e}N_i\left[\sum_{k=1}^{n}N_k v_k\sum_{j=1}^{n}\frac{\partial N_j}{\partial y}(w_x)_j\right]dA^e +\int_{A_e}N_i\left[\sum_{k=1}^{n}\frac{\partial N_k}{\partial x}u_k\sum_{j=1}^{n}N_j(w_x)_j\right]dA^e +\int_{A_e}N_i\left[\sum_{k=1}^{n}\frac{\partial N_k}{\partial x}v_k\sum_{j=1}^{n}N_j(w_y)_j\right]dA^e +\int_{A_e}N_i\left[\sum_{l=1}^{m}\frac{\partial M_l}{\partial x}q_l\right]dA^e-\int_{A_e}N_i\left[\sum_{k=1}^{n}N_k u_k\sum_{j=1}^{n}\frac{\partial N_j}{\partial x}u_j\right]dA^e -\int_{A_e}N_i\left[\sum_{k=1}^{n}N_k v_k\sum_{j=1}^{n}\frac{\partial N_j}{\partial y}u_j\right]dA^e -\int_{A_e}N_i\nu\left[\sum_{j=1}^{n}\frac{\partial^2 N_j}{\partial x^2}(w_x)_j\right]dA^e -\int_{A_e}N_i\nu\left[\sum_{j=1}^{n}\frac{\partial^2 N_j}{\partial y^2}(w_x)_j\right]dA^e=0. \tag{4.9}$$

The outer summation is over all the elements in the domain and the inner summation is over the appropriate number of nodes in an element. In our case considered here, $n=8$ and $m=4$. From vector calculus and the Green's theorem, the second order terms can be reduced as

$$-\nu\int_{A_e}N_i\left[\sum_{j=1}^{n}\frac{\partial^2 N_j}{\partial x^2}(w_x)_j+\sum_{j=1}^{n}\frac{\partial^2 N_j}{\partial y^2}(w_x)_j\right]dA^e =\nu\int_{A_e}\left[\frac{\partial N_i}{\partial x}\sum_{j=1}^{n}\frac{\partial N_j}{\partial x}(w_x)_j+\frac{\partial N_i}{\partial y}\sum_{j=1}^{n}\frac{\partial N_j}{\partial y}(w_x)_j\right]dA^e -\nu\int_{\Gamma_e}N_i\left[\sum_{j=1}^{n}\frac{\partial N_j}{\partial n}(w_x)_j\right]d\Gamma, \tag{4.10}$$

where $\Gamma^e$ denotes the element boundary. Now, the required form of the last two terms on the LHS of the Eq. (4.9), is, the RHS of the above equation. The implied suffices for the Eq. (4.9) are such that $l=1\ldots4$, $j=1\ldots8$, $k=1\ldots8$, $i=1\ldots8$, $i_e=1\ldots n_e$. The corresponding momentum equation in the $y$-direction is obtained by simply interchanging $x$, $y$ and $u$, $v$. The required set of equations is completed by defining the continuity equation

$$\sum_{i_e=1}^{n_e}\int_{A_e}M_i\left[\sum_{j=1}^{n}\frac{\partial N_j}{\partial x}(w_x)_j+\sum_{j=1}^{n}\frac{\partial N_j}{\partial y}(w_y)_j\right]dA^e=0, \tag{4.11}$$

where the weighting function is now taken as $M_i$ associated with the four noded quadrilateral element. The assembled matrix equation takes the form

$$A\chi=F+B, \tag{4.12}$$

where the chosen form of $\chi$ is

$$\chi_k=\begin{bmatrix}(w_x)_k\\ q_k\\ (w_y)_k\end{bmatrix}. \tag{4.13}$$

Each coefficient in the matrix $A$ has the form

$$a_{ik}=\int_{A_e}\begin{bmatrix}c_{11}&c_{12}&c_{13}\\ c_{21}&c_{22}&c_{23}\\ c_{31}&c_{32}&c_{33}\end{bmatrix}dA_e-\int_{\Gamma_e}\begin{bmatrix}D_{11}&0&0\\ 0&0&0\\ 0&0&D_{33}\end{bmatrix}d\Gamma, \tag{4.14}$$

where implying the summation convention, the coefficients are

$$C_{11}=-N_iN_k(w_x)_k\frac{\partial N_j}{\partial x}-N_iN_k(w_y)_k\frac{\partial N_j}{\partial y} +\nu\left(\frac{\partial N_i}{\partial x}\frac{\partial N_j}{\partial x}+\frac{\partial N_i}{\partial y}\frac{\partial N_j}{\partial y}\right)+N_i\frac{\partial N_k}{\partial x}(w_x)_kN_j,$$

$$C_{12}=N_i\frac{\partial M_l}{\partial x}, \quad C_{13}=N_i\frac{\partial N_k}{\partial x}(w_y)_kN_j,$$

$$C_{21}=M_i\frac{\partial N_j}{\partial x}, \quad C_{22}=0, \quad C_{23}=M_i\frac{\partial N_j}{\partial y},$$

$$C_{31}=N_i\frac{\partial N_k}{\partial y}(w_x)_k N_j,\quad C_{32}=N_i\frac{\partial M_l}{\partial y},$$

$$C_{33}=-N_iN_k(w_x)_k\frac{\partial N_j}{\partial x}-N_iN_k(w_y)_k\frac{\partial N_j}{\partial y}+\nu\left(\frac{\partial N_i}{\partial x}\frac{\partial N_j}{\partial x}+\frac{\partial N_i}{\partial y}\frac{\partial N_j}{\partial y}\right)+N_i\frac{\partial N_k}{\partial y}(w_y)_k N_j,$$

$$D_{11}=\nu N_i\frac{\partial N_j}{\partial n},\quad D_{33}=\nu N_i\frac{\partial N_j}{\partial n}. \tag{4.15}$$

The surface integral term in the Eq. (4.14) corresponds to that part of the element on a boundary, where the essential boundary conditions are applied and is therefore not required. On other boundaries, natural boundary conditions are imposed and these appear in the right hand vector as illustrated below. The first column vector is written as

$$F_i=\sum_{i_e=1}^{n_e}\int_{A_e}\begin{bmatrix}F_1\\F_2\\F_3\end{bmatrix}dA^e, \tag{4.16}$$

where

$$F_1=N_i\left[N_k(w_x)_k\frac{\partial N_j}{\partial x}(w_x)_j+N_k(w_y)_k\frac{\partial N_j}{\partial y}(w_y)_j\right],$$

$$F_2=0,$$

$$F_3=N_i\left[N_k(w_x)_k\frac{\partial N_j}{\partial x}(w_y)_j+N_k(w_y)_k\frac{\partial N_j}{\partial y}(w_y)_j\right].$$

Similarly, the second component of the right-hand side is

$$B_i=\sum_{i_e=1}^{n_e}\int_{A_e}\begin{bmatrix}B_1\\B_2\\B_3\end{bmatrix}dA^e, \tag{4.17}$$

where

$$B_1=\nu N_i\frac{\partial(w_x)_k}{\partial n},\quad B_2=0,\quad B_3=\nu N_i\frac{\partial(w_y)_k}{\partial n}.$$

The mesh is the same as used for the solution of Navier-Stokes equations, but the boundary conditions are as shown in Fig. 2. When solving the co-state equation, the velocity on the outer boundary is also zero apart from being zero on the boundary of the body. Whereas, the physical significance of zero velocity on the boundary of the body is no-slip, that on the outer boundary is no boundary layer solution in the inviscid region away from the body.

The steady-state equations of laminar flow are solved numerically using FEM on a digital computer. The existing FEM codes can be used to solve them. The Navier-Stokes equation is quasi-linear and requires an iterative procedure. The co-state equation is linear but requires the solution of Navier-Stokes equation in the convective terms as well as in the right hand side force vector. The anology can be drawn to the advection-diffusion equation (energy equation, the solution of which is the temperature field), which requires the velocity components in the convective terms. Even though the co-state equation is linear, the solution method is not that straightforward. Recognizing its similarity to Navier-Stokes equation, it is possible to solve this equation on a digital computer, but not without significant changes in the standard code, which is originally written for the solution of Navier-Stokes equation.

We already have conventional versions of the codes (FIDAP (Engelman and Hasbani, 1984)) and the in-house code at UConn) for modeling the laminar flow governed by Navier-Stokes equation. Since the co-state equations are linear elliptic equations, converting the existing Navier-Stokes code to model the co-state equations is a logical step. The conversion involves

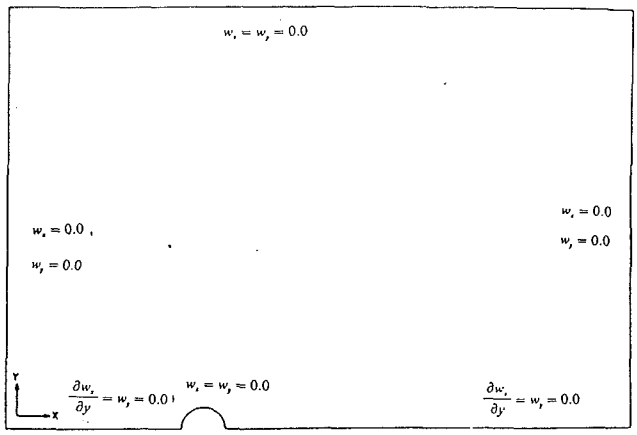


**Fig. 2 Flow domain with boundary conditions for co-state equation. The velocity on the outer boundary is zero apart from being zero on the boundary of the body.**

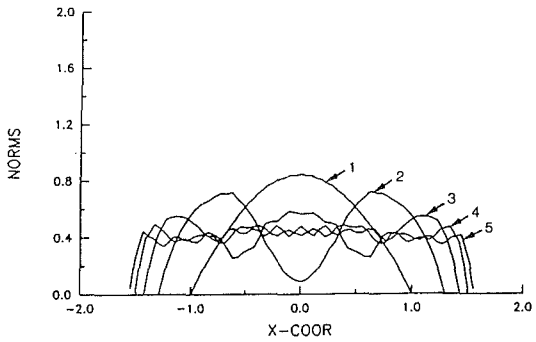


***Fig. 3 Optimality criterion: Re = 0 (initial shape: semicircle). The optimality criterion (Eq. (4.1)), i.e., the norm squared values $|\partial U/\partial n|^2$ evaluated at the nodes are shown as a function of x-coordinate, for the first 5 profiles in succession.***

significant changes in the matrix and RHS formulation as shown explicitly under Section 4. After forming the matrix equation, the application of boundary conditions and the solution method follow the standard procedure that exists in a typical FEM code such as the one we used here to solve for the laminar flow field. The conversion described was not all that difficult (for an experienced FEM user) but significant and the new adapted code is a valuable addition to our existing laminar flow model code.

## 5 Results

As a demonstration, a test case (for more examples refer to (Ganesh, 1989)) will be shown for a Reynolds number of 20, for a semicircular profile. However, as a bench mark solution test, the minimum drag profile evolution at zero Reynolds number, viz., for Stokes flow will be demonstrated first.

Since Stokes flow over a body is symmetric, a symmetric domain is chosen with the body centrally located and discretized similar to the one as shown in Fig. 1. The far field boundaries are set at a distance of ten times the diameter of the body from the center of the body. The number of quadrilateral elements and the number of nodes are 384 and 1241, respectively. The number of elements on the boundary of the profile is 64 (the number of nodes if 65). Defining the average element size '$h$' as the square root of the total area of the domain divided by the number of elements in the domain, the average element size, $h=(A/N_e)^{0.5}$ is 1.44 units. The optimality criterion (Eq. (4.1)), i.e., the norm squared values $|\partial U/\partial n|^2$ as a function of $x$-coordinate, for the five profiles evolved in succession is shown in Fig. 3 and the corresponding profiles are shown in Fig. 4. The final profile is of prolate spheroidal

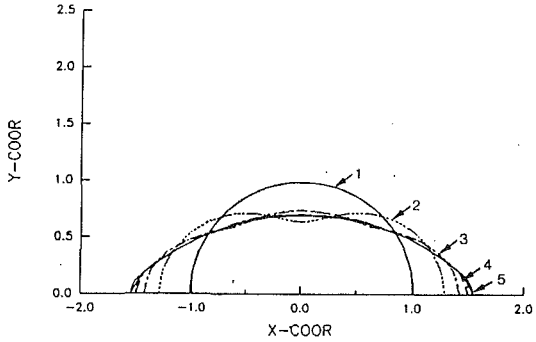


Fig. 4 Profiles evolved from semicircle: Re = 0. The profiles corresponding to the optimality criterion shown in Fig. 3 are shown.

**Table 1 Seeking optimum step size by profile search for Re = 0 (initial profile: semicircle): drag and energy dissipation rate as a function of undetermined multiplier for the first iteration.**

| No | λ | $D_b$ | $D_m$ | $D_e$ | $E_t$ |
|---|---|---|---|---|---|
| 1 | 0.6000 | 57.82310 | 57.03763 | 58.26151 | 58.25447 |
| 2 | 0.6500 | 57.88420 | 57.00323 | 58.22634 | 58.21930 |
| 3 | 0.7000 | 57.98720 | 56.99051 | 58.21359 | 58.20654 |
| 4 | 0.7500 | 58.09820 | 56.97049 | 58.19341 | 58.18635 |
| 5 | 0.8000 | 58.24180 | 56.96888 | 58.19244 | 58.18537 |
| 6 | 0.8500 | 58.41790 | 56.98435 | 58.20909 | 58.20201 |
| 7 | 0.9000 | 58.61730 | 57.01421 | 58.24036 | 58.23327 |

cross-section and the corresponding optimality criterion is almost constant everywhere on the boundary of the body as it should be for a minimum drag body (Eq. (4.1)). These results are also in good agreement with the results obtained by Sano and Sakai (1983). In this example, a sparse mesh compared to the one used in the above reference is used to obtain the same result. The reduction in drag (actually in energy dissipation rate, but in Stokes flow, energy dissipation rate and the drag on the body are numerically equal) from a circular profile to the cross-section of a prolate spheroid is 5.3 percent. The reduction in drag for the fifth profile from the fourth one is 0.05 percent and the iteration is stopped because this change is well within the convergence criterion limit of 0.1 percent. Table 1 lists the values of the drag calculated from Eq. (2.2), Eq. (2.6), and Eq. (2.9) and the energy dissipation rate calculated from Eq. (2.3), as a function of λ, for the first iteration. The optimum step size $\lambda_{opt}$, is that λ corresponding to which the energy dissipation rate is the minimum. The minimum occurs at a value of 0.8 and hence the first profile after the first iteration is the one corresponding to λ equal to 0.8.

The optimum step sizes for the second, third, fourth, and the fifth profiles are 0.35, 0.2, 0.12, and 0.06, respectively. The same type of profiles search is conducted at every step made in the negative gradient direction. This direction is the inward normal direction to the profile. Along a nonstraight boundary, there is a discontinuity in the slope of the approximated boundary and hence the normal direction is not uniquely defined. An appropriate and unique normal direction may be determined, however, by invoking mass conservation arguments, when dealing with an incompressible fluid (Engelman et al., 1982). For each profile searched, the mesh has to be moved, the flow field solution has to be obtained and the engineering criterion, viz., the energy dissipation rate has to be evaluated, using the preprocessor, solver and the post-processor respectively and it takes 14 minutes to complete all the three. Assuming, on the average, twenty searches per step, for the five steps shown here, it takes 1400 minutes, i.e., a whole day on the mini-computer used.

For the flow over a semicircular starting profile at a Reynolds number of 20, the domain chosen has the same topology as the one shown in Fig. 1. The inlet boundary is four times the diameter of the body in front of the body, the exit boundary

**Table 2 Seeking optimum step size by profile search for Re = 20 (initial profile: semicircle): drag and energy dissipation rate as a function of undetermined multiplier for the first iteration.**

| No | λ | $D_b$ | $D_m$ | $D_e$ | $E_t$ |
|---|---|---|---|---|---|
| 1 | 0.0070 | 1.178570 | 1.184469 | 1.188428 | 1.088181 |
| 2 | 0.0075 | 1.178070 | 1.183912 | 1.187865 | 1.087630 |
| 3 | 0.0080 | 1.177710 | 1.183442 | 1.187397 | 1.087160 |
| 4 | 0.0105 | 1.176970 | 1.181535 | 1.185512 | 1.085200 |
| 5 | 0.0110 | 1.177390 | 1.181568 | 1.185564 | 1.085174 |
| 6 | 0.0115 | 1.177920 | 1.181686 | 1.185695 | 1.085216 |
| 7 | 0.0120 | 1.178580 | 1.181871 | 1.185904 | 1.085324 |

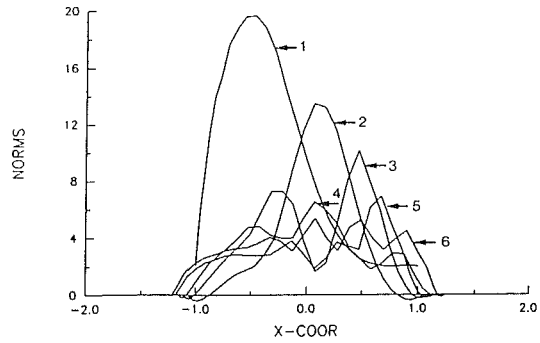


Fig. 5 R-norms: Re = 20 (initial profile: semicircle). The optimality criterion $|\partial U/\partial n|^2 + 2[(\partial U/\partial n)\cdot(\partial W/\partial n)]$ (Eq. (4.3)), called as R-norm in the figure) evaluated at the nodes are shown as a function of *x*-coordinate, for the first 6 profiles evolved in succession.

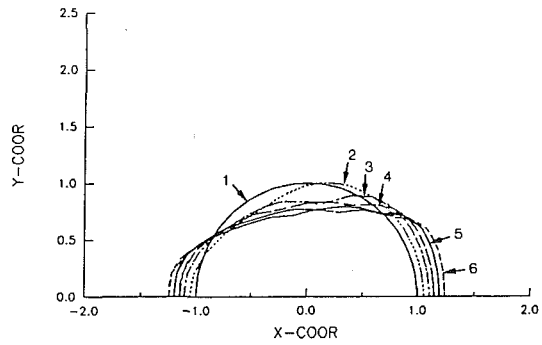


Fig. 6 Profiles evolved from semicircle: Re = 20. The profiles corresponding to the optimality criterion shown in Fig. 5 are shown.

is ten times the diameter behind the body and the third boundary parallel to the symmetry boundary is ten times the diameter away from the body. In this example, the number of quadrilateral elements and the nodes in the domain are 379 and 1230 respectively. The number of elements on the boundary of the profile is 32 (the number of nodes is 33). The average element size *h*, as defined in the previous section 1.213 units. The norm $|\partial \mathbf{U}/\partial n|$, the co-state norm $|\partial \mathbf{W}/\partial n|$ and the optimality criterion $|\partial \mathbf{U}/\partial n|^2 + 2[(\partial \mathbf{U}/\partial n)(\partial \mathbf{W}/\partial n)]$ called as R-norm in the figure) are evaluated at the nodes. Table 2 lists the values of the engineering criterion, viz., the drag and the energy dissipation rate calculated from the equations mentioned under Section 2 as a function of λ.

The optimum step size $\lambda_{opt}$, is found as explained in the last section. From Table 2 $\lambda_{opt}$ is found to be 0.0105. For each profile searched, the pre-processing solution of Navier-Stokes equation to obtain flow field and the post-processing take about 50 minutes. The pre-processing, solution of co-state equation which needs to be obtained only once per step and the post-processing at every step take about 20 minutes. Assuming on the average, twenty searches per step, it takes 1020 minutes, i.e., 17 hours for one iteration or step and a total of 102 hours at least for all the six iterations. This is an indication of how time consuming the optimum design process in fluid

mechanics can be. The $\lambda_{opt}$ values for the 2nd, 3rd, 4th, 5th, and the 6th profiles are 0.0175, 0.0140, 0.0175, 0.0165, and 0.021, respectively. The reduction in drag evaluated is about 15 percent from the starting profile to the last profile. The optimality criterion evaluated at the nodes, i.e., the R-norms are shown in Fig. 5 for the six iterations. The profiles evolved in the 1st, 2nd, 3rd, 4th, 5th, and the 6th iterations are superimposed and shown in Fig. 6.

## 6 Closure

This paper addressed a natural problem of obtaining the minimum drag profile in laminar flow. It was accomplished in an orderly and a logical manner using Pironneau's algorithm. The engineering criteria used in the algorithm, viz., the drag and the energy dissipation rate were evaluated numerically using FEM, by directly integrating the stresses on the boundary of the body and using the conservation equations. The optimization criterion, viz., the norm and the R-norm were also evaluated numerically using FEM. The paper described an attempt to help make evolution of minimum drag profiles possible in the laminar regime, particularly in the intermediate Reynolds number range, thus bridging the gap between Stokes flow and high Reynolds number laminar flow contributions by other authors. The establishment of the finite element technique required for the solution of the co-state equation played a major role in this effort, among other things. Instead of a boundary layer splicing method, a tedious and cumbersome procedure, a direct numerical simulation of the governing differential equations was resorted to. This paper demonstrated how an optimum design problem in fluid mechanics can be solved using the computer as the engineer's numerical laboratory. It must be observed that the amount of computation, hence, the time needed, is determined by the moving meshes and programming the simulation of moving meshes, is rather a time-consuming task. Even the example in the simplest of the flows, i.e., the Stokes flow, consumes a total of 24 hours on the mini-computer MicroVAX II/GPX. For Reynolds numbers of 20, the time consumed was at least 100 hours, despite using coarse meshes. The storage and the speed of the computer had been the primary limitations that restrict the examples to a relatively low Reynolds numbers. Many optimization problems in the industry such as the optimum wing problem (minimum drag for a given lift), minimum drag body for a given surface area and a minimum drag shell for a given body can be attempted following a similar procedure demonstrated here. It is presumed that the optimal control theory can provide us, in the not-too-distant future, with the necessary optimality criteria for minimum drag bodies in the unsteady laminar and the turbulent flow regimes. Hence, industries, engineers and students wishing to solve minimum drag problems in these regimes, can follow a similar approach put forth in this paper.


## Acknowledgment

The author wishes to dedicate this paper to late Wallace W. Bowley, Professor of Mechanical Engineering, University of Connecticut, Storrs, CT and vividly remembers his advice and encouragements throughout this research work. His sudden heavenly abode shocked all his students who were inspired by his teaching and research. The author is indebted to Dr. Alan F. Haught, Manager (Thermal Sciences), United Technologies Research Center, East Hartford, CT, for his permission to use FIDAP at UTRC and thankful for his constructive criticism and many valuable suggestions.


## References


Bird, R. B., Stewart, W. E., and Lightfoot, E. N., 1960, *Transport Phenomena*, Wiley, pp. 82, 133 and 731.

Engelman, M. S., Sani, R. L., and Gresho, P. M., 1982, "The Implementation of Normal and/or Tangential Boundary Conditions in Finite Element Codes for Incompressible Fluid Flow", *International Journal for Numerical Methods in Fluids*, Vol. 2, pp. 225–238.

Engelman, M. S., and Hasbani, I., 1984, FIDAP, Rev. 4.0, *Users Manual*, Fluid Dynamics International, Inc., Evanston, IL 60201.

Fung, Y. C., 1977, *A First Course in Continuum Mechanics*, Prentice-Hall, Englewood Cliffs, NJ, second edition, p. 70.

Ganesh, R. K., 1989, "The Minimum Drag Profile in Laminar Flow: A Numerical Way", Ph.D. dissertation, The University of Connecticut.

Ganesh, R. K., 1991, "Evaluation of the Drag Force by Integrating the Energy Dissipation Rate in Stokes Flow for 2D Domains Using the FEM", *International Journal for Numerical Methods in Fluids*, Vol. 13, No. 5, pp. 557–578.

Glowinski, R., and Pironneau, O., 1975, "On the Numerical Computation of the Minimum Drag Profile in Laminar Flow", *Journal of Fluid Mechanics*, Vol. 72, Part 2, pp. 385–389.

Johnson, L. W., and Riess, R. D., *Numerical Analysis*, Addison-Wesley, pp. 509–514.

Kirk, D. E., *Optimal Control Theory: An Introduction*, Prentice-Hall, Englewood Cliffs, NJ, p. 187.

Pironneau, O., 1973, "On Optimum Profiles in Stokes Flow", *Journal of Fluid Mechanics*, Vol. 59, Part 1, pp. 117–128.

Pironneau, O., 1974, "On Optimum Design in Fluid Mechanics," *Journal of Fluid Mechanics*, Vol. 64, Part I, pp. 97–110.

Pironneau, O., 1984, *Optimal Shape Design for Elliptic Systems*, Springer series in *Computational Physics*, pp. 27, 68.

Sano, M., and Sakai, H., 1983, "Numerical Determination of Minimum Drag Profile in Stokes Flow", *Transactions of the Japan Society for Aeronautical and Space Sciences*, Vol. 26, No. 71.

Taylor, C., and Hood, P., 1973, "A Numerical Solution of the Navier-Stokes Equations Using the Finite Element Technique", *Computers & Fluid*, Pergamon Press, Vol. 1, pp. 73–100.

Taylor, C., and Hughes, T. G., 1981, *Finite Element Programming of the Navier-Stokes Equations*, W. S. Atkins and Ptrs., Swansea, U.K.

Watson, S. R., 1971, "Towards the Minimum Drag on a Body of Given Volume in Slow Viscous Flow", *Journal, Institute of Mathematics and Its Applications*, pp. 367–376.

**P. K. Maciejewski**
Mechanical Engineering Department,
University of Pittsburgh,
Pittsburgh, PA 15261

**R. J. Moffat**
Department of Mechanical Engineering,
Stanford University,
Stanford, CA 94305

# Interpreting Orthogonal Triple-Wire Data From Very High Turbulence Flows

*For turbulence intensities of up to 30 percent, an orthogonal triple-wire probe can be used to make accurate measurements of the instantaneous velocity vector. Above this limit difficulties arise in the interpretation of the data due to the problem described as rectification. This paper presents a means by which data from an orthogonal triple-wire probe may be interpreted for single point measurements in Gaussian turbulence with intensity up to 50 percent resulting in unbiased estimates of the velocity mean vector, Reynolds stress tensor, and time correlation coefficients.*

## Introduction

Researchers commonly use hot wire anemometers in the study of air boundary layers, but, since a hot wire probe responds in a similar manner to either forward or backward motion in the flow, very high levels of turbulence create an uncertain relationship between the output from these anemometers and the statistics of the velocity field being measured. The studies of Tutu and Chevray[1] (1975) and Andreopoulos[2] (1983) help set limits for the domain on which instantaneous velocity measurements can be made with hot wire probes without significant errors due to the physics of the response of these probes to turbulent fluctuations. Tutu and Chevray (1975) present the problem for cross-wire probes, analyzing the response of the probe to high levels of turbulence assuming a trivariate normal distribution function for the component velocities and a simple model for the rectification of negative instantaneous velocities. Andreopoulos (1983) performs a similar analysis for triple-wire probes, concluding that mean velocities and turbulence intensities can be measured accurately at turbulence intensities of up to 30 percent.

The present study proposes to extend the domain on which an orthogonal triple wire can be reliably employed, beyond the limits set by previous investigations of the problem of rectification, by presenting a method for interpreting data from orthogonal triple-wires for turbulence intensities of up to 50 percent for situations when the underlying velocity distribution is trivariate normal or nearly so.

## The Nature of the Errors

Hot wire anemometers incur deterministic errors when subjected to highly turbulent velocity fluctuations. Tutu and Chevray (1975) identify two important physical problems in the use of an orthogonal cross-wire probe in turbulent flows of high intensity. First, the binormal ($W$-component for a cross-wire probe) fluctuations contributed significantly to the anemometer output and become misinterpreted in the values of the means and fluctuations of the $U$ and $V$ components. Second, very large turbulent fluctuations at low mean velocities may be "rectified" due to the inability of the hot wire probe to distinguish the direction of the velocity vector. Consider the following response equation for a single wire normal to the mean flow direction:

$$U_{\text{eff}}^2 = k_1 U^2 + k_2 V^2 + k_3 W^2 \tag{1}$$

where $U_{\text{eff}}$ is the instantaneous effective cooling velocity on the wire and $k_1$, $k_2$, and $k_3$ are the directional sensitivity coefficients for the wire. Suppose $U_{\text{eff}}$ is used to estimate $U$. For high levels of turbulent fluctuations, not only do the $V$ and $W$ components bias the estimate of $U$, but also a negative value for $U$ cannot be distinguished from a positive value.

While both cross-wire and single-wire probes suffer both types of errors, an orthogonal triple-wire probe identifies the bi-normal component on each wire, alleviating the problem of inter-component cross-talk and leaving only the problem of rectification. Figure 1 is a sketch of a typical orthogonal triple-wire probe. Velocity components in the wire coordinate system, denoted $X_j$ or $(X, Y, Z)$, are related to velocity components in the laboratory coordinate system, denoted by $U_i$ or $(U, V, W)$, through the geometry of the probe, the pitch angle $\omega$, and the roll angle $\alpha$. The response equations for the orthogonal triple-wire relate the effective cooling velocities on the wires, $U_{\text{eff},i}$, to the component velocities in the wire coordinate system, $X_j$, as follows:

$$U_{\text{eff},i}^2 = K_{ij} X_j^2 \tag{2}$$

where $K_{ij}$ is a matrix of directional sensitivities (typically as-

[1]Tutu, K. N., and Chevray, R., 1975, "Cross-wire Anemometry in High Intensity Turbulence," *Journal of Fluid Mechanics*, Vol. 71, pp. 785–801.

[2]Andreopoulos, J., 1983, "Statistical Errors Associated with Probe Geometry and Turbulence Institute in Triple Hot-Wire Anemometry," *J. Phys. E: Sci. Instrum.*, Vol. 16, pp. 1264–1271.

Contributed by the Fluids Engineering Division for publication in the JOURNAL OF FLUIDS ENGINEERING. Manuscript received by the Fluids Engineering Division June 7, 1993; revised manuscript received September 28, 1993. Associate Technical Editor: D. M. Bushnell.

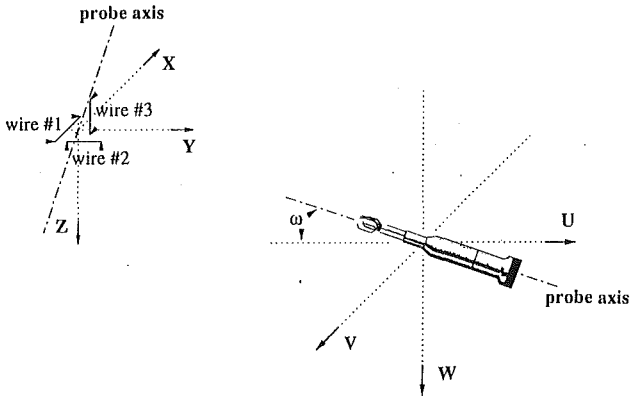


**Fig. 1 The orthogonal triple-wire probe. Wire (*X*, *Y*, *Z*) and laboratory (*U*, *V*, *W*) coordinate systems**

sumed constant). The effective cooling velocities, $U_{\text{eff},i}$, are related to the squares of the component velocities in wire coordinates, $X_j$, disregarding any directional information about $X_j$. A simple rotation relates the velocity vector in the laboratory coordinate system, $U_j$, to the velocity vector in the wire coordinate system, $X_j$, as follows:

$$U_i = C_{ij} X_j \tag{3}$$

where $C_{ij}$ is a coordinate rotation matrix accounting for wire geometry including probe pitch and roll angles. In practice one would estimate $U_{\text{eff},i}$ from the component anemometer bridge output voltages, $E_i$, and then estimate the component velocities, $X_j$, via Eq. (2), assuming the direction of each component velocity is positive. Conceptually, rectification errors occur when the instantaneous velocity vector falls outside the first octant in $X_j$ velocity space.

## The Impact of Rectification Errors on Velocity Statistics

A one-dimensional, idealized illustration of the rectification process and its influence on the sample distribution of velocity vectors is presented in Fig. 2. The example presented in Fig. 2 assumes that all of the velocity fluctuations occur in the $U$ component of velocity and that there is no prong or probe-stem interference with the velocity vector. Under these assumptions, negative velocities become interpreted as positive velocities of the original magnitude, shifting the mean of the overall distribution of velocities to the right and reducing its variance.

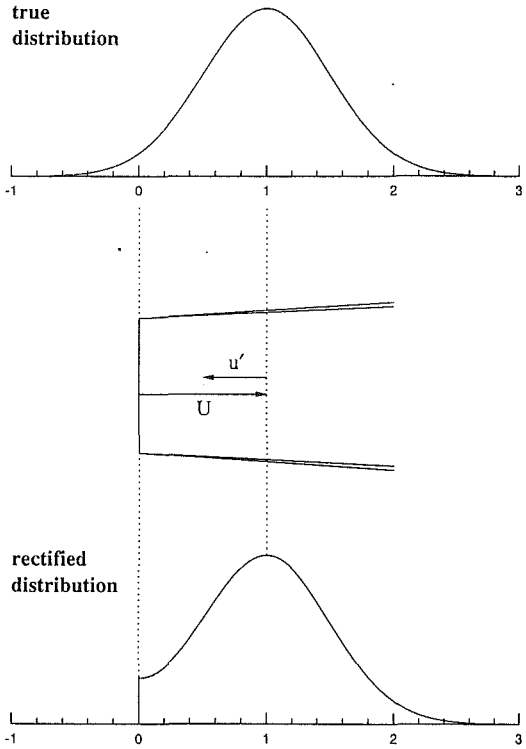


**Fig. 2 Schematic of the rectification process**

Although three-dimensional cases are more complicated than this simplified one-dimensional example, the influence of rectification errors on velocity statistics can generally be understood through the distortion of the distribution of velocity vectors. Rectification errors translate into incongruities between the "true" underlying distribution of velocity vectors and a measured/interpreted sample distribution. In three-dimensional cases, estimates for the moments of the velocity joint distribution function (e.g., the mean vector, Reynolds stress tensor, time correlations, etc.) are biased as a consequence of these incongruities.

A simulation of triple-wire probe response to high turbulence was used to identify which regions of the velocity joint distribution function are affected by rectification errors and to provide insight into new ways to interpret samples containing

## Nomenclature

$C_{ij}$ = coordinate rotation matrix
$C_{ij}^T$ = transpose of the coordinate rotation matrix
CDF = cumulative distribution function
Cov = covariance
$E_i$ = hot wire bridge voltage for $i$th channel
$f$ = frequency
$I(\ )$ = indicator function
$k_1, k_2, k_3$ = hot wire probe directional sensitivity coefficients
$K_{ij}$ = matrix of directional sensitivity coefficients
$M$ = sample median
$N$ = sample size
PSD = power spectral density function
$Q_t, Z_t$ = random variables
$R_{ij}$ = Reynolds stress tensor
$r_\tau$ = empirical autocorrelation coefficient for time lag $\tau$
$t$ = time
$U, V, W$ = velocities in laboratory coordinate system
$U_j$ = $j$th component of velocity in laboratory coordinates
$\mathrm{U_j}$ = $j$th component of velocity at time lag $\tau$
$U_{\text{eff},i}$ = hot wire effective velocity for the $i$th channel
$u', v', w'$ = standard deviation in $U$, $V$, and $W$, respectively
$X, Y, Z$ = velocities in (triple) wire coordinate system
$X_j$ = $j$th component of velocity in wire coordinates
$\mathrm{X_j}$ = $j$th component of velocity in wire coordinates at time lag $\tau$
$\alpha$ = triple-wire probe roll angle
$\gamma$ = empirical standard deviation
$\mu$ = mean
$\rho$ = correlation coefficient
$\rho_\tau$ = autocorrelation coefficient for time lag $\tau$
$\sigma$ = standard deviation
$\tau$ = time lag between observations in a stationary time series
$\omega$ = triple-wire probe pitch angle

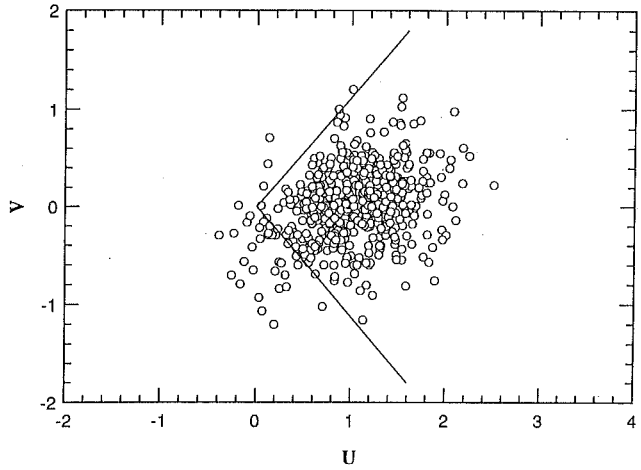


Fig. 3(*a*) Simulated "true" velocity vectors

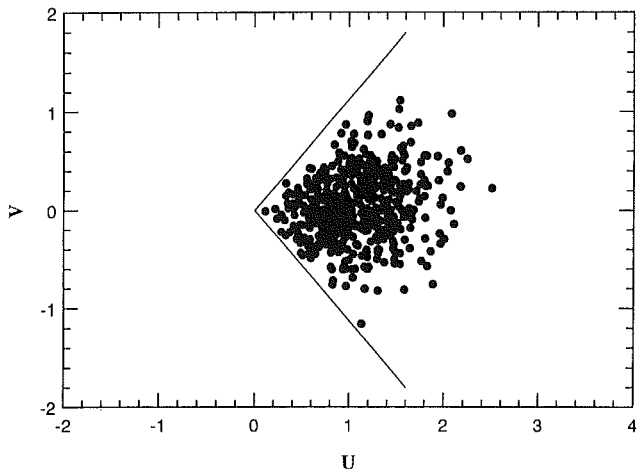


Fig. 3(*b*) Simulated response of triple-wire probe to velocity vectors plotted in Fig. 3(*a*)

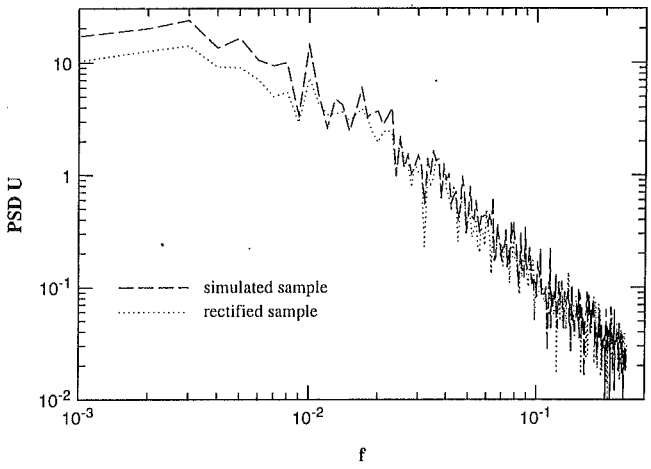


Fig. 4 Rectification affects the spectrum of component velocities

observations subject to rectification errors. The simulation was performed in two parts. First, a random sample from the "true" velocity distribution was simulated by selecting vectors from a trivariate normal distribution having a specified mean vector, Reynolds stress tensor, and $U$-component autocorrelation function. Then the response of the triple-wire probe was simulated by interpreting the sample from the "true" distribution through the response equations for the triple-wire probe, Eqs. (1)–(3) above. Details of the simulation of the velocity field are given in Appendix A.

Figure 3 illustrates the simulated response of an orthogonal triple-wire probe ($\omega = 0$ deg, $\alpha = 90$ deg) to high turbulence, with the data represented in the $U$-$V$ plane. For this simulation $u'/U = 0.5$, $v' = w' = 0.8u'$, and the correlation coefficient between $u'$ and $v'$ equals 0.3. The lines in Fig. 3 represent planes bounding the first octant of the velocity space in wire coordinates. The hollow dots in Fig. 3(*a*) correspond to "true" data points and the solid dots in Fig. 3(*b*) correspond to a mapping of the same true data points onto the $U$-$V$ plane after rectification. If a velocity vector does not suffer an error due to rectification, a solid dot in Fig. 3(*b*)is plotted at the same coordinates as the hollow dot in Fig. 3(*a*) corresponding to the true velocity. If the velocity vector suffers rectification, then the true velocity plotted in Fig. 3(*a*) is mapped into a new coordinate location within the cone of interpretation in Fig. 3(*b*). It should be noted that some of the data points that fall near but still within the planes bounding the first octant of the velocity space in wire coordinates in Fig. 3(*a*) appear as rectified in Fig. 3(*b*). This occurs when a velocity vector presented in Fig. 3(*a*) has a nonzero component in the $W$ direction (not shown in Fig. 3(*a*)) that is sufficiently large to place the data point outside the first octant of the velocity space in wire coordinates. The result is that the data point appears as rectified in Fig. 3(*b*).

Consider the statistics one might calculate if one had access to the true velocity readings, i.e., the hollow dots in Fig. 3(*a*), and compare them to those one would calculate using the "rectified" velocity reading, i.e., the solid dots in Fig. 3(*b*). Using the "rectified" data, one would overpredict the means of both $U$ and $V$, underpredict the variance of both $U$ and $V$, and underpredict the correlation between $U$ and $V$. Note that if the correlation coefficient between $u'$ and $v'$ had been zero instead of 0.3, the mean value of $V$ would be unbiased, but the variance of $V$ would still be underestimated.

Figure 4 shows the power spectral density function for the $U$-component of velocity for a simulated turbulence of $u'/U = 0.5$, $v' = w' = u'$. The effects of rectification are apparent in the low frequency, energy containing portion of the spectrum, although it isn't clear from Fig. 4 how this problem arises. Reconsidering the problem in the time domain one could construct a bivariate plot of $U(t = 0)$ and $U(t = \tau)$ (where $\tau$ = lag time between observations in a stationary time series) that would display the same features as Fig. 3 did for $U$ and $V$. In such a plot, the correlation between $U(t = 0)$ and $U(t = \tau)$ would then represent the autocorrelation for $U$ for time lag $\tau$. The errors in the estimates of the autocorrelations due to rectification result in the errors seen in the spectrum in Fig. 4. These errors are concentrated in the portion of the spectrum containing the largest fluctuations in the turbulence.

Figures 5 and 6 show the simulated errors in the cumulative distribution functions of the individual components of velocity for both the laboratory coordinate velocities, ($U$, $V$, $W$), and the wire coordinate velocities, ($X$, $Y$, $Z$), for $u'/U = 0.5$, $u' = v' = w'$, and with the mean velocity vector aligned with the axis of the probe stem. Figure 5 shows that in the laboratory coordinates, rectification affects the entire distribution for each component velocity. The $U$ component is primarily affected from the low side of the distribution, while $V$ and $W$ are affected on both sides. This is due to the geometry of the probe and its orientation to the mean velocity vector. Figure 6 shows the corresponding errors in the velocity components in wire coordinates. In the wire coordinate system the errors only affect one side of the distribution for each component. Observations in the wire coordinate velocities above their respective medians are unaffected by rectification for turbulence intensities of 50 percent. This fact can be used as the basis for a technique for interpreting triple wire data in high turbulence.

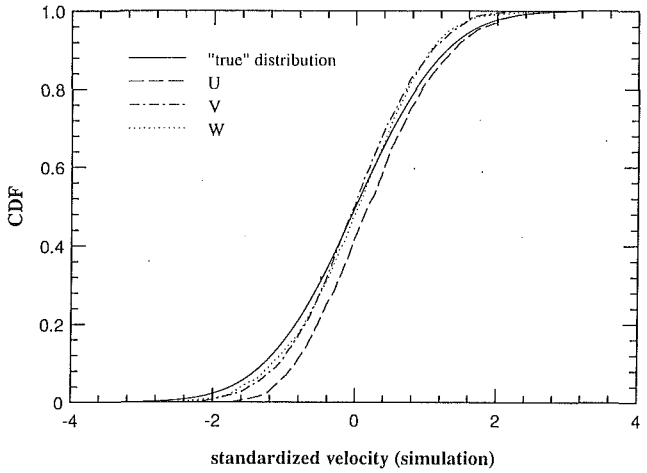


Fig. 5 In laboratory coordinates, rectification entirely distorts the velocity distributions

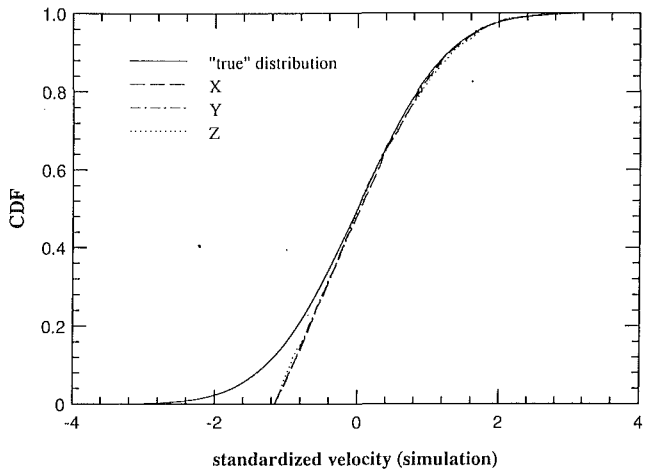


Fig. 6 In wire coordinates, rectification only distorts one side of the velocity distributions

## Median Based Estimators

The rectification of the velocity signal by hot wire anemometers operating in highly turbulent flows causes significant errors in the conventional estimates of the mean velocity vector, the Reynolds stress tensor, the one-dimensional power spectrum, etc. Biased estimates of the moments of the velocity joint distribution function occur because "rectified" measurements contaminate certain regions of the distribution. Can one infer the moments of the underlying true cumulative distribution function (CDF) given the partially distorted, rectified CDF? In the wire coordinate system rectification errors contaminate the marginal distributions for $X_j$ for low values. Are there measures of location (the center of the distributions) and scale (measure of deviations) which resist the errors in the low velocity tails of these distributions?

In the literature of statistics, Robinson[3] (1980) discusses the problem of estimating autocorrelation functions for a stationary Gaussian time series, $Q_t$ ($t = 1, 2, \ldots, n$), that has been censored, i.e., a time series in which some of the data is selectively missing or excluded from the analysis. He specifically considers the univariate case where observations fall below the median value are censored but observations at or above the median are measured without error. Under these assumptions, Robinson (1980) proves that

$$\lim_{n\to\infty} M = \mu$$

$$\lim_{n\to\infty} \gamma = \sigma$$

$$\lim_{n\to\infty} r_\tau = \rho_\tau$$

where $M$ is the sample median and $\gamma$ and $r_\tau$ are defined as follows:

$$\gamma = \left\{\sum_{s=1}^{n} \frac{1}{N} I(Z_s>0)\right\}^{-1}\left\{\sum_{t=1}^{n} Z_t^2 I(Z_t>0)\right\}$$

$$r_\tau = 2\sqrt{2\pi}\delta_\tau - 1$$

where

$$Z_t = Q_t - M$$

$$\delta_\tau = \sum_{t=1}^{n-1} \frac{1}{N-\tau}\frac{Z_t}{\sqrt{\gamma}} I(Z_t>0 \text{ and } Z_{t+\tau}>0)$$

[3]Robinson, P. M., 1980, "Estimation and Forecasting for Time Series Containing Censored or Missing Observations," *Time Series Analysis*, O. D. Anderson, ed., North-Holland Publishing Co., pp. 167-182.

Robinson (1980) concludes that an unbiased estimate of the autocorrelation function for the true time series can be made from the censored time series using estimators based on the median of the series and observations greater than the median.

Robinson's (1980) statistical analyses of censored data can be extended to the interpretation of rectified triple-wire data. Following Robinson's (1980) logic, the correlation between two components can be estimated by

$$r_{uv} = 2\sqrt{2\pi}\delta_{uv} - 1$$

where

$$\delta_{uv} = \sum_{u=1}^{n} \frac{1}{N}\frac{Z_u}{\sqrt{\gamma}} I(Z_u>0 \text{ and } Z_v>0)$$

Furthermore, under the assumptions of Robinson's (1980) analysis it can be shown that

$$\lim_{n\to\infty} r_{uv} = \rho_{uv}$$

This last result can be used to estimate both the autocorrelation of $U$ for time lag $\tau$ (from the bivariate CDF of $U(t = 0)$ and $U(t = \tau)$) and the components of the Reynolds shear stress.

For cases where the contamination of the marginal distributions of $X_j$ due to rectification is limited to values below their respective medians and it is reasonable to assume that the underlying joint distribution is Gaussian, the following statements are true:

(1) For each component $X_j$, the median is an unbiased estimate of the mean.

(2) For each component $X_j$, $\gamma_j$ is an unbiased estimate of the Reynolds normal stress for that component.

(3) For each pair of components $(X_i, X_j)$, $r_{ij}\gamma_i\gamma_j$ is an unbiased estimate for the Reynolds shear stress between those two components (no summation on $i$ and $j$).

(4) For each pair of components $(X_i(0), X_j(\tau))$, $r_\tau$ is an unbiased estimate for the time correlation between components $X_i$ and $X_j$ for time lag $\tau$.

The statistics for the components of velocity in wire coordinates determine the corresponding statistics in laboratory coordinates by the following relationships:

$$U_i = C_{ij}X_j \tag{4}$$

$$R_{ij,\text{lab}} = C_{ik}R_{kl,\text{wire}}C_{lj}^T \tag{5}$$

$$\text{Cov}(U_\alpha, U_\beta)_{\text{lab}} = C_{\alpha j}C_{\beta k}\text{Cov}(X_j, X_k)_{\text{wire}} \tag{6}$$

## Experimental Validation of the Technique

The usefulness of the estimators proposed in the previous section depends on two assumptions. The first is that the true underlying distribution function is Gaussian. The second is that the contamination of the marginal distributions of $X_j$ due to rectification is limited to values below the respective medians of $X_j$. The first assumption depends on the flow in which one measures and will be addressed in the next section. The second assumption depends on the response of the probe to high turbulence and will be addressed presently.

Using a simulation and a model for rectification errors, it is easy to answer the question: Will rectification errors due to a specified level of turbulence be restricted to values below the medians of $X_j$? It would be convenient to be able to use simulations of the response of the probe as the sole arbiter in setting limits on levels of turbulence below which the Reynolds stresses could be estimated accurately using the relations above, but there are compelling reasons to require experimental confirmations of the simulations.

There are two questions which must be answered experimentally. First, is the rectification experienced by the probe the same as the mathematical rectification used to simulate probe response? This cannot strictly be the case, since for high turbulence prong and even probe stem interference is certain to occur for some values of the instantaneous velocity vector. Nonetheless, the measured "rectified" joint CDF may be acceptably close to the mathematically rectified joint CDF. If this is the case, one could test hypotheses about the underlying distribution using the simulation. Second, even if not exact, can the simulations be used to set the limits on the domain on which the proposed estimators can be applied? In other words, is the penetration of real rectification errors into the velocity joint CDF about the same as the penetration predicted by means of the probe simulation?

A calibrated, qualified, orthogonal triple wire probe[4] was placed in a free jet at a location where the turbulence intensity was high but did not exceed 30 percent (an accepted upper limit for reasonably accurate measurements). Once the desired statistics had been measured for this location in the free jet, the probe, while remaining at the same point in the flow field, was then pitched to force the instantaneous velocity vector outside the acceptable cone for a significant proportion of the total sample in subsequent tests. The probe started at 0 degrees and was subsequently pitched to 20 and 30 degrees. (As the probe was pitched to 20 and 30 degrees, there were instances when the equation for the wire velocities in terms of the effective cooling velocities, Eq. (2), could not be solved. This was due to instantaneous interference with a prong, causing wires to "see" different velocities. When this type of error occurred components for which the equations cannot be solved were set to zero. While this interpretation would bias mean based estimators it does not affect median based estimators.) Since the results of the experiment were to be compared to the results for the probe simulation run under the same conditions as the experiment, the measurements for the probe pitched at 0 degrees were used to establish the inputs to the simulation. The simulation was then run with the probe pitched at 0, 20, and 30 degrees to the mean flow direction.

Figure 7 compares the results from the experiment to the results from the simulation of the experiment. Figures 7(*a*) and 7(*b*) show that while the actual rectification for the $X$ component of velocity differs from the simulated rectification, both

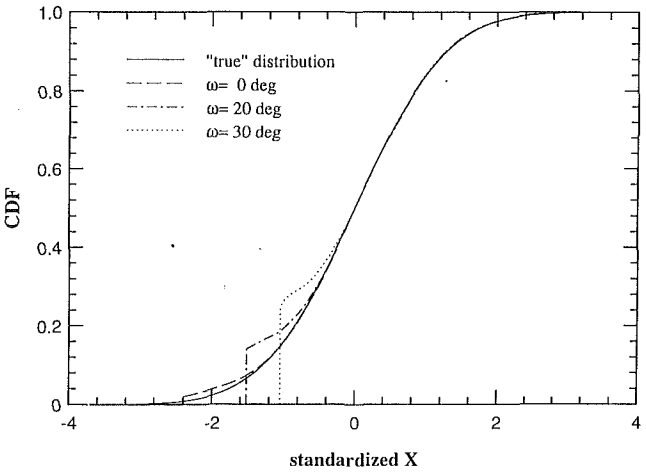


Fig. 7(*a*) Empirical distribution of $X$ for rectification experiment

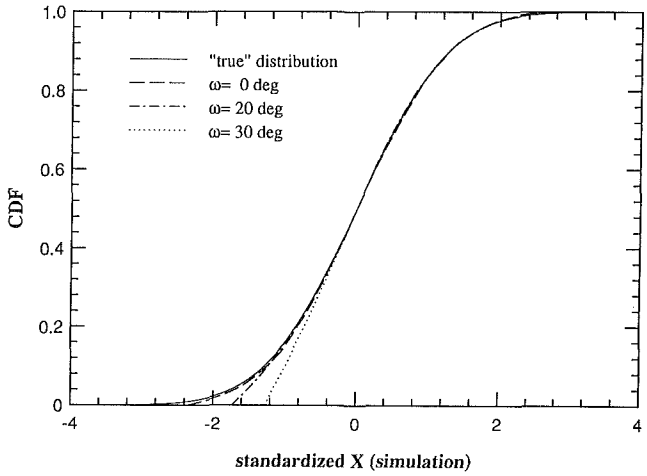


Fig. 7(*b*) Simulated distribution of $X$ for rectification experiment

the experiment and the simulation agree on the location of the point beyond which the distribution is unaffected. Similar results have been obtained for the $Y$ and $Z$ components as well. While the simulation cannot be used to account for actual rectification errors, it can be used to set accurate limits for the physical conditions under which the proposed median based estimators will resist errors.

## Discussion

The errors incurred by an orthogonal triple wire probe operating in high turbulence are deterministic, not random. The errors in the statistics of the velocity field are repeatedly biased. Conventional estimators (e.g., means and moments) are highly sensitive to rectification errors, but median based estimators resist these errors for turbulence intensities up to 50 percent. From a simulation at $u'/U = 0.5$, the errors in wire velocity component medians are 1 percent. At $u'/U = 0.7$, errors in these medians are only 5 percent.

The assumption that the underlying distribution is Gaussian (on which these procedures rest) can be partially tested. One could run a Kolmogorov-Smirnov test on the hypothesis that the "uncontaminated" portion of the distribution has a Gaussian shape. It should be noted that such a test cannot prove that the underlying distributions are as assumed. It only tests whether or not the available "uncontaminated" data are consistent with this assumption.

The proposed measures of turbulence come purely from the need to resist the deterministic errors incurred by hot wire probes in highly turbulent flow fields. Does it make sense from

[4]Details of the calibration and qualification procedures associated with the use of the triple wire probe are considered to be either established practices or special issues that fall outside the scope of the concerns of this paper. The details of the procedures associated with the present implementation can be found in the following: Maciejewski, P. K., and Moffat, R. J., 1989, "Heat Transfer with Very High Free-Stream Turbulence," Report No. HMT-42, Thermosciences Division of Mechanical Engineering, Stanford University.

a physical point of view to use these measures? From an empirical point of view, it is not clear which measures of turbulence will correlate with other parameters of interest. There is no a priori reason to prefer the mean to the median. The strongest argument for maintaining the conventional moments measures of turbulence is that we are familiar with how to think about them in the context of the Reynolds averaged equations. For Gaussian distributions the median based estimators proposed in this paper estimate the moments measures and can be used directly to close moments models. For underlying distributions that are non-Gaussian, one must either relate the median based measures to the expected moments measures and use existing turbulence models or develop new models which employ median based estimators directly.

## Recommendations

If it is reasonable to assume the underlying velocity joint distribution function is Gaussian, the median based estimators presented above yield unbiased estimates of the mean vector, Reynolds stress tensor, and two-component time correlations. One can use these estimators on data taken with an orthogonal triple wire probe for flows with turbulence intensities in the neighborhood of 50 percent. Simulations of the probe response can be used to establish the limits of reliable use. If the underlying distribution is significantly non-Gaussian, then further precautions should be taken in interpreting triple-wire data in very high turbulence.

## Acknowledgments

This study was conducted with the support of the NASA Hot Section Technology Program as NASA NAG 3-522. The work was initiated under the technical administration of Dr. John Rhode and continued under Dr. Raymond Gaugler, both of the Lewis Research Laboratories.

## APPENDIX A

### Simulating High Turbulence at a Point

A random sample from a trivariate normal distribution with a specified mean vector and covariance matrix (Reynolds stress tensor) simulates a sample from the "true" population of velocity vectors, $U_{ij}$ ($i$th observation, $j$th component). Individual components of the sample are then correlated in time using a first order autoregessive model given by

$$U'_{ij}(t) = \alpha_j U'_{ij}(t-1) + U_{ij}(t)$$

where $U'_{ij}(0) = U_{ij}(0)$, and $U_{ij} \sim N(\mu_j, \sigma_j^2)$ and $\alpha_j$ are specified by the user. This model simulates a time series having component autocorrelation functions given by

$$\rho_j(\tau) = \alpha_j^{\tau}$$

component integral scale given by

$$T_j = -1/\ln(\alpha_j)$$

and component spectra given by

$$\mathrm{PSD}_j(f) = -2\ln(\alpha_j)/\{(\ln(\alpha_j))^2 + (2\pi f)^2\}$$

This model provides a simulated sample from the population of velocity vectors with an underlying analytic joint pdf and analytic component spectra. The sample joint pdf and component spectra can be compared directly to their underlying true counterparts.

# Supersonic Flow Calculations Using a Reynolds-Stress and a Thermal Eddy Diffusivity Turbulence Model

**T. P. Sommer**
Graduate Assistant.

**R. M. C. So**
Professor.

**H. S. Zhang**
Graduate Assistant.

Mechanical and Aerospace Engineering,
Arizona State University,
Tempe, AZ 85287

*A second-order model for the velocity field and a two-equation model for the temperature field are used to calculate supersonic boundary layers assuming negligible real gas effects. The modeled equations are formulated on the basis of an incompressible assumption and then extended to supersonic flows by invoking Morkovin's hypothesis, which proposes that compressibility effects are completely accounted for by mean density variations alone. In order to calculate the near-wall flow accurately, correcting functions are proposed to render the modeled equations asymptotically consistent with the behavior of the exact equations near the wall and, at the same time, display the proper dependence on the molecular Prandtl number. Thus formulated, the near-wall second-order turbulence model for heat transfer is applicable to supersonic flows with different Prandtl numbers. The model is validated against supersonic flows with free-stream Mach numbers as high as 10 and wall temperature ratios as low as 0.3. Among the flow cases considered, the momentum thickness Reynolds number varies from ~4000 to ~21,000. Good correlation with measurements of mean velocity and temperature is obtained. Discernible improvements in the law-of-the-wall are observed, especially in the range where the log-law applies.*

## Introduction

Until recently, it was not possible to calculate supersonic flat plate turbulent boundary layers accurately when the free-stream Mach numbers were higher than 5 (Bradshaw et al., 1991). The reason can be traced to an incorrect estimate of the near-wall flow using wall functions (Zhang et al., 1992). With the advent of supercomputers and numerical techniques, it was possible to numerically simulate simple turbulent flows with and without heat transfer (Moser and Moin, 1987; Kim et al., 1987; Mansour et al., 1988; Spalart, 1988; Kim and Moin, 1989; Kasagi et al., 1991). Consequently, asymptotically correct near-wall two-equation models for the velocity and temperature fields have been proposed (So et al., 1991a; Nagano and Kim, 1988; Nagano et al., 1991; Sommer et al., 1992). These models were based on conventional high-Reynolds-number models with near-wall correcting functions that were derived to satisfy the asymptotic behavior of the exact equations. As such, the models were formulated for fluids with Prandtl number $\mathrm{Pr} \approx 1$ (So and Sommer, 1994). These models have been applied to calculate a wide variety of incompressible flows with and without heat transfer, including direct simulation data, and good agreement was obtained for all flow cases tested. Furthermore, the question of appropriate thermal boundary conditions for the fluctuating temperature at the wall has been investigated by Sommer et al. (1994). Their investigation showed that even though zero fluctuating temperature at the wall is not physically valid for most wall thermal boundary conditions, the assumption leads to very reasonable results for the entire mean field and for the fluctuating temperature field away from the wall for the different wall thermal boundary condition cases considered by Sommer et al. (1994). Consequently, the conventionally assumed zero wall temperature variance boundary condition for the two-equation thermal eddy diffusivity model is quite valid. Extensions to second-order models have been proposed and validated (Lai and So, 1990a,b; So et al., 1991b). Again, the high-Reynolds-number second-order models were found to give good results when they were modified to yield asymptotically correct near-wall behavior. The modifications were in the form of near-wall correcting functions added to the Reynolds-stress and dissipation-rate equations.

These successes, therefore, justify the extension of the near-wall correcting functions to supersonic flows. The extension was first carried out with two-equation models (Zhang et al., 1992) assuming the validity of Morkovin's hypothesis (1962) and the results indicated that, with an asymptotically consistent

Contributed by the Fluids Engineering Division for publication in the JOURNAL OF FLUIDS ENGINEERING. Manuscript received by the Fluids Engineering Division April 25, 1993; revised manuscript received February 1, 1994. Associate Technical Editor: O. Baysal.

near-wall correction, the models were able to mimic supersonic flows up to a free-stream Mach number of 10 with an adiabatic wall. In this first attempt, real gas effects were neglected and the turbulent Prandtl number, $Pr_t$, was assumed to be 0.9. On the other hand, the calculations of supersonic flows with cooled wall boundary condition and high Mach numbers were not as satisfactory. Strictly speaking, there is no dynamic similarity between momentum and heat transport, even in incompressible flows (Antonia and Kim, 1991). Therefore, the constant $Pr_t$ assumption needs to be relaxed. An attempt for supersonic flows has been carried out (Sommer et al., 1993) and the variable $Pr_t$ model used was a modification of the two-equation incompressible model proposed by Sommer et al. (1992). Therefore, the proposed model was applicable to flows with $Pr \approx 1$ only. The variable $Pr_t$ calculations assuming negligible real gas effects were in good agreement with measurements (Fernholz and Finley, 1977; Kussoy and Horstman, 1991) and gave significant improvement over those obtained assuming constant $Pr_t$. The same methodology has been applied to modify second-order models for supersonic flows (Zhang et al., 1993a) and these calculations with constant $Pr_t$ were found to give improvements over those reported by Zhang et al. (1992), especially the calculations of high Mach number flows with low wall temperature ratios. This mean that, for the first time, a model to treat complex compressible flows is available. However, the second-order model is still limited by the constant $Pr_t$ assumption and by the fact that the model is only applicable to fluids with $Pr \approx 1$.

Most engineering flows of importance involve fluids whose Prandtl numbers vary with temperature and the range of variation could be large. Furthermore, some fluids have a Pr that is vastly different from 1. In view of this, an appropriate variable $Pr_t$ model for flows with heat transfer would be one that could handle a wide variety of Pr in addition to being able to account for variable Pr effect. This means that a more general incompressible heat transfer model to those proposed by Nagano and Kim (1988), Nagano et al. (1991) and Sommer et al. (1992) has to be formulated and validated before its extension to supersonic flows. The task has been attempted by So and Sommer (1994). Their approach is based on the proposal of Sommer et al. (1992). In addition to requiring the modeled equations to satisfy the asymptotic behavior of their exact counterparts, they also try to model the correcting functions so that the parametric dependence on Pr of the near-wall flow is properly accounted for. The result is a variable $Pr_t$ model that could correctly predict incompressible heat transfer with Pr that varies from a low of $10^{-2}$ to a high of $10^3$. The model is applicable to flows with constant wall heat flux as well as constant wall temperature boundary conditions and the predictions are in good agreement with such diverse data as those given by Kader (1981), Kim and Moin (1989), and Kasagi et al. (1991).

The present objective is to formulate a second-order variable $Pr_t$ model for supersonic flows that is valid for a wide range of Pr. This is accomplished by relaxing the constant $Pr_t$ assumption made in the second-order model of Zhang et al. (1993a) and by extending the heat transfer model of So and Sommer (1994) to supersonic flows. In the present work, Morkovin's hypothesis (1962) is again invoked and the approach taken is similar to that outlined in Sommer et al. (1992). Consequently, the second-order modeled equations of Zhang et al. (1993b) for the velocity field and the two-equation model of So and Sommer (1994) for the temperature field are extended to supersonic flows. An established boundary-layer code (Anderson and Lewis, 1971) is modified to solve the set of governing equations and the calculations of compressible boundary layers with adiabatic and cooled wall boundary conditions over a wide range of Mach numbers are compared with measurements (Fernholz and Finley, 1977; Kussoy and Horstman, 1991) and the constant $Pr_t$ calculations of Zhang et al. (1993a).

## Mathematical Formulation

The supersonic flow of an ideal gas with real gas effects, bulk viscosity and body forces neglected is considered. A density-weighted average is used to decompose the fluctuating quantities, besides pressure and density, into a mass-weighted mean part and a mass-weighted fluctuating part. On the other hand, the pressure and density are decomposed using Reynolds averaging, which results in a time-averaged mean part and a time-averaged fluctuating part. For any variable $F$, the mass-weighted mean is denoted by $\tilde{F}$, the mass-weighted fluctuating part by $f$, the time-averaged mean by $\overline{F}$ and the time-averaged fluctuating part by $f'$. The fluid density is taken to be $\rho$, the dynamic viscosity $\mu$, the thermal conductivity $k$, the specific heat at constant pressure $C_p$, and the gas constant is denoted by $R$. In terms of these variables and the pressure $p$, the temperature $\Theta$, and the $i$th component of the velocity $u_i$, the mean equations of motions for compressible turbulence can be written as:

$$\frac{\partial \overline{\rho}}{\partial t} + (\overline{\rho}\tilde{U}_i)_{,i} = 0, \tag{1}$$

$$\frac{\partial \overline{\rho}\tilde{U}_i}{\partial t} + (\overline{\rho}\tilde{U}_i\tilde{U}_j)_{,j} = -\overline{P}_{,i} - \frac{2}{3}(\overline{\mu}\tilde{U}_{j,j})_{,i} + [\overline{\mu}(\tilde{U}_{i,j} + \tilde{U}_{j,i})]_{,j} - (\overline{\rho}\tau_{ij})_{,j}, \tag{2}$$

$$\frac{\partial \overline{\rho}\overline{C}_p\tilde{\Theta}}{\partial t} + (\overline{\rho}\tilde{U}_i\overline{C}_p\tilde{\Theta})_{,i} = \frac{\partial \overline{P}}{\partial t} - \tilde{U}_i\overline{P}_{,i} + \overline{u}_i\overline{P}_{,i} + \overline{u_i p'_{,i}} + \overline{\sigma}_{ij}\tilde{U}_{i,j} + \overline{\sigma}_{ij}\overline{u}_{i,j} + \overline{\rho}\epsilon - (\overline{\rho}\overline{C}_p Q_i)_{,i} + (\overline{k}\tilde{\Theta}_{,i})_{,i}, \tag{3}$$

$$\overline{P} = \overline{\rho}R\tilde{\Theta}, \tag{4}$$

where $(\bullet)_{,i}$ denotes a gradient with respect to the spatial coordinate $x_i$, the Einstein summation convention applies to repeated indices, and the Reynolds stress tensor, the Reynolds heat flux vector, the turbulent dissipation rate are defined as $\tau_{ij} = \widetilde{u_i u_j}$, $Q_i = \widetilde{u_i\theta}$, $\overline{\rho}\epsilon = \overline{\sigma_{ij}u_{i,j}}$, respectively. The mean and fluctuating viscous stress tensor is given by:

$$\overline{\sigma}_{ij} = -\frac{2}{3}\overline{\mu}\tilde{U}_{k,k}\delta_{ij} + \overline{\mu}(\tilde{U}_{i,j} + \tilde{U}_{j,i}), \tag{5a}$$

$$\sigma_{ij} = -\frac{2}{3}\overline{\mu}u_{k,k}\delta_{ij} + \overline{\mu}(u_{i,j} + u_{j,i}). \tag{5b}$$

When deriving these equations, additional assumptions are made regarding the neglect of turbulent fluctuations of dynamic viscosity, thermal conductivity and specific heat. Also, according to Speziale and Sarkar (1991), the velocity-pressure gradient correlation term $\overline{u_i p'_{,i}}$ can be written in the equivalent form as

$$\overline{u_i p'_{,i}} = -(\overline{\rho}R\tilde{\Theta}\overline{u}_i)_{,i} + (\overline{\rho}Ru_i\theta)_{,i} - \overline{p'u_{i,i}}. \tag{6}$$

From these equations, it can be seen that, to achieve closure, models are required for the Reynolds stress tensor $\tau_{ij}$, the Reynolds heat flux vector $Q_i$, the pressure dilatation correlation $\overline{p'u_{i,i}}$, the turbulent dissipation rate $\epsilon$ and the mass flux vector $\overline{u}_i$. In the following, appropriate near-wall models are proposed for $\tau_{ij}$, $Q_i$, and $\epsilon$, while Morkovin's hypothesis (1962) is invoked to justify the neglect of $\overline{p'u_{i,i}}$ and $\overline{u}_i$ in the modeling of supersonic turbulent flows. The models for $\tau_{ij}$, and $\epsilon$ are presented first and this is followed by a discussion of the model for $Q_i$.

## Second-Order Model for the Velocity Field

The modeling of the Reynolds stress tensor is provided by the Reynolds-stress transport equation which is closed by postulating models for the terms representing turbulent diffusion, viscous dissipation and velocity-pressure gradient correlation in the exact equation. Incompressible models for these terms are proposed. Usually the models are formulated for high

Reynolds-number flows, therefore, they are not suitable for near-wall flow calculations. Furthermore, the modeled equation is not valid at the wall. Consequently, some kind of wall functions have to be invoked to connect the modeled equation to the wall so that the wall boundary conditions for the Reynolds stresses can be satisfied. This approach is not satisfactory because it is too restrictive in the sense that the wall functions proposed are very much flow-type dependent and thus render the Reynolds-stress model less general compared to other models that are not as sophisticate or are of lower order. Various remedies have been proposed. However, the most promising approach is to modify the modeled equations so that they are valid for near-wall flows.

The approach taken by Zhang et al. (1993b) is to derive near-wall correcting functions for the Reynolds-stress transport equation and the conventional dissipation-rate equation. Certain constraints are imposed and these include the requirements that the wall boundary conditions for the Reynolds stresses and the dissipation rate have to be satisfied exactly and that, to the lowest order of the wall normal coordinate $x_2$, the near-wall behavior of the modeled equations is consistent with that of the exact equations. The correcting functions derived by Zhang et al. (1993b) give asymptotically correct matching up to order $x_2$. Of course, more accurate correcting functions can be derived; however, these fairly simple near-wall models are found to give results that are in good agreement with measurements covering a wide range of flow Reynolds numbers (Zhang et al., 1993b). These successes prompt the extension of the incompressible modeled equations to supersonic flows by invoking Morkovin's hypothesis (1962) and the results are extremely encouraging (Zhang et al., 1993a). In view of this, Zhang et al.'s (1993a) modeled Reynolds-stress equations are adopted in the present work.

The compressible Reynolds-stress equation in symbolic form and written similarly to its incompressible counterpart is given by:

$$C_{ij} = D^{\nu}_{ij} + D^{T}_{ij} + P_{ij} + \Pi_{ij} - \epsilon_{ij} + G_{ij} + T_{ij}, \tag{7}$$

where

$$C_{ij} = \frac{\partial}{\partial t}[\overline{\rho}\tau_{ij}] + [\overline{\rho}\tilde{U}_k\tau_{ij}]_{,k}, \tag{7a}$$

$$D^{\nu}_{ij} = [\overline{u_i\sigma_{jk}} + \overline{u_j\sigma_{ik}}]_{,k}, \tag{7b}$$

$$D^{T}_{ij} = [\overline{\rho\, u_i u_j u_k}]_{,k}, \tag{7c}$$

$$P_{ij} = -[\overline{\rho}\tau_{ik}\tilde{U}_{j,k} + \overline{\rho}\tau_{jk}\tilde{U}_{i,k}], \tag{7d}$$

$$\Pi_{ij} = -[\overline{u_i p'_{,j}} + \overline{u_j p'_{,i}}], \tag{7e}$$

$$\epsilon_{ij} = [\overline{u_{i,k}\sigma_{jk}} + \overline{u_{j,k}\sigma_{ik}}], \tag{7f}$$

$$G_{ij} = -[\overline{u}_i\overline{P}_{,j} + \overline{u}_j\overline{P}_{,i}], \tag{7g}$$

$$T_{ij} = [\overline{u}_i\overline{\sigma}_{jk,k} + \overline{u}_j\overline{\sigma}_{ki,k}], \tag{7h}$$

are, respectively, the convection of $\tau_{ij}$, the viscous diffusion of $\tau_{ij}$, the turbulent diffusion of $\tau_{ij}$, the production of $\tau_{ij}$ by mean shear, the velocity-pressure gradient correlation, the viscous dissipation rate of $\tau_{ij}$, and the interactions of compressibility effects with mean pressure and mean viscous shear. The terms (7$g$) and (7$h$) arise as a result of compressibility and are identically zero for incompressible flows. Therefore, if Morkovin's hypothesis (1962) is invoked, the terms (7$g$) and (7$h$) can be neglected and the turbulent diffusion, viscous dissipation and velocity-pressure gradient correlation terms can be modeled as in constant-density flows. Consistent with this assumption, the term $\overline{p'u_{i,i}}$ in (6) is also neglected. Finally, the viscous diffusion term $D^{\nu}_{ij}$ is approximated by $[\overline{\mu}\ \tau_{ij,k}]_{,k}$. Thus simplified, (7) can be closed by adopting the near-wall models proposed by Zhang et al. (1993b). Without derivation, these models are given as:

$$D^{T}_{ij} = \left[ C_s\overline{\rho}\frac{K}{\epsilon}(\tau_{kl}\tau_{ij,l} + \tau_{jl}\tau_{ki,l} + \tau_{il}\tau_{jk,l}) \right]_{,k}, \tag{8}$$

$$\Pi_{ij} = \Phi_{ij} + \Phi^{R}_{ij} + \Phi^{w}_{ij}, \tag{9}$$

$$\epsilon_{ij} = \frac{2}{3}\overline{\rho}\epsilon\delta_{ij} + \overline{\rho}\epsilon^{w}_{ij}. \tag{10}$$

Here, $\Phi_{ij}$ is given by the high-Reynolds-number model of Launder et al. (1975), $\Phi^{R}_{ij}$ is the "pressure echo" term, and $\Phi^{w}_{ij}$ and $\epsilon^{w}_{ij}$ are near-wall corrections. Zhang et al. (1993b) have shown that, to order $x_2^2$, the near-wall correction terms are not affected by the presence of the "pressure echo" term. Therefore, the proposal for $\Phi^{w}_{ij}$ is applicable irrespective of whether the "pressure echo" term is included in the modeling of $\Pi_{ij}$ or not. The models for these different terms can now be generalized for compressible flows as:

$$\Phi_{ij} = -C_1\overline{\rho}\frac{\epsilon}{K}\left(\tau_{ij} - \frac{2}{3}K\delta_{ij}\right) - \alpha_1\left(P_{ij} - \frac{2}{3}\tilde{P}\delta_{ij}\right) - \beta_1\left(D_{ij} - \frac{2}{3}\tilde{P}\delta_{ij}\right) - \gamma_1\overline{\rho}KS_{ij}, \tag{11}$$

$$\Phi^{R}_{ij} = C_w\overline{\rho}KS_{ij}(K^{3/2}/\epsilon x_2), \tag{12}$$

$$\Phi^{w}_{ij} = f_{w1}\left[ C_1\overline{\rho}\frac{\epsilon}{K}\left(\tau_{ij} - \frac{2}{3}K\delta_{ij}\right) - \overline{\rho}\frac{\epsilon}{K}(\tau_{ik}n_kn_j + \tau_{jk}n_kn_i) + \alpha^*\left(P_{ij} - \frac{2}{3}\tilde{P}\delta_{ij}\right)\right], \tag{13}$$

$$\epsilon^{w}_{ij} = f_{w1}\left[ -\frac{2}{3}\epsilon\delta_{ij} + \frac{\epsilon}{K}\frac{(\tau_{ij} + \tau_{ik}n_kn_i + \tau_{jk}n_kn_i + n_in_j\tau_{kl}n_kn_l)}{(1 + 3\tau_{kl}n_kn_l/2K)}\right], \tag{14}$$

where $K = \tau_{ii}/2$ is the turbulent kinetic energy, $\tilde{P} = P_{ii}/2$ is the production of $K$, $S_{ij} = (\tilde{U}_{i,j} + \tilde{U}_{j,i}) - (2\tilde{U}_{k,k}\delta_{ij})/3$ and $D_{ij} = -(\overline{\rho}\tau_{ik}\tilde{U}_{k,j} + \overline{\rho}\tau_{jk}\tilde{U}_{k,i})$. The damping function is defined as $f_{w1} = \exp[-(\mathrm{Re}_t/150)^2]$ while the turbulent Reynolds number is given by $\mathrm{Re}_t = K^2/\overline{\nu}\epsilon$. Unit normal to the wall is denoted by $n_i$ and the $C$'s are model constants whose values are chosen to be the same as those given by Zhang et al. (1993b). Furthermore, the model constants $\alpha_1$, $\beta_1$, and $\gamma_1$, are related to a single constant $C_2$ and the relations are as given by Launder et al. (1975). For ease of reference later on, the second-order model with the term $\Phi^{R}_{ij}$ included is referred to as LRR/WR, while the model with the term $\Phi^{R}_{ij}$ excluded is denoted as LRR.

It has been suggested by Sarkar et al. (1991) that the dissipation rate $\epsilon$ could be decomposed into a solenoidal part and a compressible part so that $\epsilon = \epsilon_s + \epsilon_c$. The solenoidal dissipation rate is associated with the energy cascade, therefore, it approaches its incompressible limit correctly. Consistent with Morkovin's hypothesis (1962), the compressible part of $\epsilon$ is neglected in the present formulation and $\epsilon$ is taken to be given by $\epsilon_s$ alone. A modeled dissipation-rate equation similar to its incompressible counterpart can be written for compressible flows as:

$$\frac{\partial\overline{\rho}\epsilon}{\partial t} + (\overline{\rho}\epsilon\tilde{U}_k)_{,k} = (\overline{\mu}\epsilon_{,k})_{,k} + \left(C_\epsilon\overline{\rho}\frac{K}{\epsilon}\tau_{ki}\epsilon_{,i}\right)_{,k} + C_{\epsilon 1}\overline{\rho}\frac{\epsilon}{K}\tilde{P} - C_{\epsilon 2}\frac{\overline{\rho}\epsilon\tilde{\epsilon}}{K} + \xi. \tag{15}$$

The near-wall correcting function $\xi$ of Zhang et al. (1993b) can be generalized for compressible flows to give

$$\xi = f_{w2}\overline{\rho}\left(-2\frac{\epsilon\tilde{\epsilon}}{K} + 1.5\frac{\bar{\epsilon}^2}{K} - 1.5C_{\epsilon 1}\frac{\epsilon}{K}\tilde{P}\right). \tag{16}$$

In (16), $\tilde{\epsilon}$ and $\bar{\epsilon}$ are defined by $\overline{\rho}\tilde{\epsilon} = \overline{\rho}\epsilon - 2\overline{\mu}(\partial\sqrt{K}/\partial x_2)^2$ and $\overline{\rho}\bar{\epsilon} = \overline{\rho}\epsilon - 2\overline{\mu}K/x_2^2$, respectively, and the damping function is

given by $f_{w2}=\exp[-(\mathrm{Re}_t/40)^2]$. Again, the $C$'s are model constants and their values specified by Zhang et al. (1993b) are adopted.

For the sake of completeness, the model constants used are specified as $C_1=1.5$, $C_2=0.4$, $C_{\epsilon 1}=1.5$, $C_{\epsilon 2}=1.83$, $C_s=0.11$, $C_\epsilon=0.1$, $\alpha^*=0.45$ and $\alpha_1=(8+C_2)/11$, $\beta_1=(8C_2-2)/11$ and $\gamma_1=(30C_2-2)/55$. The constant $C_w$ is introduced as a result of "pressure echo" modeling in the velocity-pressure gradient correlation. For compressible flow calculations, a generally valid relation is given by Zhang et al. (1993a) as: $C_w=(C_w)_{\mathrm{in}}-(5.8\times10^{-4})M_\infty$ for $M_\infty>2.5$, where $M_\infty$ is the free-stream Mach number. For $M_\infty\le 2.5$, $C_w=(C_w)_{\mathrm{in}}$, where $(C_w)_{\mathrm{in}}$ is given by: $(C_w)_{\mathrm{in}}=4.14\times10^{-3}+3\times10^{-3}(\log \mathrm{Re}_\theta)$ for $\mathrm{Re}_\theta\le 5.500$ and $(C_w)_{\mathrm{in}}=0.0153$ for $\mathrm{Re}_\theta>5{,}500$. Here, $\mathrm{Re}_\theta$ is the momentum thickness Reynolds number. Finally, the boundary conditions for the mean and turbulent velocity field are given by:

$$\tilde{U}=\tilde{V}=\tilde{W}=K=\tau_{ij}=0;\quad \epsilon=2\overline{\nu}_w(\partial\sqrt{K}/\partial y)^2. \tag{17}$$

## Two-Equation Model for the Temperature Field

In the previous section, a near-wall second-order model is outlined for the velocity field. Since it is advisable to calculate turbulent heat transfer using a turbulence model of equal or lesser order (So et al., 1992), a two-equation model for the temperature field would be most appropriate for the present work. Therefore, gradient transport is assumed and the $i$th component of the turbulent heat flux is given by $-Q_i=-\widetilde{u_i\theta}=\alpha_t(\partial\tilde{\Theta}/\partial x_i)$, where $\alpha_t$ is the thermal eddy diffusivity. Dimensionally, $\alpha_t$ is the product of a velocity scale and a length scale. A characteristic velocity scale for turbulent flow is $K^{1/2}$. If the interactions between momentum and heat transport are to be modeled properly, an appropriate length scale would be one given by a combination of $K^{1/2}$ and the time scales of both the thermal and velocity fields. The time scale characteristic of the thermal field can be evaluated from the temperature variance $\tilde{\theta}^2$ and its dissipation rate $\epsilon_\theta$, while the time scale for the velocity field is given by $K$ and its dissipation rate $\epsilon$. In view of this, the simplest proposal for $\alpha_t$ will be:

$$\alpha_t=C_\lambda f_\lambda K[K\tilde{\theta}^2/\epsilon\epsilon_\theta]^{1/2}, \tag{18}$$

where the velocity scale $K^{1/2}$ is multiplied by the combined time scale $[K\tilde{\theta}^2/\epsilon\epsilon_\theta]^{1/2}$ to give an appropriate length scale for the definition of $\alpha_t$, $C_\lambda$ is a model constant and $f_\lambda$ is a damping function to be defined. A constant value of $C_\lambda=0.11$ has been put forward by Nagano and Kim (1988) and adopted by Sommer et al. (1992, 1993). Furthermore, $C_\lambda=0.10$ has been assumed by Nagano et al. (1991). In all these calculations, the 0.1 value is found to give good results for the flow cases tested. Therefore, it is prudent to assume a value not too different from 0.1. For the present, $C_\lambda=0.095$ is found to give the best results. As for $f_\lambda$, it has to be parametric in Pr, otherwise, the model cannot be applied to calculate heat transfer in fluids with vastly different Pr. In the following, a near-wall model for $\alpha_t$ is first discussed, then the appropriate expression for $f_\lambda$ is presented.

Since $K$ and $\epsilon$ are defined by the solution of the modeled equations outlined in the previous section, $\alpha_t$ can be determined by solving two equations governing the transport of $\tilde{\theta}^2$ and $\epsilon_\theta$. For incompressible flows, various modeled equations for $\tilde{\theta}^2$ and $\epsilon_\theta$ have been proposed (Launder, 1976). These equations are formulated for high-Reynolds-number flows, therefore, they cannot be used consistently with other near-wall models. Several near-wall two-equation models have been put forward by Nagano and Kim (1988), Nagano et al. (1991), Sommer et al. (1992, 1993), and So and Sommer (1994). One of these models is asymptotically incorrect and gives a zero $\epsilon_\theta$ at the wall (Nagano and Kim, 1988); therefore, it is not consistent with the behavior of the near-wall turbulence model described above. The other models give asymptotically correct results near a wall and are appropriate for the present application. With the exception of So and Sommer (1994), most of the models formulated to-date are, strictly speaking, valid for fluids with $\mathrm{Pr}\approx 1$. If the compressible turbulence model for heat transfer is to be general enough for fluids with vastly different Pr, then the appropriate incompressible model to be adopted for extension to compressible flow is that proposed by So and Sommer (1994). Therefore, the present approach adopts that model as a base and proceeds to generalize it for supersonic turbulent flows.

Again, Morkovin's hypothesis (1962) is invoked in order to extend the incompressible model to compressible flows. Since the incompressible modeled equations for $\tilde{\theta}^2$ and $\epsilon_\theta$ have been given by So and Sommer (1994) and their extensions to compressible flows are straight forward, these equations can be written down without derivation as:

$$\overline{\rho}\frac{\partial\tilde{\theta}^2}{\partial t}+\overline{\rho}\tilde{U}_k\frac{\partial\tilde{\theta}^2}{\partial x_k}=\frac{\partial}{\partial x_k}\left(\overline{\rho}\,\overline{\alpha}\frac{\partial\tilde{\theta}^2}{\partial x_k}\right)+\frac{\partial}{\partial x_k}\left(C_{\theta^2}\overline{\rho}\tau_{kj}\frac{K}{\epsilon}\frac{\partial\tilde{\theta}^2}{\partial x_j}\right)-2\overline{\rho}Q_k\frac{\partial\tilde{\Theta}}{\partial x_k}-2\overline{\rho}\epsilon_\theta, \tag{19}$$

$$\overline{\rho}\frac{\partial\epsilon_\theta}{\partial t}+\overline{\rho}\tilde{U}_k\frac{\partial\epsilon_\theta}{\partial x_k}=\frac{\partial}{\partial x_k}\left(\overline{\rho}\,\overline{\alpha}\frac{\partial\epsilon_\theta}{\partial x_k}\right)+\frac{\partial}{\partial x_k}\left(C_{\epsilon\theta}\overline{\rho}\tau_{kj}\frac{K}{\epsilon}\frac{\partial\epsilon_\theta}{\partial x_j}\right)+C_{d1}\frac{\epsilon_\theta}{\tilde{\theta}^2}P_\theta+C_{d2}\frac{\epsilon}{K}P_\theta-C_{d3}\frac{\epsilon_\theta}{K}P_{uv}-C_{d4}\frac{\tilde{\epsilon}_\theta}{\tilde{\theta}^2}\overline{\rho}\epsilon_\theta-C_{d5}\frac{\tilde{\epsilon}_\theta}{K}\overline{\rho}\epsilon_\theta+\xi_{\epsilon\theta}, \tag{20}$$

where the effects of both thermal ($\tilde{\theta}^2/\epsilon_\theta$) and velocity ($K/\epsilon$) time scale on the dissipation of $\tilde{\theta}^2$ are modeled into the $\epsilon_\theta$ equation. In these equations, $\overline{\alpha}$ is the mean thermal diffusivity $P_\theta=-\overline{\rho}Q_k(\partial\tilde{\Theta}/\partial x_k)$ is turbulence production due to mean temperature gradients, $\xi_{\epsilon\theta}$ is a near-wall correcting function, $\tilde{\epsilon}_\theta=\epsilon_\theta-\overline{\alpha}(\partial\sqrt{\tilde{\theta}^2}/\partial x_2)^2$ and the $C$'s are model constants to be defined later.

If the proposed model is to approach the high-Reynolds-number limit correctly, the model constants in (19) and (20) cannot differ from conventional values adopted by other researchers. A generally acceptable set of constants for the $C$'s are given by: $C_{\theta^2}=0.11$, $C_{\epsilon\theta}=0.11$, $C_{d1}=1.8$, $C_{d2}=0$, $C_{d3}=0.72$, $C_{d4}=2.2$ and $C_{d5}=0.8$. In other words, the near-wall correcting function $\xi_{\epsilon\theta}$ has to be determined so that (19) and (20) would approach their high-Reynolds-number counterparts correctly, i.e., $\xi_{\epsilon\theta}$ would asymptote to zero away from a wall. When these constraints are used to derived $\xi_{\epsilon\theta}$ correct to order $x_2$ near a wall, the following expression is obtained:

$$\xi_{\epsilon\theta}=f_{w,\epsilon\theta}\overline{\rho}\left[(C_{d4}-4)\frac{\epsilon_\theta}{\tilde{\theta}^2}\tilde{\epsilon}_\theta+C_{d5}\frac{\tilde{\epsilon}}{K}\epsilon_\theta-\frac{\epsilon_\theta^{*2}}{\tilde{\theta}^2}+(2-C_{d1}-C_{d2}\mathrm{Pr})\frac{\epsilon_\theta}{\tilde{\theta}^2}P_\theta^*\right], \tag{21}$$

where $P_\theta^*$ is the mean production term in $P_\theta$ due to $\partial\tilde{\Theta}/\partial x_1$ alone and $\epsilon_\theta^*=\epsilon_\theta-\overline{\alpha}\tilde{\theta}^2/x_2^2$. The presence of $P_\theta^*$ is a consequence of the constant wall heat flux boundary condition where $\partial\tilde{\Theta}/\partial x_1$ is finite. Therefore, the near-wall correcting function is valid for all thermal wall boundary conditions. A damping function $f_{w,\epsilon\theta}=\exp[-(\mathrm{Re}_t/80)^2]$ is introduced to ensure that the contribution of $\xi_{\epsilon\theta}$ would vanish away from the wall. Thus formulated, the model has no new constants compared to its high-Reynolds-number counterpart.

With the exception of Nagano and Kim (1988), the various damping functions proposed for $f_\lambda$ satisfy the requirement that $\alpha_t$ behave like $x_2^3$ as a wall is approached. This is consistent with the exact near-wall behavior of the normal heat flux. If, in addition, the model is to work well with flows having dif-

ferent Pr, then $f_\lambda$ has to be parametric in Pr. When these requirements are used to deduce an expression for $f_\lambda$, the following is obtained (So and Sommer, 1994):

$$f_\lambda = C_{\lambda 1}(1 - f_{\lambda 1})/\mathrm{Re}_t^{1/4} + f_{\lambda 1}, \tag{22}$$

where $C_{\lambda 1}$ is a model constant taken to be parametric in Pr, the damping function $f_{\lambda 1}$ is defined by $f_{\lambda 1} = [1 - \exp(-x_2^+/A^+)]^2$, $x_2^+ = x_2 u_\tau/\bar{\nu}$ is a normal coordinate made dimensionless by the local length scale $\bar{\nu}/u_\tau$ and the model constant $A^+$ is also assumed to be parametric in Pr. The friction velocity $u_\tau$ is defined as $(\tau_w/\bar{\rho})^{1/2}$. Typically, for flows with $\mathrm{Pr} \approx 1$, the values for $C_{\lambda 1}$ and $A^+$ are 0.1 and 40, respectively. Their variations with Pr have been determined by So and Sommer (1994) and are given by: $A^+ = 10/\mathrm{Pr}$ for $\mathrm{Pr} < 0.25$ and $A^+ = 39/\mathrm{Pr}^{1/16}$ for $\mathrm{Pr} \geq 0.25$; $C_{\lambda 1} = 0.4/\mathrm{Pr}^{1/4}$ for $\mathrm{Pr} < 0.1$ and $C_{\lambda 1} = 0.07/\mathrm{Pr}$ for $\mathrm{Pr} \geq 0.1$.

Finally, the wall boundary conditions for the temperature field and $\bar{\theta}^2$ and $\epsilon_\theta$ can be stated as follows. At the wall, the thermal boundary conditions can either be adiabatic or constant temperature, while $\bar{\theta}^2 = 0$ and $(\epsilon_\theta)_w = \bar{\alpha}(\partial\sqrt{\bar{\theta}^2}/\partial x_2)^2$ are appropriate for both thermal wall boundary conditions.

## Results and Discussion

The ability of the near-wall models to calculate heat transfer in fluids with widely different Pr is illustrated first. Since Zhang et al. (1993b) have found that the LRR model with near-wall corrections failed to give good results for boundary-layer flows with adverse pressure gradient effects, the present calculations are carried out using the LRR/WR model with near-wall corrections only. This means solving the modeled equations with a nonzero $C_w$ for all cases examined in this paper. Hereafter, the LRR/WR model with near-wall corrections and the two-equation thermal eddy diffusivity model are simply referred to as the present model. In these calculations, fully developed pipe and channel flows with adiabatic and constant wall temperature boundary conditions are considered. Therefore, the governing equations outlined above can be reduced to ordinary differential equations and solved fairly easily by some standard numerical techniques, such as Newton iteration or relaxation methods. Both high and low Reynolds-number flows are calculated and compared with measurements and direct numerical simulation (DNS) data. Some sample comparisons with the empirical temperature log-law of Kader (1981) and with the DNS data of Kim and Moin (1989) are shown here.

In Kader's (1981) study, an empirical temperature log-law is proposed after careful analysis of numerous temperature measurements in pipe and channel flows with widely different Pr. The resultant log-law is found to correlate well with measurements over a broad range of Reynolds number and Pr. Since a more careful comparison with this empirical log-law has been given by So and Sommer (1994), only a representative comparison in the Pr range $10 < \mathrm{Pr} < 100$ is shown in Fig. 1. In this figure, $\Theta^+ = \bar{\Theta}/\Theta_\tau$, $y^+ = y u_\tau/\nu$, $y$ is the normal coordinate to the wall and $\Theta_\tau$ is the friction temperature. The model calculations are in very good agreement with Kader's temperature log-law. Such good agreement extends to Pr as low as 0.025 and as high as $10^3$. A sample comparison with low-Reynolds-number channel flows is carried out with the constant wall temperature DNS data of Kim and Moin (1989). The Reynolds number based on $u_\tau$ is 180 and three different values of Pr are investigated. These are: $\mathrm{Pr} = 0.1$, 0.71, and 2. The velocity field comparisons have been given by So and Sommer (1994) and the results are in good agreement with DNS data. Here, only the comparisons with $\Theta^+$ and $\theta_{\mathrm{rms}} = (\bar{\theta}^2)^{1/2}/\Theta_\tau$, the root-mean square temperature variance, are shown in Figs. 2 and 3, respectively. It can be seen that the calculated mean temperature profiles agree well with DNS data and their dependence on Pr is modeled correctly (Fig. 2). A slight discrepancy exists in the prediction of the maximum $\theta_{\mathrm{rms}}$ and this is most notable for the case where $\mathrm{Pr} = 2$ (Fig. 3). In general, the heat transfer model gives good predictions of incompressible flows with widely different Pr.

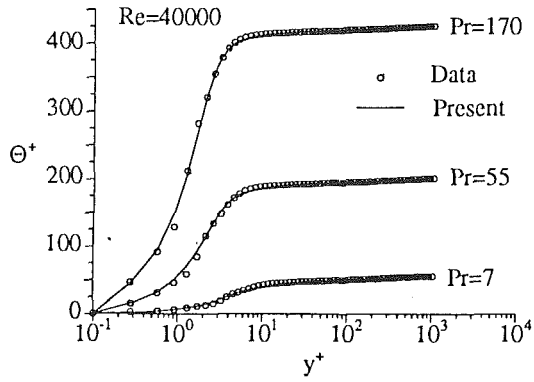


Fig. 1 Comparison of calculated $\Theta^+$ with data (Kader, 1981) for incompressible flows with different Pr

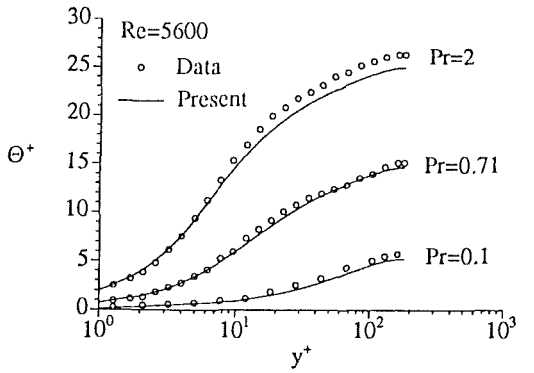


Fig. 2 Comparison of calculated $\Theta^+$ with direct simulation data (Kim and Moin, 1989) for three values of Pr

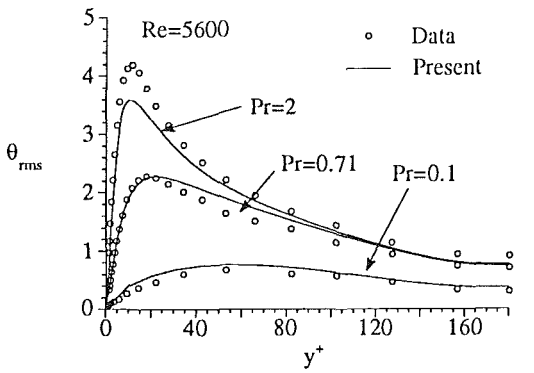


Fig. 3 Comparison of calculated $\Theta_{\mathrm{rms}}$ with direct simulation (Kim and Moin, 1989) for three values of Pr

The compressible flow calculations are compared with the measurements of Fernholz and Finley (1977) and Kussoy and Horstman (1991), and the constant $\mathrm{Pr}_t$ model of Zhang et al. (1993a). This way, the validity of the constant $\mathrm{Pr}_t$ assumption for compressible flows can be examined. Measurements obtained under both adiabatic and cooled wall boundary conditions are considered. In this preliminary attempt, all calculated cases are limited to flat plate boundary layers only, while attempts to calculate complex supersonic flows will be discussed in a subsequent report. Two adiabatic cases are chosen from Fernholz and Finley (1977). The free-stream Mach numbers of these two cases are $M_\infty = 2.244$ and 10.31, while the corre-

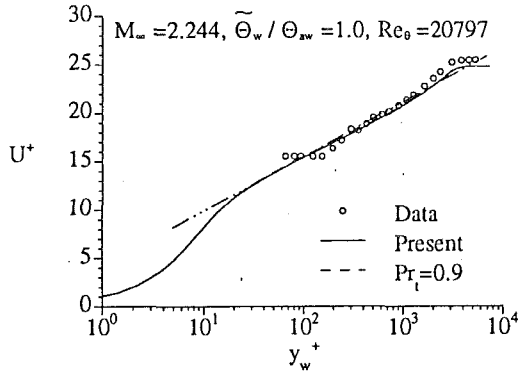


Fig. 4 Comparison of calculated $U^+$ with experimental data (Fernholz and Finley, 1977) for the $M_\infty = 2.244$ case

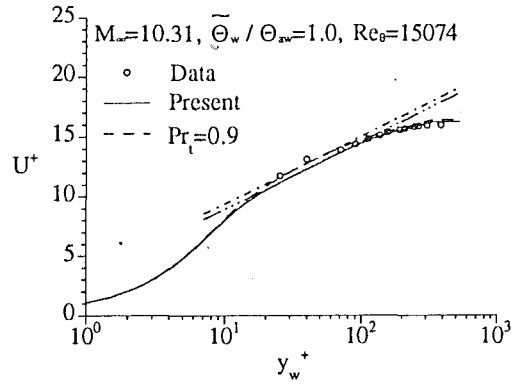


Fig. 6 Comparison of calculated $U^+$ with experimental data (Fernholz and Finley, 1977) for the $M_\infty = 10.31$ case

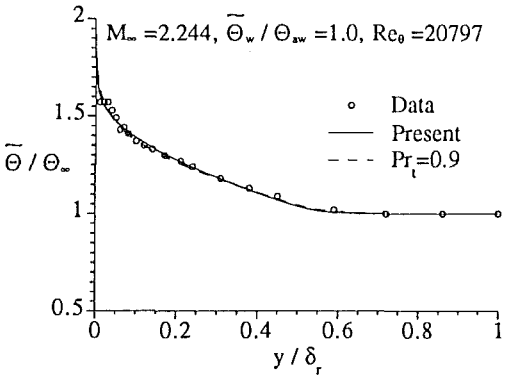


Fig. 5 Comparison of calculated $\tilde{\Theta}/\Theta_\infty$ with experimental data (Fernholz and Finley, 1977) for the $M_\infty = 2.244$ case

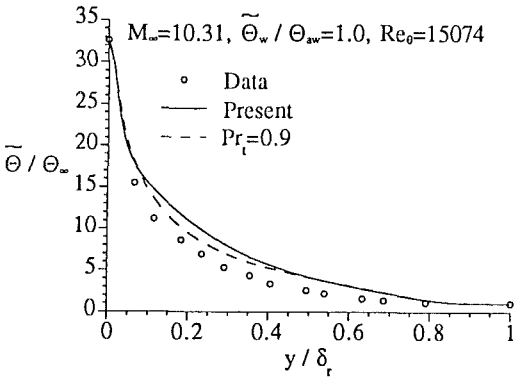


Fig. 7 Comparison of calculated $\tilde{\Theta}/\Theta_\infty$ with experimental data (Fernholz and Finley, 1977) for the $M_\infty = 10.31$ case

sponding momentum thickness Reynolds number, $R_\theta$, are 20,797 and 15,074, respectively. In addition to mean velocity, wall friction is also reported. Therefore, the comparisons are made with the mean velocity profiles in semi-log plots of $U^+$ versus $\ln y_w^+$, where $U^+ = \tilde{U}/u_\tau$ and $y_w^+ = y u_\tau/\bar{\nu}_w$. Calculations are made of the skin friction coefficient, $C_f = 2\tau_w/\bar{\rho}_\infty U_\infty^2$ and the heat transfer coefficient, $C_h = q_w/\bar{\rho}_\infty U_\infty \bar{C}_p(\Theta_w - \Theta_{aw})$, where $q_w$ is the wall heat flux. Furthermore, comparisons are made with the mean temperature profiles in the form of $\tilde{\Theta}/\Theta_\infty$ versus $y/\delta$, where $\Theta_\infty$ is the free-stream temperature and $\delta$ is the measured boundary-layer thickness. However, these are not independent comparisons because the temperature profiles are inferred from the measured velocity profiles by assuming constant total enthalpy and pressure across the boundary layers. In order to verify the present heat transfer model, comparisons with supersonic cooled wall boundary layers are carried out. Only one case is presented and this has a wall temperature ratio $\Theta_w/\Theta_{aw} = 0.3$. The data are extracted from Kussoy and Horstman (1991). The corresponding $M_\infty$ and $R_\theta$ are 3,939 and 4,600, respectively. Since the measurements of velocity and temperature are obtained independently, the performance of the compressible heat transfer model can be evaluated. Again, the skin friction coefficient and the heat transfer coefficient are calculated and compared with measurements.

Comparisons with the cases where an adiabatic wall boundary condition is specified are presented first. These results are shown in Figs. 4–7. Only the mean velocity (Figs. 4 and 6) and mean temperature (Figs. 5 and 7) profiles are compared. The measured velocity profiles can be correlated by the log-law (Zhang et al., 1992a)

$$U^+ = \frac{1}{\kappa}\ln y_w^+ + B \tag{23}$$

where $\kappa$ is the von Karman constant. At low Mach numbers, the log-law with $\kappa = 0.41$ and $B = 4.3$ correlates well with data and model calculations (see log-law plotted in Fig. 4). As Mach number increases, $B$ decreases with Mach numbers and at $M_\infty = 10.31$, the $B$ value determined from the present model is 3.35 while that from the constant $Pr_t$ model is 3.8. Both models give the same von Karman constant, i.e., $\kappa = 0.41$. However, the present model yields a longer range log-law compared to the constant $Pr_t$ model and is more consistent with measurements (see the log-laws plotted in Fig. 6). Therefore, the $B$ value thus determined is more reliable (Fig. 6). As for the temperature comparison (Figs. 5 and 7), again, there is little difference between the two model predictions at low Mach numbers. At $M_\infty = 10.31$, there is a slight discrepancy between the present model and that of the constant $Pr_t$ model in the region bounded by $0.1 < y/\delta < 0.5$. It seems that the present model over-predicts the mean temperature in this region. Since the mean temperature data are inferred from the mean velocity measurements and the assumption of constant total enthalpy, it follows that a high measured velocity would lead to a low temperature estimation. The measured velocities seem to be high compared to the log-law in this region, therefore, the inferred temperatures are low. Measurements of $C_f \times 10^{-3}$ for the $M_\infty = 2.244$ and 10.31 cases are 1.62 and 0.24, respectively. The corresponding values determined from the constant $Pr_t$ model of Zhang et al. (1993a) are 1.69 and 0.24, while the present model gives 1.71 and 0.24, respectively. As far as the prediction of $C_f$ is concerned, both models are quite good. In other words, the integral boundary-layer parameters are not as much affected by the model used to calculate the flow.

The cooled wall results are compared in Figs. 8 and 9. It has been demonstrated by Zhang et al. (1992) that the von Karman constant changes as the wall temperature ratio de-

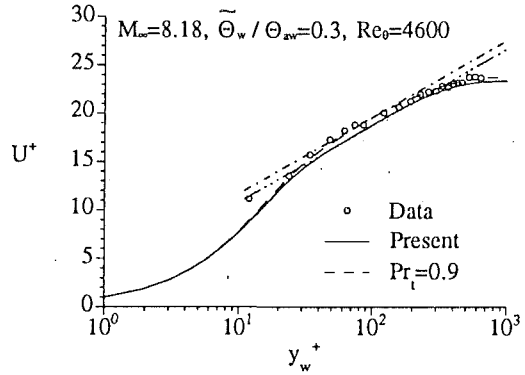


Fig. 8 Comparison of calculated $U^+$ with experimental data (Kussoy and Horstman, 1991) for the $M_\infty = 8.18$ case

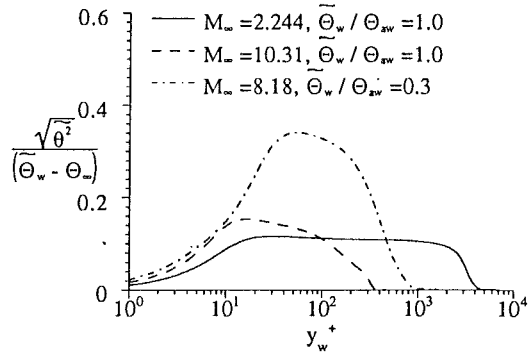


Fig. 10 Distributions of $\sqrt{\tilde{\theta}^2}/(\tilde{\Theta}_w - \Theta_\infty)$ across the boundary layers for both adiabatic and cooled wall boundary conditions

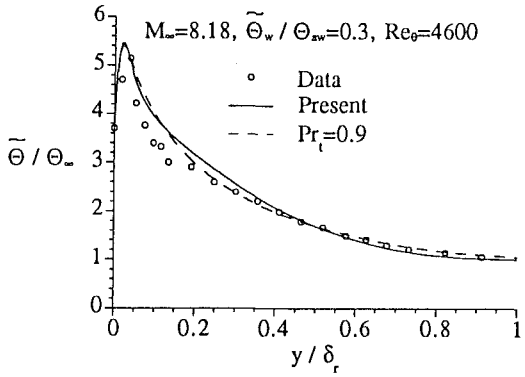


Fig. 9 Comparison of calculated $\tilde{\Theta}/\Theta_\infty$ with experimental data (Kussoy and Horstman, 1991) for the $M_\infty = 8.18$ case

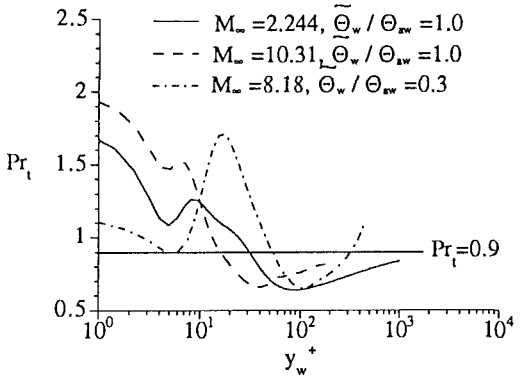


Fig. 11 Distributions of $Pr_t$ across the boundary layers for both adiabatic and cooled wall boundary conditions

creases. Furthermore, $B$ also varies as $\Theta_w/\Theta_{aw}$ decreases. The same behavior is predicted by the constant $Pr_t$ model and the present model. When $\Theta_w/\Theta_{aw}$ decreases to 0.3, the $\kappa$ and $B$ values determined from the model calculations are: 0.29 and 2.87 from the present model and 0.29 and 3.74 from the constant $Pr_t$ model (see the log-laws plotted in Fig. 8), respectively. It is difficult to say which set of values agrees better with measurements. However, as before, the present model yields a longer range of log-law compared to the constant $Pr_t$ model and is consistent with the measurements. In view of this, it can be said that the set of values determined from the present model is more reliable. There is little difference in the predicted mean temperature at low values of $\Theta_w/\Theta_{aw}$. As $\Theta_w/\Theta_{aw}$ decreases to 0.3, a slight discrepancy exists between the model predictions in the region bounded by $0.1 < y/\delta < 0.5$ (Fig. 9), which is the same as observed in the $M_\infty = 10.31$ case with an adiabatic wall boundary condition. This time, the mean temperatures are measured independently and they seem to agree better with the predictions of the constant $Pr_t$ model. The measured $C_f \times 10^{-3}$ and $C_h \times 10^{-3}$ for the $M_\infty = 8.18$ case are 0.98 and 0.53, respectively, while the corresponding calculated values are 0.95 and 0.57 from the constant $Pr_t$ model and 0.99 and 0.60 from the present model. It can be seen that there is an improvement in the prediction of $C_f$ but a deterioration in the calculation of $C_h$ when the present model is used to simulate the temperature field. However, according to Kussoy and Horstman (1991), the measurement of $C_h$ is not as accurate as that of $C_f$. Therefore, it might turn out that there is no deterioration in the prediction of $C_h$ after all.

Finally, some sample plots of the temperature variance $\tilde{\theta}^2$ and turbulent Prandtl number $Pr_t$ are shown in Figs. 10 and 11, respectively. The root mean square temperature variance normalized by $(\Theta_w - \Theta_\infty)$ is shown in Fig. 10. It can be seen that, as $M_\infty$ increases, the maximum $\tilde{\theta}^2$ increases. The same is true when $\Theta_w/\Theta_{aw}$ decreases; however, the increase in substantially larger than that due to Mach number enhancement. Therefore, these results indicate that temperature fluctuations are promoted by compressibility and most significantly by wall cooling. The calculated $Pr_t$ is not constant across the boundary layers (Fig. 11). For an adiabatic wall boundary condition, the calculated $Pr_t$ reaches a maximum of about 2 at the wall and decreases rapidly to about 1.5 in the region $4 < y_w^+ < 8$. Thereafter, $Pr_t$ continues to decrease towards the edge of the boundary layer. Essentially the same trend is followed by the $M_\infty = 2.244$ case, except that the level is lower. On the other hand, $Pr_t$ has a value of about 1.1 at the wall for the cooled wall case. Its value decreases to a minimum at $y_w^+ = 6$ and then rises to a maximum of about 1.7 at $y_w^+ = 20$. At the edge of the boundary layer, the value of $Pr_t$ is about 1.0, which is substantially higher than the values attained in the adiabatic wall cases. The constant $Pr_t$ model calculations show that, irrespective of the fact that $Pr_t$ varies significantly across the boundary layers, a constant value of 0.9 yields mean flow results that are as good as the present model. As for the turbulence statistics, no reliable data is available for comparisons. Therefore, the merit of the present model versus that of constant $Pr_t$ cannot be commented on in this work.

## Conclusions

A two-equation turbulence model for the temperature field is proposed for supersonic flows. The model equations are derived directly from their incompressible counterparts by invoking Morkovin's hypothesis, where it is postulated that compressibility effects could be accounted for by the variations of mean density alone, A thermal eddy diffusivity is assumed and it is determined from the temperature variance and its dissi-

pation rate, whose transport equations are modeled and solved in the present approach. The thermal eddy diffusivity is taken to be the product of a turbulence velocity scale and a length scale. It is further assumed that the turbulence velocity scale and an appropriately defined time scale can be used to define the length scale. Both thermal and velocity time scales are used to determine the appropriate time scale. This is necessary because the interactions of the velocity and temperature fields have to be accounted for properly. The present approach invokes a second-order compressible turbulence model for the velocity field. The model equations are applied to study supersonic flows with free stream Mach numbers and wall temperature ratios that vary from 2.244 to 10.31 and 0.3 to 1.0, respectively. In calculating these supersonic flows, real gas effects are neglected. The calculated results are compared with measurements covering the same range of Mach numbers and wall temperature ratios. A similar model assuming the turbulent Prandtl number to be 0.9 is used to calculate the test cases and the results compared with the variable $Pr_t$ model calculations and measurements.

The two model calculations yield results that are in good agreement with measurements. One possible difference is in the prediction of the range of the log-law. The present model predicts a longer range for all test cases examined compared to the constant $Pr_t$ model. In the test cases studied, the longer log-law range seem to be more consistent with measurements. Thus compared, the constant $Pr_t$ assumption is found to be valid for the range of Mach numbers and wall temperature ratios investigated. On the other hand, compared to the constant $Pr_t$ calculations, the present model over-predicts slightly the mean temperature in the range $0<y/\delta<0.5$ at high Mach numbers and low wall temperature ratios. Consequently, the relative merits of the present model and the constant $Pr_t$ model have to be further analyzed by comparing the calculations with accurately measured turbulence statistics, which are presently lacking.

## Acknowledgments

Funding support under grant no. NAG-1-1080 from NASA Langley Research Center, Hampton, VA 23665, is gratefully acknowledged.

## References

Anderson, E. C., and Lewis, C. H., 1971, "Laminar or Turbulent Boundary-Layer Flows of Perfect Gases or Reacting Gas Mixtures in Chemical Equilibrium," NASA CR-1893.

Antonia, R. A., and Kim, J., 1991, "Turbulent Prandtl Number in the Near-Wall Region of a Turbulent Channel Flow," *Journal of Heat and Mass Transfer*, Vol. 34, pp. 1905–1908.

Bradshaw, P., Launder, B. E., and Lumley, J. L., 1991, "Collaborative Testing of Turbulence Models," ASME JOURNAL OF FLUIDS ENGINEERING, Vol. 113, pp. 3–4.

Fernholz, H. H., and Finley, P. J., 1977, "A Critical Compilation of Compressible Turbulent Boundary Layer Data," AGARDograph No. 223.

Kader, B. A., 1981, "Temperature and Concentration Profiles in Fully Turbulent Boundary Layers," *International Journal of Heat and Mass Transfer*, Vol. 24, pp. 1541–1544.

Kasagi, N., Tomita, Y., and Kuroda, A., 1991, "Direct Numerical Simulation of the Passive Scalar Field in a Two-Dimensional Turbulent Channel Flow," *Proceedings of the 3rd ASME-JSME Thermal Engineering Joint Conference*, Vol. 3, pp. 175–182.

Kim, J., and Moin, P., 1989, "Transport of Passive Scalars in a Turbulent Channel Flow," *Turbulent Shear Flows 6*, Springer-Verlag, Berlin, pp. 85–96.

Kim, J., Moin, P., and Moser, R. D., 1987, "Turbulence Statistics in Fully Developed Channel Flow at Low Reynolds Number," *Journal of Fluid Mechanics*, Vol. 177, pp.133–186.

Kussoy, M. I., and Horstman, K. C., 1991, "Documentation of Two- and Three-Dimensional Shock-Wave/Turbulent Boundary-Layer Interaction Flows at Mach 8.18," NASA-TM-103838.

Lai, Y. G., and So, R. M. C., 1990a, "On Near-Wall Turbulent Flow Modeling," *Journal of Fluid Mechanics*, Vol. 221, pp. 641–673.

Lai, Y. G., and So, R. M. C., 1990b, "Near-Wall Modeling of Turbulent Heat Fluxes," *International Journal of Heat and Mass Transfer*, Vol. 33, pp. 1429–1440.

Launder, B. E., Reece, G. J., and Rodi, W., 1975, "Progress in the Development of a Reynolds Stress Turbulence Closure," *Journal of Fluid Mechanics*, Vol. 68, pp. 537–566.

Launder, B. E., 1976, "Heat and Mass Transport," *Turbulence—Topics in Applied Physics*, Vol. 12, P. Bradshaw, ed., Springer, Berlin, pp. 232–287.

Mansour, N. N., Kim, J., and Moin, P., 1988, "Reynolds-Stress and Dissipation-Rate Budgets in a Turbulent Channel Flow," *Journal of Fluid Mechanics*, Vol. 194, pp. 15–44.

Morkovin, M., 1962, "Effects of Compressibility on Turbulent Flows," *Mecanique de la Turbulence*, CNRS, A. Favre, ed., Gordon and Breach, pp. 367–380.

Moser, R. D., and Moin, P., 1987, "The Effects of Curvature in Wall Bounded Turbulent Flow," *Journal of Fluid Mechanics*, Vol. 175, pp. 479–510.

Nagano, Y., and Kim, C., 1988, "A Two-Equation Model for Heat Transport in Wall Turbulent Shear Flow," ASME *Journal of Heat Transfer*, Vol. 110, pp. 583–589.

Nagano, Y, Tagawa, M., and Tsuji, T., 1991, "An Improved Two-Equation Heat Transfer Model for Wall Turbulent Shear Flows," *Proceedings of the 3rd ASME-JSME Thermal Engineering Joint Conference*, Vol. 3, pp. 233–240.

Sarkar, S., Erlebacher, G., Hussaini, M. Y., and Kreiss, H. O., 1991, "The Analysis and Modeling of Dilatational Terms in Compressible Turbulence," *Journal of Fluid Mechanics*, Vol. 227, pp. 473–493.

So, R. M. C., Zhang, H. S., and Speziale,C. G., 1991b, "Near-Wall Modeling of the Dissipation-Rate Equation," *AIAA Journal*, Vol. 29, pp. 2069–2076.

So, R. M. C., Lai, Y. G., Zhang, H. S., and Hwang, B. C., 1991a, "Second-Order Near-Wall Turbulence Closures: A Review," *AIAA Journal*, Vol. 29, pp. 1819–1835.

So, R. M. C., Yuan, S. P., and Sommer, T. P., 1992, "A Hierarchy of Near-Wall Closures for Turbulent Heat Transfer," *Trends in Heat, Mass & Momentum Transfer*, Vol. 2, pp. 203–221.

So, R. M. C., and Sommer, T. P., 1994, "A Near-Wall Eddy Conductivity Model for Fluids with Different Prandtl Numbers," ASME *Journal of Heat Transfer*, to appear.

Sommer, T. P., So, R. M. C., and Lai, Y. G., 1992, "A Near-Wall Two-Equation Model for Turbulent Heat Fluxes," *International Journal of Heat and Mass Transfer*, Vol. 35, pp. 3375–3387.

Sommer, T. P., So, R. M. C., and Zhang, H. S., 1993, "A Near-Wall Variable-Prandtl-Number Turbulence Model for Compressible Flows," *AIAA Journal*, Vol. 31, pp. 27–35.

Sommer, T. P., So, R. M. C., and Zhang, H. S., 1994, "Heat Transfer Modeling and the Assumption of Zero Wall Temperature Fluctuations," ASME *Journal of Heat Transfer*, to appear.

Spalart, P. R., 1988, "Direct Simulation of a Turbulent Boundary Layer up to $R_\theta = 1410$," *Journal of Fluid Mechanics*, Vol. 187, pp. 61–98.

Speziale, C. G., and Sarkar, S., 1991, "Second-Order Closure Models for Supersonic Turbulence-Flows," AIAA Paper No. 91-0217.

Zhang, H. S., So, R. M. C., Speziale, C. G., and Lai, Y. G., 1992, "A Near-Wall Two-Equation Model for Compressible Turbulent Flows," AIAA Paper No. 92-0442; also *AIAA Journal*, Vol. 31, pp. 196–199.

Zhang, H. S., So, R. M. C., Speziale, C. G., and Gatski, T. B., 1993a, "A Near-Wall Second-Order Closure for Compressible Turbulent Flows," *Near-Wall Turbulent Flows*, R. M. C. So, C. G. Speziale, and B. E. Launder, eds., Elsevier, Amsterdam, The Netherlands, pp. 209–218.

Zhang, H. S., So, R. M. C., and Zhu, M. L., 1993b, "A Near-Wall Reynolds-Stress Turbulence Model and Its Application to Wall-Bounded Flows," *Proceedings, Ninth Symposium on Turbulent Shear Flows*, pp. 8.2.1–8.2.6.

# The Wavenumber-Phase Velocity Representation for the Turbulent Wall-Pressure Spectrum

**Ronald L. Panton**
Mechanical Engineering Department,
University of Texas,
Austin, TX 78712
Fellow ASME

**Gilles Robert**
Laboratorie de Mecanique des
Fluids et d'Acoustique,
Ecole Centrale de Lyon,
69131 Ecully Cedex, France

*Wall-pressure fluctuations can be represented by a spectrum level that is a function of flow-direction wavenumber and frequnecy, $\Phi(k_1, \omega)$. In the theory developed herein the frequency is replaced by a phase speed; $\omega = ck_1$. At low wavenumbers the spectrum is a universal function if nondimensionalized by the friction velocity $u^*$ and the boundary layer thickness $\delta$, while at high wavenumbers another universal function holds if nondimensionalized by $u^*$ and viscosity $\nu$. The theory predicts that at moderate wavenumbers the spectrum must be of the form $\Phi^+(k_1^+, \omega^+ = c^+k_1^+) = k_1^+ - 2P^+(\Delta c^+)$ where $P^+(\Delta c^+)$ is a universal function. Here $\Delta c^+$ is the difference between the phase speed and the speed for which the maximum of $\Phi^+$ occurs. Similar laws exist in outer variables. New measurements of the wall-pressure are given for a large Reynolds number range; $45{,}000 < Re = U_0\delta/\nu < 113{,}000$. The scaling laws described above were tested with the experimental results and found to be valid. An experimentally determined curve for $P^+(\Delta c^+)$ is given.*

## Introduction

In the general situation where a boundary layer develops slowly, the flow only depends on the local properties; the layer thickness, friction velocity, fluid density, pressure gradient, and the characteristic Mach number and Reynolds number of the flow. This paper deals with incompressible flow where the Mach number is nearly zero. As in the general theory of turbulent boundary layers the development is organized as the limiting behavior for high Reynolds numbers. Although the data we will present are for zero-pressure gradients, the theory is also applicable to flows with pressure gradients.

It is well-known that turbulent boundary layers have two distinctively different layers; the outer inviscid layer and the inner wall layer. These layers are not mutually exclusive but have a region of overlap, the "log region." The extent of the overlap region increases directly with the Reynolds number. Because the wall pressure is influenced by turbulent motions from throughout the boundary layer, changes in boundary layer overlap structure are reflected by changes in the spectrum. In this paper, we develop a theory that accounts for the expansion of the frequency range in a rational way.

Over the last thirty years numerous measurements of the wall-pressure field have been made. Even though approaches exist which seek to characterize the signature of wall pressure from coherent turbulent structures (Dinkelacker, 1977; Wilczynski and Casarella, 1993) experimental studies generally concern the statistical description of the wall-pressure field. Results for $R_{pp}(\xi, \zeta, \tau)$ are presented in physical and temporal space (for example, Willmarth, 1975) and Panton, 1980). Related quantities have been studied in physical and frequency space, $S_{pp}(\xi, \zeta, \omega)$, by among others, Bull (1967), Blake (1970), Willmarth (1970), for aerodynamic boundary layers, and by Carey (1967), Bakewell (1968), and Benarrous (1979) for hydrodynamic boundary layers. Fourier transforming the results obtained in physical space (Wills, 1970; Karangelen et al., 1991); Manoha, 1991) gives one access to a continuous representation of the cross-spectrum in $k-\omega$ space.

## Theory

A physical characteristic of turbulent wall layers is that the fluctuations, which have a small characteristic velocity, are convected with a much larger velocity. The crudest approximation is that the convection velocity is a constant fraction of the free-stream velocity. A much better approximation is that the convection velocity is approximately the local mean velocity. The physical process of convection is emphasized by introducing a phase velocity defined by

$$c = \omega/k_1 \tag{1}$$

With this substitution the spectrum function $\Phi(k_1, \omega)$ can be given as a function of $k_1$, and $c$.

$$\Phi = (k_1, ck_1) \tag{2}$$

(Wills (1970) used this approach to separated acoustic noise from his measurements.) The physical picture is that the pressure fluctuations are primarily the result of superimposed components of wavenumber $k_1$, being convected at a speed $c$ over the wall. At a specific point on the wall it is expected that turbulent fluctuations of small scale convected at a low speed will produce the same frequency as a large fluctuation con-

Contributed by the Fluids Engineering Division for publication in the JOURNAL OF FLUIDS ENGINEERING. Manuscript received by the Fluids Engineering Division January 25, 1993; revised manuscript received September 29, 1993. Associate Technical Editor: D. M. Bushnell.

vected at a high speed. By using $c$ and $k_1$ as independent variables the contributions of different size eddys to the same frequency are separated.

It is a fact that the extent of influence of a turbulent fluctuation is proportional to its size. The largest fluctuations have a spatial scale about the size of the boundary layer thickness, while the smallest scales are related to the thickness of the viscous sublayer. Thus, a small eddy that is in the outer layer is not felt on the wall. This is particularly true as the Reynolds number becomes high and the outer layer is large compared to the inner layer. If it is valid that the highest wavenumber portion of the spectrum comes only from the inner layer then the proper nondimensional variables are scaled with the inner scales $u_*$ and $\nu$, that is

$$\Phi^+ = \frac{\Phi(k_1, \omega)}{\rho^2 \nu^2 u_*}, \quad k_1^+ = \frac{k_1 \nu}{u_*}, \quad c^+ = \frac{c}{u_*} \tag{3}$$

In this form the spectrum $\Phi^+$ should be nearly independent of the Reynolds number in the region of high $k_1$. Moreover, this portion of the spectrum should not be influenced greatly by an external pressure gradient.

At the other end of the spectrum, the largest turbulent eddys exist only in the outer layer and have a size scaled by the boundary layer thickness $\delta$. The intensity of fluctuation in these eddys also scales with $u^*$. The appropriate outer scaling (the use of $u^*$ and $\delta$ for scaling the frequency spectrum was proposed long ago and has been experimentally confirmed by Farabee and Casarella, 1991) is

$$\Sigma = \frac{\Phi(k_1, \omega)}{\rho^2 u_*^3 \delta^2}, \quad K_1 = k_1 \delta, \quad C = \frac{c - U_\infty}{u^*} \tag{4}$$

At low wavenumbers this form for $\Sigma$ should be roughly independent of the Reynolds number, however, it will be sensitive to the pressure gradient. An important assumption is that the phase velocity is expressed as a defect law; an analogy with the mean velocity profile where it is known to be the correct form.

The ratio of outer and inner scales is the Reynolds number

$$\mathrm{Re}_* = \frac{u_* \delta}{\nu} \tag{5}$$

Inner and outer spectrum variables, defined above, are simply related through this Reynolds number. The relations are

$$\Sigma = \Phi^+ \mathrm{Re}_*^{-2}, \quad K_1 = k_1^+ \mathrm{Re}_*, \quad C = c^+ - U_\infty / u_* \tag{6}$$

It should be noted that $U_\infty / u_*$ is a function of the Reynolds number.

Next, we consider the ridge in the $k_1 - c$ plane where $\Phi$ has a local maximum for constant wavenumber ($\partial\Phi, \partial c = 0$). The values along the ridge are noted by the subscript max and the location is the curve $c^+_{\max} = c^+_{\max}(k_1^+)$.

$$\Sigma_{\max}(K_1) = \Sigma(K_1, K_1\, C_{\max})$$

$$\Phi^+_{\max}(k_1^+) = \Phi^+(k_1^+, c^+_{\max} k_1^+) \tag{7}$$

The curve $c^+_{\max}$ can be considered as the convective velocity of the pressure fluctuations. As with the complete spectra these maxima functions are independent of Reynolds number in the inner and outer scaling at high and low wavenumbers, respectively. Of interest in the current paper is the overlap convective law given by Panton and Linebarger (1974).

$$c^+_{\max} = \frac{c_{\max}}{u_*} = -\frac{1}{\kappa} \ln(k_1^+) + C \tag{8}$$

The constants here are the same as those in the mean velocity law (note that conversion of Eq. (8)) from $k_1^+$ to $K_1$ is accomplished using the friction law;

$$\frac{U_\infty}{u_*} = \frac{1}{\kappa} \ln(\mathrm{Re}_*) + C + \frac{2\Pi}{\kappa}.$$

Assume that there is an overlap region in $\Phi_{\max}$ as a function of $k_1$ where both inner and outer scaling are valid. That is, there is a region of intermediate wavenumbers where both expressions in Eq. (7) are valid

$$\Sigma_{\max} = \Phi^+_{\max} \mathrm{Re}_*^{-2} \tag{9}$$

Since this is a finite region we may differentiate Eq. (9) with respect to $K_1$ to obtain

$$\frac{d\,\Sigma_{\max}}{dK_1} = \frac{d(\Phi^+_{\max} \mathrm{Re}_*^{-2})}{dk_1^+} \frac{dk_1^+}{dK_1}$$

Using the relation $K_1 = k_1^+ \mathrm{Re}_*$, separating variables, and considering $K_1$ and $k_1^+$ to be independent (for fixed $K_1$, $\mathrm{Re}_*$ could be changed) leads to

$$K_1^3 \frac{d\,\Sigma_{\max}}{dK_1} = (k_1^+)^3 \frac{d\Phi^+_{\max}}{dk_1^+} = \text{Constant} = A' \tag{10}$$

One of the two differential equations that result is

$$d\,\Sigma_{\max} = A' K_1^{-3}\, dK_1$$

Thus, in the range of wavenumbers where there is an overlap, the behavior of the maximum values must be

$$\Sigma_{\max} = A K_1^{-2} + C_1 \tag{10a}$$

Similar arguments produce the inner form of this relation

## Nomenclature

$c$ = phase speed
$c_{\max}$ = convection velocity
$f$ = frequency
$k_1$ = streamwise wavenumber
$p$ = pressure fluctuation
$Re_*$ = Reynolds number $u_* \delta / \nu$
$R_{pp}(\xi, \zeta, \tau)$ = cross-correlation function
$S_{pp}(f)$ = wall-pressure power spectral density
$S_{pp}(\omega)$ = wall-pressure spec-trum: $4\pi S_{pp}(\omega) = S_{pp}(f)$
$S_{pp}(\xi, \zeta, \omega)$ = wall-pressure cross-spectrum
$U_\infty$ = free-stream velocity
$u_*$ = friction velocity
$\alpha$ = coefficient for streamwise decay of coherence
$\delta^*$ = displacement thickness
$\delta$ = boundary layer thickness
$\rho$ = density
$\Phi(k_1, k_2, \omega)$ = wavenumber and frequency cross-spectrum
$\Phi(k_1, \omega)$ = integrated wavenumber spectrum
$\nu$ = kinematic viscosity
$\tau$ = time delay
$\tau_0$ = mean wall shear stress ($\tau_0 = \rho u^{*2}$)
$\xi, \zeta$ = streamwise and transverse separation distance
$\omega$ = angular frequency, $2\pi f$
$P^+(c^+, k_1^+)$ = spectrum function
$R_{pp}(\xi, \zeta, \tau)$ = $p(x, z, t) \cdot p(x+\xi, z+\zeta, t+\tau)$
$S_{pp}(\xi, \zeta, \omega)$ = $1/2\pi \int R_{pp}(\xi, \zeta, \tau) \cdot \exp(-i\omega\tau)$ $d\xi\, d\zeta\, d\tau$—
$\Phi(k_1, k_3, \omega)$ = $1/8\pi^3 \int R_{pp}(\xi, \zeta, \tau) \cdot \exp(i(k_1\xi + k_3\xi - \omega\tau))d\xi\, d\zeta\, d\tau$
$\Phi(k_1, \omega)$ = $\int \Phi(k_1, k_3, \omega) dk_3$

$$\Phi^+_{max} = A\ k_1^{+-2} + C_2 \qquad (10b)$$

Back substitution into Eq. (9) shows that the constants are zero. Equations (10) were previously given by Panton (1990).

The essential mathematical element of the argument above is that a function of the single variable, $k_1$, has an overlap region which expands with Reynolds number. Any other mathematical property of the spectra where $c$ is eliminated to leave only the independent variable $k_1$ can be similarly treated. Here we extend the argument to prove that the spectra in the overlap region must also have a universal shape. Consider the integral below over $c^+$ with $k_1^+$ as a parameter

$$I^+(k_1^+) \equiv \int \Phi + (k_1^+, c^+ k_1^+) d(c^+ k_1^+) \qquad (11a)$$
$$k_1^+ = \text{constant}$$

Transforming the integral into outer variables yields

$$I^+(k_1^+) = \text{Re}^* \int \Sigma(K_1, CK_1)\, d(CK_1) \equiv \text{Re}^* \mathbf{I}(K_1) \qquad (11b)$$

Applying the same overlap argument as above to the functions $I^+(k_1^+)$ and $\mathbf{I}(K_1)$ shows that we should expect a range of moderate wavenumbers where the integrals must have the following trends

$$I^+(k_1^+) = B\ k_1^{+-1} \qquad \mathbf{I}(K_1) = B\ K_1^{-1} \qquad (12)$$

Next, consider that the expressions in Eq. (12) can be solved for the constant $B$

$$B = k_1^+ I^+(k_1^+) = \int k_1^{+2}\, \Phi^+(k_1^+, c^+ k_1^+)\, dc^+ \qquad (13)$$

Let the integrand be denoted by $P^+$

$$P^+(c_1^+, k_1^+) \equiv k_1^{+2} \Phi^+(k_1^+, c^+\ k_1^+) \qquad (14)$$

Consider $P^+$ as a function of $c^+$ with $k_1$ as a parameter. Furthermore, note that there is no change in the level of $P^+$ when it is expressed in outer variables.

$$P^+(c^+, k_1^+) = k_1^{+2}\Phi^+ = \left(\frac{K_1}{\text{Re}^*}\right)^2 \Sigma\ \text{Re}^{*2}$$
$$= K_1^2 \Sigma = \mathbf{P}(C, K_1) \qquad (15)$$

We will call $P^+$ or $P$ the *spectrum function*.

For constant wavenumber the peaks of the $P^+$ curves can be lined up by introducing the variable

$$\Delta c^+ = c^+ - c^+_{max}(k_1) \qquad (16)$$

In the overlap range $c^+_{max}$ is given by Eq. (10). Likewise, the outer representation should be based on the defect velocity

$$\Delta C \equiv C - C_{max} = \Delta c + \qquad (17)$$

Equations (15) and (17) imply that any statement about $P^+(c^+, k_1^+)$ also applies to $P(C, K_1)$.

Next we will show that $P^+$ has a universal form, that is $P^+(c^+, k_1^+) = P^+(\Delta c^+)$ for any $k_1^+$ is in the overlap region. To prove this consider a new integral from the maximum $c^+_{max}$ to an arbitrary point $c^+_{max} + \Delta c^+$

$$I_2^+(k_1^+; \Delta c^+) = \int_{c^+_{max}}^{c^+_{max} + \Delta c+} P^+(c^+, k_1^+)\, dc^+$$

Since $P^+(c^+, k_1^+) = P(C, K_1)$, Eq. (15), and $\Delta C = \Delta c^+$, Eq. (17), the value of this integral is unchanged when it is transformed into outer variables, that is

$$I_2^+(k_1^+; \Delta c^+) = \int_{C_{max}}^{C_{max} + \Delta C} \mathbf{P}(C, K_1)\, dC = I_2(K_1; \Delta C) \qquad (18)$$

Therefore, the overlap arguments can be applied to show that $I_2^+$ is constant (for fixed $\Delta c^+$) over the range of overlap wavenumbers. Equally as important is the fact that the argument is good for any choice of $\Delta c^+ = \Delta C$.

Figure 1 shows the integral for a certain value of $\Delta c^+$ for two different wavenumbers. Assume the opposite of what we desire to prove; namely, that the curves for two different overlap wavenumbers are distinct as shown. Since the integrals are equal by Eq. (18) there must be a crossover point between $c^+_{max}$ and $c^+_{max} + \Delta c^+$. If this were true we could immediately choose the crossover point as a new $\Delta c+$ and the integrals to this new value would be different. This contradicts the known fact in Eq. (18), hence the curves $P^+(\Delta c^+) = \mathbf{P}(\Delta C)$ must be identical (universal) for all $k_1^+$ in the overlap region.

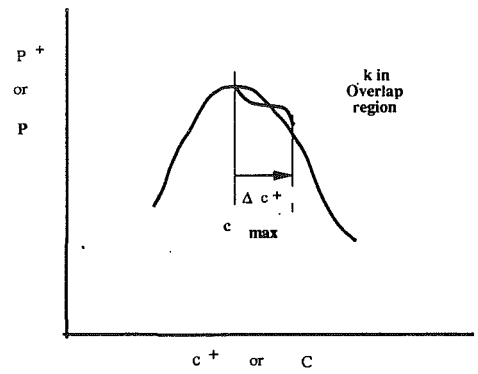


**Fig. 1 Spectrum function $P^+(c^+)$. Two curves for distinct wavenumbers.**

**Table 1 Boundary layer characteristics**

| | | | | | |
|---|---|---|---|---|---|
| $Uo$ m/s | 20 | 30 | 40 | 50 | 60 |
| $u^*$ m/s | 0.826 | 1.18 | 1.56 | 1.9 | 2.19 |
| $\delta$ m | 0.0358 | 0.0358* | 0.0359 | 0.0358* | 0.0359 |
| $\Pi$ | 0.16 | 0.16* | 0.087 | 0.16* | 0.27 |
| $C$ | 5.082 | 5.082* | 5.018 | 5.082* | 5.52 |
| $d^+$ | 166 | 238 | 314 | 385 | |
| $\text{Re}_*$ | 1908 | 2725 | 3662 | 4400 | 5086 |

*Extrapolated values from 20 m/s.

As an aside we note that if one deals with the complete spectrum with zero spanwise separation $\Phi^+_{pp}(k_1^+, k_3^+ = 0, c + k_1^+)$, as opposed to the spectrum that is integrated over $k_3^+$, the corresponding result is $\Phi^+_{pp}(k_1^+, k_3^+ = 0, c^+ k_1^+) = k_1^{+-3} \mathbf{P}^+_{pp}(\Delta c^+_1 k_1^+)$.

We summarize the results with the following statements. For high wavenumbers the spectrum function $P^+(\Delta c^+, k_1^+)$ depends on $k_1^+$ but should be independent of the Reynolds number. Similarly, for low wavenumbers the outer representation $P(\Delta C, K_1)$ should be roughly independent of Reynolds number. The range of overlap wavenumbers that connects these representations expands directly with increasing Reynolds number. It has been shown that within an overlap range of wavenumbers, denoted by $K_{1\,min}$ to $k^+_{1\,max}$, the spectrum function is a universal function $P^+(\Delta c^+)$; in other words, $P^+(\Delta c^+, k_1^+)$ becomes independent of $k_1^+$.

Moreover, it has previously been proposed, Panton and Linebarger (1974), that the convection velocity $c^+_{max}$ is a universal function for high wavenumbers, $C_{max}$ is a universal function for low wavenumbers, and the overlap region is given by Eqs. (18).

## Comparison with Experiments

The theory was tested by measurement made in the wind tunnel of the Acoustics Center at Ecole Centrale de Lyon. The tunnel, illustrated in Fig. 2 and described more fully in Robert (1993), was especially constructed to minimize acoustic contamination by upstream machinery and ambient noise.

The mean velocity profiles, shown in Fig. 3, were measured with a Pitot tube for three flow speeds: 20, 40, 60 m/s. These profiles were used to determine the parameters $u^*$, $\delta$, and $\Pi$ by the methods which are fully given by Robert (1993). The values, see Table 1, are consistent with the different laws directing the characteristics of the boundary layer at different speeds. The wake components, $\Pi$, are variable and somewhat smaller than the nominal value of 0.6. Casarella and coworkers

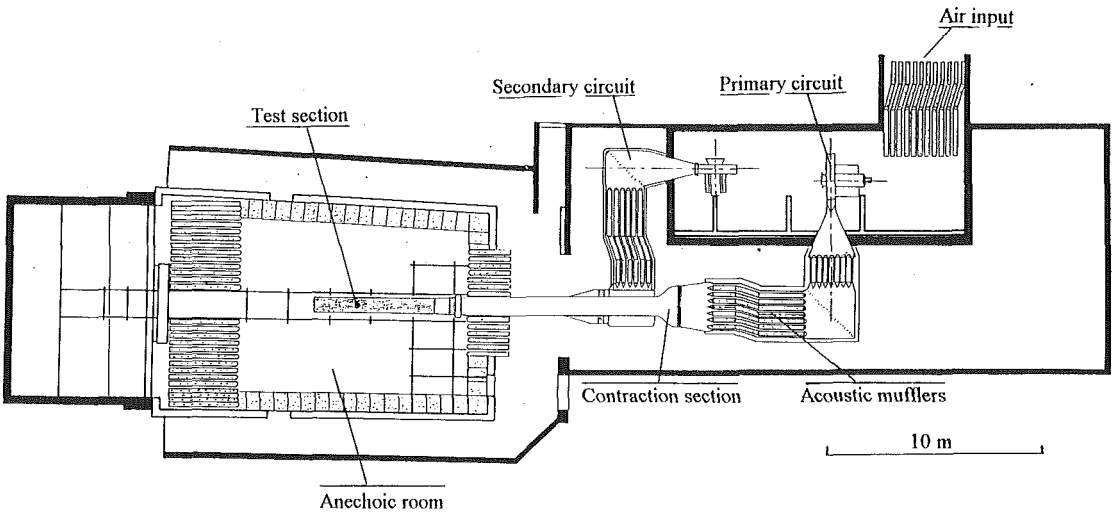


Fig. 2 The anachoic wind tunnel facility at Ecole Centrale de Lyon

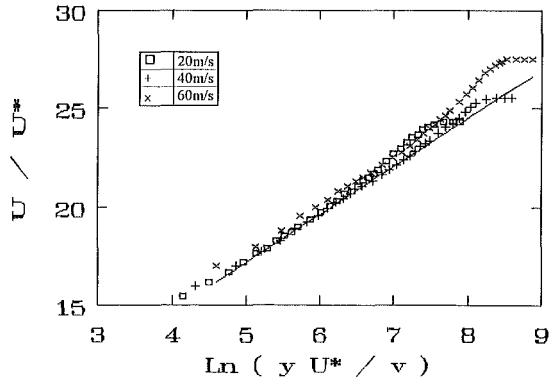


Fig. 3 Boundary layer velocity profiles. Law of the wall coordinates.

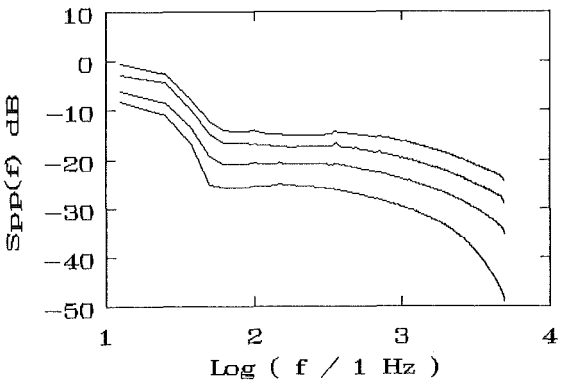


Fig. 4 Wall pressure frequency spectra in dB (ref 1 $Pa^2$/Hz) for 20, 30, 40, and 50 m/s. Note that the origin is shifted for each curve.

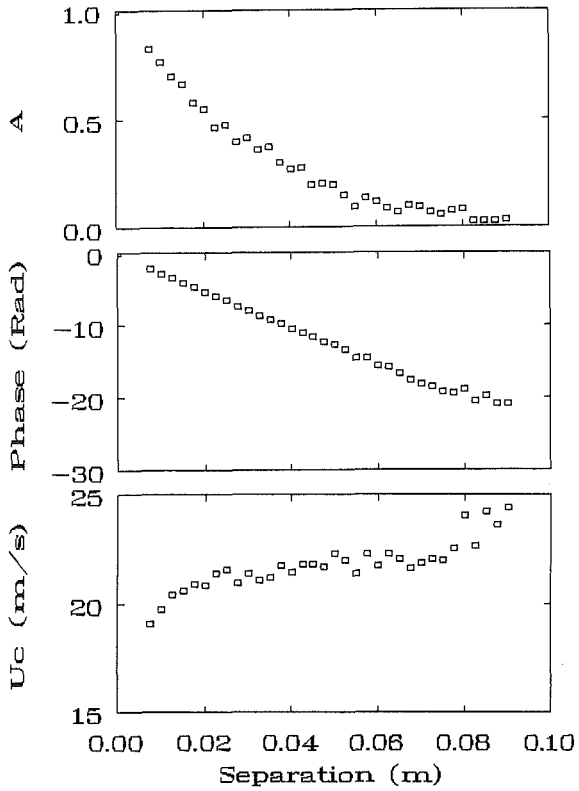


Fig. 5 Streamwise cross-spectrum of the wall pressure for $U_o = 30$ m/s and $f = 900$ Hz; (*a*) coherence function, (*b*) phase function, (*c*) convection velocity

(private communication) have noted that the method of tripping has a large and longlasting effect on this value.

The frequency spectra measurements are presented for the four velocities in Fig. 4. In this figure one can observe some strong energetic levels at very low frequencies. These levels comes from stationary acoustic waves that occur in the test section between the upstream convergent and the exit section. In what follows we will limit the displays to frequencies above 50 Hz. The spectra levels obtained in the present study are roughly 1dB lower than those of Farabee and Casarella (1991).

A more precise description of the wall-pressure field is obtained with the cross-spectrum $S_{pp}(\xi, \zeta, \omega)$. Below we discuss only the behavior with respect to $\xi$. In general, the cross-spectrum is a complex function that is often represented by the coherence function $A(\xi, \omega) = |S_{pp}(\xi, 0, \omega)|/(S_{p1}(\omega) S_{p2}(\omega))^{0.5}$ together with a phase function $\Theta(\xi, \omega)$. The coherence expresses the decreasing activity of the pressure field associated with the $\omega$ frequency when it is convected over a distance $\xi$. A (different) convection velocity is obtained from $U_c(\xi, \omega) = \omega\xi/\Theta(\xi, \omega)$. A typical example of the evolution of these three functions is shown in Fig. 5. At a given frequency, the coherence function shows a nearly exponential decrease with $\xi$ while the phase increases almost, but not quite, linearly. The departure of the phase from linearity is easier to see in the convection velocity which increases slightly with the separation.

For a given frequency the cross-spectrum $\Phi(k_1, \omega)$ was ob-

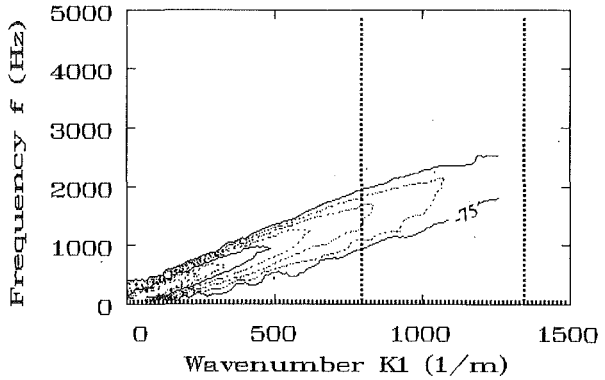


Fig. 6 Contour plot of streamwise wave number frequency spectrum of wall pressure in dB (ref 1 $Pa^2$ m/Hz) with increments of 2.5 dB for $U_o = 20$ m/s. Frequency (50 Hz) and wave number limits (1 db and 3db loss from microphone spatial sensitivity) are given by dashed line.

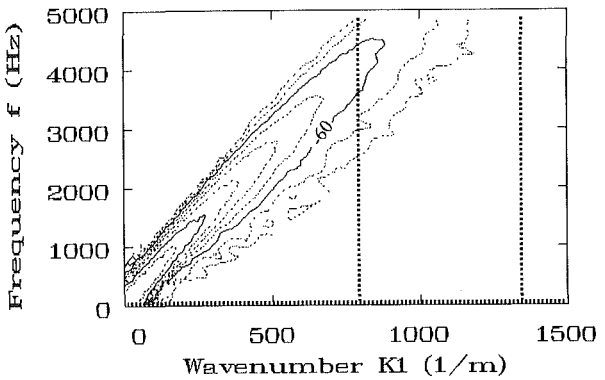


Fig. 7 Contour plot of streamwise wave number frequency spectrum of wall pressure in dB (ref 1 Pa2 m/Hz) with increments of 2.5 dB for $U_o = 20$ m/s.

tained by a fast Fourier Transform over the space variable $\xi$ of the cross-spectrum $S_{pp}(\xi, 0, \omega)$. A typical wavenumber cross-spectrum presents a principal peak that characterizes the convected nature of the wall-pressure field. The evolution of the convection peak is presented as a function of frequency for the two extreme Reynolds numbers in Figs. 6 and 7. Two types of limit lines are shown on the figures; one for the 50Hz acoustic standing waves mentioned earlier and the second corresponding to two estimates for the transducer resolution. The estimates were made considering a one db and three db loss of response for a circular diaphragm with a radius 80 percent of the microphone radius.

The increase of the flow velocity, and thus the convection velocities, manifests itself in the straightening of the convection contours towards the frequency axis. As Wills (1970) and Choi and Moin (1990) have observed, the convection ridge has a tendency to broaden when the frequency rises. This broadening is induced by the reduction of the correlation lengths at high frequencies. The ridge presents a strong asymmetry with an abrupt fall of level toward the low wavenumbers. This behavior is equally observable in the results of Willis and Choi and Moin but less so than in those of Karangelen et al. (1991). This asymmetry cannot come from the FFT process on the cross-spectrum modulus because it only acts grossly and in a symmetrical fashion on the width of the convection peak. It comes instead from the nonlinearity of the phase $\Theta$ as a function of the separation. That is to say the evolution of the convection velocity with the separation. A constant convection velocity, that is $\Theta$ a linear function, would only induce a symmetrical convection peak centered on $\omega/U_c$ in the wavenumber space.

The experimental results were reprocessed into the form $\mathbf{P}(\Delta C, K_1)$ and contour plots for wind tunnel speeds of 20,

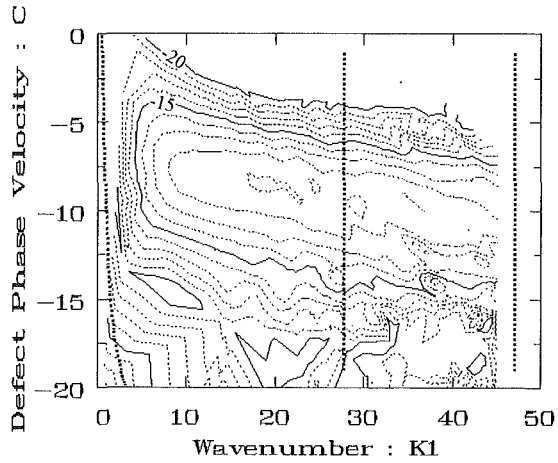


Fig. 8 Spectrum function $P(K, C)$. Level in dB (5 dB between solid lines) $U_o = 20$ m/s, $Re^* = 1908$. Frequency and wave number limits given by dashed line.

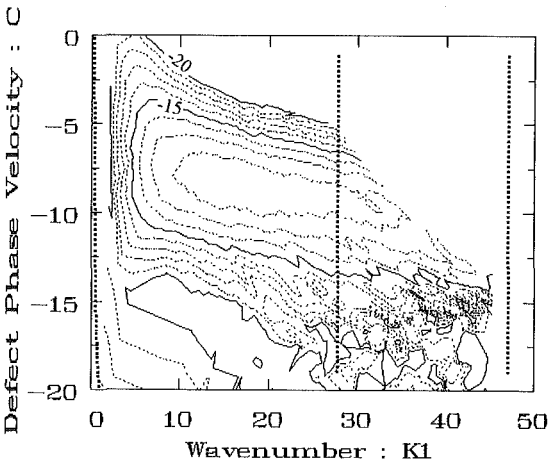


Fig. 9 Spectrum function $P(K, C)$. Level in dB (5 dB between solid lines) $U_o = 50$ m/s, $Re^* = 4400$. Frequency and wave number limits given by dashed line.

30, 40, and 50 m/s, $Re^* = 1900$ to 4500, and plotted in contour maps. The extreme cases are given in Figs. 8 and 9. Note that all of the data presented are made dimensionless by boundary layer parameters and not by the rms of the signals. The limit lines for acoustic interference and transducer resolution are again shown.

The overlap region where $\mathbf{P}(\Delta C, K_1)$ is only a function of $\Delta C$ is also evident. This is seen more accurately in Figs. 10 through 12 where cuts at constant wavenumber for the different Reynolds number are plotted. At $K_1 = 10$ the overlap region has not been reached as the peak of the curves are noticeably lower than those of the other figures. Comparison of the remaining curves with each other shows no significant difference. For reference a curve fit to the data (from $K_1 = 20$, and 30) is plotted. The equation that resulted is

$$10 \text{ Log } P = A + B\Delta C + C(\Delta C)^2 + D(\Delta C)^3 + E(\Delta C)^4 + F(\Delta C)^5 \quad (19)$$

$$A = -11.09,\ B = 0.05333,\ C = -0.3851,$$

$$D = -0.03458,\ E = 0.005006,\ F = 0.0007544$$

The free-stream speed, $C = 0$, is an effective maximum for the phase speed.

The drop-off in the spectrum at very low wavenumbers is shown in Fig. 13. Here cuts of the spectrum function are made at constant wavenumbers and the data from the two extreme Reynolds number grouped on a single graph. The similarity

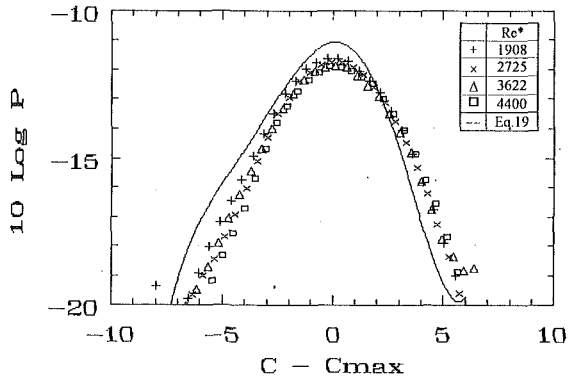


Fig. 10 Spectrum function at $K_1 = 10$ for all Re*

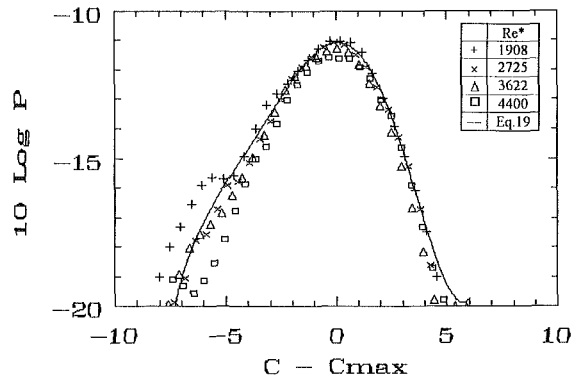


Fig. 11 Spectrum function at $K_1 = 20$ for Re*

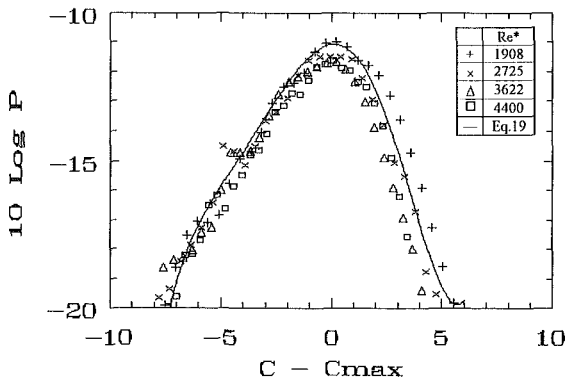


Fig. 12 Spectrum function at $K_1 = 30$ for all Re*

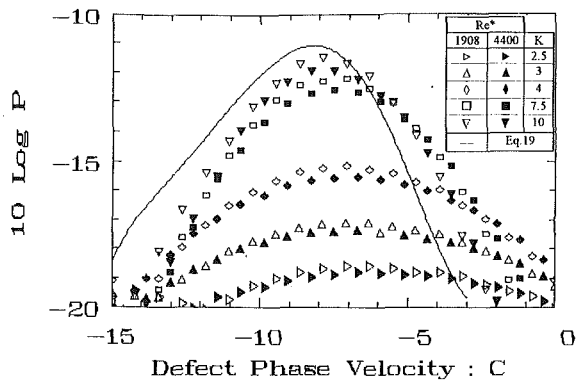


Fig. 13 Spectrum function for low wavenumbers at different $K$ for Re* = 1908 and 4400.

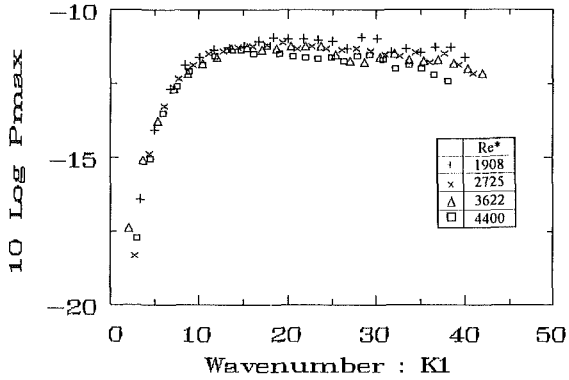


Fig. 14 Maximum of spectrum function for all Re*

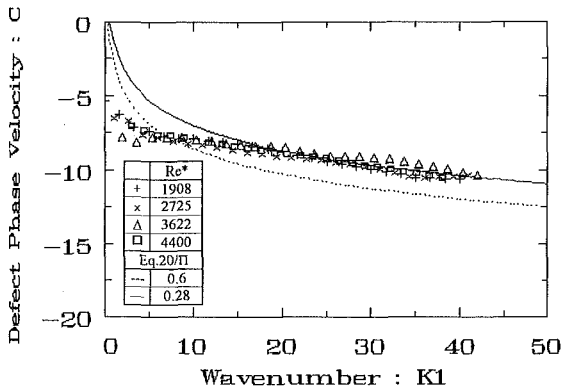


Fig. 15 Convective velocity

with Reynolds number is very good and confirms, at least for these values, that the low wavenumber spectrum is independent of Re* (see also Fig. 14). Theoretically these wavenumbers are sensitive to pressure gradient. As the wavenumber decreases the content at low phase velocities remains about the same, the peak decreases and moves slightly to higher velocities, and the content at high phase velocities broadens noticeably. For example, at a wavenumber of $K_1 = 4$ the curves rise rapidly from $C = 0$, essentially the free-stream velocity. Although the spectrum levels at low $K_1$ and high velocities are quite low the broadening is to be expected physically. It is well-known that boundary layers have potential fluctuations out to distances considerably larger than $y = \delta$. Explicit evidence of the connection between the potential fluctuations and the wall pressure has been obtained by correlating a hot wire at distances greater than $\delta$ and a wall microphone. Such data have been given by Farabee and Casarella (1991) and Panton et al. (1980).

The drop-off of the maximum values of the spectrum function is presented in Fig. 14 for all Reynolds numbers. Again the curves correlate very well. There is negligible contribution to the spectrum function (seven db down from the peak) for wavenumbers less than $K_1 = 2.5$. The value for which the level reaches a constant, 10 log $P = -11$, marks the lower end of the overlap region and is about $K_{min} = 14$ (the corresponding wavelength is $\Lambda_{min} = 0.45\ \delta$). This is a little higher than the value of $K_{min} = 6$ chosen by Karangelen et al. (1991). The data show a slight downward trend at higher wavenumbers, however, the accuracy of the calculation and scatter of the results are becoming larger so this is probably not an actual physical trend.

The convective velocities $C_{max}$ $(K_1)$ for all Reynolds numbers are given on Fig. 15. The different Reynolds numbers correlate very well in terms of these variables, especially when one notes that blunt contours give difficulty in obtaining $C_{max}$ when $K_1$

is low. For the overlap region of wavenumbers the theoretical relation obtained by rearranging Eq. (8) is

$$C_{\max} = -\frac{1}{\kappa} \ln (K_1) - \frac{2\Pi}{\kappa} \tag{20}$$

This equation is shown on Fig. 15 for two values of the wave strength constant Π, 0.28, and 0.6. The values 0.28 is a fit to the data of the figure while 0.6 is the number most often given as typical of zero pressure gradient boundary layers. For comparison recall (Table 1) that the tested velocity profiles yielded values of 0.09 to 0.27. The fact that the detailed nature of the outer flow is very important to the low wavenumber spectrum was emphasized by Farabee and Casarella (1991) and we concur on this point.

The deviation from the overlap law, a wake law if you like, occurs toward lower values of the velocity. This is in agreement with the results presented recently in Karangelen et al. (1991) but in the opposite direction from the older data of Wills (1970). Also noted from Figs. 8 and 9 that the contours are very broad and blunt in this region. The results do not approach the free-stream as $K_1 \rightarrow 0$. This means that there are always very low wavenumber components within the boundary layer traveling at low velocities that are as important as the low wavenumber potential motions in the free-stream.

Because of transducer spatial resolution and the minimum spacing between microphones, the data do not extend to high enough wavenumbers to see the drop off in the spectrum function from viscous effects. We can guess that this begins for wavelengths about twice the buffer layer thickness. $\lambda^+ = 100$ or $k^+_{\max} = k_1 \nu / u^*]_{\max} = 0.0625$. For a Reynolds number of $\mathrm{Re}^* = 1000$ this is equivalent to $K_1 = 62$, a value beyond the range of the measurements.

## Conclusions

The wall pressure fluctuations under a turbulent wall layer have been discussed in terms of a spectrum function with streamwise wavenumber $k_1$ and phase velocity $c$ as variables. The conversion of the frequency into a wavenumber and phase velocity, $\omega = k_1 c$, allows a theory that postulates an overlap range of wavenumbers where both inner and outer variables are valid. The most important theoretical conclusion is that the spectrum in the overlap region is of the form $\Phi^+(k_1^+, \omega^+ = c^+ k_1^+) = (k_1^+)^{-2} P^+(\Delta c^+)$ in inner variables or $\Sigma = K_1^{-2} \mathbf{P}(\Delta C)$ in outer variables. Here $\Delta c^+ = \Delta C$ is the difference between the phase speed and the speed for which the maximum of $\Phi^+$ occurs. Experimental data validate the overlap form and show that $\mathbf{P}(\Delta C) = P^+(\Delta c^+)$ is an asymmetric function. This representation is valid from $k_1 \delta]_{\min} = 14$ to some value of $k_1 \nu / u^*]_{\max}$ (about 0.0625?) which is too high for the experiments to resolve. The overlap convective law for $c_{\max}$ from previous theory was also verified.

For values of the wavenumber lower than $K_{\min}$ the spectrum function $\mathbf{P}(K_1, C)$ falls rapidly and is seven db down from the peak when the wavenumber is $K_1 = 2.5$. Also at low wavenumbers the spectrum funciton broadens and shows a small contribution from the potential motions as $c \rightarrow U_\infty$. At least in the range of experiments covered by the experiments, $\mathrm{Re}^* = 1000$ to 4,500 the low wavenumber convective events scale are independent of Reynolds number when scaled on outer variables including a defect phase velocity.


## Acknowledgment

The first author expresses appreciation to the Rhone-Alpe Region of France for a Bourse d'Accueil and to the University of Texas for a Research Assignment.

This experimental program was sponsored by the Direction des Recherches et Etutes Techniques.


## References


Bakewell, H. P., 1968, "Turbulent Wall Pressure Fluctuations on a Body of Revolution," *Journal of Acoustical Society of America*, Vol. 43, No. 6, pp. 1358-1363.

Benarrous, E., 1979, "Contribution à l'étude des fluctuations de pression pariétale sous une couche limite turbulente," Thèse No. 897, Univ. Claude Bernard, Lyon, France.

Blake, W. K., 1970, "Turbulent Boundary-Layer Wall-Pressure Fluctuations on Smooth and Rough Walls," *Journal of Fluid Mechanics*, Vol. 44, Part 4, pp. 637-660.

Blake, W. K., and Chase, D. M., 1971, "Wavenumber-Frequency Spectra of Turbulent Boundary Layer Pressure Measured by Microphone Arrays," *Journal of Acoustical Society of America*, Vol. 49, No. 3, Part 2.

Bull, M. K., 1967, "Wall-Pressure Fluctuations Associated With Subsonic Turbulent Boundary Layer Flow," *Journal of Fluid Mechanics*, Vol. 28, Part 4, pp. 719-754.

Carey, G. F., Chlupsa, J. E., and Schloemer, H. H., "Acoustic Turbulent Water-Flow Tunnel," *Journal of Acoustical Society of America*, Vol. 41, No. 2, 1967, pp. 373-379.

Choi, H., and Moin, P., 1990, "On the Space-Time Characteristics of Wall-Pressure Fluctuations," *The Physics of Fluids*, Vol A2 (8), Aug. pp. 1450-1460.

Dinkelacker, A., Hessel, M., Meier, G.E.A., and Schewe G., 1977, "Investigation of Pressure Fluctuations Beneath a Turbulent Boundary Layer by Means of an Optical Method," *The Physics of Fluids*, Vol. 20, No. 10, Part II, Oct.

Farabee, T. M., and Geib, F. E. Jr., 1976, "Measurement of Boundary Layer Pressure Fields with an Array of Pressure Transducers in a Subsonic Flow," Naval Ship Research and Development Center, Ship Acoustics Department Research and Development Report 76-0031.

Farabee, T. M., and Casarella, M. J., 1991, "Spectral Features of Wall Pressure Fluctuations Beneath Turbulent Boundary Layers," *Physics of Fluids*, Vol. 3, pp. 2410-2420.

Karangelen, C. C., Casarella, M. J., and Farabee, T. M., 1991b, "Wavenumber-Frequency Spectra of Turbulent Wall Pressure Fluctuations," ASME Winter Annual Meeting, NCA-Vol. 11/FED-Vol. 130, pp. 37-44, submitted to ASME *Journal of Vibrations and Acoustics*.

Manoha, E., 1991, "Wall Pressure Wavenumber-Frequency Spectrum Beneath a Turbulent Boundary Layer Measured With Transducer Arrays Calibrated With an Acoustical Method," ASME Winter Annual Meeting, NCA-Vol. 11/FED-Vol. 130, pp. 21-35.

Panton, R. L., and Linebarger, J. H., 1974, "Wall Pressure Spectra Calculations for Equilibrium Boundary Layers," *Journal of Fluid Mechanics*, Vol. 65, pp. 261-287.

Panton, R. L., Goldman, A. L., Lowery, R. L., and Reischman, M. M., 1980, "Low-Frequency Pressure Fluctuations in Axisymmetric Turbulent Boundary Layers," *Journal of Fluid Mechanics*, Vol. 97, Part 2, pp. 299-319.

Panton, R. L., 1990, "Inner-Outer Structure of Wall-Pressure Correlation Function," Kline and Afgan, *Near Wall Turbulence*, pp. 381-396.

Roberts, Gilles, 1993, "The Wall-Pressure Spectrum Under a Turbulent Boundary Layer: Part 1, Experiments," ASME Winter Annual Meeting, FED-Vol. 155, pp. 37-43.

Wilczynski, V., and Casarella, M. J., 1993, "The Relationship Between Organized Structures and Wall Pressure Fluctuations," ASME Winter Annual Meeting, NCA-Vol. 11/FED-Vol. 150, pp. 59.

Willmarth, W. W., 1975, "Pressure Fluctuations Beneath Turbulent Boundary Layers," *Annual Review of Fluid Mechanics*, Vol. 7, pp. 13-38.

Willmarth, W. W., and Yang, C. S. 1970, "Wall-Pressure Fluctuations Beneath Turbulent Boundary Layers on a Flat Plate and a Cylinder," *Journal of Fluid Mechanics*, Vol. 11, Part 1, pp. 47-80.

Wills, J. A. B., 1970, "Measurements of the Wave-Number/Phase Velocity Spectrum of Wall Pressure Beneath a Turbulent Boundary Layer," *Journal of Fluid Mechanics*, Vol. 45, Part 1, pp. 65-90.

# Experimental Determination of Transition to Turbulence in a Rectangular Channel With Eddy Promoters

**J. S. Kapat**
Department of Mechanical Engineering,
Clemson University,
Clemson, SC 29634-0921

**J. Ratnathicam**
OECO Corporation,
Milwaukee, OR

**B. B. Mikić**
Department of Mechanical Engineering,
Massachusetts Institute of Technology,
Cambridge, MA

*We report on laminar-to-turbulent transition in a rectangular channel in the presence of periodically placed cylindrical eddy promoters. Transition is identified through the analysis of power spectral density (PSD) of velocity fluctuations. Placement of the eddy promoters in the channel, depending on the geometric configuration, can significantly reduce the value of Reynolds number at transition. The critical Reynolds number (based on the average velocity and the channel height) ranges from 1500 (for an unobstructed channel) to about 400 (for the most unstable configuration we have deployed). For all the configurations tested, demarcation of transition can be correlated with the expression:* $Re_\tau \equiv \sqrt{\bar{\tau}_{w,av}/\rho}\, H/2/\nu = 44 \sim 51$, *where* $\bar{\tau}_{w,av}$ *is the spatially averaged value of mean wall shear stress and H is the channel height.*

## 1 Introduction

Heat transfer enhancement plays an important role in the performance of many engineering systems; heat exchangers, gas turbine blades, and electronic components are few such examples. For almost all of these applications, the task of the design engineer is to optimize the rate of heat transfer for given systems parameters (or equivalently, to minimize cost of operation for a given rate of heat removal).

Studies have shown that the critical Reynolds number associated with transition to turbulence is lower for the geometries modified for transport enhancement (e.g., with eddy promoters or wall grooves) than for the equivalent system without any modification (Thomas, 1966; Kozlu, 1989; Greiner et al., 1990). Although the "early" transition is associated with very effective enhancement of heat transfer, presently, there is no developed procedure to predict the transition for a geometry of this type, nor any accepted qualitative explanation for the observed "premature" transition. These preliminary results suggest that, in view of the role of this type of geometries in heat transfer augmentation, we might significantly benefit from a systematic investigation of laminar-to-turbulent transition in these flow configurations.

Information concerning transition to turbulence is important for various other reasons as well. First, laminar-to-turbulent transition is one of the still unresolved problems. Second, turbulence plays a significant role in many engineering applications. However we still do not have any general criterion that correlates transition in all flow configurations: the value of critical Reynolds number is system specific (e.g., Eckert and Irvine, 1956; Obot, 1988) and is also frequently dependent on initial perturbation (e.g., Joseph, 1976).

Laminar flow characteristics are largely determined by the boundary conditions, the nature of the driving forces, the extent of ambient noise and flow configuration. On the other hand, there are several features (e.g., dynamics of the smallest scales, energy cascading, Reynolds transport) which are universal characteristics of any turbulent flow. This suggests that perhaps it is the internal dynamics (and not the evolution) of turbulence which contributes not only to the universal nature of a turbulent flow, but may prove useful in forming a general criterion for transition (Mikić, 1990), which would be based on the condition for maintenance of turbulence.

The central argument in the proposed approach is this: in wall bounded flows, the system capacity to sustain turbulence is determined by the system's ability to supply high vorticity fluid from the wall region (where vorticity is generated) to the core. Or in the mechanistic terms, for turbulence to be sustained, the time required for convection of vorticity from the wall region to the core must be smaller than the time within which the transported vorticity would be dissipated. Since this supply of vorticity occurs via perturbation motions and since these motions are correlated with friction velocity, the Reynolds number based on friction velocity is a good candidate for demarcation of cessation of turbulence (Mikić et al., 1992).

The primary objective of the present work is to provide a comprehensive set of experimental data on transition and compare the findings with the proposed demarcation criterion.

## 2 Experimental Procedure

Experiments were performed with air as the fluid. The air temperature was controlled to within ±2°C. Different flow

Contributed by the Fluids Engineering Division for publication in the JOURNAL OF FLUIDS ENGINEERING. Manuscript received by the Fluids Engineering Division July 28, 1993; revised manuscript received November 19, 1993. Associate Technical Editor: W. S. Saric.

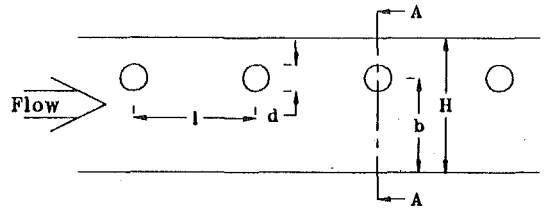


a) Side view of a rectangular channel with eddy promoters

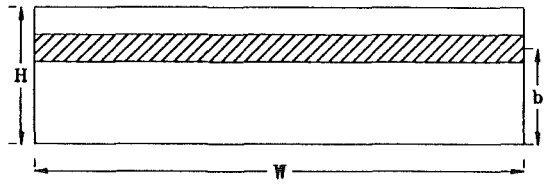


b) Cross-sectional view at A–A

Fig. 1 A schematic view of the flow configuration with eddy promoters

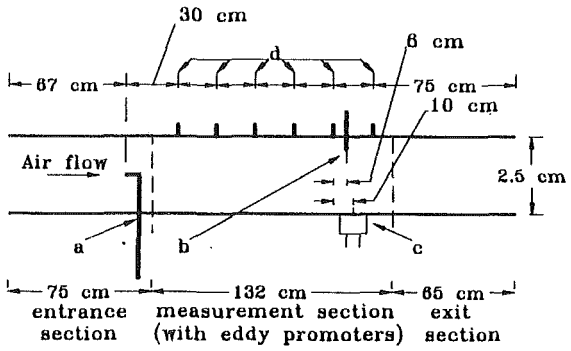


a. Pitot-static probe
b. hot-wire anemometer
c. shear probe
d. 6 pressure taps (at 20 cm interval)

Fig. 2 Layout of the test section

**Table 1 Parameters in different flow configuration**

| Name | $l/H$ | $d/H$ | $W/H$ |
|---|---|---|---|
| 825C | 7.76 | 0.196 | 8.63 |
| 425C | 3.88 | 0.196 | 8.63 |
| 225C | 1.94 | 0.196 | 8.63 |
| 125C | 0.97 | 0.196 | 8.63 |
| 835C | 7.76 | 0.309 | 8.63 |
| 435C | 3.88 | 0.309 | 8.63 |
| Plain | | | 8.91 |

control devices (e.g., screens, honeycombs, diverging-converging sections) were deployed to straighten the flow and break large eddies before air entered the test section. The fluctuation intensity at the entrance to the test section was less than 5 percent. A more detailed description of the wind tunnel has been reported by Kapat (1991).

A schematic of the flow geometry is shown in Fig. 1. A rectangular test section with aspect ratio ($W/H$) of 8.91 (with height $H=0.02568$ m) was used. Cylindrical rods, with diameter $d$ and placed perpendicular to the flow, were used as eddy promoters. In all the experiments reported here, the cylinders were placed in the midplane such that $b/H=0.5$.

The configuration of the unobstructed channel and six different eddy promoter configurations were tested. The values of different flow parameters for these seven cases are tabulated in the Table 1.

The layout of the whole test section is shown in Fig. 2. The test section was made of three segments. A Pitot tube and a thermocouple were inserted through the bottom surface of the 75 cm-long first part that did not contain any eddy promoters. The pitot tube was traversed to measure the velocity profile at a fixed location. The average velocity ($V_{av}$) obtained from this profile was used in all of the subsequent Reynolds number calculation. However, because of the finite aspect ratio, $V_{av}$ was not the same as the true average velocity averaged over the whole cross-section: the former was at most 6.99 percent higher than the later.

The eddy promoters, a hotwire and several static wall pressure taps were placed in the 132 cm-long middle segment. The pressure taps were mounted along the center of the test section at equal distances from the side walls. The hotwire was located at a point 4 cm from the centerline. The purpose of the 65 cm-long last portion of the test section was to isolate the middle segment of the test section from the exit conditions.

The separation between consecutive static pressure taps at the wall were integral multiples of the geometric periodicity in cylinder deployment for all of the configurations tested. This ensured that if the drop of pressure over two consecutive intervals between pressure taps were found to be "close enough" to the pressure drop over the adjacent upstream interval, then the flow can be assumed to be fully developed (Patankar et al., 1977). In all the tests, the difference between pressure drops over consecutive intervals were less than 3 percent around the measurement location. All differential pressure measurements were performed with an MKS-398 Baratron pressure transducer equipped with a one torr sensing head.

The nature of velocity fluctuations in the flow field was monitored with the hot wire anemometer probe (TSI model 1211-T1.5) in conjunction with a constant temperature bridge, TSI model 1053. The hot wire was oriented such that the streamwise component of velocity was normal to the wire and the spanwise component was binormal to the wire. The fluctuating voltage signal from the anemometer bridge output was fed into a single channel spectrum analyzer, model Genrad 2512A, to determine the oscillogram as well as the frequency spectrum of the signal.

Transition was determined through monitoring of the fluctuating voltage that was applied to the hot wire in the constant temperature mode of operation. For fluctuation intensity of upto 25 percent, the voltage fluctuations were proportional to the velocity fluctuations within 10 percent error limit (Hinze, 1975). However, a strict proportionality was not needed in this study since the qualitative nature of PSD (power spectral density) of the voltage fluctuations was all that was used to demarcate transition. The PSD was also used to determine the major frequencies, if any, present in the flow.

The local mean wall shear stress was measured with a sublayer-fence-type shear probe (Hanratty and Campbell, 1983) mounted at a fixed location on the bottom wall. All of the cylinders were mounted on a movable rail to allow the measurement of the streamwise profile of the wall shear stress with a single fixed probe. At any relative position of the eddy promoters, there were a minimum of six cylinders upstream of the shear probe. The flow was found to become fully developed after only three of four cylinders; this was in agreement with Sparrow and Tao (1983). From the measured profile of wall shear stress, the spatially averaged value of the mean wall shear stress ($\bar{\tau}_{w,av}$) was calculated.

For each different flow setting for different geometric configurations, the Reynolds number was calculated $\mathrm{Re}=V_{av}H/\nu$. Besides Re, a Reynolds number based on "friction velocity" was also calculated; this number was defined as $\mathrm{Re}_\tau=\sqrt{\bar{\tau}_{w,av}/\rho}\,H/2/\nu$. This number is hereafter referred to as shear Reynolds number.

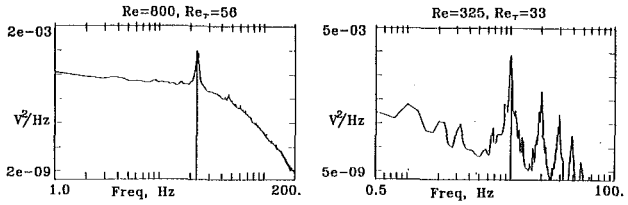


Fig. 3 Spectra of velocity fluctuations for 225C configuration

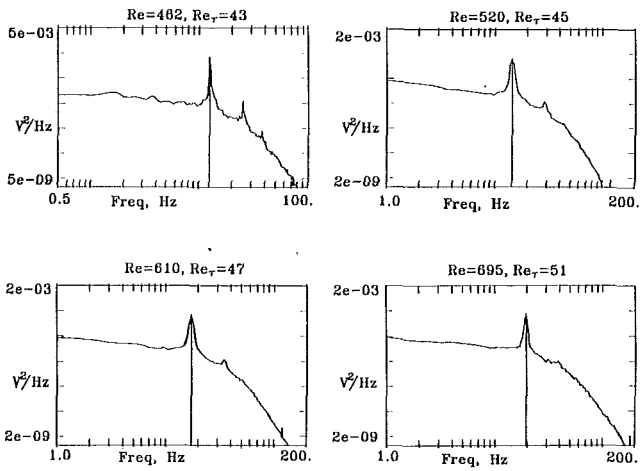


Fig. 4 Spectra of velocity fluctuations for 225C configuration

## 3 Experimental Uncertainties

An uncertainty analysis (Figliola and Beasley, 1991) indicated that the 95 percent confidence interval for Re was ±9 percent of the mean; the same for $Re_\tau$ was found to be ±8 percent. The spectral resolution in all PSD-graphs was either 0.5 Hz or 1.0 Hz. The precision error in the calculation of the power spectral density caused the 95 percent confidence interval to be ±8.5 percent of the mean; the bias error in that calculation is estimated to be −3.3 percent of the mean (Bendat and Piersol, 1986).

## 4 Results and Discussion

The unobstructed channel configuration was tested first. The friction factor was measured for different flow rates and there was a good agreement with the data available in the literature. The wall shear stress was then calculated from the experimentally observed fully developed pressure gradient. This calculated shear stress was used to calibrate the shear probe.

In our system, in the absence of any (intentionally induced) perturbations, as flow rate was gradually increased in the unobstructed channel, a critical Reynolds number of 2250 was obtained through the study of oscilloscope trace of anemometer voltage as well as through the study of PSD of ac-coupled signal from the anemometer bridge. As long as the flow remained laminar or turbulent, the qualitative nature of the spectra did not change. The PSD for the laminar case corresponded to the noise level in the measurement system, whereas for a turbulent flow, PSD had the broadband appearance characteristic of a continuous cascading of eddies in a turbulent flow (Bradshaw, 1971; Ahlers and Behringer, 1978). The oscilloscope trace changed from a steady signal to a fluctuating signal at the transition.

The critical Reynolds number was found to depend on disturbances created at the entry to the test section. The lowest observed value for the critical Reynolds number in an unobstructed channel was 1500 which agreed with previously reported results (Shah and Bhatti, 1987). When transition was approached from the turbulent side, the observed critical Reynolds number was found to be 1500, irrespective of the disturbances created at the entry to the test section.

In the presence of eddy promoters, no hysteresis had been noticed: the critical Reynolds number was not found to depend on whether transition was approached from the laminar regime or from the turbulent regime. However, to be consistent with the procedure adopted for the unobstructed channel, here also, all the flow parameters at transition were obtained by decreasing the flow rate from a turbulent one.

In the presence of the eddy promoters, oscillograms of the voltage (or velocity) fluctuations could not be used directly to separate the two flow regimes since for these cases even in the laminar regime one would observe fluctuations at multiple frequencies which correspond to TS wave frequency and/or primary eddying frequency and higher harmonics. A qualitative study of PSD, however, indicated that the nature of the spectrum changed significantly as the flow rate was reduced past the point of transition. Figure 3 shows spectra for two different flow rates in 225C configuration. The first of these two spectra corresponds to Re = 800. Although there is a peak in the spectrum at the primary vortex shedding frequency, the spectrum has a broadband appearance, which indicates existence of energy cascading characteristic of a turbulent flow. On the other hand, the second spectrum (Re = 325) contains few discrete peaks, corresponding to the primary vortex shedding frequency and its harmonics, indicative of a laminar flow. The spectra for several intermediate Reynolds numbers were also examined. According to those spectra (Fig. 4), the broadband appearance of the spectrum gradually disappeared and higher harmonics of the primary vortex shedding frequency gradually appeared as the flow rate was reduced past the Reynolds number range of 610–695. For this reason, transition in 225C configuration was said to occur over that range of settings. For all other configurations, ranges of Reynolds number over which transition occurred were similarly obtained.

Use of a range, rather than a single value, to demarcate transition is perhaps unconventional: nevertheless, as was already commented by Bradshaw (1978), "it is not useful to agonize about the exact point at which the motion can properly be called 'turbulence'."

A single value of the critical Reynolds number was also calculated by an independent second approach. In this approach, the modified Reynolds number ($Re_\tau$) was plotted as a function of Reynolds number (Re). Two best-fit curves of the form $Re_\tau = aRe^b$ were drawn: one through the points that correspond to the laminar regime and the others that correspond to the turbulent regime. The point of intersection of those two curves gave the critical values for Reynolds number and modified Reynolds number. The curves for the flow configuration 425C is shown in Fig. 5. The figure also shows good agreement between experiment and numerical simulation for laminar flows. The numerical simulation was done using the spectral element code Nekton. The details about numerical simulation can be found in Karniadakis et al. (1988) and Kapat (1991).

The relocation of the hot wire to different points in the flow relative to the cylinders did not produce any qualitatively different PSD for the same flow rates and geometry: the conclusion about the critical range of Reynolds number was not found to depend on the hot wire location.

The results from all the configurations tested is reported in Table 2. We find that the critical Reynolds number at the transition was reduced by more than a factor of three from 1500 to 400, as we changed the geometry from the plain channel to the 435C configuration. On the other hand, the shear Reynolds number ($Re_\tau$) remained almost invariant within the bounds of experimental accuracy.

The primary role of the eddy promoters in the laminar regime (and also the only role if the promoters are of sufficiently small

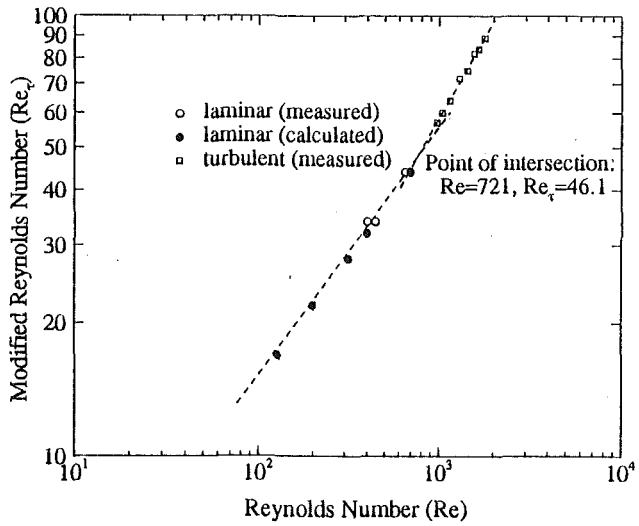


Fig. 5 Calculation of critical Reynolds number for 425C configuration

**Table 2 Values of shear and classical Reynolds numbers at transition**

| Geometry | Re | $Re_\tau$ |
|---|---|---|
| A. Plain Channel | 1465–1584 | 49–52 |
| B. 825C | 880–988 | 49–53 |
| C. 425C | 698–815 | 46–51 |
| D. 225C | 610–695 | 47–51 |
| E. 125C | 574–615 | 44–48 |
| F. 835C | 560–668 | 43–49 |
| G. 435C | 380–430 | 41–46 |

cross-section or far apart) is to destabilize the flow by exciting the Tollmien-Schlichting (TS) waves (Karniadakis et al., 1988). This destabilization increases momentum transfer, with corresponding increase in the value of wall shear stress. As the separation between the cylinders is decreased, or their diameter is increased, the cylinders cannot be viewed as mere perturbations to the mean flow: for those cases vorticity generation at the channel-walls next to the cylinders and on the cylinder surfaces becomes a significant fraction of the total vorticity generation in the system. For the cases of small separation and/or large diameter, one would expect a departure from the trend of the cases with large separation and small diameter, since $Re_\tau$ does not take into account the shear stress (and vorticity generation) at the cylinder surface. In accord with the above expectation, the values of $Re_\tau$ at transition, for the configurations 125C and 435C (with dense spacing and larger $d$, respectively), are somewhat lower than the other cases in the series.

## 5 Conclusion

In a number of transport enhancement schemes that use flow destabilization to augment transport, transition has been observed at a lower Reynolds number in the presence of flow destabilizing elements. The phenomenon of the "early" transition has neither been systematically investigated, nor has there been any suggestion why it occurs. The present work is the first systematic effort to study this phenomenon of "early" transition.

Experiments were carried out in a rectangular channel containing periodically placed cylindrical eddy promoters. Experimental results confirmed the earlier observation: the presence of the eddy promoters induces transition at a much lower Reynolds number values than in the unobstructed channel. The critical Reynolds number decreases, by more than a factor of three, from 1500 for plain channel to about 400. For all the cases in our investigation, transition can be correlated with the following expression based on shear Reynolds number,

$$\mathrm{Re}_\tau = \sqrt{\frac{\bar{\tau}_{w,av}}{\rho}}\,\frac{H/2}{\nu} = 44 \sim 51. \qquad (1)$$

## References


Ahlers, G., and Behringer, R. P., 1978, "The Rayleigh-Bénard Instability and the Evolution of Turbulence," *Progress of Theoretical Physics, Supplement*, No. 64, pp. 186–201.

Bendat, J. S., and Piersol, A. G., 1986, *Random Data*, Wiley, New York, pp. 278–286.

Bradshaw, P., 1971, *An Introduction to Turbulence and its Measurements*, Pergamon Press, New York, p. 32.

Bradshaw, P., 1978, "Introduction," *Turbulence*, P. Bradshaw, ed., Springer-Verlag, New York, p. 12.

Figliola, R. S., and Beasley, D. E., 1991, *Theory and Design for Mechanical Measurements*, Wiley, New York, ch. 5.

Eckert, E. R. G., and Irvine, Jr., T. F., 1956, "Flow in Corners of Passages With Noncircular Cross Sections," *Trans. ASME*, pp. 709–718.

Greiner, M., Chen, R. F., and Wirtz, R. A., 1990, "Heat Transfer Augmentation Through Wall-Shape-Induced Flow Destabilization," ASME Paper 90-F-1468, ASME, New York.

Hanratty, T. J., and Campbell, J. A., 1983, "Measurement of Wall Shear Stress," *Fluid Mechanics Measurements*, R. J. Goldstein, ed., Hemisphere Publishing, New York, pp. 571–572.

Hinze, J. O., 1975, *Turbulence*, McGraw-Hill, New York, pp. 85–112.

Joseph, D. D., 1976, *Stability of Fluid Motions*, Springer-Verlag, New York, pp. 8–10.

Karniadakis, G. E., Mikić, B. B., and Patera, A. T., 1988, "Minimum Dissipation Transport Enhancement by Flow Destabilization," *Journal of Fluid Mechanics*, Vol. 192, pp. 365–391.

Kapat, J. S., 1991, "Transition to Turbulence in Rectangular Channels with Eddy Promoters: Implications to Heat Transfer Augmentation," ScD thesis, MIT.

Kozlu, H., 1989, "Experimental Investigation of Optimal Heat Removal From a Surface," PhD thesis, MIT.

Mikić, B. B., 1988, "On Destabilization of Shear Flows: Concept of Admissible System Perturbations," *International Communications in Heat and Mass Transfer*, Vol. 15, No. 6, pp. 799–811.

Mikić, B. B., 1990, "Turbulent Transition," *Some Unanswered Questions in Fluid Mechanics*, L. M. Trefethen and R. L. Panton, eds., *Applied Mechanics Reviews*, Vol. 43, pp. 156–157.

Mikić, B. B., Kapat, J. S., and Ratnathicam, J., 1992, "Transition to Turbulence in Systems with Eddy Promoters: Implication for Question of Turbulence," *Physics of Fluids A: Fluid Dynamics*, Vol. 4, No. 8, pp. 1854–1855.

Obot, N. T., 1988, "Determination of Incompressible Flow Friction in Smooth Circular and Noncircular Passages: A Generalized Approach Including Validation of the Nearly Century Old Hydraulic Diameter Concept," ASME Paper 88-WA/FE-1, ASME, New York.

Patankar, S. V., Liu, C. H., and Sparrow, E. M., 1977, "Fully Developed Flow and Heat Transfer in Ducts Having Streamwise Periodic Variations of Cross Sectional Area," ASME *Journal of Heat Transfer*, Vol. 99, No. 2, pp. 180–186.

Shah, R. K., and Bhatti, M. S., 1987, "Laminar Convective Heat Transfer in Ducts," *Handbook of Single-Phase Convective Heat Transfer*, S. Kakaç et al., ed., Wiley, New York.

Sparrow, E. M., and Tao, W. Q., 1983, "Enhanced Heat Transfer in a Rectangular Duct with Streamwise-Periodic Disturbances at One Principal Wall," ASME *Journal of Heat Transfer*, Vol. 105, No. 4, pp. 851–861.

Thomas, D. G., 1966, "Forced Convection Mass Transfer: Part III. Increased Mass Transfer from a Flat Plate Caused by the Wake from Cylinders Located Near the Edge of the Boundary Layer," *AIChE Journal*, Vol. 6, No. 4, pp. 124–130.

# Friction Factor for Flow in Rectangular Ducts With One Side Rib-Roughened

B. Youn

C. Yuen

A. F. Mills

Department of Mechanical, Aerospace & Nuclear Engineering, University of California, Los Angeles, CA 90024

*Numerical simulations of incompressible turbulent flow through rectangular ducts with one side rib-roughened were performed to determine pressure drop. The "PHOENICS" software package was used for the computations, which required provision of a wall function for transverse rib-roughened surfaces. The present study was conducted in the range of $10^5 \le$ Reynolds number $\le 10^7$, $0.01 \le$ rib height to hydraulic diameter ratio $\le 0.04$, $10 \le$ pitch to rib height ratio $\le 40$. Using the numerical results, friction factor charts for various aspect ratios were generated. The numerical results agreed well with experimental data that was obtained for $10^5 <$ Reynolds number $< 2 \times 10^5$. In addition, a scheme for predicting friction factor using existing correlations for smooth and rough walls was developed.*

## Introduction

Considerable research has been directed to the enhancement of heat transfer in heat exchangers through the use of artificially roughened surfaces. However, there is the concomitant increase in pressure drop which can result in an unacceptable increase in required pumping power. Thus the engineer requires friction factor data for candidate enhanced surfaces.

Our primary concern is the design of active cooling system for hypersonic aircraft (NASP). Hypersonic aircraft surfaces are exposed to severe heat fluxes due to aerodynamic heating and fuel combustion. Active cooling is a promising candidate for this purpose, where cryogenic hydrogen fuel is circulated through a cooling panel underneath the aircraft skin to keep temperatures under the material limit. It may be beneficial to selectively insert wall roughness only in areas exposed to intensive heat flux to minimize pressure drop. The present work is concerned with a single duct as shown in Fig. 1, where transverse ribs are inserted on the heated side only. The duct size can be specified by width $W$ and height $H$ and the roughness element can be described by rib height $h_r$ and spacing $p$.

The governing conservation equations were numerically solved to obtain friction data using the software package PHOENICS (Parabolic Hyperbolic Or Elliptic Numerical Integration Code Series) developed by CHAM (Concentration Heat And Momentum) Ltd., London, England. This package uses the finite volume method described in Patankar (1980). The key assumptions involved in the present work are:

1. The flow is parabolic in downstream direction—axial diffusion is negligible.
2. The rib width is small relative to the rib spacing and its effect is negligible.

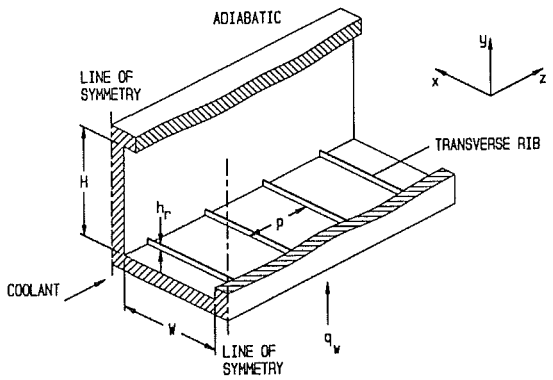


**Fig. 1 Geometry of a single duct of a cooling panel with one side rib-roughened**

3. The $k$-$\epsilon$ turbulence model is adequate.
4. The effect of wall roughness can be adequately accounted for by using an appropriate empirical wall function.

In addition to the numerical study, experimental measurements were made for a limited Reynolds number range, in order to validate the numerical method.

## Governing Equations

The governing equations for steady state turbulent flow through the rectangular duct shown in Fig. 2 with axial diffusion, body force and bulk viscosity effects neglected are (all variables are time-averaged quantities):

Mass:

$$\frac{\partial v_x}{\partial x} + \frac{\partial v_y}{\partial y} + \frac{\partial v_z}{\partial z} = 0 \qquad (1)$$

Contributed by the Fluids Engineering Division for publication in the JOURNAL OF FLUIDS ENGINEERING. Manuscript received by the Fluids Engineering Division July 2, 1993; revised manuscript received December 23, 1993. Associate Technical Editor: T. T. Huang.

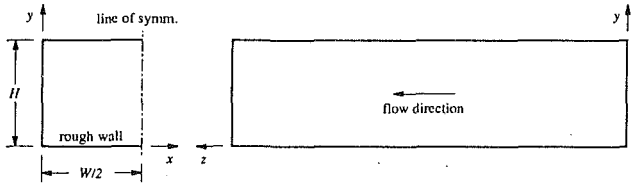


**Fig. 2 Computation domain and coordinate system for rectangular duct**

$x$-momentum:

$$\rho\left[\frac{\partial(v_x^2)}{\partial x}+\frac{\partial(v_yv_x)}{\partial y}+\frac{\partial(v_zv_x)}{\partial z}\right]-\frac{\partial}{\partial x}\left[(\mu_\ell+\mu_t)\frac{\partial v_x}{\partial x}\right]-\frac{\partial}{\partial y}\left[(\mu_\ell+\mu_t)\frac{\partial v_x}{\partial y}\right]=-\frac{\partial P}{\partial x} \quad (2)$$

$y$-momentum:

$$\rho\left[\frac{\partial(v_xv_y)}{\partial x}+\frac{\partial(v_y^2)}{\partial y}+\frac{\partial(v_zv_x)}{\partial z}\right]-\frac{\partial}{\partial x}\left[(\mu_\ell+\mu_t)\frac{\partial v_y}{\partial x}\right]-\frac{\partial}{\partial y}\left[(\mu_\ell+\mu_t)\frac{\partial v_y}{\partial y}\right]=-\frac{\partial P}{\partial y} \quad (3)$$

$z$-momentum:

$$\rho\left[\frac{\partial(v_xv_z)}{\partial x}+\frac{\partial(v_yv_z)}{\partial y}+\frac{\partial(v_z^2)}{\partial z}\right]-\frac{\partial}{\partial x}\left[(\mu_\ell+\mu_t)\frac{\partial v_z}{\partial x}\right]-\frac{\partial}{\partial y}\left[(\mu_\ell+\mu_t)\frac{\partial v_z}{\partial y}\right]=-\frac{\partial P}{\partial z} \quad (4)$$

where subscripts $\ell$ and $t$ denote laminar and turbulent respectively.

An appropriate turbulence model is required to specify the turbulent viscosity $\mu_t$. The $k$-$\epsilon$ model was chosen for the present work, and the basis of this model is the solution of the transport equations for the turbulence kinetic energy $k$ $(=\overline{v_x'^2+v_y'^2+v_z'^2}/2)$ and its dissipation rate $\epsilon$, which are coupled to the governing equations via the relation

$$\mu_t=\rho C_\mu\frac{k^2}{\epsilon} \quad (5)$$

Among the various $k$-$\epsilon$ model equations, the following form is recommended by a number of workers, e.g., Jones and Launder (1972), and Launder and Spalding (1974):

Turbulence kinetic energy:

$$\rho\left[\frac{\partial(v_xk)}{\partial x}+\frac{\partial(v_yk)}{\partial y}+\frac{\partial(v_zk)}{\partial z}\right]-\frac{\partial}{\partial x}\left[\left(\mu_\ell+\frac{\mu_t}{\sigma_k}\right)\frac{\partial k}{\partial x}\right]-\frac{\partial}{\partial y}\left[\left(\mu_\ell+\frac{\mu_t}{\sigma_k}\right)\frac{\partial k}{\partial y}\right]=\mu_t\Phi-\rho\epsilon \quad (6)$$

Dissipation rate:

$$\rho\left[\frac{\partial(v_x\epsilon)}{\partial x}+\frac{\partial(v_y\epsilon)}{\partial y}+\frac{\partial(v_z\epsilon)}{\partial z}\right]-\frac{\partial}{\partial x}\left[\left(\mu_\ell+\frac{\mu_t}{\sigma_\epsilon}\right)\frac{\partial\epsilon}{\partial x}\right]-\frac{\partial}{\partial y}\left[\left(\mu_\ell+\frac{\mu_t}{\sigma_\epsilon}\right)\frac{\partial\epsilon}{\partial y}\right]=C_1\mu_t\frac{\epsilon}{k}\Phi-\rho C_2\frac{\epsilon^2}{k} \quad (7)$$

where the viscous dissipation function $\Phi$ is defined by

$$\Phi=2\left[\left(\frac{\partial v_x}{\partial x}\right)^2+\left(\frac{\partial v_y}{\partial y}\right)^2+\left(\frac{\partial v_z}{\partial z}\right)^2\right]+\left(\frac{\partial v_y}{\partial x}+\frac{\partial v_x}{\partial y}\right)^2+\left(\frac{\partial v_z}{\partial y}+\frac{\partial v_y}{\partial z}\right)^2+\left(\frac{\partial v_x}{\partial z}+\frac{\partial v_z}{\partial x}\right)^2 \quad (8)$$

The most widely accepted values for the empirical constants are

$$\sigma_k=1.0,\quad \sigma_\epsilon=1.3,\quad C_1=1.44,\quad C_2=1.92,\quad C_\mu=0.09$$

## Boundary Conditions

At the inlet, uniform profiles for all the dependent variables are employed for simplicity:

## Nomenclature

$a$ = distance from rough wall to the zero shear plane
$b$ = distance from smooth wall to the zero shear plane
$C_1$, $C_2$, $C_\mu$ = $k$-$\epsilon$ model constants
$D$ = diameter of circular tube
$D_h$ = hydraulic diameter of rectangular duct $(= 2WH/(W+H))$
$E$ = constant in logarithmic velocity profile
$f$ = friction factor $(= 8\tau_w/(\rho u_b^2))$
$h_r$ = rib height
$h_r^+$ = dimensionless $h_r$ $(= u^*h_r/\nu)$
$k$ = turbulence kinetic energy $(= \overline{v_x'^2+v_y'^2+v_z'^2}/2)$
$k_s$ = equivalent sand grain roughness
$p$ = rib pitch
$P$ = pressure
$R_h$ = hydraulic radius of rectangular duct $(= WH/(W+H))$
Re = Reynolds number $(= u_bD/\nu$ or $u_bD_h/\nu)$
$u$ = velocity component in flow direction $(= v_z)$
$u^*$ = friction velocity $(= \sqrt{\tau_w/\rho})$
$u^+$ = dimensionless velocity $(= u/u^*)$
$u_h^+$ = roughness function
$v_x$, $v_y$, $v_z$ = time-averaged velocity component in $x$, $y$, $z$ direction
$W$ = width of rectangular duct
$x$, $y$, $z$ = rectangular coordinates
$y$ = distance from the wall
$y^+$ = dimensionless $y$ $(= u^*y/\nu)$
$\delta$ = distance from wall to near-wall grid point
$\epsilon$ = dissipation rate of turbulence energy
$\kappa$ = von Karman constant
$\mu_\ell$ = laminar viscosity
$\mu_t$ = turbulent viscosity
$\nu_\ell$ = laminar kinematic viscosity
$\nu_t$ = turbulent kinematic viscosity
$\rho$ = density
$\sigma_k$ = diffusion Prandtl number for $k$
$\sigma_\epsilon$ = diffusion Prandtl number for $\epsilon$
$\tau_w$ = wall shear stress
$\Phi$ = viscous dissipation function

**Subscripts**

$b$ = bulk
$h$ = hydraulic
$in$ = inlet
$\ell$ = laminar
$t$ = turbulent
$w$ = wall

**Superscripts**

$+$ = inner variable

$$v_x(z=0)=0 \tag{9}$$

$$v_y(z=0)=0 \tag{10}$$

$$v_z(z=0)=v_{in} \tag{11}$$

$$k(z=0)=k_{in} \tag{12}$$

$$\epsilon(z=0)=\epsilon_{in} \tag{13}$$

$v_{in}$ is an input parameter to be specified, and it is generally reported that the choice of $k_{in}$ and $\epsilon_{in}$ makes little influence on the results. For the present work, the following inlet conditions for $k$ and $\epsilon$ have been used:

$$k_{in}=0.0025v_{in}^2 \tag{14}$$

$$\epsilon_{in}=\frac{1.6k_{in}^{1.5}}{R_h} \tag{15}$$

where $R_h$ denotes the hydraulic radius of duct.

No-slip and impermeable wall conditions are imposed:

$$v_x=v_y=v_z=0 \quad \text{for} \quad x=0,\ y=0,\ y=H \tag{16}$$

Obviously the turbulence kinetic energy is zero at the wall:

$$k(x=0,\ y=0,\ y=H)=0 \tag{17}$$

Among the several options for wall boundary condition for $\epsilon$ the one derived by Patel et al. (1985) has been chosen because of its simplicity:

$$\left.\frac{\partial\epsilon}{\partial x}\right|_{x=0}=\left.\frac{\partial\epsilon}{\partial y}\right|_{y=0,\ y=H}=0 \tag{18}$$

At the line of symmetry the following conditions are implied:

$$v_x(x=W/2)=0 \tag{19}$$

$$\frac{\partial v_y}{\partial x}=\frac{\partial v_z}{\partial x}=\frac{\partial k}{\partial x}=\frac{\partial\epsilon}{\partial x}=0 \quad \text{for} \quad x=W/2 \tag{20}$$

## Wall Function

When numerical methods are used to analyze turbulent flow, it is convenient to adopt wall functions to bridge the buffer region and the viscous sublayer with a single computation cell. In this way a considerable amount of CPU time and computer memory can be saved. In addition, the wall function approach allows the rough wall flow to be solved as a parabolic problem by using empirical wall functions.

The wall function concept is based on the logarithmic velocity profile:

$$u^+=\frac{1}{\kappa}\ln(Ey^+) \tag{21}$$

where $u$ and $y$ denote velocity components in flow direction and normal distance from the wall respectively. $\kappa=0.41$ and $E=10.0$ where used in the present work. Applying the logarithmic velocity profile, Eq. (21), for $y=\delta$ gives the following implicit equation for $\tau_w$:

$$u_\delta\sqrt{\frac{\rho}{\tau_w}}=\frac{1}{\kappa}\ln\left(E\frac{\delta}{\nu}\sqrt{\frac{\tau_w}{\tau}}\right) \tag{22}$$

Experimental data from the pioneering work by Nikuradse (1950) show that the effects of wall roughness are confined to the inner region only, changing the intercept of the logarithmic velocity profile such that

$$u^+=\frac{1}{k}\ln\frac{y}{h_r}+u_h^+ \tag{23}$$

where $h_r$ is roughness height and $u_h^+$ is called the "roughness function." Also it has been found that, when the roughness element protrudes into the turbulent core (the "fully rough") regime, $y^+>60$), the friction factor is a function of geometric parameters of the roughness element only, that is to say, $u_h^+$ is a function of geometric parameters only.

Assuming that the logarithmic velocity profile, Eq. (23) is valid approximately over the entire crosssection of a circular tube and using the definition of bulk velocity, we obtain the following expressions for $u_h^+$ and $f$,

$$u_h^+=\sqrt{\frac{8}{f}}-\frac{1}{\kappa}\ln\frac{R}{h_r}+3.75 \tag{24}$$

$$f=8\left(\frac{1}{\kappa}\ln\frac{R}{h_r}+u_h^+-3.75\right)^{-2} \tag{25}$$

Webb et al. (1971) performed experiments for flow in round tubes having a repeated-rib roughness in the range of $0.01<h_r/D<0.04$ and $10<p/h_r<40$, and developed the following correlation of the roughness function for the fully rough regime ($h_r^+>35$):

$$u_h^+=0.95\left(\frac{p}{h_r}\right)^{0.53} \tag{26}$$

However, the above correlation is derived from Eq. (24), which is based on several assumptions, and thus will not recover the original values for $f$ when employed in a numerical solution procedure. Wassel and Mills (1979) empirically adjusted the above correlation to secure a better agreement between numerical results and experimental data to obtain

$$u_h^+=\left(1-\frac{h_r}{R_h}\right)\left(\frac{p}{h_r}\right)^{0.5} \tag{27}$$

Figures 3(*a*) and (*b*) show the comparison of experimental data and computed results using Eq. (26) and Eq. (27), respectively, which demonstrates a considerable improvement by employing the modified correlation. We will assume that wall functions based on experimental data for round tubes are also valid for square ducts provided that the roughness height is small compared to the hydraulic radius.

## Numerical Method

As mentioned earlier, the PHOENICS code (version 1.4) was used to solve the governing equations. The PHOENICS code can solve any partial differential equation that can be expressed in the form

$$\frac{\partial}{\partial t}(\rho\phi)+\text{div}(\rho\mathbf{v}\phi-\Gamma_\phi\,\text{grad}\,\phi)=S_\phi \tag{28}$$

where

- $t$: time
- $\mathbf{v}$: velocity vector
- $\phi$: general dependent variable, e.g., velocity component, $k$ or $\epsilon$
- $\Gamma_\phi$: exchange coefficient for $\phi$, e.g., viscosity
- $S_\phi$: source term, e.g., pressure gradient

It can be easily seen that the governing equations discussed in the previous section are in the form of Eq. (28).

The PHOENICS code uses the finite volume method described in Patankar (1980). Integrating Eq. (28) over a control volume of finite size (finite volume cell) gives a discretized finite-volume equation. It uses the SIMPLE (Semi-Implicit Method for Pressure-Linked Equations) scheme developed by Patankar and Spalding (1972) to solve for pressure. This method combines the continuity equation with the momentum equation and derives an equation for a pressure correction $P'$ to be added to the current iteration value of pressure in the same form as for the other dependent variables.

The solution scheme for solving parabolic flows is as follows:

1. Guess the values for each dependent variable (e.g., pressure, velocity component, $k$, $\epsilon$) at the first $z$-slab.

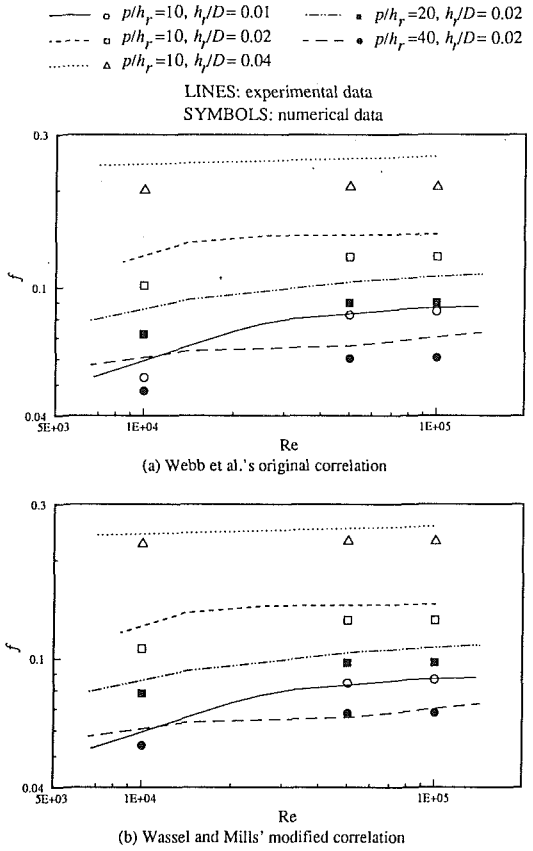


(a) Webb et al.'s original correlation

(b) Wassel and Mills' modified correlation

**Fig. 3 Comparison of $f$ with experimental data for rough circular pipe**

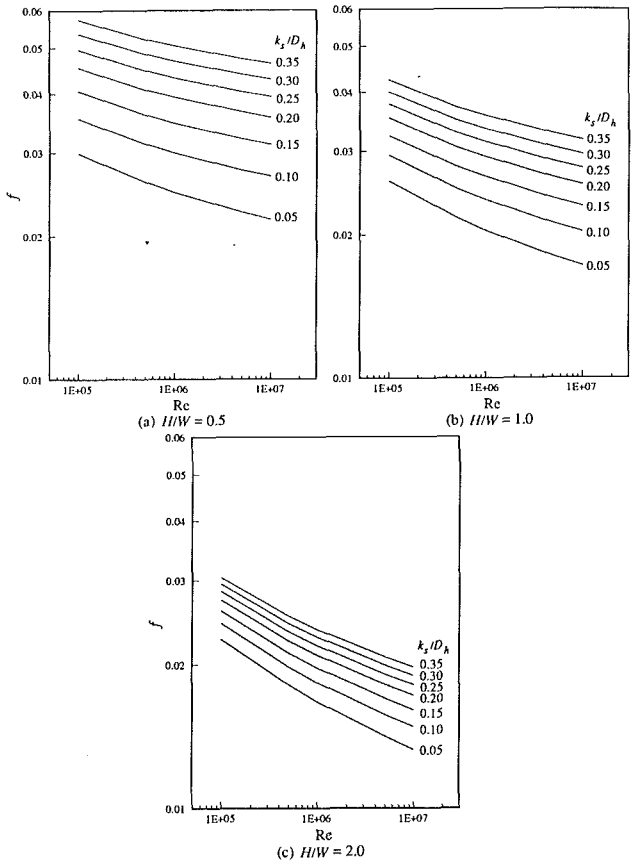


(a) $H/W = 0.5$ (b) $H/W = 1.0$

(c) $H/W = 2.0$

**Fig. 4 Friction factor charts for various aspect ratios**

2. Solve the discretized linear simultaneous equations for each dependent variable using an iterative method similar to Stone's SIP (Strongly Implicit Procedure).
3. Repeat Step 2 using new values until convergence is attained. Iteration is essential since the discretized equations are generally nonlinear.
4. Repeat Steps 2–3 for each $z$-slab.

PHOENICS provides the $k$-$\epsilon$ turbulence model as a built-in option, however, no wall function for rough surfaces is given. Thus the rough wall function using Eq. (27) was implemented in the user-section called 'GROUND.' The numerical scheme used in PHOENICS is 1st-order accurate as a whole. All the convergence criteria are chosen to be sufficiently smaller than the truncation error, and numerical errors in the friction factors are estimated to be no greater than 5 percent.

## Numerical Results

It is known that the friction factor for a developed flow inside a fully rough duct is a function of roughness parameters only, and charts or formulas for this type of flow are well established. However, for the present problem $f$ also depends on Reynolds number and aspect ratio $H/W$ since only one side is roughened, that is,

$$f = f(\mathrm{Re},\ H/W,\ h_r/D_h,\ p/h_r) \tag{29}$$

Here two parameters are required for specifying roughness size, $h_r$ and $p$, however, these can be reduced to a single parameter by introducing equivalent sand grain roughness $k_s$. Examination of Nikuradse's (1950) experimental data shows $u_h^+ = 8.5$ for sand grain roughness for the fully rough regime. Thus, for sand grain roughness, Eq. (25) becomes

$$f = 8\left(\frac{1}{\kappa}\ln\frac{R}{k_s} + 4.75\right)^{-2} \tag{30}$$

and the equivalent sand grain roughness is obtained by comparing Eqs. (25) and (30):

$$k_s = h_r \exp[\kappa(8.5 - u_h^+)] \tag{31}$$

Now $f$ is a function of Re, $H/W$ and $k_s/D_h$:

$$f = f(\mathrm{Re},\ H/W,\ k_s/D_h) \tag{32}$$

Friction factor charts (numerical data) for fully developed flow in rectangular duct with one side rib-roughened are presented in Fig. 4. There exists no previous work for this particular geometry and thus no comparison with other data can be made.

## Experimental Validation

Three square ducts were constructed, one smooth and two rib-roughened on one side. The smooth duct was used to check the experimental technique. The two rib-roughened ducts, one with $k_s/D_h = 0.27$ and the other with $k_s/D_h = 0.17$ were tested to validate the numerical results. An existing water loop was used, which limited the maximum attainable Reynolds number to $2 \times 10^5$. The pressure drop was measured using a Micro Switch 16 PC pressure transducer connected to an ACRO data acquisition system, and the flow rate was measured using an ITT Barton Model No. 7286 turbine flow meter. After confirming the experimental technique using the smooth duct (by comparing measured friction factors at Reynolds numbers based on hydraulic diameter with Nikuradse's results for a round tube), the rib-roughened ducts were tested. Table 1 compares the experimentally obtained friction factors with the numerical predictions. The maximum deviation is 7.9 percent with significantly lower deviations for the larger rib height.

The uncertainties associated with the various instrumenta-

**Table 1 Comparison of experimental results with numerical predictions**

| $k_s/D_h$ | Re | $f_{experimental}$ | $f_{numerical}$ | % error |
|---|---|---|---|---|
| 0.27 | $1.95\times10^5$ | 0.0374 | 0.0368 | −1.62 |
| 0.27 | $1.75\times10^5$ | 0.0376 | 0.0372 | −0.98 |
| 0.27 | $1.51\times10^5$ | 0.0380 | 0.0377 | −0.69 |
| 0.27 | $1.25\times10^5$ | 0.0384 | 0.0381 | −0.75 |
| 0.27 | $1.13\times10^5$ | 0.0385 | 0.0384 | −0.29 |
| 0.27 | $1.01\times10^5$ | 0.0383 | 0.0389 | 1.54 |
| 0.17 | $2.08\times10^5$ | 0.0307 | 0.0317 | 3.18 |
| 0.17 | $1.82\times10^5$ | 0.0310 | 0.0321 | 3.68 |
| 0.17 | $1.57\times10^5$ | 0.0312 | 0.0325 | 4.15 |
| 0.17 | $1.30\times10^5$ | 0.0308 | 0.0330 | 7.06 |
| 0.17 | $1.21\times10^5$ | 0.0320 | 0.0333 | 4.03 |
| 0.17 | $1.06\times10^5$ | 0.0310 | 0.0335 | 7.94 |

tion and equipment used are listed below according to the manufacturer's specifications.

| | |
|---|---|
| Pressure Transducer: | ±1.25 percent |
| ACRO Data Acquisition System: | ±0.1 percent |
| Turbine Flow Meter: | ±0.25 percent linearity |
| Duct Hydraulic Diameter: | ±0.03 mm |

An error propagation analysis yielded an expected uncertainty of 1.47 percent while the precision from the measured data was 1.65 percent. Thus one can conclude that there is little bias in any of the instrumentation utilized and the precision of the experimentally measured data is acceptable. Special care was taken to ensure that the pressure drop measurement was not falsified by changes in dynamic head. The pressure taps were located in machined end pieces with a tolerance of 0.03 mm on the duct width to give a maximum error of ±1 percent in the pressure drop. It was not possible to impose such a tight tolerance on the welded test sections. Note also that it is not practical to measure pressures along the test section for the same reason, and also because it would be necessary to locate the pressure taps very precisely relative to rib locations.

## Proposed Correlation

To correlate the data we will decompose the rectangular duct under the consideration into two pairs of parallel plates (vertical and horizontal channels) of infinite width as shown in Fig. 5. It is straightforward to calculate friction factor $f_1$ for the vertical channel using existing correlations since both plates are smooth. The most widely recommended correlation for friction factor of turbulent flow in smooth duct is Petukhov's (1970) correlation,

$$f=(0.79\ln \mathrm{Re}-1.64)^{-2} \tag{33}$$

Then the friction factor for the vertical channel becomes

$$f_1=(0.79\ln \mathrm{Re}_{2W}-1.64)^{-2} \tag{34}$$

For the horizontal channel, we postulate that the $\tau=0$ plane divides the flow into two regions, and that they do not influence each other. Also the bulk velocity $u_b$ can be assumed to be identical for both regions since the velocity profile for turbulent flow is almost flat. Then the friction factors $f_2$ and $f_3$ can be calculated such that

$$f_2=\left(0.86\ln\frac{2a}{k_s}+1.68\right)^{-2} \tag{35}$$

$$f_3=(0.79\ln \mathrm{Re}_{4b}-1.64)^{-2} \tag{36}$$

using Eqs. (30) and (33), respectively. By considering a momentum balance we obtain the following relation:

$$\frac{b}{a}=\frac{\tau_{w3}}{\tau_{w2}}=\frac{f_3}{f_2} \tag{37}$$

since the pressure is constant over the entire crossection in the fully developed state. By iteratively solving Eqs. (35)–(37) we can obtain $f_2$ and $f_3$.

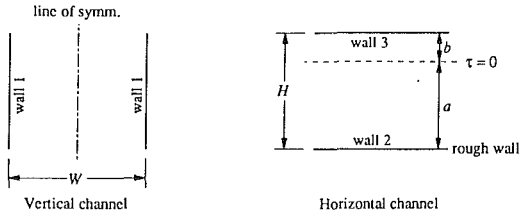


**Fig. 5 Decomposition of rectangular duct into vertical and horizontal channels**

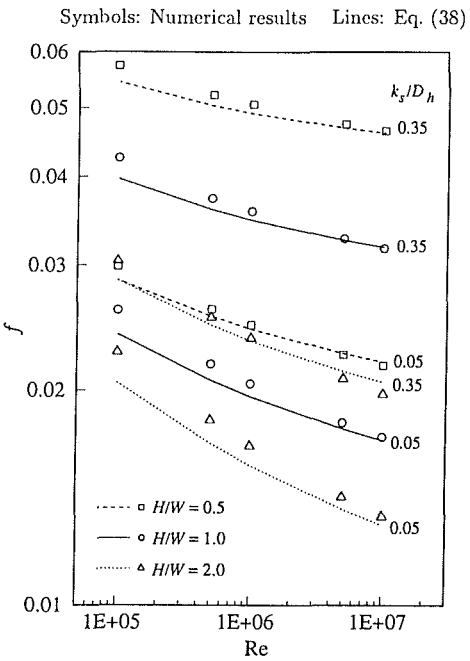


**Fig. 6 Comparison of computed *f* and prediction by Eq. (38)**

Then, assuming that the total shear force for the rectangular duct can be approximated by the sum of the shear forces for the vertical and horizontal channels, the overall friction factor is calculated such that

$$f=\frac{2Hf_1+W(f_2+f_3)}{2(W+H)} \tag{38}$$

The last assumption is reasonable since the velocity profile for turbulent flow is almost flat except the very near-wall region where the molecular viscosity effect is dominant. Velocity profiles for the near-wall region are considered to be almost independent of duct shape. This approximation is not valid for the corner regions, however, these regions are too small to influence the overall flow characteristics. The agreement between the numerical results and predictions by Eq. (38) is generally good as shown in Fig. 6. The discrepancy is relatively larger for lower Reynolds number, which is natural since the corner effects become more dominant for lower Reynolds number.

To get a better agreement with the computed data, $a/H$ was calculated from the computed friction factor using Eqs. (33)–(38) and curve-fitted as a function of $\mathrm{Re}_{2H}$ and $k_s/H$ such that

$$\frac{a}{H}=0.536+4.48\times10^{-5}\log \mathrm{Re}_{2H}+0.326\log\frac{k_s}{H_2}-0.079\log \mathrm{Re}_{2H}\log\frac{k_s}{H}+6.38\times10^{-3}(\log \mathrm{Re}_{2H})^2-0.254\left(\log\frac{k_s}{H}\right)^2 \tag{39}$$

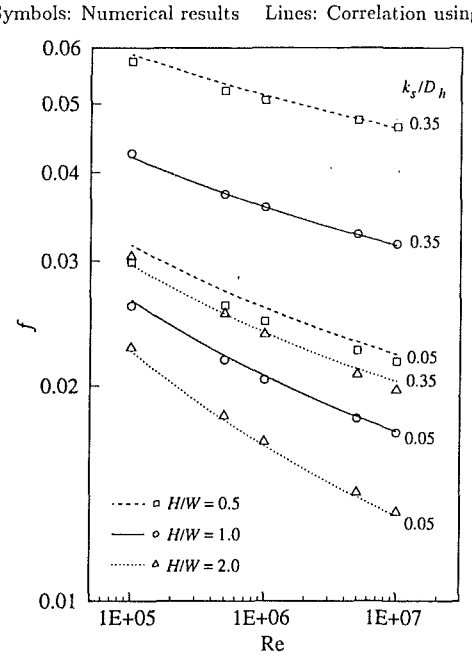


**Fig. 7 Comparison of computed $f$ and correlation using Eq. (39)**

which is valid for $10^5 \leq \mathrm{Re} \leq 10^7$ and $0.5 \leq H/W \leq 2.0$. The friction factors calculated using the above correlation for $a/H$ are compared with the numerical results in Fig. 7.

## Summary

Incompressible flow through rectangular ducts with one side rib-roughened was numerically solved to obtain friction factor data. Flow through a circular tube was also solved to verify the computer code and rough wall function since no previous work on the rectangular duct is available. About 10 minutes CPU time on an IBM 3090 computer was required for the rectangular duct.

Friction factor charts were generated for various aspect ratios based on the numerical results. A superposition method for predicting friction factor for channel flow with smooth and rough walls mixed was introduced and was demonstrated to agree with the numerical results well except for the case of low Reynolds number. A correlation based on the numerical results was suggested for predicting friction factor using the above superposition method. The superposition and correlation methods presented in this study can be extended to any geometry where smooth and rough walls are mixed or various roughness sizes are present.

## Acknowledgments

This work was funded by the National Aeronautics and Space Administration Ames-Dryden Flight Research Facility through the U.C.L.A. Laboratory for Flight Systems Research, director, Professor A. V. Balakrishnan. The NASA Technical Officer was Mr. R. D. Quinn, and the funding was facilitated by Dr. K. Illif of NASA Dryden. Computer time was supplied by the U.C.L.A. Office of Academic Computing. Technical support for the experimental work was provided by Messers G. Roytshteyn, H. Kasper, and D. Cooper.

## References

Jones, W. P., and Launder, B. E., 1972, "The Prediction of Laminarization with a Two-Equation Model of Turbulence," *International Journal of Heat and Mass Transfer*, Vol. 15, pp. 301–314.

Launder, B. E., and Spalding, D. B., 1974, "The Numerical Computation of Turbulent Flows," *Computer Methods in Applied Mechanics and Engineering*, Vol. 3, pp. 269–289.

Nikuradse, J., 1950, "Laws of Flow in Rough Pipes," NACA TM-1292.

Patankar, S. V., 1980, *Numerical Heat Transfer and Fluid Flow*, McGraw-Hill.

Patankar, S. V., and Spalding, D. B., 1972, "A Calculation Procedure for Heat, Mass and Momentum Transfer in Three-Dimensional Parabolic Flows," *International Journal of Heat and Mass Transfer*, Vol. 15, p. 1787.

Patel, V. C., Rodi, W., and Scheuerer, G., 1985, "Turbulence Models for Near-Wall and Low Reynolds Number Flow: A Review," *AIAA Journal*, Vol. 23, No. 9, pp. 1308–1319.

Petukhov, B. S., 1970, *Advances in Heat Transfer*, Vol. 6, Academic Press, New York.

PHOENICS Instruction Course Lecture Notes, CHAM Ltd., 40 High St., Wimbledon, London, SW19 5A4, England.

Wassel, A. T., and Mills, A. F., 1979, "Calculation of Variable Property Turbulent Friction and Heat Transfer in Rough Pipes," ASME *Journal of Heat Transfer*, Vol. 101, pp. 469–474.

Webb, R. L., Eckert, E. R. G., and Goldstein, R. J., 1971, "Heat Transfer and Friction in Tubes with Repeated-Rib Roughness," *International Journal of Heat and Mass Transfer*, Vol. 14, pp. 601–618.

# Quantitative Visualization of Surface Flows on Rotating Disks

**H.-M. Tzeng**

**A. C. Munce**

**L. Crawforth**

IBM Research Division,
Almaden Research Center,
650 Harry Road,
San Jose, CA 95120-6099

*A novel scheme for the visualization of surface flows is developed. It utilizes the strong adhesion forces between micrometer-sized particles and solid surfaces to register the surface streaklines, or equivalently, streamlines for steady flows. Fluorescent particles are used to allow the spectral separation of particle fluorescence emission from morphology-related elastic light scattering from the surface. This scheme was employed to investigate the surface flow on rotating disks in a disk-drive-like environment. Trajectories of the streaklines were digitized and quantitatively analyzed using image processing for orientation and spatial distribution. The surface streaklines provide information about the boundary layers on the disk while the spreading angle of the jets in the self-pumped through-flow reveal details about the bulk flow outside the boundary layer. The spiral angle of the streaklines over a major portion of the disk surface was found to be in good agreement with the theory for laminar Ekman boundary layers. The spreading of the streaklines, reflecting the width of the self-pumped jets emanating from holes in the hub, was found to increase linearly with radius.*

## Introduction

In many practical situations, one is concerned with the flow in the vicinity of solid boundaries, e.g., the deposition of particles on turbine blades which can lead to deteriorated performance. In hard disk drives, maintaining ultra-thin ($< 5$ nm) layers of lubricant on disk surfaces is vital to reliable disk-drive operation. For such thin lubrication films, the major force affecting lubricant migration is the air shearing stress near the disk surface. It is therefore of great interest to understand the characteristics and to estimate key attributes of the flow near the disks. We are motivated to identify a suitable approach for investigating the surface flow on disks in a disk-drive environment.

A common technique for visualizing the surface flow is the oil-film technique (see, for example, Merzkirch, 1987, and references therein). Independent of flow conditions, the trajectory of an 100-$\mu$m diameter silicon-oil droplet is always a straight radial line at a speed of 3600 revolutions per minute (rpm), which is typical of current hard disk drives. Therefore, the centrifugal effect in rotating flows excludes the oil-film visualization technique as a viable approach to study the surface flow on disks. A variation to the oil-film technique is a fluorescence scheme which was employed by Gessner and Chan (1983) who sprayed paint of an oil mixture containing fluorescence pigments on test surfaces. After exposure to the flow, the oil-film coated surface was illuminated by an ultraviolet source to reveal the surface flow pattern. One of the advantages exhibited by the fluorescence scheme is its tolerance to surface roughness because the elastic surface scattering can be separated in wavelength from the fluorescence signal.

Abrahamson et al. (1991) studied an externally-pumped through-flow in a water-tank model of disk drives. At $\mathrm{Re} = 5.6 \times 10^5$, they observed that the through-flow affected the inner region of the disk space by forming discrete jets which emanated from holes drilled in spacer rings. At the entrance region to the disk space, a cross-flow instability was observed. The water-tank-based technique provided a convenient means to envision the global flow structure between disks. However, boundary layers on the disks were not observed.

We have developed a new scheme to investigate surface flow that circumvents the problem arising from centrifugal forces acting on the oil film. The scheme is based on measurements of streakline trajectory due to deposition of airborne, fluorescent particles on surfaces. In this paper, we demonstrate this scheme for the visualization of Ekman boundary layers on rotating surfaces with self-pumped through-flows. First the operating principle will be described along with the experimental apparatus used to perform the measurements. The results for one particular disk-drive-like flow will be given and discussed in detail. A simple analysis for the Ekman boundary layers in this type of flow allows for several physical insights to be drawn from the measurements.

## Visualization Principle

The underlying principle of this scheme is that a record of streaklines on a surface in a steady flow is the same as the streamlines on the surface (Batchelor, 1967), i.e.,

$$\frac{ds}{v_s} = \frac{dn}{v_n}. \tag{1}$$

Contributed by the Fluids Engineering Division for publication in the JOURNAL OF FLUIDS ENGINEERING. Manuscript received by the Fluids Engineering Division February 26, 1993; revised manuscript received October 27, 1993. Associate Technical Editor: M. Gharib.

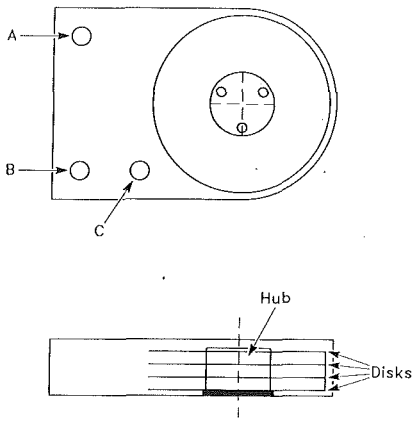


Fig. 1 Schematic of the test apparatus

Therefore, a measurement of the streakline trajectories allows the determination of ratio between velocity components.

As pointed out in the preceding section, the oil-film technique is not suitable for rotating flows due to the excess centrifuging force on the film. However, the strong adhesion force between micrometer-sized particles and surfaces lends itself as an ideal method for investigating surface flows. For example, a 2-$\mu$m polystyrene latex (PSL) sphere (density of 1.05 g/cm$^3$) is held onto a silicon substrate by a van der Waals force of approximately 0.5 dyne; while the centrifugal force is about $4\times10^{-6}$ dyne at a rotation rate of 3600 rpm (Bowling, 1988). Once a particle is deposited on the disk surface, it becomes firmly attached. The use of micrometer-sized PSL particles also ensures that fluctuations in the flow will be followed (Durst et al., 1981). Furthermore, the smallness of these particles introduces minimal perturbation to the flow.

A collection of these particle depositions serves as a 'permanent' record revealing the surface streaklines. Since the flow is in steady motion, these streaklines are the same as the streamlines. Consequently, a measurement of the slope of the trajectory enables the deduction of the ratio of the two orthogonal velocity components on the surface.

## Experimental Apparatus

The fluorescence-imaging scheme was applied to a through-flow generated by a test apparatus that was modelled after the hard disk drive (Fig. 1). Through-flows were induced by the rotation of a set of four industry-standard 3.5 in. ($R_2=47.5$ mm) disks that were mounted, at equal axial distances ($h=0.084$), on a hub. The disks were rotated at a uniform speed of 3600 rpm ($\Omega=377$ rad/s).

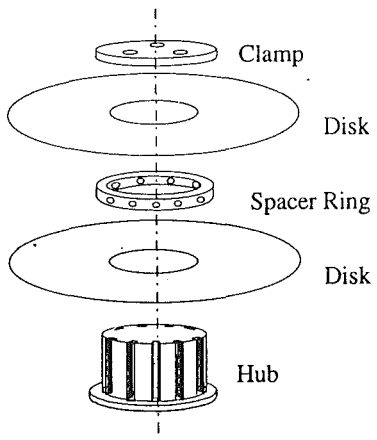


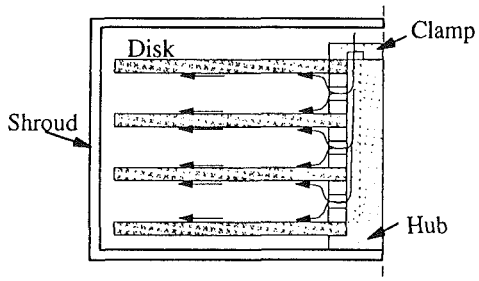


Fig. 2 Flow path of the through-flow system. (*a*) Exploded view of the key components. (*b*) Schematic of the path of through-flow.

To generate a self-pumped through-flow, the hub was provided with rectangular grooves to pass the flow as indicated in Fig. 2(*a*). The through-flow geometry consisted of nine hub grooves (rectangular cross-section of 2 mm $\times$ 2 mm), three disk clamp openings (diameter of 2.5 mm), and three spacer rings each having nine circular apertures (diameter $\phi_a=2.36$ mm) to pass the flow. In operation, the pressure differential between the inner and outer radii drove the flow through holes in the top clamp, down the grooves on the hub, and out the holes in the spacer rings into the space between the disks. Upon entering the disk space, the through-flow, in the form of discrete, circular jets, is entrained into the boundary layer on the disk by Coriolis forces arising from a tangential velocity deficit. The flow is transported radially outward in the disk boundary layers to return along the shroud and top cover into the top clamp again.

The opening area of the spacer ring apertures was 9.1 percent of the surface area. There was an annular gap (0.76 mm high

## Nomenclature

$H$ = disk-to-disk spacing
$I(R)$ = fluorescence intensity
$I_t$ = total fluorescence intensity on the disk
$i$ = normalized fluorescence intensity, $I(R)/I_t$
$R$ = radius
$r$ = normalized radius, $R/R_2$
Re = disk Reynolds number, $\Omega R_2^2/\nu$
$R_2$ = disk outer radius, 47.5 mm
$\Delta R$ = a small radial distance
$(R, \theta, z)$ = polar coordinate with origin at disk center
$(r, s)$ = local orthogonal coordinate
$(U, V)$ = radial and circumferential velocity relative to a laboratory observer
$(u, v)$ = radial and circumferential velocity relative to the disk
$\bar{v}$ = time-averaged circumferential velocity relative to the disk
$v_s, v_r$ = local velocity components in r and s directions
$W_{1/2}$ = spiral width at half of local maximum
$w_{1/2}$ = $W_{1/2}/\phi_a$
$\alpha$ = spiral angle
$\alpha_0$ = spiral angle in the inner to intermediate radii
$\Delta\theta$ = a small change in $\theta$
$\delta$ = thickness of boundary on disk
$\epsilon$ = Rossby number, $(\Omega R - V)/\Omega R$
$\mu$ = dynamic viscosity
$\nu$ = kinetic viscosity, $\nu = \mu/\rho$
$\rho$ = fluid density
$\phi_a$ = diameter of apertures on spacer rings, 2.36 mm
$\Omega$ = disk rotational rate (rad/s)

by 7 mm wide) between the clamp and hub to distribute the flow to individual grooves. Each of the nine apertures on the spacer rings was aligned with the grooves on the hub. Three of the nine grooves were connected directly to the three openings on the disk clamp. In order to enter the remaining six grooves, the flow had to negotiate through the annular gap on the disk clamp. Because of the disparity of flow impedances among these grooves, a nonuniformity in the distribution of particle concentration among grooves was anticipated.

The disks employed were of the thin-film, magnetic type. To reduce the stiction between magnetic sensors and disks during spin-up, disks are often textured (i.e., roughened) to a root-mean-square roughness of $\approx 50$ nm, which will have a negligible effect on the boundary layer that has a thickness of about 200 $\mu$m at $\mathrm{Re} = 5.7 \times 10^4$. The textured disk surfaces, like other rough surfaces, enhance elastic light scattering (Beckmann and Spizzichino, 1987). To obtain satisfactory surface streakline images, this elastic scattering had to be suppressed by spectral filtering as described below.

Aerosol particles were produced by drying atomized water droplets containing PSL spheres. Fluorescent PSL spheres of 1.85 $\mu$m diameter (Duke Scientific Inc., catalog No. R185) were first mixed in filtered (by PALL Filters, 99.8 percent efficiency at 0.2 $\mu$m), deionized water at a concentration of $10^7/\mathrm{cm}^3$. At this concentration level, it was found that more than 80 percent of the final aerosol particles were at the same size as the primary PSL spheres. Aerosols of the water droplets pass through two diffusion dryers (TSI model 3062) connected in series, and then a charge neutralizer (TSI model 3012) to achieve a Boltzmann equilibrium distribution. The dried, charge-neutralized aerosols were introduced into the tester via an inlet (port A in Fig. 1). Excess flow in the tester was vented out through an exhaust (port B in Fig. 1) on the cover plate. The absolute pressure in the tester was monitored at location C during the course of the test to prevent infiltration of ambient particles and to avoid adverse perturbation to the interior flow. After exposure to aerosol injection for 48 hours, disks were removed from the tester for interrogation.

The smallness of the micrometer-sized particles utilized to reveal the flow pattern required an intense light source with good beam stability and quality. Since the PSL spheres were impregnated with a Rhodamine dye which had an absorption band extending from ultraviolet to green in the visible spectrum, an argon-ion laser, lasing at wavelengths of 488 and 514.5 nm, was used as the light source. The laser employed in the investigation (Spectral-Physics model 171-17) was operated at roughly 1 Watt of power in the 514.5 nm line. The optical arrangement of the imaging system is displayed in Fig. 3. Two laser beams of equal-intensity were produced from the incoming laser beam. Each beam was expanded by a spherical lens (focal length of 3 cm) to fill the entire disk surface. Each beam was set at an angle of about 30 deg with respect to the disk surface normal. An overlap of these two beams improved the uniformity of laser illumination on the disk sample.

Important to the success of the fluorescence-imaging scheme is the selection of appropriate color filters to block the elastic light scattering at the incident laser wavelengths. The peak of fluorescence emission from the Rhodamine dye molecules imbedded in the PSL spheres is shifted from the excitation laser wavelength by about 70 nm. With an excitation wavelength at 514.5 nm, the peak of the fluorescence emission is at 585 nm. One problem that was observed is that because of the finite sharpness of the filter cut-off and the relative strength of the elastic scattering signal, it was necessary to move the cut-off wavelength of the filter to a value longer than the centerline of the fluorescent emission to get better separation between the excitation and emission wavelengths. Therefore, an orange color filter, such as the Schott OG610, which has a cut-off wavelength of 610 nm, served well to separate the bulk of the fluorescence emission from the elastic scattering. Since a single

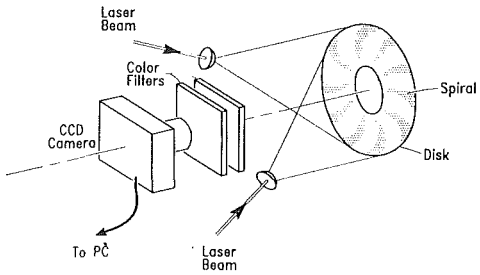


**Fig. 3 Visualization setup**

color filter has an extinction ratio of $1{:}10^4$, it was found that two filters, placed back-to-back in front of the collection lens, were needed to fully block the elastic scattering.

Fluorescent images of the deposition patterns due to the fluorescent PSL spheres was recorded by a cooled, high-resolution CCD (charge-coupled device) detector (Spectral Source, model HPC-1). Each image contained $1024 \times 1024$ pixels and covered the entire illuminated disk surface. The image was digitized with a 16-bit resolution. To fully utilize the dynamic range of the CCD camera system while remaining in the linear regime of the detector, the exposure time was set to 4 s, achieving pixel values of about $2 \times 10^4$, which corresponds to 14–15 bits.

Each pixel in the image was corrected for variations in responsivity in the detector array and dark field current due to thermal noises. The nonuniformity of the laser illumination was corrected by recording an image when the disk sample was replaced by a flat, white surface. Subsequent fluorescent images were normalized by the field response to the white-target image. The corrected images were uploaded to a host mainframe computer to perform further image processing to extract the desired flow quantities.

## Image Analysis

Once the images of the surface streaklines had been recorded, the orientation of the spiral streaklines was quantitatively determined as follows. Referring to Fig. 4, an angular profile of the fluorescence intensity at a fixed radius, OA ($=R$), was extracted from the image. An adjacent profile, at radius OB ($=R+\Delta R$), was also extracted and found to be displaced by a small angle, AOB ($=\Delta\theta$). Each profile is divided into 720 bins for calculations. A cross-correlation between these two profiles is computed to determine its maximum. The angular shift at the maximum correlation is the angular displacement, $\Delta\theta$, between the two profiles. The spiral angle of a streakline, $\alpha$, can then be expressed as

$$\alpha = \mathrm{atan}\left(\frac{\Delta R}{R\Delta\theta}\right). \tag{2}$$

The rate of spread of the spiral trajectory is another piece of information that can be extracted from the image. A straightforward approach is to measure the half-width of a trajectory, the width where the intensity is 50 percent that of the local peak intensity. In comparing the change in the half-width with radius, the underlying assumption is that the intensity profiles are similar. In the present study, it is found that the intensity profiles of the spiral trajectory in the outer-radii region deviate from those in the inner-radii region. As a result, the spread rate of the spiral trajectory exhibits peculiar behavior near the disk edge. To circumvent this difficulty, an alternate definition of the half-width was proposed. It is based on a determination of a width that encompasses 50 percent of the total fluorescence emission at a fixed radius. With this integral approach, the half-width of the trajectory is found to be less sensitive to the shape of the intensity profile.

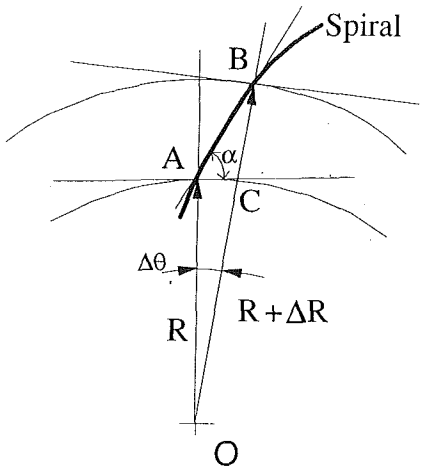


Fig. 4 Trajectory of the surface streaklines. The spiral angle $\alpha$ is defined as the angle between the centerline of a trajectory and a tangent to an arc concentric with the disk.

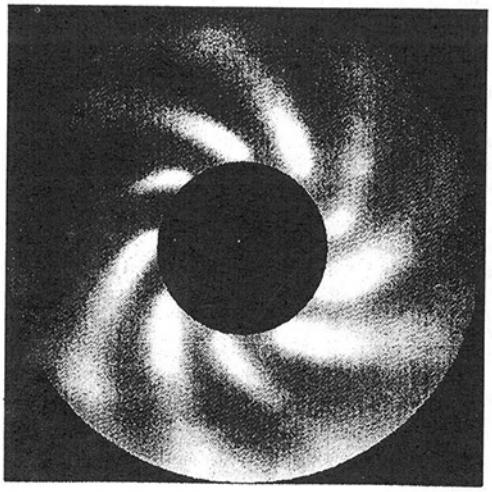

Fig. 5 A typical pattern of surface trajectory on a disk operated at Re = 5.7 x $10^4$. The uncertainty in Re is 430 due primarily to the room temperature variation (1°C).

## Results and Discussion

Figure 5 displays a typical pattern of streaklines on a disk exposed to the through-flow. One of the most prominent features in the picture is the nine spiral trajectories extending over the entire disk surface. The bright portion of these spirals begins at the outer radius of the spacer ring. These spirals are in opposite rotation sense to the disk. The intensity from one spiral to the next is not uniform, presumably due to the disparity in flow geometry among the different spacer ring holes.

Curve (a) in Fig. 6 displays the variation of spiral angle with radius. In the inner to intermediate region ($0.50 < r < 0.78$), the spiral angle is close to being constant at 48 deg. However, it increases with radius in the outer-radii region $r > 0.78$. The measurement uncertainty in the spiral angle is 1.5 deg.

The through-flow spreads as it travels radially outward along the disk surface. The averaged half-width of the bright spiral trajectories is displayed by Curve (b) in Fig. 6. The half-width increases linearly with radius for $0.5 < r < 0.78$, while deviating slightly from linear for $r > 0.78$. It is worth noting that the deviation from the linear increase occurs at approximately the same radius that the spiral angle deviates from a constant value. A linear regression of the half-width leads to the following result:

$$w_{1/2} = -1.67 + 7.80\, r \tag{3}$$

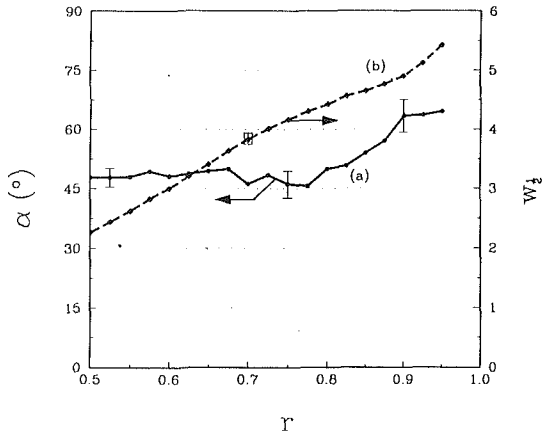


Fig. 6 The spiral angle (Curve a) and the half-width (Curve b) of spiral trajectory on disk plotted as a function of radius. Uncertainties in the measurements of spiral angle and half-width are indicated.

with the correlation coefficient for the regression exceeding 0.99.

The flow enters the disk cavity in the form of discrete, circular jets and is brought close to the boundary layer on the disk by Coriolis forces arising from a velocity deficit (see Eq. (4)). The surface streaklines are essentially a projection of the through-flow onto the disk surface. It is known that the width of a laminar circular jet scales linearly with streamwise distance (Schlichting, 1968). The data in Fig. 6 demonstrate that jets in this rotating flow bear the same linear scaling relationship to radius.

## Analysis

As we are interested in the surface flow on the rotating disks, it is more convenient to attach the reference coordinate to the disk. In the inner- to mid-radii region of $r \leq 0.8$ the velocity difference between the bulk of the flow and the disk is less than 10 percent. With a corresponding Rossby number $\epsilon < 0.1$, it is a good approximation to neglect nonlinear inertia terms from the equations of motion. It follows that the Coriolis and viscous terms dominate and the following Ekman-layer equations can be obtained (Ekman, 1905).

$$-2\Omega(v-\bar{v}) = \frac{\mu}{\rho}\frac{\partial^2 u}{\partial z^2} \tag{4}$$

and

$$-2\Omega u = \frac{\mu}{\rho}\frac{\partial^2 v}{\partial z^2}. \tag{5}$$

The boundary conditions are

$$u = v = 0 \quad \text{at} \quad z = 0, \quad \text{and} \quad u = 0,\ v = \bar{v} \quad \text{as} \quad z \to \infty. \tag{6}$$

When the flow is laminar, Eqs. (4)–(6) can be solved to yield

$$u = -\bar{v}\, e^{-z/\delta} \sin\frac{z}{\delta} \tag{7}$$

and

$$v = -\bar{v}\left(1 - e^{-z/\delta}\cos\frac{z}{\delta}\right) \tag{8}$$

where $\delta = (\nu/\Omega)^{1/2}$. From Eqs. (7) and (8), it can be readily shown that the ratio between these two velocity components approaches unity for small $z$, i.e., a spiral angle of 45 deg at the disk surface. For a fully developed turbulent boundary layer the spiral angle can be shown to be 29 deg, if the 1/7 power-law profiles are used (see, for example, Owen, 1988). The Reynolds number for the experimental data in Fig. 6 was

$Re = 5.7 \times 10^4$, and therefore based on previous studies (Schlichting, 1968) one would anticipate that the boundary layers should be laminar up to about $Re = 3 \times 10^5$. The fact that spiral angles in this study are close to 45 deg over a large range of radii is in agreement with this prediction. The deviation in spiral angle at the larger radii from the laminar value is likely due to the fact that near the shroud the flow becomes highly three dimensional and the approximations of Eqs. (4)–(6) no longer apply.

A measurement of the spiral angles associated with the surface streaklines also allows us to gain insight about the thickness of the Ekman layer. Using an approach developed by Prandtl (1949), Schlichting (1968) showed that

$$\delta^2 \propto \left(\frac{\nu}{\Omega}\right) \tan \alpha. \tag{9}$$

In the inner-radii region ($0.5 < r < 0.78$) where the direction of the flow near the disk is independent of the radius, the thickness of the Ekman layer becomes independent of radius and

$$\delta \propto \left(\frac{\nu}{\Omega}\right)^{1/2}. \tag{10}$$

In the outer-radii region, the thickness of the Ekman layer apparently grows with radius in proportion to $(\tan \alpha)^{1/2}$. For example, the thickness, of the Ekman layer at $r = 0.9$ is 1.7 times that in the inner-radii region.

It is interesting to note that the spiral streaklines extend over the entire disk surface. In the radial region, where the spiral angle is close to a constant value, the centerlines of the spiral trajectories are logarithmic spirals which, in a polar coordinate system, can be described by

$$R_n = \exp(\tan \alpha_0(\theta_n - \theta_{o,n})) \tag{11}$$

where a subscript $n$ denotes the $n$th spiral.

## Conclusion

A novel surface visualization scheme was developed based on the adhesion of micrometer-sized particles on solid surfaces. The adhesion of these fine particles gives rise to streaklines, which are equivalent to surface streamlines in steady flows. Since the surface streaklines are firmly held onto the dark surface, taking images of the surface streaklines is relatively easy. With the advance of cooled, high-resolution detectors, the exposure time can be extended for optimal image quality. Further, computer-aided image processing not only improves the image quality but also enables quantitative analyses of flow properties.

This scheme proves useful to the understanding of a self-pumped through-flow in a disk-drive-like environment. The characteristics of the surface flow on rotating disks, in the presence of superimposed through-flows, are revealed. Interestingly, information can be obtained about not only the boundary layer flow, but certain characteristics of the bulk flow. The results thus obtained complement not only previous qualitative visualizations but also quantitative velocity measurements of the bulk flow in similar test systems.

Though demonstrated for a self-pumped through-flow in a disk-drive like environment, the scheme can be applied to other flows. A major advantage of this fluorescence-based imaging method over other schemes based on elastic scattering is that it is insensitive to surface roughness or the reflective properties of the test specimen. Thus it is particularly useful for investigations on the deposition and corrosion of particles on turbine blades that occur in practical applications.

## References


Abrahamson, S. D., Chiang, C., and Eaton, J. K., 1991, "Flow Structure in Head-Disk Assemblies and Implications for Design," ASME *Advances in Information and Storage Systems*, Vol. 1, pp. 111–132.

Batchelor, G. K., 1967, *An Introduction to Fluid Dynamics*, Cambridge University Press, pp. 71–72.

Beckmann, P., and Spizzichino, A., 1987, *The Scattering of Electromagnetic Waves from Rough Surfaces*, Artech House.

Bowling, R. A., 1988, "A Theoretical Review of Particle Adhesion," *Particles on Surfaces*, K. L. Mittal, ed., Plenum Press, pp. 129–142.

Durst, F., Melling, A., and Whitelaw, J. H., 1981, *Principles and Practice of Laser-Doppler Anemometry*, Second Edition, Academic Press, pp. 281–292.

Ekman, V. W., 1905, "On the Influence of the Earth's Rotation on Ocean Currents," *Arkiv For Matematik, Astronomi Och Fysik*, Vol. 2, No. 11.

Gessner, F. B., and Chan, Y. L., 1983, "Flow in a Rectangular Diffuser with Local Flow Detachment in the Corner Region," *Trans. ASME*, Vol. 105, pp. 204–211.

Merzkirch, W., 1987, *Flow Visualization*, Second Edition, Academic Press, pp. 82–87.

Owen, J. M., 1988, "Air-cooled Gas-Turbine Discs: a Review of Recent Research," *International Journal of Heat and Fluid Flows*, Vol. 9, No. 4, pp. 354–365.

Schlichting, H., 1968, *Boundary Layer Theory*, McGraw-Hill, p. 94.

# Time-Dependent Conjugate Heat Transfer Characteristics of Self-Sustained Oscillatory Flows in a Grooved Channel

**J. S. Nigen**
Graduate Student.

**C. H. Amon**
Associate Professor.
Mem. ASME

Department of Mechanical Engineering and
Engineering Design Research Center,
Carnegie Mellon University
Pittsburgh, PA 15213

*Convective heat transport in a grooved channel is numerically investigated using a time-dependent formulation. Conjugate conduction/convection and uniform heat-flux representations for the solid domain are considered. For the conjugate representation, the solid domain is composed of multiple materials and concentrated heat generation. The associated cooling flows include laminar and transitional regimes. Steady and time-dependent contours of the streamfunction and local skin-friction coefficients are presented. Additionally, local distributions of Nusselt number and surface temperature are displayed for both the conjugate and convection-only representations. These results are contrasted over the range of Reynolds numbers explored to demonstrate the significance of including time-dependency and conjugation in the study of convective heat transport. Such considerations are found to be important in the design and analysis of heat exchanger configurations with spatially varying material composition and concentrated heat generation.*

## Introduction

Industrial applications of transport phenomena entail the achievement of performance objectives, as well as the satisfaction of limiting constraints. In many situations, size and acoustic output play crucial roles in the selection of a design. Therefore, an increasing amount of research has focused on the enhancement of transport rates without violating these constraints. One successful technique is the modification of the initially specified geometry. An objective of geometric variation is to increase the total area from which heat is removed, as exemplified by the addition of fins. Another objective is the reduction of thermal resistances through the thinning of the boundary layer, which may be achieved by surface segmentation. Surface segmentation causes a repetitive pattern of boundary layer initiation, growth, and separation resulting in a reduction of transport resistance normal to these surfaces. Segmented geometries such as communicating channels (Amon and Mikic, 1991; Majumdar and Amon, 1992), furrowed channel (Stephanoff et al., 1980), ribbed channel (Greiner et al., 1990), and grooved channel (Lehmann and Wirtz, 1985; Nigen and Amon, 1991) have been demonstrated to reduce boundary layer thickness and are employed in both compact heat and mass transfer applications.

The fluid flow in these segmented geometries can be partitioned into two distinct regions: the bypass and the groove regions (Fig. 1). The bypass region (Moffat and Ortega, 1988) consists of the portion of the channel in which fluid flows from inlet to outlet, while the groove regions consist of the locations wherein fluid remains trapped between the bypass flow and the channel surfaces. The flow patterns exhibited in the bypass and groove regions differ greatly in that a mostly parallel flow structure is present in the bypass region, which is separated by a shear layer from recirculating zones within the groove regions. The shear layer partitioning the flow regions prohibits convective exchange of fluid. The combination of the above factors results in a disparity in convective performance between the different regions.

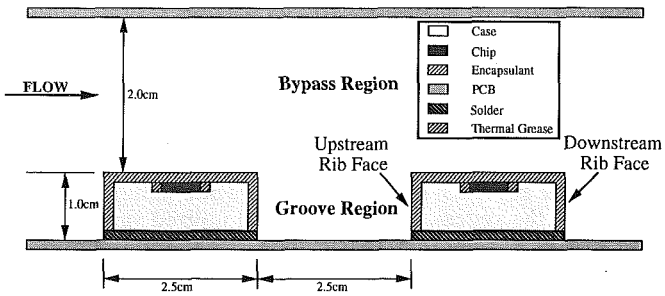


**Fig. 1 Schematic of the package, overall geometry, and flow regions**

Flows in these geometries have been found to undergo transition from a steady, parallel flow structure in the bypass region to a time-dependent, nonparallel flow structure above a geometrically-dependent critical Reynolds number (Ghaddar et al., 1986a; Amon and Patera, 1989; Pereira and Sousa, 1993). For

Contributed by the Fluids Engineering Division for publication in the JOURNAL OF FLUIDS ENGINEERING. Manuscript received by the Fluids Engineering Division March 23, 1993; revised manuscript received August 27, 1993. Associate Technical Editor: J. A. C. Humphrey.

a range of Reynolds numbers, the resulting supercritical bypass flow structure is composed of two-dimensional, self-sustained oscillations, indicative of Tollmien-Schlichting waves that interact with the shear layer and recirculating zones within the groove regions. The associated time-dependent flow patterns yield convective exchange between the groove and bypass regions, resulting in significant transport augmentation (Ghaddar et al., 1986b; Nigen and Amon, 1991). However, this improvement in transport tends to be nonuniform over the exchanger surfaces.

In applications where spatial variations of temperature are important because of operational and/or reliability considerations, neglecting nonuniform heat transfer may result in unacceptable performance. An additional source of temperature variations, other than that associated with convective phenomena, is caused by variations in material composition or concentrated heat generation. Electronic systems are examples of such spatially nonhomogeneous and thermally sensitive systems. The analysis of electronic systems is further complicated by their multicomponent composition, which frequently includes power supplies, storage devices, printed circuit boards (PCBs), as well as other components.

An approach to analyzing sub-components of electronic systems is to numerically solve the heat equation within the solid domain (Hardisty and Abboud, 1987; Aghazadeh and Mallik, 1990). Boundary conditions are then applied at the solid-fluid interface based upon empirically generated heat transfer coefficient correlations. These empirical correlations are frequently determined through the use of idealized boundary conditions, such as uniform heat flux or temperature. This approach has been used to evaluate the relative impact of varying the material composition or internal structure of a configuration upon its operating temperature. The accuracy of the temperature predictions for the modeled domain is, therefore, highly dependent upon the appropriateness of the assumed boundary conditions, as described by Humphrey et al. (1993). Although these idealized boundary conditions effectively model some heat exchanger configurations, their adequacy would be adversely affected by the large degree of spatial variation and the concentration of heat generation in some configurations, such as electronic packages. More accurate spatially-varying heat transfer coefficients would enable a better assessment of heat-exchanger design modifications (Nigen and Amon, 1992). Furthermore, an asymmetrical distribution of convective performance along a surface may require an asymmetrical design to minimize thermal gradients and operating temperatures.

Another approach is to conduct conjugate simulations of a region of the system. Researchers have utilized variations of the SIMPLE algorithm to simulate steady-state conjugate problems for configurations with either inflow/outflow or periodic boundary conditions (Patankar et al., 1977; Davalath and Bayazitoglu, 1987; Zebib and Wo, 1989). The SIMPLE algorithm has also been employed in a study of a single-material iterated rib geometry (Yuan, 1992) yielding consistently lower Nusselt numbers for the conjugate simulations than the nonconjugate counterpart, in the range of Reynolds numbers considered. Some previous investigations accounted for material variation and concentration of heat generation within the modeled solid domain. However, all of these simulations lacked time dependency and the complex internal structure contained within most electronic systems. Furthermore, the effect of contact resistance, which can be significant, was neglected in the modeling of the solid domain.

The present study involves both conjugate conduction/convection and convection-only simulations. A time-dependent formulation is implemented and a multimaterial, internal structure of an electronic component, is incorporated. The modeled component consists of five different materials, contact resistance, and concentrated heat generation. Convection-only and conjugate conduction/convection simulations are carried out for both subcritical and supercritical Reynolds number flows. The resulting time-dependent flow patterns are analyzed and the associated local skin-friction coefficient distributions are presented. Time-averaged and space-varying Nusselt numbers, surface temperatures, and heat fluxes are determined. The resulting distributions of surface temperatures and Nusselt numbers are contrasted, and the effect of Reynolds number is investigated. Furthermore, the conjugate results are compared with those of the convection-only simulations to evaluate the degree to which conjugation alters convective performance. Notice that direct comparisons are only appropriate with respect to the specific geometry considered for variations in the internal structure of the package, as well as in the geometric proportions of the groove, would cause differences in the quantitative results. However, this investigation allows for an assessment of the importance of including time dependency and spatial variations in the modeling of multimaterial heat exchangers with concentrated heat sources, such as those encountered in electronics cooling.

## Problem Formulation

The grooved-channel geometry is comprised of surface-mounted electronic packages and a PCB. The internal structure of the chip carrier (Fig. 1) includes an encapsulant, case, thermal grease, chip, and solder with the corresponding material properties indicated in Table 1. Contact resistance is modeled by assigning an effective thermal conductivity (Table 1) such that the thermal resistance obtained is commensurate with empirical data from Yovanovich and Antonetti (1988). Numerical experiments have demonstrated that internal temperature distributions differ greatly if contact resistance is not accounted for in the modeling procedure. Additionally, the configuration is modeled as two-dimensional, thereby, converting the chip carriers into ribs. The densely packed PCBs found in most electronic systems exhibit more spatial variation in the streamwise direction than across the packages, which supports this assertion (Garimella and Eibeck, 1990,1991; Chyu et al., 1993). However, three-dimensional effects are still important and their omission represents a deficiency of the current model.

The thermo-fluid characteristics associated with the grooved channel are computed through direct numerical simulation of the time-dependent, two-dimensional, incompressible Navier–Stokes and energy equations. Buoyancy effects are neglected because of the small pertinent spatial scale (2H) and low temperature differences, which are later verified by the simula-

## Nomenclature

$c_p$ = specific heat
$H$ = half-channel height
$k$ = thermal conductivity
Nu = Nusselt number: $(QH/(k(T_{wall} - T_{bulk}))$
$Q$ = heat flux
Re = Reynolds number: $(3VH)/(2\upsilon)$
$T$ = temperature
$T_{wall}$ = local-wall temperature
$T_{bulk}$ = bulk-mean temperature at the leading edge of the rib
$\Delta T$ = difference between the local-wall and bulk-mean temperatures
$V$ = channel-averaged velocity

**Greek Symbols**

$\upsilon$ = kinematic viscosity
$\rho$ = density

Table 1

| Component | $k$ (W/cm°C) | $\rho c_p$(KJ/cm$^3$°C) | $u'''$ (W/cm$^3$) |
|---|---|---|---|
| Case | $2.04\times10^{-1}$ | 3.47 | --- |
| Chip | $1.25\times10^{-2}$ | 1.74 | 5.1842 |
| Encapsulate | $6.99\times10^{-3}$ | 3.16 | --- |
| PCB | $7.4\times10^{-3}$ | 2.27 | --- |
| Solder | $1.0\times10^{-3}$ | 1.47 | --- |
| Thermal Grease | $9.614\times10^{-3}$ | 1.71 | --- |
| Air | $2.851\times10^{-4}$ | $1.534\times10^{-4}$ | |

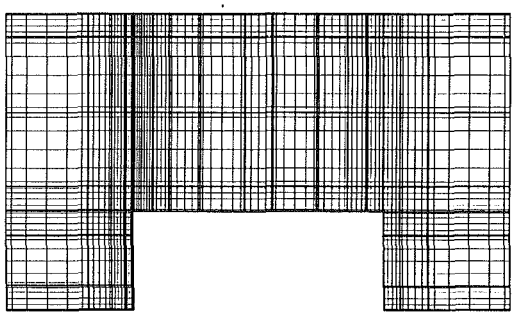

**Fig. 2 Spectral element discretization of the computational domain. Darker lines indicate macro-element boundaries and lighter lines represent internal node discretizations.**

tions. Likewise, viscous dissipation is neglected. It should be noted that the dimensions of the grooved channel and streamwise velocities considered in this study are representative of those encountered in electronics-cooling applications.

The boundary conditions for the velocity are no-slip at the solid-fluid interfaces and periodicity at the inflow and outflow of the domain, which represent the periodically fully developed region of the grooved channel. Such regions have been experimentally observed after the fourth or fifth rib (Lehmann and Wirtz, 1985). The imposed boundary conditions for the energy equation are adiabatic along the upper wall and either uniform flux for the convection-only simulations or continuity of both temperature and heat flux along the grooved wall for the conjugate simulations. Periodicity of temperature is imposed at the inflow and outflow of the domain by subtracting the equivalent rise in bulk-mean temperature on a point-by-point basis.

Initial value solvers are utilized and the solutions are iterated in time until either a steady or time-periodic state is achieved. The spectral element technique is employed for the spatial domain and finite differences for the temporal domain (Patera, 1984; Amon, 1993). The spectral element technique is a hybrid approach in which the physical domain is subdivided into a series of macro-elements, as in finite methodologies, upon which tensor products of high-order orthogonal expansions are projected at collocation points, as in spectral techniques. The macro-elements and internal nodes, comprising the discretization of the grooved channel, are shown in Fig. 2. The nonuniform elemental discretization used in this investigation resulted from a mesh refinement study that indicated the necessity of increased resolution at the corners to localize singularities. The asymmetric elemental discretization is a consequence of the higher gradients associated with the contraction of the flow at the upstream portion of the domain, relative to the expansion at the downstream portion.

The nonlinear convective, viscous, and dynamic-pressure terms of the Navier–Stokes equations are solved separately in a semi-implicit, three-step temporal discretization. This results in solving a wave-like equation for the nonlinear convective terms and then elliptic Poisson and modified-Helmholtz equations for the dynamic pressure and viscous terms, repectively. The convective step is formulated using a pseudo-spectral approach, thus allowing for efficient treatment of the nonlinear terms. For the viscous and pressure steps of the Navier Stokes

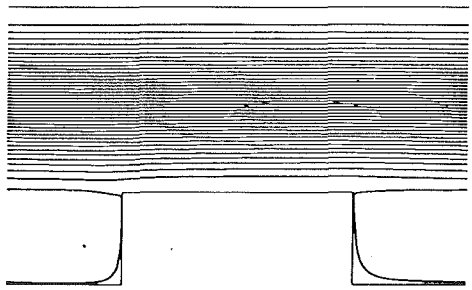

**Fig. 3 Subcritical streamline pattern at Re = 261**

equations, as well as the decoupled energy equation, discrete equations are generated for each element by inserting the interpolants and the transformed nodal collocation values into the variationally-formulated weak form of the corresponding equation. Then a Galerkin weighted-residual technique is applied and the resulting equations are integrated, requiring stationarity at each collocation point.

Once the system of discrete equations is obtained for each element, the global matrix is assembled using direct stiffness summation. This approach results in decoupling the boundary nodes from the internal nodes of each macro-element. In this fashion, the boundary nodes are determined serially, after which, the internal nodes may be determined in parallel, permitting efficient implementation on parallel computer architectures. The variational formulation automatically satisfies $C^0$ across elemental boundaries, while interfacial continuity of flux is achieved through convergence. This alleviates the necessity of a patching technique, usually required to obtain interfacial continuity in other multidomain spectral formulations.

The accuracy of the spectral-element solution may be affected either by increasing the total number of macro-elements, obtaining algebraic convergence, or by increasing the order of the local expansions, achieving nearly-exponential convergence. Adequate resolution was verified by contrasting the flow characteristics using both 7th and 9th order local expansions, as well as using different macro-elemental discretizations. The results from the simulations for the final macro-elemental discretization with 7th and 9th order expansions, yielded virtually identical results, indicating that the lower resolution was adequate for this investigation. Furthermore, the discretization used for the conjugate simulations was more constrained by geometric resolution of the package sub-components than by numerical accuracy concerns.

## Flow Patterns

The flow behavior can be categorized, depending on the Reynolds number, into subcritical and supercritical regimes. In the subcritical regime, the bypass flow is essentially parallel, as evidenced by the streamlines in Fig. 3. A boundary layer grows unhindered along the top surface until reaching its fully-developed thickness. However, the bottom surface, due to its segmentation, causes a boundary layer to initiate and then separate along each successive rib. The separated boundary layer forms a wake that extends downstream. The subcritical bypass flow essentially lacks transverse mixing and therefore, does not fully homogenize the wake before it reaches the next downstream package. This results in a finite boundary layer thickness at the leading edge of each package within the periodically fully developed region. For larger subcritical Reynolds numbers, the incoming flow becomes less homogeneous because of the increase in the streamwise momentum, without a corresponding increase in transverse mixing.

The corresponding subcritical groove flow is steady and

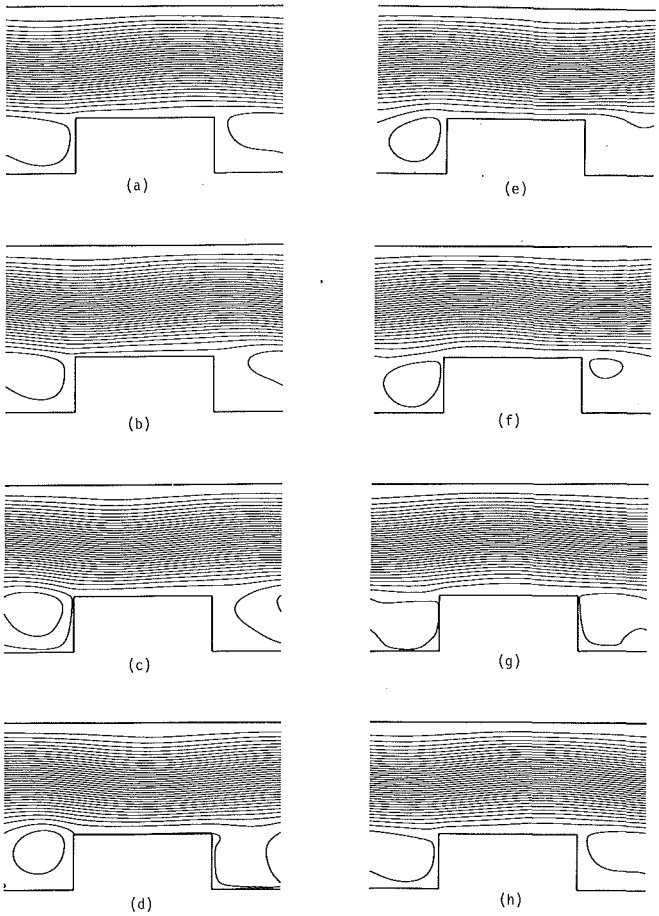


**Fig. 4 Supercritical streamline sequence at equally spaced time increments within one cycle of oscillation at Re = 592**

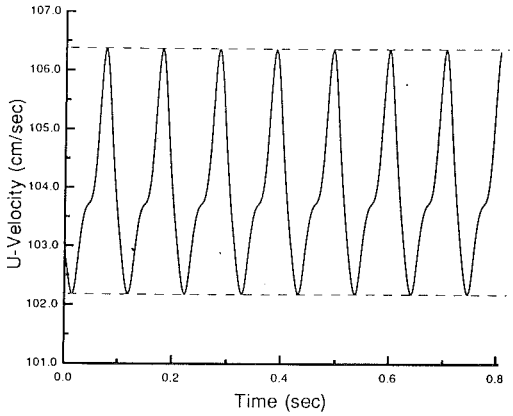


**Fig. 5 Time history of streamwise velocity at a point centered above the groove**

composed of one large recirculation zone that is segregated from the bypass region by a shear layer. As the Reynolds number is increased, additional momentum is imparted to the recirculating zone, increasing its rotational strength and displacing it downstream within the groove. This causes larger velocity gradients along the upstream rib face, while diminishing the velocity gradients along the downstream rib face. In the subcritical regime, the shear layer remains intact, preventing convective exchange of fluid between the groove and bypass regions.

For the grooved-channel geometry considered in this study, the critical Reynolds number for the onset of self-sustained oscillations is between 550 and 555. As the Reynolds number is increased above this critical value, the bypass and groove flows exhibit several important differences. The parallel streamlines of the subscritical bypass flow are replaced by a time-dependent sequence of curved streamlines (Fig. 4). These oscillations correspond to Tollmien-Schlichting traveling waves (Ghaddar et al., 1986a; Amon and Patera, 1989) with a frequency of 9.42 Hz for a Reynolds number of 592 in this geometry. The presence of self-sustained oscillations and the bounded periodic nature of the velocity fluctuations is verified by examining the time history of the U-velocity for a point centered above the groove (Fig. 5).

The transverse momentum carried by the wavy bypass flow induces a time-dependent boundary layer thickness at each streamwise location along the top wall. The effect upon the grooved wall is far more complex. First, the time-dependent transverse momentum of the traveling waves causes large-scale mixing within the bypass region. This large-scale mixing partially homogenizes the wake, resulting in a more uniform velocity distribution at the leading edge of the package. Second, the time-dependent interaction between the recirculating zones and the traveling waves results in an expansion of the upstream recirculating zone into the bypass region. This serves to divert the wake above the package and away from its leading edge (Figs. 4(*c–e*)). Furthermore, the bypass flow periodically penetrates through the shear layer into the groove region (Figs. 4(*d–f*)), resulting in a direct exchange of fluid. As the bypass flow enters the groove, it separates over the downstream corner of the rib (Fig. 4(*d*)), inducing the growth of a downstream recirculating zone (Figs. 4(*e, f*)). This recirculating zone grows and is displaced downstream until it contacts the preexisting recirculation zone (Fig. 4(*g*)). The two recirculation zones coalesce (Fig. 4(*a*)) and the sequence is periodically repeated in time, synchronized with the cycle of the traveling waves in the bypass region.

## Skin-Friction Coefficients

The effect of the time-dependent flow structure can be better understood by examining the wall shear stress. A nondimensional skin-friction coefficient is defined as the wall shear stress normalized by one-half the mean streamwise momentum of the bypass flow. A sign convention is adopted such that the direction of the velocity dictates the sign of the skin-friction coefficient. In this manner, rotational directions of recirculating zones can be clearly discerned.

The skin-friction coefficient distribution along the grooved wall, corresponding to the subcritical flow pattern of Fig. 3, is displayed in Fig. 6. The distribution along the top surface of the rib exhibits the classical behavior associated with boundary-layer growth, except in the vicinity of the downstream corner. The no-slip condition is relaxed after the flow separates from the rib, causing the fluid near the corner to accelerate, which increases the local skin friction. Additionally, the velocity deficit associated with the wake from the preceding package is evidenced by the finite value of skin friction at the leading edge of the package.

As previously noted, along the upstream rib face and groove, negative skin-friction coefficients correspond to clockwise rotation, while positive values indicate counter-clockwise rotation. The distribution along the upstream groove and rib face indicates the presence of a single, large clockwise-rotating recirculating zone. The magnitude of the skin-friction coefficient along the downstream rib face and groove is much lower than along the other surfaces for this Reynolds number. The large clockwise-rotating recirculating zone within the groove region is centered within the upstream portion of the groove, leading to smaller magnitudes of skin-friction coefficients.

The time-dependent skin-friction coefficient distribution

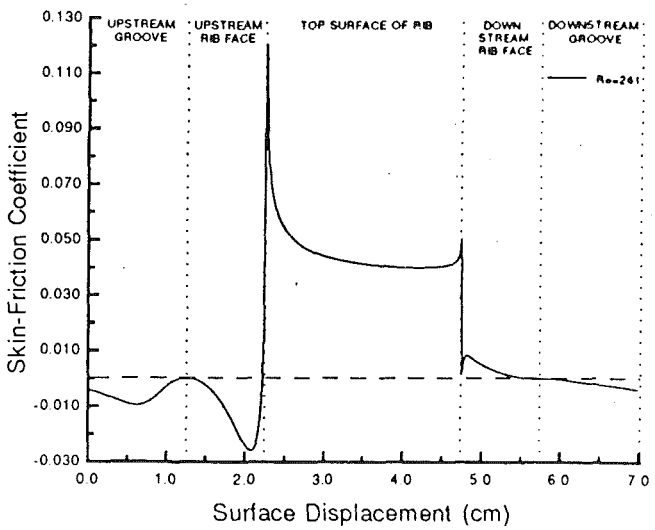


**Fig. 6 Subcritical skin-friction coefficient distribution at Re = 261**

corresponding to the supercritical flow regime (Fig. 4) is displayed in Fig. 7, for one cycle of oscillation. The magnitude of the skin-friction coefficient along the top surface of the rib is smaller for the supercritical flow than for the subcritical flow. This is a consequence of the increased streamwise momentum of the bypass flow without the small-scale mixing present in turbulent flows. Therefore, the velocity profile retains an essentially parabolic shape, leading to significantly less shear stress along the solid-fluid interface than in turbulent flows. This feature of transitional flows makes them particularly attractive relative to pumping power requirements. However, within the groove region, the magnitude of the shear stress increases because of the time-dependent disruption of the shear layer, which directly exposes the recirculating regions to the bypass flow. This time-dependent interaction causes the rotational strength of the recirculating zones to substantially increase, particularly so for the upstream recirculating zone.

The most discernible effect of the supercritical flow structure on the distribution of the skin-friction coefficient is the departure from the classical boundary-layer behavior along the top surface of the rib. The traveling waves affect the growth of the boundary layer along this surface through two mechanisms. The first is related to the interaction of the traveling waves with the recirculating zones in the groove. As previously described, for a portion of the periodic cycle, the upstream recirculating zone expands into the bypass region, diverting the wake over the top surface of the rib and displacing the reattachment point downstream. This results, for this portion of the flow sequence, in an increased skin-friction coefficient in the streamwise direction (Figs. 7(*d*, *e*)). The second effect is associated with the passing of the traveling waves crests and troughs. Namely, the transverse momentum of the traveling waves periodically compresses and expands the boundary layer, thereby increasing and decreasing the skin-friction with the position of the trough (Figs. 7(*e*, *f*)) and crest (Figs. 7 (*a*, *g*)), respectively.

The effect of the time-dependent supercritical flow structure upon the skin-friction coefficient distribution within the groove region is more complex. Recall that within the upstream portion of the groove, negative values of skin friction correspond to clockwise rotation, while within the downstream portion, clockwise rotation is indicated by negative values along the groove and positive values along the the rib face. The changes in sign that occur over a periodic cycle, along the groove surface, indicate that both counter-clockwise and clockwise rotating recirculating zones are created by the interaction between the traveling waves and the shear layer.

## Convection-Only Simulations

Next, the effect of the flow regime on the time-averaged difference between the surface and bulk-mean temperatures ($\Delta T$) is presented in Fig. 8. For the convection-only simulations, uniform heat flux at the solid-fluid interface is specified as the boundary condition. To satisfy this boundary condition, the wall temperature must adjust in accordance with the temperature of the fluid in the near-wall region of the boundary layer. Therefore, the temperature distribution along the wall is governed by a combination of the local fluid temperature and the wall shear stress, both being strongly related to upstream effects.

As shown in Fig. 8, the distributions of $\Delta T$ along the top surface of the rib are quite similar for all the Reynolds numbers explored. However, the largest $\Delta T$ is exhibited by the near critical Reynolds number case (Re = 550), followed by the subcritical (Re = 261) and then the supercritical cases (Re = 600, 693). As previously described, within the subcritical flow regime the wake from the preceding rib is not fully homogenized. Therefore, the thermal boundary layer initiates with a finite thickness. As the boundary layer grows along the rib surface, its temperature increases to compensate for the energy diffused away from the wall. In the supercritical case, the wake is more completely homogenized, requiring a lower surface temperature at the leading edge of the rib to satisfy the constant flux boundary condition. Additionally, the supercritical bypass flow induces higher diffusion rates along the top surface of the rib, resulting in a more rapid increase in wall temperature than in the subcritical cases.

As the flow becomes supercritical, the $\Delta T$ is substantially reduced due to the transverse momentum and time-dependent nature of the supercritical bypass flow. In fact, all of the surfaces along the grooved wall experience a reduction in temperature. The waviness of the supercritical flow structure results in transverse convective transport, inducing large-scale mixing and a reduction of the effects associated with the wake. It should be noted that the traveling waves do not fully homogenize the temperature distribution within the fluid, as in a turbulent flow, and upstream effects remain important in considering local transport behavior.

The variations in convective behavior along the grooved surface can be clearly visualized by examining the local distribution of the time-averaged Nusselt number, shown in Fig. 9. Along the top surface of the rib, the Nusselt numbers decrease slightly with Reynolds number throughout the subcritical regime. However, this behavior reverses in the supercritical flow regime, as the Nusselt number increases significantly with Reynolds number. The Nusselt number within the groove region continuously increases with Reynolds number for both subcritical and supercritical flows, suggesting that the recirculating flow patterns within the groove significantly minimize any resistance associated with upstream effects.

In summary, the supercritical flow structure increases convective heat transport through three mechanisms. First, the traveling waves in the bypass region induce fluctuations in the velocity components. These fluctuations periodically increase the shear stress substantially above subscritical values, resulting in increased diffusion at the solid-fluid interface. Second, the supercritical bypass flow contains fluctuations in normal velocity, which partially homogenize the temperature distribution within the bypass flow and wake. Last, the supercritical flow structure disrupts the shear layer separating the groove and bypass flows. This disruption results in direct convective exchange between the groove and bypass flows, increasing surface transport rates. Therefore, the supercritical flow structure increases heat transport by both increasing diffusion at the solid-fluid interface and inducing large-scale mixing within and between the groove and bypass regions.

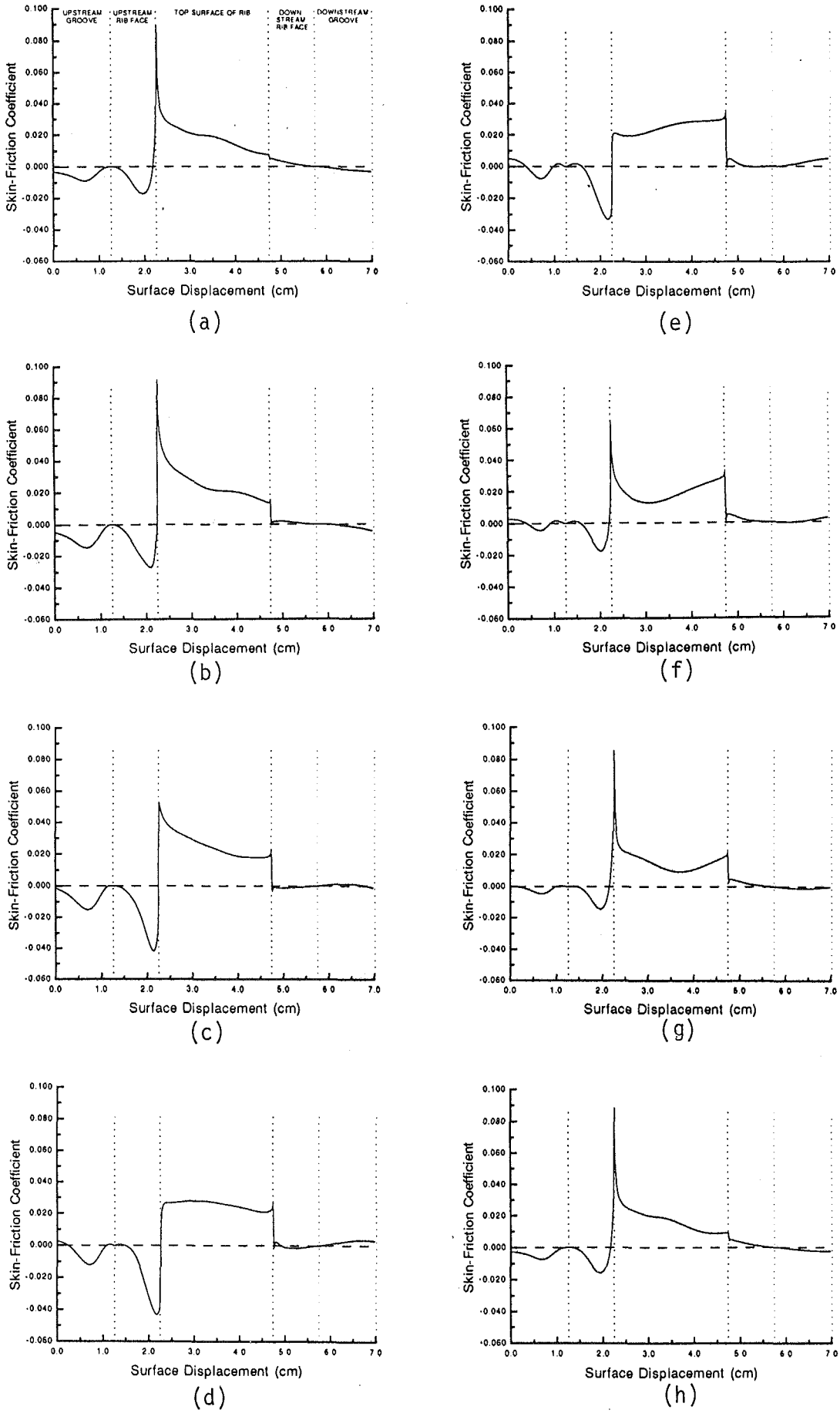


**Fig. 7 Supercritical skin-friction coefficient distribution within one cycle of oscillation at Re = 592**

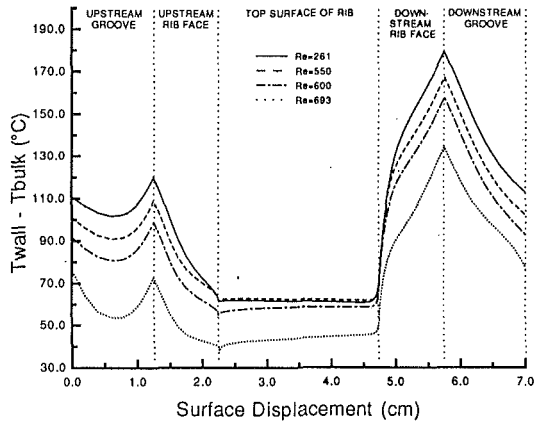


Fig. 8 $T_{wall} - T_{bulk}$ versus surface displacement for convection-only simulations

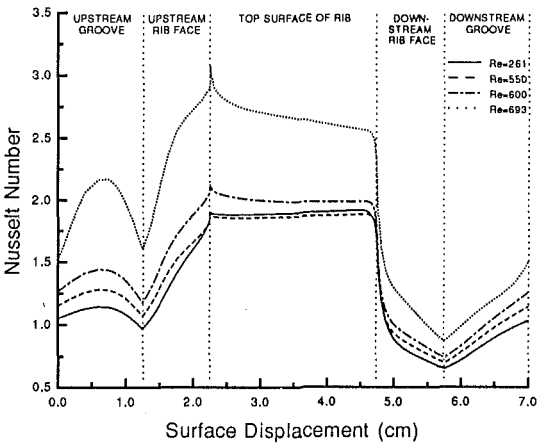


Fig. 9 Time-averaged Nusselt number distribution for convection-only simulations

## Conjugate Conduction/Convection Simulations

In the conjugate simulations, heat is generated within the chip, conducted through the package to the surface, and convected into the cooling fluid. The local thermal-fluid characteristics, as well as the composition and distribution of heat generation within the solid region dictate the local convective performance. Consequently, because of the additional internal resistances, the surface temperature distribution (Fig. 10) exhibits a different pattern than in the convection-only simulations (Fig. 8). The concentrated heat generation produces a maximum $\Delta T$ directly above the location of the chip. This differs from the convection-only simulations in which the top surface of the rib displays the lowest $\Delta T$ and the groove surface the highest. In fact, for the conjugate case, the groove surface displays the lowest $\Delta T$.

Contrary to the convection-only case, the $\Delta T$ increases from the subcritical to the supercritical flow regime, for the range of Reynolds numbers explored. In the convection-only case, the uniform flux boundary condition applied at the solid-fluid interface mandates that the product of the heat transfer coefficient and the temperature difference be constant. At supercritical Reynolds numbers, higher heat transfer coefficients result because of the combination of better flow homogenization and higher diffusive rates. Therefore, the $\Delta T$ must decrease to satisfy the uniform heat-flux boundary condition. However, the conjugate problem must satisfy a different boundary condition, namely continuity of flux and temperature at the solid-fluid interface. As the Reynolds number increases within the range of this study, more heat is convected from the package surface (Fig. 12), causing larger internal temperature gradients. To satisfy the continuity of flux boundary condition, the temperature gradient within the fluid must similarly increase. Physically, as heat is removed from the package by the cooling fluid, the bulk temperature increases. Therefore, the surface temperature must likewise increase in order to maintain the temperature gradient at the solid-fluid interface.

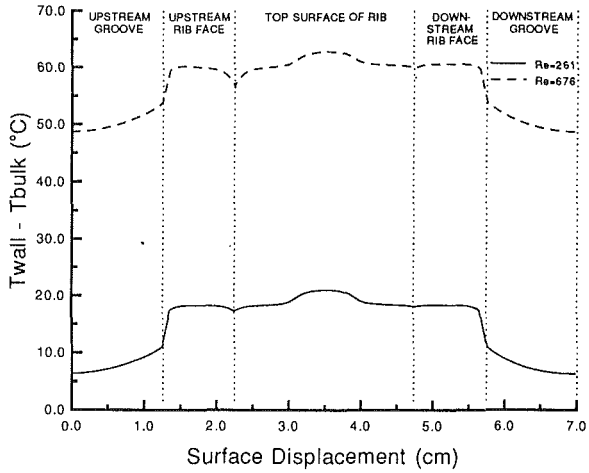


Fig. 10 $T_{wall} - T_{bulk}$ versus surface displacement for conjugate simulations

The time-averaged local Nusselt number distribution along the grooved wall, for the conjugate simulation, is shown in Fig. 11. The fluid contained within the groove region is convectively heated along the upstream and downstream rib faces. In the subcritical case, the shear layer separating the groove and bypass flows remains intact, prohibiting convective exchange of fluid. Therefore, the recirculating fluid becomes hotter than the groove surface temperature. This temperature gradient causes heat to be transferred from the fluid to the groove surface, producing negative values of Nusselt number along the upstream and downstream groove surfaces (Fig. 11). As the bypass flow becomes oscillatory and disrupts the shear layer, the fluid within the groove is convectively cooled. Therefore, the temperature gradient along the groove surface is reduced and the Nusselt numbers become increasingly less negative. It should be noted that in three-dimensional configurations, the thermal gradients would be lower because of convection from the sides of the groove region, an important effect not captured by the two-dimensional model.

A local rise in Nusselt number occurs along the exposed surface corresponding to the location of the solder. This local increase is a consequence of the nonintimate contact between the PCB and the package, which reduces the convective resistance to the cooling fluid, relative to the conductive resistance into the PCB.

The distribution of Nusselt number along the top of the rib is affected by the thermal wake from the preceding rib, the growth of the boundary layer, the material composition of the package, and the location of heat generation. The combination of these effects leads to an exponential decline from the upstream to the downstream corner, with a local rise directly over the location of the chip.

Although the distributions and magnitudes of Nusselt numbers for both the subcritical and supercritical flow regimes are similar, the total amount of heat transferred to the fluid is quite different. This can be seen by examining the spatial distribution of the heat flux along the solid-fluid interface (Fig. 12). The increase in shear stress caused by the oscillatory flow,

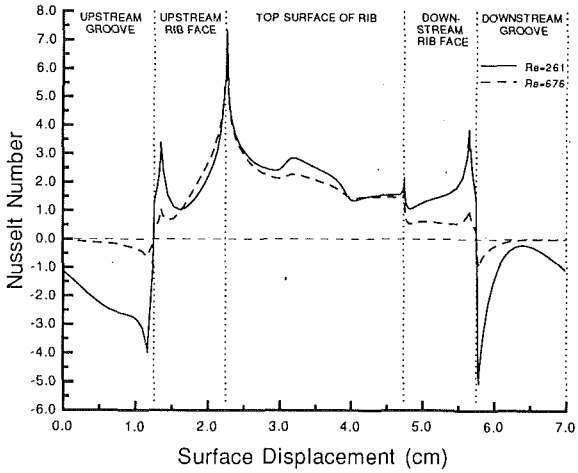


Fig. 11 Time-averaged Nusselt number distribution for conjugate simulations

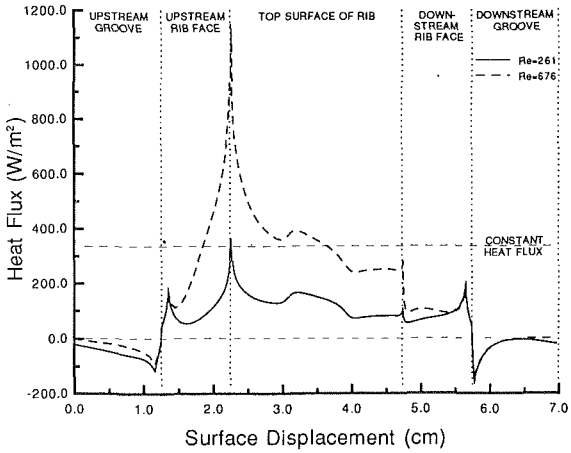


Fig. 12 Heat flux versus surface displacement for conjugate simulations

most significantly affects both the upstream rib face and the top surface of the rib (Fig. 7). A corresponding increase in heat flux is clearly depicted in the distributions along these surfaces. It should be noted that the heat flux specified as a boundary condition for convection-only simulations is independent of Reynolds number. However, for the conjugate case, the heat flux obtained at the solid-fluid interface is 58.59 W/$m^2$ and 180.25 W/$m^2$, for the subcritical (Re = 261) and supercritical (Re = 676) flows, respectively. Therefore, the heat flux at the solid-fluid interface is strongly dependent upon the Reynolds number and is not accounted for in the convection-only case. The remaining energy not transferred to the cooling fluid is conducted through the PCB to the next upstream package, thereby, satisfying global energy conservation.

## Conclusions

Forced convective heat exchangers consisting of complex, multimaterial solid domains with concentrated heat generation exhibit different thermal performance than uniform heat-flux representations. In fact, thermal performance characteristics, such as heat being transferred from the fluid to the groove surface and local variations along the rib surfaces, are absent from the uniform heat-flux approximation. In applications with imposed limits on thermal gradients or local temperatures, neglecting these conjugate effects may result in unacceptable cooling behavior. Additionally, it has been shown that increases in the Reynolds number produce varied transport effects dependent upon both the geometric region and flow regime.

The importance of considering time-dependent flow characteristics, the significance of increasing the Reynolds number from a time-invariant subcritical to a time-dependent supercritical flow regime, and the mechanisms for supercritical heat transport enhancement are identified. Similarly, conjugate conduction/convection effects are demonstrated to significantly influence heat transport and need to be accounted for in the design and analysis of heat exchanger configurations, such as those found in the electronic equipment.

## Acknowledgment

*This work has been supported by the Engineering Design Research Center, a National Science Foundation/Engineering Research Center, under cooperative agreement EDC-8943164 and by the National Science Foundation Grant CTS-9311072.*

## References

Aghazadeh, M., and Mallik, D., 1990, "Thermal Characteristics of Single and Multilayer High Performance PQFD Packages," *IEEE Trans. Comps., Hydrids, Manuf. Technol.*, Vol. 13, No. 4, pp. 975–979.

Amon, C. H., 1993, "Spectral Element-Fourier Method for Transitional Flows in Complex Geometries," *AIAA Journal*, Vol. 31, No. 1, pp. 42–48.

Amon, C. H., and Mikic, B. B., 1991, "Spectral Element Simulations of Unsteady Forced Convective Heat Transfer: Application to Compact Heat Exchanger Geometries," *Numerical Heat Transfer*, Part A, Vol. 19, pp. 1–19.

Amon, C. H., and Patera, A. T., 1989, "Numerical Calculation of Stable Three-Dimensional Tertiary States in Grooved-Channel Flow," *Physics of Fluids A*, Vol. 1, No. 12, pp. 2001–2009.

Chyu, M. K., Natarajan, V., and Chiou, J. S., 1993, "Heat Transfer from Arrays of Cubes Exposed to an External Boundary Layer Flow," *Enhanced Cooling Techniques for Electronics Applications*, ASME HTD-Vol. 263, pp. 79–87.

Davalath, J., and Bayazitoglu, Y., 1987, "Forced Convection Cooling Across Rectangular Blocks," ASME *Journal of Heat Transfer*, Vol. 109, pp. 321–328.

Garimella, S. V., and Eibeck, P. A., 1990, "Heat Transfer Characteristics of an Array of Protruding Elements in Single Phase Forced Convection," *International Journal of Heat Mass Transfer*, Vol. 33, No. 12, pp. 2659–2669.

Garimella, S. V., and Eibeck, P. A., 1991, "Effect of Spanwise Spacing on the Heat Transfer from an Array of Protruding Elements in Forced Convection," *International Journal of Heat Mass Transfer*, Vol. 34, No. 9, pp. 2427–2430.

Ghaddar, N. K., Korczak, K. Z., Mikic, B. B., and Patera, A. T., 1986a, "Numerical Investigation of Incompressible Flow in Grooved Channels. Part 1. Stability and Self-Sustained Oscillations," *Journal of Fluid Mechanics*, Vol. 163, pp. 99–127.

Ghaddar, N. K., Magen, M., Mikic, B. B., and Patera, A. T., 1986b, "Numerical Investigation of Incompressible Flow in Grooved Channels. Part 2. Resonance and Oscillatory Heat-Transfer Enhancement," *Journal of Fluid Mechanics*, Vol. 168, pp. 541–567.

Greiner, M., Chen, R.-F., and Wirtz, R. A., 1990, "Heat Transfer Augmentation Through Wall-Shape-Induced Flow Destabilization," *Journal of Heat Transfer*, Vol. 112, pp. 336–341.

Hardisty, H., and Abboud, J. B., 1987, "Thermal Analysis of a Dual-in-Line Package using the Finite Element Method," *IEEE Proc., Part 1: Solid State and Electronic Devices*, Vol. 134, No. 1, pp. 23–31.

Humphrey, J. A. C., Devaraknoda, R., and Queipo, N., 1993, "Interactive Computational-Experimental Methodologies (ICEME) for Thermofluids Research: Application to the Optimized Packaging of Heated Electronic Components," *Computers and Computing in Heat Transfer Science and Engineering*, W. Nakayama and K. T. Yang, eds., CRC Press, Begell House, pp. 293–317.

Lehmann, G. L., and Wirtz, R. A., 1985, "The Effect of Variations in Stream-Wise Spacing and Length on Convection from Surface Mounted Rectangular Components," *Heat Transfer in Electronic Equipment*, HTD-Vol. 48, pp. 39–47.

Majumdar, D., and Amon, C. H., 1992, "Heat and Momentum Transport in Oscillatory Viscous Flows," ASME *Journal of Heat Transfer*, Vol. 114, pp. 866–875.

Moffat, R. J., and Ortega, A., 1988, "Direct Air-Cooling of Electronic Components," *Advances in Thermal Modeling of Electronic Components and Systems*, Vol. 1, Avram Bar-Cohen and Allan D. Kraus, eds., Hemisphere Publishing, New York, pp. 129–282.

Nigen, J. S., and Amon, C. H., 1991, "Forced Convective Cooling Enhancement of Surface-Mounted Electronic Package Configurations through Self-Sustained Oscillatory Flows," *Heat Transfer in Electronic Equipment*, ASME HTD-Vol. 171, pp. 39–46.

Nigen, J. S., and Amon, C. H., 1992, "Concurrent Thermal Designs of PCB's:

Balancing Accuracy with Time Constraints," *IEEE Trans. Comps., Hybrids, Manuf. Technol.*, Vol. 15, No. 5, pp. 850–859.

Patankar, S. V., Liu, C. H., and Sparrow, E. M., 1977, "Fully Developed Flow and Heat Transfer in Ducts Having Streamwise Periodic Variation of Cross Section," ASME *Journal of Heat Transfer*, Vol. 99, pp. 180–186.

Patera, A. T., 1984, "A Spectral Element Method for Fluid Dynamics: Laminar Flow in a Channel Expansion," *Journal of Computational Physics*, Vol. 54, pp. 468–488.

Pereira, J. C. F., and Sousa, J. M. M., 1993, "Finite Volume Calculations of Self-Sustained Oscillations in a Grooved Channel," *Journal of Computational Physics*, Vol. 106, pp. 19–29.

Stephanoff, K. D., Sobey, I. J., and Bellhouse, B. J., 1980, "On Flow Through Furrowed Channels. Part 2. Observed Flow Patterns," *Journal of Fluid Mechanics*, Vol. 96, pp. 27–32.

Yovanovich, M. M., and Antonetti, V. W., 1988, "Application of Thermal Contact Resistance Theory to Electronic Packages," *Advances in Thermal Modeling of Electronic Components and Systems*, Vol. 1, Avram Bar-Cohen and Allan D. Kraus, eds., Hemisphere Publishing, New York, pp. 79–128.

Yuan, T. D., 1992, "Thermal Modeling of Integrated Heat Exchangers with Alternating Ribs," *Proc. Inter. Society Conf. on Thermal Phenomena in Electronic Systems: I-Therm III*, pp. 96–101.

Zebib, A., and Wo, Y. K., 1989, "A Two-Dimensional Conjugate Heat Transfer Model for Forced Air Cooling of an Electronic Device," ASME *Journal of Electronic Packaging*, Vol. 111, pp. 41–45.

# Evaluation of Flip-Flop Jet Nozzles for Use as Practical Excitation Devices

**Ganesh Raman**
Senior Research Engineer,
NYMA, Inc.,
NASA Lewis Research Center Group,
Brookpark, OH 44142

**Edward J. Rice**
Lewis Distinguished Research Associate,
Retired.
NASA Lewis Research Center,
Cleveland, OH 44135

**David M. Cornelius**
OAI/NASA Summer Student Intern,
Department of Aeronautics and Astronautics,
Stanford University,
Stanford, CA 94305

*This paper describes the flowfield characteristics of the flip-flop jet nozzle and the potential for using this nozzle as a practical excitation device. It appears from the existing body of published information that there is a lack of data on the parameters affecting the operation of such nozzles and on the mechanism of operation of these nozzles. An attempt is made in the present work to study the important parameters affecting the operation and performance of a flip-flop jet nozzle. Measurements were carried out to systematically assess the effect of varying the nozzle pressure ratio (NPR) as well as the length and volume of the feedback tube on the frequency of oscillation of this device. Flow visualization was used to obtain a better understanding of the jet flowfield and of the processes occurring within the feedback tube. The frequency of oscillation of the flip-flop jet depended significantly on the feedback tube length and volume as well as on the nozzle pressure ratio. In contrast, the coherent velocity perturbation levels did not depend on the above-mentioned parameters. The data presented in this paper would be useful for modeling such flip-flop excitation devices that are potentially useful for controlling practical shear flows.*

## Introduction

Although evidence of the use of fluid power dates back to ancient civilization (Tokaty, 1971; Morris, 1973), only recently has significant progress been made in the development of control devices that do not use moving parts, for example; turbulence amplifiers, wall attachment devices, active and passive momentum interaction devices, and vortex devices (see Morris, 1973). In the 1970's fluid control techniques were applied to jet nozzles in a pioneering paper on "flip-flop jet nozzles" by Viets (1975) and Viets et al. (1975a). Despite all the work that exists in this area, the understanding of the operation of such devices is far from complete.

The potential for using flip-flop jets for the control of practical shear flows is the driving force behind the present investigation. Methods such as acoustic excitation (Crow and Champagne, 1971; Ahuja et al., 1982; Raman and Rice, 1991) used for controlling shear flows in fundamental research experiments are not likely to be effective under practical conditions. In recent years, a variety of novel fluid flow control devices have been developed. Examples of such devices are the whistler nozzle (Hill and Greene, 1977), tabs at the jet exit (Ahuja and Brown, 1989; Zaman et al., 1994), suction at the jet exit periphery (Strykowski et al., 1992) and transverse injection using auxiliary jets (Davis, 1982). Other recent concepts include bifurcating jets (Parekh et al., 1987), hydrodynamic excitation (Brown and Ahuja, 1990), the use of piezoelectric actuators (Wiltse and Glezer, 1993), and the use of artificially induced screech (Rice and Raman, 1993). The flip-flop jet provides yet another possibility for the control of practical flows. In pursuit of the above goal there has been a recent renewal of interest in flip-flop jets (Schreck, 1992; Raman et al., 1993; and Raman and Rice, 1993). Other applications of flip-flop jets such as in two-phase flow (Morris et al., 1992) and in foam spreading (Viets et al., 1975b) have also been reported.

The parameters affecting the operation of a bistable fluid amplifier and a wall attachment fluidic oscillator were studied by Warren (1962) and Beale and Lawyer (1974), respectively. Subsequent work by Viets (1975) and Viets et al. (1975a) suggested that the nozzle pressure ratio as well as feedback tube length and volume played a role in determining the frequency of the flip-flop jet, but no clear relationships were established. The objective of the present work is to study the effect of the nozzle pressure ratio (NPR = ratio of plenum pressure to ambient pressure, $P_o/P_a$) and feedback tube length and volume on the operation of the flip-flop jet nozzle.

## Experimental Details

The research facility included a plenum tank (15.24 cm diameter, 1.82 m long) to which various nozzles could be attached. The plenum tank was supplied by compressed air at pressures up to 350 kPa (50 Psig) at 80°F. After passing through a filter that removed any dirt or dust that might break the hot-

Contributed by the Fluids Engineering Division for publication in the JOURNAL OF FLUIDS ENGINEERING. Manuscript received by the Fluids Engineering Division October 21, 1993; revised manuscript received April 24, 1994. Associate Technical Editor: Wing-Fai Ng.

Table 1 Description of nozzle parameter

| NOZZLE PARAMETER | SYMBOL | LARGE SCALE NOZZLE DIMENSION (mm, cubic mm) | MINIATURE NOZZLE DIMENSIONS (mm, cubic mm) |
|---|---|---|---|
| Smaller Dimension of Inner Nozzle | h | 6.35 | 2.34 |
| Larger Dimension of Inner Nozzle | b | 69.85 | 19.05 |
| Aspect Ratio (b/h) | s | 11.0 | 8.15 |
| Smaller Dimension of Flip-Flop Attachment | H | 26.98 | 7.0 |
| Larger Dimension of Flip-Flop Attachment | B | 69.85 | 19.05 |
| Aspect Ratio (B/H) | S | 2.58 | 2.72 |
| Width of Feedback Slot | w | 25.4 | 3.17 |
| Axial Dimension of Flip-Flop Attachment | $L_{ff}$ | 25.4 | 15.87 |
| Length of Feedback Tube | L | 444.5 | 304.8-1625.6 |
| Diameter of Feedback Tube | d | 43.88 ($d_e$) | 9.5-19.1 |
| Volume of Feedback Tube | Vol | 672,194 | 21,604-465,596 |
| Nozzle Pressure Ratio | NPR | Flow Visualization Only | 1.3-2.0 |
| Exit Geometry | - | Divergent Walls 3.6° Half Angle | Divergent Walls 5° Half Angle |

film probes, the air entered the plenum axially. The nozzle pressure ratio was varied by changing the plenum pressure. The plenum also had pipe fittings for injecting smoke for the visualization studies. The streamwise velocity (mean and fluctuating) was measured using a single sensor hot-film probe (TSI Inc. model 1210-20) in conjunction with Dantec 55M01 and 55M10 circuits and a Dantec 55M25 linearizer. The single hot-film probe was oriented such that it was most sensitive to the streamwise velocity. The large scale flip-flop nozzle described in Table I and shown in Fig. 1(*a*), was used only for the flow visualization study. For the parametric study, a miniature nozzle (Fig. 1(*b*) and 1(*c*)) was used. The nozzle has three parts: the convergent rectangular slot nozzle, a nozzle attachment with control ports, and a feedback tube that connects the control ports. The exit (center) of the inner rectangular nozzle is the origin of the coordinate system shown in Fig. 1(*a*). The frequency of pressure oscillation in the feedback tube was measured using one of the piezoresistive pressure transducers (see Fig. 1(*b*)). The unsteady velocity and pressure signals were analyzed using a 2 channel B&K spectrum analyzer.

## Results and Discussion

**Flowfield Characteristics.** Figure 2 shows smoke flow visualization photographs of the flip-flop jet. The visualization was carried out at very low speeds (~10 m/s) and was made possible by filling the plenum chamber with smoke and illuminating the flowfield with bright continuous light (750 W). The still pictures cover an axial extent of up to $x/h = 25$ and show the two phases of oscillation of the jet. During phase 1, the jet is attached to the bottom wall and during the other phase to the top wall. The details of the operation of such nozzles will be discussed in a later section.

Figure 3(*a*) shows the mean velocity contours in the flip-flop jet flow-field when the jet was operated at a NPR of 1.02. In Fig. 3(*a*) the mean velocity is expressed as a fraction of the jet's exit velocity. It is to be noted that the potential core is virtually absent due to the oscillation of the jet in the transverse direction. The outer edge of the jet is denoted by the $\overline{U}/\overline{U}_e = 0.03$ contour. Due to flow reversals near the outer edge of the jet the hot-film measurements are not meaningful for lower velocities. The total velocity fluctuations in the jet are

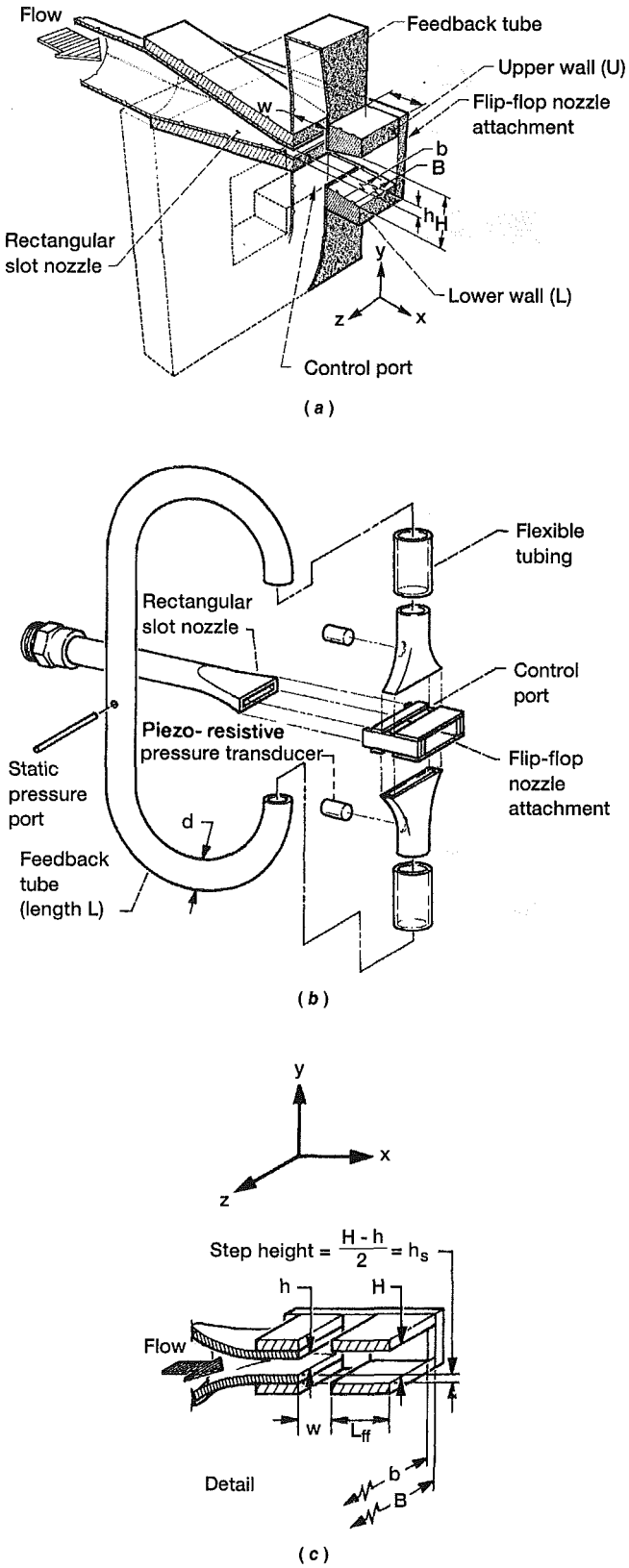


**Fig. 1 Schematic of flip-flop jet nozzle. (*a*) Large scale flip-flop nozzle; (*b*) miniature flip-flop nozzle; (*c*) detail of miniature scale nozzle.**

shown in Fig. 3(*b*). The velocity fluctuation level in the contour plot is expressed as a percentage of the jet exit velocity. The velocity fluctuations shown in Fig. 3(*b*) include the coherent oscillations due to the flapping of the jet as well as randomly occurring velocity fluctuations attributed to fine scale turbu-

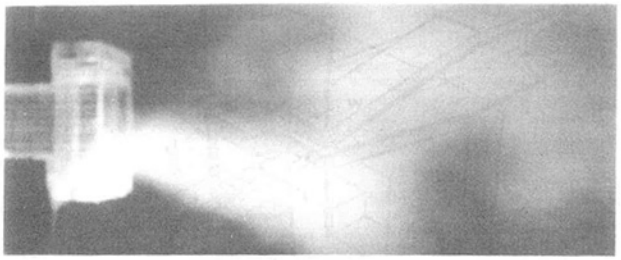

(a)

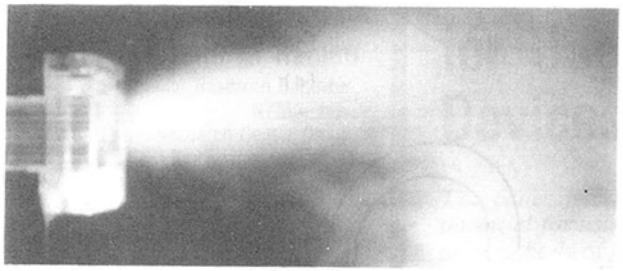

(b)

Fig. 2 Flow visualization of the two phases of oscillation. (*a*) Phase 1 of oscillation; (*b*) Phase 2 of oscillation.

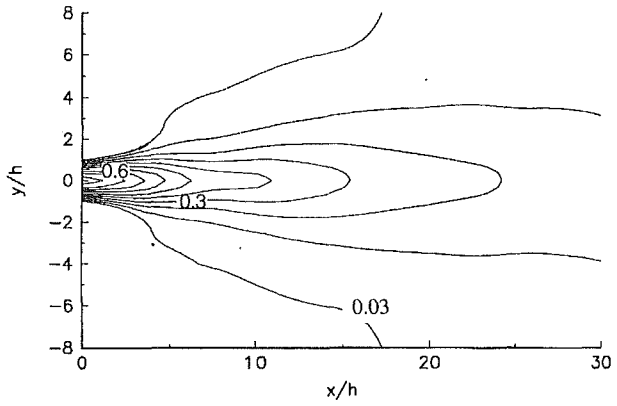


(a)

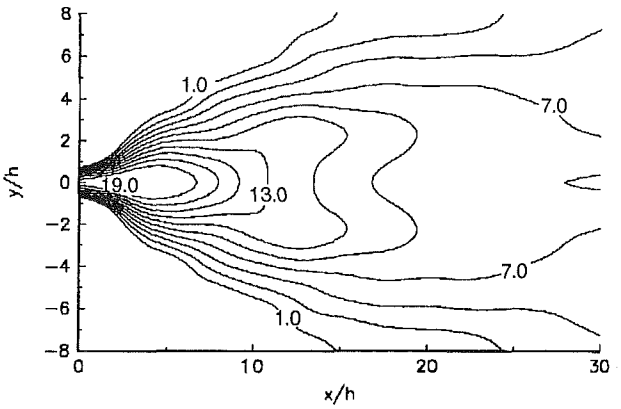


(b)

Fig. 3 Characterization of the flow-field of a flip-flop jet. (*a*) Contours of mean velocity; (*b*) contours of total fluctuating velocity level.

lence. The coherent velocity fluctuations could be occurring at the flapping frequency and at its harmonics. Figure 4(*a*) shows the coherent fluctuating velocity level in the flip-flop jet. The coherent velocities were obtained by signal enhancement with respect to a reference hot-film probe signal. The reference probe (hot-film) was located in the shear layer close to the jet exit ($x/h \simeq 0$, $y/h = 1.5$, $z/h = 0$). The measurement probe (hot-film) was moved throughout the flowfield in the $xy$ plane ($z/h = 0$). The signal enhancement process can be explained by assuming that a time varying signal, $A(t)$, consists of a periodic part, $p(t)$, and uncorrelated noise, $n(t)$. When a cross-spectrum average is obtained between the measurement probe signal and the reference probe signal the periodic part adds coherently (amplitude summation) and the uncorrelated random noise adds incoherently (power summation). Thus, after many averages the random part is averaged out and the coherent part is extracted. From Fig. 4(*a*) it can be seen that very high coherent fluctuation levels can be obtained even far downstream from the jet's exit. It is this feature of the flip-flop jet that makes it attractive for use as an excitation device in practical flows. Figure 4(*b*) shows the relative phase (obtained from the phase of the averaged cross-spectrum) between the stationary probe and the traversed probe. It is clear that events occurring on either side of the jet are 180° out-of-phase. This is proof that the flapping persists even at downstream stations. Note that for the data presented in Figs. 3 and 4 the errors are large (~ 10%) for $x/h < 5$. Details of experimental errors are provided in the section on "Estimates of Measurement Uncertainty."

## Observations on the Mechanism of Operation

When the jet from the inner nozzle (see Fig. 1(*b*)) exhausts into the region between the two plates of the flip-flop attachment, a small pressure gradient could cause the jet to attach (or detach) from either wall. With the help of the feedback tube this process repeats and results in an oscillating jet flow. An explanation for the operation of such nozzles based on wave propagation in the feedback tube was first provided by Viets (1975). However, his paper also stated that such an explanation would not be adequate for short feedback tubes. The frequencies of oscillation measured in the present work, however, are much lower than the frequencies expected based on the length of the feedback tube and the speed of propagation of pressure waves (sound) in the feedback tube. This suggests that for the lengths used in the present work the phenomenon is not controlled only by wave propagation. This also indicates that additional processes would have to be considered in order to provide a complete explanation of the operation of the flip-flop jet nozzle. In this context it needs to be mentioned that Viets et al. (1975a) did indicate that the volume of the feedback tube could be a factor, but their work did not attempt to assess the influence of this factor, nor did they document the volumes of the feedback tubes used in their work.

## Relationship Between Events in the Feedback Tube and in the Shear Layer

Figure 5 shows flow visualization photographs of the events at the nozzle exit. Smoke is injected near the nozzle lip using an external tube. The two phases shown in Figs. 5(*a*) and 5(*b*) correspond to the two phases of jet oscillation shown in Figs. 2(*a*) and 2(*b*). Figure 5(*a*) shows smoke being drawn into the nozzle when the jet in 2(*a*) is attached to the bottom and 5(*b*) shows smoke being blown away when the jet in 2(*b*) flips to the top.

The unsteady pressure time traces measured on either side of the feedback tube displayed a sinusoidal shape with a pressure difference of about 14.2 kPa at a nozzle pressure ratio of 1.8. When the jet was attached to the lower wall, the absolute pressure at that control port was measured to be 53.25 kPa, while the corresponding pressure at the other port was 67.45 kPa. Since the two control ports are connected by the feedback tube, the equalization of pressure occurs by a certain mass of

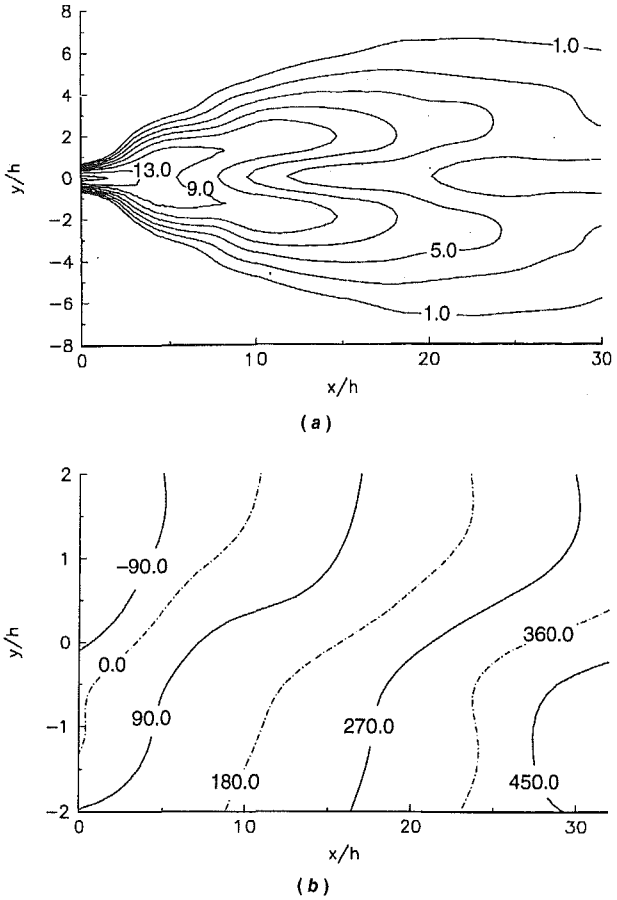


**Fig. 4 Characterization of velocity fluctuations at the frequency of oscillation of the flip-flop jet. (*a*) Contours of coherent velocity fluctuation levels; (*b*) relative phase between fixed and traversed probes.**

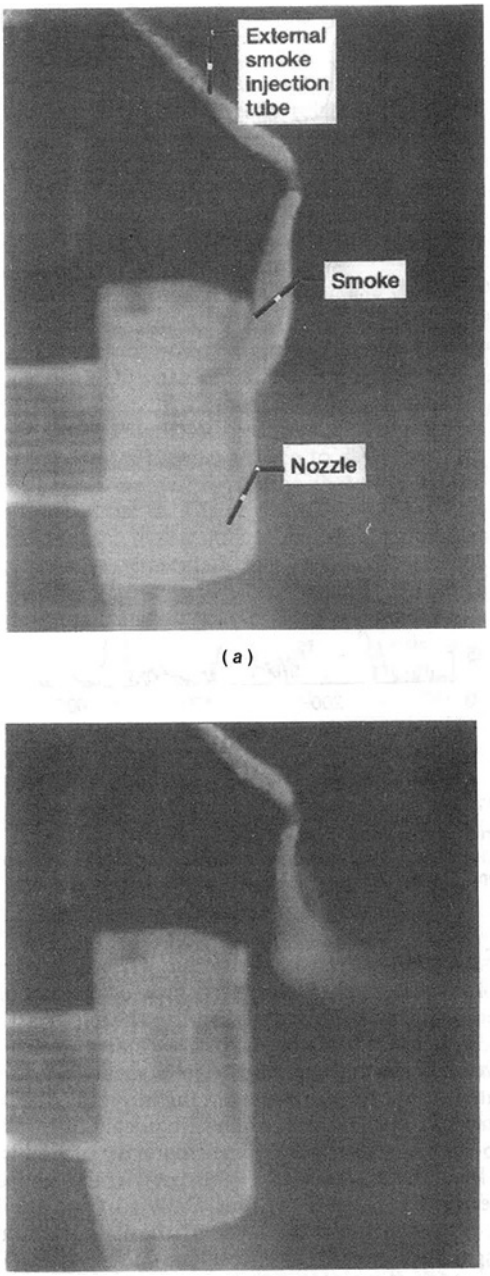


**Fig. 5 Flow visualization of events at the nozzle exit. (*a*) Smoke being drawn into the nozzle at the top; (*b*) smoke being blown away from the nozzle at the top.**

fluid being drawn in through port 2 (shown by the inflow of smoke into the nozzle in Fig. 5(*a*)). The equalization of pressure causes the jet to detach from the lower wall and attach to the upper wall (shown by smoke being blown away near the upper wall in Fig. 5(*b*)). The process then repeats itself.

In an attempt to visualize the events within the feedback tube, another experiment was performed. The feedback tube (metal) was replaced with a transparent tygon tube with a small column of alcohol in the tube. When the flip-flop nozzle was run in this condition, the column of alcohol was visually seen to oscillate at the frequency at which the jet flapped. As the nozzle pressure ratio was increased, the oscillation frequency of the column of alcohol increased as did its amplitude of oscillation (displacement of the alcohol column from its equilibrium position). It should be noted here that while the frequency of oscillation of the alcohol column is an indication of the frequency of flapping of the jet, the amplitude of oscillation is an indication of the volume of air that is alternately being pumped from one side to another during alternate pressure equalization. Although the trends were clear, it was not possible to keep track of the change of frequency and changes in the amplitude of oscillation of the alcohol column for small changes in nozzle pressure ratio. Therefore all the observations should be interpreted with caution and treated as qualitative. It should be pointed out that at a given nozzle pressure ratio, the nozzle with alcohol in the feedback tube oscillated at a lower frequency than the nozzle with no alcohol in the feedback tube. Although the alcohol does interfere with the process, it at least provides a qualitative picture of what is happening.

Figure 6(*a*) shows a spectrum from a hot-film probe located near the jet exit shear layer. The hot-film was positioned at the transverse location where the maximum velocity fluctuation was recorded. Figure 6(*b*) shows a spectrum from the piezoresistive pressure transducer in the feedback tube. Figures 6(*a*) and 6(*b*) represent simultaneous averaged spectra of velocity oscillations in the shear layer and pressure oscillations in the feedback tube. In both measurements the same dominant frequency ($f$) and three harmonics ($2f$, $3f$, and $4f$) were observed. Figure 6(*c*) represents the linear spectral coherence between the two signals. The following notation is necessary to introduce the linear spectral coherence. For two signals (varying with time), $A(t)$ and $B(t)$, autospectra, $G_{AA}$ and $G_{BB}$, can be represented as $A(f) \cdot A^*(f)$ and $B(f) \cdot B^*(f)$, respectively. Note that '$f$' denotes the frequency domain, the overbar denotes an average value, and the asterisk the complex conjugate. The cross-spectrum $G_{AB}$ can be represented as $\overline{A^*(f) \cdot B(f)}$. The linear spectral coherence, $\gamma^2(f)$, is defined to be

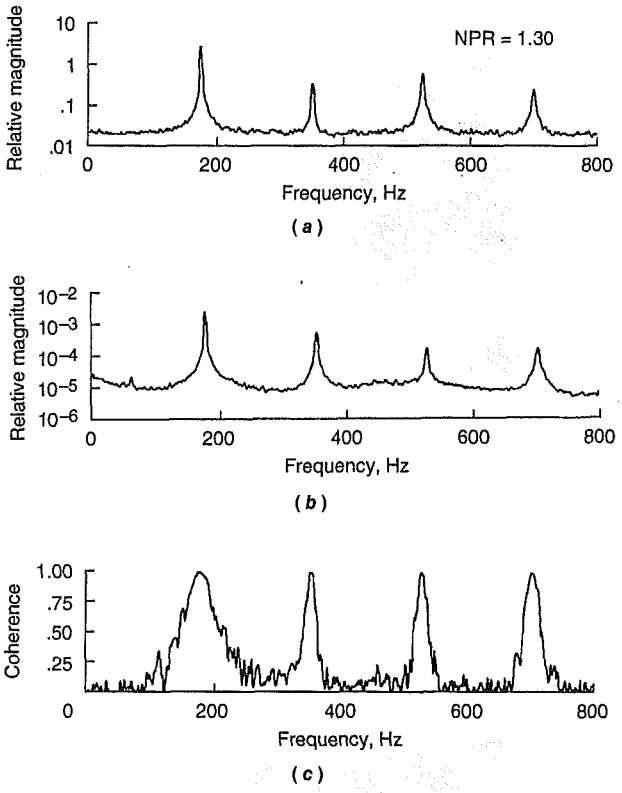


**Fig. 6 Velocity and pressure spectra. (*a*) Spectrum of unsteady velocity measured in the shear layer at the jet exit; (*b*) spectrum of pressure oscillations measured in the feedback tube; (*c*) linear spectral coherence function.**

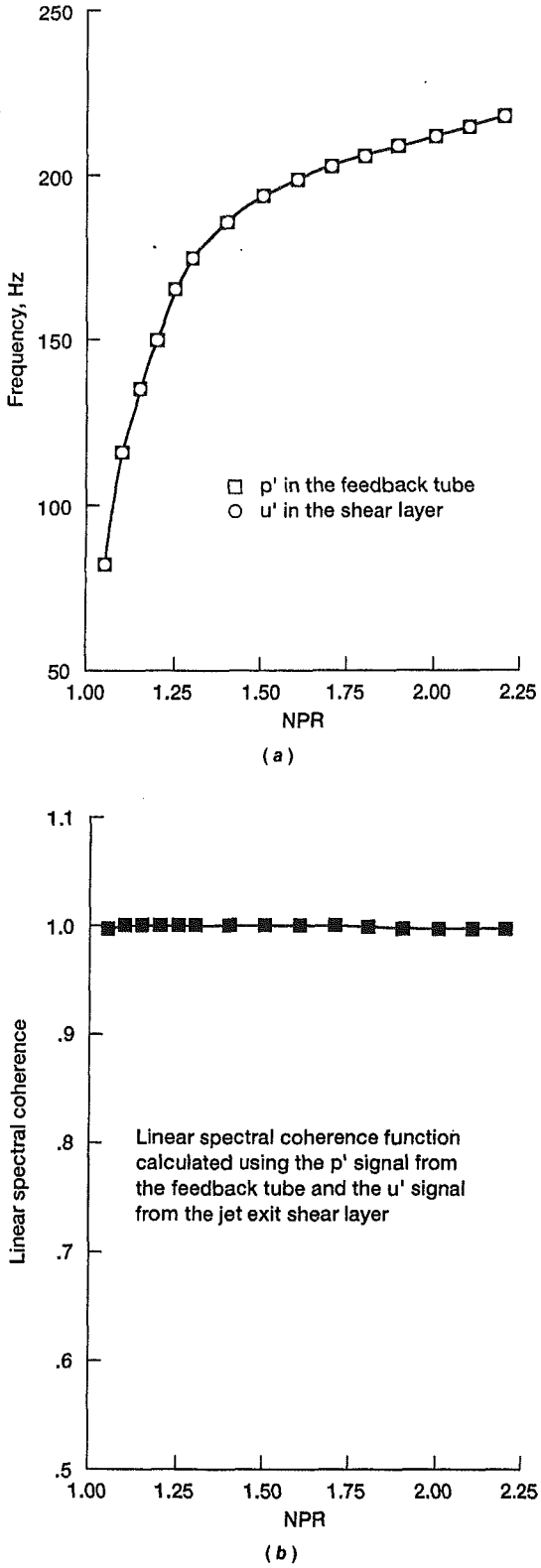


**Fig. 7 Relationship between pressure oscillations in the feedback tube and velocity perturbations in the shear layer at various nozzle pressure ratios. (*a*) Frequency of oscillation versus nozzle pressure ratio; (*b*) linear spectral coherence versus nozzle pressure ratio.**

$|G_{AB}|^2/G_{AA}\cdot G_{bb}$. Note that $0 \le \gamma^2 \le 1$. The utility of $\gamma^2(f)$ lies in the fact that it expresses the degree of linear correlation between $A(f)$ and $B(f)$. At $f$ and its harmonics the linear spectral coherence is almost 1.00. This indicates that the coherent velocity fluctuations in the jet's shear layer are highly correlated to the pressure oscillations in the feedback tube.

Figure 7(*a*) shows a plot of the frequency of oscillation of the flip-flop jet versus NPR. The frequency of oscillation obtained from the unsteady pressure signal in the feedback tube was seen to be the same as that obtained from the hot-film measurements in the shear layer of the jet. In addition, the linear spectral coherence at the oscillation frequency (Fig. 7(*b*)) between the two signals was 1.0, thus indicating a strong correlation between the pressure signals in the feedback tube and the coherent velocity signals in the jet's shear layer for the entire NPR range. It should be emphasized that in addition to the high coherence noted from Fig. 7(*b*) there is other evidence to prove that the jet oscillations are caused by the processes occurring in the feedback tube. First, when the feedback tube is disconnected the jet oscillation stops. Second, when the control ports are sealed off, the flip-flop jet oscillations cease. It is therefore the pressure oscillations in the feedback tube that are responsible for the oscillatory nature of the flip-flop jet. Note that for the data in the next section (Figs. 8–10) the frequency of oscillation of the flip-flop jet was measured using one of the piezoresistive pressure transducers in the feedback tube (see Fig. 1(*b*)).

## Effect of Varying Nozzle Parameters on the Frequency of Oscillation

The operation of the flip-flop jet nozzle depends on a multitude of parameters. It is impractical to vary each of those parameters while keeping the others constant. The present work only attempts to vary a limited set of parameters which are believed to be important for the operation of this device. These important parameters are the nozzle pressure ratio, as well as the feedback tube length and volume.

A case where both length and volume of the feedback tube

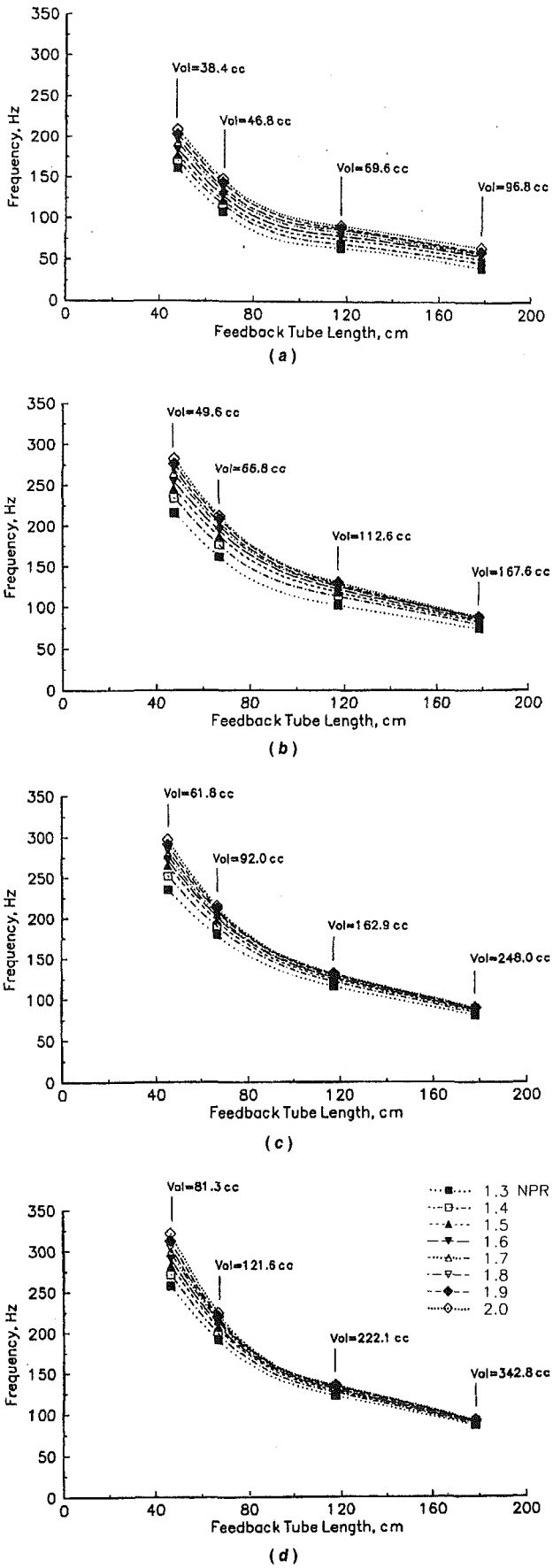


**Fig. 8 Effect of simultaneous variation of length and volume of the feedback tube. The feedback tube diameters ($D$) for the various cases were: (*a*) $D = 0.754$ cm; (*b*) $D = 1.072$ cm; (*c*) $D = 1.334$ cm; (*d*) $D = 1.588$ cm**

are varied simultaneously is shown in Fig. 8(*a–d*). To obtain the data for this case the feedback tube length was varied for a constant diameter tube. An increase in the length also automatically increased the volume. Note that in Fig. 8(*a–d*) the volume and length do not directly relate using the diameter given. This is due to the noncircular cross section of the feedback tube where it connects to the control port (see Fig. 1(*b*)). The frequency of oscillation of the flip-flop jet is seen to decrease with an increase in the length of the constant diameter tube. The frequency of oscillation was also seen to increase with increase in the nozzle pressure ratio.

The variation of the oscillation frequency versus feedback tube length for constant feedback tube volumes is shown in Fig. 9(*a–d*) for various nozzle pressure ratios. In order to keep the volume constant for the various feedback tube lengths, feedback tubes of smaller diameters had to be used for longer lengths. When the length was increased at a constant volume, the frequency of oscillation was seen to decrease. This observation can be rationalized by noting that with a longer tube it takes a longer time for the pressures between the two ports to equalize. Again, higher nozzle pressure ratios resulted in higher frequencies of oscillation.

The variation of the oscillation frequency versus feedback tube volume for constant length feedback tubes is shown in Fig. 10 for various nozzle pressure ratios. In order to keep the length constant for various feedback tube volumes, feedback tubes of various diameters were used. For a constant length and NPR, the frequency of oscillation increased as the volume of the feedback tube was increased. This increase in frequency with increase in volume is more pronounced for the case of short feedback tube lengths. It follows that the jet oscillation cannot be explained in terms of wave propagation in a tube for short tube lengths. The fact that wave propagation could not account for the frequency of oscillation of flip-flop jets with short feedback tube lengths was also reported by Viets (1975). It appears from Fig. 10 that the greater cross-sectional area (larger volume) of the feedback tube lowers the resistance to the pressure equalization process in the feedback tube. The time for the equalization of the pressure is therefore much shorter, resulting in higher frequencies of oscillation. As before, higher NPRs resulted in higher frequencies of oscillation.

It is to be noted that a limited attempt was made to present the data in a universal non-dimensional form. However, the non-dimensional model did not collapse all the data points. The dimensional data documented in this paper would still be valuable for future modeling of this device.

## Effect of Varying Nozzle Parameters on the Coherent Excitation Levels

The evaluation of the flip-flop jet nozzle as an excitation device would not be complete without a careful documentation of the coherent velocity perturbation levels capable of being produced by this device. In order to quantify these levels a hot-film probe was positioned at various downstream stations and the maximum coherent velocity perturbation level was recorded. The effect of the feedback tube length and volume, as well as the effect of nozzle pressure ratio (NPR), will be discussed next. It is important to note that an overall picture of the coherent velocity field produced by the flip-flop jet was shown in Fig. 4(*a*) for one set of conditions. However, that jet was operated at a very low nozzle pressure ratio (NPR = 1.02). Since it is impractical to collect data similar to that presented in Fig. 4(*a*) for several feedback tube lengths, volumes and nozzle pressure ratios, only the maximum coherent velocity perturbation level at three different axial stations was obtained.

Figure 11(*a*) shows a plot of the peak coherent velocity perturbation level versus feedback tube length for a constant feedback tube volume of 95 cc. It can be seen that the velocity

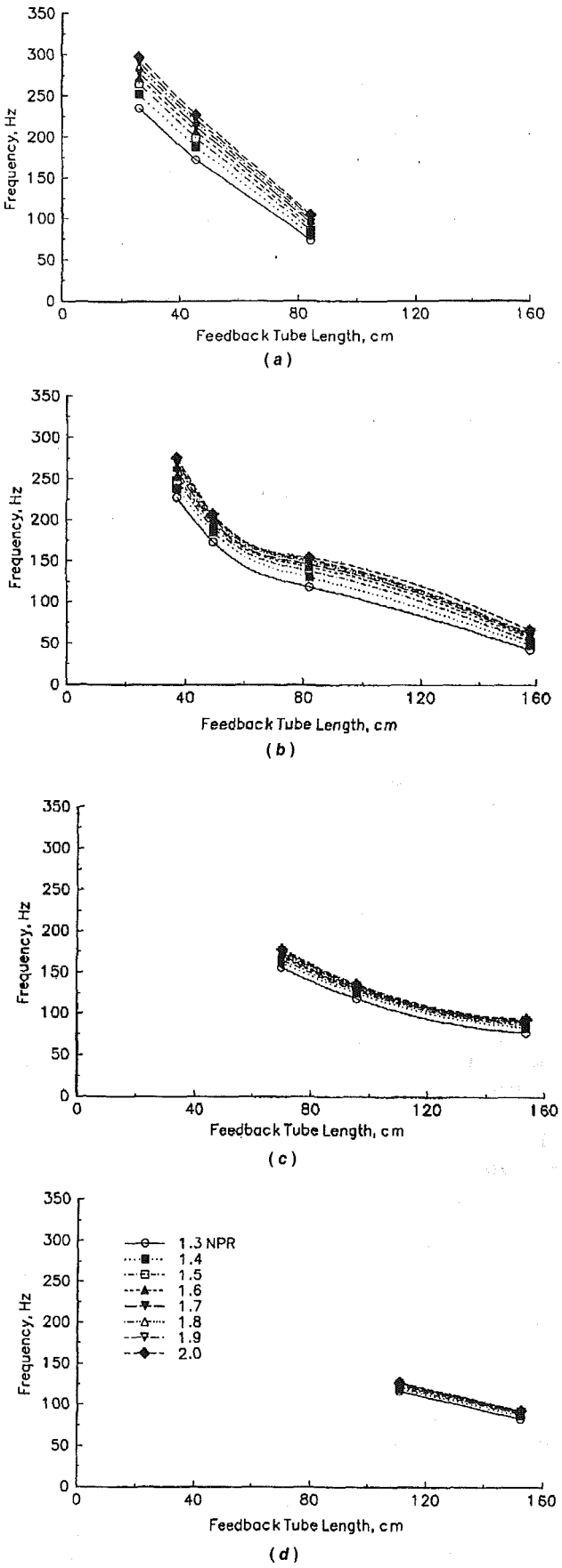


Fig. 9 Effect of varying the length of feedback tube with volume constant. The feedback tube volumes (Vol) for the four constant volume cases were: (*a*) Vol = 62 cc; (*b*) Vol = 95 cc; (*c*) Vol = 160 cc; (*d*) Vol = 240 cc

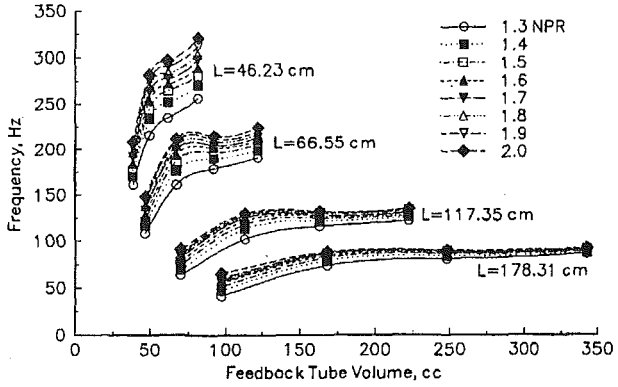


Fig. 10 Effect of volume of feedback tube with length constant. The feedback tube lengths (*L*) for the four constant length cases were: (*a*) *L* = 46.23 cm; (*b*) *L* = 66.55 cm; (*c*) *L* = 117.35 cm; (*d*) *L* = 178.31 cm

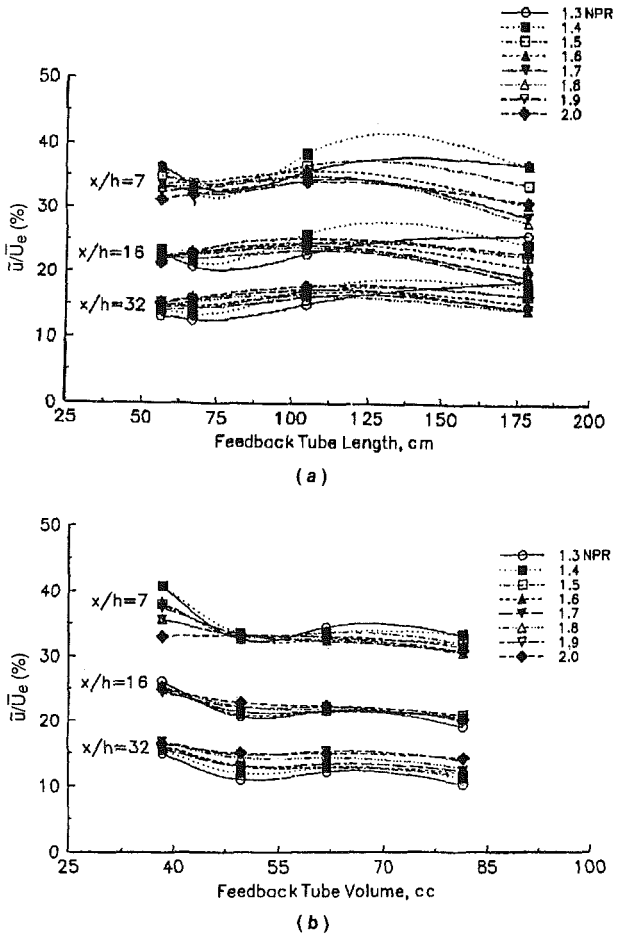


Fig. 11 Effect of varying nozzle parameters on coherent velocity perturbation levels. (*a*) Effect of feedback tube length for a constant feedback tube volume of 95 cc; (*b*) Effect of feedback tube volume for a constant feedback tube length of 46.23 cm.

perturbation levels are around 35% at $x/h = 7$, around 20 percent at $x/h = 16$, and around 15 percent at $x/h = 32$. It appears that at low feedback tube lengths the effect of varying the NPR is not so significant, whereas at a feedback tube length of 175 cm there is a considerable effect of the NPR on the coherent velocity perturbation levels.

Figure 11(*b*) shows data similar to that discussed in Fig. 11(*a*). However, the effect of varying the feedback tube volume at a constant feedback tube length is addressed here. The coherent velocity perturbation levels are of the same order as discussed in connection with Fig. 11(*a*) at the three axial sta-

tions. With the possible exception occurring at the $x/h=7$ location, there appears to be no significant variation in the coherent velocity levels with volume or with nozzle pressure ratio. The conclusions to be made from Figs. 11(*a*) and 11(*b*) are that the magnitude of the normalized coherent velocity perturbation levels that could be produced by the flip-flop jet excitation device depend mainly on the axial location at which the levels are measured. There is no significant change with feedback tube length or volume. There is a limited dependence on NPR for some cases. It should be emphasized that these observations are in contrast to the observations for the frequency of oscillation of the flip-flop jet. The frequency of oscillation depended considerably on the feedback tube length, volume, and the nozzle pressure ratio.

## Potential For Use as an Excitation Device

For jet mixing control applications, miniature flip-flop exciter jets could be used on either side of the exit of a larger scale primary nozzle. For such an application, the frequency of operation of the flip-flop jets should fall within the range of frequencies of the natural instability in the primary flow. In addition, the mass flow through the flip-flop jets should be small compared to that from the primary jet. Further, multiple flip-flop exciter nozzles operating at a prescribed phase difference could be used to excite the primary flow into various modes of instability. These phasing schemes were described by Raman and Rice (1993). Future work should focus on applying flip-flop excitation devices to jet mixing control applications.

## Estimates of Measurement Uncertainty

Estimates for the uncertainty in the measurements were obtained using the methods described by Moffat (1985). For the single component hot-film probes the calibration uncertainty was 2 percent and the first order uncertainty was $<0.5$ percent, yielding a total uncertainty of 2.1 percent. However, when the probe was placed near the exit of the flip-flop jet ($x/h<5$) the errors were much larger ($\sim 10$ percent). The above estimates are valid for the data in Figs. 3, 4, Figs. 6 and 7 (velocity data only), and Fig. 11.

Estimates for the uncertainty in the piezoresistive pressure transducers were reported in an earlier paper (Raman and Rice, 1993). The calibration uncertainty was 1.5 percent and the first order uncertainty 0.3 percent, yielding a total uncertainty of 1.53 percent. Since the same pressure transducers were used under similar conditions in the present work, the earlier estimates are valid here. The estimates provided in this paragraph are valid for the data in Figs. 6 and 7 (pressure oscillation data only) and Figs. 8–10. In addition, it should be noted that the uncertainty in the frequency measurement (Figs. 6–10) was $\pm 1$ Hz and that in the phase measurement (Fig. 4(*b*)) $\pm 5$ deg.

## Concluding Remarks

The flip-flop jet nozzle was evaluated for use as an excitation device for the control of practical shear flows. The effect of the important nozzle parameters, i.e., the feedback tube length, volume and nozzle pressure ratio on the frequency of oscillation and the coherent velocity perturbation levels was investigated. It was found that the frequency of oscillation of the flip-flop jet depended significantly on the feedback tube length and volume as well as the nozzle pressure ratio. In contrast, the coherent normalized velocity perturbation level did not depend on the above parameters. The data presented in this paper would be valuable for future modeling of this device.

In summary, when the flip-flop jet nozzle is used as an excitation device the nozzle parameters need to be carefully selected so that the frequency of oscillation of the flip-flop jet matches that of the natural instability of the flow being excited. However, the coherent normalized velocity perturbation levels that this device is capable of producing are by far independent of the nozzle parameters and depend only on the location at which these are measured. If one desires higher velocity perturbation levels, then the flip-flop jets would have to be located closer to (or built into) the primary flow being excited. As a final note, the velocity perturbation levels that the flip-flop device is capable of producing are much greater than the levels produced using conventional excitation sources. Future research within our group at NASA Lewis Research Center will focus on applying these devices for the control of practical shear flows.

## Acknowledgments

The experiments reported in this paper were done when the first author was with Sverdrup Technology, Inc. The authors would like to thank Dr. B. Wendt, Dr. H. Viets, and Mr. John M. Abbott for providing suggestions and for their encouragement. In addition, the authors would like to thank Ms. Tammy Langhals for her help in the production of this document.

## References

Ahuja, K. K., and Brown, W. H., 1989, "Shear Flow Control by Mechanical Tabs," AIAA Paper 89-0994.

Ahuja, K. K., Lepicovsky, J., Tam, C. K. W., Morris, P. J., and Burrin, R. H., 1982, "Tone-excited Jets, Theory and Experiments," NASA CR-3538.

Beale, R. B., and Lawyer, M. T., 1974, "Development of a Wall-Attachment Fluidic Oscillator Applied to Volume Flow Metering," *Flow—Its Measurement and Control in Science and Industry*, Vol. 1, Part II, Dowdell, R. B., ed., Instrument Society of America, pp. 989–996.

Brown, W. H., and Ahuja, K. K., 1990, "Jet Mixing Enhancement by Hydrodynamic Excitation," AIAA Paper 90-4005.

Crow, S. C., and Champagne, F. H., 1971, "Orderly Structure in Jet Turbulence," *Journal of Fluid Mechanics*, Vol. 48, pp. 547–591.

Davis, M. R., 1982, "Variable Control of Jet Decay," *AIAA Journal*, Vol. 20, pp. 606–609.

Hill, W. G., and Greene, P. R., 1977, "Increased Turbulent Jet Mixing Rates Obtained by Self-Excited Acoustic Oscillations," ASME JOURNAL OF FLUIDS ENGINEERING, Vol. 99, pp. 520–525.

Moffat, R. J., 1985, "Using Uncertainty Analysis in the Planning of an Experiment," ASME JOURNAL OF FLUIDS ENGINEERING, Vol. 107, pp. 173–178.

Morris, G. J., Jurewicz, J. T., and Palmer, G. M., 1992, "Gas-Solid Flow in a Fluidically Oscillating Jet," ASME JOURNAL OF FLUIDS ENGINEERING, Vol. 114, pp. 362–366.

Morris, N. M., 1973, *An Introduction to Fluid Logic*, McGraw Hill Book Co., UK.

Parekh, D. E., Reynolds, W. C., and Mungal, M. G., 1987, "Bifurcation of Round Air Jets by Dual-Mode Acoustic Excitation," AIAA Paper 87-0164.

Raman, G., Hailye, M., and Rice, E., 1993, "Flip-Flop Jet Nozzle Extended to Supersonic Flows," *AIAA Journal*, Vol. 31, No. 6, pp. 1028–1035.

Raman, G., and Rice, E. J., 1991, "Axisymmetric Jet Forced by Fundamental and Subharmonic Tones," *AIAA Journal*, Vol. 29, pp. 1114–1122.

Raman, G., and Rice, E. J., 1993, "Development of Phased Twin Flip-Flop Jets," ASME Paper 93-WA/NCA-25.

Rice, E. J., and Raman, G., 1993, "Enhanced Mixing of a Rectangular Supersonic Jet by Natural and Induced Screech," AIAA Paper 93-3263.

Schreck, S., 1992, "Application of a Flip-Flop Nozzle on Plume Mixing Enhancement," Presented at the First NASA/Industry High Speed Research, Nozzle Symposium, NASA LeRC, Cleveland, OH (to be published as a NASA CP).

Strykowski, P. J., Krothapalli, A., and Wishart, D., 1992, "The Enhancement of Mixing in High Speed Heated Jets Using a Counterflowing Nozzle," AIAA Paper 92-3262.

Tokaty, G. A., 1971, "A History and Philosophy of Fluid Mechanics," G. T. Foulis and Co. Ltd., UK.

Viets, H., 1975, "Flip-Flop Jet Nozzle," *AIAA Journal*, Vol. 13, pp. 1375–1379.

Viets, H., Blaster, D., and Toms, H. L., Jr., 1975a, "Time Dependent Fuel Injectors," AIAA Paper 75-1305.

Viets, H., Blaster, D., and Toms, H. L., Jr., 1975b, "Feasibility Study of Unsteady Foam Generators," DOD-AGFSRS-75-6, Wright-Patterson Air Force Base.

Warren, R. W., 1962, "Some Parameters Affecting the Design of Bistable Fluid Amplifiers," *Symposium on Fluid Jet Control Devices*, Winter Annual Meeting of the ASME, New York.

Wiltse, J. M., and Glezer, A., 1993, "Manipulation of Free Shear Flows using Piezoelectric Actuators," *Journal of Fluid Mechanics*, Vol. 249, pp. 261–285.

Zaman, K. B. M. Q., Reeder, M. F., and Samimy, M., 1994, "Control of an Axisymmetric Jet Using Vortex Generators," *Physics of Fluids*, Vol. 6, No. 2, pp. 778–793.

F. M. Donovan, Jr.

R. W. McIlwain

Mechanical Engineering Department,
The University of South Alabama,
Mobile, AL 36688

D. H. Mittmann

B. C. Taylor

Biomedical Engineering Department,
The University of Akron,
Akron, OH 44325

# Experimental Correlations to Predict Fluid Resistance for Simple Pulsatile Laminar Flow of Incompressible Fluids in Rigid Tubes

*The effects of oscillatory amplitude and frequency on fluid resistance for pulsatile incompressible laminar flow in rigid tubes were investigated analytically and experimentally. Analytical results predict that oscillations will have no effect on average resistance, defined as average pressure drop divided by average flow rate. The effect of oscillatory flow amplitude on total fluid resistance was obtained analytically. These results were verified experimentally. Equations are presented which allow the calculation of total fluid resistance for laminar, incompressible pulsatile flow in rigid tubes as a function of tube dimensions, fluid properties, frequency of oscillation and oscillatory flow amplitude.*

## Introduction

Pulsatile flow is encountered in physiology (circulatory system, respiratory system), prosthetic devices in biomedicine (cardiac support and replacement, mechanical respiratory support, jet ventilation) and engineering (positive displacement pump systems, IC engines, pulse combustors). The behavior of these systems is affected by fluid resistance, however, no correlation exists which allows the determination of fluid resistance for pulsatile flow. In the present context, pulsatile flow consists of steady flow with sinusoidal oscillations superimposed; oscillatory flow consists of sinusoidal oscillations with no net flow.

Womersley (1955), McDonald (1960), Jager et al. (1965) and others have shown that, in oscillating fluids, the interaction between viscous and inertial effects alters the velocity profile so that it no longer resembles the parabola of steady flow. Womersley noted that the resistance and inertance could be expressed as functions of a single nondimensional parameter, $\alpha$, defined as

$$\alpha = r_o \sqrt{\frac{\omega}{\nu}} \tag{1}$$

Ury (1962), Linford et al. (1965), Sergeev (1966), and Merkli and Thomann (1975) have demonstrated that resistance calculations based on Womersley's equations are accurate at low values of $\alpha$ but they suspected a transition from laminar to turbulent flow at high $\alpha$ where predicted and experimental results diverged.

Donovan et al. (1991) solved the Navier-Stokes equation for incompressible one-dimensional oscillatory flow of fluids in a circular pipe with no net flow rate, and found that the analytical resistance and inertance predictions agreed with Womersley's predictions. However, these authors demonstrated that the one-dimensional analytical predictions of resistance did not agree with experimental results for values of $\alpha$ up to 1000. They also demonstrated that the differences encountered were not due to turbulence. They published a correlation which can be used to calculate the resistance as a function of $\alpha$ for oscillatory laminar flow in rigid tubes.

The authors speculated that the increased resistance observed at high $\alpha$ may be due to secondary flows. If this were true, then it would be expected that the addition of oscillations to steady flow would increase the average steady flow resistance.

The present study was done to answer two questions for pulsatile laminar flow of incompressible fluids in rigid circular tubes:

1. What effect does fluid oscillation have on the average resistance as calculated from average flow and average pressure drop?
2. How is the total fluid resistance affected by the ratio of oscillatory flow amplitude to steady flow rate?

## Analytical Predictions

The Navier-Stokes equation for an incompressible constant viscosity fluid element in a circular constant area rigid tube

Contributed by the Fluids Engineering Division for publication in the JOURNAL OF FLUIDS ENGINEERING. Manuscript received by the Fluids Engineering Division November 6, 1992; revised manuscript received November 1, 1993. Associate Technical Editor: R.L. Panton.

with no radial or tangential velocity component and fully developed flow may be written as

$$\frac{\partial u}{\partial t}-\frac{\nu}{r}\frac{\partial}{\partial r}\left[r\frac{\partial u}{\partial r}\right]=\frac{(P_1-P_2)}{\rho L} \tag{2}$$

where $P_1$ and $P_2$ are pressures at the tube entrance and exit, respectively.

Donovan et al. (1991) demonstrated that the fluid resistance for this system being driven by a harmonic pressure difference is given by

$$R=\frac{\int_0^\tau (P_1-P_2)Q dt}{\int_0^\tau Q^2 dt} \tag{3}$$

The relationship of this resistance to energy dissipation rate is

$$\dot{E}=R\frac{1}{\tau}\int_0^\tau Q^2 dt \tag{4}$$

In order to produce pulsatile flow in the tube, let the driving pressure be defined as

$$P_1-P_2=A_{\text{osc}}\sin(\omega t+\theta)+A_{\text{std}} \tag{5}$$

and let elapsed time be very large, so that initial transients have died out resulting in steady state conditions.

Define the velocity in terms of an oscillatory component and a steady state component

$$u=u_{\text{osc}}+u_{\text{std}} \tag{6}$$

Substitution of Eqs. (5) and (6) into Eq. (2) and application of the principle of superposition produced the following equations:

$$\frac{\partial u_{\text{osc}}}{\partial t}-\frac{\nu}{r}\frac{\partial}{\partial r}\left[r\frac{\partial u_{\text{osc}}}{\partial r}\right]=\frac{A_{\text{osc}}\sin(\omega t+\theta)}{\rho L} \tag{7}$$

$$\frac{\partial u_{\text{std}}}{\partial t}-\frac{\nu}{r}\frac{\partial}{\partial r}\left[r\frac{\partial u_{\text{std}}}{\partial r}\right]=\frac{A_{\text{std}}}{\rho L} \tag{8}$$

The solution to Eq. (8) is presented by Donovan et al. (1991) and has the form

$$u_{\text{osc}}=\frac{A_{\text{osc}}G}{\rho L\omega}\sin(\omega t+\theta+\phi) \tag{9}$$

where $G$ and $\phi$ are gain and phase which are functions of $r$ and $\alpha$.

The oscillatory component of the volumetric flow rate is determined by integrating the oscillatory component of velocity over the radius

$$Q_{\text{osc}}=2\pi\int_0^{r_0} u_{\text{osc}} r dr \tag{10}$$

and an oscillatory resistance can be calculated by

$$R_{\text{osc}}=\frac{\int_0^\tau A_{\text{osc}}\sin(\omega t+\theta)Q_{\text{osc}}dt}{\int_0^\tau Q_{\text{osc}}^2 dt} \tag{11}$$

Solution of Eq. (8) yields the fully developed laminar flow equations:

$$u_{\text{std}}=\frac{A_{\text{std}}(r_0^2-r^2)}{4\mu L} \tag{12}$$

$$Q_{\text{std}}=\frac{\pi A_{\text{std}} r_0^4}{8\mu L} \tag{13}$$

from which the steady flow resistance can be calculated to be the same as fully developed laminar steady flow resistance.

$$R_{\text{lam}}=\frac{8\mu L}{\pi r_0^4} \tag{14}$$

The total flow rate is the sum of the oscillatory and steady components of flow

$$Q_{\text{tot}}=Q_{\text{osc}}+Q_{\text{std}} \tag{15}$$

and the total fluid resistance is given by

$$R_{\text{tot}}=\frac{\int_0^\tau [A_{\text{osc}}\sin(\omega t+\theta)+A_{\text{std}}]Q_{\text{tot}}dt}{\int_0^\tau Q_{\text{tot}}^2 dt} \tag{16}$$

## Nomenclature

$A_1$ = phase angle of pressure measurement P1, rad
$A_2$ = phase angle of pressure measurement P2, rad
$A_3$ = phase angle of compliance volume measurement, rad
$A_{\text{osc}}$ = amplitude of oscillatory component of driving pressure, Pa
$A_{\text{std}}$ = amplitude of steady component of driving pressure, Pa
$B_1$ = steady component of pressure measurement P1, Pa
$B_2$ = steady component of pressure measurement P2, Pa
$B_3$ = steady component of volume in compliance chamber, $m^3$
$C_1$ = oscillatory amplitude of pressure measurement P1, Pa
$C_2$ = oscillatory amplitude of pressure measurement P2, Pa
$C_3$ = oscillatory amplitude of volume in compliance chamber, $m^3$
$\dot{E}$ = energy dissipation rate, W
$G$ = gain, none
$L$ = length of tube, m
$P$ = pressure, Pa
$Q$ = volumetric flow rate, $m^3/s$
$Q_{\text{osc}}$ = oscillatory component of volumetric flow rate, $m^3/s$
$Q_{\text{std}}$ = steady component of volumetric flow rate, $m^3/s$
$Q_{\text{tot}}$ = total volumetric flow rate, $m^3/s$
$R$ = resistance, $Pa\cdot s/m^3$
$\text{Re}_{\text{max}}$ = Reynold's number based on maximum flow rate, none
$R_{\text{lam}}$ = resistance based on fully developed laminar flow, $Pa\cdot s/m^3$
$R_{\text{osc}}$ = resistance based on oscillatory component of flow, $Pa\cdot s/m^3$
$R_{\text{tot}}$ = total flow resistance, $Pa\cdot s/m^3$
$r$ = radial distance from center of tube, m
$r_o$ = radius of tube, m
$t$ = time, s
$u$ = axial velocity, m/s
$u_{\text{osc}}$ = oscillatory component of axial velocity, m/s
$u_{\text{std}}$ = steady component of axial velocity, m/s
$V$ = volume of water in compliance chamber, $m^3$
$\alpha$ = dimensionless parameter, none
$\theta$ = driving pressure phase angle, rad
$\mu$ = dynamic viscosity, $N\cdot s/m^2$
$\nu$ = kinematic viscosity, $m^2/s$
$\rho$ = fluid density, $kg/m^3$
$\tau$ = period of oscillation, s
$\phi$ = phase angle, rad
$\omega$ = frequency, rad/s

Donovan et al. (1991) showed that the shape of the velocity profile for oscillatory flow depends only on $\alpha$, subsequently, the value of the dimensionless oscillatory resistance, $R_{osc}/R_{lam}$ depends only on $\alpha$. For simple pulsatile flow, the shape of the velocity profile is determined by the sum of $u_{osc}$ and $u_{std}$ and will depend on both $\alpha$ and the flow ratio $Q_{osc}/Q_{std}$. Since the total resistance is determined entirely by the shape of the velocity profile, the dimensionless total resistance $R_{tot}/R_{lam}$ will be a function of $\alpha$ and flow ratio only. If oscillatory flow amplitude is small, $R_{tot}$ approaches the steady flow resistance $R_{lam}$. At large oscillatory amplitudes $R_{tot}$ approaches the oscillatory resistance $R_{osc}$ as defined by Eq. (11).

The dimensionless total resistance, $R_{tot}/R_{lam}$, approaches unity at small flow ratios and approaches a value dependent on $\alpha$ at high flow ratios. The normalized dimensionless resistance ratio

$$\frac{R_{tot}-R_{lam}}{R_{osc}-R_{lam}}$$

approaches zero at small flow ratios and one at large flow ratios, regardless of the value of $\alpha$. Values of the normalized dimensionless resistance ratio during transition from steady flow at low flow ratios to oscillatory flow at high flow ratios were calculated analytically using Eqs. (9) through (16) for a number of different values of $\alpha$ ranging from 1 to 64. The analytical result is shown as the solid line in Fig. 4. The shape of the transition is independent of $\alpha$.

Since the analytical results are dependent only on $\alpha$ and the flow ratio, they are valid for any incompressible fluid in a circular pipe. The analytical solution predicts that the presence of oscillatory flow will have no effect on the average resistance defined as the average pressure drop divided by average flow rate. The analytical solution also predicts that the presence of a steady flow component will have no effect on the oscillatory resistance as defined by Eq. (11). The oscillatory resistance is the total resistance that would be seen in simple oscillatory flow if there were no net flow.

## Experimental Methods

Three series of experiments were performed. The purpose of the first series was to measure the effect of oscillations on the steady flow resistance. The objectives of the second and third series were to determine the effects of oscillatory flow amplitude on total fluid resistance. Two different apparatuses (hereafter referred to as apparatus I and apparatus II) were used. The basic test arrangement is shown in Fig. 1.

Water was supplied to the apparatus at constant pressure with the pressure drop across the inlet valve maintained at or above 100 times the pulse pressure amplitude on the downstream side of the valve. This guaranteed that less than 0.5 percent of the oscillatory volume passed through the inlet valve so that at least 99.5 percent of the oscillatory volume flowed into and out of the air compliance chamber.

The air compliance chamber provided a means of measuring the oscillatory component of volumetric flow rate. The chamber was statically calibrated by injecting known volumes into the chamber and recording the value of the signal from the pressure transducer on top of the chamber. This was an isothermal calibration. Since the air compliance is used for a dynamic measurement, the effect of compression and expansion on temperature was taken into account. The thermal time constant of the air chamber was calculated to be 1.4 seconds for apparatus I and 0.4 seconds for apparatus II. The minimum frequencies used were 0.4 Hz and 3 Hz, respectively, so the air chamber experienced essentially adiabatic compression and expansion. This necessitated dividing the volume indicated by the static calibration by the specific heat ratio for air to correct to the dynamic conditions in use.

Entrance and exit lengths ranging from 70 to 153 diameters were provided on each end of the test section to reduce the effects of the valves and fittings at each end of the tube.

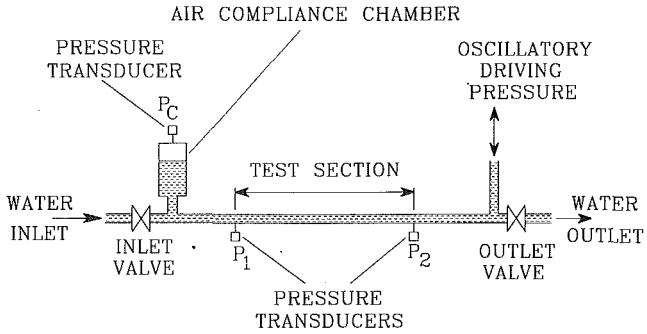


**Fig. 1 Water filled rigid tube test section**

Oscillatory flow was introduced into the system through the side arm located near the outlet valve. The outlet valve was used to maintain positive pressure in the system. Some of the oscillatory flow escaped through the outlet valve but this had no effect on the measurement of oscillations in the test section, since the air compliance chamber was located on the opposite end. No net flow of water was allowed to enter through the oscillatory driving pressure side arm.

The average flow rate through the test section was determined by measuring the time required to capture a known volume of water leaving the system in a beaker. The uncertainty for steady (net) flow measurement was estimated to be $\pm 2.5$ percent. The volume transducer and pressure transducers were calibrated at the beginning of each test.

## Steady Flow Resistance Measurements and Results

The steady flow resistance measurements were accomplished using apparatus I. A constant pressure of 414,000 Pa (60 psi) was maintained upstream of the inlet valve by a Tuthill® gear pump with an internal bypass pressure relief. The oscillatory flow was generated by a motor driven crank and piston provided with a compliance chamber to remove high frequency harmonics. A measured frequency response curve for the oscillatory driving system showed one secondary harmonic with twice the frequency and approximately 0.001 of the amplitude of the primary harmonic.

The air compliance chamber was a 9.5 cm diameter plexiglas cylinder with a piezoresistive pressure transducer mounted at the top. The precision limit for oscillatory flow measurements was estimated to be $\pm 0.1$ percent with $\pm 10$ percent bias for an uncertainty of $\pm 10$ percent.

The test section consisted of a 3 m length of 8.16 mm diameter copper refrigeration pipe with a 1.25 m entrance length on each end. Piezoresistive pressure transducer systems with sensitivities of 533 Pa/Volt were placed at the beginning and end of the test section. Since only the average pressures were of interest in this series of tests, the outputs of these transducers were low pass filtered at a cut-off frequency of 0.1 Hz.

The transducer output data were collected with an IBM DACA 12 bit A/D board. The precision of the pressure readings was estimated to be $\pm 1.0$ Pa with a bias limit of $\pm 4.9$ Pa which produced an uncertainty of $\pm 5.0$ Pa.

Data were sampled at 20 Hz for 25.6 seconds and stored in binary files. These files were translated into ASCII and analyzed by a Microsoft QuickBASIC program to determine peak flow rate, steady flow rate, frequency of oscillation and average pressures at each end of the test section.

The maximum Reynold's number was calculated as:

$$\mathrm{Re}_{max}=\frac{2[Q_{std}+|Q_{osc}|]}{\pi r_o \nu} \tag{17}$$

where $|Q_{osc}|$ is the amplitude of oscillatory flow rate.

**Table 1 Range of values used for steady flow resistance measurements**

| Variable | Minimum value | Maximum value | Units |
|---|---|---|---|
| Frequency | 0 | 1.26 | Hz |
| $Q_{std}$ | $1.8\times10^{-7}$ | $1\times10^{-5}$ | $m^3/s$ |
| $Q_{osc}/Q_{std}$ | 0 | 74.9 | None |
| $Re_{max}$ | 46 | 3737 | None |
| $\alpha$ | 0 | 12.2 | None |

The steady flow resistance was calculated from the average flow rate and the average pressure drop

$$R_{std}=\frac{\overline{P}_1-\overline{P}_2}{Q_{std}} \tag{18}$$

where $\overline{P}_1$ and $\overline{P}_2$ are the averages of pressures $P_1$ and $P_2$.

A total of 484 data points were taken for steady flow resistance measurements over the ranges shown in Table 1.

A plot of dimensionless resistance for all of the steady flow resistance measurements is shown in Fig. 2.

The results shown in Fig. 2 give no significant indication of the onset of turbulence below a maximum Reynold's number of 2000. In the remaining results only those data points for which maximum Reynold's number is less than 2000 were used to ensure laminar flow. The experimental uncertainty of the data shown in Fig. 2. using only those data with Reynold's number below 2000 was found to be ±0.62.

The relationship between dimensionless steady flow resistance and flow ratio is shown in Fig. 3.

The experimental uncertainty of the data in Fig. 3 was found to be ±0.42. Figure 3 shows a slight increase in steady flow resistance with flow ratio. If this increase were caused by secondary flows generated by the oscillations, then the resistance of approximately two thirds of the points should have increased by a factor of 2.7 to 4.6 by the time the flow ratio reached 5. This is based on the correction factor published by Donovan et al. (1991) which requires a multiplier on viscosity of 2.7 and 4.6 for $\alpha$ of 3.5 and 12, respectively. These are the values of $\alpha$ about which most of the steady flow resistance data are grouped. The most probable cause of the increase in resistance with flow ratio is the slight disturbance caused by the pressure taps at each end of the test section which add small entrance and exit losses as resistances proportional to flow rate. The oscillatory frequency was found to have a negligible effect on dimensionless steady flow resistance.

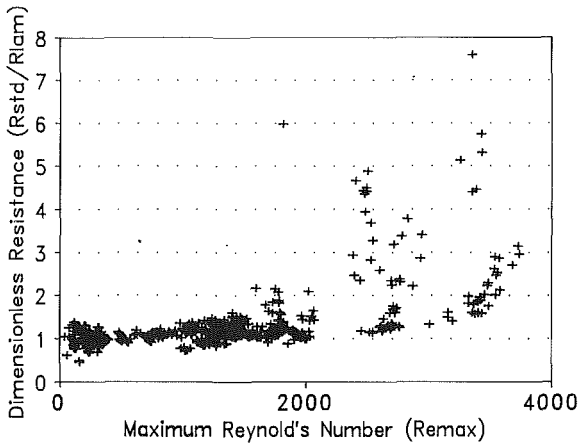


**Fig. 2 Variation of dimensionless steady flow resistance with maximum Reynolds number**

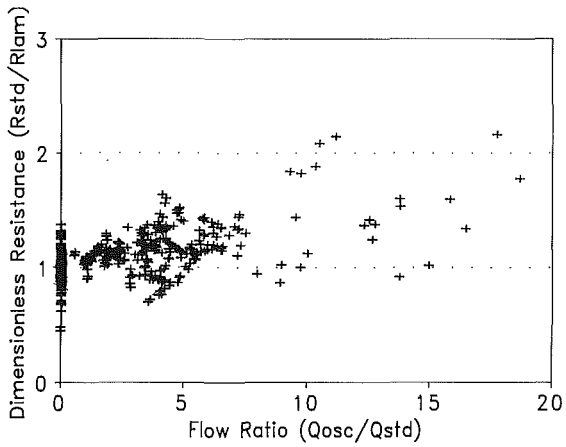


**Fig. 3 Variation of dimensionless steady laminar flow resistance with flow ratio**

## Total Resistance Measurements and Results

Two series of total resistance measurements were made using apparatus I and II, respectively. In the first series, in which apparatus II was used, a constant pressure of 689,000 Pa (100 psi) was maintained upstream of the inlet valve by the laboratory water supply system. A compliance air volume of approximately 4 liters in the supply line filtered minor pressure variations from the supply. The oscillatory flow was generated by a solenoid valve-controlled air supply driving a water filled U tube with air at each end. The driving air was restricted by a valve so the U tube was driven by a triangular pressure wave. The frequency of the driving pressure was determined by a function generator which operated the valve. For each frequency, the mass of water in the U tube was adjusted to resonance, which provided a sinusoidal pressure to the oscillatory driving pressure side arm of the test system. The average standard deviation of the pressure signal from a pure sine wave for this series of tests was found to be 4.8 percent of the oscillatory pressure amplitude.

The air compliance chamber was a 2 cm diameter plexiglas cylinder with a Microswitch PK236PC piezoresistive bridge pressure transducer mounted at the top. The precision limit for measurement of oscillatory flow rate was estimated to be ±0.1 percent with ±10 percent bias, resulting in an uncertainty of ±10 percent.

The test section consisted of two different tubes. The first was a 2.02 m length of 4.57 mm diameter aluminum tubing with entrance and exit lengths of 0.5 m on each end. The second was a 2.22 m length of 7.1 mm diameter aluminum tubing with entrance and exit lengths of 0.5 m on each end. Microswitch PK236PC piezoresistive bridge pressure transducers were placed at the beginning and end of the test section.

Transducer outputs were collected with an Apple IIe computer using an A/D system with 12 bit precision and a sampling rate of 406 samples per second. The precision of these pressure readings was estimated to be ±7.4 Pa with bias limit of ±350 Pa due to drift. The uncertainty of these readings was ±350 Pa.

Data were collected over two complete cycles and stored on disk files in ASCII. The files were transferred to an IBM compatible disk and analyzed by a Microsoft QuickBASIC program. A gradient search optimization technique was used to perform a least squares fit of sine wave equations to the volume and pressure data. The resulting equations were of the form

$$P_1=C_1\sin(\omega t+A_1)+B_1 \tag{19}$$

$$P_2=C_2\sin(\omega t+A_2)+B_2 \tag{20}$$

$$V=C_3\sin(\omega t+A_3)+B_3 \tag{21}$$

**Table 2 Range of values used for total flow resistance measurements**

| Variable | Minimum value | Maximum value | Units |
|---|---|---|---|
| Frequency | 0.47 | 6.77 | Hz |
| $Q_{std}$ | $1.27\times10^{-8}$ | $4.3\times10^{-6}$ | $m^3/s$ |
| $Q_{osc}/Q_{std}$ | 0.16 | 55.8 | None |
| $Re_{max}$ | 98 | 1554 | None |
| $\alpha$ | 7.4 | 28.0 | None |

The equation for the oscillatory driving pressure was determined from Eqs. (19) and (20) to be

$$P_1 - P_2 = A_{osc}\sin(\omega t + \theta) + A_{std} \tag{22}$$

where $A_{osc}$, $\theta$ and $A_{std}$ are defined by the equations

$$A = C_1\cos(A_1) - C_2\cos(A_2)$$

$$B = C_1\sin(A_1) - C_2\sin(A_2)$$

$$A_{osc} = \sqrt{A^2 + B^2}$$

$$\theta = \arctan\left(\frac{B}{A}\right)$$

$$A_{std} = B_1 - B_2$$

The equation for the oscillatory flow rate was determined from Eq. (21) to be

$$Q_{osc} = -\omega C_3\cos(\omega t + A_3) \tag{23}$$

The total flow rate is the sum of the oscillatory and steady components of flow as shown in Eq. (15).

The oscillatory resistance was calculated by substituting Eq. (23) into Eq. (11) and performing the indicated operations. The resulting equation is

$$R_{osc} = \frac{-A_{osc}\sin(\theta - A_3)}{\omega C_3} \tag{24}$$

The steady flow resistance was calculated by the equation

$$R_{std} = \frac{A_{std}}{Q_{std}} \tag{25}$$

The total resistance was calculated by using Eq. (15) to determine the equation for total flow rate, substituting the total flow rate equation into Eq. (16) and performing the indicated operations. The result is

$$R_{tot} = \frac{-A_{osc}C_3\sin(\theta - A_3) + 2A_{std}Q_{std}/\omega}{\omega C_3^2 + 2Q_{std}/\omega} \tag{26}$$

A total of 70 data points were taken for total flow resistance measurements using apparatus II.

Apparatus I was used in the second series of total resistance measurements. The low-pass filter was removed from the pressure transducer to allow measurement of oscillatory signals, and the system operated as described in the section on steady flow resistance measurements. The sampling rate was increased to 50 Hz. The analysis was accomplished as with apparatus II. A total of 109 data points were taken for total flow resistance measurements in the series using apparatus I.

The ranges of values for the total flow resistance measurements are shown in Table 2.

Total flow experimental resistances are compared to the analytically predicted curve in Fig. 4. The values of $R_{tot}$ and $R_{osc}$ were determined from the experimental data while $R_{lam}$ was calculated using Eq. (14).

The uncertainty of the experimental results shown in Fig. 4 is $\pm 0.1$. Figure 4 verifies that the total resistance relationship predicted by the mathematical analysis is followed by the experimental data.

The effect of oscillatory frequency on dimensionless oscillatory resistance compared to the dimensionless resistance results and correlation for pure oscillatory flow published by Donovan et al. (1991) is shown in Fig. 5.

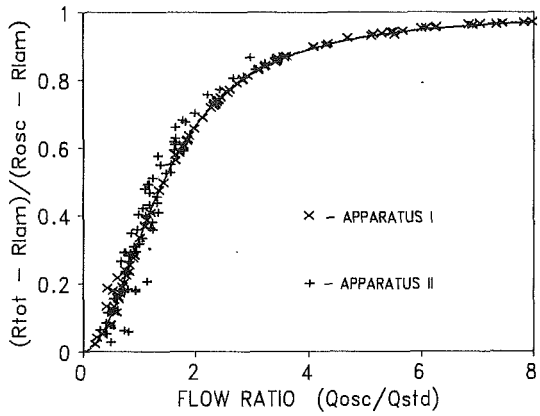


**Fig. 4 Experimental results compared to the analytical curve**

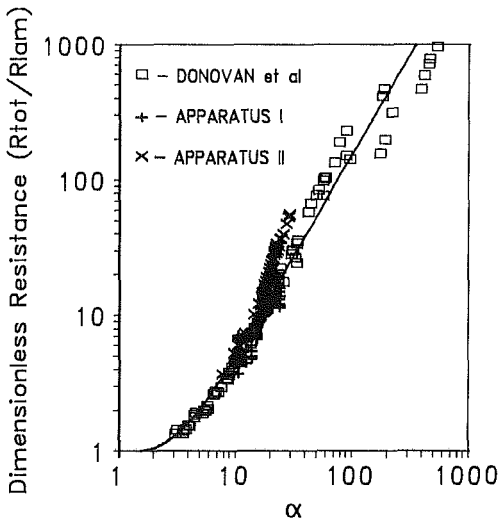


**Fig. 5 Dimensionless oscillatory resistance compared to data and correlation from Donovan et al. (1991)**

The experimental uncertainty of the results shown in Fig. 5 is $\pm 60$ percent. The oscillatory resistances calculated using the results from apparatus II agree with the experimental curve determined by Donovan et al. (1991), as shown in Fig. 5. The same result is obtained with about one third of the data from apparatus I. The remaining results from apparatus I indicate oscillatory resistance higher than predicted by the correlation. When compared to all of the experimental data presented by Donovan et al., the results from apparatus I fall only slightly outside their experimental scatter.

The analytical curve presented in Fig. 4 is represented by the equation

$$\frac{(R_{tot} - R_{lam})}{(R_{osc} - R_{lam})} = \frac{\left(\frac{Q_{osc}}{Q_{std}}\right)^2}{2 + \left(\frac{Q_{osc}}{Q_{std}}\right)^2} \pm 0.008 \tag{27}$$

The dimensionless resistance curve presented in Fig. 5 can be used to determine the oscillatory resistance as a function of $\alpha$ for pulsatile flow, and is represented by the equation

$$\frac{R_{osc}}{R_{lam}} = \frac{1}{1 + 0.25\alpha^{1.5}} + 0.166\alpha^{1.49} \pm 6 \text{ percent} \tag{28}$$

This equation is applicable for $\alpha$ between 0 and 1000.

## Discussion of Uncertainty Calculations

The experimental uncertainties stated for quantities plotted in Figs. 2 through 5 were determined by calculating the standard deviation of the dependent variable relative to the linear regression line (Figs. 2 and 3) or relative to the analytical curve (Figs. 4 and 5), and doubling the standard deviation to obtain the uncertainty at a confidence level of 95 percent. The uncertainties of the predicted curves as represented by Eqs. (27) and (28) were calculated by applying the central limit theorem to determine the standard deviations of the estimation of the population means, represented by the equations, and multiplying the standard deviations by 2 to obtain the uncertainties at confidence levels of 95 percent.

## Conclusions

The following conclusions were reached concerning pulsatile laminar flow of incompressible fluids in rigid circular tubes:

1. Flow oscillation has no significant effect on the average resistance defined as the average pressure drop divided by the average flow rate. This was verified by the experimental results for flow ratios from 0 to 8.
2. The total fluid resistance changes from the fully developed laminar flow resistance at very low flow ratios to the pure oscillatory resistance at high flow ratios. The transition is about 89 percent complete at a flow ratio of 4, as shown in Fig. 4.
3. The total fluid resistance can be calculated by the following procedure:
   (*a*) Calculate the laminar flow resistance ($R_{lam}$) from Poiseuille's law (presented in Eq. (14)).
   (*b*) Calculate the value of $\alpha$ using Eq. (1).
   (*c*) Use Eq. (28) and the laminar flow resistance value to calculate the oscillatory resistance ($R_{osc}$).
   (*d*) Calculate the total resistance ($R_{tot}$) using Eq. (27) and the values of laminar flow resistance and oscillatory resistance determined in steps a and c.


## Acknowledgment

This research was funded in part by the National Science Foundation, grant No. EID-9154390.


## References


Donovan, F. M., Taylor, B. C., and Su, M. C., 1991, "One-Dimensional Computer Analysis of Oscillatory Flow in Rigid Tubes," ASME *Journal of Biomechanical Engineering*, Vol. 113, pp. 476–484.

Jager, G. N., Westerhof, N., Noordergraaf, A., 1965, "Oscillatory Flow Impedance in an Electrical Analog of the Arterial System: Representation of the Sleeve Effect and Non-Newtonian Properties of Blood," *Circulation Research*, Vol. 16, pp. 121–133.

Linford, R. G., and Ryan, N. W., 1965, "Pulsatile Flow in Rigid Tubes," *Journal of Applied Physiology*, Vol. 20, pp. 1078–1082.

McDonald, D. A., 1960, *Blood Flow in Arteries*, Arnold & Co., London, Chapter 11, The Design of Manometers, pp. 234–257.

Merkli, P., and Thomann, H., 1975, "Transition to Turbulence in Oscillating Pipe Flow," *Journal of Fluid Mechanics*, Vol. 68, pp. 567–575.

Sergeev, S. I., 1966, "Fluid Oscillations in Pipes at Moderate Reynolds Numbers," *Fluid Dynamics*, Vol. 1, pp. 121–122.

Ury, J. F., 1962, "Viscous Damping in Oscillating Liquid Columns, Its Magnitude and Limits," *International Journal of Mechanics and Science*, Vol. 4, pp. 349–369.

Womersley, J. R., 1955, "Method for the Calculation of Velocity, Rate of Flow and Viscous Drag in Arteries When the Pressure Gradient is Known," *Journal of Physiology*, Vol. 127, pp. 553–563.

**Baby Chacko**
Research Scholar,
Department of Mechanical Engineering.

**V. Balabaskaran**
Associate Professor,
Department of Mechanical Engineering.

**E. G. Tulapurkara**
Professor,
Department of Aerospace Engineering.

**H. C. Radha Krishna***
Professor,
Department of Mechanical Engineering.

Indian Institute of Technology,
Madras, India 600036

# Performance of S-Cambered Profiles With Cut-Off Trailing Edges

*The aerodynamic characteristics of an S-cambered profile are studied under forward and reversed flow conditions. The profile chord is cut by 3, 6, and 9 percent of the chord at the sharp trailing edge end and the performances of these profiles are compared. It is found that with increase in length of cutting the lift coefficient increases in forward direction and decreases in reverse direction of flow. Cutting off the sharp trailing edge improves the lift-drag characteristics in forward mode and deteriorates in the reverse mode.*

## I Introduction

In tidal power plants, an axial flow hydraulic machine undergoes turbining as well as pumping operations in forward and reverse directions of flow. A single machine which can work as a turbine and as a pump in both the directions of flow is known as Fully Reversible Pump-turbine. Many investigators (Kar, 1962; Kelly, 1970; Anton et al., 1977) have studied the possibility of using a single cambered blade profile for a Fully Reversible Axial Pump-turbine runner. When such a profile is used for the Fully Reversible Axial Pump-turbine, the runner blades need to be rotated through about 180 deg so that the leading edge faces the flow during the reverse mode of operation also. If this rotation is not effected the efficiency in the reverse mode would be very low. These difficulties were overcome by using double cambered S-profile blades (Ravindran and Radha Krishna, 1979, 1979a; La Rance 1966; Alexsapolski et al., 1972; Ren, 1984). However, the available aerodynamic data on such profiles is inadequate for the design of runners using profiles of this kind. Further, moderately thick trailing edge is desirable from the point of view of reduced erosion of blade trailing edge. Hence aerofoils with varying amounts of cut-off at the trailing edge are studied in this investigation.

Some information is available on the effects of blunt trailing edge on the aerodynamic characteristics of conventional aerofoils (Smith and Schaefer, 1950; Hoerner, 1975; Ramjee et al., 1986). However, such information is not available on S-profile blades which is needed to support a better design of Fully Reversible Axial Pump-turbine. Smith and Schaefer (1950) have measured lift, drag and pitching moments characteristics of three aerofoil sections formed by cutting 1.5, 4, and 12.5 percent of the original chord from the trailing edge of NACA 0012 aerofoil section. Their results indicate that as the length of cut at trailing edge end increases, there is little change in the maximum lift coefficient, but drag increases. Hoerner (1975) found that a 40 percent thick aerofoil with an aspect ratio 4 gives increased lift coefficient with blunt trailing edge compared to the profile with sharp trailing edge. Experimental and theoretical investigations of Ramjee et al. (1986) on NACA 0012 aerofoil section showed that maximum lift coefficient and the slope of the lift curve are slightly higher for wings with blunt trailing edge as compared to the wing with sharp trailing edge.

The results of an experimental study on the effect of trailing edge cutting off on the aerodynamic performance of lightly cambered S-profiles are reported in this paper. Experiments were carried out for both forward and reversed flow conditions.

## II Test-Setup and Experimentation

**Wind Tunnel.** All the experiments reported in this paper were carried out in the low speed wind tunnel facility available at the Aerospace Engineering Department, I. I. T., Madras (Fig. 1). It is an open circuit suction type wind tunnel having $700 \times 1000$ mm test suction. The free-stream velocity at the test section was kept at about 34 m/s during the experiments.

**Details of the Profiles.** The profile under investigation is obtained by combining an 'S' shaped camber line and Gö775 thickness distribution. The S-shaped camber line consists of two symmetrical parabolas having maximum cambers of 2.5 percent chord. The choice of maximum camber is based on

*Present Address: Faculty of Mechanical Engineering, Universiti Technologi Malaysia, Johor Bahru, Malaysia.

Contributed by the Fluids Engineering Division for publication in the JOURNAL OF FLUIDS ENGINEERING. Manuscript received by the Fluids Engineering Division September 23, 1991; revised manuscript received December 7, 1993. Associate Technical Editor: R. L. Panton.

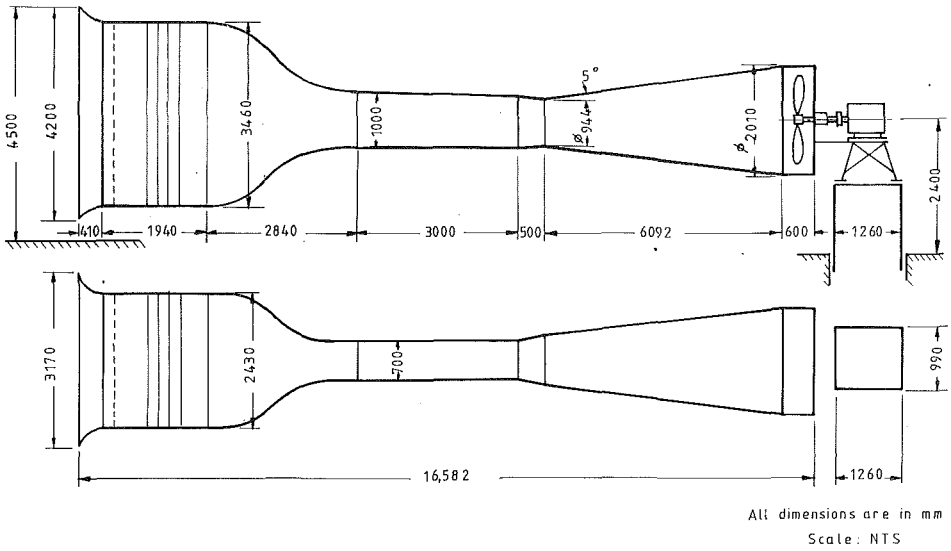


Fig. 1 Low turbulence subsonic wind tunnel

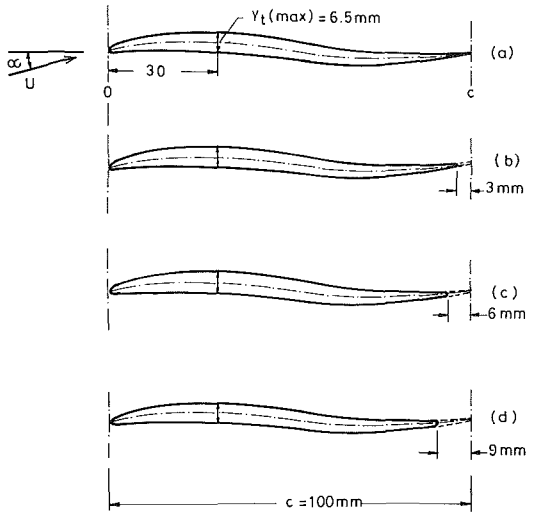


Fig. 2 Profiles with cut-off trailing edge


Fig. 3 Profile in reverse mode

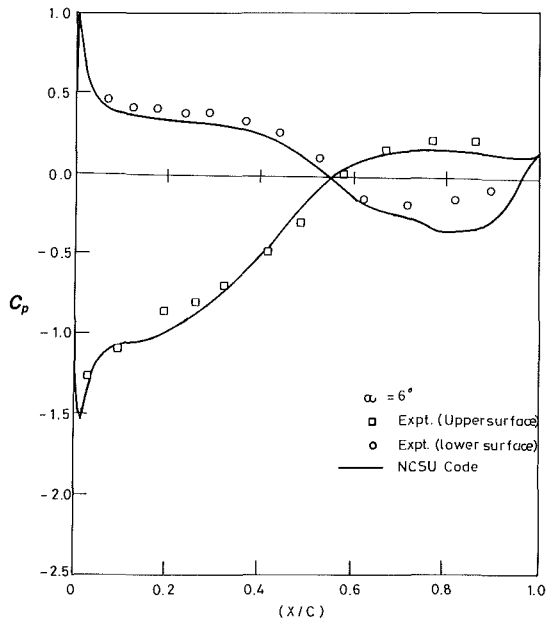


Fig. 4 $C_p$ distribution at $\alpha = 6$ deg for uncut profile (Uncertainty in $C_p = 3.3$ percent 20:1 odd)

Radha Krishna et al.'s (1979) investigation which showed that a maximum camber of 2.5 percent of chord gave an optimum performance for tidal plant applications. Gö775 thickness distribution has been chosen as it has a smooth potential flow velocity distribution which is favorable to reduce the chance of occurrence of cavitation. The profile has a chord of 100 mm and maximum thickness ratio of 6.5 percent. These values are typical of low head model turbine runners (Suryanarayanan, 1981).

**Fabrication of Blades.** Eight blades of 400 mm span and 100 mm chord length were die-moulded using fibre glass reinforced plastic material. Later, pairs of 400 mm long blades were carefully joined to get four 800 mm span blades. 24 stainless steel tubes of diameter 0.8 mm were embedded inside the blades while casting. Along the central region of the blade span, 0.5 mm diameter pressure tappings were drilled normal to the blade surface. Trailing edges of three blades were cut by 3, 6, and 9 percent of the original chord length and rounded off to obtain three new profiles as shown in Figs. 2(*b*) to 2(*d*).

## Nomenclature

$c$ = profile chord
$C_d$ = profile drag coefficient
$C_l$ = profile lift coefficient
$C_p$ = coefficient of pressure
$p$ = static pressure
$p_\infty$ = free-stream static pressure
Re = Reynolds number
$U$ = free-stream velocity
$\alpha$ = angle of attack
$\alpha_{01}$ = zero-lift angle
$\nu$ = kinematic viscosity
$\rho$ = density of air

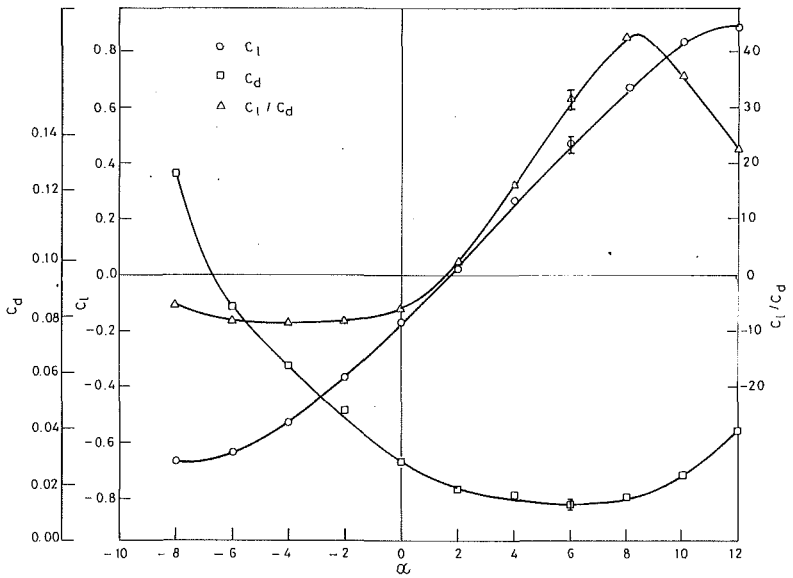


Fig. 5 Lift and drag characteristics of the uncut profile in forward mode

Table 1 Comparison of profiles in forward mode

| Cut length %c | 0 | 3 | 6 | 9 |
|---|---|---|---|---|
| $dC_l/d\alpha^\circ$ | 0.1043 | 0.1121 | 0.1086 | 0.1133 |
| $C_{l\max}$ | 0.90 | 0.85 | 0.90 | 0.85 |
| $C_{d\min}$ | 0.0135 | 0.0135 | 0.0165 | 0.0175 |
| $\alpha_{stall}$,deg | 11.5 | 10.5 | 10.5 | 9.5 |
| $(C_l/C_d)_{\max}$ | 43 | 47 | 43 | 44 |

Table 2 Comparison of profiles in reverse mode

| Cut length %c | 0 | 3 | 6 | 9 |
|---|---|---|---|---|
| $dC_l/d\alpha^\circ$ | 0.1094 | 0.1208 | 0.1320 | 0.1216 |
| $C_{l\max}$ | 0.84 | 0.76 | 0.73 | 0.69 |
| $C_{d\min}$ | 0.0210 | 0.0210 | 0.0210 | 0.0180 |
| $\alpha_{stall}$,deg | 9.0 | 9.0 | 8.5 | 8.5 |
| $(C_l/C_d)_{\max}$ | 17 | 17.5 | 17.0 | 13 |

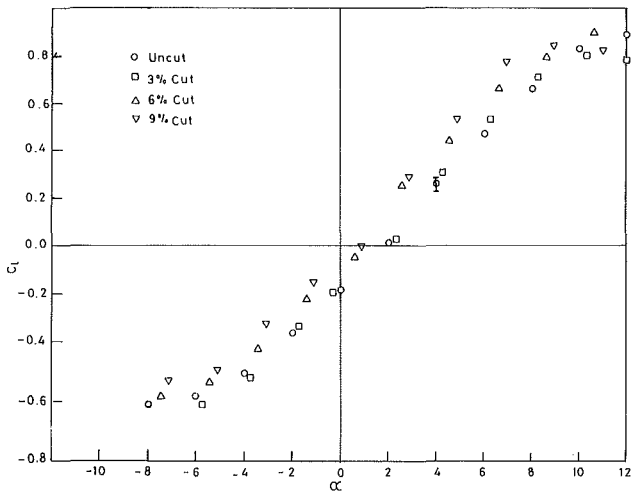


Fig. 6 Effect of cutting off trailing edge on the lift characteristics of the profile in forward mode

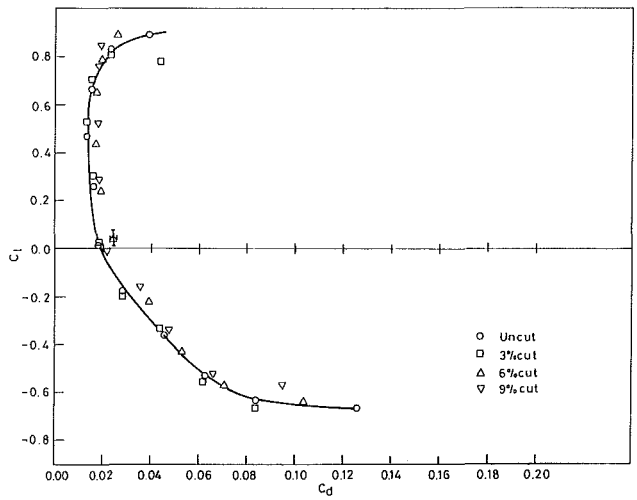


Fig. 7 Effect of cutting off trailing on the drag polar of the profile in the forward mode

**Experimentation.** The blade of span 800 mm was fixed between two Aluminium disks mounted on the side walls of the 700 mm wide wind tunnel test section. The extra length of the blade was allowed to protrude outside the test section and the ends were carefully sealed. The discs could be rotated to provide the required angle of attack which was varied from $-8$ to $+12$ deg at intervals of 2 deg. The surface static pressure, $p$ was measured using micromanometer along with a scanning box made by M/s Furness Controls, U.K. The free-stream total and static pressures were measured using a pitot static tube. The velocity inside the tunnel was kept constant at 34 m/s throughout the experiments. The Reynolds number, ($\mathrm{Re} = U \cdot c/\nu$), during the experiments was $2.2 \times 10^5$, where $U$ is the free-stream velocity, $c$ is the chord length, and $\nu$ is the kinematic viscosity of air. It may be added that in practical turbomachine applications the Reynolds number based on the blade chord is below $5 \times 10^5$ and that there is no influence of Reynolds number in the range between $2 \times 10^5$ and $5 \times 10^6$ (Rhoden, 1952; Horlock, 1958, p. 72; Gostelow, 1984, p. 27). Measurements in both forward and reverse flow mode were carried out on the surfaces of the four profiles and in the wake, for various angles of attack. Figure 3 shows the blade and flow direction in the reverse mode. The objective was to understand the aerodynamic characteristics of S-profile with progressive cutting of the trailing edge kept in both directions of flow. From measured pressure distribution the pressure coefficient, $C_p$, was calculated as:

$$C_p = \frac{p - p_\infty}{1/2\rho U^2}$$

## III Calculation of Lift and Drag Coefficients

The lift coefficient ($C_l$) is generally obtained by integrating the distribution of pressure coefficient ($C_p$). In the present investigation, totally 24 holes are located on the upper and lower surfaces put together for measuring $C_p$. The first pressure tapping on the upper surface is at 3 percent of the chord and that on the lower surface is at 7 percent from the leading edge. More pressure tappings could not be accommodated in this region due to the thinness of the blade (6.5 percent) and small chord (100 mm). To carry out the integration to obtain $C_l$, the pressure distribution needs to be smoothed and extrapolated up to the leading and trailing edges. Following practice was adopted: (i) The smoothed curves for $C_p$ were extrapolated to the trailing edge such that $C_p$ is same on both upper and lower surfaces at the trailing edge. The value of $C_p$ at the trailing edge was found to be generally between $\pm 0.2$. This value is close to the range of values for $C_p$ at trailing edge given by Young (1989, p. 200). (ii) Near the leading edge the extrapolation is not so simple because $C_p$ reaches a value of 1 on one of the surfaces and has a minimum at the other. To seek some guideline from theoretical results, computations were done using the surface vorticity technique which treats the fluid as inviscid. The agreement between the theory and experiment was not satisfactory. Subsequently, computations were done using a code called SRISTI developed at National Aeronautical Laboratory, Bangalore, India. This code is based on the NCSU (North Carolina State University) code of Smetana (1975). In this code, the flow past the aerofoil is computed using potential flow techniques and subsequently the boundary layer is computed using an integral method. The typical results for uncut profile at 6 deg angle of attack are shown in Fig. 4. It is noticed that though the predictions are not very good near the trailing edge, the calculated distribution captures the trends of the $C_p$ distribution, near the leading edge region. The trends indicated by computed results were used to extrapolate experimental $C_p$ distribution near trailing edge. It may be added that the comparison was not so favorable at all angles of attack, but the computations did give clear indication of the trend. Plausible distribution of $C_p$ which would enclose the experimental $C_p$ distribution near the leading edge, were tried out and it was found that the uncertainty in values of $C_l$ due to smoothing was within $\pm 0.03$. This is indicated by error bars in the graphs.

The drag coefficient was obtained using the standard technique of velocity distribution in the wake behind the body. The measurements were done at 3 chords behind the blade, where the static pressure across the wake was almost uniform. The lift and drag coefficients for the profiles with trailing edge cut-off are based on the shortened chord. The angle of attack for these profiles is measured with respect to the modified chord of the cut-off profile. Typical readings of free stream static pressure, free-stream total pressure, and surface static pressure are $79 \pm 0.5$ mm, $5 \pm 0.1$ mm, $195 \pm 0.5$ mm of water column below atmosphere pressure respectively. This gives an error of $\pm 0.25$ percent in the free-stream velocity and $\pm 3.3$ percent in the coefficient of pressure at 20:1 odds.

## IV Results and Discussion

**Flow Over the Profiles in Forward Mode.** Typical pressure distributions, ($C_p$) for the uncut profile, in the forward mode are shown in Fig. 4 for $\alpha = 6$ deg. The aerodynamic characteristics (viz. variations of $C_l$, $C_d$ and $C_l/C_d$ with angle of attack) for this profile are shown in Fig. 5. For small angles of attack in both negative and positive directions, the lift coefficient varies linearly with angle of attack, with $dC_l/d\alpha$ having a value around 0.11 per degree (Table 1). Contrary to the case of conventional aerofoils for which zero-lift-angle ($\alpha_{01}$) is negative, an *S*-shaped profile shows a positive $\alpha_{01}$.

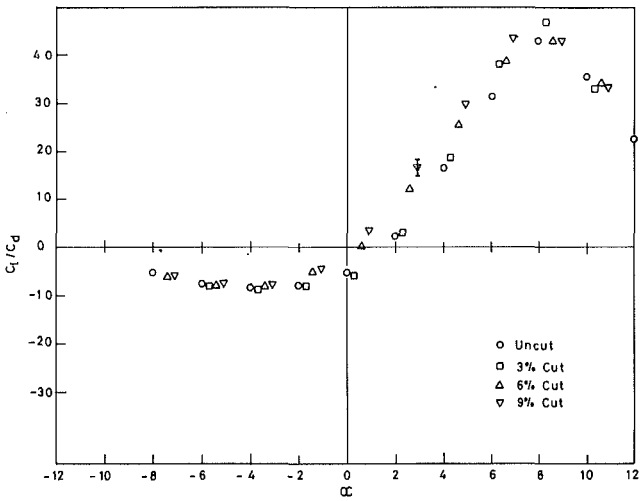


**Fig. 8 Effect of cutting off the trailing edge on the $C_l/C_d$ characteristics of the profile in forward mode**

The drag coefficient is fairly small and almost constant for $\alpha$ between $+2$ and $+8$ deg, beyond which the drag rises rapidly. This characteristic is similar to that of conventional aerofoils with small camber.

$C_l/C_d$ curve shows that it reaches a maximum of 43 at around 8 deg in positive direction and attains a value of 9 at $-4$ deg in negative direction. The variations of experimental lift coefficient with $\alpha$ for different lengths of cut are presented in Fig. 6. At a given positive angle of attack increase in lift coefficient can be observed as length of the cut increases. The reason for this increase in lift is the removal of negative camber in rear portion of the profile. After cutting off the trailing edge, the effective camberline will have a higher positive camber in the first half than negative camber in the second half. Hence the portion which gives the negative lift is partially removed by cutting at the trailing edge end. Other contributing factor for the higher lift of the profiles with cut off trailing edge could be the slight increase in thickness to chord ratio of the profile. However the $C_{l\max}$ values for profiles are around 0.85. The values of maximum lift coefficient, $C_{l\max}$, slope of lift curve $dC_l/d\alpha$ deg and angle of stall, $\alpha_{stall}$, are presented in Table 1. The trend was similar to the one observed by Ramjee et al. for NACA 0012 aerofoil. Ramjee et al. (1986) experiments on NACA 0012 profile showed a decrease in the value of $C_{l\max}$ when cut-off exceeds 15 percent. However, for the present case with the *S*-profile, trailing edge cut-off more than 9 percent was not investigated as the $C_{l\max}$ for reversed flow conditions was found to decrease significantly with the trailing edge cut-off (Table 2). As in the case of NACA0012 profile here also there was a slight decrease in the value $\alpha_{stall}$ as the amount of cut increases.

Drag characteristics for the profiles with cut-off trailing edge are compared in Fig. 7. For almost entire range of lift coefficient the profile with 3 percent cut shows almost equal drag coefficient as the uncut profile. The reason for this may be that the trailing edge separation is not influenced by small cut at the trailing edge. On the other hand, for the same lift coefficient, the profiles with 6 and 9 percent cut show slightly higher $C_d$ value compared to the other profiles. However, at negative angles of attack the profiles with 6 and 9 percent cut-off trailing edge seem to have lesser $C_d$ value compared to other profiles.

$C_l/C_d$ characteristics are compared for different lengths of cut in Fig. 8. Profiles with cut-off trailing edge are found to give slightly higher values of $(C_l/C_d)_{\max}$ and wider peaks compared to uncut profile. This may be because the increase in

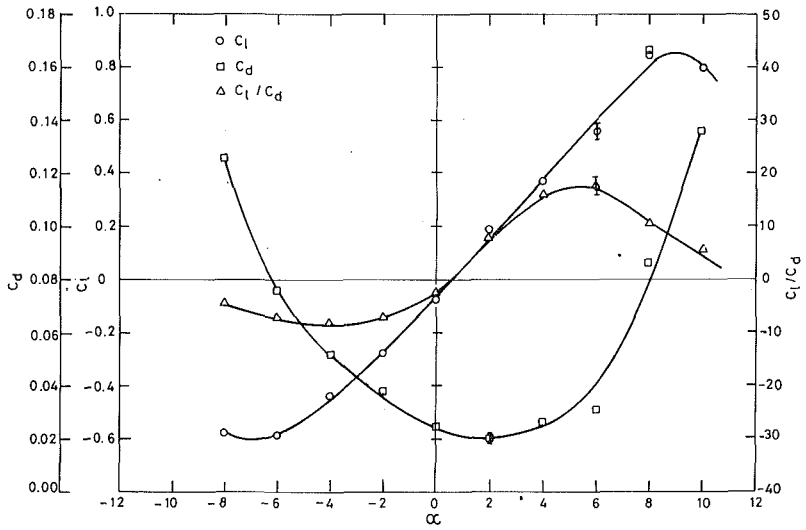


Fig. 9 Lift and drag characteristics of the uncut profile in reverse mode

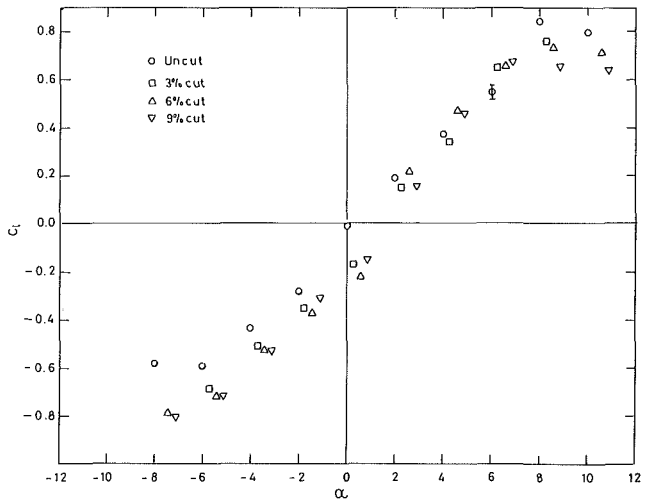


Fig. 10 Effect of cutting off the trailing edge on the lift characteristics of the profile in reverse mode

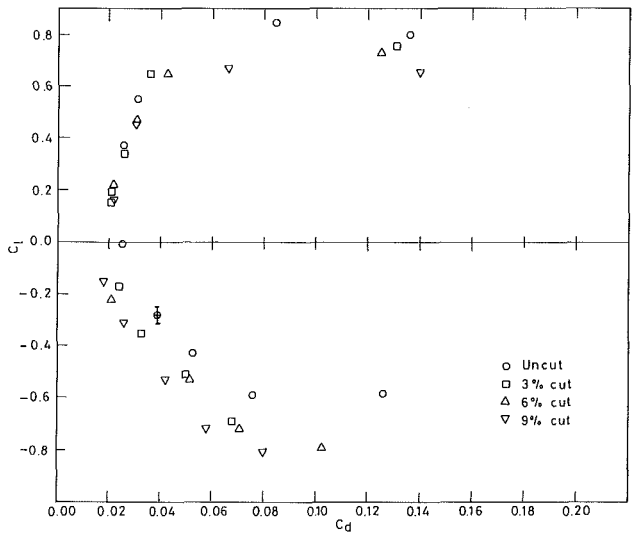


Fig. 11 Effect of the cutting off the trailing edge on the drag polar of the profile in reverse mode

lift coefficient is more predominant than the increase in drag coefficient for the profiles with trailing edge cut off.

**Flow Over the Profiles in Reverse Mode.** The variations of $C_l$, $C_d$ and $C_l/C_d$ with $\alpha$ for uncut profile in reverse flow mode are shown in Fig. 9. The $C_l$ versus $\alpha$, $C_l$ versus $C_d$ and $C_l/C_d$ versus $\alpha$ curves for profiles with 3, 6, and 9 percent cut in the reverse flow mode are shown in Figs. 10, 11, and 12. The values of $dC_l/d\alpha$, $C_{l\max}$, $C_{d\min}$, and $\alpha_{stall}$ are tabulated in Table 2. It is seen that though $dC_l/d\alpha$ is higher in the reverse mode when compared to the forward mode, $\alpha_{stall}$ is lower and hence $C_{l\max}$ is lower in the reverse mode. However, $C_{l\max}$ decreases as the length of cut increases. This behavior is in contrast to that in the forward mode where $C_{l\max}$ almost remains constant. This penalty in $C_{l\max}$ value for reverse mode is due to the reduced camber in the first half of the profile and it is well known that camber in the first half has strong influence on $C_{l\max}$. $C_{d\min}$ is much higher in the reverse mode and hence $(C_l/C_d)_{\max}$ is much lower.

## Conclusions

Based on the above studies on the aerodynamic characteristics of the profiles with different length of cut at the trailing

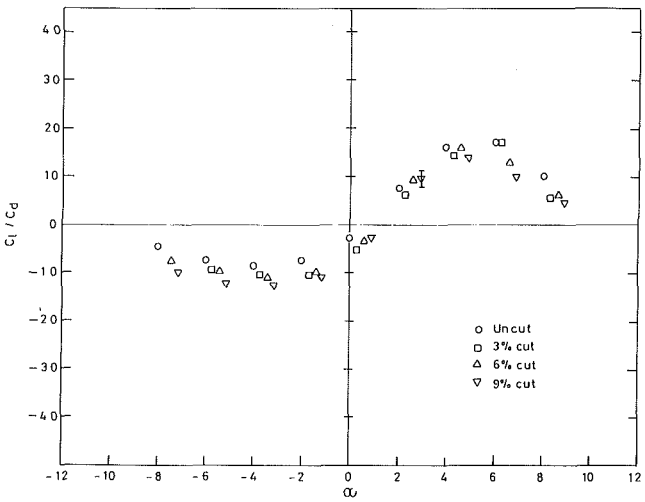


Fig. 12 Effect of cutting off the trailing edge on the $C_l/C_d$ characteristics of the profile in reverse mode

edge, in forward and reversed directions of flow, the following conclusions can be drawn.

1) Cutting off trailing edge can vary the aerodynamic characteristics of the S-profile appreciably.

2) At low angles of attack with increase in length of cut, the lift coefficient increases in forward direction and decreases in reversed direction. However, $C_{l\max}$ is almost same for all profiles in forward mode but decreases with increase of cut in reverse mode.

3) A small cut (3 percent) does not cause much variation to the drag coefficient of the profile in both directions.

4) Cutting of the sharp end improves the $C_l/C_d$ characteristics in forward flow and deteriorates in the reverse mode.

5) Comparing the $C_l/C_d$ values for forward and reverse mode for profiles with different length of cut, it is seen that a small cut of about 3 percent would give an overall advantage in the aerodynamic characteristics for both directions of flow.

## Acknowledgments

The authors are thankful to Mr. V. S. Narayanan for running the SRISTI code for various profiles and to Dr. P. Ramamoorthy of N. A. L., Bangalore for providing the object code of SRISTI.

## References

Alexsapolski, D., YA, Tishenko, A. K., and Kruthko, M. P., 1972, "Experimental Axial Reversible Pumps," Kharkov Polytechnical Institute, USSR, Report on Hydraulic Machines.

Anton, I., Anton, V., and Maithe, A., 1977, "Air Foil Cascades Working under Normal and Reversed Flow," *Revue Roumaine des Sciences Techniques Se'rie de Mechanique Applique'e*, Tome 22, Bucarest, pp. 63–74.

Gostelow, J. P., 1984, *Cascade Aerodynamics*, Pergamon, Oxford.

Hoerner, S. F., 1975, *Fluid Dynamic Lift*, Hoerner Fluid Dynamics, NJ.

Horlock, J. H., 1958, *Axial Flow Compressors*, Butterworths Scientific Publications, London, England.

Kar, R. N., 1962, "Reversed Flow Through Kaplan Runner," *Water Power*, Vol. 14, p. 281.

Kelly, G. R., 1970, "The Characteristics of Flow Through Reversible Pump-Turbine Blading," Ph.D. thesis, University of Edinburg, England.

"La Rance Tidal Power Scheme—An Unprecedented Achievement," 1966, *Revue Franc, aise de l' Energee*, p. 183.

Radha Krishna, H. C., Aswathanarayana, P. A., and Ramachandran, Rm., 1979, "Some Flow Studies on S-Cambered Aerofoils," *Proceedings of the 6th Conference on Fluid Machinery*, Budapest, Hungary, pp. 917–925.

Ramachandran, Rm., Radha Krishna, H. C., and Aswathanarayana, P. A., 1986, "Cascade Experiments over S-Blade Profiles," *ASCE Journal of Energy Engineering*, Vol. 112, pp. 37–50.

Ramjee, V., Tulapurkara, E. G., Balabaskaran, V., 1986, "Experimental and Theoretical Study of Wings with Blunt Trailing Edges," *Journal of Aircraft*, Vol. 23, pp. 349–352.

Ravindran, M., and Radha Krishna, H. C., 1979, "Characteristics of a Fully Reversible Axial Pump-Turbine for Application in Tidal Power Plants," *Proceedings of the International Conference on Future Energy Concepts*, London, pp. 156–158.

Ravindran, M., and Radha Krishna, H. C., 1979a, "Influence of Blade Profiles on the Performance of Fully Reversible Axial Pump-Turbine," *Proceedings of the 6th Conference on Fluid Machinery*, Budapest, Hungary, Vol. 2, pp. 926–935.

Ren, H. G., 1984, "Bulb Turbine Using Tidal Energy for Generating Electric Power from Both Directions in China," ASME Winter Annual Meeting, New Orleans, LA, pp. 13–20.

Rhoden, H. G., 1952, "Effects of Reynolds Number on the Flow of Air Through a Cascade of Compressor Blades," Aeronautical Research Council, London, Reports and Memoranda, No. 2919.

Smetana, F. O., 1975, "Light Aircraft Lift, Drag and Moment Prediction—A Review and Analysis," National Aeronautics and Space Administration Contractor Report No. 2523.

Smith, H. A., and Schaefer, R. F., 1950, "Aerodynamic Characteristics at Reynolds Number of $3 * 10^6$ and $6 * 10^6$ of Three Airfoil Sections Formed by Cutting off Various Amounts from the Rear Portion of the NACA 0012 Airfoil Section," National Advisory Committee for Aeronautics Technical Note No. 2074.

Suryanarayan, A., 1980, "Aerodynamic Performance of Highly Reflexed Profile for Fully Reversible Hydraulic Machines," M.S. thesis, Indian Institute of Science, Bangalore, India.

Young, A. D., 1989, *Boundary Layers*, B.S.P. Professional Books, London.

# Actively Controlled Radial Flow Pumping System: Manipulation of Spectral Content of Wakes and Wake-Blade Interactions

O. Akin

D. Rockwell

Department of Mechanical Engineering and Mechanics, Lehigh University, Bethlehem, PA 18015

*A unique, actively controlled pumping system allows independent control of inflow and impeller perturbations, as well as the phase shift between them. The basic configurations of an impeller and an impeller-diffuser blade system have been investigated, with the objective of manipulating the spectral content of the unsteadiness of the near-wake at the impeller discharge. Substantial alteration of the discrete spectral components can be attained. A central feature is the generation of a number of nonlinear interaction components, corresponding to sum and difference frequencies, of the forcing- and blade passing-frequencies and their harmonics. With proper choice of perturbation conditions, it is possible to attenuate the inflow perturbation, as well as to alter the magnitudes of the blade passing component and its harmonics.*

## 1 Introduction

Unsteadiness past blade arrays in rotating machines is of central importance. It can arise from unsteady inlet conditions or from the existence of upstream blading. For rotating machines of the axial flow type, a wide variety of investigations have addressed unsteady loading on blading. Experimental studies of Dring et al. (1982), Franke and Henderson (1979), and Gallus et al. (1980) assess the two major types of contributions to the blade loading: potential flow distortion; and impingement of the wake upon the blade. A possibility for reducing the noise level involves use of a "wake canceling" effect between successive rows of blades, as addressed by Walker and Oliver (1972). On the theoretical side, Kemp and Sears (1953, 1955) originally addressed the loading on thin airfoils with small turning by use of linearized potential flow techniques. Subsequent investigations, such as those of Horlock (1968) and Naumann and Yeh (1973) characterize, respectively, the effects of simultaneous transverse and chordwise gusts upon the blading and the effects of blade camber. Unsteady loading arising from purely potential flow distortion, fully accounting for finite thickness and turning of the blades, has been addressed by Parker and Watson (1972) and Casper et al. (1980), and the extensive range of studies cited therein. Rotating machines of the radial or centrifugal flow class typically exhibit more complex flow behavior than that occurring in axial flow machines. Nevertheless, flow-blade interactions analogous to those of the axial flow category can be present. Cumpsty (1977) characterizes a range of unresolved issues inherent to the category of radial flow machines.

In radial flow machines, the spacing between the impeller and (stationary) diffuser blading is typically small, providing the potential for generation of large-amplitude pressure fluctuations. Arndt et al. (1989, 1990) determined the large-amplitude pressure and lift fluctuations in a diffuser pump due to impeller blade-diffuser blade interactions. For volute pumps and centrifugal blowers, no stationary diffuser (stator) vanes are present. However, the existence of the rotating impeller in presence of the tongue (or cutoff or cutwater) is a major source of noise generation. Embleton (1963), Simpson et al. (1967), and Blake (1986) address several aspects of noise generation from this class of machines. Several types of geometrical modifications are suggested by Neise (1976, 1982) for attenuation of the discrete and broadband noise. The complex flow patterns that can occur in these types of radial flow systems have been revealed by Inoue and Cumpsty (1984) with hot wire and surface pressure measurements, by Paone et al. (1989), Dong et al. (1992a,b), and Akin and Rockwell (1992) using whole field measurement techniques and by Elholm et al. (1992) via flow visualization complemented with laser anemometry.

In rotating machines, global instabilities can occur on a scale larger than the instabilities associated with a single blade. Examples include impeller rotating stall, diffuser instability, and surge. The many features of these complex phenomena are assessed by Abdelhamid et al. (1979), Frigne and Van den Braembussche (1984), Kinoshita and Senoo (1988), and Otugen and Hwang (1988).

Unsteadiness of the inflow is, of course, expected to influence the overall dynamic performance characteristics of a ra-

Contributed by the Fluids Engineering Division for publication in the JOURNAL OF FLUIDS ENGINEERING. Manuscript received by the Fluids Engineering Division September 28, 1992; revised manuscript received February 23, 1994. Associate Technical Editor: N. A. Cumpsty.

dial flow machine. Anderson et al. (1971) have determined the overall resistance and inertness of a radial-bladed centrifugal pump subjected to sinusoidal fluctuations of the flow rate. Fanelli (1972) formulates a model for determining the internal impedance of a hydraulic machine in the presence of unsteady throughflow. Such a framework, when combined with knowledge of the complex types of unsteadiness in a machine, can provide a unified basis for analysis.

The issue arises as to whether it is possible to manipulate the spectral content of fluctuations occurring in rotating machinery by imposing perturbations on the nominally-steady inflow, the impeller, or a combination of them. In a practical sense, in contrast to inflow perturbation, significant perturbations of the impeller rotation rate are unlikely to occur. Nevertheless, the aim of the present study is to gain insight into flow control concepts; the simultaneous existence of inflow and impeller perturbations allows a phase shift between them, and a study of the general theme of phase-shifting concepts. Using different approaches, other investigators have demonstrated the success of controlling instabilities in axial and radial flow machines. In these studies, emphasis has been on the control of surge-type instabilities, as addressed by Pinsley (1988) and Huang (1988), and rotating-stall instabilities, described by Dugundji et al. (1989). These observations suggest that the flow structure in radial flow machines may be susceptible to control. In the present study, the active control is of the open-loop (non-feedback) type. If the nature of the unsteadiness can be modified using the approaches described in this study, then equivalent or analogous techniques may be employed in practice in order to minimize flow-induced loading and noise generation.

The objective of this investigation is to determine the response of the flow through a free impeller and an impeller-diffuser blade system, typical of the configurations employed in radial flow pumping systems. The overall goal is to determine the degree to which the spectral content of the impeller wake can be controlled for cases with and without a stationary diffuser blade. Of particular interest is the possible generation of nonlinear interaction components in the wake spectra, along with possible attentuation of the inflow perturbation component as well as the blade passing component, and the consequence of the spectral alterations in relation to the broadband (background) level of the flow fluctuations.

## 2 Experimental System and Techniques

A transparent, actively controlled rotating machine was employed, in order to facilitate optically based measurements of the velocity field. Figure 1 is an overview of the system. The inflow was controlled by the motion of the piston within the duct; various combinations of mean and perturbed flow could be generated by programming the Compumotor at the end of the drive train. Likewise, the rate of rotation of the impeller, consisting of mean and perturbation components, could be controlled by the Compumotor mounted on top of the reservoir. The impeller, shown in Figs. 2(*a*) and 2(*b*), as well as

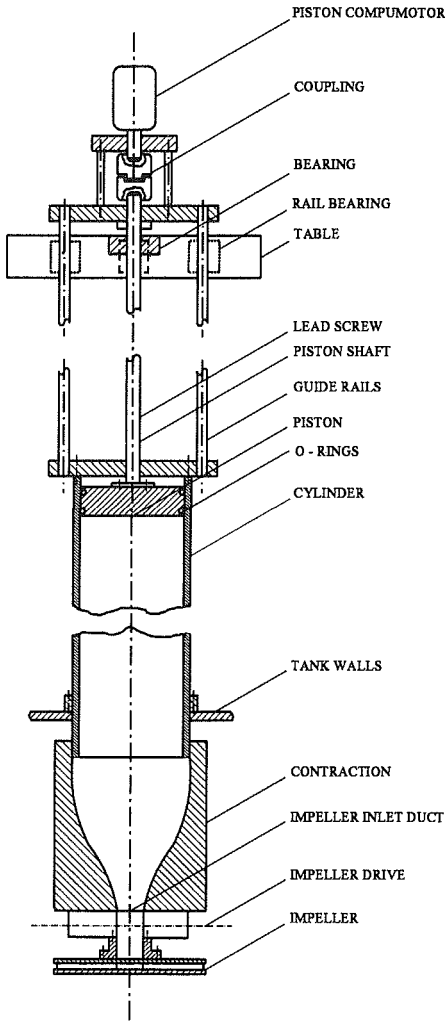


**Fig. 1 Overview of transparent, actively controlled rotating machine**

## Nomenclature

$b$ = width of impeller discharge (mm)
$D$ = diameter of impeller discharge (mm)
$e$ = probe location measured from discharge of impeller (mm)
$f_{BP}$ = blade passing frequency (c/s)
$f_{F_i}$ = forcing frequency of impeller perturbation (c/s)
$f_{F_p}$ = forcing frequency of inlet flow perturbation (c/s)
$f_F$ = forcing frequency when inlet flow perturbation frequency is equal to impeller perturbation; or, spectral component at forcing frequency in response spectrum (c/s)
$m, n$ = integers
$Q$ = volume flow into impeller ($m^3/s$)
$r_i$ = impeller radius (mm)
$\overline{V}_p$ = mean inflow velocity (m/s)
$\tilde{V}_p$ = fluctuating inflow velocity (m/s)
$\tilde{V}_p/\overline{V}_p$ = amplitude of inflow perturbation
$\overline{V}_i$ = mean tangential velocity of impeller (m/s)
$\tilde{V}_i$ = fluctuating tangential velocity of impeller (m/s)
$V^*$ = power spectral density of fluctuating velocity $\tilde{V}$
$\tilde{V}_i/\overline{V}_i$ = amplitude of impeller perturbation
$\alpha$ = angle of leading-edge of diffuser blade relative to trailing-edge of impeller
$\beta_1$ = impeller blade angle (inlet)
$\beta_2$ = impeller blade angle (discharge)
$\Omega$ = rotation rate of impeller (rev/sec)
$\Phi$ = flow coefficient = $Q/\pi bD\overline{V}_i$
$\psi_{ip}$ = phase shift between inlet flow and impeller perturbations (radians)

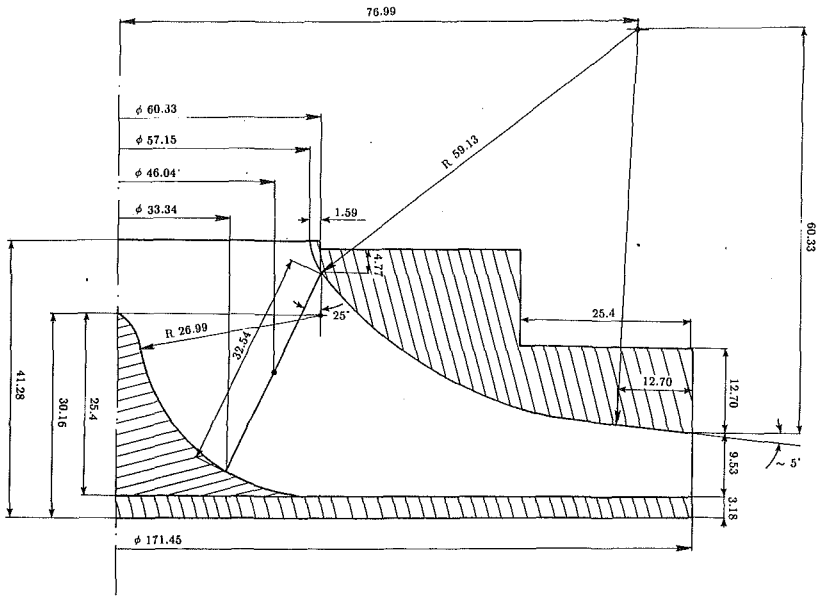


Fig. 2(*a*) Detailed dimensions of the six-bladed impeller, side view

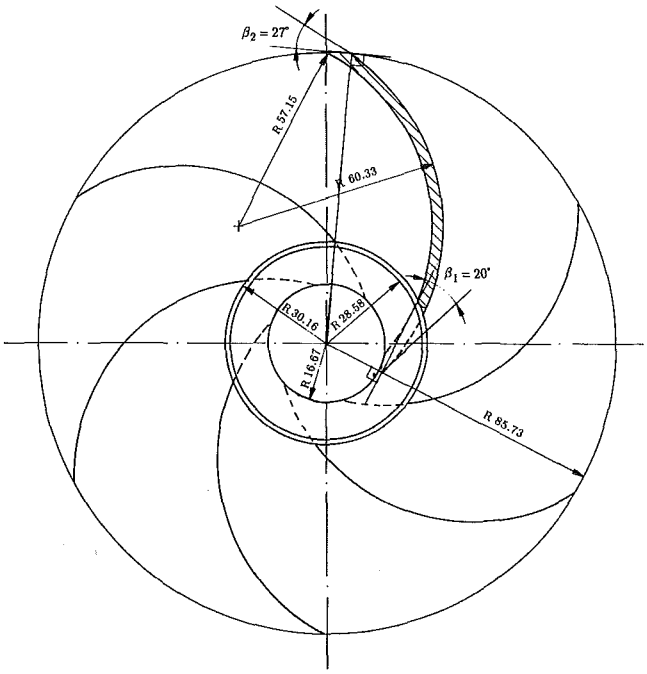


Fig. 2(*b*) Detailed dimensions of the impeller, plan view

the diffuser walls and diffuser blade (not shown) were machined from Plexiglas, making the system fully transparent. Full details of the system design are given by Akin (1991). The internal diameter and the length of the piston were 229 mm and 813 mm, respectively. For the experiments described herein, the ranges of operating conditions were as follows. The rotation rate $\Omega$ of the impeller was varied over the range $0.5 \leq \Omega \leq 1.7$ rev/s, and correspondingly the tangential velocity $\overline{V}_i$ of the impeller over values $0.27 \text{ m/s} \leq \overline{V}_i \leq 0.92$ m/s. The inflow velocity $\overline{V}_p$ at the eye of the impeller was in the range $0.1 \leq \overline{V}_p \leq 0.2$ m/s. Perturbation levels of the inflow and impeller could be adjusted within the ranges of $0.05 \leq \tilde{V}_p / \overline{V}_p \leq 0.30$ and $0.05 \leq \tilde{V}_i / \overline{V}_i \leq 0.30$ by programming the respective Compumotors. Since the system was operated in a blowdown mode, it was necessary to allow a minimum number of impeller rotations before a stationary response was attained. Extensive study of velocity records showed that a criterion of nine rotations, corresponding to 54 blade passings, was adequate.

Cross-sectional and plan views of the six-bladed impeller are shown in Figs. 2(*a*) and 2(*b*). Blades were constructed by the Single Arc Method (Lazarkiewicz and Troskolanski, 1965) with constant thickness from the leading- to the trailing-edge. The inlet and discharge blade angles, $\beta_1$ and $\beta_2$ are $\beta = 20$ deg and $\beta_2 = 27$ deg.

Velocity measurements were performed at the impeller outlet using a laser-Doppler anemometer (LDA) described in detail by Akin (1991). The control volume of the LDA was positioned at the midspan of the diffuser discharge and at the radial locations described in the subsequent text. The region of primary interest was the near-wake of the impeller, where amplification of fluctuations and generation of sum and difference frequencies occurs. Movement of the LDA control volume to different locations, extending over radial distances of the order of the trailing-edge thickness of the impeller, showed the same general form of velocity spectra. The same predominant peaks were present, but their relative amplitudes were altered. At large distances, secondary spectral peaks were rapidly attenuated due to turbulent mixing.

Spectra of the velocity fluctuations were obtained using a data acquisition and processing system based on the laboratory microcomputer, as described by Akin (1991). The analog signal from the counter processor was employed to filter frequencies above the Nyquist frequency, which was 50 Hz. This corresponded to a sampling frequency $\Delta f = 100$ Hz and a sampling time $\Delta t = 0.01$ s. For each set of acquired data, this corresponded to approximately 61 to 208 passages of the impeller blade. Moreover, each spectrum obtained using this sampling was averaged together with 12 other spectra to provide, in effect, an averaging over a total of 732 to 2496 passages of the impeller blade.

## 3 Response to Imposed Forcing: Generation of Multiple Spectral Components in Wake of Free Impeller

The unsteady velocity was measured at the discharge of the free impeller for various types of unsteady inflow and impeller perturbation conditions. These perturbations were imposed using the techniques described in Section 2. The principal classes of forcing involved: controlled perturbations of the inflow velocity $\tilde{V}_p$ at a frequency $f_{F_p}$; simultaneous perturbations of

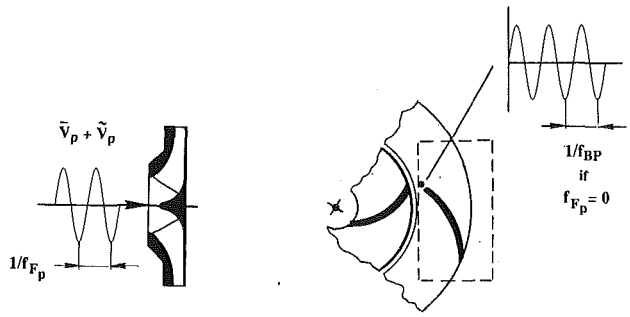


**Fig. 3 Generation of modulated spectral components of flow structure—hypothesized mechanisms**

the inflow $\tilde{V}_p$ and impeller tangential velocity $\tilde{V}_i$ at frequency $f_F$ with zero phase shift between them, referred to as a synchronized condition; and simultaneous forcing of the inflow $\tilde{V}_p$ and impeller velocities $\tilde{V}_i$ with variable phase shift $\psi_{ip}$ between them.

The unsteady velocity fluctuation in the tangential direction was characterized at a location immediately outside the impeller discharge, corresponding to $e/r_i = 0.037$ in which $r_i$ is the radius of the impeller. In all experiments, the flow coefficient $\Phi$ was maintained at a value of $\Phi = 0.111$, corresponding to an inlet velocity $\overline{V}_p = 0.2$ m/s at the entrance of the impeller and a rotational speed of the impeller of 1.7 rev/s corresponding to a blade passing frequency $f_{BP} = 10.2$ Hz. The amplitude of the inlet flow perturbation was in the range of $0.05 \leq \tilde{V}_p/\overline{V}_p \leq 0.30$. Unless otherwise noted, all forcing conditions described in the following correspond to the highest amplitude $\tilde{V}_p/\overline{V}_p = 0.30$.

**3.1 Overview of Concepts of Manipulating Spectral Response.** In order to provide a framework for the manipulations of the spectral content of the velocity fluctuations to be described in the figures that follow, it is insightful to consider simplified interpretations of the velocity fluctuations at the fixed location of measurement, as described in the schematic of Fig. 3. These concepts hold irrespective of whether or not a diffuser blade is in place. (In the first series of experiments, it is not in place; in the second, it is.) The inflow perturbation at frequency $f_{F_p}$ and period $1/f_{F_p}$ enters the eye of the impeller as represented in the left schematic. At the discharge of the impeller, represented by the point immediately to the right of the impeller blade tip in the right-hand schematic, the period of the detected fluctuation can be expected to be the inverse of the blade passing frequency, i.e., $1/f_{BP}$, if the inflow perturbation is not applied, i.e., if $f_{F_p} = 0$. Of course, in the actual flow, spectral analysis of the fluctuation at this location will show not only the component $f_{BP}$ but also its higher harmonics $2f_{BP}$, $3f_{BP}$, and so on. Now if the inflow perturbation is applied at $f_{F_p}$, then, in a strictly linear sense, the velocity fluctuation at the fixed location indicated in Fig. 3 can be expected to exhibit a difference frequency component $f_{F_p} - f_{BP}$. In the presence of higher amplitude and nonlinear effects, the nonlinear harmonic components of this difference frequency will be present. Depending upon the phase coherence between the components $f_{F_p}$ and $f_{BP}$, as well as between the harmonics of $f_{F_p}$ and $f_{BP}$, it may be possible to generate a large number of nonlinear difference components having the form of, for example, in $f_{F_p} + nf_{BP}$ where $\eta$ is an integer. We therefore have, on the basis of relatively simple reasoning, grounds for expecting generation of a variety of spectral peaks, traceable to a basic concept of difference frequency.

Even for simple flow configurations such as the separation of a shear layer from a trailing-edge (Miksad, 1972, 1973), it is possible to generate a variety of sum and/or difference frequency components when two different frequencies are applied to the shear layer from two different perturbations (loudspeaker) systems. The occurrence of possible sum/difference frequencies depends upon the phase coherence between the various spectral components. In self-excited systems, such as the impingement of a shear layer on the downstream corner of a cavity (Knisely and Rockwell, 1982), analogous sum and difference frequency components arise. Miksad (1973) and Knisely and Rockwell (1982) have demonstrated the essential feature of phase coherence between the interacting spectral components using bicoherence concepts. These concepts of nonlinear interaction are expected to apply to the present configuration; the occurrence of unsteady separated flow not only in the wake of the impeller blade, but also within the impeller, provides the possibility for a rich variety of interaction phenomena.

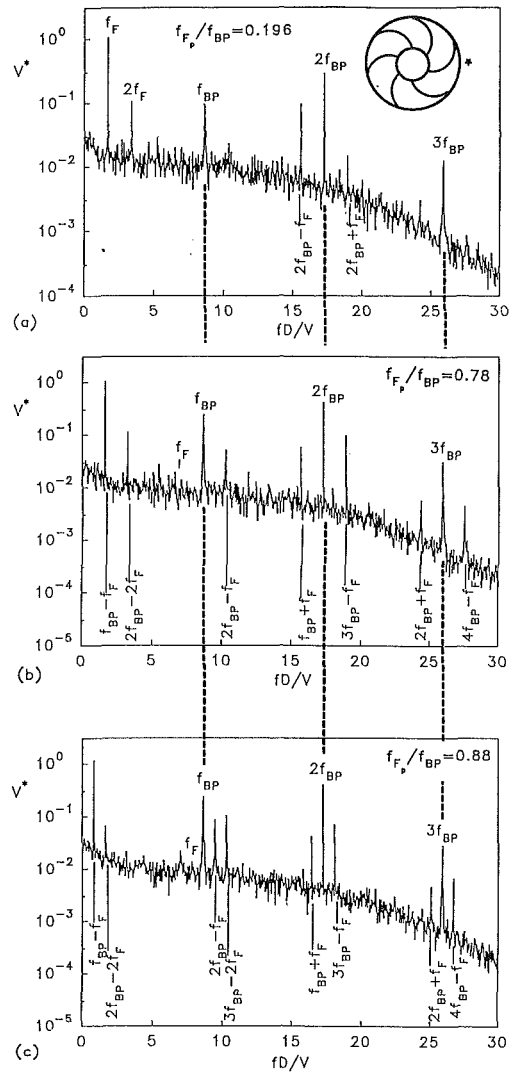


**Fig. 4(*a, b, c*) Spectrum of velocity fluctuations for active control in the form of inlet flow perturbations with an amplitude of 30 percent where the ratio of the forcing frequency to the blade passing frequency is: (*a*) 0.196, (*b*) 0.78, and (*c*) 0.88**

**3.2 Effect of Inflow Perturbations.** The first type of control perturbation involves forced unsteadiness of the inlet flow at a constant (steady) rotation rate of the impeller. In absence of the applied perturbation (not shown), only the blade passing frequency $f_{BP}$ and its higher harmonics $2f_{BP}$ and $3f_{BP}$ are present. The degree to which these inherent blade passing components are matched to, or interact with, the imposed perturbation are expected to influence the extent to which the spectrum can be manipulated.

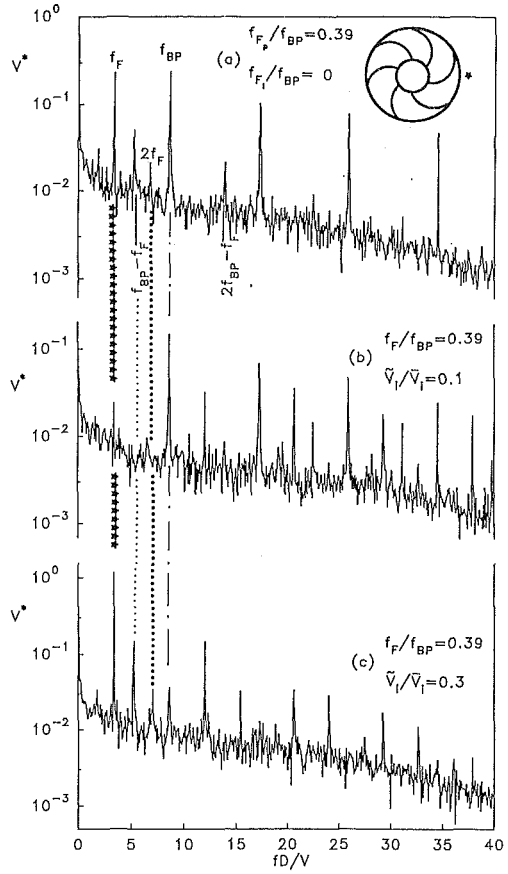


**Fig. 5 Spectrum of velocity fluctuations for: active control in the form of: (*a*) inlet flow perturbations with an amplitude of 30 percent where the ratio of the forcing frequency to the blade passing frequency is 0.39, (*b*) simultaneous forcing of the impeller with an amplitude of 10 percent, and (*c*) simultaneous forcing of the impeller with an amplitude of 30 percent**

As shown in Fig. 4(*a*), forcing the inlet flow at a frequency of $f_{F_p}/f_{BP}=0.196$ produces a predominant component in the spectrum at the forcing frequency $f_F$; the only other indications of the forcing correspond to its first harmonic $2f_F$ and to its sum and difference frequencies with the second harmonic of the blade passing frequency, i.e., $2f_{BP}\pm f_F$. An increase of the forcing frequency to a value of $f_{F_p}/f_{BP}=0.78$ produces, as illustrated in Fig. 4(*b*), the remarkable result of complete attenuation of the spectral component at the forcing frequency $f_F$. Remaining are the difference frequency components between the blade passing and forcing frequencies. Pronounced sum and different interaction components with the second, third, and fourth harmonics of the blade passing frequency are also evident. This suppression of the component at the forcing frequency $f_F$ persists to higher values of excitation frequency $f_{F_p}=0.88$, as illustrated in Fig. 4(*c*). Again, suppression is achieved at the expense of introducing nonlinear interaction components corresponding to sum and difference frequencies of the higher harmonics of the blade-passing frequency and the forcing frequency. The suppression of the component $f_F$ may be related to the concept of coalescence of frequencies in globally unstable wake systems, one corresponding to the forcing component, and the other to a self-excited component (Staubli and Rockwell, 1987).

Viewing the spectra of Fig. 4 as a whole, and comparing the broadband background level of the fluctuations, the imposed perturbations produce no significant change in the broadband content. Therefore, we conclude that the effect of the imposed perturbations is to cause a redistribution of energy among discrete spectral components. In fact, in those cases where the component at the forcing frequency $f_F$ is attentuated, the number of higher order spectral peaks associated with nonlinear interactions increases.

**3.3 Effect of Simultaneous Inflow and Impeller Perturbations.** As illustrated in the foregoing, it is possible to attenuate the component at the forcing frequency $f_F$ provided the value of $f_F$ is of the order of 80 percent or more of the blade passing frequency $f_{BP}$. This type of attentuation can be achieved at considerably lower values of forcing frequency by simultaneous excitation of the impeller, as illustrated in Fig. 5. In these cases, the impeller perturbation is represented by perturbations of its tangential velocity $\tilde{V}_i$ at the same frequency as the inlet flow perturbations $\tilde{V}_p$. In all cases, there is zero phase shift between these two types of perturbations; in other words, they are synchronized. At the lower value of impeller perturbation amplitude, represented by Fig. 5(*b*), the peak at the forcing frequency $f_F$ is reduced by about one order of magnitude relative to the case of no impeller perturbation shown in Fig. 5(*a*). An increase in the amplitude of the impeller perturbation, represented by Fig. 5(*c*) produces large amplitudes at the forcing frequency $f_F$. Akin (1991) considers in detail the decrease, then increase, of the component at $f_F$ over a range of perturbation amplitude and finds complete attenuation of the forcing component $f_F$ for a dimensionless impeller perturbation amplitude $\tilde{V}_i/\bar{V}_i=0.08$. Furthermore, as is evident by comparing Fig. 5(*c*) with 5(*b*), the increase in amplitude of component $f_F$ is accompanied by a substantial decrease in the amplitude of the component $f_{BP}$. Apparently, the large amplitude tangential velocity perturbation imposed by the impeller overwhelms the velocity perturbation induced by the blade passing.

**3.4 Effect of Simultaneous Inflow and Impeller Perturbations With Variable Phase Angle Between Them.** The effect of varying the phase angle between the inflow and impeller perturbations is shown in Fig. 6. As a reference, the case of no applied perturbation is shown in Fig. 6(*a*). The predominance of the blade passing frequency $f_{BP}$ and its higher harmonics $nf_{BP}$ is clearly evident. Figure 6(*b*) represents the case of an inflow perturbation, but with no impeller perturbation other than the component at the forcing frequency $f_F$ and its harmonic $2f_F$; there are only two identifiable peaks, which are due to nonlinear interaction. Figure 6c shows the case of perturbations of both the inflow and the impeller, with zero phase shift $\psi_{ip}=0$ between them, corresponding to synchronized excitation. The nonlinear interaction peaks correspond to difference frequencies between the blade passing frequency $f_{BP}$, its harmonics, and the forcing frequency $f_F$, i.e., $mf_{BP}\pm f_F$ where $m$ is an integer. The number of nonlinear interaction peaks increases but the amplitude of the peak at the forcing frequency decreases drastically, relative to the case of Fig. 6(*b*). As illustrated in Fig. 6(*d*), introduction of a phase shift between the impeller and the inflow of $\psi_{ip}=\pi/4$ produces a pronounced interaction component $3f_F/2$ due to the interaction of the subharmonic $f_F/2$ with the forcing frequency $f_F$; also, the amplitude of the peak at the forcing frequency increases, even exceeding the case of Fig. 6(*b*), for which the impeller is not perturbed. This general form of the spectral content persists for a phase shift of $\psi_{ip}=\pi/2$ (Fig. 6(*e*)).

Viewing together the spectra given in Fig. 6, it is evident that substantial manipulation of the discrete spectra components can be attained, at least for the discrete components in the low-frequency range of the spectrum, by variation of the phase angle between the inflow and impeller perturbations.

## 4 Response to Imposed Forcing: Generation of Multiple Spectral Components in Impeller-Vaneless Diffuser and Impeller-Diffuser Blade System

In this phase of the investigation, the same impeller was

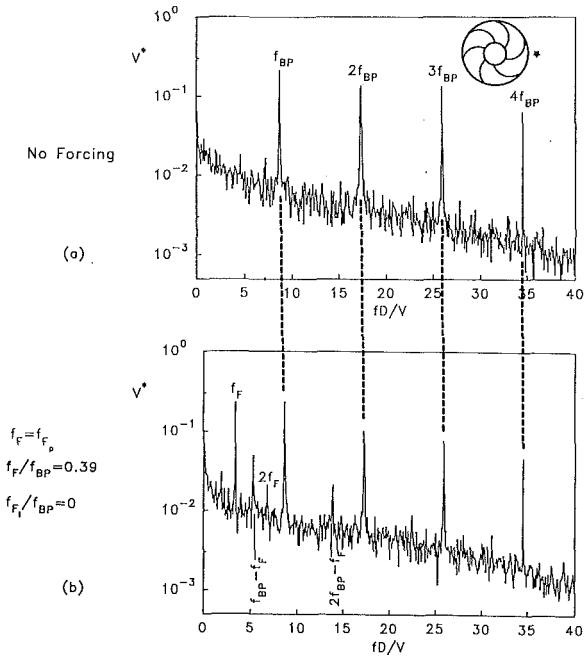


**Fig. 6(*a*, *b*) Spectrum of velocity fluctuations for: (*a*) no active control and (*b*) active control in the form of inlet flow perturbation with an amplitude of 30 percent where the ratio of the forcing frequency to the blade passing frequency is 0.39**

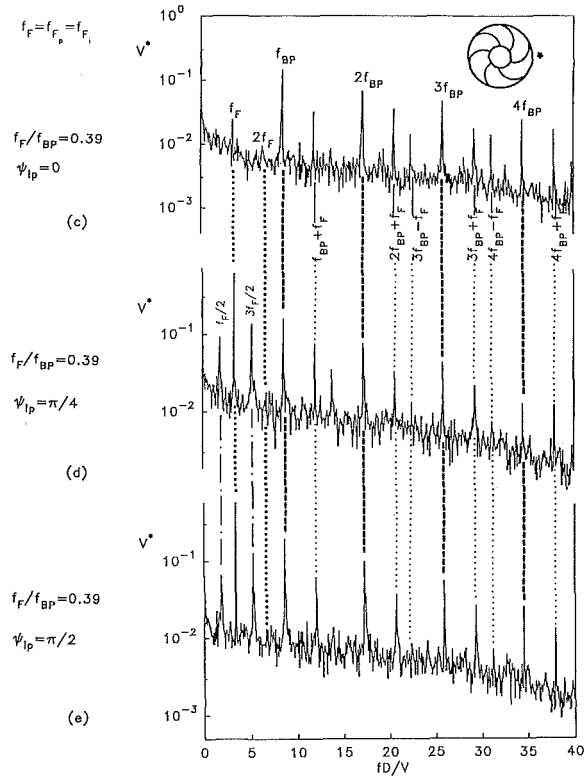


**Fig. 6(*c*, *d*, *e*) Spectrum of velocity fluctuations for: (*c*) simultaneous forcing of the impeller with an amplitude of 10 percent and zero phase angle, (*d*) phase angle of $\pi/4$, and (*e*) $\pi/2$**

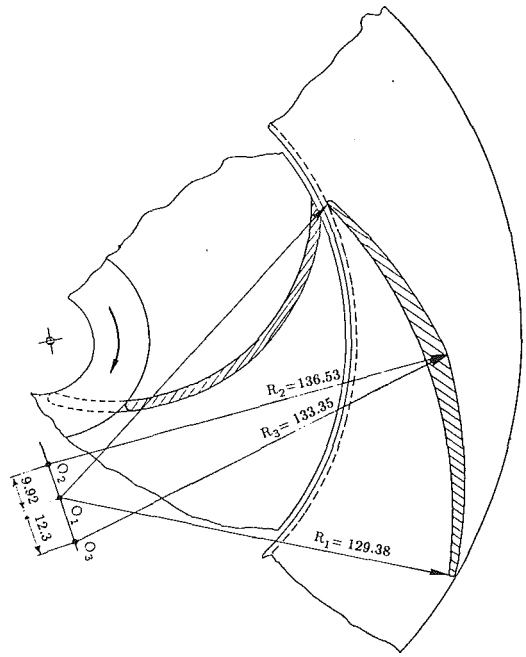


**Fig. 7 Dimensions of diffuser blade**

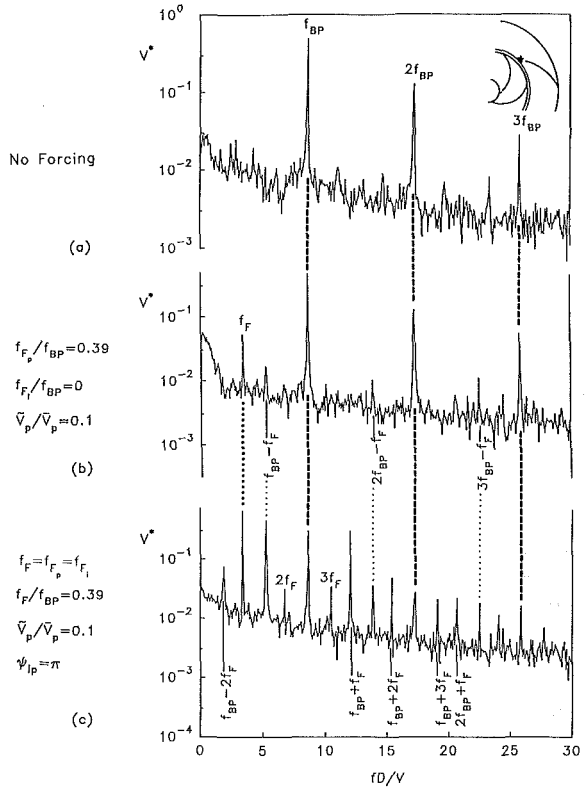


**Fig. 8 Spectrum of velocity fluctuations for: (*a*) no active control, (*b*) active control in the form of inlet flow perturbations with an amplitude of 10 percent where the ratio of the forcing frequency to the blade passing frequency is 0.39, and (*c*) phase angle of $\pi$ between the inlet flow perturbation at $f_{F_p}$ and the impeller perturbation at $f_{F_i}$**

employed. Diffuser discs (endwalls) and later a single diffuser blade were added, as defined in detail by Akin (1991). The ratio of the diameter of the diffuser to the diameter of the impeller was 1.6. The gap between the discharge of the impeller and the diffuser inlet was 1.6 mm. The width of the diffuser, which was constant from inlet to discharge, was chosen 10 percent smaller than the breadth of the impeller discharge.

For subsequent experiments, a single diffuser blade was mounted within the diffuser (Fig. 7). This single blade allowed more extensive optical access than a complete cascade. The gap between the exit of the impeller blade and the leading-

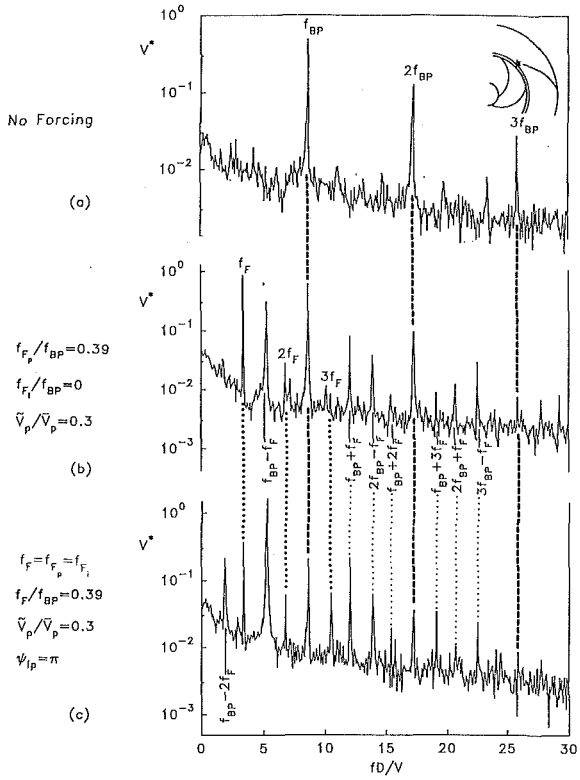


**Fig. 9 Spectrum of the velocity fluctuations for: (*a*) no active control, (*b*) active control in the form of the inlet flow perturbations with an amplitude of 30 percent where the ratio of the forcing frequency to the blade passing frequency is 0.39, and (*c*) phase angle of $\pi$ between the inlet flow perturbation at $f_{F_p}$ and the impeller perturbation at $f_{F_i}$**

edge of the diffuser blade was 3.2 mm. The diffuser blade was designed according to criteria described by Lazarkiewicz and Troskolanski (1965). The angle of the geometrical tangent of the leading-edge of the blade, relative to that of the trailing-edge of the impeller was 15 deg. Measurements of the velocity fluctuations were made at a distance of 4.8 mm upstream of the leading-edge of the diffuser blade and at a radial location approximately midway between the leading-edge of the blade and the trailing-edge of the impeller blade. This location, which lies in the region of maximum flow distortion, is indicated by the star in Figs. 8 to 12.

Experiments were carried out for the same basic classes of perturbations as for the free impeller, described in Section 4: in the absence of perturbations; and with various combinations of inflow and impeller perturbations.

In the absence of perturbations, the spectrum takes the form shown in Fig. 8(*a*). The blade passing frequency $f_{BP}$ and its higher harmonics $nf_{BP}$ are substantially above the broadband (background) level. In the presence of relatively low amplitude perturbations of the inflow, $\tilde{V}_p/\bar{V}_p=0.1$, the forcing frequency $f_F$ is evident along with barely discernible difference frequencies between the blade-passing frequency $f_{BP}$, its higher harmonics $nf_{BP}$ and the forcing frequency $f_F$. When both inflow and impeller perturbations are imposed, with a phase angle of $\psi_{ip}=\pi$ between them, the spectrum takes the form shown in Fig. 8(*c*). Not only is the component at the forcing frequency substantially larger, but also the number of nonlinear interaction components involving sum and difference frequency components has increased markedly.

Corresponding experimental results are given in Fig. 9 for a larger amplitude of the inflow perturbation. Figure 9(*a*) shows the case of no applied perturbation. As indicated in Fig. 9(*b*), the discrete component at the forcing frequency $f_F$, as well as the nonlinear sum and difference components, increase

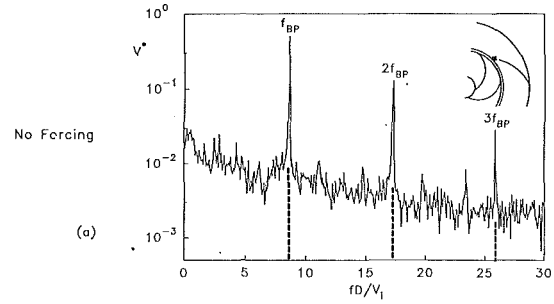


**Fig. 10(*a*) Spectrum of velocity fluctuations for: (*a*) no active control**

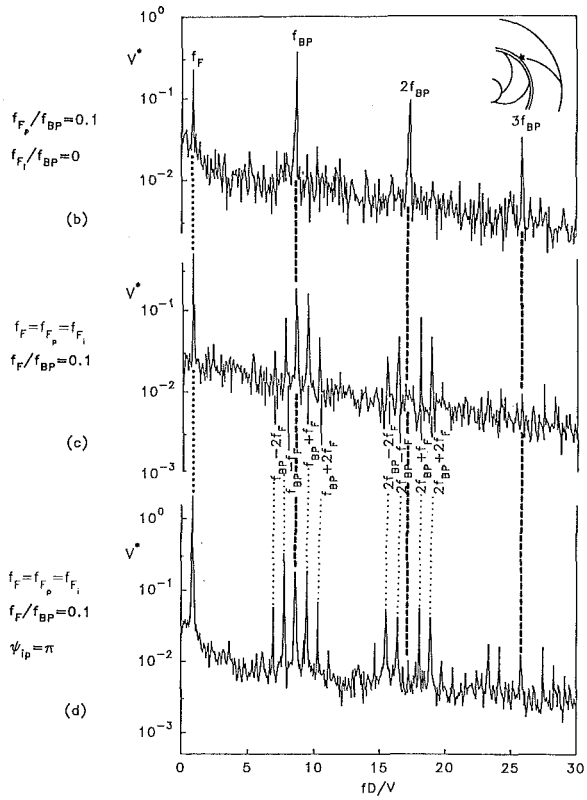


**Fig. 10(*b, c, d*) Spectrum of velocity fluctuations for: (*b*) active control in the form of inlet flow perturbation with an amplitude of 10 percent and where the ratio of the forcing frequency to the blade passing frequency is 0.1, (*c*) simultaneous forcing of the inlet flow and the impeller and zero phase angle, and (*d*) phase angle of $\pi$ between the inlet flow perturbation at $f_{F_p}$ and the impeller perturbation at $f_{F_i}$. Amplitude of impeller perturbation is $\tilde{V}_i/\bar{V}_i=0.10$.**

substantially. As shown in Fig. 9(*c*), the relative amplitudes of the spectral components can be manipulated by simultaneous excitation of the impeller and the inflow (i.e. piston) with a phase angle $\psi_{ip}=0$ between them. In this case, for example, a difference frequency component $f_{BP}-f_F$ dominates the component at the forcing frequency $f_F$.

Viewing together the spectra shown in Figs. 8 and 9, it is evident that the number and strength of the nonlinear interaction components can be enhanced in one of two ways: by increasing the amplitude of the inflow perturbation component (compare Figs. 8(*b*) and 9(*b*)), or by excitation of both the impeller and the inflow with an appropriate phase angle between them (compare Figs. 8(*b*) and 8(*c*) and 9(*b*) and 9(*c*)).

In the event that the forcing $f_F$ and blade-passing $f_{BP}$ components are well separated, it is expected that the strength of the nonlinear interaction between them, and in turn the amplitudes of the interaction components in the spectrum, will

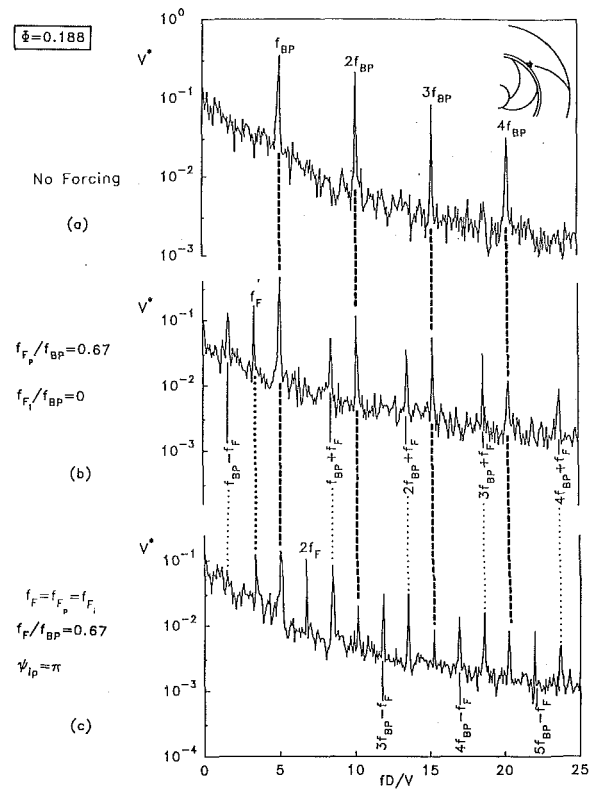


Fig. 11 Spectrum of velocity fluctuations at off-design condition with a flow coefficient of 0.188, for: (*a*) no active control, (*b*) active control in the form of inlet flow perturbations with an amplitude of 30 percent and ratio of forcing frequency to blade passing frequency of 0.67, and (*c*) phase angle of $\pi$ between the inlet flow perturbation at $f_{F_p}$ and the impeller perturbation at $f_{F_i}$. Amplitude of impeller perturbation is $\tilde{V}_i/\overline{V}_i=0.10$.

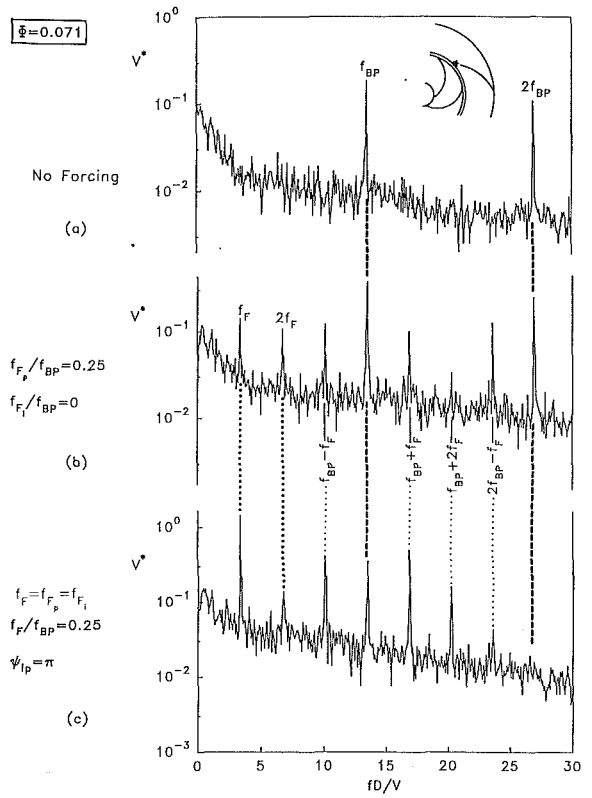


Fig. 12 Spectrum of velocity fluctuations, at off design condition with a flow coefficient is 0.071, for: (*a*) no active control, (*b*) active control in the form of inlet flow perturbations with an amplitude of 30 percent and the ratio of the forcing frequency to the blade passing frequency is 0.25, and (*c*) phase angle of $\pi$ between the inlet flow perturbation at $f_{F_p}$ and the impeller perturbation at $f_{F_i}$. Amplitude of impeller perturbation is $\tilde{V}_i/\overline{V}_i=0.10$.

be smaller than for the preceding cases. The effect of a relatively low forcing frequency is illustrated in Fig. 10. In this case, the forcing frequency is one order of magnitude lower than the blade passing frequency. Figure 10(*a*) represents the case of no applied perturbation. In Fig. 10(*b*), only the inflow is perturbed, and there is no indication of interaction between the forcing $f_F$ and blade passing $f_{BP}$ components. This is due to the fact that the essential condition for nonlinear interaction, namely phase coherence between spectral components, cannot be attained if the forcing and blade passing frequencies are widely separated. On the other hand, Fig. 10(*c*) shows that if both the inflow and impeller are subjected to perturbations at the same frequency and amplitude with zero phase angle between them, then there is a dramatic increase in the number of spectral components involving sum and difference combinations of the blade passing and forcing frequencies and their higher harmonics. In contrast to the previous cases of forcing at a frequency close to the blade passing frequency, the sum and difference combinations take the form of well-defined sidebands (about $f_F$, $2f_F$, $3f_F$) of progressively decreasing amplitude. This cluster of spectral peaks is characteristic of amplitude-/frequency-modulated response; in this case, the carrier component is $f_{BP}$ and the modulating component is $f_F$. The occurrence of the sum and difference frequencies in Fig. 10(*c*) is accompanied by a significant attenuation of the blade passing component $f_{BP}$ and almost complete disappearance of the peaks at its first and second harmonic components. Figure 10(*d*) shows that alteration of the phase angle between the inflow and impeller perturbations has a relatively minor effect on the spectrum. The broadband (background) level of the spectra shown in Figs. 10(*a*) through 10(*d*) does not change significantly for the various excitation conditions. There appears to be simply a redistribution of energy over the discrete spectral components when forcing is applied.

The spectrum of the velocity fluctuations at the discharge of the vaned diffuser shows, however, a decrease of the broadband noise level (Akin, 1991). As shown therein, even in the case of phase-shifted inflow and impeller forcing, the peaks at the forcing and blade passing frequencies can be barely detected.

Up to this point, all experiments described were at the impeller design condition $\Phi=0.111$. In order to examine the response of the system at off-design conditions, two different, extreme values of flow coefficients $\Phi=0.071$ and 0.188 were investigated. These values of $\Phi$ were generated by keeping $\overline{V}_p$ constant ($\overline{V}_p=0.1$ m/s) and varying $\overline{V}_i$, i.e., $\Omega$. The values of the parameters for the off-design condition, relative to those for the design condition ($\Phi=0.111$) are: $\Phi=0.071$ ($\Omega=1.32$ rev/s, $f_{BP}=7.97$ Hz); $\Phi=0.111$ ($\Omega=0.85$ rev/s, $f_{BP}=5.10$ Hz); $\Phi=0.188$ ($\Omega=0.5$ rev/s, $f_{BP}=3.0$ Hz). For the case of the high flow coefficient, $\Phi=0.188$, shown in Fig. 11, the case of no inflow or impeller perturbation is represented by the spectrum of Fig. 11(*a*). It exhibits relatively high amplitude broadband (background) level at low frequencies, most likely due to the occurrence of stall phenomena, i.e., large-scale flow separation in the vicinity of the trailing-edge of the impeller as determined by flow visualization. Application of an inflow perturbation, as illustrated in Fig. 11(*b*), actually decreases the broadband level in the low frequency range but at the expense of pronounced components at the forcing frequency $f_F$ and its sum and difference frequencies with the blade passing component $f_{BP}$. If both the inflow and impeller are perturbed, with a phase

angle $\psi_{ip} = \pi$ between them, as illustrated in Fig. 11(*c*), then the background level returns to a relatively high value and the amplitudes of the discrete components below the blade passing frequency are attenuated.

At the other extreme value of flow coefficient, $\Phi = 0.071$, shown in Fig. 12, it is evident that the low frequency, broadband level again is higher than that corresponding to the on-design condition. Application of an inflow perturbation, shown in Fig. 12(*b*) produces discrete components at the forcing and nonlinear interaction components. As illustrated in Fig. 12(*c*), it is possible to manipulate the relative amplitudes of these components by introducing a phase angle $\psi_{ip} = \pi$ between the inflow and impeller perturbation components. For example, the amplitude of the component at the forcing frequency $f_F$ increases by about one order of magnitude and the first harmonic of the blade passing frequency $2f_{BP}$ is entirely attenuated.

## 5 Concluding Remarks

It has been demonstrated that the spectral content of the near-wake (discharge) of a free impeller as well as the interaction region of an impeller-diffuser blade system, can be manipulated by perturbations of the inflow into the impeller, perturbations of the impeller rotation rate, and combinations of these classes of perturbations. The spectral content can be altered, in some cases substantially, not only at the design flow condition but also for flow coefficients well above and below it. Although it is possible to modify the discrete spectral components, the background (broadband) level is, in general, relatively uninfluenced. The only exception occurs at off-design flow coefficients where it is possible to modify the amplitude of low frequency, broadband fluctuations. Generally speaking, modification of the spectral content involves transfer of energy between discrete spectral components. All of the observed spectral components correspond to the blade passing frequency, the forcing frequency, their harmonics, or their sum/difference nonlinear interactions.

There are several general observations that can be made as a result of considering not only the spectra indicated here but also additional spectra (Akin, 1991) over a wide range of excitation conditions:

(*a*) The number of sum and difference frequencies occurring in the spectra, which are due to nonlinear interactions, increases as the value of the forcing frequency approaches the blade passing frequency.

(*b*) As the amplitude of either the inflow or impeller perturbation increases, it tends to induce nonlinear interactions over a wide frequency range, in particular at higher frequency in the spectra.

(*c*) Under certain excitation conditions, it is possible to attain a nearly complete attenuation of the inflow perturbation. This attenuation tends to occur when the excitation frequency is sufficiently high relative to the passing frequency, in particular when it reaches a value of about 80 percent of the blade passing frequency.

(*d*) At sufficiently large amplitude of the inflow perturbation, it is possible to significantly reduce the amplitude of the spectral component at the blade-passing frequency; this is achieved, however, at the expense of substantial components at other frequencies.

(*e*) Simultaneous inflow and impeller perturbations, with a prescribed phase angle between them, can drastically alter the number and amplitude of nonlinear interaction peaks.

## Acknowledgments

The authors gratefully acknowledge the support of the Office of Naval Research under ONR-ARI Grant N00014-89-J-1799.

## References

Abdelhamid, A. N., Colwill, W. H., and Barrows, J. F., 1979, "Experimental Investigation of Unsteady Phenomena in Vaneless Diffusers," *Trans. ASME*, Vol. 101, pp. 52–60.

Anderson, D. A., Blade, R. J., and Stevans, W., 1971, "Response of a Radial-Bladed Centrifugal Pump to Sinusoidal Disturbance for Non-Cavitating Flow," NASA Technical Note D-6556.

Akin, O., 1991, "Unsteady Flow in an Actively-Controlled Centrifugal Pump," M.S. Thesis, Department of Mechanical Engineering and Mechanics, Lehigh University, Bethelehem, PA.

Akin, O., and Rockwell, D., 1993, "Flow Structure in a Radial Flow Pumping System Using High-Image-Density Particle Image Velocimetry," ASME JOURNAL OF FLUIDS ENGINEERING, published in this issue pp. 538–544.

Arndt, N., Acosta, A. J., Brennen, C. E., and Caughey, T. K., 1989, "Rotor-Stator Interaction in a Diffuser Pump," ASME *Journal of Turbomachinery*, Vol. 111, July, pp. 213–221.

Arndt, N., Acosta, A. J., Brennen, C. E., and Caughey, T. K., 1990, "Experimental Investigation of Rotor-Stator Interaction in a Centrifugal Pump with Several Vaned Diffusers," ASME *Journal of Turbomachinery*, Vol. 112, Jan., pp. 98–108.

Blake, W. K., 1986, *Mechanics of Flow-Induced Sound and Vibration*, Vol. 2, Complex Flow Structure Interactions, Academic Press, Inc.

Casper, J. R., Hobbs, D. E., and Davis, R. L., 1980, "Calculation of Two-Dimensional Potential Cascade Flow Using Finite Area Methods," *AIAA Journal*, Vol. 18, No. 1, Jan., pp. 103–109.

Cumpsty, N. A., 1977, "Review—A Critical Review of Turbomachinery Noise," ASME JOURNAL OF FLUIDS ENGINEERING, Vol. 99, June, pp. 278–293.

Dong, R., Chu, S., and Katz, J., 1991, "Quantitative Visualization of the Flow within the Volute of a Centrifugal Pump," ASME FED-Vol. 107, *General Topics in Fluids Engineering*, American Society of Mechanical Engineers, pp. 113–124.

Dong, R., Chu, S., and Katz, J., 1992a, "Quantitative Visualization of the Flow within the Volute of a Centrifugal Pump. Part A: Technique," ASME JOURNAL OF FLUIDS ENGINEERING, Vol. 114, Sept., pp. 390–395.

Dong, R., Chu, S., and Katz, J., 1992b, "Quantitative Visualization of the Flow within the Volute of a Centrifugal Pump. Part B: Results and Analysis," ASME JOURNAL OF FLUIDS ENGINEERING, Vol. 114, Sept., pp. 396–403.

Dring, R. P., Joslyn, H. D., Hardin, L. W., and Wagner, J. H., 1982, "Turbine Rotor-Stator Interaction," ASME *Journal of Engineering for Power*, Vol. 104, Oct., pp. 729–742.

Dugundji, J., Epstein, A. H., Garnier, V., Greitzer, E. M., Guenette, G., Paduano, J., Silkowski, P., Simon, J., and Valavani, L., 1989, "A Progress Report on Active Control of Flow Instabilities: Rotating Stall Stabilization in Axial Compressors," AIAA Second Shear Flow Conference, March 13–16, Tempe, AZ, Paper No. AIAA-89-1008.

Elholm, T., Ayder, E., and Van den Braembussche, R., 1992, "Experimental Study of the Swirling Flow in the Volute of a Centrifugal Pump," ASME *Journal of Turbomachinery*, Vol. 114, Apr., pp. 366–372.

Embleton, T. F. W., 1963, "Experimental Study of Noise Reduction in Centrifugal Blowers," *The Journal of the Acoustical Society of America*, Vol. 35, No. 5, pp. 700–705.

Fanelli, M., 1972, "Further Considerations of the Dynamic Behavior of Hydraulic Turbo-Machinery," *Water Power*, June, pp. 208–222.

Franke, G. F., and Henderson, R. E., 1979, "Unsteady Stator Response to Upstream Rotor Blades," AIAA Paper 79-0579, AIAA Fifth Aeroacoustics Conference, Seattle, Washington, Mar. 12–14.

Frigne, P., and Van den Braembussche, R., 1984, "Distinction Between Different Types of Propeller and Diffuser Rotating Stall in a Centrifugal Compressor with Vaneless Diffuser," ASME *Journal of Engineering for Gas Turbines and Power*, Vol. 6, pp. 468–474.

Gallus, H. E., Lambertz, J., and Wallmann, T. H., 1980, "Blade-Row Interaction in Axial-Flow Subsonic Compressor Stages," ASME *Journal of Engineering for Power*, Vol. 102, Jan., pp.169–177.

Horlock, J. H., 1968, "Fluctuating Lift Forces on Airfoils Moving Through Transverse and Chordwise Gusts," ASME *Journal of Basic Engineering*, pp. 494–500.

Huang, X., 1988, "Active Control of Aerodynamic Instabilities," Ph.D. Thesis, Cambridge University Engineering Department.

Inoue, M., and Cumpsty, N. A., 1984, "Experimental Study of Centrifugal Impeller Discharge Flow in the Vaneless and Vaned Diffusers," ASME *Journal of Engineering for Gas Turbines and Power*, Vol. 106, Apr., pp. 455-467.

Kemp, N. H., and Sears, W. R., 1953, "Aerodynamic Interference Between Moving Blade Rows," *Journal of the Aeronautical Sciences*, Vol. 20, No. 9, pp. 585–597.

Kemp, N. H., and Sears, W. R., 1955, "The Unsteady Forces Due to Viscous Wakes in Turbomachines," *Journal of the Aeronautical Sciences*, Vol. 22, No. 7, pp. 478–483.

Kinoshita, Y., and Senoo, Y., 1988, "Rotating Stall Induced in Vaneless Diffusers of Very Low Specific Seed Blowers," ASME *Journal of Engineering for Gas Turbines and Power*, Vol. 107, Apr., pp. 514–521.

Knisely, C., and Rockwell, D., 1982, "Self-Sustained Low-Frequency Components in an Impinging Shear Layer," *Journal of Fluid Mechanics*, Vol. 116, pp. 157–186.

Lazarkiewicz, S., and Troskolanski, A. T., 1965, *Impeller Pumps*, Pergamon Press, New York.

Miksad, R. W., 1972, "Experiments on the Nonlinear Stages of Free-Shear-Layer Transition," *Journal of Fluid Mechanics*, Vol. 56, pp. 695–719.

Miksad, R. W., 1973, "Experiments on Nonlinear Interactions in the Transition of a Free Shear Layer," *Journal of Fluid Mechanics*, Vol. 59, pp. 1–21.

Naumann, H., and Yeh, H., 1973, "Lift and Pressure Fluctuations of a Cambered Airfoil Under Periodic Gusts and Applications in Turbomachinery," ASME *Journal of Engineering for Power*, pp. 1–10.

Neise, W., 1976, "Noise Reduction in Centrifugal Fans: A Literature Survey," *Journal of Sound and Vibration*, Vol. 45, No. 3, pp. 375–403.

Neise, W., 1982, "Review of Noise Reduction Methods for Centrifugal Fans," ASME *Journal of Engineering for Industry*, Vol. 104, May, pp. 141–161.

Otugen, M. V., and Hwang, B. C., 1988, "The Effect of Diffuser Geometry on Rotating Stall Behavior," ASME Paper No. 88-GT-153.

Paone, N., Riethmuller, M. L., and Van den Braembussche, R. A., 1989, "Experimental Investigation of Flow in the Vaneless Diffuser of a Centrifugal Pump by Particle Image Displacement Velocimetry," *Experiments in Fluids*, Vol. 7, pp. 371–378.

Parker, R., and Watson, J. F., 1972, "Interaction Effects Between Blade Rows and Turbomachines," *Proceedings of the Institute of Mechanical Engineering*, Vol. 186, No. 21, pp. 331–340.

Pinsley, J. E., 1988, "Active Control of Centrifugal Compressor Surge," M.S. thesis, Department of Aeronautics and Astronautics, MIT.

Simpson, H. C., Clark, T. A., and Weir, G. A., 1967, "A Theoretical Investigation of Hydraulic Noise in Pumps," *Journal of Sound and Vibration*, Vol. 5, No. 3, pp. 456–488.

Staubli, T., and Rockwell, D., 1987, "Interaction of an Unstable Planar Jet with an Oscillating Leading Edge," *Journal of Fluid Mechanics*, Vol. 176, pp. 135–167.

Walker, J. J., and Oliver, A. R., 1972, "The Effect of Interaction Between Wakes from Blade Rows in an Axial Flow Compressor on a Noise Generated by Blade Interaction," ASME Paper No. 72-GT-15, contributed by the Gas Turbine Division for presentation at the Gas Turbine and Fluids Engineering Conference and Product Show, San Francisco, CA, Mar. 26–30, 1972.

# Flow Structure in a Radial Flow Pumping System Using High-Image-Density Particle Image Velocimetry

O. Akin

D. Rockwell

Department of Mechanical Engineering and Mechanics,
354 Packard Laboratory,
19 Memorial Drive West,
Lehigh University,
Bethlehem, PA 18015

*Use of high-image-density particle image velocimetry (PIV) allows characterization of the instantaneous structure of wake and wake-blade interactions in a simulated rotating machine. The distribution of vorticity over an entire plane within the pumping system is related to the instantaneous pressure source terms in the wake of the impeller. Comparison of instantaneous and ensemble-averaged vorticity contours shows that limited ensemble-averaging can produce a substantial reduction in vorticity levels associated with the instantaneous pressure source terms. When the wake from the impeller interacts with a stationary diffuser blade, the instantaneous processes of flow separation and reattachment can be effectively characterized using combinations of instantaneous streamline patterns and contours of constant vorticity. Moreover, active control of the inflow into the pumping system allows substantial modification of these vorticity distributions.*

## 1 Introduction

In rotating machinery of the radial flow type, a variety of complex flow phenomena can be present. The structure of the flow depends, of course, on the geometrical configuration of impeller and diffuser blades, in addition to the usual flow parameters. For volute pumps and centrifugal blowers, no stationary diffuser (stator) vanes are present. Depending upon the application, the efficiency, overall performance, and/or noise generation may be of interest. The focus of the present study is on those features of the flow pattern that are linked to the noise generation. Neither measurement of the overall pump noise nor a general solution to pump noise is pursued; rather, a framework is established for assessing possible source(s) of noise generation, in relation to the distortion of the flow field.

Paone et al. (1989) have characterized the nature of the wake from a rotating impeller blade, exhausting into a vaneless diffuser, using a whole field particle image velocimetry (PIV). Depending upon the flow coefficient of the rotating machine, quasi-organized concentrations of vorticity were observed in the wake region. Using an analogous whole field PIV technique, Dong et al. (1992a,b) have determined the turbulent flow structure in the volute of a centrifugal pump; they identified, among other features, a pulsating flow phenomenon, which depended on the location of the impeller blade relative to the tongue.

In certain pump and fan configurations, the wakes from the rotating impeller blades interact with a downstream diffuser blade or with the cutoff (or cutwater) of the pump. Due to this impingement process, the noise generation is particularly troublesome. Embleton (1963), Simpson et al. (1967), and Blake (1986) describe the primary features of the noise generation within these types of rotating machines. It is possible to attenuate the noise sources by appropriate geometric modifications, as addressed by Neise (1976, 1982). Arndt et al. (1989, 1990) have shown that the pressure fluctuations generated on the surface of a stationary diffuser blade can have very large amplitudes, due to the small spacing between the impeller and diffuser blades. In all of these systems, the flow patterns are particularly complex, and insight into the instantaneous flow structure has been difficult to achieve.

The major objective of the present investigation is to examine the detailed structure of the free wake of an impeller exhausting into a vaneless diffuser and the interaction of this wake with a stationary diffuser blade. In doing so, emphasis is given to acquisition of instantaneous distributions of vorticity over an entire plane of the flow, and their interpretation as a potential source of structural loading and noise generation.

## 2 Experimental Systems and Techniques

The pumping system employed in this investigation involved a unique, actively controlled rotating machine, illustrated in the overview of Fig. 1 and described in detail by Akin (1991). Distilled water was used as the working fluid. The inflow of this machine was controlled by motion of the piston within the duct, allowing generation of various combinations of mean and perturbed flow. During a given run, the water initially in the cylinder was forced through the impeller by the motion of

Contributed by the Fluids Engineering Division for publication in the JOURNAL OF FLUIDS ENGINEERING. Manuscript received by the Fluids Engineering Division October 20, 1992; revised manuscript received October 6, 1993. Associate Technical Editor: L. Nelik.

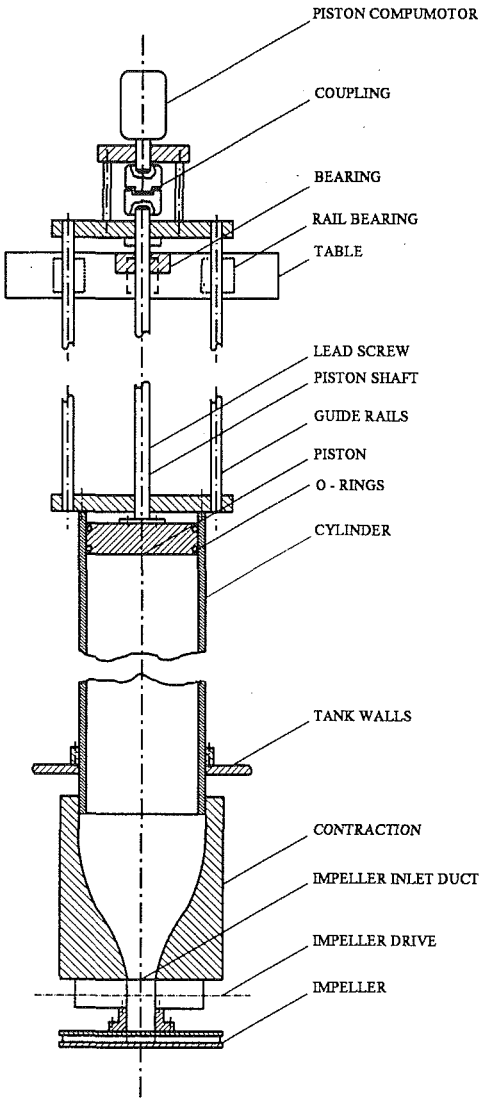


**Fig. 1 Overview of actively controlled pumping system**

the piston. This water was collected in a free-surface reservoir (not shown). To prepare for a subsequent run, the water was drawn into the cylinder by running the piston in reverse. The flow system was therefore a closed system operating in a blow-down mode. The functional form of the inlet flow was determined by the computer-controlled, high-resolution stepper motor (Akin, 1991) located at the end of the piston drive train. Only harmonic perturbations are considered in the present study. The rotation of the shaft of the computer-controlled motor was converted to translating motion of the piston via a lead screw. The rate of rotation of the impeller was controlled by the same type of motor located above the exhaust reservoir of the pump system (not shown in Fig. 1) and connected to the impeller by a drive chain.

Details of the impeller and impeller-diffuser system are given in the thesis of Akin (1991) and by Akin and Rockwell (1992). The radial flow impeller had six blades. The blades were constructed by the single arc method with constant thickness from the leading- to the trailing-edge of each blade. An overview of the cross-section of the impeller-vaneless diffuser system is given in Fig. 2(*a*). The critical dimensions are:

$$D_1 = 57.15 \text{ mm} \quad D_4 = 177.8 \text{ mm} \quad b_{1m} = 32.45 \text{ mm}$$
$$D_2 = 171.45 \text{ mm} \quad D_5 = 279.4 \text{ mm} \quad b_2 = 9.53 \text{ mm}$$
$$D_3 = 174.63 \text{ mm} \quad b_3 = b_5 = 8.26 \text{ mm}$$

The vaneless diffuser was transformed into a so-called vaned diffuser by mounting a blade between the disks of Fig. 2(*a*). Figure 2(*b*) shows a plan view of the impeller and the diffuser blade. The diffuser blade angle $\alpha$ is computed as $\alpha = 15$ deg. The ratio of the gap between this blade and the impeller discharge to the impeller radius was 0.037, corresponding to an absolute distance of 3.17 mm at the leading edge. This single diffuser blade is not meant to simulate a complete cascade of blades in an actual pump; the thrust of this study is to illustrate the major features of the flow distortion past a blade.

For the present experiment, the rotation rate $\omega$ of the impeller was $\omega = 0.5$ revolutions/second, the inflow velocity $\overline{V}_p$ at the eye of the impeller = 0.1 m/s, and the tangential velocity $\overline{V}_i$ of the impeller was 0.27 m/s, corresponding to a Reynolds number based on the diameter $D_1$ of the inlet of the impeller $\mathrm{Re}_{D_1} = 6250$. Perturbation levels of the inflow had values in the range of $\tilde{V}_p/\overline{V}_p \leq 0.3$. The value of the flow coefficient $\Phi$ was 0.188. This particular value was selected, since it led to particularly coherent patterns of vortex formation in the wake of the impeller blade.

For the high-image-density technique of particle image velocimetry, the water was seeded with metallic-coated particles having a diameter of twelve microns. A laser sheet located midway between the parallel walls of the diffuser was generated by deflecting the beam of a four watt continuous wavelength Argon-ion laser beam from a 72-faceted polygonal mirror rotating at a rate corresponding to a scanning frequency $f_s = 1080$ cycles/second. A multiple-exposure photograph of the parti-

## Nomenclature

$b$ = width of impeller or diffuser (m)
$b_2$ = width of impeller discharge
$d_I$ = interrogation laser beam diameter (mm)
$D$ = characteristic diameter of impeller or diffuser (m)
$DB$ = diffuser blade
$D_1$ = diameter of impeller inlet (m)
$D_2$ = diameter of impeller discharge (m)
$f_{BP}$ = blade passing frequency of impeller (c/s)
$f_s$ = scanning frequency of laser beam (c/s)
$f_p$ = frequency of piston oscillation, i.e., inflow perturbation velocity (c/s)
$IB$ = impeller blade
$M$ = magnification of camera lens
$Q$ = volume flow into impeller ($m^3/s$)
$\mathrm{Re}_{D_1}$ = $\overline{V}_p D \overline{V}_1/\nu$ = Reynolds number
$u$ = flow velocity in diffuser in $x$ direction (m/s)
$v$ = flow velocity in diffuser in $y$ direction (m/s)
$\overline{V}_1$ = tangential velocity of impeller (at discharge) (m/s)
$\overline{V}_p$ = time mean inflow velocity (m/s)
$\tilde{V}_p$ = magnitude of inflow velocity perturbation (m/s)
$\Delta l$ = effective grid size in plane of laser sheet (mm)
$\Delta\omega$ = incremental value of vorticity (1/s)
$\phi$ = phase shift between inflow velocity perturbation $\tilde{V}_p$ and position of impeller blade
$\Phi$ = flow coefficient = $Q/\pi D_2 b_2 \overline{V}_i$
$\nu$ = kinematic viscosity ($m^2/s$)
$\omega$ = vorticity (1/s)
$\omega_{\max}$ = maximum value of vorticity (1/s)
$\omega_{\min}$ = minimum value of vorticity (1/s)

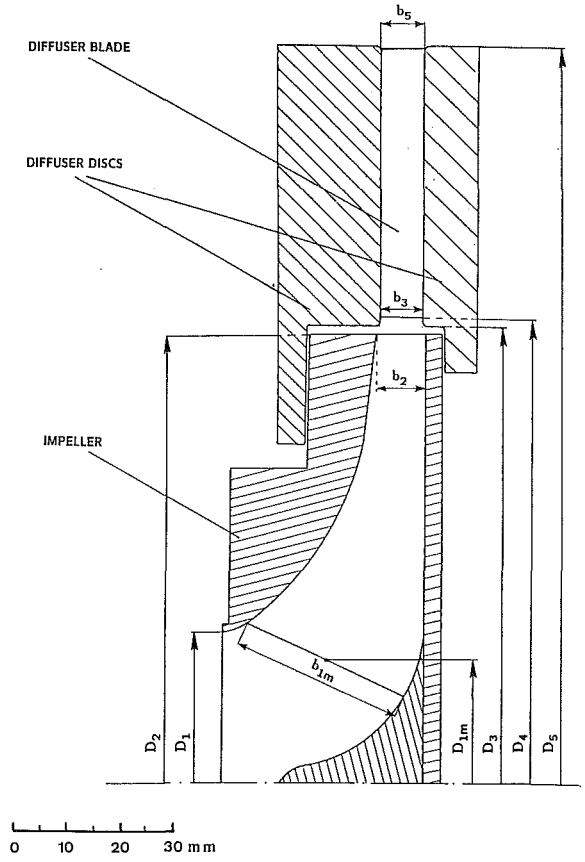


Fig. 2(*a*) Cross-sectional view of impeller-diffuser system

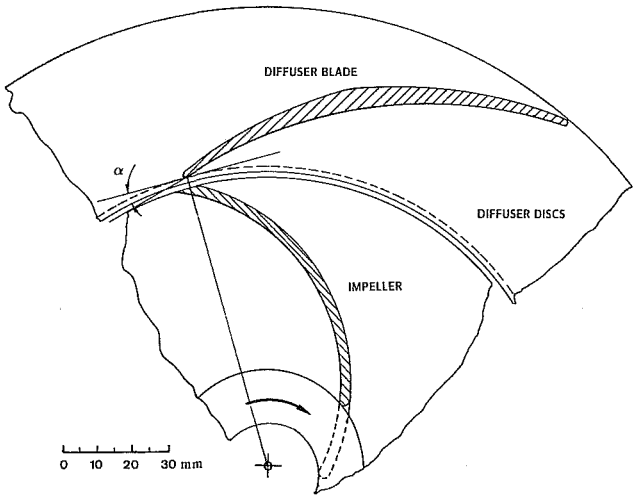


Fig. 2(*b*) Plan view of impeller-diffuser blade system

cles in the laser sheet provided the pattern of images that were analyzed to give the velocity field. The particle images were recorded using a 35 mm F-3 Nikon camera, then interrogated using a fringe analysis system. This technique, as well as its advantages and limitations, are described by Rockwell et al. (1992) and Rockwell et al. (1993).

In this particular experiment, only the largest scale eddies were of interest. Consequently, the magnification $M$ of the lens was selected as $M = 0.378$ in order to provide an overview of the distortion of the largest eddies; the interrogation beam diameter $d_I$ relative to the magnification $M$ was $d_I/M = 2.674$ mm; the image was interrogated with a 50 percent overlap in order to satisfy the Nyquist criterion, thereby giving an effective grid size $\Delta l/M = 1.32$ mm. This grid size corresponds to 1.4 percent of the total length of the image of Fig. 7. For the images shown in Fig. 7, this corresponds to a grid of $71 \times 48$ velocity vectors or a total of 3380 vectors over the entire image. Processing of the velocity field resulting from the interrogation involved application of a Gaussian filter with a factor $p = 1.3$. Contours of constant vorticity were then constructed using the program surfer, which simply fits a spline through the data points, i.e. no additional filtering of the data was done at this stage. A tension factor of 0.1 was employed for the spline fits. In general, the distance between the linearly-interpolated contours of constant vorticity in Fig. 7 corresponds to a distance of about one-third to one grid spacing $\Delta l$, depending upon the family of contours considered. For all contours of constant vorticity, the values of $\omega_{min}$, $\omega_{max}$, and $\Delta\omega$ were maintained constant in order to provide a comparison of the different regions of vorticity concentration.

Regarding the experimental uncertainty, the instantaneous velocity and vorticity are estimated to be accurate to within 1 and 7 percent, respectively, of their time values.

## 3 Wake Structure in Vaneless Diffuser

When the wake from the rotating impeller blade exhausts into the vaneless diffuser, the instantaneous velocity field and streamline patterns take the forms shown in Fig. 3. The field of view is indicated by the dashed-box, and the instantaneous location of the rotating impeller blade by the solid thick line, in the schematic at the lower left. Moreover, the discharge of the vaneless diffuser is represented by the inner circular arc, and the discharge of the vaneless diffuser by the outer (larger) radius circular arc. The instantaneous distribution of velocity and the corresponding streamline pattern in the laboratory reference frame are shown in the left column of Fig. 3, while the corresponding plots in a biased reference frame are given in the right column. These biased plots correspond to subtracting the spatially-averaged (over the entire image) velocities in the $x$ and $y$ direction from the velocity field given in the left image. In this biased frame, the ordered pattern of velocity vectors in the lower left portion of the velocity field suggests that vorticity concentrations are formed in the wake from the impeller. The corresponding streamline exhibits four quadrants of streamlines that have the same direction within each quadrant. This overall streamline pattern has a form similar to the one for which a saddle point forms (Perry and Steiner, 1987). A saddle point involves the interaction of four streamlines. For the image of Fig. 3, however, no such interaction occurs in the central region. From a physical standpoint, the streamline pattern in the biased frame shows that there is instantaneous flow from the reservoir into the vaneless diffuser (see top region of image), as well as large-scale circulating flow within the diffuser (see left, right, and bottom regions of image).

**3.1 Comparison of Distributions of Instantaneous Vorticity and Pressure Sources.** Since the vorticity field involves derivatives of the velocity, the vorticity distribution is independent of the reference frame of the observer. The instantaneous contours of constant vorticity corresponding to the images of Fig. 3 are given in the top image of Fig. 4. The impeller blade of interest is designated in the schematic at the bottom of Fig. 4. The wake from this blade exhibits highly pronounced concentrations of positive vorticity. In contrast, the contours of constant vorticity of negative sign are much weaker and more distributed. We therefore conclude that the process of vortex formation from the trailing-edge of the impeller blade does not give rise to a classical Kármán vortex street. Instead, its vorticity concentrations have a form typical of those occurring in mixing-layer configurations. This form of the vorticity field arises from the substantial difference in freestream velocity on either side of the trailing-edge of the impeller. Qualitative visualization (not shown here) of the re-

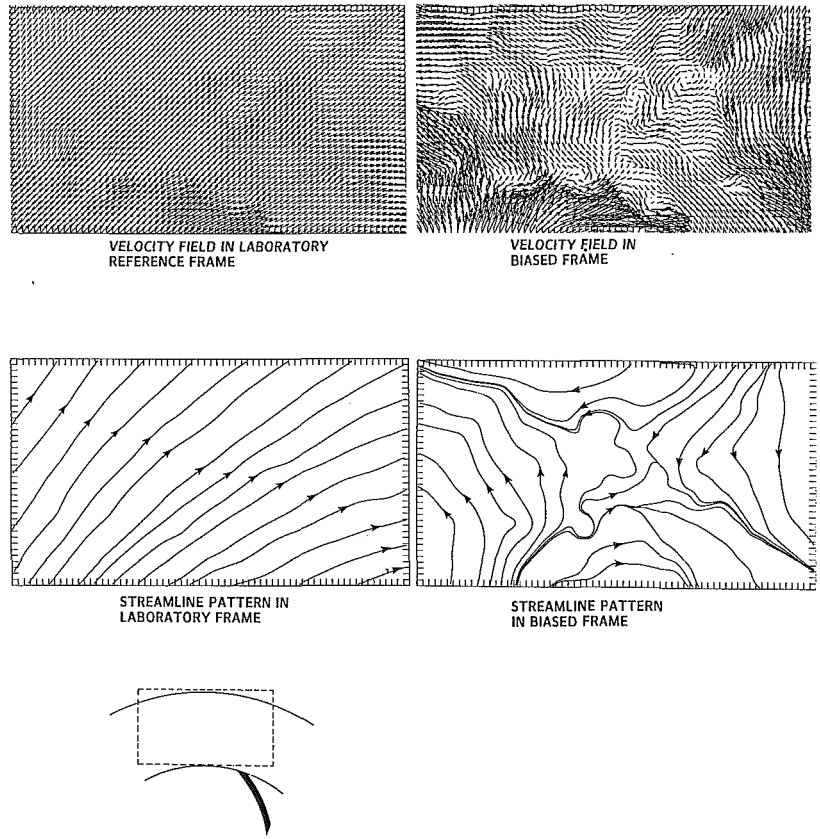


**Fig. 3 Instantaneous velocity fields and streamline patterns in laboratory and bias reference frames**

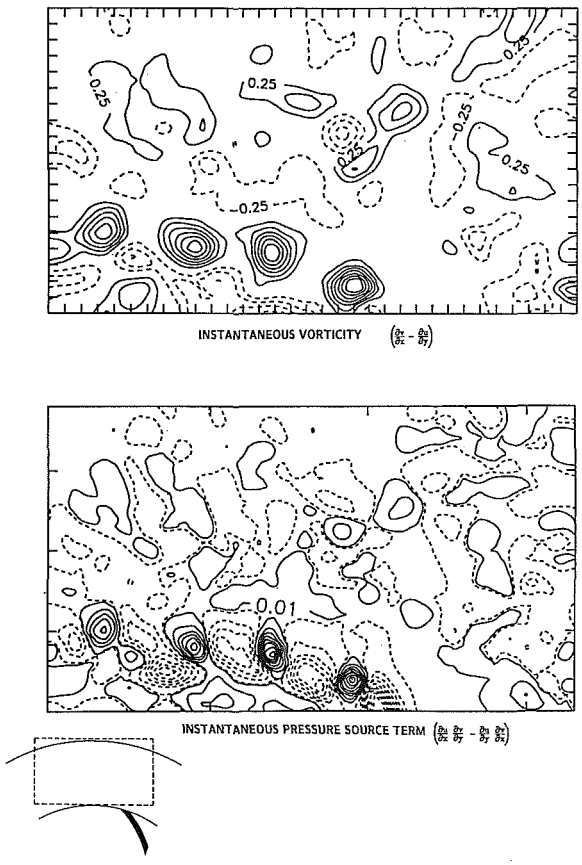


**Fig. 4 Instantaneous vorticity and pressure source terms of wake in vaneless diffuser**

gion of flow near the trailing-edge suggests occurrence of unstalled and stalled domains on either side of the trailing-edge.

It is insightful to calculate, for the same instantaneous velocity field, the instantaneous pressure source term $(\partial u/\partial x)(\partial v/\partial y) - (\partial u/\partial y)(\partial v/\partial x)$ shown in the bottom plot of Fig. 4. In free space, this term represents the forcing function of the Lighthill analogy that relates the far-field sound to the near-field flow distortion; in the vicinity of solid surfaces, such as the impeller blade, the boundary conditions must be properly accounted for in formulating a deductive theory of surface effects for the noise generation (Crighton, 1975). It is evident that highly concentrated, positive contributions to the instantaneous pressure source term are essentially coincident with the concentrations of vorticity. In addition, generally weaker concentrations of negative pressure sources occur between these positive concentrations. At locations away from this highly coherent wake, i.e., at larger values of radius, the concentrations of vorticity and the pressure sources are much weaker and more irregular. Apparently the severe adverse pressure gradient existing in the radial direction in the vaneless diffuser rapidly reduces the degree of coherence of the vortical structures at increasing values of radius.

**3.2 Decomposition of Instantaneous Pressure Source Terms.** It is insightful to consider the relative contributions of the voriticity-related and the rate-of-strain related contributions to the instantaneous pressure source. These two types of contributions are illustrated in the middle and lower images of Fig. 5. In general, the predominant contributions to the pressure source are from the vorticity-related term shown in the middle image. Regarding the rate-of-strain related contribution, it has its highest degree of concentration centered at the junction between the positive and the negative contributions of the vorticity-related source terms, as indicated by the vertical line connecting the middle and lower images.

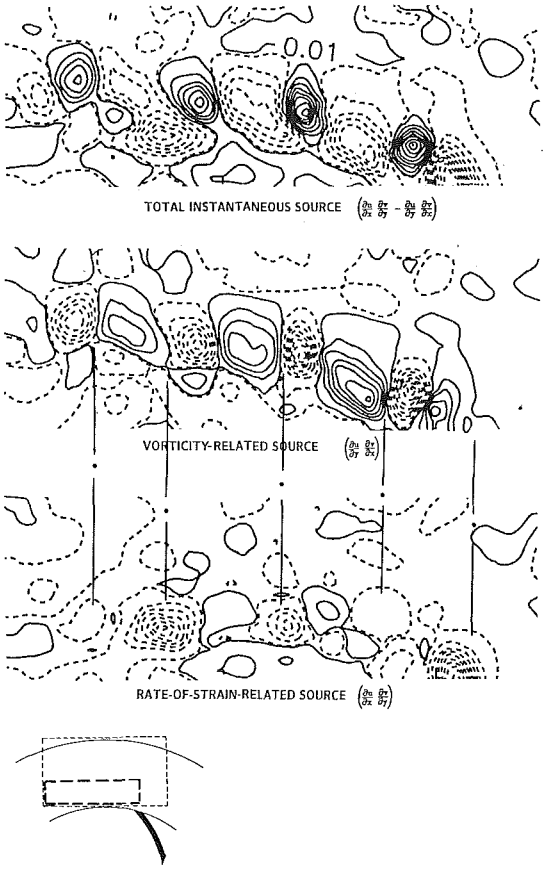


Fig. 5 Decomposition of total instantaneous pressure source into vorticity-related and rate-of-strain-related source contributions

Of course, we expect a very substantial, if not the predominant source of pressure fluctuations, to be due to the flow distortion in the immediate vicinity of the trailing-edge of the rotating impeller blade (Curle, 1955). This study focuses only on the free portion of the wake, in order to illustrate the principal contributions of the fully separated, free wake to the pressure source terms. An effort is currently underway to characterize the region in the vicinity of the trailing-edge.

**3.3 Ensemble-Average of Vorticity Fields.** In order to illustrate the variation of the flow structure from one instantaneous realization to the next, three representative, instantaneous realizations of the positive distributions of vorticity are shown in the three images of Fig. 6. In all cases, the highest concentrations of vorticity occur in the wake formed from the impeller blade indicated in the schematic at the bottom of Fig. 6. These concentrations of vorticity, as well as the concentrations formed from two previous impeller blades, are connected by the relative streamlines shown in the image at the upper left. It is evident that there are substantial levels of vorticity in the wakes from the previous two blades. However, these concentrations are irregular in form and randomly located relative to the pattern of vortices formed from the blade shown in the schematic. An ensemble-average of these three instantaneous realizations of the vorticity contours produces the pattern shown at the bottom right of Fig. 6. It is evident that the vorticity concentrations formed from the previous two blades are much weaker than their instantaneous counterparts. Since the instantaneous pressure source terms will be a function of the degree of concentration of the instantaneous vorticity, it is evident that the ensemble-averaged distributions of vorticity will not provide a proper representation of the instantaneous pressure source.

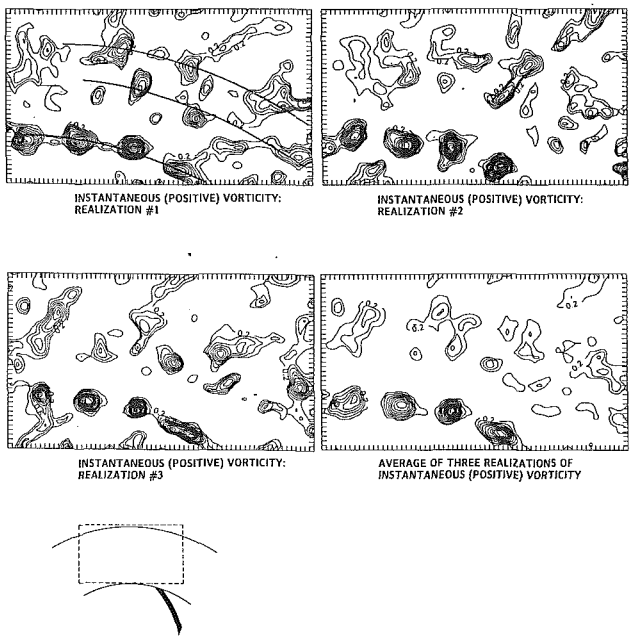


Fig. 6 Comparison of instantaneous realizations of vorticity at three different instants with ensemble-average representation

## 4 Structure of Impeller Wake-Diffuser Blade Interaction

Interaction of the wake from the rotating impeller blade with a stationary diffuser blade can produce complex distortions of the incident vorticity fields, as well as generation of additional vorticity due to the unsteady pressure gradients along the surface of the blade. In turn, the unsteady lift acting on the diffuser blade, and thereby the radiated noise, are a function of the rate-of-change of the moment of vorticity taken in the volume surrounding the diffuser blade (Howe, 1989). With this concept in mind, it is of obvious importance to determine the instantaneous vorticity field surrounding the diffuser blade. Moreover, if this vorticity field can be manipulated by active control of the inlet flow through the pump, then the unsteady loading and noise can be controlled as well. In the following, the instantaneous streamlines and contours of constant vorticity are described for cases with and without control of the inlet flow.

**4.1 Overview of Instantaneous Streamline Patterns.** Streamline patterns are shown in Fig. 7 for the cases with no active control (upper image) and active control at two instants of time (middle and bottom images). In all cases, the instantaneous location of the rotating impeller blade, relative to the stationary diffuser blade, is exactly the same. In order to determine the response of flow structure to controlled perturbations of the inflow, the piston (see Fig. 1) was forced at a frequency $f_{BP}$ of the impeller. For the case of no control, corresponding to $f_p/f_{BP}=0$, there is separation of flow along the upper surface above the diffuser blade; details of this separated flow region are not indicated by the streamline pattern.

The issue arises as to whether the nature of the separated flow pattern can be altered by perturbations of the inflow. When the inflow into the eye of the impeller is forced at a frequency $f_p/f_{BP}=0.67$, and an amplitude of $\tilde{V}_p/\overline{V}_p=0.2$, then it is possible to generate reattachment of the separated flow (middle image) or a separated flow region of much larger extent (bottom image). These markedly different streamline patterns occur for different phase angles $\phi$ of the inflow perturbations relative to the instantaneous position of the diffuser blade. At

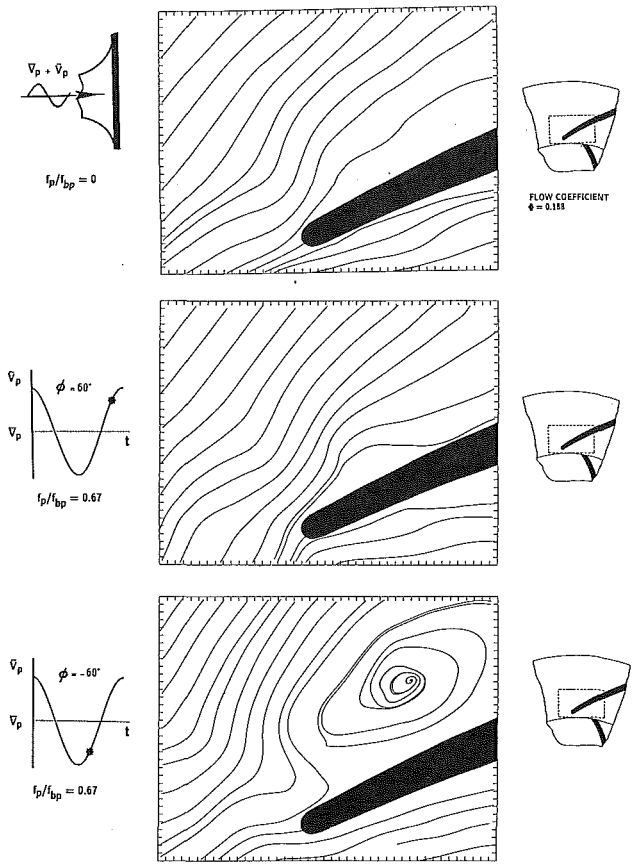


Fig. 7 Instantaneous streamline patterns in vicinity of leading-edge of diffuser blade for cases of: no inflow disturbance; inflow disturbance at a phase shift $\phi = 60$ deg; and perturbation with phase shift $\phi = -60$ deg of inflow fluctuation relative to blade position. Inflow perturbation frequency $f_p$ relative to blade-passing $f_{bp}$ is $f_p/f_{BP} \cong 0.67$; amplitude of inflow velocity $\tilde{V}_p$ relative to mean inflow velocity $V_p$ is $\tilde{V}_p/\bar{V}_p = 0.2$.

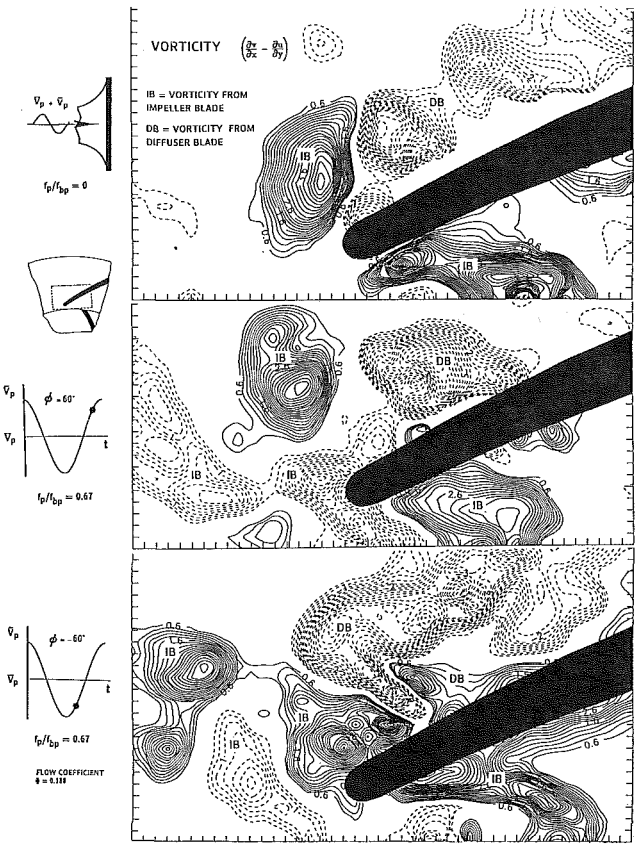


Fig. 8 Instantaneous contours of constant vorticity originating from impeller blade (IB) and diffuser blade (DB) for same conditions as given in Fig. 7. Solid and dashed lines represent positive and negative contours of vorticity, respectively.

$\phi = 60$ deg, the reattachment condition is attained, while at $\phi = -60$ deg, the large-scale separated region in generated. It is characterized by an outward-spiraling vortex motion, known in the field of topology as an unstable focus (Perry and Steiner, 1987). Although the streamline patterns are of interest in examining certain of the overall features of the flow pattern they are not adequate for characterizing the detailed distortion of the flow field. In fact, it is not possible to deduce the existence and location of concentrations of vorticity based on these patterns.

**4.2 Overview of Vorticity Fields.** The instantaneous contours of constant vorticity corresponding to the streamline patterns of Fig. 7 are shown in Fig. 8. When identifying the positive (solid line) and negative (dashed line) concentrations of vorticity, it is insightful to designate whether the vorticity is generated from the surface of the upstream impeller blade or the stationary diffuser blade. These two different sources of vorticity are indicated in the plots of Fig. 8 by the symbols IB (Impeller Blade) and DB (Diffuser Blade). For the case of no active control of the inlet flow, represented by the vorticity contours in the top image, there are large concentrations of positive vorticity from the upstream impeller blade that impinge upon the downstream diffuser blade. This interaction process imposes an unsteady pressure gradient along the leading-edge of the diffuser blade and, in turn, the occurrence of flow separation and the subsequent formation of concentrations of vorticity along the separated shear layer above the surface of the diffuser blade. The sign of these concentrations of vorticity is negative, as represented by the contours of dashed lines. When the inflow perturbation is applied, then not only large-scale positive concentrations of vorticity are formed from the upstream impeller blade, but also negative concentrations as well. The negative concentration of vorticity above the diffuser blade arises from separation from the leading-edge of the blade. Downstream of this concentration of vorticity, the flow reattaches. (Compare middle image of Fig. 7.) At a different phase angle $\phi = -60$ deg, represented by the image at the bottom of Fig. 8, the relative locations of the concentrations of vorticity from the upstream impeller blade are substantially displaced relative to those of the case of $\phi = -60$ deg represented in the middle image. The large-scale region of negative vorticity above the diffuser blade is associated with the very large vortex existing above the blade. (Compare bottom image of Fig. 7.) Moreover, there is a region of positive vorticity above the diffuser blade, due to flow separation from the surface of the blade, induced by the large scale, clockwise vortex above the blade.

It is evident that very substantial manipulation of the vorticity field incident upon the blade, as well as that generated from it, can be induced by suitable active control of the inlet flow.

## 5 Conclusions

High image-density particle image velocimetry provides a basis for determining the instantaneous velocity field and thereby the instantaneous contours of constant vorticity over an entire plane within a complex, rotating flow configuration such as a pumping system. A major advantage of this approach is that the instantaneous contours of constant vorticity can be related to the instantaneous pressure source terms at precisely

the same instant of time. Moreover, this instantaneous pressure source term is easily decomposed into its vorticity-related and rate-of-strain related contributions.

The importance of considering the instantaneous contours of vorticity, rather than the traditional ensemble-averaged contours such as would be obtained from classical point measurement techniques, is underscored by direct comparison of images of vorticity contours obtained at successive instants with a limited ensemble-average. Averaging as few as three images results in substantial attenuation of the degree of concentration and peak values of concentrations of vorticity that are not repetitive in space and time. As a consequence, the pressure source terms associated with the generation of far field sound will not be properly represented by the ensemble-averaging process.

In a similar fashion, particle image velocimetry provides a direct relationship between processes of separation and reattachment, suggested by instantaneous streamline patterns, in relation to the corresponding instantaneous vorticity fields. The high sensitivity of these instantaneous vorticity fields to active (open-loop) control is demonstrated by application of perturbations of the inflow into the eye of the pump impeller. The global PIV technique allows rapid assessment of the distortion of the vorticity field incident upon the stationary diffuser blade, as well as generation of new concentrations of vorticity from its surface.

## Acknowledgments

The authors are grateful to the Office of Naval Research (Grant N00014-89-J-1799) for support of this research program.

## References

Akin, O., 1991, "Unsteady Flow in an Actively-Controlled Centrifugal Pump," M.S. thesis, Department of Mechanical Engineering and Mechanics, Lehigh University, Bethlehem, PA.

Akin, O., and Rockwell, D., 1992, "Actively Controlled Radial Flow Pumping System: Manipulation of Spectral Content of Wakes and Wake-Blade Interactions," published in this issue pp. 528–537.

Arndt, N., Acosta, A. J., Brennen, C. E., and Caughey, T. K., 1989, "Rotor-Stator Interaction in a Diffuser Pump," ASME *Journal of Turbomachinery*, Vol. 111, July, pp. 213–221.

Arndt, N., Acosta, A. J., Brennen, C. E., and Caughey, T. K., 1990, "Experimental Investigation of Rotor-Stator Interaction in a Centrifugal Pump with Several Vaned Diffusers," ASME *Journal of Turbomachinery*, Vol. 112, January, pp. 98–108.

Blake, W. K., 1986, *Mechanics of Flow-Induced Sound and Vibration, Vol. 2, Complex Flow Structure Interactions*, Academic Press.

Crighton, D. G., 1975, "Basic Principles of Aerodynamic Noise Generation," *Progress in Aerospace Sciences*, Pergamon Press, Great Britain, Vol. 16, No. 1, pp. 31–96.

Curle, N., 1955, "The Influence of Solid Boundaries Upon Aerodynamic Sound," *Proceedings of Royal Society of London*, Series A, Vol. 231, pp. 505–514.

Dong, R., Chu, S., and Katz, J., 1992a, "Quantitative Visualization of the Flow Within the Volute of a Centrifugal Pump. Part A: Technique," ASME JOURNAL OF FLUIDS ENGINEERING, Vol. 114, Sept., pp. 390–395.

Dong, R., Chu, S., and Katz, J., 1992b, "Quantitative Visualization of the Flow Within the Volute of a Centrifugal Pump. Part B: Results and Analysis," ASME JOURNAL OF FLUIDS ENGINEERING, Vol. 114, Sept., pp. 396–403.

Embleton, T. F. W., 1963, "Experimental Study of Noise Reduction in Centrifugal Blowers," *The Journal of the Acoustical Society of America*, Vol. 35, No. 5, pp. 700–705.

Howe, M. S., 1989, "On Unsteady Surface Forces and Sound Produced by the Normal Chopping of Rectilinear Vortex," *Journal of Fluid Mechanics*, Vol. 206, pp. 131–153.

Neise, W., 1976, "Noise Reduction in Centrifugal Fans: A Literature Survey," *Journal of Sound and Vibration*, Vol. 45, No. 3, pp. 374–403.

Neise, W., 1982, "Review of Noise Reduction Methods for Centrifugal Fans," ASME *Journal of Engineering for Industry*, May, Vol. 104, pp. 141–161.

Paone, N., Riethmuller, M. L., and Van den Braembussche, R. A., 1989, "Experimental Investigation of the Flow in the Vaneless Diffuser of a Centrifugal Pump by Particle Image Displacement Velocimetry," *Experiments in Fluids*, Vol. 7, pp. 371–378.

Perry, A. E., and Steiner, T. R., 1987, "Large-Scale Vortex Structures in Turbulent Wakes Behind Bluff Bodies. Part 1. Vortex Formation," *Journal of Fluid Mechanics*, Vol. 174, pp. 233–270.

Rockwell, D., Magness, C., Robinson, O., Towfighi, J., Aking, O., Gu, W., and Corcoran, T., 1992, *Instantaneous Structure of Unsteady Separated Flows Via Particle Image Velocimetry*. Lehigh University, Department of Mechanical Engineering and Mechanics, Fluid Mechanics Laboratories Report PI-1, Feb.

Rockwell, D., Magness, C., Towfighi, J., Akin, O., and Corcoran, T., 1993, "High Image-Density Particle Image Velocimetry Using Laser Scanning Techniques," *Experiments in Fluids*, Vol. 14, pp. 181–192.

Simpson, H. C., Clark, T. A., and Weir, G. A., 1967, "A Theoretical Investigation of Hydraulic Noise in Pumps," *Journal of Sound and Vibration*, Vol. 5, No. 3, pp. 456–488.

# An Experimental Investigation of Cross-Flow Turbine Efficiency

**Venkappayya R. Desai**
Visiting Lecturer,
Department of Civil Engineering,
Indian Institute of Technology,
Kharagpur-721302 India

**Nadim M. Aziz**
Associate Professor,
Department of Civil Engineering,
Clemson University,
Clemson, SC 29634-0911

*An experimental investigation was conducted to study the effect of some geometric parameters on the efficiency of the cross-flow turbine. Turbine models were constructed with three different numbers of blades, three different angles of water entry to the runner, and three different inner-to-outer diameter ratios. Nozzles were also constructed for the experiments to match the three different angles of water entry to the runner. A total of 27 runners were tested with the three nozzles. The results of the experiments clearly indicated that efficiency increased with increase in the number of blades. Moreover, it was determined that an increase in the angle of attack beyond 24 deg does not improve the maximum turbine efficiency. In addition, as a result of these experiments, it was determined that for a 24 deg angle of attack 0.68 was the most efficient inner-to-outer diameter ratio, whereas for higher angles of attack the maximum efficiency decreases with an increase in the diameter ratio from 0.60 to 0.75.*

## Introduction

Hydropower is one of the most desirable energy resources to be utilized, if it is as competitive economically as any other energy source. One economical measure in hydropower is the efficiency of turbines, which is the subject of the study reported here.

In conventional low head hydroelectric stations, axial turbines such as propeller turbines or bulb turbines are generally used. The technology for these machines is well established with sufficient know-how compiled. At present, the cross-flow turbine is gaining acceptance in small and ultra low head establishments because of its remarkably simple structure. This interest has resulted in several such turbines being used in several locations around the country.

The cross-flow turbine (CFT) is composed of two major parts, the runner and the nozzle. The runner is of closed type made of at least two circular side walls with the blades fixed to these walls along the periphery. The blades are circular and make a certain angle with the tangent to the outer periphery ($\beta$). On the other hand, the nozzle directs the flow into the runner at a specified angle of attack ($\alpha$). The nozzle has a rectangular cross-section with a curved back wall. Figure 1 shows details of the CFT and is used here as a definition sketch for the parameters of this study. Figure 2 shows the orientation and profile of the blades.

A portion of the water jet hits the turbine blades twice, initially from outside the runner to inside (first stage) and later from inside the runner to outside (second stage). The portion of the water jet that crosses the runner twice is called the crossed flow or simply "cross-flow"; hence the name cross-flow turbine. The portion of the jet which crosses the runner only once is called the uncrossed flow. Figure 3 illustrates a typical flow pattern in a CFT.

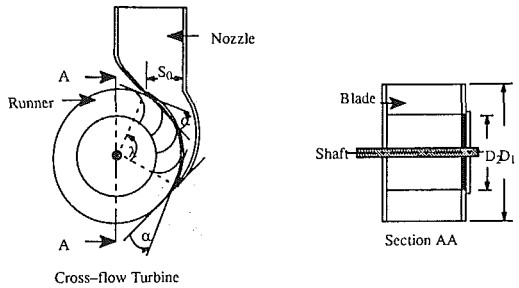


Fig. 1 Definition sketch of the CFT


Fig. 2 Orientation and the profile of a typical blade

## Literature Review

The experimental research on CFT was initiated by Mockmore and Merryfield (1949) who constructed a runner made out of steel. The side disks were cut out of 6.4 mm. steel plates with an outer diameter of 332.7 mm. A 305-mm. wide runner was used having 20 blades cut out of 2.8 mm. steel, bent to a radius of 54.4 mm. The head values were 2.74 m, 3.05 m, 3.66 m, 4.27 m., 4.88 m., and 5.49 m. measured to the shaft center.

Contributed by the Fluids Engineering Division for publication in the JOURNAL OF FLUIDS ENGINEERING. Manuscript received by the Fluids Engineering Division February 26, 1993; revised manuscript received September 23, 1993. Associate Technical Editor: L. Nelik.

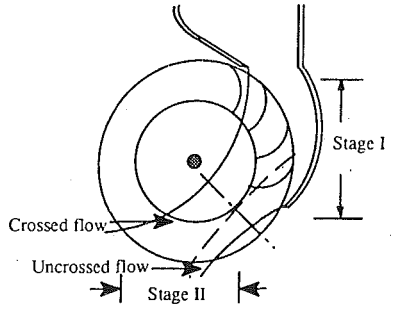


**Fig. 3 A typical flow pattern in a CFT**

The flow rate was 0.06 $m^3$/sec. at 4.88 m. head. At maximum power, the actual shaft speeds were compared to the computed speeds for various heads. The computed speed was expressed in terms of head and outer diameter.

The maximum efficiency of 68 percent was measured under 4.88 m. Mockmore and Merryfield concluded that the BHP is proportional to $H^{1.5}$, where H is the head, and at a constant head the maximum efficiency will occur at a constant speed practically for all gate openings.

Varga (1959) conducted experiments to measure the pressure distribution along the nozzle walls. A total of 24 gaging points were provided covering the upper and lower sections as well as the side walls of the nozzle. All gaging points were connected to a multi-manometer system. Pressure distributions along the walls were measured with and without the runner, and a trajectory network was constructed, similar to a flow net. The maximum efficiency reported in these experiments was 77 percent. Varga inferred that the CFT works as an impulse turbine only in the range of well-defined speeds with its upper limit being the point of maximum efficiency. It was also confirmed that at maximum efficiency the ratio of the peripheral and absolute velocities are equal to half the cosine of the angle of attack at the first stage inlet. Varga (1959) also concluded that the momentum required for regulation of the CFT can be determined by the trajectory network and the pressure distributions along the nozzle walls.

Nakase et al. (1982) studied experimentally the effect of nozzle shape on the performance of the CFT. They used nozzles of different rear wall shapes, and concluded that circular arc and logarithmic spiral shapes were both equally more efficient than an intermediate shape. Similarly, a nozzle with an entry arc of 90° was found to be more efficient than nozzles with entry arcs of 30, 60, and 120 deg. The most suitable value of the nozzle throat width ratio ($2S_0/D_1\lambda$) was found to be 0.26, changing slightly with the nozzle entry arc. The absolute maximum efficiency obtained was 82 percent.

Johnson et al. (1982) designed and tested a CFT with a wooden casing, PVC runner plates and vanes, and polymer-coated wooden nozzles and guide vanes. The tests indicated that a single, non-segmented design can achieve efficiencies of 60 to 80 percent over a wide range of flow rates and heads, at various runner speeds. For a runner with 18 blades, the maximum efficiency was obtained at a head of 0.91 m. to 1.07 m. The root mean square uncertainty in the measured turbine efficiency was ±6 percent. The best results were obtained when the water in the draft tube was just at the bottom of the runner. They also concluded that with proper nozzle design, efficiency will remain high up to a nozzle entry arc of 120 deg.

Hothersall (1985) tested runners with 20 and 21 blades having a diameter ratio of 0.66, with the nozzles of 60 and 130 deg entry arcs. At a net head of 6.71 m, the maximum efficiency was estimated as 75%.

Khosrowpanah et al. (1988) were probably the first to attempt a parametric study of the CFT nozzle as well as the runner. The experimental work involved the study of the effect of the number of blades, runner diameter, and nozzle entry arc under flow/head variations. Water was admitted vertically through nozzles with entry arcs of 58, 78, and 90 deg. Khosrowpanah concluded that the maximum efficiency of the CFT increases with an increase in the nozzle entry arc from 58 to 90 deg and decreases slightly with a decrease in runner diameter at constant runner width. For the four runners tested, Khosrowpanah observed that maximum efficiency (80 percent) was when the nozzle throat width ratio ($2S_0/D_1\lambda$) was 0.41 and the speed ratio was 0.54, and that the number of blades has only a moderate effect on efficiency and power output. The runner with 15 blades was found to be more efficient than the runners with either 10 or 20 blades.

Durgin and Fay (1984) built an acrylic model of the CFT and tested nozzles with entry arcs ranging from 50 to 80 deg and obtained a maximum efficiency of 66 percent. This maximum efficiency compared very well with their theoretical prediction. They also extracted the cross-flow by introducing a pipe with a slot to determine the power produced by the first stage as 83 percent while the rest of the power came from the second stage.

Chiatti and Ruscitti (1988) introduced an internal rotating deflection element inside the blade crown to guide the stream and to avoid the effect due to the convergence of the jet at the shaft center. Their prototype runner diameter was 250 mm, with 24 blades of 145 mm length. The full load jet width, design power, and the design speed were 4 mm, 140 KW, and 3000 rpm respectively. The test bed was equipped with a digital speed meter and a brake mounted on an oscillating support with a dynamometer having a least count of 0.05 Newton. The maximum overall efficiency obtained was about 75 percent with the uncertainty of ±3 percent. The optimum inlet angle and the deviator-to-blade phase angle were close to the theoretical values as provided by the design procedure.

Fiuzat and Akerkar (1989 and 1991) studied the effect of the angle of attack in addition to nozzle entry arc and nozzle configuration on CFT efficiency. The results indicated that a vertical nozzle configuration is more efficient than both the horizontal and slant (45 deg) configurations. They also confirmed the earlier observation by Nakase (1982) and Kosrowpanah (1984) that a nozzle entry arc of 90 deg was the optimum. Fiuzat and Akerkar also concluded that efficiency increases with an increase in the angle of attack from 16 to 24 deg, thus

## Nomenclature

$D_1$ = runner outer diameter
$D_2$ = runner inner diameter
$H$ = total head
$N_b$ = number of blades
$n$ = shaft rotational speed
$P_{in}$ = input power
$P_{out}$ = output power measured at the shaft center
$Q$ = flow rate
$S_0$ = nozzle throat width
$T$ = shaft torque
$u_1$ = peripheral velocity at the first stage inlet
$V_1$ = absolute velocity at the first stage inlet
$\alpha$ = angle of attack for the water flowing through the turbine
$\beta$ = blade inlet angle
$\beta_2$ = blade exit angle at the first stage
$\gamma$ = specific weight of water
$\eta$ = efficiency
$\lambda$ = nozzle entry arc

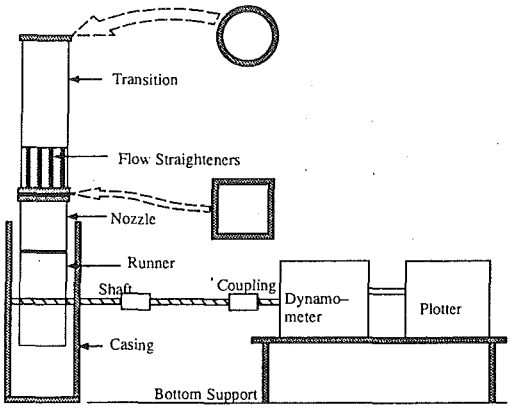


**Fig. 4 A schematic diagram of the experimental setup**

contradicting the Banki theory of CFT. The present investigation primarily aims at studying the impact of a further increase in the angle of attack beyond 24 deg.

From the above discussion it is clear that the efficiency of the cross flow turbine has been observed to vary with the amount of crossflow, the number of blades in the runner, the angle of attack, and the inner-to-outer diameter ratio of the runner. The efficiency improving tests of the research reported in this paper are an extension of the work of Nakase et al. (1982), Khosrowpanah et al. (1988), and Fiuzat and Akerkar (1989 and 1991).

## Equipment and Model Components

Cross-flow turbine models including the runners, blades, and nozzles were built and tested at the Clemson Hydraulics Laboratory. Acrylic was used to construct the runners, blades, and nozzles. The transparent material was instrumental in flow visualization. An 11.3 N-m, dynamometer was used for torque and rotational speed measurements. Two pumps with capacities 7.46 kw and 18.64 kw were utilized to maintain a constant head during the tests.

A total of 27 runners were constructed using 12.7 mm. acrylic sheets and 3.2 mm-thick cylindrical pipes. The acrylic sheets were used for the sidewalls of the runners and the cylindrical pipes were used for the blades. The side walls were cut out of acrylic with one of the sides having a hole and a key-way to hold the shaft and the runner. The other side wall was in the form of an annulus with outer and inner diameters corresponding to the outer and inner diameters of the runner. On the side walls, 3.2 mm-wide grooves were cut in the shape of circular arc whose inner and outer radii were the inner and outer radii of the blades as shown in Fig. 2. A schematic diagram of the experimental set-up is shown in Fig. 4.

Three nozzles were constructed from 6.4 mm.-thick acrylic sheets with a nozzle entry arc ($\lambda$) of 90 deg and a nozzle throat width ratio ($2S_0/D_1\lambda$) of 0.41, respectively. These are the same values used by Khosrowpanah et al. (1988), and Fiuzat and Akerkar (1989 and 1991) and produced the best performance. The rear wall of the nozzles (shown in Fig. 1) was constructed to have a spiral shape such that the water jet entering the turbine experiences a uniform acceleration.

## Experimental Procedure

The experimental study involved the measurement of four parameters: shaft torque, shaft rotational speed, flow rate, and total pressure. An 11.3 N-m dynamometer was used to measure torque and angular speed and was controlled by an automatic speed controller. The controller was used to bring the runner rotating at maximum speed (zero torque) to a halt. The duration of this process was 40 seconds. This is called the automatic speed control. The electronic setup transmitted the angular speed and torque to a plotter which produced a speed versus torque plot. The controller can also be used to generate discrete torque versus speed by disabling the automatic speed control and run the test at specified torque or speed. This is known as the manual speed control method.

Theoretically, the results obtained by the automatic and manual speed control of the dynamometer should be the same. Since the dynamometer used in this study did not have built-in inertia correction, the shaft speed under the automatic speed control were smaller than the corresponding values obtained by manual speed control. Hence in this paper, most of the results are reported only for manual speed control.

Total pressure was measured at a section in the prismatic portion of the nozzle wherein the variation in the total pressure across the nozzle cross-section was negligible. Total pressure was measured by means of a standard Pitot tube and U-tube water manometer. Since the experimental set-up was the same for all the tests, the total pressure varied with only the flow rate. Hence, the manometer reading for total pressure was calibrated with respect to the manometer reading for discharge.

The flow rate was measured by means of an orifice-meter which was introduced in a straight reach of the pipeline. The calibration of the orifice-meter was done by means of a weighing tank.

## Data Analysis

The performance of turbines is measured by their efficiencies. In general, efficiency is an indication of what percentage of the input to the turbine is converted into power. Efficiency ($\eta$) is defined as follows:

$$\eta = \frac{P_{\text{out}}}{P_{\text{in}}} 100\% \tag{1}$$

where

$$P_{\text{out}} = \frac{2\pi nT}{60} \tag{2}$$

and

$$\text{IHP} = \gamma \text{HQ}. \tag{3}$$

The efficiency values are plotted against the speed ratio ($u_1/V_1$) defined as:

$$\frac{u_1}{V_1} = \frac{\pi D_1 n}{60\sqrt{2gH}}. \tag{4}$$

Among previous studies, the experiments of Khosrowpanah et al. (1988) include runners with 15 and 20 blades. Likewise, Johnson et al. (1982), Nakase et al. (1982), Khosrowpanah et al. (1988), and Fiuzat and Akerkar (1989) have constructed runners with a diameter ratio of 0.68. However, these runners had either 15 or 16 deg angle of attack and an entirely different experimental setup, resulting in different head values for the same flow rate.

Only Fiuzat (1988) and Akerkar (1989) have tested the 24 deg angle of attack, but no studies are available on 28 and 32 deg angles. In that study the first stage blade exit angle ($\beta_2$ in Fig. 2) was different from the present value of 90 deg. Also, in the data of Fiuzat (1988) and Akerkar (1989), there is a lot of variation in the total head with the shaft rotational speed at every flow rate. Apparently, the total head inside the nozzle might have been measured while the runner was in. Possibly, this could have resulted in backing up of water inside the nozzle leading to a variation in the total head. Whereas in the present study, the total pressure head was measured inside the nozzle without the runner consistent with Nakase et al. (1982), and Khosrowpanah et al. (1988). Therefore under the present circumstances, comparison with any of the previous studies is not possible.

Table 1 Runner parameters and maximum overall turbine efficiencies

| Runner # | Angle of Attack α° | Diameter Ratio $D_2/D_1$ | Number of Blades $N_b$ | Maximum Efficiency η % |
|---|---|---|---|---|
| 1 | 24 | 0.60 | 15 | 64.1 |
| 2 | | | 20 | 64.4 |
| 3 | | | 25 | 74.5 (80.6) |
| 4 | | 0.68 | 15 | 59.1 |
| 5 | | | 20 | 70.7 |
| 6 | | | 25 | 76.7 (84.5) |
| 7 | | 0.75 | 15 | 50.6 |
| 8 | | | 20 | 63.3 |
| 9 | | | 25 | 71.9 |
| 10 | 28 | 0.60 | 15 | 63.7 |
| 11 | | | 20 | 71.1 |
| 12 | | | 25 | 71.7 (78.0) |
| 13 | | 0.68 | 15 | 56.5 |
| 14 | | | 20 | 65.2 |
| 15 | | | 25 | 66.7 (73.9) |
| 16 | | 0.75 | 15 | 49.8 |
| 17 | | | 20 | 59.6 |
| 18 | | | 25 | 65.2 |
| 19 | 32 | 0.60 | 15 | 58.3 |
| 20 | | | 20 | 64.8 |
| 21 | | | 25 | 66.7 (73.7) |
| 22 | | 0.68 | 15 | 55.6 |
| 23 | | | 20 | 63.1 |
| 24 | | | 25 | 64.3 (71.0) |
| 25 | | 0.75 | 15 | 46.4 |
| 26 | | | 20 | 55.1 |
| 27 | | | 25 | 62.7 |

*Numbers in parentheses are efficiencies obtained by the manual speed control method.*

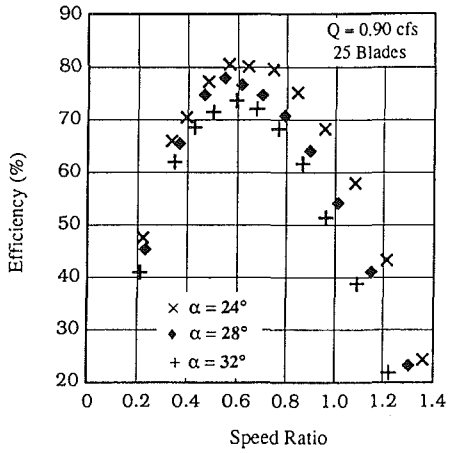


Fig. 5 Impact of angle of attack on CFT efficiency at a diameter ratio 0.60

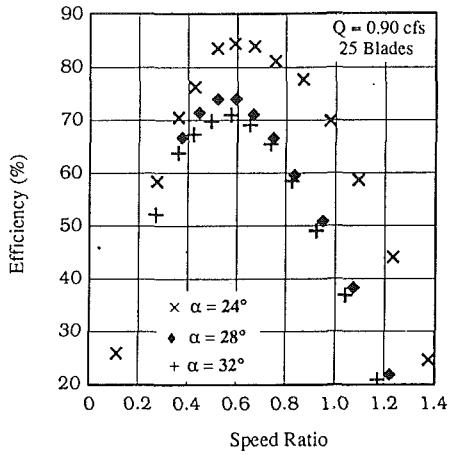


Fig. 6 Impact of angle of attack on CFT efficiency at a diameter ratio of 0.68

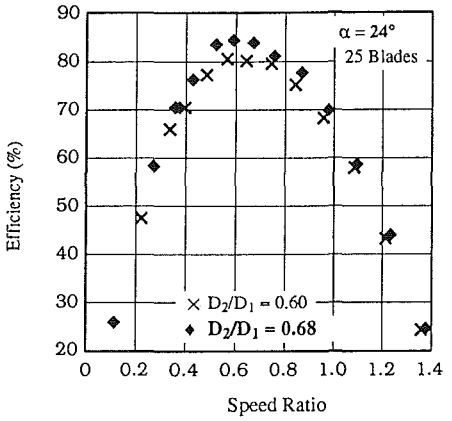


Fig. 7 The impact of diameter ratio on CFT efficiency

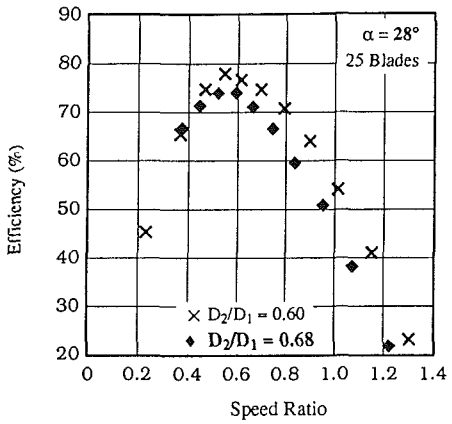


Fig. 8 The impact of diameter ratio on CFT efficiency

## Results.

The maximum overall turbine efficiencies for all runners are listed in Table 1. Only the highly efficient runners were tested by the manual speed control method. These runners had 25 blades and a diameter ratio of either 0.60 or 0.68. The remaining runners were tested only in automatic speed control (without inertia correction) and hence, the influence of the number of blades reported here is not corrected for inertia effects Table 1 indicates that runner #6 is the most efficient of all the runners tested and has the following parameters: $\alpha = 24$ deg, $D_2/D_1 = 0.68$, and $N_b = 25$.

## Discussion

The impact of the angle of attack on efficiency of the cross-flow turbine is shown in Figs. 5 and 6. Figure 5 shows the effect of angle of attack at a diameter ratio of 0.60, while Fig.6 shows its effect at a diameter ratio of 0.68. These plots indicate that an increase in the value of the angle of attack from 24 to 32 deg results in a decrease in the maximum efficiency. The behavior can be explained as follows: since an increase in $\alpha$ is always associated with an increase in $\beta$, at angles of attack higher than 24 deg the water jet is deflected toward the runner center in the first stage, possibly leading to a retardation effect in the second stage.

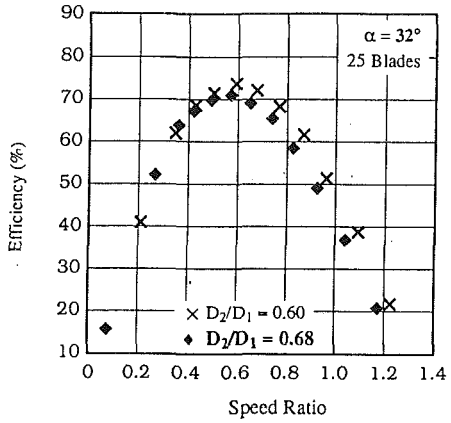


Fig. 9 The impact of diameter ratio on CFT efficiency

Table 2 Coefficients of the fitted equations and their 99 percent confidence limits

| Independent Variable | Dependent Variable | Equation | Values of the Coefficients | Lower Limit of 99% Confidence | Upper Limit of 99% Confidence |
|---|---|---|---|---|---|
| $\log h_q$ | log Q | $\log Q = a + b^* \log h_q$ | a = −9.616E−2<br>b = 0.499 | −9.758E−2<br>0.496 | −9.475E−2<br>0.502 |
| Flow Manometer Reading ($h_q$, m.) | Total Head (H, m.) | $H = a + b^* h_q$ | a = 1.599<br>b = 0.536 | 1.534<br>0.519 | 1.664<br>0.553 |

Table 3 Lower and upper bound estimates of the input power parameters

| Parameter | Lower bound Estimate | Most Probable Estimate | Upper Bound Estimate |
|---|---|---|---|
| Flow Rate (Q, $m^3$/sec.) | 2.566E−2 | 2.577E−2 | 2.585E−2 |
| Total Pressure Head (H, m.) | 0.332 | 0.344 | 0.356 |
| Water Specific Weight ($\gamma$ N/$m^3$) | 9773.5 | 9786.1 | 9797.1 |

Table 4 Lower and upper bound estimates for the rotational speed and maximum efficiency

| Runner | Parameter | Lower bound Estimate | Most Probable Estimate | Upper Bound Estimate |
|---|---|---|---|---|
| # 3 | N at $\eta_{max}$ (rpm) | 102.3 | 102.9 | 103.5 |
| | $\eta_{max}$ (%) | 77.1 | 81.4 | 84.6 |
| # 6 | N at $\eta_{max}$ (rpm) | 94.3 | 95.5 | 96.8 |
| | $\eta_{max}$ (%) | 79.1 | 84.5 | 88.1 |
| # 12 | N at $\eta_{max}$ (rpm) | 87.5 | 88.5 | 89.5 |
| | $\eta_{max}$ (%) | 73.5 | 78.0 | 81.5 |
| # 15 | N at $\eta_{max}$ (rpm) | 87.4 | 87.9 | 88.3 |
| | $\eta_{max}$ (%) | 70.2 | 74.1 | 77.0 |
| # 21 | N at $\eta_{max}$ (rpm) | 95.0 | 96.0 | 97.0 |
| | $\eta_{max}$ (%) | 69.9 | 73.9 | 77.4 |
| # 24 | N at $\eta_{max}$ (rpm) | 91.8 | 93.0 | 94.3 |
| | $\eta_{max}$ (%) | 67.4 | 71.0 | 75.1 |

Figures 7, 8 and 9 explain the effect of the diameter ratio on the CFT efficiency at angles of attack 24, 28 and 32 deg, respectively. An increase in the diameter ratio is always associated with a decrease in the blade arc length. From Figs. 8 and 9, it is evident that at angles of attack higher than 24 deg, the increase in the diameter ratio leads to a reduction in the force due to jet impact and hence a reduction in the power produced whereas Fig. 7 indicates that the reduction in the jet impact force is dominated by the effect of a lower angle of attack. Hence at $\alpha = 24$ deg, the runner with diameter ratio 0.68 is more efficient than the runners with diameter ratios of 0.60 or 0.75.

A summary of the effect of number of blades on the performance of the turbine is presented in Table 1. This table

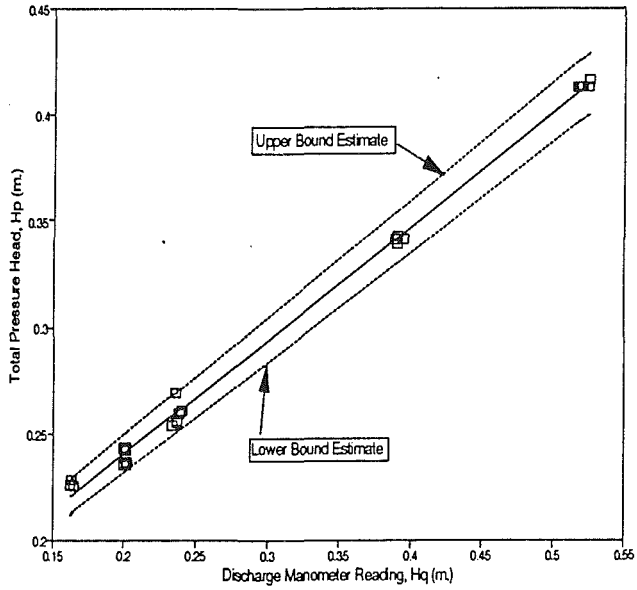


Fig. 10 Sensitivity of the total head to the fitted equation

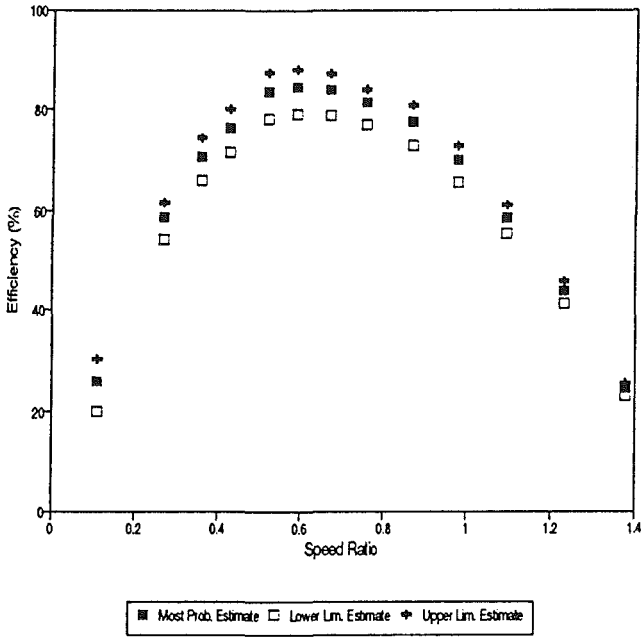


Fig. 11 Sensitivity of the efficiency to the combined effect of curve-fittings

indicates a significant improvement in the performance of the turbine as a result of increasing the number of blades either from 15 to 20 or from 20 to 25. This may be explained by the fact that an increase in the number of blades results in more energy transfer between water and the turbine blades.

## Uncertainty and Sensitivity Analysis

The uncertainty estimates are based on the sensitivity analysis. The sensitivity analysis is performed at 99 percent confidence limits for the coefficients in the fitted equations. All nozzle-runner combinations reported in Figs. 4 through 8 are used for the uncertainty analysis. Table 2 lists the coefficients of the fitted equations and their 99 percent confidence limits.

The lower and upper limits of 99 percent confidence limit were used to compute the lower bound and upper bound estimates of the dependent parameters $Q$ and $H$. The lower and upper limits for the specific weight of water are entered from

standard tables for properties of water assuming an uncertainty of $\pm 0.5°C$ in the water temperature. Table 3 shows these lower and upper bound estimates.

For the rotational speed ($N$), the lower and upper bound estimates are computed either by actual observation of the torque-speed plots or by the lower and upper limits of the 99 percent confidence limits for the coefficients of the fitted cubic curves, at the maximum efficiency point. This actually depends on whether the maximum efficiency was at a measured point or at an interpolated point, obtained by solving the mathematical condition for the maximum efficiency. According to this mathematical condition, at the maximum efficiency point the BHP is maximum or in other words, the partial derivative of the product of torque and speed is zero. These estimates of $N$ are substituted in the expressions for brake horsepower at the maximum efficiency point and the input horsepower (i.e., Equations (2) and (3), respectively). The lower and upper bounds of the maximum efficiency are then determined. Table 4 lists the most probable estimates and the lower and upper bound estimates for the maximum efficiency and the corresponding rotational speed.

Figure 10 shows the sensitivity of the straight line fit for the total head. The uncertainty is very high at low flow rates. Figure 11 illustrates the combined influence of the two fitted equations for the flow rate and the total head on the efficiency.

For the sensitivity plot of the flow rate, both the upper and lower bound estimates were overlapping, and hence it is not shown here. The sensitivity and analysis for Runner #6 results in an uncertainty in the maximum efficiency of $-5.4$ to $+3.6$ percent. The mean value of uncertainty for all the nozzle-runner combinations reported in Figs. 4 through 8 is-4.3 to 3.5 percent. Nevertheless, the uncertainty in either the torque or the speed always lies within the limiting values, as recommended in the ASME PTC 18-1949 (i.e., $\pm 3$ and $\pm 1$ percent, respectively).

## Conclusions

The experiments and data analysis reported in this article clearly indicate the significance of the geometric design parameters of the cross-flow turbine on its overall performance. This research indicates that the efficiency of the turbine improves as the number of runner blades increases from 15 to 25. The increase in the angle of attack, however, did not improve the turbine performance in the range of 24 to 32 degrees. Finally, the ratio the inner to the outer diameter of the runner was shown to produce a higher turbine efficiency at 0.68 as compared to that at either 0.60 or 0.75.

These results when combined together improve the efficiency of the cross flow turbine to a more acceptable range than what has been previously reported. This, in combination with the fact that the cross-flow turbine is environmentally desirable and economical, will provide a means for utilization in small hydropower environments.

## Acknowledgments

This research was funded by the Department of Energy, Bonneville Power Administration, Portland, Oregon.

## References

Aziz, N. M., and Desai, V. R., 1991, "An Experimental Study of the Effect of Some Design Parameters on Cross-flow Turbine Efficiency," Engineering Report #1W-91, Department of Civil Engineering, Clemson University, Clemson, SC.

Chiatti, G., and Ruscitti, R., 1988, "Performance Tests of a New Hydraulic Impulse Turbine," *Small Hydro '88*, An International Conference and Trade Show, Vol. 2.

Durgin, W. W., and Fay, W. K., 1984, "Some Fluid Flow Characteristics of a Cross-flow Type Hydraulic Turbine," *Small Hydropower Fluid Machinery*, ASME Winter Annual Meeting, New Orleans, LA, pp. 77–83.

Fiuzat, A. A., and Akerkar, B. P., 1989, "The Use of Interior Guide Tube in Cross-flow Turbines," *Waterpower '89*, Niagara Falls, NY, Vol. 2, pp. 1111–1119.

Fiuzat, A. A., and Akerkar, B. P, 1991, "Power Outputs of Two Stages of Cross-Flow Turbine," *ASCE Journal of Energy Engineering*, Vol. 117, No. 2, Aug. pp. 57–70.

Hothersall, R., 1985, "A Review of the Cross-flow Turbine," *Waterpower '85*, Las Vegas, NV, Vol. 2, pp. 914–923.

Johnson, W., Ely, R., and White, F., 1982, "Design and Testing of a Inexpensive Cross-Flow Turbine," *Small Hydro-power Fluid Machinery*, ASME Winter Annual Meeting of Phoenix, AZ, pp. 129–133.

Khosrowpanah, S., Fiuzat, A. A., and Albertson, M. L., 1988, "Experimental Study of Cross-flow Turbine," ASCE *Journal of Hydraulic Engineering*, Vol. 114, No. 3, Mar. pp. 299–314.

Mockmore, C. A., and Merryfield, F., 1949, "The Banki Water Turbine," *Engineering Experiment Station Bulletin Series No. 25*, Oregon State College, Corvallis, OR, Feb.

Nakase, Y., Fukutomi, J., Watanabe, T., Suetsugu, T., and Kubota, T., 1982, "A Study of Cross-flow Turbine (Effects of Nozzle Shape on its Performance)," *Small Hydro Power Fluid Machinery*, ASME Winter Annual Meeting of the ASME, Phoenix, AZ, pp. 13–18.

Varga, J., 1959, "Tests with the Banki Water Turbine," *Acta Technica*, Vol. XXVII/1-2, Academia Hungaricae, pp. 79–102.

# A Correlation of Leakage Vortex Cavitation in Axial-Flow Pumps

**K. J. Farrell**
Research Assistant.

**M. L. Billet**
Senior Scientist.

Applied Research Laboratory,
The Pennsylvania State University,
State College, PA 16804

*Tip clearance flow in turbomachinery can lead to losses in efficiency and stall margin. In liquid handling turbomachinery, the vortical flow field, formed from the interaction of the leakage flow with the through-flow, is subject to cavitation. Furthermore, this flow field is complex and not well understood. A correlation of variables which predict the vortex minimum pressure has been formulated. Measurements of the important variables for this correlation have been made on a high Reynolds number ($3 \times 10^6$) axial-flow test rig. The correlation has been applied to the measured data and other data sets from the literature with good agreement. An optimum tip clearance has been theoretically identified as experiments have shown. Observations of cavitation indicate a second vortex originating along the suction side trailing edge.*

## Introduction

The relative motion of a blade and the casing requires a finite clearance between the blade tip and the end-wall to avoid rubbing. The relative motion of the blade tip and the end-wall and the pressure difference across the blade tip create the tip clearance flow. In the end-wall region, the flow does not receive the theoretical momentum increase, and the interactions of this tip clearance flow with the incoming secondary flows, blade boundary layer, and end-wall boundary layer disturb the through-flow in a significant portion of the blade passage, as shown schematically in Fig. 1. The tip clearance flow between the rotor tip and end-wall intersects the flow over the suction side of the blade which has a different magnitude and direction. The two flows form a vortex sheet which eventually rolls up to form the leakage vortex.

Axial-flow pumps and compressors are subject to many of the same design considerations in regard to tip clearance flows; however, in pumps, which are liquid handling machinery, the dynamic interaction of the blade tip with the casing boundary layer and the leakage flow may lead to cavitation in addition to energy losses. Cavitation occurring in the tip clearance flow region of an axial-flow pump can be classified into three types: gap, blade-end, and leakage vortex cavitation. Gap cavitation occurs in the clearance itself due to separation of the clearance flow as it travels around the blade end. It is usually prevented by rounding the intersections of the leading edge and pressure surface with the tip surface (Gearhart, 1966). However, in the aero-engine community, where cavitation is not a concern, the intersection of the pressure surface and the tip surface is made sharp to promote separation and maximize the flow blockage in the clearance. Blade-end cavitation occurs at the leading edge when clearances are small and is due primarily to the stretching of boundary layer vorticity. Leakage vortex cavitation results from the low pressure region in the vortex formed by the interaction of the clearance flow with the through-flow. Of the three types, leakage vortex cavitation is the most problematic and least understood. A correlation which predicts the inception index for leakage vortex cavitation as a function of blade geometry and flow variables would be useful for the pump designer and is the motivation for this study.

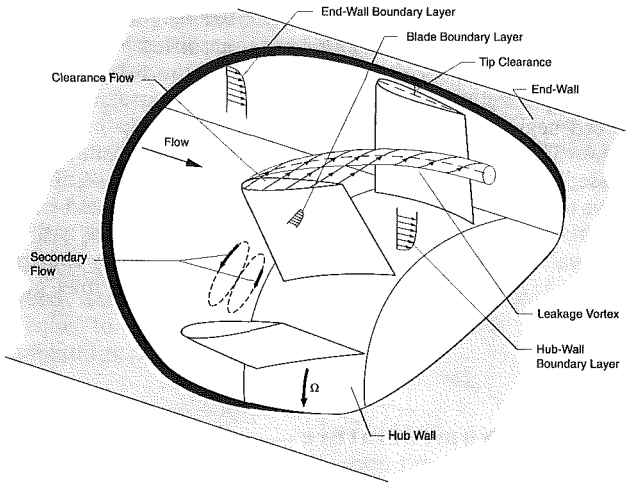


**Fig. 1 Flowfield in the end-wall region**

## Experimental Facilities and Procedures

The High Reynolds Number Pump (HIREP) facility was designed and constructed in order to study tip clearance flow. The rig consists of a 1.07-meter diameter axial-flow pump coupled with 1.22-meter diameter downstream, regenerative turbine in the 1.22-meter diameter by 4.3-meter long test section of the Garfield Thomas Water Tunnel of the Applied Research Laboratory Penn State. The impeller in the lower

Contributed by the Fluids Engineering Division for publication in the JOURNAL OF FLUIDS ENGINEERING. Manuscript received by the Fluids Engineering Division January 30, 1993; revised manuscript received September 15, 1993. Associate Technical Editor: A. Prosperetti.

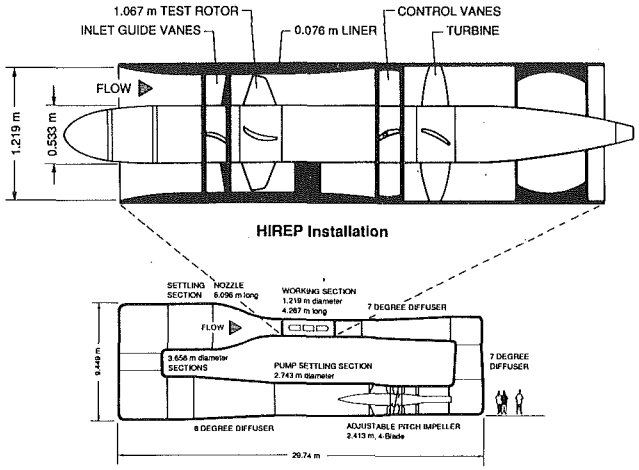


**Fig. 2 Schematic of 1.22-meter diameter Garfield Thomas water tunnel**

loop of the water tunnel provides sufficient energy to overcome the losses incurred in the rig and the flow loop. A schematic of the facility is given in Fig. 2. Further details concerning the HIREP facility and the instrumentation systems are given by Farrell et al. (1987).

The pump stage consists of inlet guide vanes (IGV's) and a rotor capable of absorbing 1 MW at a through-flow velocity of 15 m/s. The hub/annulus wall diameter ratio of the rotor stage is 0.5. The specifications of the rotor tip are as follows: chord, 206 mm; solidity, 0.43; maximum thickness, 21 mm; stagger angle, 53.4 degrees; and camber height, 0.2 percent chord. The thickness distribution is a modified NACA-66 series. The blade section stack-up was nearly radial. The IGV's were approximately one rotor chord length upstream and produced negligible turning at the tip; the rotor tip inflow was axial. The IGV's may have introduced an unsteadiness, discussed subsequently, in the vortex structure and position relative to the rotor blade. Spacers of various thicknesses beneath the blase bases were used to adjust the tip clearance with the end-wall. The pump flow coefficient was adjusted by changing the blade angles on the turbine rotor and turbine inlet guide vanes.

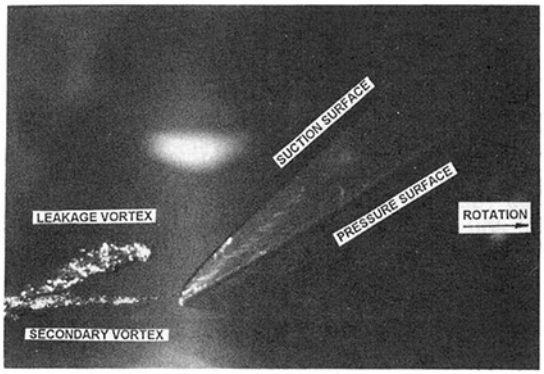


**Fig. 3 Photograph of multiple cavitating vortices at the rotor tip**

## Cavitation Results

A typical photograph of leakage vortex cavitation in the HIREP pump is shown in Fig. 3. The location of the vortex along the blade chord was observed to vary with gap spacing for constant flow coefficient. For very small gaps the cavitating vortex was observed to emanate near the blade leading edge, and for large gaps the vortex moved near the trailing edge. The cavitation index varied with tip clearance, Reynolds number, and flow coefficient. Desinent cavitation indices were measured on the HIREP pump rotor for three ranges of flow coefficient, 1.26–1.28, 1.33–1.35, and 1.37–1.39, and for through-flow velocities of 7.9, 9.4, and 11.0 m/s. These ranges of flow coefficient bracket the design value of 1.33.

The data showed a decrease in cavitation index with decreasing levels of gas content, as determined by the van Slyke apparatus. A procedure was developed to account for the air content effects so that cavitation data obtained at different air content levels could be compared on the same basis (see Billet and Holl, 1981; and Holl, 1960). Cavitation indices for Blade A are presented in Fig. 4 before and after the air content correction procedure was applied.

The values of leakage vortex cavitation index obtained for this experiment are given for three rotor blades in Figs. 4, 5, and 6 as a function of the ratio of tip clearance to maximum tip thickness, $\lambda$. Note that the cavitation index reported is normalized by a dynamic pressure based on the tip speed. The static pressure was measured at the pump stage inlet. For the

## Nomenclature

$A$ = projected tip surface area; empirical constant
$A_p$ = pump annulus area
$c$ = blade tip chord
$C_{P_{\min}}$ = minimum pressure coefficient, $(P_{\min} - P_\infty)/1/2\rho U^2$
$C_{L_0}$ = tip left coefficient at zero clearance condition
$C_{L_{\text{tip}}}$ = tip left coefficient, tip lift/$1/2\rho W_\infty^2 A$
$D$ = pump rotor diameter
$h$ = tip clearance
$k_s$ = empirical constant
$K$ = retained lift fraction
$n$ = rotational speed (rev/s)
$P_v$ = vapor pressure
$P_\infty$ = static pressure
$r_c$ = vortex core radius
$\text{Re}_c$ = blade tip chord relative Reynolds number, $W_\infty c/\nu$
$t_m$ = maximum tip thickness
$U$ = tip speed
$V_x$ = through-flow velocity
$W_1$ = inlet relative velocity at tip
$W_\infty$ = free-stream relative velocity at tip (outside boundary layer)
$y$ = contour path coordinate for line integral
$\epsilon$ = tip clearance over tip chord, $h/c$
$\Gamma$ = circulation
$\kappa$ = correction factor for air content level effects when scaling model data
$\lambda$ = tip clearance over maximum tip thickness, $h/t_m$
$\nu$ = kinematic viscosity
$\xi$ = coordinate along vortex sheet
$\rho$ = fluid density
$\sigma$ = desinent cavitation index, $(P_\infty - P_v)/1/2\rho U^2$
$\phi$ = flow coefficient, $V_x A_p/nD^3$ or $(V_x/U)A_p\pi/D^2$
$\zeta$ = vortex core radius over maximum tip thickness, $r_c/t_m$

### Subscripts

0 = zero-clearance value
$v$ = leakage vortex; normalization by $1/2\rho V_x^2$
sec = secondary flow
scrape = scraping vortex formed on pressure side
shed = free vorticity shed from rotor blade
tip = blade tip section
$w$ = normalization by $1/2\rho W_\infty^2$

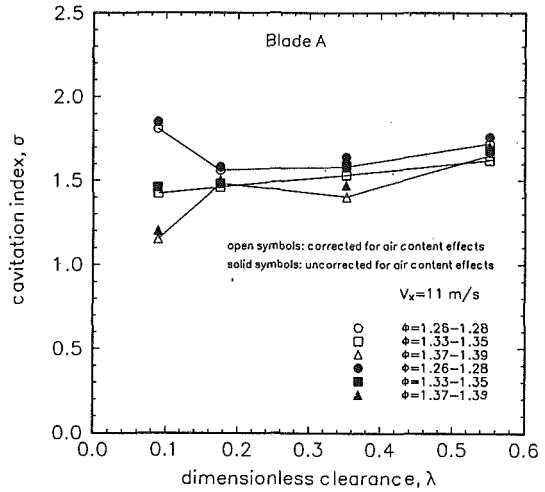


**Fig. 4 Cavitation index versus clearance for blade A, illustrating air content correction**

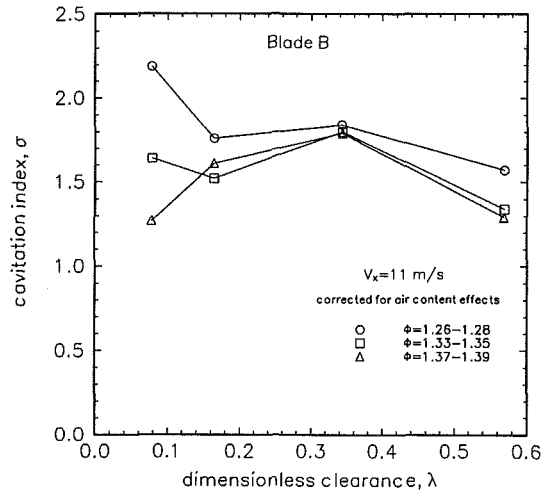


**Fig. 5 Cavitation index versus clearance for blade B**

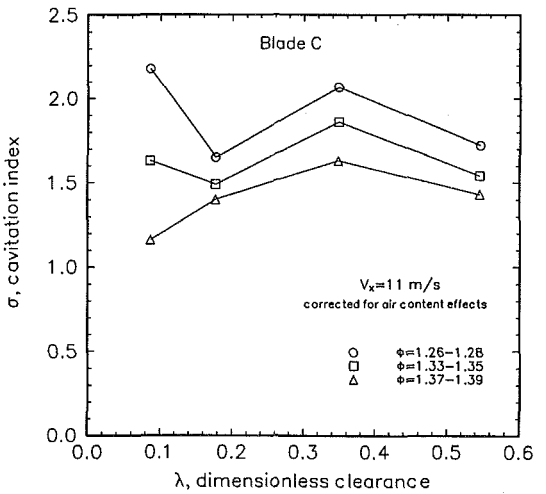


**Fig. 6 Cavitation index versus clearance for blade C**

low and medium flow coefficient ranges, the curves show a minimum occurring near $\lambda \simeq 0.2$. An optimum tip clearance for cavitation performance was also noted by Rains (1954), Mitchell (1958), and Shuba (1983). Janigro and Ferrini (1973)

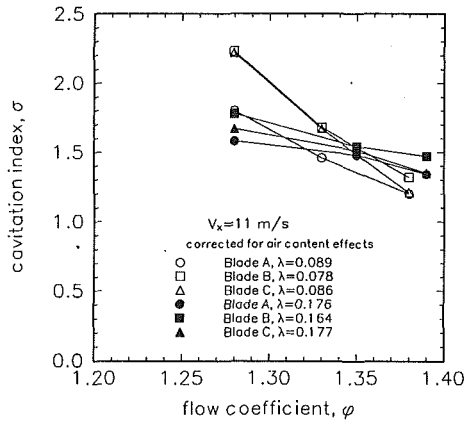


**Fig. 7 Cavitation index versus flow coefficient for $\lambda \simeq 0.08$ and $\lambda \simeq 0.17$**

noted a similar relationship with tip clearance in the cavitation performance of inducers evaluated by Acosta (1958) and Henderson and Tucker (1962). Mitchell and Shuba noted that for clearances less than $\lambda \simeq 0.15$, gap cavitation was observed, and for clearances greater than $\lambda \simeq 0.15$, leakage vortex cavitation was observed for all clearances. For the present data, leakage vortex cavitation was the limiting form for all tip clearances tested. From $\lambda \simeq 0.2$ to $\lambda \simeq 0.3$, the cavitation index generally increased. From $\lambda \simeq 0.3$ to $\lambda \simeq 0.5$, the cavitation index exhibited blade-to-blade variability; two of the blades showed a decrease while one showed an increase. In the limit as the tip clearance is increased, all of the tip lift is shed into the trailing vortex, and none is retained at the end-wall. The cavitation index should then asymptotically approach a value representative of a unshrouded pump, i.e., no casing. In Fig. 7, the cavitation data are presented as a function of flow coefficient for tip clearances $\lambda \simeq 0.08$ and $\lambda \simeq 0.17$. The leakage vortex cavitation is more sensitive to flow coefficient for smaller clearances.

## Model Development

Classical cavitation theory, which ignores bubble dynamic effects, states that cavitation will occur when the local pressure is equal to the vapor pressure. For a Rankine vortex, the minimum pressure is given by

$$C_{P_{\min}} = -2\left[\frac{\Gamma}{2\pi r_c U}\right]^2. \tag{1}$$

Inherent in Eq. (1) is the assumption that the vortex roll-up is complete, i.e., all of the vorticity is in the vortex core. Observations of the flow field and cavitation indices of a tip vortex by Stinebring, Farrell and Billet (1991) showed clearly that the minimum pressure of a trailing vortex occurs in the formation region, while some vorticity remains outside the core region. The validity of using this relationship in the correlation model will be discussed. Observations from the present data and the literature show that the cavitation index is a function of geometrical and flow parameters: tip clearance, blade chord, blade thickness, flow coefficient, tip left coefficient, rotational speed, end-wall boundary layer ($W_1$), and the Reynolds number. The circulation and vortex core size must be determined as a function of these parameters.

**Vortex Circulation.** The circulation in the leakage vortex is comprised of vorticity generated and shed near the tip:

$$\Gamma_v = \sum \Gamma_{i,\ \text{shed}} \cong \oint -\left(\frac{\partial \Gamma}{\partial y}\right) dy + \Gamma_{\text{sec}} + \Gamma_{\text{scraping}} + \ldots \tag{2}$$

The first term above represents the free vorticity shed from a

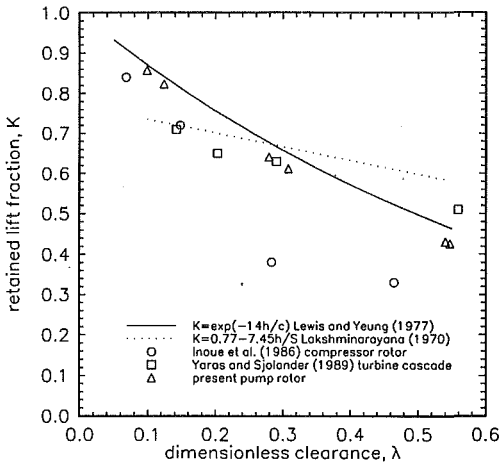


Fig. 8 Retained lift fraction versus clearance

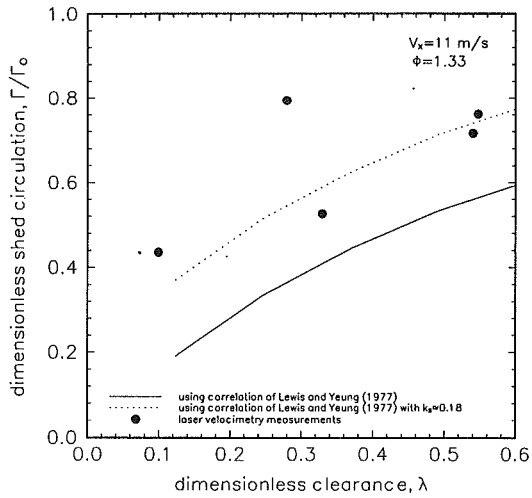


Fig. 9 Vortex circulation versus clearance

blade tip and is the dominant term in the equation. Usually the clearance is large enough and the turning small enough so as not to generate strong secondary vorticity. In fact, the secondary vorticity was found to be an order of magnitude less than the shed vorticity in the pump used by Shuba (1983). The size of the tip clearance also minimizes the scraping vorticity which forms on the pressure side of the blade. A secondary vortex which feeds into the large leakage vortex was visible from the cavitation photographs, Fig. 3. However, based on cavitation inception data for this vortex, it appears that its circulation is significantly less than the circulation in the leakage vortex, and thus it is not considered in the model. This vortex appears to be formed by the separated flow at the trailing edge of the blade. Thus free vorticity is the dominant term of the right-hand side of Eq. (2).

Lakshminarayana and Horlock (1962) suggested that only part of the blade's bound vorticity is shed downstream into the tip leakage vortex. The fluid in the clearance experiences a lift force as shown by measurements of static pressure on the end-wall in cascade with tip clearance (Lewis and Yeung, 1977; Yaras et al., 1988; and Yaras and Sjolander, 1989). Inoue et al. (1986) measured the circulation in the tip leakage vortex for a compressor rotor. For smaller clearances a larger fraction of the blade lift was retained at the end-wall, while for larger clearances, the blade lift was shed as circulation in the tip leakage vortex.

To quantify the shed lift effect, the value of lift on the blade tip was measured as a function of tip clearance. The outer ten percent of the rotor blade span was instrumented with a two-component force balance. The tip lift was measured as a function of flow coefficient and tip clearance. The present data showed good agreement with the empirical correlation of Lewis and Yeung (1977) and the measured data of Yaras and Sjolander (1989), while Lakshminarayana's (1970) cascade relation over-predicted the retained lift as illustrated in Fig. 8 for large clearances. Using the relation of Lewis and Yeung (1977), the circulation shed from the blade tip section can be expressed as

$$\Gamma_{\text{tip, shed}} = C_{L_0}(\phi) W_1 \frac{c}{2} [1 - e^{-14\epsilon}]. \tag{3}$$

Laser velocimetry was used to measure the tip inlet, exit, and clearance flows at several axial locations. Surveys of the exit flow provided data relative to the leakage vortex circulation and core size. Figure 9 shows a comparison of Eq. (3) above with the vortex circulation values determined from the laser data. The scatter in the LV data is attributed to the spatial wandering or meandering of the vortex (Baker et al., 1974; Straka and Farrell, 1991). While this effect on the circulation cannot be quantified, it is estimated from the analysis of the data by Straka and Farrell (1992) that it is smaller than the effect on the vortex core size and velocity distribution. The movement of the vortex through the LV control volume has the erroneous effect of enlarging the vortex core size and reducing the magnitude of the maximum tangential velocity.

Equation (3) underestimates the total circulation in the leakage vortex in spite of the total roll-up assumption, however the trend appears to be correct. Additional shed circulation exists due to the spanwise loading gradient and is a measure of the amount of span at the tip involved in the process. This additional circulation can be correlated with an averaged tip circulation, $\Gamma_0$,.which can be expressed as

$$\Gamma_v \cong \oint -\left(\frac{\partial \Gamma}{\partial y}\right) dy \cong \Gamma_{\text{tip, shed}} + k_s \Gamma_0. \tag{4}$$

In the present investigation, the constant $k_s$ can be determined explicitly.

**Vortex Core Size.** The expression for the minimum pressure of a vortex requires knowledge of the vortex core size as a function of the tip lift coefficient, the tip clearance, and the location of minimum pressure along the blade chord. Borrowing from Rains (1954) and using Lakshminarayana's and Horlock's (1962, 1967) assumption that the sheet radius and core radius are equal, Shuba expressed the resultant leakage vortex core radius as

$$r_c = 0.14\, \epsilon^{-0.85} (C_{L_{\text{tip, shed}}})^{0.425} (\xi/c)^{0.825} \tag{5}$$

Shuba, however, provided no experimental verification of the above.

Figure 10 compares the time-mean vortex core radius, as measured with the laser velocimeter as a function of the dimensionless tip clearance, with values calculated from Shuba's expression above. The measured vortex size was found to decrease with increasing tip clearance, contrary to Eq. (5). Intuitively, the vortex core size would scale with the clearance, since the clearance is a length scale for the leakage flow; and this was the observation of Storer and Cumpsty (1990) in a turbine cascade.

Several phenomena occurred which may explain this trend. First, as shown in Fig. 3, a secondary vortex was generated on the rotor blade suction side. The roll-up of this vortex with the leakage vortex appeared to be partially responsible for the increase in the unsteadiness of the core. The two vortices intersected at the blade trailing edge, just upstream of the LV measurement locations, 13 and 68 mm downstream of the rotor trailing edge. The secondary vortex generated appears to have

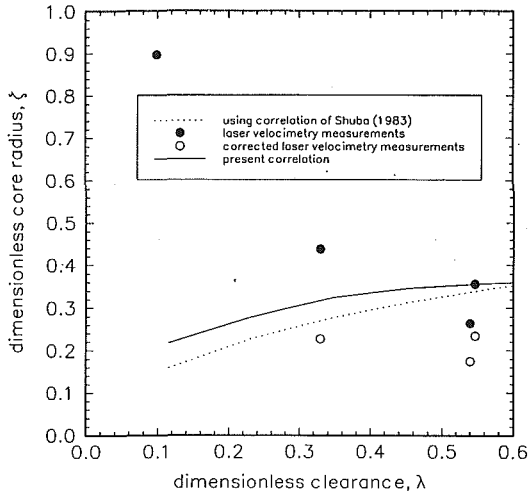


Fig. 10 Vortex core radius versus clearance

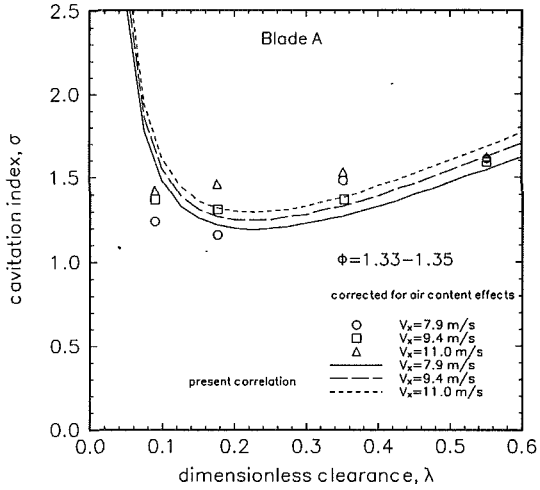


Fig. 11 Correlation model predictions compared to present data for several flow coefficients

a substantial influence on the stability of the leakage vortex system. For smaller tip clearances, the upstream end of the leakage vortex formed near the leading edge of the blade. Thus the two corotating vortices originated nearly a blade tip chord apart, and their initial interaction near the tip trailing edge may have formed a large diameter structure. Observations of the cavitating vortices showed that their axes intersected at a large included angle and confirmed the enlargement phenomenon which was observed with the LV. For large tip clearances, the two vortices originated near the same location at the trailing edge of the blade, and the leakage vortex did not appear to change drastically in structure.

Second, the vortices generated with small tip clearances wandered or meandered substantially, probably due to inlet flow distortions from upstream vanes, ingested freestream turbulence, and/or the instability of the vortex sheet. The wandering phenomenon distorts the vortex as measured with the laser velocimeter as mentioned earlier; the core size is enlarged and the maximum tangential velocity is reduced (Baker et al., 1974, Straka and Farrell, 1992). Straka and Farrell (1992) analyzed the effect of vortex wandering on the present LV data with a numerical model of the phenomenon. Even with the large uncertainty concerning the characteristics of the wandering motion, the vortex cores were shown to be substantially enlarged, as shown in Fig. 10.

Shuba's (1983) correlation for the vortex core radius yields values which are smaller than the measured data at larger clearances, where the LV core measurements are probably the least effected by the interaction and wandering phenomena discussed above. In a similar manner as the retained lift, the vortex core radius can be expressed as

$$r_c = (1 - e^{-6\lambda}) r_{c_{h\to\infty}}. \tag{6}$$

For the present investigation, the leakage vortex core radius at the largest tip clearance is taken as the estimator for $r_{c,h\to\infty}$, since we believe it to be least affected by the multiple vortex interaction and wandering phenomena. The present database is insufficient to determine a relationship for $r_{c,h\to\infty}$ as a function of the tip lift coefficient and the tip geometry. However, for the unshrouded pump condition, it is postulated that the leakage vortex core size is weakly dependent upon the tip lift coefficient and strongly dependent on the tip geometry and Reynolds number. Based on the measured cavitation indices, changes in the operating flow coefficient do not substantially affect the cavitation performance, except for small clearances (Fig.7). Moreover, the flow coefficient affects the circulation in the vortex directly. Therefore, the assumption of a weak relationship between core size and tip lift coefficient is reasonable.

McCormick (1962) and Gearhart and Ross (1983) noted the dependency of the cavitation index on the Reynolds number in scaling vortex cavitation data. McCormick emphasized that the vortex core radius is comprised principally of the pressure side boundary layer flow. For a flat plate turbulent flow, the boundary layer thickness is inversely proportional to the Reynolds number raised to the one-seventh power. The length scale for the leakage flow is proportional to the chord length, $c$. Thus, for an empirical approximation applying to conventional axial-flow pumps, the vortex core radius can be expressed as

$$r_{c_{h\to\infty}} = Ac\mathrm{Re}_c^{-1/7} \tag{7}$$

where $A$ is a constant. The value of $A \simeq 0.36$ was determined by applying Eq. (7) to the LV measurements of vortex core radii, corrected for wandering. Equation (7) was then applied to the other data sets using the appropriate chord length and Reynolds number.

**Vortex Minimum Pressure.** A correlation model of leakage vortex cavitation can be formed by substituting the expressions for the leakage vortex circulation (Eq. (4)) and the vortex core size (Eqs. (6) and (7)) into the expression for the minimum pressure in the vortex:

$$\sigma \cong \frac{\kappa}{8\pi^2 A^2} C_{L_0}^2 \left[ \frac{W_1(1 - e^{-14\epsilon}) + W_\infty k_s}{(1 - e^{-6\lambda}) U} \right]^2 Re_c^{2/7}. \tag{8}$$

Equation (8) contains all of the known parameters which influence the leakage vortex cavitation index: tip clearance, blade chord, blade thickness, flow coefficient, tip lift coefficient, rotational speed, end-wall boundary layer ($W_1$), and the Reynolds number. The factor $\kappa$ accounts for effects of air content level.

Since the velocity distributions of the leakage vortices were measured with the laser velocimeter, the total circulation is known, and thus the constant $k_s = 0.18$, which was correlated with the two-dimensional circulation of the tip section $\Gamma_0$, is known *a priori*. However, for other data sets from the literature, where measurements of the leakage vortex flow field are not available, the same value of $k_s = 0.18$ was used and found to correlate the data.

**Application.** The results of applying the correlation model to the High Reynolds Number Pump are illustrated in Fig. 11 for the three flow coefficient ranges tested. The model predicts the existence of an "optimum" clearance at $\lambda \simeq 0.2$. As small

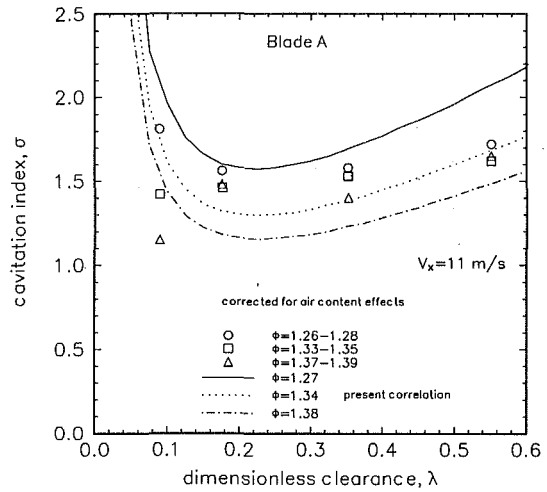


**Fig. 12 Correlation model predictions compared to present data for several axial velocities**

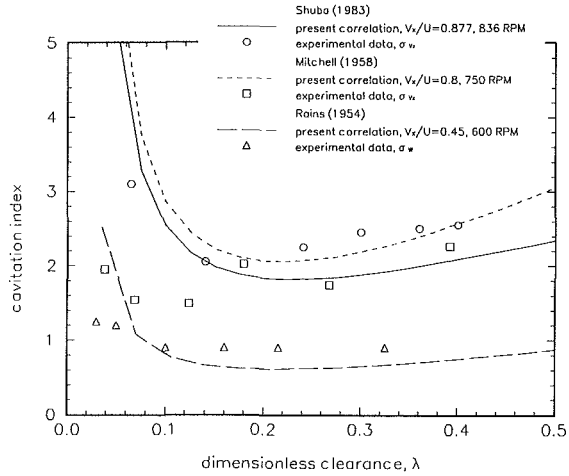


**Fig. 13 Correlation model predictions compared to data of Shuba (1983), Mitchell (1958), and Rains (1954)**

clearances less than $\lambda \simeq 0.15$ are approached, the correlation predicts increasing values of the cavitation index. However, from the data, this trend is a strong function of flow coefficient as shown in Fig. 7. Blade tip static pressure measurements indicate that the $\sigma$-$\phi$ trend at small clearances was not due to the change in tip lift coefficient alone; the scraping vortex was suggested as a contributor. Further, measurements of blade tip surface pressures indicate the existence of a critical gap Reynolds number between $\lambda \simeq 0.07$ and $\lambda \simeq 0.16$, which separates two regimes for the leakage flow. At small clearance values, the leakage flow should be modeled using a potential flow analysis; for larger clearances values, a viscous flow model, as presented in this paper, is appropriate. Thus for small clearances, Eq. (8) is not applicable. The ability of the model to account for changes in Reynolds number can be evaluated in Fig. 12. The predicted spread in the cavitation index over the limited velocity range compares well with the experimental data. When scaling model scale cavitation data to a larger scale pump, the correlation of Eq. (8) collapses to

$$\sigma_{\text{large scale}} = \sigma_{\text{model scale}}(\text{Re}_{c_{\text{large scale}}}/\text{Re}_{c_{\text{model scale}}})^{2/7}\kappa. \quad (9)$$

In the investigation of Shuba (1983), the tip lift and vortex core size were not measured. Equation (8) was used to calculate an estimate for $r_{c,h\to\infty}$. The tip lift coefficient was obtained from the design database. Similar to the treatment of the HIREP data, additional circulation was included in the correlation model; a value of $k_s = 0.18$ was used. The correlation results and the data are shown in Fig. 13 for the conditions $V_x/U = 0.877$ and 836 rpm. The correlation predicts a shallower cavitation bucket compared to the present HIREP data, and the trend compares well with the experimental data. Note that for normal operating clearances in the range of 0.1 to 0.2 (dimensionless), the correlation does very well.

The correlation model of leakage vortex cavitation was also applied to the experimental investigation of Mitchell (1958). Howell's cascade correlations were used to estimate a tip lift coefficient for the circular arc blades. The vortex core radius at infinite gap was calculated from Eq. (7), and $k_s = 0.18$ was used to include additional circulation in the model. The correlation model generally overpredicted the cavitation indices for the conditions $V_x/U = 0.8$ and 750 rpm, as shown in Fig. 13, except near $\lambda \simeq 0.2$. The trend appears reasonable, however.

The data of Rains (1954) was used as a final application of the correlation model as shown in Fig. 13. Using the tip lift coefficient given by Rains and a value of $r_{c,h\to\infty}$ from Eq. (7), the cavitation indices were calculated at the design flow coefficient, $V_x/U = 0.45$ and 600 rpm. Again using a value of $k_s = 0.18$, the model underpredicted the data for large clearance values.

## Conclusions

The cavitation and tip flow studies of a high Reynolds number axial-flow pump have provided useful insight into the physics of the tip clearance flow. A correlation model of flow and geometrical parameters has been formulated for the prediction of leakage vortex cavitation by the pump designer, and is simplified below:

$$\sigma \cong 0.0977\ \kappa C_{L_0}^2 \left[\frac{W_1(1-e^{-14\epsilon}) + 0.18\ W_\infty}{(1-e^{-6\lambda})U}\right]^2 \text{Re}_c^{0.29}. \quad (10)$$

As a result of this investigation, a number of conclusions can be made:

1. Leakage vortex cavitation was observed for all tip clearances tested. The location of the cavitating vortex origin moved along the chord line, depending on the size of the tip clearance.
2. The leakage vortex flow field was further complicated by the interaction of another vortex at the suction side trailing edge tip. The cavitation index of this vortex is substantially less than the cavitation index of the leakage vortex.
3. The highest measured cavitation indices were observed for the smallest tip clearances. Generally, cavitation minima occurred near $\lambda \simeq 0.2$.
4. Laser velocimeter measurements indicated that the circulation shed from the blade tip (outer ten percent span) did not account for all of the circulation in the leakage vortex, even though roll-up was not complete. An additional value of $0.18\ \Gamma_0$ appears to correlate the data.
5. The correlation model presented in Eq. (8) simplifies to a simple Reynolds number scaling relationship in Eq. (9) when projecting large scale cavitation performance from model scale tests. The Reynolds number dependence arises from the pressure side boundary layer flow passing through the clearance and rolling-up into the leakage vortex.
6. The applicability of the model is limited to clearances greater than approximately $\lambda \simeq 0.1$, but this covers normal operating clearances for pumps. For smaller clearances, a potential model of the leakage flow is more appropriate.

## Uncertainty

The uncertainty associated with the measurements reported herein are as follows: $\sigma$, $\pm 5\%$; $C_L$, $+2\%$; $V_x$, $\pm 1\%$, $U$, $\pm 0.5\%$; and $h$, $\pm 0.1$ mm. The effect of the vortex wandering

on the laser velocimetry measurements of vortex core size and circulation is significant and has been discussed previously.

## Acknowledgment

The effort described herein was sponsored by the U.S. Navy.

## References

Acosta, A. J., 1958, "An Experimental Study of Cavitating Inducers," *Proceedings of the Second Symposium on Naval Hydrodynamics*, ONR/ACR-38, pp. 533–577.

Baker, G. R., et al., 1974, "Laser Anemometer Measurements of Trailing Vortices in Water," *Journal of Fluid Mechanics*, Vol. 65, Part 2, pp. 325–336.

Billet, M. L., and Holl, J. W., 1981, "Scale Effects on Various Types of Cavitation," ASME JOURNAL OF FLUIDS ENGINEERING.

Farrell, K. J., McBride, M. W., and Billet, M. L., 1987, "High Reynolds Number Pump Facility for Cavitation Research," *International Symposium on Cavitation Research Facilities and Techniques*, ASME FED Vol. 57.

Gearhart, W. S., 1966, "Tip Clearance Cavitation in Shrouded Underwater Propulsors," *AIAA Journal of Aircraft*, Vol. 3, No. 2.

Gearhart, W. S., and Ross, J. R., 1983, "Tip Leakage Effects," Applied Research Laboratory Penn State Technical Memorandum 83-20.

Henderson and Tucker, 1962, "Performance Investigation of Some High Speed Pump Inducers," R.P.E. Technical Note 214.

Holl, J. W., 1960, "An Effect of Air Content on the Occurrence of Cavitation," ASME *Journal of Basic Engineering*, pp. 941–946.

Inoue, M., Kuroumaru, M., and Fukuhara, M., 1986, "Behavior of Tip Leakage Flow Behind an Axial Compressor Rotor," ASME *Journal of Engineering for Gas Turbines and Power*, Vol. 108, pp. 7–15.

Janigro, A., and Ferrini, F., 1973, "Inducer Pumps," von Karman Institute for Fluid Dynamics, Lecture Series 61.

Lakshminarayana, B., 1970, "Methods of Predicting the Tip Clearance Effects in Axial Flow Turbomachinery," ASME *Journal of Basic Engineering*.

Lakshminarayana, B., and Horlock, J. H., 1967, "Leakage and Secondary Flows in Compressor Cascades," Aeronautical Research Council (U. K.), R & M No. 3483.

Lakshminarayana, B., and Horlock J. H., 1962, "Tip Clearance Flow and Losses for an Isolated Compressor Blade," Aeronautical Research Council (U. K.), R & M No. 3316.

Lewis, R. I., and Yeung, E. H. C., 1977, "Vortex Shedding Mechanisms in Relation to Tip Clearance Flows and Losses in Axial Fans," Aeronautical Research Council (U. K.), R & M No. 3829.

McCormick, B. W., 1962, "On Cavitation Produced by a Vortex Trailing from a Lifting Surface," ASME *Journal of Basic Engineering*.

Mitchell, A. B., 1958, "An Experimental Investigation of Cavitation Inception in the Rotor Blade Tip Region of an Axial Flow Pump," Admiralty Research Laboratory, ARL/R1/G/HY/11/2.

Rains, D. A., 1954, "Tip Clearance Flows in Axial Flow Compressors and Pumps," Hydromechanics and Mechanical Engineering Laboratories, California Institute of Technology.

Storer, J. A., and Cumpsty, N. A., 1990, "Tip Leakage Flow in Compressors," ASME Paper 90-GT-127, Gas Turbine Institute and Aeroengine Congress and Exposition, Brussels, Belgium.

Shuba, B. H., 1983, "An Investigation of Tip-wall Vortex Cavitation in an Axial-flow Pump," Master's thesis, The Pennsylvania State University, Dept. of Aerospace Engineering.

Straka, W. A., and Farrell, K. J., 1992, "An Investigation of Vortex Wandering in a High Reynolds Number Axial-flow Pump," *Experiments in Fluids*, 13, 163–170.

Yaras, M., Zhu, Y., and Sjolander, S. A., 1988, "Flow Field in the Tip Gap of a Planar Cascade of Turbine Blades," ASME Paper 88-GT-29.

Yaras, M., and Sjolander, S. A., 1989, "Development of the Tip-Leakage Flow Downstream of a Planar Cascade of Turbine Blades: Vorticity Field," ASME Paper 89-GT-55.

**E. A. Baskharone**
Associate Professor.
Mem. ASME

**A. S. Daniel**
Graduate Research Assistant.

**S. J. Hensel**[2]
Graduate Research Assistant.

Department of Mechanical Engineering,
Texas A&M University,
College Station, TX 77843

# Rotordynamic Effects of the Shroud-to-Housing Leakage Flow in Centrifugal Pumps[1]

*The fluid/shroud interaction forces acting on a pump impeller that is precessing around the housing centerline, are computed and the rotordynamic coefficients deduced. The numerical procedure utilized is an upgraded version of a finite-element-based perturbation model, initially devised for simple see-through annular seals. The computational model accounts for the complex flow structure in the shroud-to-housing secondary flow passage, which includes a tight-clearance face seal. The model also facilitates the mutual interaction between the primary and secondary flows near the impeller inlet and discharge stations. The numerical results are compared to existing experimental data, as well as the results of a simpler and widely used numerical model. Sources of discrepancies between the numerical results are identified, and a comprehensive assessment made in light of the experimental data.*

## Introduction

Frequent mechanical failure of turbomachinery rotating components, due to fluid-induced vibration, has been reported over the past two decades. The most common instability mechanism in this case is one where the impeller whirls around the housing centerline at a subsynchronous whirl frequency (e.g., Childs and Moyer, 1985). Serious efforts are now being devoted to the development of reliable predictive tools for capturing the dynamics of fluid-encompassed rotors and testing ways to enhance the fluid restoring forces.

Rotordynamic forces on shrouded pump impellers have particularly been the subject of an increasing number of experimental and numerical investigations. Of the experimental studies, those by Bolleter et al. (1989) and Guinzburg et al. (1993) are perhaps the most comprehensive. In both cases, the fluid-exerted forces were reported to have a more or less parabolic dependency on the impeller whirl frequency. This dependency was approximated with a least-square fit to obtain the direct and cross-coupled stiffness, damping and inertia coefficients of the fluid/shroud system.

Perhaps the simplest, and most popular, numerical tool in this area is the bulk-flow model devised by Childs (1983). This model was later upgraded (Childs, 1989) and used to compute the rotordynamic coefficients of two leakage-passage configurations, both corresponding to the same impeller geometry and operating conditions. Results of this study were compared to the experimental data by Bolleter et al. (1989). More detailed models of the fluid/rotor interaction problem have also been reported by Tam et al. (1988) as well as Dietzen and Nordmann (1988). However, attention in these two studies was focused on simple annular seals and journal bearings.

The current study is the first such attempt, known to the authors, where a full-scale unsplit secondary passage of a pump stage is under investigation within a framework which tolerates such real flow effects as separation and recirculation. The study is an extension of the model previously published by Baskharone and Hensel (1991a) for a simple untapered annular seal. The idea of utilizing segments of the primary flow passage in defining the computational domain (Fig. 1) was first outlined (also by Baskharone and Hensel, 1989) as a means of facilitating the calculation of the primary/secondary flow interaction effects. However, the published analysis, then, merely presented the idea, but treated the secondary flow as strictly laminar and, as a result, had no appreciable engineering value. The current study is, therefore, one which expands previously devised ideas, by the authors, and applies the outcome to a traditionally complex problem for which an equally detailed solution is simply non-existing.

## Analysis

Figure 1 shows a schematic of a hydraulic pump stage, with a face seal as a leakage-control device (Bolleter et al., 1989). Shown on the same figure is the computational domain for solving the centered-rotor (zeroth-order) flow-governing equations. In addition to the secondary shroud-to-housing flow passage, the selected domain also includes two primary-flow segments, which are naturally connected to the secondary passage near the impeller inlet and discharge stations. The ob-

[1] This research was funded by NASA-Marshall Space Flight Center, Huntsville, Alabama, Contract No. NAS8-37821 (technical monitor: James Cannon), and the Texas A&M Turbomachinery Research Consortium.

[2] Currently with Westinghouse Savannah River Laboratory, Aiken, SC, Mem. ASME.

Contributed by the Fluids Engineering Division for publication in the JOURNAL OF FLUIDS ENGINEERING. Manuscript received by the Fluids Engineering Division May 17, 1993; revised manuscript received December 7, 1993. Associate Technical Editor: L. Nelik.

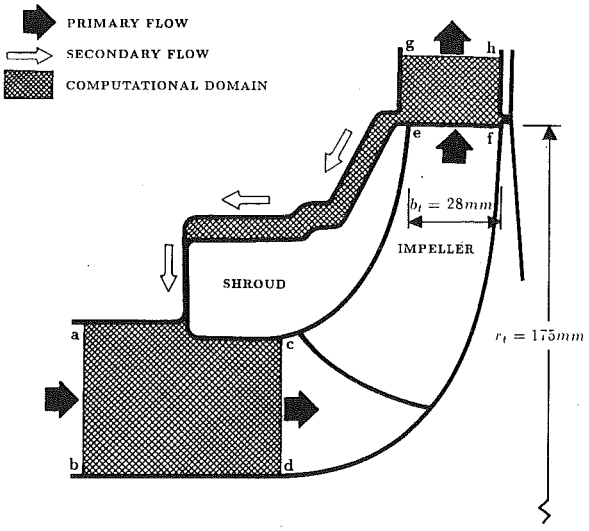


Fig. 1 Definition of the computational domain

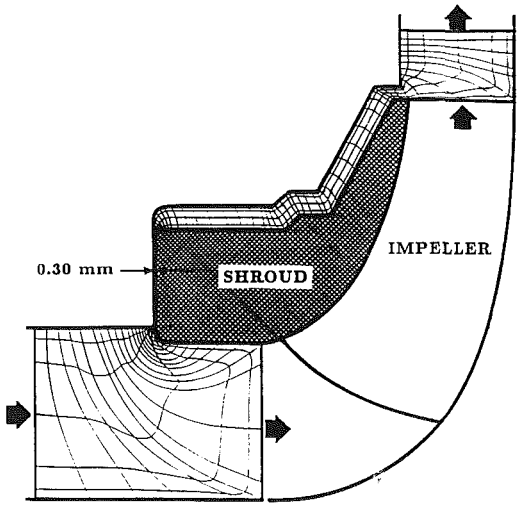


Fig. 2 Finite-element discretization model for the centered-impeller operation mode

jective here is to alleviate the need for specifying, assuming, or iteratively obtaining the secondary-passage inlet flow conditions. Of these common choices, Childs, for instance, has reportedly utilized the iterative approach, whereby the secondary passage was isolated, and the flow solution iteratively obtained under the condition that the streamwise pressure differential, across the passage, is identical to that across the impeller (Childs, 1989). Such approach is understandably appropriate, considering that the secondary flow in this case is treated as one layer with no cross-flow gradients taken into account. However, this and any other equivalent simplifications would fall between insufficient and inadequate in the current detailed flow model where inlet and exit velocity profiles will also have to be prescribed, should the passage be isolated. Contouring the computational domain in the manner seen in Fig. 1 has the effect of converting the secondary passage inlet and exit flow conditions into internal variables to be part of the numerical solution. Note that the passage inlet and exit swirl profiles, which have a predominant effect on the impeller stability, are included among these variables.

Figure 2 shows the finite-element discretization model which was created for the centered-rotor operation mode. The model is composed of non-overlapping nine-noded bi-quadratic elements of the Lagrangian type (Zienkiewicz, 1971). These elements are generally curve-sided, a feature which had a highly favorable effect in matching the domain boundaries. Intensity of the finite elements are, by reference to Fig. 2, much higher in regions where pronounced gradients of the flow thermophysical properties are anticipated.

**Flow-Governing Equations.** In order to eliminate the flow field time-dependency, that is imparted by the impeller whirling motion (Fig. 3), the flow conservation laws are cast in a frame of reference that is attached to the rotor, being the impeller-shroud assembly, and whirls with it. The time-averaged flow equations, now expressed in terms of relative velocity components, include such terms as the Coriolis and centripetal acceleration components. These equations, as well as their finite-element equivalent, were previously published by Baskharone and Hensel (1991b). The published model also contained a modified version of Baldwin and Lomax turbulence closure (1978).

**Boundary Conditions.** Referring to the flow-permeable

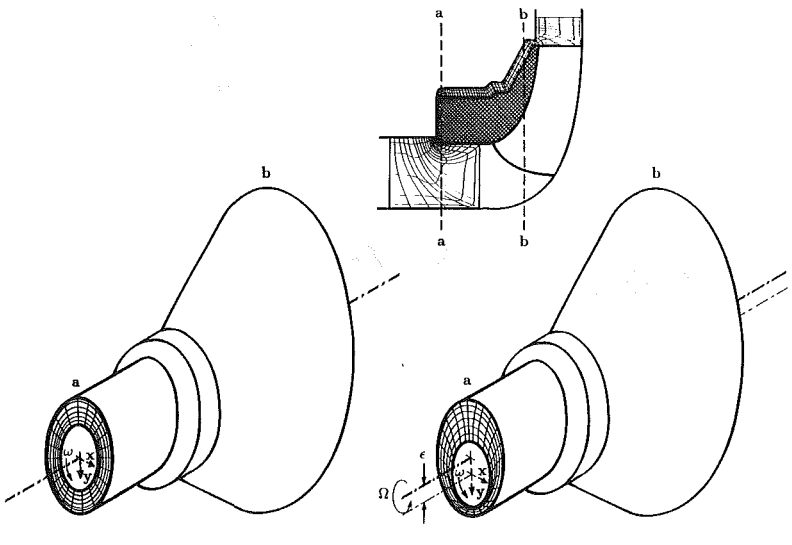


Fig. 3 Distortion of the shroud-to-housing finite element assembly due to the impeller whirl

boundary segments in Fig. 1, the boundary conditions over these segments are as follows:

(*i*) *Stage Inlet Station.* This is the boundary segment a-b in Fig. 1, which is located sufficiently far upstream from the impeller. Fully developed flow is assumed at this location, giving rise to the following boundary condition:

$$\frac{\partial V_r}{\partial z}=\frac{\partial V_\theta}{\partial z}=\frac{\partial V_z}{\partial z}=0$$

In addition, the stage-inlet static pressure is specified at the node midway between the endwalls on this station.

(*ii*) *Impeller Inlet and Exit Stations.* These are labeled c-d and e-f in Fig. 1. Fixed profiles of the velocity components, corresponding to the stage operating conditions, are imposed over these boundary segments. Note that the operating conditions here involve the primary impeller passage, and do not include the secondary mass flow rate.

(*iii*) *Stage Exit Station.* The flow behavior at this station (designated g-h in Fig. 1) is viewed as predominantly confined to satisfying the mass and angular momentum conservation equations in a global sense. In their derivative forms, these can be expressed as follows:

$$\frac{\partial V_r}{\partial r}=-\frac{V_r}{r} \quad \text{and} \quad \frac{\partial V_\theta}{\partial r}=-\frac{V_\theta}{r}$$

These two boundary conditions are linear and are, therefore, introduced non-iteratively in the numerical solution process. Moreover, a zero normal derivative of $V_z$ is imposed over this station, and the stage-exit static pressure is specified at the computational node midway between the endwalls.

As for the solid boundary segments in Fig. 1, namely those of the housing and shroud as well as the hub surface segment b-d, the no-slip boundary condition applies as follows:

$$V_r=0, \quad V_z=0 \quad \text{and} \quad V_\theta=C$$

where $C$ is equal to $(\omega r)$ and zero for rotating and nonrotating boundary segments, respectively.

**Perturbation Model.** As the impeller enters the whirling motion depicted in Fig. 3, the flow properties including, in particular, the shroud pressure distribution, assume nonaxisymmetric patterns. The current perturbation model perceives such deviation, from that of the centered-impeller, as the result of infinitesimally small distortions in the finite-element grid due to the eccentricity "$\epsilon$" of the impeller axis of rotation (Fig. 3). Expansion of the flow-governing equations, in their finite-element form, as functions of "$\epsilon$" is then carried out and, in the end, gives rise to the differential changes of the flow variables. Of these differential changes, those associated with the shroud pressure distribution are then isolated and integrated over the entire shroud surface. The result in this case is the rate, with respect to $\epsilon$, at which the fluid reaction forces (restoring or aggravating) are exerted on the shroud. The fluid/shroud interaction forces are then analyzed at various whirl frequencies to determine the stiffness, damping and inertia coefficients with which the fluid contributes to the shroud whirling motion.

Aside from the different geometry and boundary conditions in the current study, the perturbation model just described is virtually identical to that by Baskharone and Hensel (1991a) where the much simpler case of a straight annular seal was analyzed. However, since the basic approach development has already been published, and for the sake of compactness, the interested reader is referred to the two "companion" papers by Baskharone and Hensel (1991a, 1991b).

## Results and Discussion

A centrifugal pump stage, which was the subject of rotordynamic measurements by Bolleter et al. (1989), was chosen as a test case in the current study. This is schematically shown in Fig. 1, and has been previously selected for rotordynamic analysis by Childs (1989). The stage dimensions and operating conditions were reported by Bolleter et al. (1989) as follows:

Impeller tip radius = 175 mm
Impeller outlet width = 28 mm
Impeller speed = 2000 rpm
Working medium is water at 30°C
Volumetric flow rate = 130 l/s
Total head = 68 m
Reynolds' number (based on the tip speed and radius = $8.02\times10^6$

Figures 4, 5, and 6 present the most significant features of

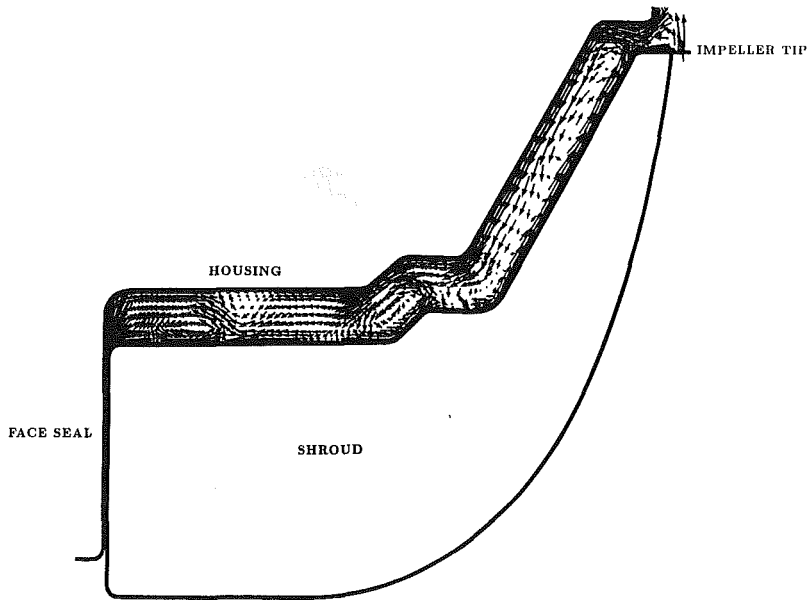


**Fig. 4 Vector plot of meridional velocity component for the centered-impeller operation mode**

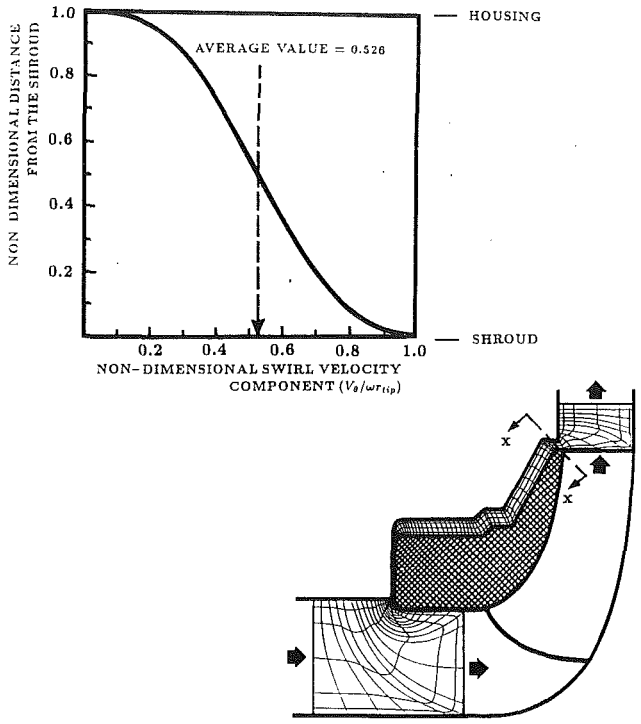


**Fig. 5 Distribution of the non-dimensional swirl velocity component at the leakage-passage inlet station**

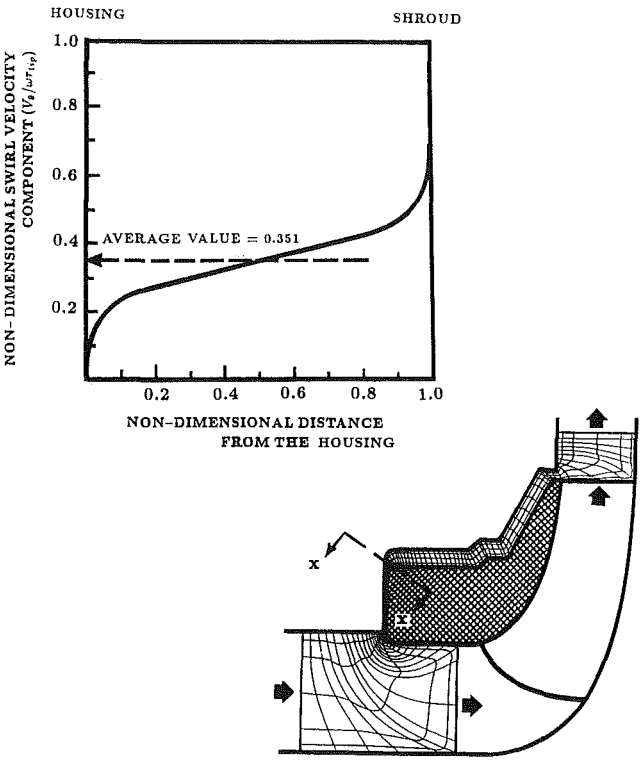


**Fig. 6 Distribution of the non-dimensional swirl-velocity component at the face-seal inlet station**

the centered-impeller flow structure in the secondary passage. The complexity of this flow field is most apparent in Fig. 4, which is a vector plot of the meridional velocity component in the shroud-to-housing passage. The flow pattern in this figure is characterized by massive separation and recirculation zones in virtually all segments of the passage. This characteristic is the result of the flow tendency to migrate radially outwards near the "spinning" shroud (due to the locally high centrifugal force and the flow viscosity), which is opposed by the tendency to proceed radially inwards near the housing (due to the static pressure differential across the flow passage). Such flow behavior is generally consistent with experimental observation (e.g., Guelich et al., 1987), but was never part of a rotordynamic analysis to the authors' best knowledge. Equally important are the swirl velocity profiles in Figs. 5 and 6 at the leakage-passage and the seal inlet stations (Figs. 5 and 6, respectively). This is due to the well-established fact that the flow swirl in the leakage passage acts as a major destabilizing factor. Examination of the cross-flow swirl velocity distributions in Figs. 5 and 6 reveals significantly large boundary layer thicknesses at the solid walls, with a rather narrow "core flow" region as the flow passage contracts just upstream of the face seal (Fig. 6). The relatively small value of the swirl velocity in Fig. 6 is a natural outcome of the "no-slip" condition that prevails at the shroud surface, giving rise to a swirl velocity which is relatively small at this radial location by comparison.

Prior to the full-scale execution of our perturbation model, a grid-dependency study was conducted. The independent variable here was the number of computational planes in the circumferential direction (Fig. 3), whereby the fluid-exerted forces at an arbitrarily fixed whirl-frequency ratio ($\Omega/\omega$) of 0.3, were monitored. Results of this numerical experimentation phase are shown in Fig. 7 in the form of tangential and radial components of the net shroud force. The figure clearly shows that the force trends begin to level out for a circumferential plane count of 9. As a result, the impeller rotordynamic analysis was conducted in its entirety using this value in a compromise between the precision of the numerical results, on one hand, and the consumption of computational resources, on the other.

Results of the perturbation analysis, as fluid-exerted forces on the shroud, are shown in Fig. 8 for a range of whirl frequency ratio ($\Omega/\omega$) between $-1.25$ and $+1.25$. The fluid-exerted forces in this figure, as well as Fig. 8, are nondimensionalized in the same manner proposed by Bolleter et al. (1989), namely:

$$\overline{F}_r = \frac{\dfrac{\partial F_r}{\partial \epsilon}}{\pi r_t^2 \rho b_t \omega^2}$$

$$\overline{F}_\theta = \frac{\dfrac{\partial F_\theta}{\partial \epsilon}}{\pi r_t^2 \rho b_t \omega^2}$$

where $\epsilon$ is the orbit radius of the impeller axis (Fig. 3), $r_t$ is the impeller tip radius, $b_t$ is the impeller outlet width, $\rho$ is the fluid density, and $\omega$ is the shaft angular speed (in rad./s). Reproduced on the same figure are the experimental measurements of Bolleter et al. (1989), and the forces computed by Childs (1989) using a bulk-flow perturbation model. Of these, Childs' results are shown for pre-imposed inlet swirl values of 0.5 and 0.6 of the impeller tip speed. The reader is reminded that this ratio, in the current computational procedure, is treated as unknown to be produced in the solution of the zeroth-order flow field, and that our computed average value is, by reference to Fig. 6, 0.526 of the impeller tip speed. As seen in Fig. 8, the bulk-flow model produces rather sharp force fluctuations, initially thought of as resonance-like, for the elevated inlet swirl ratio of 0.6, within a narrow range of whirl-frequency ratio around 0.3. These fluctuations are neither confirmed by the current results nor the experimental data. The fact that such drastic change in the force trends corresponds to modest changes in the inlet swirl ratio, by comparison to the smooth flow trends obtained for a swirl ratio of 0.5 (Fig. 8), was equally surprising. However, the point should be made that the seal-inlet swirl velocity in Childs' study was significantly higher than (roughly double) the computed value in the

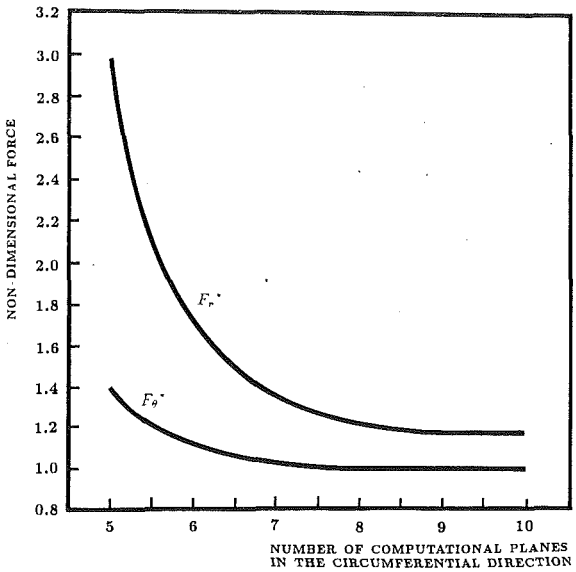


Fig. 7 Dependency of the fluid-exerted forces on the grid resolution in the circumferential direction

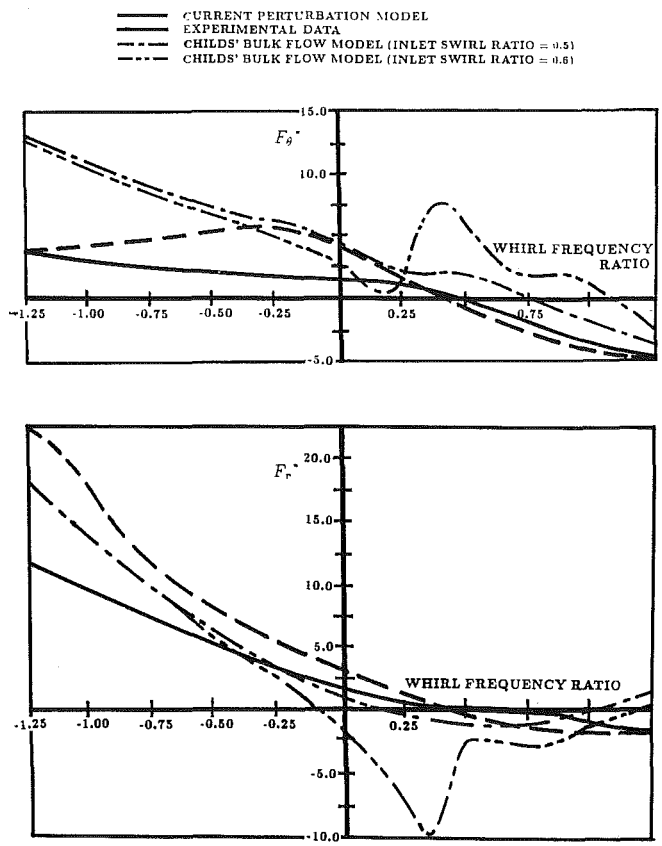


Fig. 8 Comparison of the shroud forces with experimental and numerical data

current study (Fig. 6). Knowing that the seal-inlet swirl velocity deviation, between the two numerical studies, grows even wider as the leakage-passage inlet swirl velocity is elevated, it would perhaps be natural to expect the type of disagreement between the two sets of results, as seen in Fig. 8.

Next, the direct and cross-coupled stiffness, damping and inertia (added mass) coefficients of the fluid/shroud interaction were computed. The computational procedure here is essentially equivalent to that previously outlined by Baskharone and Hensel (1991a) for an annular seal problem. The calculated

**Table 1 Comparison of the impeller rotordynamic coefficients with experimental and numerical data**

| | Current Perturbation Model | Exp. data (Bolleter et al., 1989) | Bulk-flow model (Childs, 1989) Inlet-swirl ratio = 0.5 |
|---|---|---|---|
| $K$ (MN/m) | −0.268 | −0.500 | −0.042 |
| $k$ (MN/m) | 0.165 | 0.600 | 0.288 |
| $C$ (Ns/m) | 1640.8 | 2570 | 2020 |
| $c$ (Ns/m) | 2916.3 | 7610 | 2290 |
| $M$ (kg) | 5.034 | 29.6 | 8.96 |
| $m$ (kg) | 3.035 | 10.800 | −0.009 |

rotordynamic coefficients are shown in Table 1 versus the experimental results of Bolleter et al. (1989) and the numerical results of the bulk-flow model (Childs, 1989). Of these the results by Childs correspond to an externally-prescribed leakage-passage inlet swirl ratio of 0.5 which, by reference to Fig. 8, gives rise to smooth trends of the fluid reaction force components. Referring to Table 1, it seems that the bulk-flow model significantly underestimates the direct stiffness and cross-coupled inertia coefficients, particularly the former. Otherwise, the rotordynamic coefficients produced by the two perturbation analyses appear to be of comparable magnitudes.

In appraising the current numerical results in Table 1, the fact should be emphasized that a significantly better agreement with the experimental data was not initially anticipated. Despite our success in incorporating (to a reasonable extent) the primary/secondary flow interaction within the pump stage (Fig. 1), it is the intolerance of our perturbation model to the force contributions of the impeller primary flow which led to such modest expectations in the first place. These contributions were independently confirmed, by Ohashi and Shoji (1984) and Jery et al. (1984), to be comparable to those developed in the secondary flow passage. Consider, for example, the newly-computed and measured stiffness coefficients in Table 1. As reported by Adkins (1985), the impeller primary-flow contributions to these coefficients may be as high as one half of their measured magnitudes. Examination of Table 1 reveals that the ratios of computed-to-measured stiffness coefficients are very much consistent with Adkin's observation.

## Concluding Remarks

A perturbation model, originally devised for simple annular seals, has been upgraded and applied to the problem of fluid/shroud interaction in a typical pump stage. The computed rotordynamic coefficients are compared to existing experimental and numerical data. Comparison of the computed rotordynamic coefficients with experimental measurements revealed that the former coefficients are commonly less in magnitude than their experimental counterparts. This is consistent with documented observations that the impeller primary flow effects (suppressed in the current study) amount to substantial percentages of the rotordynamic coefficients. On the other hand, the current results seem closer to the experimental values for those coefficients where a substantial disagreement, with the existing numerical data, occurs. A primary source of discrepancies between the newly-computed sets of rotordynamic parameters and their numerical counterparts (Childs, 1989) was identified to be the seal-inlet swirl velocity magnitude. In the current analysis, this key variable is part of the zeroth-order (centered-impeller) flow solution and, as such, is a function of not only the pump operating conditions but also the manner in which the leakage passage is naturally connected to the seal segment of the secondary passage. The authors believe that the value of the current perturbation model would be enhanced by integrating the impeller primary flow passage into the computational domain. Such upgrade, which is major in nature, is currently in progress.

## Acknowledgment

This study was funded by NASA-Marshall Space Flight Center (Huntsville, Alabama), contract no. NAS8-37821, technical monitor: James Cannon. Partial funding was also provided by the Texas A&M Turbomachinery Research Consortium.

## References

Adkins, D. R., 1985, "Analyses of Hydrodynamic Forces on Centrifugal Pump Impellers," Report No. 200.23, California Institute of Technology.

Baldwin, B. S., and Lomax, H., 1978, "Thin Layer Approximation and Algebraic Model for Separated Turbulent Flows," AIAA Paper No. 78-257.

Baskharone, E. A., and Hensel, S. J., 1989, "A New Model for Leakage Prediction in Shrouded-Impeller Turbopumps," ASME JOURNAL OF FLUIDS ENGINEERING, Vol. 111, pp. 118–123.

Baskharone, E. A., and Hensel, S. J., 1991a, "A Finite-Element Perturbation Approach to Fluid/Rotor Interaction in Turbomachinery Elements. Part 1: Theory," ASME JOURNAL OF FLUIDS ENGINEERING, Vol. 113, No. 3, pp. 353–361.

Baskharone, E. A., and Hensel, S. J., 1991b, "A Finite-Element Perturbation Approach to Fluid/Rotor Interaction in Turbomachinery Elements. Part 2: Application," ASME JOURNAL OF FLUIDS ENGINEERING, Vol. 113, No. 3, pp. 362–367.

Bolleter, U., Leibundgut, E., and Sturchler, R., 1989, "Hydraulic Interaction and Excitation Forces of High Head Pump Impellers," presented at the Third Joint ASCE/ASME Mechanics Conference, University of California, La Jolla, CA.

Childs, D. W., 1983, "Finite Length Solutions for Rotordynamic Coefficients of Turbulent Annular Seals," ASME *Journal of Lubrication Technology*, Vol. 105, pp. 437–445.

Childs, D. W., and Moyer, D., 1985, "Vibration Characteristics of the High Pressure Oxygen Turbopump of the Space Shuttle Main Engine," ASME *Journal of Engineering for Gas Turbine and Power*, Vol. 107, pp. 152–159.

Childs, D. W., 1989, "Fluid-Structure Interaction Forces at Pump-Impeller Shroud Surfaces for Rotordynamic Calculations," ASME *Journal of Vibration, Stress and Reliability in Design*, Vol. 111, pp. 216–225.

Dietzen, F. J., and Nordmann, R., 1988, "Calculating Rotordynamic Coefficients of Seals by Finite Difference Techniques," ASME *Journal of Tribology*, Vol. 109, pp. 388–394.

Guelich, J., Florjancic, D., and Pace, S. E., 1987, "Influence of Flow Between Impeller and Casing on Part-Load Performance of Centrifugal Pumps," *Rotating Machinery Dynamics*, ASME Publication DE-Vol. 2, pp. 227-235.

Guinzburg, A., Brennen, C. E., Acosta, A. J., and Caughey, T. K., 1993, "The Effect of Inlet Swirl on the Rotordynamic Shroud Forces in a Centrifugal Pump," ASME *Journal of Engineering for Gas Turbines and Power*, Vol. 115, pp. 287–293.

Jery, B., Acosta, A. J., Brennen, C. E., and Caughey, T. K., 1984, "Hydrodynamic Impeller Stiffness, Damping and Inertia in the Rotordynamics of Centrifugal Pumps," NASA Conference Publication 2338, pp. 137–160.

Ohashi, H., and Shoji, H., 1984, "Lateral Fluid Forces Acting on a Whirling Centrifugal Impeller in Vaneless and Vaned Diffuser," NASA Conference Publication 2338, pp. 109–122.

Tam, L. T., Prezkwas, A. J., Muszynska, A., Hendricks, R. C., Braun, M. J., and Mullen, R. L., 1988, "Numerical and Analytical Study of Fluid Dynamic Forces in Seals and Bearings," ASME *Journal of Vibration, Acoustics, Stress, and Reliability in Design*, Vol. 110, pp. 315–325.

Zienkiewicz, O. C., 1971, *The Finite Element Method in Engineering Science*, McGraw-Hill, New York, NY.

# Perturbed Flow Structure in an Annular Seal Due to Synchronous Whirl[1]

**E. A. Baskharone**
Associate Professor,
Department of Mechanical Engineering,
Texas A&M University,
College Station, Texas 77843.
Mem. ASME

*This paper provides a thorough examination of the flow field resulting from synchronous whirl of an eccentric rotor in an annular seal under typical operating conditions. A new finite-element-based perturbation model is employed in the analysis, whereby perturbations in the flow thermophysical properties are attributed to virtual distortions in the rotor-to-housing finite element assembly. The numerical results are compared to a recent set of experimental data for a hydraulic seal with typical geometrical configurations and a synchronously whirling rotor. Despite the common perception that perturbation analyses are categorically confined to small rotor eccentricities, good agreement between the computed flow field and the experimental data is obtained for an eccentricity/clearance ratio of 50 percent. The agreement between the two sets of data is notably better at axial locations where the real-rig flow admission losses have diminished, and up to the seal discharge station. This attests to the accuracy of this untraditional and highly versatile perturbation model in predicting the rotordynamic characteristics of this and a wide variety of conceptually similar fluid/rotor interaction problems.*

## Introduction

An unstable operation mode of annular seals is known as cylindrical whirl (Fig. 1), in which the rotor axis precesses around the housing centerline at a finite frequency ($\Omega$). Of the possible vibration mechanisms in this case is synchronous whirl, where the whirl frequency is identical to the rotor speed, and is primarily caused by mass imbalance. In high speed pump applications, the hydrodynamic forces associated with the rotor whirl can be a major contributor to the system instability, and may indeed lead to destructive consequences.

Existing computational tools for predicting the fluid/rotor interaction forces vary in complexity from the simple and widely used bulk-flow model (Childs, 1983) to more detailed finite-difference analyses (e.g., Dietzen et al., 1987 and Tam et al., 1988). These have progressively embraced more of the flow details in the rotor-to-housing passage but, nevertheless, shared a rather disputed simplification that perturbations in the flow thermophysical properties assume a single-harmonic type of circumferential variation. While such a simplification is, for all practical purposes, applicable to the simple annular seal problem (Baskharone and Hensel, 1991b), it is unlikely that the same would hold true for secondary turbomachinery passages which, due to their complex geometry, give rise to flow separation and recirculation even under the unperturbed (centered-rotor) operation mode.

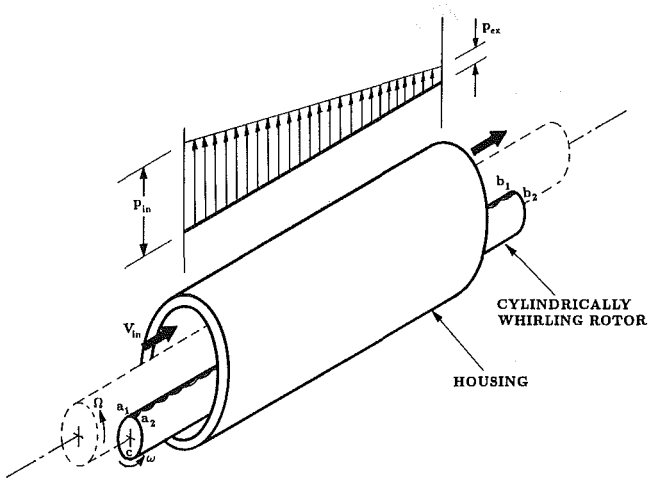


Fig. 1 Cylindrical whirl in annular seals

The current study is an extension to a recent investigation (Baskharone and Hensel, 1991a), in which an unconventional perturbation approach to the general fluid-induced vibration problem was devised. The perturbation equations, under the new strategy, were deduced from the flow-governing equations in their discrete finite-element form, rather than the differential form as is traditionally the case. As a result, limitations on the circumferential perturbation pattern and/or the rotor-ex-

[1]This research was sponsored by the Texas A&M Turbomachinery Research Consortium. Partial Funding was also provided by NASA-Marshall Space Flight Center (Huntsville, Alabama), Contract No. NAS8-37821, Technical Monitor: James Cannon.

Contributed by the Fluids Engineering Division for publication in the JOURNAL OF FLUIDS ENGINEERING. Manuscript received by the Fluids Engineering Division March 10, 1993; revised manuscript received August 17, 1993. Associate Technical Editor: L. Nelik.

citation degrees of freedom, were totally alleviated. The new perturbation model was utilized in computing the rotordynamic coefficients associated with cylindrical and conical rotor whirl (Baskharone and Hensel, 1991b, 1991c), as well as a compound rotor excitation that is composed of the two whirling modes (Baskharone and Hensel, 1991d).

Validation of the new perturbation model has so far been focused on verifying the results in a "macroscopic" sense, with the net integrated rotor forces, and the corresponding rotordynamic coefficients being the only variables under examination. In this paper, however, fine details of the perturbed rotor-to-housing flow field are rigorously verified. The intention here is to provide a better understanding of the source of rotordynamic forces which, in turn, should serve the design process itself. The current study was first and foremost motivated by the recent availability of detailed LDA flow measurements in a typical annular seal with a synchronously whirling rotor (Morrison et al., 1992). The outcome of this experimental study is utilized here for the purpose of comparison.

The seal geometry and operating conditions in the current study are identical to those of Morrison et al. (1992). With a seal length of 37.3 mm, a rotor diameter of 164.1 mm, and a nominal clearance of 1.27 mm, this seal was tested at a rotor speed of 3600 rpm using water as the working medium. These variables gave rise to a Reynolds number (Re) of 24,000 and a Taylor number (Ta) of 6600. At all times, the rotor whirl frequency was identical to the spinning speed, and the eccentricity ratio ($\epsilon/c$) was fixed at 50 percent in the test rig.

## Computational Development

**Centered-Rotor Flow Field.** The perturbation procedure is initiated by computing this "zeroth-order" flow field, which is clearly axisymmetric. Details of the flow-governing equations, turbulence closure, and finite-element formulation of this relatively simple problem were all discussed by Baskharone and Hensel (1991b), where two sample cases (including the seal under consideration here) were presented. Comparison of the through-flow and swirl velocity profiles in the rotor-to-housing passage with the experimental data previously reported by Morrison et al. (1991), was also presented, and the agreement between the two sets of data was encouraging.

**Perturbation Analysis.** The centered-rotor flow solution, referenced above, was used in the current study as input to the perturbation analysis phase of the computational procedure. Devised by Baskharone and Hensel (1991a), the perturbation model here is based on what was generically termed the "virtually" deformable finite element concept, where the perturbed flow equations emerge from expansion of the finite-element equations in terms of the rotor eccentricity $\epsilon$. Since no circumferential pattern is pre-imposed on the perturbations of the flow properties, the problem at this point shifts to the fully three-dimensional type, as the rotor eccentricity destroys the flow axisymmetry (Fig. 2). Simultaneously, the flow problem is cast in a rotating-translating frame of reference, which is attached to the whirling rotor at all times (Fig. 2) in order to eliminate the time dependency of the flow field in this case.

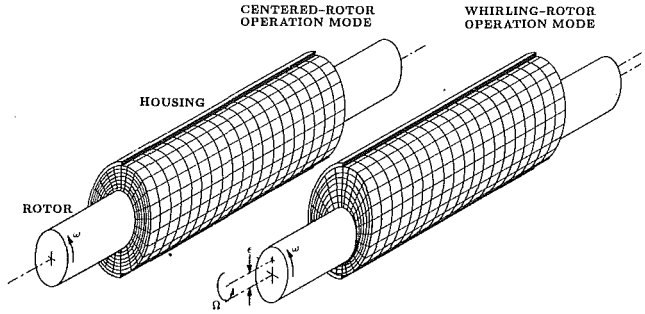


Fig. 2 Distortion of the rotor-to-housing finite element assembly as a result of the rotor eccentricity

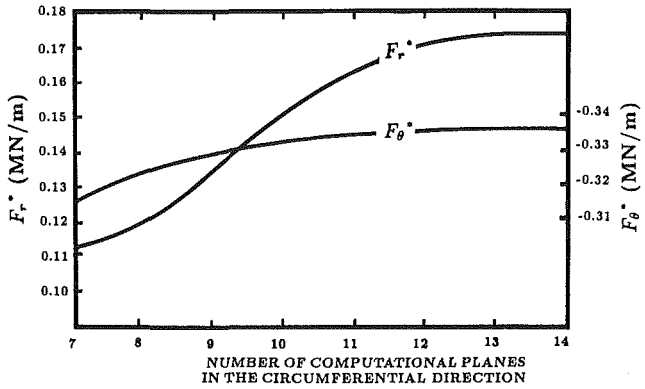


Fig. 3 Relationship between the fluid-exerted forces and the grid resolution in the tangential direction

**Grid Dependency.** As would naturally be anticipated, the perturbated flow resolution is dependent on the grid resolution which, as the domain three-dimensionality prevails, translates into the number of computational stations in the circumferential direction (Fig. 2). Investigation of this dependency was carried out by varying this number and computing the fluid-exerted forces on the rotor each time. Results of this preliminary step are shown in Fig. 3, where the fluid force components $F_r^*$ and $F_\theta^*$ are obtained by integrating the rotor-surface pressure forces, upon resolution in the radial and tangential directions, over all of the contributing finite element boundaries.

The force trends in Fig. 3 suggest that the radial force is more sensitive to the tangential grid resolution by comparison. The figure also shows that changes in the force magnitudes becomes acceptably small for a tangential computational-station count that is in excess of 11. In the current study, this parameter was selected to be 13, as a compromise between a desirably high resolution of the flow properties in the circumferential direction, on one hand, and the CPU time consumption, on the other.

## Nomenclature

$c$ = nominal seal clearance
$d$ = rotor diameter
$e$ = eccentricity ratio ($\epsilon/c$)
$F_r^*$ = radial component of the rotor force perturbation
$F_\theta^*$ = tangential component of the rotor force perturbation
$L$ = seal length
$p$ = static pressure
$p_{in}$ = seal inlet pressure
Re = Reynolds number = $2cV_{in}/\nu$
$r_i$ = rotor radius
Ta = Taylor number = $cU_i/\nu\sqrt{2c/d}$
$U_i$ = rotor surface velocity = $\omega r_i$
$V_{in}$ = seal inlet through-flow velocity
$V_r$ = radial velocity component
$V_z$ = axial velocity component
$V_\theta$ = tangential velocity component
$z$ = distance along the seal axis
$\epsilon$ = rotor eccentricity
$\nu$ = kinematic viscosity coefficient
$\rho$ = fluid density
$\Omega$ = whirl frequency
$\omega$ = rotor spinning speed
$(\ )^*$ implies the operator $\partial(\ )/\partial\epsilon$

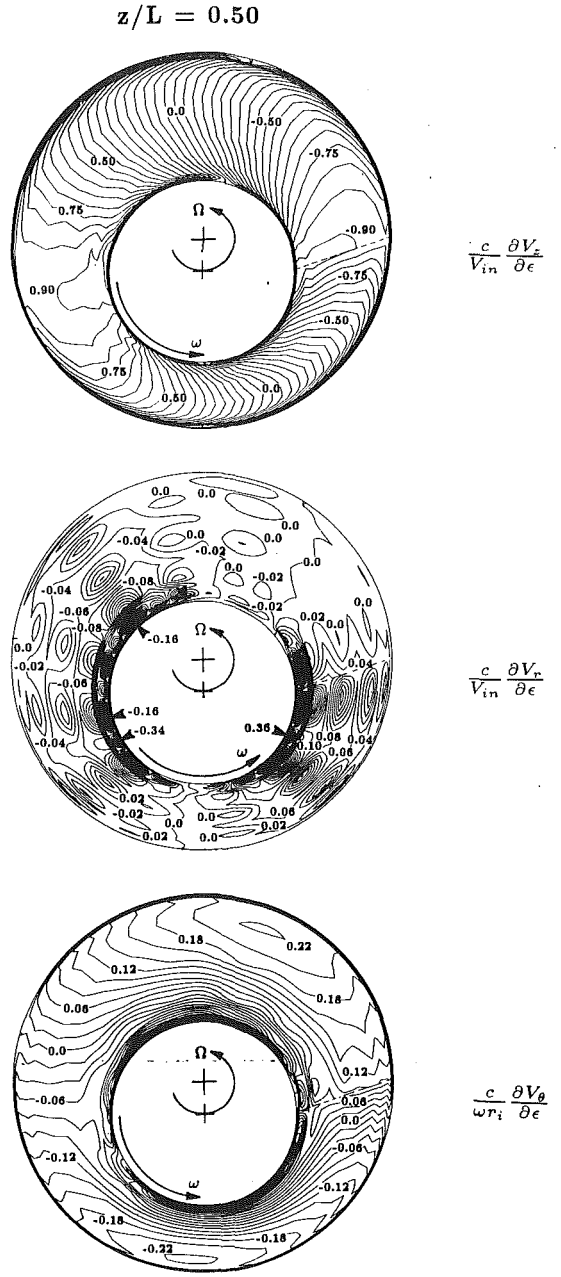


**Fig. 4 Contour plots of the velocity perturbations at 50 percent of the seal length**

## Results and Discussion

Examples of the "raw" results of the current study are shown in Fig. 4 for the seal middle cross section, as a representative axial location. These are contours of the nondimensionalized perturbations in the velocity components; namely $cV_z^*/V_{in}$, $cV_r^*/V_{in}$ and $cV_\theta^*/\omega r_i$, where:

$V_{in}$ is the seal-inlet average through-flow velocity
$\omega$ is the rotor spinning speed
$r_i$ is the rotor radius
$c$ is the seal nominal clearance

with the asterisk implying the operator $\partial/\partial\epsilon$. In this, as well as all remaining figures, the whirl frequency $\Omega$ is identical to the rotor speed $\omega$, giving rise to the case of a synchronous whirl investigated by Morrison et al. (1992). There is, however, no valid comparison between the results in Fig. 4 and Morrison's flow measurements, since the latter is a combination of the velocity perturbations and the unperturbed (centered-rotor) velocity field.

Examination of Fig. 4 reveals that the maximum perturbation of the axial velocity component occurs in the vicinity of the rotor "pressure" side (where the clearance is smaller than the nominal value), and at a tangential location that lags the minimum-clearance position, by reference to the whirl direction. The radial velocity perturbations in this figure are clearly smaller than those of the axial velocity, and attains its maximum value near the rotor pressure side as well. The difference, however, is that the radial component peaks ahead of the minimum-clearance position in the whirl direction. As for the tangential velocity perturbation in Fig. 3, the peak value appears closer to the housing, and on the "suction" side relative to the rotor.

Figure 5 shows contours of the nondimensionalized pressure perturbations ($p^*c/\rho V_{in}^2$), as well as those of the combined (centered-rotor and eccentricity-related) pressure values in the annulus at the middle of the seal length. The combined pressure values in this figure correspond to an eccentricity ratio ($\epsilon/c$) of 50 percent, and are nondimensionalized using the seal-inlet static pressure ($p_{in}$). As expected, the peak values, in each plot, occurs on the rotor pressure side, but not at the minimum clearance position as may be intuitively anticipated. Comparison of this observation, as well as those cited above in connection with the velocity perturbations, with the flow measurements by Morrison et al. (1992) was not possible, as the latter involved only the "net" velocity field in the whirling-rotor operation mode, with no pressure measurements whatsoever.

One-to-one comparisons with Morrison's experimental data are presented in Figs. 6 through 10. In these figures, the velocity component perturbations, corresponding to a rotor eccentricity ratio of 50 percent, are superimposed on the centered-rotor magnitudes. In assessing the numerical results in these figures, it was both important as well as interesting to verify a fact that was solidly stated by Morrison et al., that the maximum through-flow velocity magnitude occurs on the pressure side of the rotor, over the early seal sections, but then moves towards the suction side as the flow progresses to the seal downstream sections. Comparison of the computed velocity contours in Figs. 6 through 10 reveals that the numerical results are indeed in agreement with Morrison's observation.

It is important, in comparing the numerical and experimental sets of data, to point out that early sections of the seal (perhaps up to the mid-seal location) are those where no significant agreement would be anticipated. This is largely due to the flow admission losses which would prevail in the actual test rig, whereas the computational model treats this early seal segment as systematically, in the sense of turbulence closure and near-wall analysis, as does the entire seal. This is primarily why the velocity contours become more and more in agreement with the experimental data as the seal exit station is approached (e.g., Figs. 9 and 10). This, in particular, includes the tangential shift of the maximum axial-velocity position from a tangential location in the pressure (small clearance) region, gradually toward the suction side (Figs. 8 through 10) in a manner that is consistent with the flow measurements in these figures. In fact, one would even go further, in reviewing the flow measurements in Figs. 6 through 10, indicating that the measurements themselves do not exhibit a characteristically similar axial-velocity pattern until the 77 percent seal-length section is reached.

An interesting phenomenon, which is confirmed both by the numerical results and the flow measurements, is that of flow separation and recirculation near the seal exit station. This, by reference to Figs. 9 and 10, takes place on the rotor suction side, and is more pronounced at the tangential location marked "s" in these two figures. It is also in Figs. 9 and 10 that the numerical results yield shapes and magnitudes of the velocity

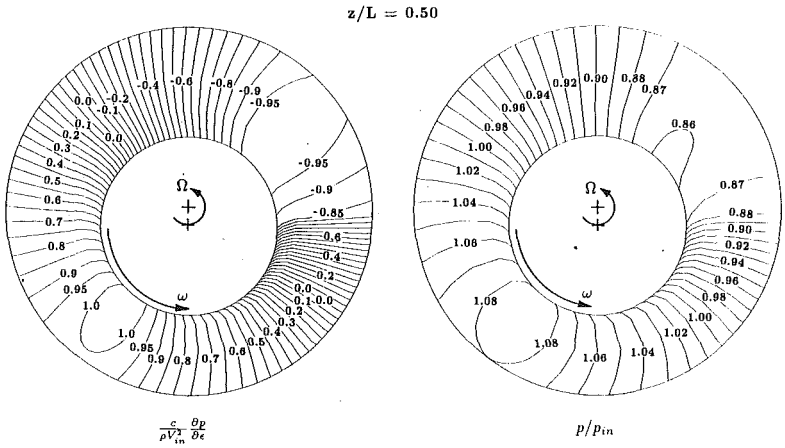


**Fig. 5 Contour plots of the pressure perturbation and the resultant pressure (for a 50 percent eccentricity ratio) at 50 percent of the seal length**

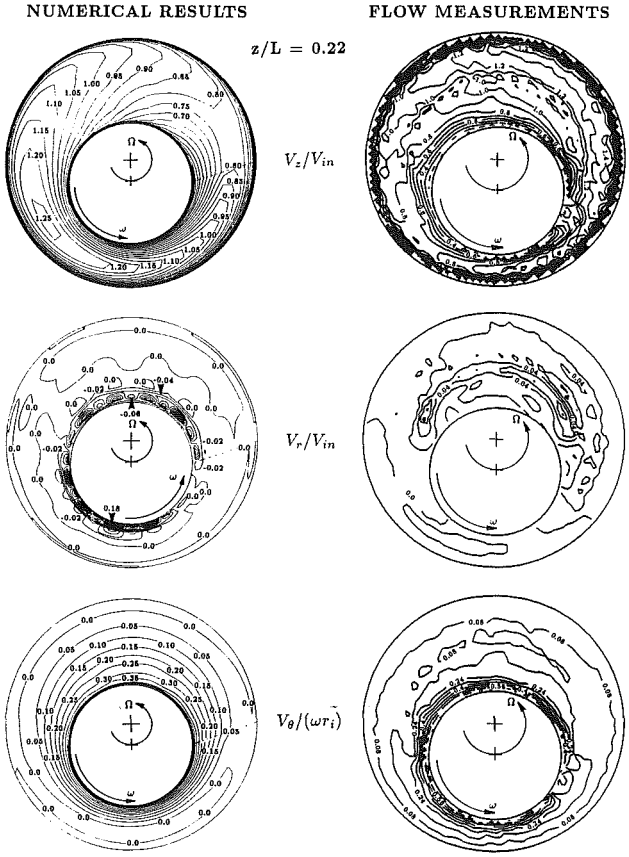


**Fig. 6 Comparison of the velocity distribution at 22 percent of the seal length (eccentricity ratio = 50 percent)**

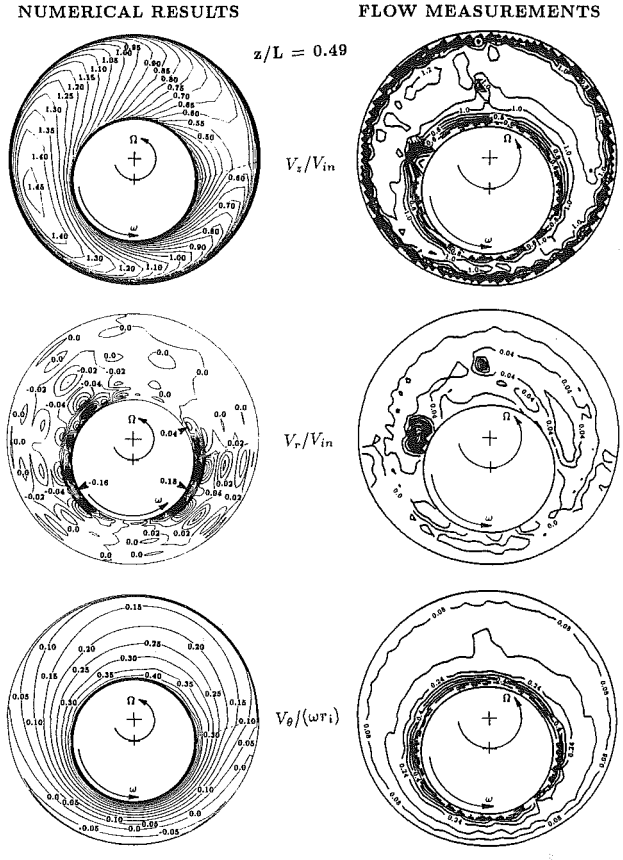


**Fig. 7 Comparison of the velocity distribution at 49 percent of the seal length (eccentricity ratio = 50 percent)**

contours which are very much consistent with the flow measurements.

Another flow structure, which is equally interesting, involves the tangential velocity distribution and pertains, in particular, to the seal sections at 49 and 77 percent of the seal length (Figs. 7 and 8). It is seen that there exists a region of reversed tangential velocity in each of these two sections near the housing at the minimum-clearance location. This implies local in-plane flow separation and recirculation in this region. Such flow behavior was apparently suspected (but not confirmed) by Morrison et al. (1992), who stated that: "if a tangential recirculation zone exists, it must be between the stator (referred to as the housing in this paper) and the first radial grid line."

Figure 11 shows a contour plot of the nondimensionalized pressure perturbation; namely ($p^*c/\rho V_{in}^2$), and the resultant (centered-rotor and whirl-related) magnitudes of the nondimensionalized pressure ($p/p_{in}$) over the rotor surface. The pressure contours in this figure are shown on the "unwrapped" rotor surface which is obtained by "splitting" the surface along the lines labeled [$a_1 - b_1$] and [$a_2 - b_2$] in Fig. 1. Due to the lack of pressure measurements in Morrison's study, no experimental verification of the results in Fig. 11 was possible.

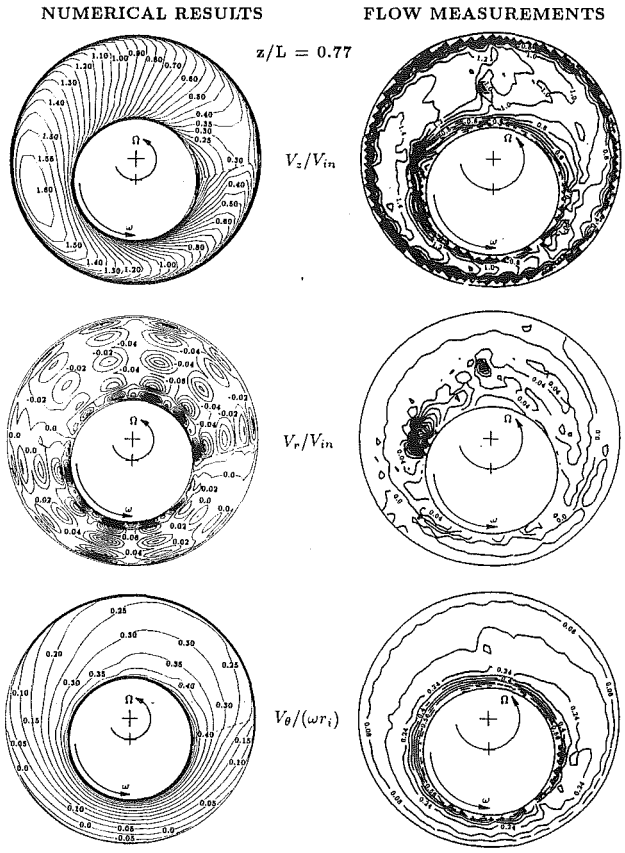


Fig. 8 Comparison of the velocity distribution at 77 percent of the seal length (eccentricity ratio = 50 percent)

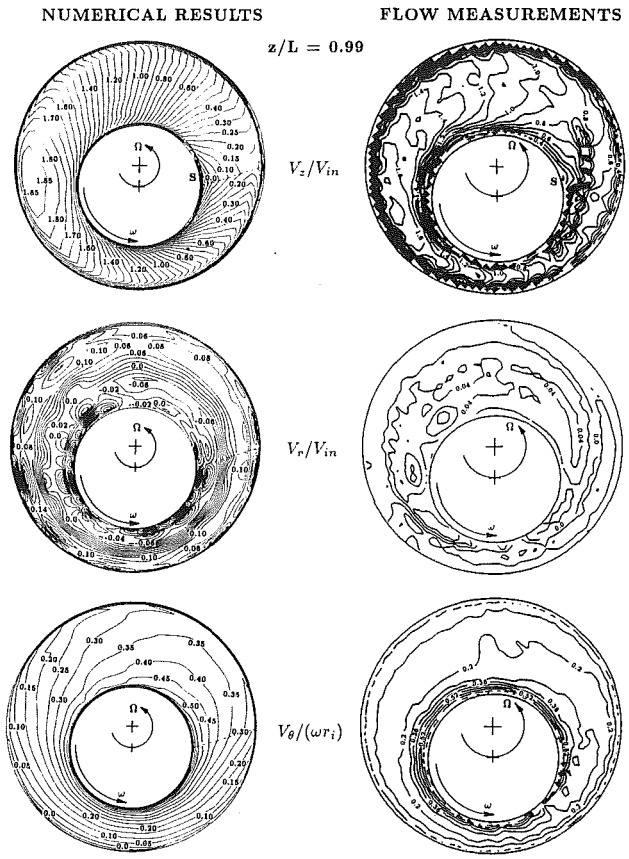


Fig. 10 Comparison of the velocity distribution at 99 percent of the seal length (eccentricity ratio = 50 percent)

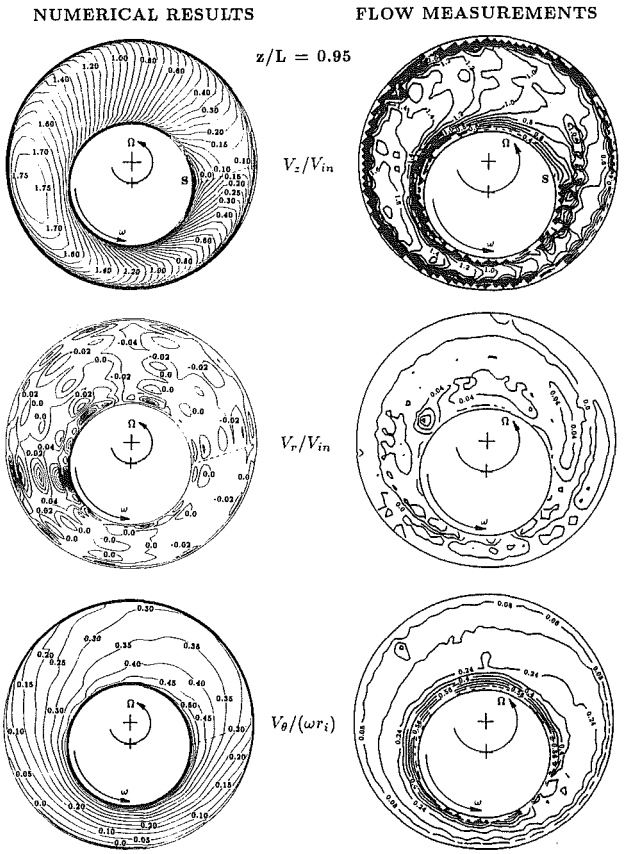


Fig. 9 Comparison of the velocity distribution at 95 percent of the seal length (eccentricity ratio = 50 percent)

Examination of the pressure contours in this figure reveals that the peak value occurs at a tangential location which lags the minimum clearance position, by reference to the whirl direction. It is conceivable, and indeed likely, that the maximum pressure location is a function of the whirl direction (forward or backward) and/or the whirl frequency ratio ($\Omega/\omega$). For the synchronous whirl case under consideration, Fig. 11 shows that the rotor surface pressure peaks to a value of approximately 1.12 of the inlet pressure near the inlet station, and that with the streamwise loss in total pressure (due to friction) this magnitude gradually declines to approximately 0.93 of the inlet pressure at the exit station. Figure 11 also shows that the maximum and minimum rotor-surface pressure locations hardly change their tangential location over the overwhelming majority of the seal length.

## Concluding Remarks

Since the development of the so-called "virtually" deformable finite-element concept (Baskharone and Hensel, 1991a), the validation of this new approach never went beyond the traditional "macroscopic" means of assessing the ultimate objective of the entire computational procedure; namely the final set of rotordynamic coefficients (Baskharone and Hensel, 1991b, c, d). Such a verification method is perhaps the least accurate, for it was always the global value of integrated rotor-surface pressure that was examined in reality. Recalling that the seal-clearance pressure field itself is among the least sensitive thermophysical properties, it is clear that the current comparative study is the most significant in appraising the mathematically rigorous computational model which centers around this categorically new finite-element-based concept.

The numerical results corresponding to a synchronously whirling rotor of an annular seal are consistent with the flow

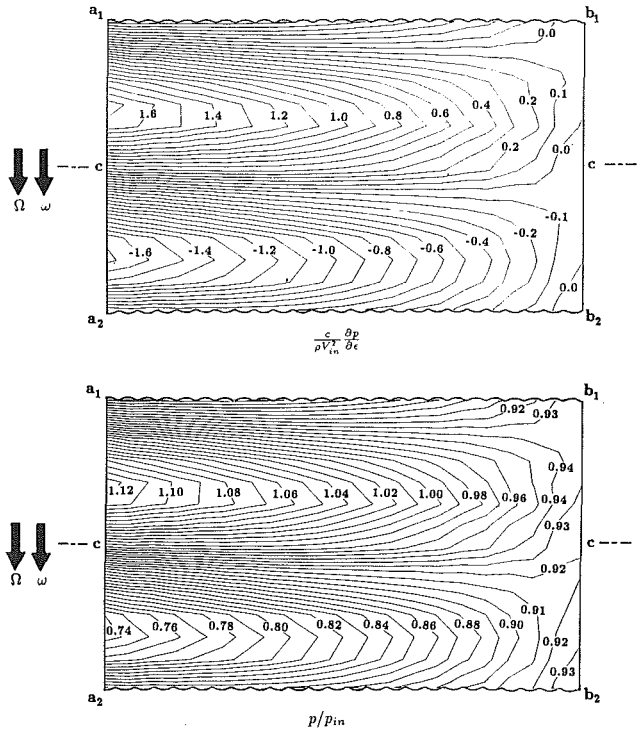


**Fig. 11 Contours of the pressure perturbation and the resultant pressure (for a 50 percent eccentricity ratio) over the rotor surface**

measurements of Morrison et al. (1992). Agreement of the two sets of results is particularly favorable over the downstream half of the seal, which is where the real-rig flow admission losses have dissipated, and characteristically similar trends of the measurements themselves take place. Contrary to the common perception that perturbation analyses are only applicable to infinitesimally small rotor eccentricities, the favorable results of this study corresponds to an eccentricity that is as high as 50 percent of the seal nominal clearance. Successful validation of the computational model, under such conditions, underscores the model accuracy and establishes it as perhaps the most versatile perturbation approach, of its nature, in the general area of rotordynamics today.

## Acknowledgment

This study was sponsored by the Texas A&M Turbomachinery Research Consortium. Partial funding was also provided by NASA-Marshall Space Flight Center (Huntsville, AL), Contract No. NAS8-37821, Technical Monitor: James Cannon.

## References

Baskharone, E. A., and Hensel, S. J., 1989, "A New Model for Leakage Prediction in Shrouded-Impeller Turbopumps," ASME JOURNAL OF FLUIDS ENGINEERING, Vol. 111, pp. 118–123.

Baskharone, E. A., and Hensel, S. J., 1991, "A Finite-Element Perturbation Approach to Fluid/Rotor Interaction in Turbomachinery Elements. Part 1: Theory," ASME JOURNAL OF FLUIDS ENGINEERING, Vol. 113, No. 3, pp. 353–361.

Baskharone, E. A, and Hensel, S. J., 1991, "A Finite-Element Perturbation Approach to Fluid/Rotor Interaction in Turbomachinery Elements. Part 2: Application," ASME JOURNAL OF FLUIDS ENGINEERING, Vol. 113, No. 3, pp. 362–367.

Baskharone, E. A., and Hensel, S. J., 1991, "Moment Coefficients of Incompressible-Flow Seals with Conically Whirling Rotors," *International Journal of Mechanical Sciences*, Vol. 33, No. 2, pp. 151–167.

Baskharone, E. A., and Hensel, S. J., 1991, "Interrelated Rotordynamic Effects of Cylindrical and Conical Whirl of Annular Seal Rotors," ASME *Journal of Tribology*, Vol. 113, No. 3, pp. 470–480.

Childs, D. W., 1983, "Finite Length Solutions for Rotordynamic Coefficients of Turbulent Annular Seals," ASME *Journal of Lubrication Technology*, Vol. 105, pp. 437–445.

Dietzen, F. J., and Nordmann, R., 1987, "Calculating Rotordynamic Coefficients of Seals by Finite Difference Techniques," ASME *Journal of Tribology*, Vol. 109, pp. 388–394.

Morrison, G. L., Johnson, M. C., and Tatterson, G. B., 1991, "Three-Dimensional Laser Anemometer Measurements in an Annular Seal," ASME *Journal of Tribology*, Vol. 113, pp. 421–427.

Morrison, G. L., DeOtte, R. E., and Thames, H. D., 1992, "Turbulence Measurements of High Shear Flow Fields in a Turbomachine Seal Configuration," presented at the Advanced Earth-To-Orbit Propulsion Technology Conference, Huntsville, AL.

Tam, L. T., Prezkwas, A. J., Muszynska, A., Hendricks, R. C., Braun, M. J., and Mullen, R. L., 1988, "Numerical and Analytical Study of Fluid Dynamic Forces in Seals and Bearings," ASME *Journal of Vibration, Acoustics, Stress, and Reliability in Design*, Vol. 110, pp. 315–325.

# A Preliminary Parametric Study of Electrorheological Dampers

Z. Lou[1]

R. D. Ervin

Transportation Research Institute,
The University of Michigan,
Ann Arbor, MI 48109

F. E. Filisko

Material Science and Engineering
Department,
The University of Michigan,
Ann Arbor, MI 48109

*In approaching the design of an electrorheology-based, semi-active suspension, the electrorheological component (ER damper) can be built as either a flow-mode, shear-mode, or mixed-mode type of damper. The source of damping force in the flow-mode is exclusively from flow-induced pressure drop across a valve, while that in the shear-mode is purely from the shear stress on a sliding surface. The dynamics of the fluid flow are included in the derivation of the zero-field damping forces. The control effectiveness is found to be strongly related to the dynamic constant (which is proportional to the square root of the vibration frequency) and, for shear- and flow-mode dampers, the ratio of the piston area to the cross-section of the ER control gap. To achieve the same performance, a flow-mode ER damper is not as compact and efficient as a shear-mode ER damper. With the same ER damping force, a mixed-mode damper is more compact than a shear-mode damper. However, the mixed-mode damper does not have as a low zero-field damping force as the shear-mode damper. The analysis is based on the assumption that the ER fluid is Bingham plastic.*

## Introduction

An electrorheological (ER) damper is a device that is able to generate a controllable damping force by employing an ER fluid. An ER fluid can change its rheological properties, most notably its effective viscosity. The wide range and the high bandwidth of the effective viscosity variation of ER fluids are two of the primary factors that have caused intense research and development activities in ER dampers. The ER damper studies so far have generally ignored the influence of the fluid dynamics, i.e., the unsteady nature of the fluid velocity, shear rates, and thus the damping force, which are all induced by the inertia of the fluid. Lou et al. (1992) have shown that the fluid inertia can limit the bandwidth of an ER valve to a level far below the bandwidth of the rheological variation of an ER fluid. Similar influence exists in ER dampers, many of which contain ER valves.

ER dampers can be classified as: flow-mode, mixed-mode, and shear-mode (Fig. 1). The configurations illustrated in Fig. 1 are generic concepts that contain simplified features to facilitate the design analysis. In practical hardware, for example, the cylinder is likely to be single-ended, rather than double-ended, and the ER control valve or area is likely to be comprised of multiple parallel or concentric plates. Among the three conceptual modes, the flow-mode damper is most similar to the traditional shock absorber except that is replaces the conventional orifice with an ER control gap or valve. The source of the damping force in this mode is exclusively from flow-induced pressure drop across the piston. The ER valve can be placed outside the cylinder (as in Fig. 1(*a*)) or within the piston component.

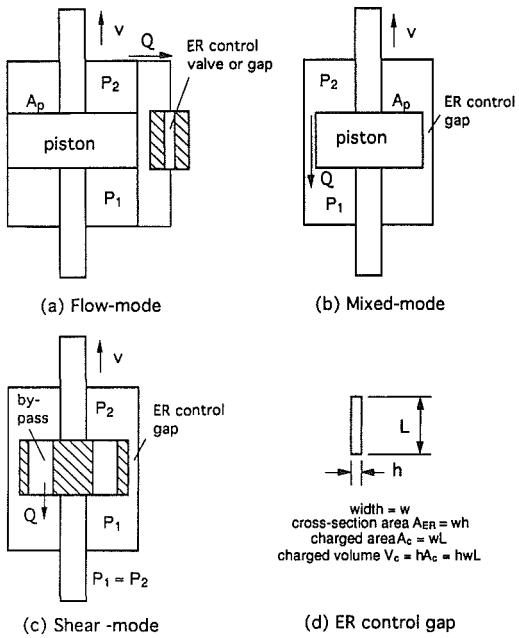


**Fig. 1 The generic concepts of the three modes of electrorheological dampers**

In the mixed-mode damper, the ER control is realized in the gap between the piston side-wall and the cylinder liner. The fluid shear stress at the shear surface also contributes to the damping force, while the flow-induced pressure drop is still present as a force component on the piston.

[1] Present address: Ford Motor Co., Electrical and Fuel Handling Div., McKean and Textile Roads, P.O. Box 922, Ypsilanti, MI 48197.

Contributed by the Fluids Engineering Division and presented at the Fluids Engineering Conference, ASME, June 20-23, 1993, Washington, D.C., of THE AMERICAN SOCIETY OF MECHANICAL ENGINEERS, FED-Vol. 164: Electrorheology Flows—1993, pp. 143-156. Manuscript received by the Fluids Engineering Division May 3, 1993; revised manuscript received November 1, 1993. Associate Technical Editor: R. Panton.

If a large bypass port is cut through the piston of a mixed-mode damper, the device becomes a simple shear-mode element. Since the fluid can flow freely through the by-pass, the pressure drop across the piston becomes negligible and only shear stresses developed along the wall contribute to the damping force.

The purpose of this study is to systematically analyze the dynamic performance of all three modes of ER dampers. Special attention is paid to (*a*) the relative magnitudes of the zero-field and ER components of the damping force under dynamic situation and (*b*) and their implication in the sizing and selection of the damping mode. For simplicity, ER fluids are assumed to be Bingham plastic. If ER fluids show a certain degree of elasticity, the assumption here will not result in significant errors for practical dampers that far out-stroke the elastic strain range and/or the low shear rate range. When the electric field strength is zero, an ER fluid is assumed to be Newtonian, with the zero-field viscosity being equal to the plastic viscosity of the Bingham model. Non-Newtonian behavior at zero-field has been reported though (Lou et al., 1990). The Bingham plastic assumption implies that the shear stress response to electric field changes is instantaneous and that the stress-shear rate relationship has no time dependency.

## Analysis

**Flow-Mode Dampers.** If the piston vibration (Fig. 1(*a*)) can be described as

$$v = v_p \sin \omega t = \omega x_p \sin \omega t \tag{1}$$

where $v$ is the piston velocity, $v_p$ the amplitude of $v$, $\omega$ the angular velocity, $t$ the time, and $x_p$ the amplitude of the piston displacement. From continuity, the amplitude of the (space-wise) mean velocity of the ER fluid in the ER valve is $(A_p/A_{ER})x_p\omega$, where $A_p$ is the piston cross-section area, and $A_{ER}$ is the ER valve cross-sectional area. The zero-field pressure drop for an equivalent steady flow of the same flow amplitude is

$$\Delta p_s = 12\eta \frac{LA_p}{h^2 A_{ER}} x_p \omega \tag{2}$$

where $L$ and $h$ are the length and gap size of the ER valve, respectively. The parameter $\eta$ is the zero-field or plastic viscosity. This pressure drop, frequently used in the literature of ER devices, does not account for the dynamic effect of a sinusoidal flow, which is fully presented in this study. The solution of an oscillatory flow of a viscoelastic medium between parallel planes induced by a sinusoidal pressure drop has been derived by Thurston (1959). The solution of an oscillatory flow induced by a sinusoidal flow rate or piston motion presented here is different only in phasic expression.

The dynamic pressure drop has a component induced by fluid inertia:

$$\Delta p_m = g_m \Delta p_s \sin\left(\omega t + \frac{\pi}{2}\right) \tag{3}$$

with

$$g_m = \frac{2}{3} h^{*2} \tag{4}$$

$$h^* = \frac{h}{2}\sqrt{\frac{\rho\omega}{2\eta}} \tag{5}$$

where $\rho$ is the density of the ER fluid. The dimensionless parameter $h^*$ is, if ignoring the constant $2\sqrt{2}$, the ratio of $h$ to $\sqrt{\eta/\rho\omega}$. The latter has the dimensions of length. It is related to the location of an overshoot in the mean velocity of an oscillatory flow in a flow-mode damper or to the penetration depth of an oscillatory shear flow in a shear-mode damper. One can thus consider $h^*$ as a dimensionless gap size. The parameter $h^*$ and its variations, including those in cylindrical flows, are called in the literature the kinetic Reynolds number, the Womersley number, dynamic constant, or dimensionless frequency. They are also related to the ratio of the flow time constant to the forcing function period (Lou and Yang, 1993). In this study, $h^*$ is named the dynamic constant instead of the dimensionless gap size because (*a*) the parameter appears only in a dynamic situation, (*b*) the practical gap size is generally in a narrow range around 1 mm, and (*c*) the frequency changes greatly in most ER fluid applications.

The functions $g_m$, called the dynamic factor of $\Delta p_m$, is 0 at $h^* = 0$ and rises proportionally with $h^{*2}$ (or with $\omega$ if other parameters in $h^*$ is fixed). Physically, the ratio of the amplitude of the inertia component of the dynamic pressure to the equivalent steady pressure drop is proportional to the frequency.

The dynamic pressure drop has another component that is induced by the wall shear stress:

## Nomenclature

$A_c$ = charged area
$A_{cf}$, $A_{cm}$, and $A_{cs}$ = flow-, mixed-, and shear-mode charged areas
$A_{ER}$ = ER valve cross-sectional area
$A_p$ = piston cross-sectional area
$A_1$, $A_2$, $A_3$, $A_4$, $A_{1um}$, $A_{2um}$, $A_{1om}$, and $A_{2om}$ = intermediate variables
$C$ = electric capacitance
$C_d$ = electric current density
$C_h$ = intermediate variable
$D_h$ = intermediate variable
$E_p$ = peak electric field strength
$F_{om}$ = mixed-mode total zero-field damping force
$F_{ERf}$ = flow-mode ER damping force
$F_{ERm}$ = mixed-mode ER damping force
$F_{ERs}$ = shear-mode ER damping force
$F_u$ = shear-mode zero-field (upper-plate) damping force
$f_{of}$ = flow-mode zero-field factor
$f_{om}$ = mixed-mode zero-field factor
$f_{os}$ = shear-mode zero-field factor
$g_l$ = dynamic factor of the shear-mode lower-plate stress
$g_m$ = dynamic factor of $\Delta p_m$
$g_o$ = dynamic factor of a flow-mode damper
$g_{om}$ = dynamic factor of a mixed-mode damper
$g_u$ = dynamic factor of (the upper-plate stress of) a shear-mode damper
$g_{um}$ = dynamic factor of the mixed-mode upper-plate stress
$g_w$ = dynamic factor of $\Delta p_w$
$h$ = gap size of an ER valve/gap
$h^*$ = dynamic constant
$L$ = ER valve/gap length
$P_{cp}$ = peak capacitive electric power
$P_{rp}$ = peak resistive electric power
$t$ = time

$$\Delta p_w = g_w \Delta p_s \sin(\omega t + \phi_w) \tag{6}$$

with

$$g_w = \frac{2}{3} h^* \frac{[(2C_h - C_h^2 - D_h^2)^2 + 4D_h^2]^{1/2}}{(2 - C_h)^2 + D_h^2} \tag{7}$$

$$\phi_w = \frac{\pi}{2} + tan^{-1}[2D_h/(2C_h - C_h^2 - D_h^2)] \tag{8}$$

$$C_h = \frac{\sin h^* \cos h^* + \sinh h^* \cosh h^*}{h^* [(\cosh h^* \cos h^*)^2 + (\sinh h^* \sin h^*)^2]} \tag{9}$$

$$D_h = \frac{\sin h^* \cos h^* - \sinh h^* \cosh h^*}{h^* [(\cosh h^* \cos h^*)^2 + (\sinh h^* \sin h^*)^2]} \tag{10}$$

The function $g_w$, called the dynamic factor of $\Delta p_w$, starts from 1.0 at $h^* = 0$, increases with $h^*$ slightly until about $h^* = 1$, and, then, rises almost proportionally with $h^*$ (or with $\sqrt{\omega}$ if other parameters in $h^*$ is fixed). Physically, the amplitude of the dynamic wall shear stress is approximately equal to that of the equivalent steady shear stress at low frequencies and grows larger at high frequencies. A solution of the wall shear rate at a low dynamic constant was presented by Thurston and Gaertner (1991).

The zero-field dynamic pressure drop $\Delta p_o$, the summation of its two components $\Delta p_w$ and $\Delta p_m$, is:

$$\Delta p_o = g_o \Delta p_s \sin(\omega t + \phi_o) \tag{11}$$

with

$$g_o = \frac{4h^{*2}}{3[(2 - C_h)^2 + D_h^2]^{1/2}} \tag{12}$$

$$\phi_o = \frac{\pi}{2} + \tan^{-1}[D_h/(2 - C_h)] \tag{13}$$

where $g_o$ and $\phi_o$ are the dynamic factor and the phase advance of the flow-mode damper, respectively. The primary value of $g_o$ is from $g_w$ at low frequencies and from $g_m$ at high frequencies. The factor $g_o$ remains close to one at low frequencies and rises proportionally with $h^{*2}$ (Fig. 2). Physically, $\Delta p_o$ is mainly to overcome the wall stress and the fluid inertia at low and high frequencies, respectively. The phase advance $\phi_o$ is 0 at $h^* = 0$ (steady state), 45 deg at about $h^* = 1$, and 90 deg as $h^*$ approaches infinite.

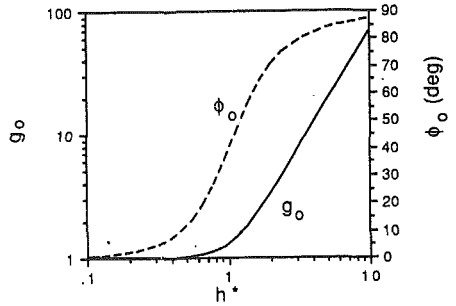


**Fig. 2 The dynamic factor $g_o$ and the phase advance $\phi_o$ of the zero-field pressure drop versus the dynamic constant $h^*$**

The above analysis has been for the zero-field situation. With the application of an electric field, a yield stress is induced. For a steady Couette flow within a narrow gap, the yield stress and the zero-field shear stress can be superposed. The linear summation is no longer valid under dynamic conditions and a numerical solution can be obtained by solving the fluid dynamic equation (Lou et al., 1993a). Analytical solutions for a dynamic Bingham fluid flow are not readily available, while numerical solutions are generally time-consuming. For a preliminary parametric study, a simplified, linear analytical approach is adopted here.

The ER pressure drop $\Delta p_{ER}$ is estimated to be

$$\Delta p_{ER} = 2\frac{L}{h}\tau_y \tag{14}$$

where $\tau_y$ is the yield stress. The time-dependency of electrorheology is not considered here, and $\Delta p_{ER}$ or $\tau_y$ involves only the amplitude of electrorheology. The ratio of $\Delta p_o$ to $\Delta p_{ER}$ is derived as

$$\frac{\Delta p_o}{\Delta p_{ER}} = f_{of} \sin(\omega t + \phi_o) \tag{15}$$

with

$$f_{of} = 6\frac{A_P}{A_{ER}}\frac{g_o}{\tau_y^*} \tag{16}$$

$$\tau_y^* = \frac{\tau_y}{\tau_o} \tag{17}$$

## Nomenclature (cont.)

$V_c$ = charged volume
$V_{cf}$, $V_{cm}$, and $V_{cs}$ = the flow-, mixed-, and shear-mode charged volumes
$v$ = piston velocity
$v_p$ = amplitude of $v$
$w$ = ER valve/gap width
$x_p$ = piston displacement amplitude
$\Delta p_{ER}$ = ER pressure drop
$\Delta p_m$ = pressure drop component induced by fluid inertia
$\Delta p_o$ = flow-mode zero-field pressure drop
$\Delta p_s$ = zero-field pressure drop for an equivalent steady flow of the same flow amplitude
$\Delta p_w$ = pressure drop component induced by the wall shear stress
$\epsilon$ = fluid dielectric constant
$\phi_l$ = phase advance of the shear-mode lower-plate stress
$\phi_o$ = flow-mode phase advance
$\phi_{om}$ = mixed-mode phase advance
$\phi_u$ = phase advance of (the upper-plate stress of) a shear-mode damper
$\phi_{um}$ = phase advance of the mixed-mode upper-plate stress
$\phi_w$ = phase advance of $\Delta p_w$
$\eta$ = zero-field viscosity
$\rho$ = fluid density
$\tau_l$ = shear-mode lower-plate shear stress
$\tau_o$ = equivalent to the zero-field shear stress between two parallel plates, with one of them fixed and the other plate moving at $v_p$
$\tau_u$ = shear-mode upper-plate shear stress
$\tau_{um}$ = mixed-mode upper-plate shear stress
$\tau_y$ = yield stress
$\tau_y^*$ = dimensionless yield stress
$\omega$ = angular velocity of the input vibration

$$\tau_o = \eta \frac{v_p}{h} \tag{18}$$

where $f_{of}$ is the zero-field factor of the flow-mode damper, a relative measure of the zero-field pressure drop. For the ER damper to be effective, $f_{of}$ has to be much less than one. The parameter $\tau_y^*$ is dimensionless; $\tau_o$ is equivalent to the zero-field shear stress between two parallel plates, with one of them fixed and the other plate moving at $v_p$.

The ER damping force on the piston of the flow-mode damper $F_{ERf}$ is calculated as

$$F_{ERf} = 2\frac{L}{h} A_p \tau_y \tag{19}$$

and it has to match the designed peak damping force. The compactness and efficiency of the device are important as well. The charged area $A_c$ (where the charged electrodes face each other) is calculated as

$$A_c = wL \tag{20}$$

where $w$ is the width of the ER valve. The charged volume $V_c$ (i.e., the volume between the charged electrodes) is calculated as

$$V_c = hA_c = wLh. \tag{21}$$

The damper electric capacitance $C$ is obtained as

$$C = \epsilon \frac{A_c}{h} \tag{22}$$

where $\epsilon$ is the fluid dielectric constant. Assuming a sinusoidal electric field strength with a peak value of $E_p$, one obtains the following peak capacitive electric power $P_{cp}$ and peak resistive electric power $P_{rp}$, respectively,

$$P_{cp} = \frac{1}{2}\epsilon\omega E_p^2 V_c \tag{23}$$

and

$$P_{rp} = C_d E_p V_c \tag{24}$$

where $C_d$ is the electric current density.

**Shear-Mode Dampers.** A practical shear-mode damper has a narrow gap whether it has a concentric or parallel arrangement of its electrodes. The fluid flow in a small gap can be approximated with a one-dimensional flow between two infinite parallel plates, with one plate (denoted arbitrarily as the lower-plate here) fixed and the other plate (the upper-plate) oscillating in its plane with a velocity

$$v = v_p \sin \omega t \tag{25}$$

Adapting the solutions of Schrag et al. (1965) to the current arrangement and a Newtonian fluid, the shear stress at the upper-plated $\tau_u$ is derived as

$$\tau_u = g_u \tau_o \sin(\omega t + \phi_u) \tag{26}$$

with

$$g_u = 2\sqrt{2}h^* \frac{\sqrt{A_1^2 + A_2^2}}{\sqrt{A_3^2 + A_4^2}}, \tag{27}$$

$$\phi_u = \frac{\pi}{4} + \tan^{-1}(A_2/A_1) - \tan^{-1}(A_4/A_3), \tag{28}$$

$$A_1 = \cosh 2h^* \cos 2h^*, \quad A_2 = \sinh 2h^* \sin 2h^*,$$

$$A_3 = \sinh 2h^* \cos 2h^*, \quad \text{and} \quad A_4 = \cosh 2h^* \sin 2h^* \tag{29}$$

where $g_u$ and $\phi_u$ are the dynamic factor and the phase advance of (the upper-plate stress of) the shear-mode damper, respectively. The dynamic factor $g_u$ is approximately equal to 1 when $h^* < 0.5$ and equal to $2\sqrt{2}h^*$ when $h^* > 0.5$ (Fig. 3). Therefore, $\tau_u$ increases with $h^*$.

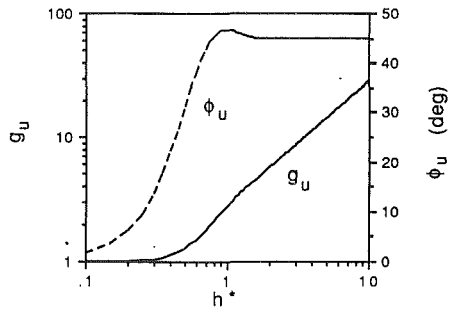


**Fig. 3 The dynamic factor ($g_u$) and the phase advance ($\phi_u$) of the upper-plate shear stress of the shear-mode damper**

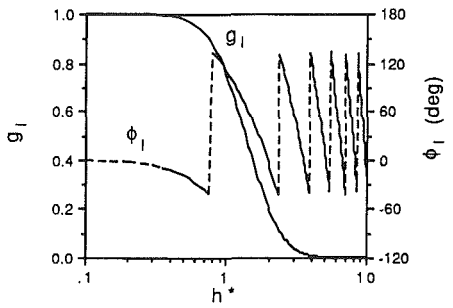


**Fig. 4 The dynamic factor ($g_l$) and the phase advance ($\phi_l$) of the lower-plate shear stress of the shear-mode damper**

The lower-plate shear stress $\tau_l$ is derived as

$$\tau_l = g_l \tau_o \sin(\omega t + \phi_l) \tag{30}$$

with

$$g_l = 2\sqrt{2}h^* \frac{1}{\sqrt{A_3^2 + A_4^2}} \tag{31}$$

$$\phi_l = \frac{\pi}{4} - \tan^{-1}(A_4/A_3) \tag{32}$$

where $g_l$ and $\phi_l$ are the dynamic factor and the phase advance of the lower-plate stress of the shear-mode damper, respectively. The dynamic factor $g_l$ is approximately equal to 1 when $h^* < 0.5$ and approaches 0 at high $h^*$ values (Fig. 4). Therefore, $\tau_l$ decreases with $h^*$. During a high-frequency oscillation, the shear waves does not fully reaches the lower-plate, and the majority of the energy is dissipated in the fluid volume immediately below the upper-plate.

As in the flow-mode damper, a simplified, linear analytical approach is adopted for dynamic flow of a Bingham fluid induced by an oscillating plate. In the shear-mode damper, no pressure drop is involved, and the damping force is directly related to the shear force on the upper-plate. The ER damping force in the shear-mode damper $F_{ERs}$ is estimated as

$$F_{ERs} = A_{cs}\tau_y, \tag{33}$$

where $A_{cs}$ is the charged area of the shear-mode damper. The zero-field (upper-plate) damping force $F_u$ is

$$F_u = A_{cs}\tau_o g_u \sin(\omega t + \phi_u) \tag{34}$$

The desired damping force of the system has to be matched by $F_{ERs}$, and $F_u$ has to be relatively small. The ratio of $F_u$ to $F_{ERs}$ is

$$\frac{F_u}{F_{ERs}} = f_{os} \sin(\omega t + \phi_u) \tag{35}$$

with

$$f_{os}=\frac{g_u}{\tau_y^*} \tag{36}$$

where $f_{os}$ is the zero-field factor of the shear-mode damper. For the damper to be effective, $f_{os}$ has to be much less than one.

**Mixed-Mode Dampers.** Because of the linear nature of the flow of a Newtonian fluid between two parallel plates, the velocity between the electrodes of a mixed-mode damper can be obtained by superposing those of the corresponding shear- and flow-mode dampers. The upper-plate shear stress $\tau_{um}$ is the summation of the shear stresses induced by Couette and Poiseuille flows:

$$\tau_{um}=\tau_o g_{um}\sin(\omega t+\phi_{um}) \tag{37}$$

with

$$g_{um}=\sqrt{A_{1um}^2+A_{2um}^2} \tag{38}$$

$$\phi_{um}=\tan^{-1}\frac{A_{2um}}{A_{1um}} \tag{39}$$

$$A_{1um}=g_u\cos\phi_u+6\frac{A_p}{A_{\mathrm{ER}}}g_w\cos\phi_w$$

and

$$A_{2um}=g_u\sin\phi_u+6\frac{A_p}{A_{\mathrm{ER}}}g_w\sin\phi_w. \tag{40}$$

where $g_{um}$ and $\phi_{um}$ are the dynamic factor and the phase advance of $\tau_{um}$, respectively.

The total zero-field damping force $F_{om}$ is derived as

$$F_{om}=A_p g_o\Delta p_s\sin(\omega t+\phi_o)+A_c g_{um}\tau_o\sin(\omega t+\phi_{um}) \tag{41}$$

and the ER control force $F_{\mathrm{ER}m}$ is as follows

$$F_{\mathrm{ER}m}=2\frac{L}{h}A_p\tau_y+A_c\tau_y \tag{42}$$

In ether of Eqs. (41) or (42), the first term on the right hand side is the force from the pressure drop, while the second term represent the force on the shearing surface.

The combination of Eqs. (41) and (42) gives

$$\frac{F_{om}}{F_{\mathrm{ER}m}}=f_{om}\sin(\omega t+\phi_{om}) \tag{43}$$

with

$$f_{om}=\frac{g_{om}}{\tau_y^*} \tag{44}$$

$$g_{om}=\frac{\sqrt{A_{1om}^2+A_{2om}^2}}{[2(A_p/A_{\mathrm{ER}})+1]} \tag{45}$$

$$\phi_{om}=\tan^{-1}\frac{A_{2om}}{A_{1om}} \tag{46}$$

$$A_{1om}=12(A_p/A_{\mathrm{ER}})^2 g_o\cos\phi_o+g_{um}\cos\phi_{um} \tag{47}$$

$$A_{2om}=12(A_p/A_{\mathrm{ER}})^2 g_o\sin\phi_o+g_{um}\sin\phi_{um} \tag{48}$$

where $f_{om}$ is the zero-field factor, $g_{om}$ the dynamic factor, and $\phi_{om}$ the phase advance of the mixed-mode damper. Both $g_{om}$ and $\phi_{om}$ increase with $h^*$ (Fig. 5). The dynamic factor $g_{om}$ also increases with $A_p/A_{\mathrm{ER}}$ because of the rising dominance of the flow action (Fig. 5(*a*)). The phase advance $\phi_{om}$ decreases with $A_p/A_{\mathrm{ER}}$ at low $h^*$ and does the opposite at high $h^*$ (Fig. 5(*b*)). A mixed-mode damper becomes a shear-mode damper when $A_p/A_{\mathrm{ER}}$ approaches zero, i.e., no more piston area.

**Flow-Mode Versus Shear-Mode.** In active damping control, one likes to generate a large ER damping force and keep the zero-field damping force as small as possible. For the same task, a shear-mode damper and a flow-mode damper therefore should have (*a*) the same ER damping force and (*b*) the same zero-field factor value. For the second requirement, one has

$$\frac{f_{of}}{f_{os}}=1. \tag{49}$$

The substitution of Eqs. (15) and (36) into Eq. (49) gives

$$A_p=\frac{g_u}{6g_o}A_{\mathrm{ER}}. \tag{50}$$

To meet the first requirement, one can derive from Eqs. (19), (20), (33), and (50) the following

$$\frac{V_{cf}}{V_{cs}}=\frac{A_{cf}}{A_{cs}}=\frac{3g_o}{g_u} \tag{51}$$

where $V_{cs}$ is the charged volume of the shear-mode damper, and $A_{cf}$ the charged area of the flow-mode damper. The both dampers are assumed to have the same gap size. The ratio $V_{cf}/V_{cs}$ is a good indicator of relative design merits of the two dampers because the charged volume is directly related to the size (Fig. 1(*d*)) and power requirement of a damper as shown in Eqs. (23) and (24). The ratio $V_{cf}/V_{cs}$, like $g_o$ or $g_u$, is a function of $h^*$ (see Fig. 6). The ratio $V_{cf}/V_{cs}$ is 3 at $h^*=0$, decreases gradually to its minimum value of 1.35 around $h^*=1$, and then increases linearly with $h^*$. To achieve the same performance, the flow-mode is not as compact and efficient as the shear-mode ER.

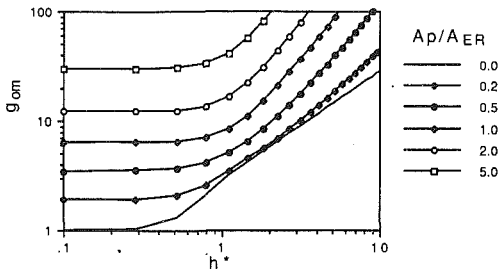


Fig. 5(*a*)

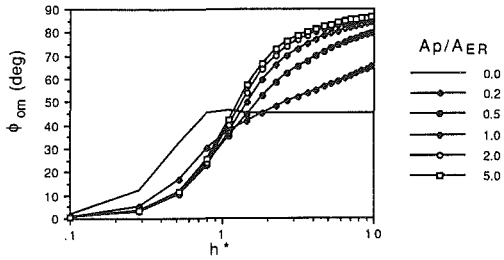


Fig. 5(*b*)

**Fig. 5** (*a*) The dynamic factor $g_{om}$ and (*b*) the phase advance $\phi_{om}$ of a mixed-mode damper versus the dynamic constant $h^*$ and the area ratio $A_p/A_{\mathrm{ER}}$

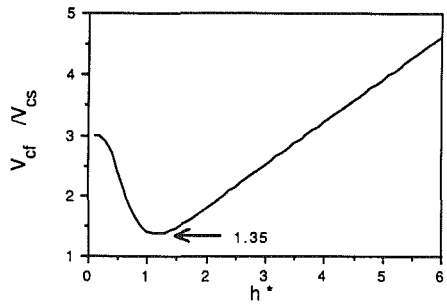


**Fig. 6** The ratio of the flow-mode charged volume ($V_{cf}$) to the shear-mode charged volume ($V_{cs}$) as a function of the dynamic constant $h^*$

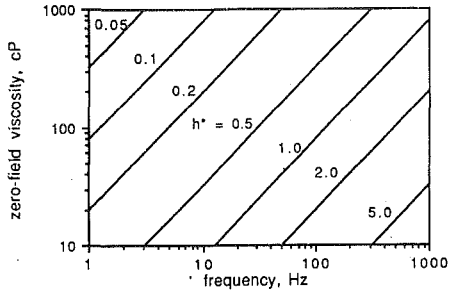


**Fig. 7 The dynamic constant $h^*$ as a function of the vibration frequency ($=\omega/2\pi$) and the zero-field viscosity ($\eta$), with the ER control gap size $h=1$ mm and the ER fluid density $\rho=1000$ kg/m$^3$**

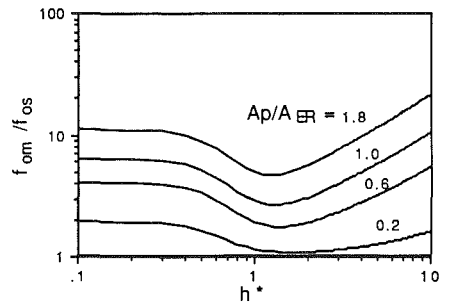


**Fig. 8 The ratio of the zero-field factor of the mixed-mode damper $f_{om}$ to that of the shear-mode damper $f_{os}$ as a function of the dynamic constant $h^*$ and the area ratio $A_p/A_{ER}$**

The significance of the dynamic constant $h^*$ is evident in Fig. 6. A practical range of $h^*$ is estimated using Eq. (5) and plotted in Fig. 7, where the fluid density $\rho$ and the gap size $h$ are chosen to be 1000 kg/m$^3$ and 1 mm, respectively. The frequency ranges from 1 to 1000 Hz, and $\eta$ ranges from 10 to 1000 cP in Fig. 7. In passenger cars, body natural frequencies are 1–2 Hz, the wheelhop frequency is around 15 Hz, and the engine mount natural frequency is 10–20 Hz (Morishita and Mitsui, 1992). The upper natural frequency limit of practical mechanical systems is probably 100 Hz. A middle-range value of the zero-field viscosity is 100 cP. For the chosen density and gap size, the dynamic constant $h^*$ varies from 0.05 to 5.0. Practical $\rho$ and $h$ values will not deviate too much from those chosen here, and the $h^*$ range in Fig. 7 is representative.

**Mixed-Mode Versus Shear-Mode.** For the ER damping force of a mixed-mode damper $F_{ERm}$ and that of a shear-mode damper $F_{ERs}$ to be equal, one obtains

$$\frac{V_{cm}}{V_{cs}}=\frac{A_{cm}}{A_{cs}}=\frac{1}{2(A_p/A_{ER})+1} \tag{52}$$

where $V_{cm}$ and $A_{cm}$ are the charged volume and area of the mixed-mode damper, respectively. The gap size $h$ is assumed to be the same. With a positive $A_p/A_{ER}$, $V_{cm}/V_{cs}<1$. With the same ER damping force, the mixed-mode damper is therefore more compact than the shear-mode damper.

The ratio of the zero-field factor of the mixed-mode damper $f_{om}$ to that of the shear-mode damper $f_{os}$ is equal to $g_{om}/g_u$ because of Eqs. (36) and (44). The ratio $f_{om}/f_{os}$ is a function of $h^*$ and $A_p/A_{ER}$, and is always greater than one for a positive $A_p/A_{ER}$ (Fig. 8). The mixed-mode damper therefore does not have as a low zero-field damping force as the comparable shear-mode damper.

## Discussions

The above analysis shows that one should avoid the flow-mode and use the shear-mode. There are two physical reasons for the conclusion. First, with a limited ER induced increase in the shear stress, a device should operate at as a low shear rate as possible to reduce the zero-field damping force and increase its effective control. The yield stress may even decreases with the shear rate (Klass and Martinek, 1967; Lou et al., 1990), which further enhances the need for a low shear rate. Second, the fluid inertia and the unsteady wall shear stress (which is higher than the steady wall shear stress) significantly increase the zero-field damping force. A flow-mode damper generally has higher shear rate and acceleration, especially with a large $A_p/A_{ER}$, than a shear-mode damper.

In the analysis, the cylinder component of a damper is fixed while the piston component vibrates. Both the components of many practical dampers can move. In most of these cases, there is a large disparity in the amplitudes of the motion for the two components, and the analysis in this study is valid. Otherwise, more appropriate boundary conditions have to be used for a finer analysis although the general conclusion from this study may still apply, at least to the first order accuracy.

For the purpose of generality, the assigned vibration in this study is sinusoidal. Road surface profiles for an automobile damper, for example, is not so. Through the use of the power spectral density function, however, one can present the surface profiles in forms of sine wave.

Shear-mode dampers can be further divided into rotary and translational types, either of which can have its own variations in the way electrodes are arranged.

The damper in Fig. 1($c$) is only one possible version of the translational type of shear-mode dampers, where the electrodes are arranged concentrically. Electrodes can also be parallel plates. Multiple electrodes are generally used to achieve a compact design. Because of the translational motion, the cylinder in Fig. 1($c$) has to be longer than the piston to keep a constant charged area. This results in a significant amount of idling surface on the cylinder at any moment.

A rotary-type shear-mode damper is able to reduce the extra surface area by having all the surface area engaged all the time. One possible version is to have a plurality of rotational shearing disks along the rotation axis (Lou et al., 1993b). An alternative is to have multiple concentric electrodes around the rotation axis. A translation-to-rotation device is needed if the motion to be damped is translational. ER fluids in shear-mode dampers are under a minimum, if any, pressure. Low pressure simplifies many design problems, especially the sealing problem. Among shear-mode dampers, a rotary damper has an additional advantage over a translational damper because the former can avoid sealing a reciprocating sliding surface, which is more prone to entrapping the solid phase of an ER fluid.

The ER fluid used in the analysis is Bingham plastic and has a time constant far smaller than those of the dampers. A practical ER fluid may not follow an ideal Bingham plastic model. As long as the practical fluid has a relatively Newtonian rheology at zero-field, a fast time response, and an effective yield stress (i.e., a finite shear stress increment at the working shear-rate range) when energized, the results from this study still apply because of the nature of the analysis in this study. The analysis is base on (1) the flow dynamics at zero-field and (2) the achievable stress increment when energized. If the ER response is close to or slower than those of the dampers, one needs to include the flow dynamics of the energized fluid as well.

## Conclusions

In this study, the dynamics of the fluid flow is included in the derivation of the zero-field damping forces of the flow-, shear-, and fixed-mode ER dampers based on an ER fluid that is Bingham plastic. The main results of the study are as follows:

- The zero-field pressure drop in a flow-mode damper is mainly to overcome the wall shear stress at low frequencies. At high frequencies (with the dynamic constant $h^*$ greater than one), the zero-field pressure counters pri-

marily the fluid inertia, and it increases with the frequency or $h^{*2}$. It also has a significant phase advance relative to the vibration at high frequencies. The level of ER control decreases with the ratio of the piston area to the ER valve cross-section $A_p/A_{ER}$.

- The zero-field pressure drop in a shear-mode damper also has to counter the fluid inertia at high frequencies. When the dynamic constant $h^*$ is greater than 0.5, the zero-field pressure increases with $h^*$ or the square root of the frequency.
- The behavior of the zero-field pressure drop in a mixed-mode damper is between those of a shear- and a flow-mode damper, and it is a function of the area ratio $A_p/A_{ER}$. The mixed-mode damper becomes a shear-mode damper when the ratio $A_p/A_{ER}$ approaches zero.
- To achieve the same performance, a flow-mode ER damper is not as compact and efficient as a shear-mode ER damper.
- With the same ER damping force, a mixed-mode damper is more compact than a shear-mode damper. However, the mixed-mode damper does not have as a low zero-field damping force as the shear-mode damper.

## Acknowledgments

The authors wish to acknowledge the financial support from the NASA-Langley Research Center, the U.S. Army Tank-Automotive Command (TACOM), Aeroquip Corporation, BASF, Chrysler Corporation, Ford Motor Company, Monroe Automotive Equipment Co., Naval Underwater Systems Center, Nissan Motors, and Tremec Trading Company.

## References

Klass, D. L., and Martinek, T. W., 1967, "Electroviscous Fluids I. Rheological Properties," *Journal of Applied Physics*, Vol. 38, pp. 67–74.

Lou, Z., Ervin, R. D., and Filisko, F. E., 1990, "The Feasibility of Using Electro-Rheological Fluids in Aircraft Flight Controls—Phase 1 Report," UM-TRI-90-10, The University of Michigan Transportation Research Institute, Ann Arbor.

Lou, Z., Ervin, R. D., and Filisko, F. E., 1992, "Behaviors of Electrorheological Valves and Bridges," *Proceedings of the International Conference on Electrorheological Fluids: Mechanism, Properties, Structure, Technology, and Applications*, Tao, R., ed., World Scientific, River Edge, NJ, pp. 398–423.

Lou, Z., Ervin, R. D., and Filisko, F. E., 1993a, "The Influence of Viscometer Dynamics on the Characterization of an Electrorheological Fluid Under Sinusoidal Electric Excitation," *Journal of Rheology*, Vol. 37, pp. 55–70.

Lou, Z., Ervin, R. D., Filisko, F. E., and Winkler, C. B., 1993b, "An Electrorheologically Controlled Semi-Active Landing Gear," SAE Technical Paper Series, No. 931403, SAE, Warrendale, PA (Also: "Electrorheologically Controlled Landing Gear," *Aerospace Engineering*, June 1993, pp. 17–22).

Lou, Z., and Yang, W. J., 1993, "A Computer Simulation of the Non-Newtonian Blood Flow at the Aortic Bifurcation," *Journal of Biomechanics*, Vol. 26, pp. 37–49.

Morishita, S., and Mitsui, J., 1992, "An Electronically Controlled Engine Mount Using Electro-Rheological Fluid," SAE Technical Paper Series, No. 922290, SAE, Inc., Warrendale, PA.

Schrag, J. L., Guess, J. F., and Thurston, G. B., 1965, "Shear-Wave Interference Observed by Optical Birefringence Induced in a Viscous Liquid," *Journal of Applied Physics*, Vol. 36, pp. 1996–2000.

Thurston, G. B., 1959, "Theory of Oscillation of a Viscoelastic Medium Between Parallel Planes," *Journal of Applied Physics*, Vol. 30, pp. 1855–1860.

Thurston, G. B., and Gaertner, E. B., 1991, 'Viscoelasticity of Electrorheological Fluids During Oscillatory Flow in a Rectangular Channel," *Journal of Rheology*, Vol. 35, pp. 1327–1343.

# Marangoni Convection With a Curved and Deforming Free Surface in a Cavity

**G. P. Sasmal**
Presently,
Division of Cardiothoracic Surgery,
Washington University School of Medicine,
St. Louis, MO

**J. I. Hochstein**

Department of Mechanical Engineering,
Memphis State University,
Memphis, TN 38152

*A finite-volume based computational model is developed to predict Marangoni convection in a cavity with a curved and deforming free surface. The two-dimensional incompressible continuity, momentum, and energy equations are solved on a staggered Cartesian grid. The free surface location is computed using the volume-of-fluid transport equation. Normal and tangential boundary conditions at the free surface are modeled using respectively a surface pressure and a continuum surface force technique. Computational predictions of thermocapillary flow in a shallow cavity are shown to be in good agreement with previously published asymptotic results. The new transient model is then used to study the influence of Marangoni number and Capillary number on thermocapillary flows in a cavity for different static contact angles. The flows are characterized by streamline and isotherm patterns. The influence of the dimensionless parameters on heat transfer rate at the cavity walls is exposed by examination of local Nusselt number profiles.*

## Introduction

For most fluids, surface tension coefficient is a contravariant function of temperature. Variation of surface tension coefficient due to a temperature gradient at a free surface can cause fluid motion from a low to a high surface tension zone. This phenomenon, known as Marangoni convection, plays an important role in material processing such as laser surface melting, crystal growth, and coating. A general review of this phenomena is presented by Ostrach (1982). The geometric simplicity of Marangoni flow in a cavity has made it an attractive configuration for many investigators seeking to expose the complex interaction between fluid mechanics and heat transfer in the presence of a deforming free surface. Many numerical and analytical studies have been limited to flows in small aspect ratio cavities with á priori specification of a flat free surface to avoid the complexity of modeling the transport processes at a curved and deforming interface.

Chen et al. (1990) performed steady state analyses for free surface flows with mild curvature in a small aspect ratio configuration using a boundary fitted curvilinear coordinate system. Sen and Davis (1982) used an asymptotic method to study thermocapillary convection in a shallow two-dimensional slot in which the interface shape is not flat. Their solutions are valid for slight deviation of interface shape from the initial domain in a small aspect ratio cavity at a low Marangoni number and low Reynolds number. Pimputkar and Ostrach (1980) allowed the free surface to deform in their transient analyses of thin liquid layers. Pressure effects due to surface curvature were neglected due to small aspect ratio of their geometry. Zebib et al. (1985) determined the interface shape by a domain perturbation method for very low Capillary number and studied high Marangoni number convection in a square cavity. Cuvelier and Drissen (1986) computed the free surface shape by three different iterative methods in their steady state analyses of two-dimensional thermocapillary flow using a finite element method.

This paper presents the development of a new computational model to predict Marangoni convection in a cavity with a curved and deforming free surface. The model is then used to study the influence of Ma and Ca on thermocapillary flows in a cavity for different static contact angles. The two-dimensional transient incompressible continuity, momentum, and energy equations are solved using a pressure correction method. The normal surface stress is modeled as an equivalent surface pressure whereas the tangential surface tension gradient force is incorporated in the momentum equations as a body force using a continuum surface force model (Kothe et al., 1991). The free surface location is computed using the volume-of-fluid transport equation (Torrey, 1985) on a fixed Cartesian grid. In contrast to most existing analytical and computational tools for the study of thermocapillary flows, á priori specification of interface shape is not required. The ability to study the transient evolution of a thermocapillary flow is also unusual in that most previous models are only capable of obtaining steady-state solutions for the model equations. In summary, the ability to model transient evolution of thermocapillary flow including significant deformation of interfaces of arbitrary topology make this a unique tool for the study of thermocapillary flows.

Contributed by the Fluids Engineering Division for publication in the JOURNAL OF FLUIDS ENGINEERING. Manuscript received by the Fluids Engineering Division April 10, 1993; revised manuscript received October 27, 1993. Associate Technical Editor: M. Gharib.

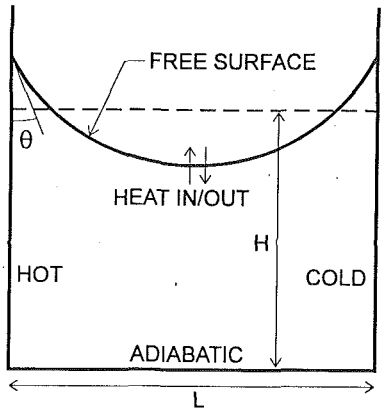


**Fig. 1 Fluid configuration in a plane 2-D cavity**

## Mathematical Formulation

The physical domain under consideration is a rectangular cavity of width $L$ containing a Newtonian fluid of average height $H$ as shown in Fig. 1. The rigid side walls at $x = 0$ and $x = L$ are maintained at constant temperature $T_{hot}$ and $T_{cold}$ respectively whereas the bottom rigid wall is insulated. The viscosity $\mu$, specific heat $c$, thermal conductivity $k$, and heat transfer coefficient at the free surface $h_c$ are constant. The surface tension coefficient is assumed to vary linearly with temperature.

$$\sigma = \sigma_{ref} + \frac{\partial \sigma}{\partial T}(T - T_{ref}) \tag{1}$$

where $\partial\sigma/\partial T$ is a negative constant for a given fluid. $\sigma_{ref}$ and $T_{ref}$ are the reference values for the surface tension coefficient and temperature respectively.

The appropriate equations for describing transient two-dimensional motion of an incompressible fluid in terms of dimensional primitive variables are:

$$\text{Continuity:} \quad \frac{\partial u}{\partial x} + \frac{\partial v}{\partial y} = 0 \tag{2}$$

$x$-momentum:

$$\frac{\partial u}{\partial t} + u\frac{\partial u}{\partial x} + v\frac{\partial u}{\partial y} = -\frac{1}{\rho}\frac{\partial P}{\partial x} + \nu\left[\frac{\partial^2 u}{\partial x^2} + \frac{\partial^2 u}{\partial y^2}\right] + \frac{1}{\rho}F_{sux}^{(t)} \tag{3}$$

$y$-momentum:

$$\frac{\partial v}{\partial t} + u\frac{\partial v}{\partial x} + v\frac{\partial v}{\partial y} = -\frac{1}{\rho}\frac{\partial P}{\partial y} + \nu\left[\frac{\partial^2 v}{\partial x^2} + \frac{\partial^2 v}{\partial y^2}\right] + \frac{1}{\rho}F_{svy}^{(t)} \tag{4}$$

where the terms $F_{sux}^{(t)}$, and $F_{svy}^{(t)}$ are the $x$- and $y$-components of the tangential surface tension gradient volume forces derived from the continuum method (Kothe, 1991). Details of how these forces are modeled will be presented in a later section. In the present study, buoyancy terms are absent from the momentum equations since the focus is on Marangoni convection in a zero gravity environment. Application of the principle of conservation of energy to the configuration of interest yields the following thermal energy transport equation.

$$\text{Energy:} \quad \frac{\partial T}{\partial t} + u\frac{\partial T}{\partial x} + v\frac{\partial T}{\partial y} = \alpha\left[\frac{\partial^2 T}{\partial x^2} + \frac{\partial^2 T}{\partial y^2}\right] \tag{5}$$

A rigid no-slip boundary condition at the cavity walls, and the thermal boundary conditions for the energy equation, are enforced by the following equalities.

$$u(0, y) = v(0, y) = 0, \quad T(0, y) = T_{HOT}$$
$$u(L, y) = v(L, y) = 0, \quad T(L, y) = T_{COLD}$$

$$u(x, 0) = v(x, 0) = 0, \quad \left.\frac{\partial T}{\partial y}\right|_{y=0} = 0 \tag{6}$$

The free surface is subject to normal, tangential, kinematic, and heat transfer boundary conditions. Although the tangential shear stress boundary condition at the free surface is explicitly incorporated in the momentum equations, it is presented here for clarity.

$$\text{Shear stress balance:} \quad \mu\left(\frac{\partial u_s}{\partial n} + \frac{\partial v_n}{\partial s}\right) = \frac{\partial \sigma}{\partial s} \tag{7}$$

$$\text{Normal stress balance:} \quad P = P_0 + 2\mu\frac{\partial v_n}{\partial n} - \sigma\kappa \tag{8}$$

where $u_s$ and $v_n$ are the tangential and normal velocity component at the free surface. $\kappa$ is the curvature of the free surface and $P_0$ is the vapor pressure in the gas region. The present model does not include dynamics for the gas phase so the vapor pressure is assumed to have a constant value. The kinematic boundary condition at the free surface requires that the fluid velocity normal to the free surface is zero with respect to the free surface and is given by:

$$\frac{\partial f}{\partial t} + u\frac{\partial f}{\partial x} + v\frac{\partial f}{\partial y} = 0, \tag{9}$$

where $f$ is the fractional volume of the fluid in a computational cell. This takes a value of unity at a point in space occupied by fluid and a value of zero if fluid does not occupy that point. The liquid-vapor interface is located at the $f = 0.5$ contour. The volume-of-fluid (VOF) algorithm solves the above equation in the full computational domain and thereby automatically satisfies the kinematic boundary condition at the free surface. Finally a heat flux balance at the free surface gives rise to the following expression:

$$-k\frac{\partial T}{\partial n} = h_c(T - T_0) \tag{10}$$

## Nomenclature

$A$ = aspect ratio
Bd = dynamic Bond number
Bo = static Bond number
Ca = capillary number
$F$ = force
Gr = Grashof number
$h_c$ = film coefficient at interface
$k$ = thermal conductivity
Ma = Marangoni number
$n$ = coordinate normal to interface
Nu = Nusselt number
$P$ = pressure
Pr = Prandtl number
Re = Reynolds number
$s$ = coordinate along interface
$t$ = time
$T$ = temperature
$t_x$, $t_y$ = components of unit tangent vector
$u$, $v$ = $x$- and $y$-component velocity
$x$, $y$ = Cartesian coordinates
$\alpha$ = thermal diffusivity
$\beta$ = coefficient of thermal expansion
$\Delta T$ = characteristic temperature difference
$\kappa$ = curvature
$\nu$ = kinematic viscosity
$\theta$ = contact angle
$\rho$ = density
$\sigma$ = surface tension coefficient
$\mu$ = dynamic viscosity

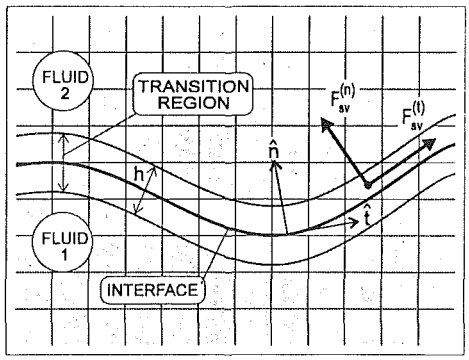


**Fig. 2 Interface transition region on a Cartesian grid**

where $T_0$ is a specified temperature distribution in the gas region.

Dimensional analysis of the governing equations and free surface boundary conditions produces several dimensionless parameters that have been identified by previous investigators. The frequently appearing dimensionless parameters are: $A = H/L$, $\mathrm{Re} = (|\partial\sigma/\partial T|\Delta TH)/(\mu\nu)$, $\mathrm{Ca} = (|\partial\sigma/\partial T|\Delta T)/\sigma_{\mathrm{ref}}$, $\mathrm{Pr} = \nu/\alpha$, $\mathrm{Ma} = (|\partial\sigma/\partial T|\Delta TH)/\mu\alpha$, $\mathrm{Nu} = (h_c H)/k$. In addition to these dimensionless parameters, the initial free surface shape must be specified through a static contact angle. Since the present study is focused on Marangoni convection in a zero gravity environment, dimensionless parameters containing the acceleration due to gravity such as Grashof number ($\mathrm{Gr} = \rho^2 g\beta\Delta TH^3/\mu^2$), Static Bond number ($\mathrm{Bo} = \rho g H^2/\sigma_{\mathrm{ref}}$), and Dynamic Bond number ($\mathrm{Bd} = \rho g L^2/(|\partial\sigma/\partial T|\Delta T)$) are zero.

## Modeling of Surface Tension and Its Gradient

The normal surface tension force was modeled using a surface pressure technique (Torrey, 1985) and can be written in terms of the surface pressure as:

$$P_s = P - P_0 = -\sigma\kappa + 2\mu\frac{\partial v_n}{\partial n}. \tag{11}$$

The curvature of the free surface ($\kappa$) is computed at an interface from a surface shape reconstruction based on the value of the VOF function in a cell and in its neighbor cells. The radius of curvature is the reciprocal of the rate-of-change of slope along the surface computed from this reconstruction. At a solid/fluid interface the specified contact angle is included in the surface reconstruction. The resulting surface pressure acts like a wall adhesion force that forces the fluid to make the specified contact angle at a solid wall but permits motion of the contact line along the solid boundary.

The tangential surface tension gradient force is computed as a cell-centered quantity. It is modeled using the VOF function as a color variable that varies continuously in a transition region of finite thickness as shown in Fig. 2. The tangential volume force derived from the continuum surface force (CSF) model (Kothe 1991) can be written as

$$\mathbf{F}_{sv}^{(t)} = \left[\hat{i}\left(t_x^2\frac{\partial\sigma}{\partial x} + t_x t_y\frac{\partial\sigma}{\partial y}\right) + \hat{j}\left(t_y^2\frac{\partial\sigma}{\partial y} + t_x t_y\frac{\partial\sigma}{\partial x}\right)\right]|\nabla f| \tag{12}$$

where the $x$- and $y$-components of the unit tangent at the free surface, $t_x$ and $t_y$, are evaluated using the gradients of the VOF function. The tangential volume force computed by Eq. (12) varies smoothly across the transition region, and is zero outside the region, because the unit tangent and VOF gradient from which it is computed have precisely these properties. The finite difference formulation used to compute $\partial\sigma/\partial x$ and $\partial\sigma/\partial y$ is biased toward the liquid side of the interface to insure that their evaluation is performed using values in the fluid cells. Sasmal (1993) presents a detailed derivation of Eq. (12) and its finite difference approximation. Using an explicit difference formulation, the $x$ and $y$ components of the tangential forces from Eq. (12) are incorporated into the momentum Eqs. (3, 4).

## Solution Procedure

The flow field is discretized into finite volumes forming a staggered Cartesian grid on which velocities are defined at cell faces and pressure at the cell center. A semi-implicit finite volume approximation to the transient two-dimensional incompressible Navier-Stokes equations reduces the problem to solving a system of nonlinear algebraic equations to advance the solution from one time level to the next. This system is solved using a successive over-relaxation procedure (Torrey, 1985). The cell-centered VOF function is then advanced using a donor-acceptor scheme specifically designed to avoid excessive diffusion and thereby to preserve steep surface slopes (Nichols, 1980). A free surface reconstruction based on the VOF function values in neighbor cells is used to approximate the surface shape in a cell as aligned predominantly with either the $x$ or the $y$ coordinate. Fluid is then transferred from the donor cell to the acceptor cell according to the velocity previously computed for the cell face, but limited to no more than the amount of fluid in the cell at the beginning of the time step. The thermal energy transport equation is discretized using an explicit finite volume approximation on the same Cartesian grid with the temperature defined as a cell-centered quantity. The thermal energy equation is solved using the new-time level velocities to compute the advection terms. The solution is advanced through time in finite size steps which are limited in magnitude by appropriate stability considerations.

All analyses conducted during this study begin with a stagnant uniform field and terminate when the flow field and temperature fields cease to change. An analysis was judged to have reached a steady state solution when all velocities and temperatures remain unchanged to 5 significant places for two successive time steps. A Silicon Graphics 4D/35 workstation served as the computational platform for all the analyses presented in the following paragraphs. The level of computational effort required to complete the analyses ranged from approximately twenty minutes of CPU time for the most rapid analyses to approximately 5 hours for the most challenging analysis.

## Results and Discussion

Before using the new computational model as a tool for investigating the influence of various dimensionless parameters on Marangoni convection with a curved and deforming free surface in a cavity, it is prudent to demonstrate the fidelity of the model in representing such a flow. A previously published solution (Sen and Davis, 1982) based on an asymptotic analysis of flow at low Marangoni and Reynolds number in a small aspect ratio cavity was selected as an appropriate test case. The asymptotic solution was obtained for a 90 deg contact angle and is valid for slight deviations from the initially specified flat interface. Using a Nusselt number of unity, heat transfer at the interface was computed based on a linear temperature distribution in the gas phase. The flow conditions for this numerical experiment are characterized by the following dimensionless parameters: $\mathrm{Re} = 1.0$, $\mathrm{Pr} = 0.2$, $A = 0.2$, $\mathrm{Nu} = 1.0$, $\mathrm{Ca} = 0.08$, and $\mathrm{Gr} = 0.0$.

Both the asymptotic analysis and the computational model predict a rise in fluid height along the cold wall and a depression of the fluid surface at the hot wall. The asymptotic analysis predicts a depression of the interface at the hot wall to height of 0.175, in excellent agreement with the computational model's prediction of 0.174. The computational model's prediction of a rise in fluid height at the cold wall to a height of 0.224 is also in excellent agreement with the asymptotic model's

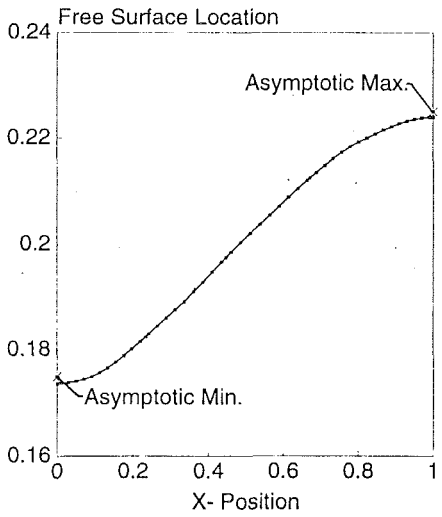


Fig. 3 Computed surface shape for low aspect ratio cavity

**Table 1 Case matrix for thermocapillary convection in a cavity (Pr = 1.0, $A$ = 1.0, Nu = 0.0, Gr = 0.0)**

| Case No. | $\theta$ | Ma | Ca |
|---|---|---|---|
| 1 | 90 deg | 10 | 0.1 |
| 2 | 90 deg | 100 | 0.1 |
| 3 | 90 deg | 100 | 0.05 |
| 4 | 90 deg | 500 | 0.05 |
| 5 | 60 deg | 10 | 0.1 |
| 6 | 60 deg | 10 | 0.05 |
| 7 | 60 deg | 100 | 0.1 |
| 8 | 60 deg | 500 | 0.05 |
| 9 | 10 deg | 10 | 0.1 |
| 10 | 10 deg | 100 | 0.1 |
| 11 | 10 deg | 500 | 0.05 |
| 12 | 120 deg | 100 | 0.1 |
| 13 | 120 deg | 500 | 0.2 |

prediction of 0.225. Similar configurations were studied by Chen et al. (1990) using a steady state computational model which iteratively adjusts a curvilinear coordinate system to fit the interface shape. Their model predicts interface shapes similar to that depicted in Fig. 3, providing additional confidence in the new computational model.

The geometric configuration used to study the dependence of thermocapillary flow on Marangoni number, Capillary number, and contact angle, is presented in Fig. 1. To eliminate the influence of interfacial heat transfer on the thermocapillary flow, the Nusselt number has been set to zero for all analyses in this study. Likewise, a value of unity was specified for both Prandtl number and aspect ratio. For a pool with a curved free surface, the aspect ratio is defined as the ratio of average fluid height, (height corresponding to a level surface enclosing the same volume), to the width. Table 1 presents the case matrix for studying the influence of Ma, Ca, and contact angle on Marangoni convection in a cavity.

The 34 × 31 nonuniform mesh displayed in Fig. 4($a$) was used to study flows with a 90 deg contact angle. The mesh is refined near the free surface to capture the details of the solution. The steady state isotherms and streamlines for the 90 deg contact angle cases are shown in Fig. 4($b$-$d$). Isotherm shapes for the low Ma number case confirm that conduction is the dominant mode of heat transfer for this case. As Ma is increased, the growth of surface tension driven convection beneath the free surface toward the cold wall is obvious in the increased distortion of the isotherms. Since the full-field isotherm and streamline patterns predicted for cases 2 (Ca = 0.1) and 3 (Ca = 0.05) are indistinguishable, only the patterns for case 2 are included in Fig. 4. However, Fig. 5 displays the

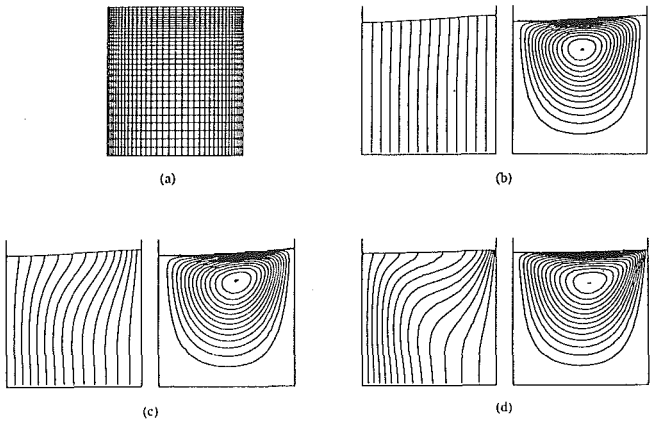


Fig. 4 Marangoni convection for a 90 deg contact angle. ($a$) 34 × 31 nonuniform mesh; Steady-state isotherms (left) and streamlines (right) for ($b$) Ma = 10, Ca = 0.1, ($c$) Ma = 100, Ca = 0.1, ($d$) Ma = 500, CA = 0.05 Isotherms are equally spaced ranging from a normalized value of +1/2 at hot wall to −1/2 at cold wall. Streamlines are also equally spaced.

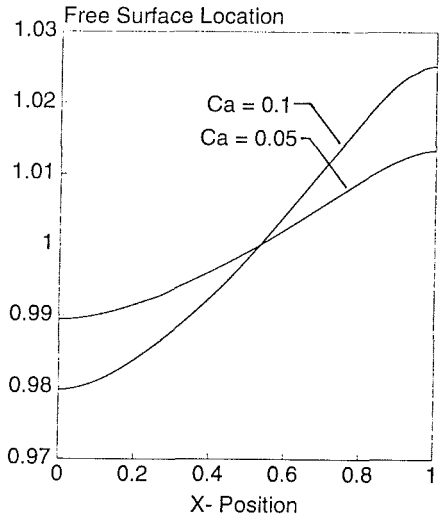


Fig. 5 Free surface deformation for Ma = 100, Ca = 0.1/0.05, $\theta$ = 90 deg

predicted interface shapes for these cases using a magnified height scale to reveal that the surface deformation does increase with increasing Ca. Interface shapes predicted by Chen et al. (1990) using their steady state model exhibited a similar dependence.

A mesh sensitivity study was executed using the two meshes displayed in Fig. 6($a$). The steady state isotherms and streamlines computed for Ma = 10, Ca = 0.1, and $\theta$ = 60 deg (case 5) using these grids are shown in Figs. 6($b$) and 6($c$). The solutions displayed in these figures are virtually identical, leading to the conclusion that the coarser mesh is acceptable for subsequent analyses. Compared to the initial static isothermal meniscus, the minimum surface height location of the final interface is shifted towards the hot wall due to an increase in fluid height at the cold wall and a decrease in height at the hot wall. Full-field isotherm and streamline displays for case 6 (Ma = 10, Ca = .05) are indistinguishable from those of case 5 and, therefore, are not presented. Figures 6($d$-$e$) show the steady state isotherms and streamlines for other 60 deg contact angle cases. They clearly show an increased isotherm distortion at higher Ma. Further, the streamline field associated with Ma = 500 shows a shifting of the vortex toward the cold wall and the streamlines being drawn further into the cold wall/interface junction.

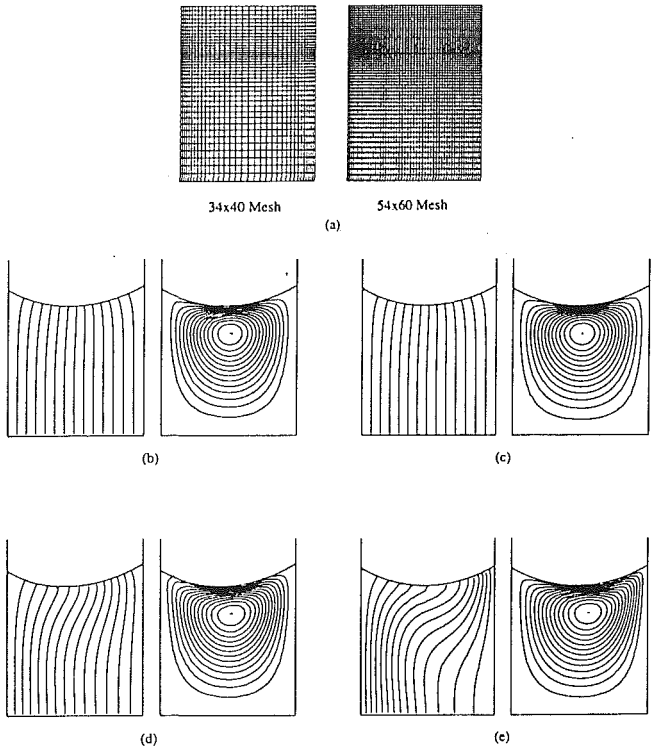


**Fig. 6 Marangoni convection for a 60 deg contact angle. (*a*) Nonuniform meshes for grid sensitivity study. Steady-state isotherms (left) and streamlines (right) for (*b*) Ma = 10, Ca = 0.1, 34 × 40 mesh, (*c*) Ma = 10, Ca = 0.1, 54 × 60 mesh, (*d*) Ma = 100, Ca = 0.1, (*e*) Ma = 500, Ca = 0.05. Isotherms are equally spaced ranging from a normalized value of + 1/2 at hot wall to − 1/2 at cold wall. Streamlines are also equally spaced.**

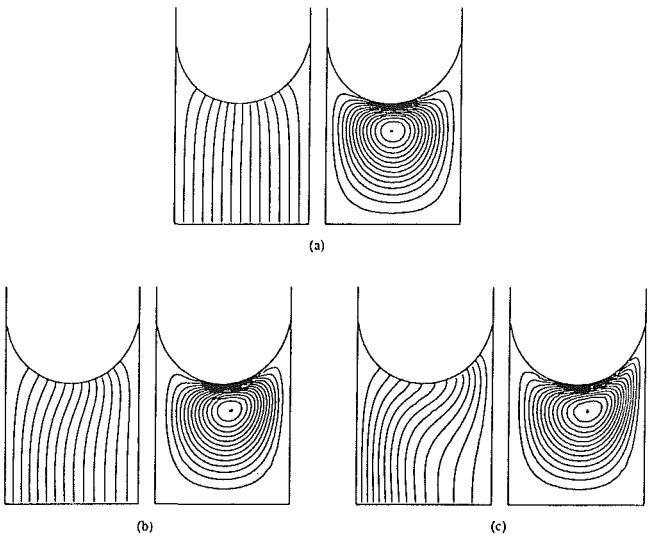


**Fig. 7 Marangoni convection for a 10 deg contact angle. Steady-state isotherms (left) and streamlines (right) for (*a*) Ma = 10, Ca = 0.1, (*b*) Ma = 100, Ca = 0.1, (*c*) Ma = 500, Ca = 0.05. Isotherms are equally spaced ranging from a normalized value of + 1/2 at hot wall to − 1/2 at cold wall. Streamlines are also equally spaced.**

Analyses of small contact angle (10 deg) flows were performed using a nonuniform 34 × 55 mesh graded to capture the flow details near the interface. Because the preceding analyses demonstrated a consistent and very small increase in free surface deformation with increasing Ca, a pair of cases designed to study this dependence was not included in the 10 deg set. Further, the small contact angle provides an even stiffer boundary condition for the surface which should hold the surface more tightly in place and permit even less difference

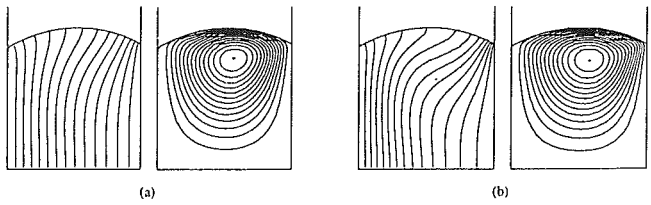


**Fig. 8 Marangoni convection for a 120 deg contact angle. Steady-state isotherms (left) and streamlines (right) for (*a*) Ma = 100, Ca = 0.1, (*b*) Ma = 500, Ca = 0.2. Isotherms are equally spaced ranging from a normalized value of + 1/2 at hot wall to − 1/2 at cold wall. Streamlines are also equally spaced.**

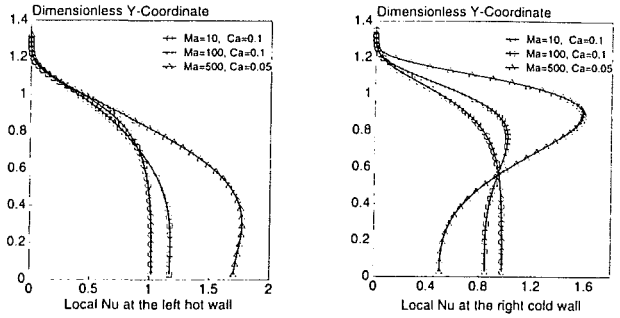


**Fig. 9 Nusselt number distribution along cavity walls for a 10 deg contact angle**

in surface deformation than was observed for the 60 and 90 deg cases. Steady state isotherms and streamlines for the 10 deg contact angle cases are shown in Fig. 7. The thermocapillary flow toward the cold wall is more pronounced than observed at the higher contact angles, distorting the isotherms as Ma increases. Figure 7(*c*) clearly depicts the shifting of the vortex toward the cold wall and the distortion of the streamlines into the cold wall interface junction with increasing Ma.

Analyses for a 120 deg contact angle were performed on a 34 × 38 nonuniform mesh. The steady state isotherms and streamlines for the two 120 deg contact angle cases are shown in Fig. 8. High capillary numbers were chosen to enhance free surface deformation. Again, the free surface rises along the cold wall and falls along the hot wall. As expected, an increased distortion of isotherms at higher Ma was observed with an accompanying translation of the vortex core and distortion of the streamlines towards the cold wall.

Graphical displays of the influence of Ma, Ca, and $\theta$ on local Nu at the cavity walls are presented in Figs. 9 to 11. The local Nu at a cavity wall was defined as the ratio of local heat flux to the heat flux for pure conduction between the hot and cold walls. Figure 9 reveals the strong dependence of local Nu on height for flow with a contact angle of 10 deg. For both cavity side-walls, and for all three cases displayed, Nu decreases rapidly with height in the vicinity of the interface and approaches zero at the free surface. This result is consistent with the isotherms, streamlines, and interface shapes depicted in Fig. 7 for these flows. Since the streamlines do not penetrate the narrow corner region in the vicinity of the contact line, it is reasonable to expect that fluid in this region is nearly stagnant and that the fluid temperature will approach the wall temperature as a steady-state is established. Without significant advective transport, this equilibration between wall and fluid temperature reduces heat transfer to near zero as reflected by the precipitous drop in Nu near the free surface. As the contact angle is increased, flow into the contact region becomes more vigorous moving the Nu maximum on the cold wall toward the free surface, (Figs. 9, 10, 11). Figure 10(*b*) shows that the maximum Nu at the cold wall has moved to the free surface for a 90 deg contact angle. Figure 11 shows that the maximum

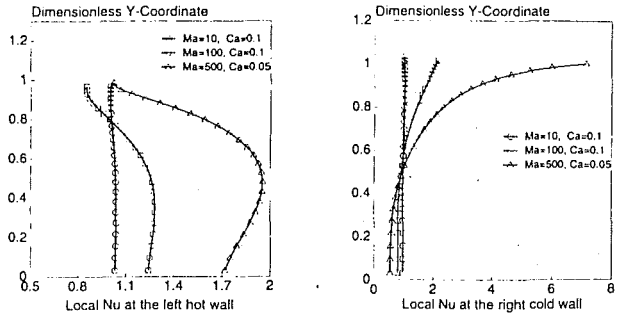


**Fig. 10 Nusselt number distribution along cavity walls for a 90 deg contact angle**

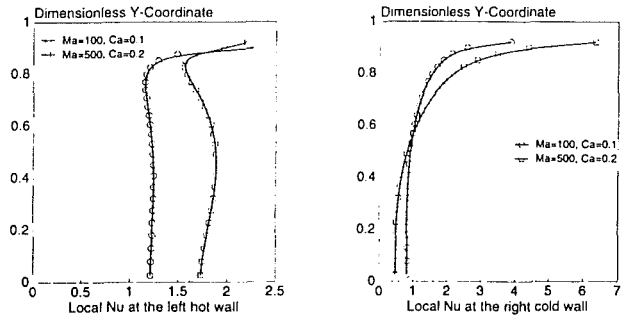


**Fig. 11 Nusselt number distribution along cavity walls for a 120 deg contact angle**

Nu on the hot wall has also moved to the free surface for flow with a 120 deg contact angle.

Figures 9 through 11 show a greater variation in Nu along a cavity wall for high Ma flow than for low Ma flow. This is consistent with the previously noted increase in intensity of vortex motion associated with increasing Ma. As flow intensity increases, advective transport enhances heat transfer leading to larger values of maximum Nu near the free surface at the cold wall. The increased heat transfer near the contact line lowers the temperature of the fluid flowing past the wall. This results in suppression of the Nu along the lower wall to values below those computed for lower Ma flow. The Nu distributions along the hot wall also show an increase of maximum Nu with increasing Ma.

It is interesting to note that although the flow patterns, temperature distributions, and Nu distributions are dependent on contact angle, the qualitative dependence of Marangoni convection on Ma and Ca is similar for all cases considered in this study.

## Summary and Conclusions

A new computational model was developed to predict thermocapillary convection in a cavity with a curved and deforming free surface. The volume-of-fluid algorithm is used to track free surface evolution through an Eulerian mesh. The normal surface tension force is modeled using a surface pressure model and the tangential surface tension gradient force is modeled using a modification of the Continuum Surface Force model. Computational predictions by this model are shown to be in good agreement with previous analytical and numerical results.

The influence of Ma and Ca on thermocapillary convection in a cavity is investigated for different static contact angles. Surface deformation is shown to increase with increasing Ca and larger distortion of isotherms is observed for higher Ma flows. For a given Ma and Ca, thermocapillary flow toward the cold wall is more pronounced for small contact angle flows than for large contact angle flows. Maximum local Nu and average Nu both increase with increasing Ma and the local maximum moves toward the free surface with increasing contact angle.

## Acknowledgments

This research was made possible by the support of the NASA Lewis Research Center under NCC3-176 and by the support of the Herff Internship of Memphis State University. The authors also wish to express their thanks to Dr. D. B. Kothe for his helpful discussions of free surface modeling.

## References

Chen, J. C., Sheu, J. C., and Jwu, S. S., 1990, "Numerical Computation of Thermocapillary Convection in a Rectangular Cavity," *Numerical Heat Transfer*, Part A, Vol. 17, pp. 287–308.

Cuvelier, C., and Drissen, J. M., 1986, "Thermocapillary Free Boundaries in Crystal Growth," *Journal of Fluid Mechanics*, Vol. 169, pp. 1–26.

Kothe, D. B., Mjolsness, R. C., and Torrey, M. D., 1991, "RIPPLE: A Computer Program for Incompressible Flows with Free Surfaces," LA-12007-MS, Los Alamos National Laboratory, New Mexico.

Nichols, B. D., Hirt, C. W., and Hotchkiss, R. S., 1980, "SOLA-VOF: A Solution Algorithm for Transient Fluid Flow with Multiple Free Boundaries," LA-8355, Los Alamos National Laboratory.

Ostrach, S., 1982, "Low Gravity Fluid Flows," *Annual Review Fluid Mechanics*, pp. 313–345.

Pimputkar, S. M., and Ostrach, S., 1980, "Transient Thermocapillary Flow in Thin Liquid Layers," *Physics of Fluids*, Vol. 23, No. 7, pp. 1281–1285.

Sasmal, G. P., 1993, "Numerical Modeling of Thermocapillary Convection with Curved and Deforming Free Surfaces," A doctoral dissertation, Memphis State University, Memphis, Tennessee.

Sen, A. K., and Davis, S. H., 1982, "Steady Thermocapillary Flows in Two-Dimensional Slots," *Journal of Fluid Mechanics*, Vol. 121, pp. 163–186.

Torrey, M. D., Cloutman, L. D., Mjolsness, R. C., and Hirt, C. W., 1985, "NASA-VOF2D: A Computer Program for Incompressible Flows with Free Surfaces," LA-10612-MS, Los Alamos National Laboratory.

Zebib, A., Homsy, G. M., and Meiburg, E., 1985, "High Marangoni Number Convection in a Square Cavity," *Physics of Fluids*, Vol. 12, pp. 3467–3476.

# The Effect of Interfacial Waves on the Transition to Slug Flow

**Eugene Kordyban**

**Abdul Hakim Okleh**

University of Detroit Mercy,
4001 W. McNichols,
Detroit, MI 48221

*It has been proposed by the authors that the transition to slug flow depends on the growth of waves in the two-phase flow and thus may predict if the laws of wave growth in closed channel are known. In this work, this proposition is tested by examining the highest waves and the transition to slug flow for air and water, air and water with surface tension reduced by addition of surface-active agents, air and water with increased viscosity by addition of corn syrup and air and ethanol. In each case it is found that the predicted transition to slug flow agrees well with experimental data. Neither a lower surface tension nor a higher viscosity has any effect on the transition to slug flow, but the use of surface active agents reduces the wave growth rate and causes the transition to slug flow to shift to higher gas velocities.*

## Introduction

The slug flow is rather unique among the two-phase flow patterns in that it is characterized by high pressure and flow rate fluctuations. The liquid slugs, driven at high velocity by the gas trapped behind them, have been known to damage conduits. Thus, the determination of the conditions under which slug flow exists is important for many industrial processes.

The first flow pattern map was introduced by Baker (1954), based strictly on experimental data. In this chart the transitions between flow patterns depend on liquid and gas flow rates modified somewhat by fluid properties. Actually, charts based on such criteria are somewhat misleading since the slugs are known to form on stationary liquid and it is the liquid level that is a better criterion for slug formation. The liquid level is not an easily measurable quantity, but it can be determined if the interfacial shear is known.

In the 70s, the transition to slug flow was studied in a more fundamental manner and a number of hypotheses were presented. Although they are based on different physical principles, they agree rather well with each other and the experimental data, but these were obtained for air and water.

More recently, Wu et al. (1987) have found that these theories do not agree well with the experimental data for hydrocarbon fluids at high pressure.

Kordyban has proposed previously (1990) that the transition to slug flow may be dependent on the rate of wave growth and used the data for wave height in air and water in support of his hypothesis.

In order to investigate this subject further, tests were conducted with water where the surface tension was reduced by the use of a surface-active agent, as well as test with water with additives to increase the viscosity.

The results obtained in this work are presented here.

Contributed by the Fluids Engineering Division for publication in the JOURNAL OF FLUIDS ENGINEERING. Manuscript received by the Fluids Engineering Division December 6, 1992; revised manuscript received December 7, 1993. Associate Technical Editor: O. C. Jones.

## Background

In 1970, Kordyban and Ranov (1970) published a paper which described an experimental and theoretical investigation into the transition to slug flow and proposed that this transition is due to the Kelvin-Helmholtz instability of nonlinear waves. They found that, in order to predict the transition, the knowledge of the wavelength is necessary. It is interesting to note that a similar conclusion was reached by Ahmed and Banerjee (1985) who performed a much more sophisticated mathematical analysis.

Wallis and Dobson (1973) were able to correlate their experimental results quite well on a $J^* - \alpha$ graph and the resulting curve was expressible by a simple equation.

$$J^* = 1/2\alpha^{3/2} \tag{1}$$

Kordyban (1977a) obtained data for the transition to slug flow in a rectangular channel. The data correlated quite well on a $J^* - \alpha$ graph, but deviated somewhat from the Wallis-Dobson equation. It did agree, however, with the relationship of Taitel and Dukler (1976) who also assumed Kelvin-Helmholtz instability as the cause for the transition to slug flow and introduced an empirical constant to account for the lower threshold of instability for nonlinear waves.

It should be noted that in the latter relationships the wavelength is not needed to predict the transition to slug flow. In fact, Wallis and Dobson, in the course of their investigation, observed various shapes of waves, while in Kordyban's experiments the wavelength varied by a factor greater than 10, and yet all the data could be correlated by a single curve. These facts seem to indicate that the wave is simply a conveyance whose crest brings the liquid surface into the high velocity field where it becomes unstable. This, in fact, was confirmed by a photographic study of unstable waves by Kordyban (1985). He found that, just prior to the formation of a slug, the hitherto smooth crest of the waves breaks up into ripples and it is one of the ripples that grows to become a slug.

There are several other relationships which were developed and all agree reasonably well with each other and with the

data, but it should be noted that all the data have been obtained for air and water at atmospheric pressure. While the ratio of densities is taken into account in the existing relationships, there is no mechanism in them to consider the role of viscosity or surface tension.

The Taitel and Dukler relationship seems to have found favor with the workers in the field, but in applying it to hydrocarbon fluids, Wu et al. (1987) have found a marked difference between it and the actual transition to slug flow in the sense that the actual transition occurs at higher gas velocities. Since their experiments were conducted in an 8-in. diameter tube at a pressure of 75 bar, the authors attribute this difference to high pressure and apply an instability analysis for linear waves developed by Wallis.

It appears rather doubtful, however, that a linear theory is really applicable here in view of the rather detailed studies of instability described previously. It is felt that the discrepancy is due to a different rate of wave growth which, as shown here, appears to be the only factor determining the transition to slug flow.

A note on the instability of liquid surface should be added here, since there appears to be some confusion on this subject. In considering the formation of slugs two instabilities should be considered. The first of these is the instability of the plane liquid surface resulting in the formation and growth of waves. This does not seem to be the Kelvin-Helmholtz instability, since the growth of waves is relatively slow and orderly. As the waves grow and approach the channel top, a second instability occurs. This is the Kelvin-Helmholtz instability which results in explosive growth of a wave which then becomes a slug. This is the instability dealt with in this work.

## Theory

Since the wavelength or shape seems to play no role in the transition to slug flow, Kordyban (1990) has proposed that the transition to slug flow may be obtained by studying the laws of wave growth. In his study of the wave instability he derived a criterion for the transition to slug flow considering the force balance on the wave.

Referring to Fig. 1, the origin is placed at the wave crest and, the upward force on an element of liquid at the crest due to aerodynamic pressure is

$$(p-p_c)dx.$$

The restoring force due to gravity is

$$g(\rho_l-\rho_g)\eta dx$$

From Bernoulli equation

$$p-p_c=\frac{\rho_g V_c^2}{2}\left[1-\left(\frac{h_c}{h_c+\eta}\right)^2\right] \tag{1}$$

In his study of aerodynamic pressure due to gas flowing over a wavy liquid surface Kordyban (1977b) found that a better agreement with experiment is obtained if the pressure difference in Eq. (1) is multiplied by 1.35. Furthermore, the term in brackets may be expanded. Thus modified Eq. (1) becomes

$$p-p_c=\frac{1.35\rho_a V_c^2}{2}\left[1-1+2\frac{\eta}{h_c}-3\frac{\eta^2}{h_c^2}+\ ,\ ,\ ,\right] \tag{2}$$

Limiting our range to the vicinity of crest where $\eta \ll h_c$ we have

$$p-p_c=\frac{1.35\rho_a V_c^2\eta}{h_c} \tag{3}$$

At instability the upward and the restoring force are equal, thus

$$(p-p_c)dx=g(\rho_l-\rho_g)\eta dx;\quad \frac{1.35V_c^2}{gh_c}\cdot\frac{\rho_g}{\rho_l-\rho_g}=1 \tag{4}$$

This equation, while derived assuming that the Kelvin-Helmholtz instability occurs first at the wave crest, rather than over the whole wave and agrees fairly well with experimental data, is not usable in practice, since $h_c$ is not an easily determinable quantity. It can be expressed, however, in Wallis-Dobson notation by the following process.

The continuity equation can be expressed as

$$JH=V_c h_c \tag{5}$$

Since, for high waves, the mean level is nearly one third of the wave height from the trough, which has been found from the work of Kordyban (1977b) for the range of gas velocities under consideration here,

$$h_c=H-h_w-\frac{2}{3}h, \tag{6}$$

and, for rectangular channel,

$$\frac{h_c}{H}=\alpha-\frac{2}{3}\frac{h}{H} \tag{7}$$

Substituting into Eq. (4) we have

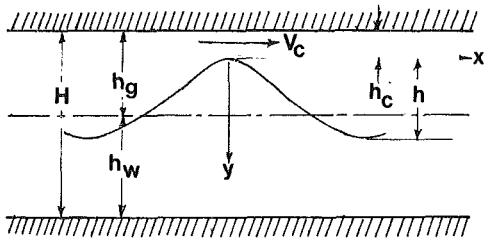


Fig. 1 Schematic of wave and associated nomenclature

## Nomenclature

$c$ = wave speed
$D$ = pipe diameter
$g$ = acceleration of gravity
$h$ = wave height
$H$ = total channel depth
$h_c$ = the distance from wave crest to the channel top
$h_w$ = liquid level
$J$ = superficial gas velocity (Wallis-Dobson relationship)
$J^*$ = $J\left[\frac{\rho_g}{\rho_l-\rho_g}\Big/gH\right]^{1/2}$
$k$ = wave number
$p$ = pressure
$P_c$ = pressure at the crest
$r$ = pipe radius
$U_{SG}$ = superficial gas velocity (Lin Hanratty relationship)
$V$ = gas velocity
$V_g$ = mean gas velocity
$V_c$ = gas velocity at the crest
$X$ = fetch, the distance from the point of tangency of the guide plate at entrance to the point of measurement
$\alpha$ = void fraction
$\lambda$ = wavelength
$\nu$ = kinematic viscosity of liquid
$\rho_g$ = gas density
$\rho_l$ = liquid density
$\sigma$ = surface tension
$\theta_c$ = defined in Fig. 12
$\eta$ = surface elevation measured from crest
$\omega$ = wave frequency

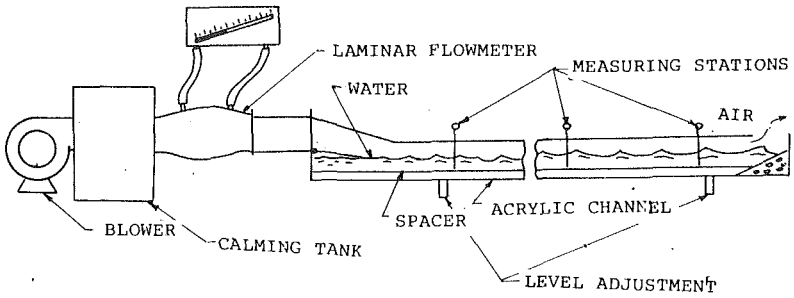


Fig. 2 Schematic of equipment and instrumentation

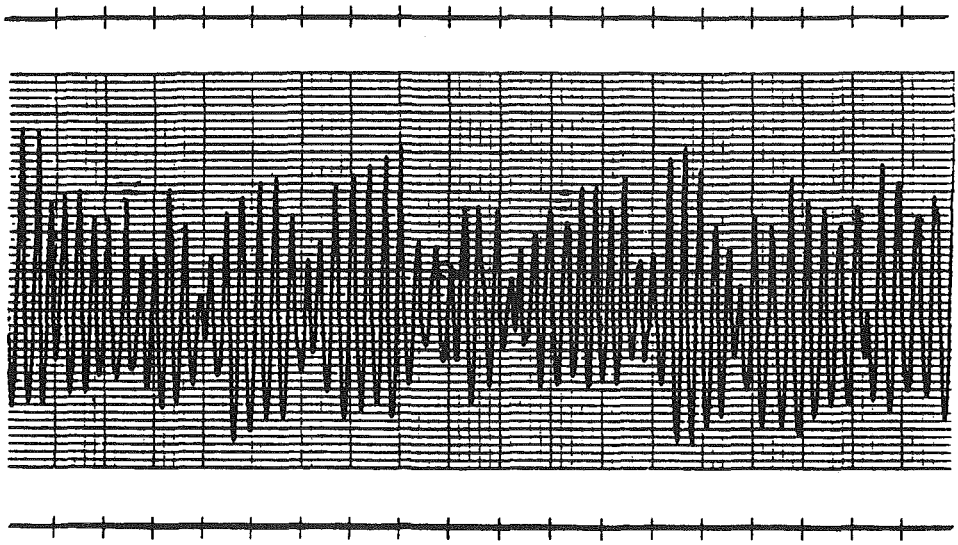

Fig. 3 Portion of oscillograph record showing waves of various heights

$$\frac{1.35J^2}{Hg\left(\alpha-\frac{2}{3}\frac{h}{H}\right)^3}\cdot\frac{\rho_g}{\rho_l-\rho_g}=1$$

and solving for $J$

$$J=\sqrt{\frac{1}{1.35}}\left[\frac{\rho_l-\rho_g}{\rho_g}\cdot Hg\left(\alpha-\frac{2}{3}\frac{h}{H}\right)^3\right]^{1/2} \tag{8}$$

and using Wallis-Dobson notation for dimensionless volume flux $J^*$, we have

$$J^*=0.861\left(\alpha-\frac{2}{3}\frac{h}{H}\right)^{3/2}=0.861\left(\frac{h_c}{H}\right)^{3/2} \tag{9}$$

Equation (9) clearly indicates the necessity for the knowledge of the wave height.

## The Wave Growth for Air and Water

**Experimental Work Equipment and Instrumentation.** The tests were conducted in a channel made of transparent acrylic plastic 10 cm deep, 15 cm wide, and about 5 m long, shown in Fig. 2. The upstream end was equipped with an air entry which contained a guide plate extending to the liquid surface. This permitted the initial tangential contact between air and water. The downstream end had a sloping beach made of screens and gravel to minimize the reflection of the waves. The channel was mounted on adjustable supports which permitted the variation of the slope.

The liquid level was measured by means of electrical conductivity gages which consisted of two parallel platinum wires 0.127 mm in diameter and about 3 mm apart located in a vertical plane in the channel. They were connected to a bridge amplifier powered by 400 Hertz a-c and the results were displayed on a recorder to permit the examination of wave characteristics and to determine the maximum wave heights. The rms value of the wave height was determined by a true rms voltmeter capable of measuring the signal accurately down to 0.1 Hertz. A band pass filter was used to determine the mean liquid level of the wavy surface. The gages were frequently calibrated by comparing their readings to those of a hook gage for level liquid surface.

**Test Procedures.** All tests were conducted on nominally stationary liquid. Two types of tests were conducted. In the first of these, the rms wave height was determined as a function of air velocity and the distance from the initial contact between air and the liquid, commonly known as fetch. For this purpose three measuring stations were employed, placed along the channel. For each water level a particular air velocity was set and the slope of the channel was adjusted to obtain equal liquid levels at all measuring stations. Once an equilibrium was attained, the measurements of the air velocity and of the wave height were taken. Since the waves produced by a particular air velocity are of variable height, it was decided to use the rms value as the significant wave height. A typical oscillograph record is shown in Fig. 3.

In the second series of tests, the transition to slug flow was determined, as well as the highest waves just prior to the formation of slugs. To accomplish this the air velocity was increased in steps for each liquid level, until it was judged that the formation of slugs was impending. At that point the velocity was increased in very small steps, while the recorder measuring the wave heights was run. This was continued until the first slugs appeared, when the value of air velocity, of the

**Table 1 Properties of liquids used in the experiments**

| Liquid | Density kg/m$^3$ | Viscosity cp | Surface tension N/m |
|---|---|---|---|
| Water | 998 | 1.0 | 0.073 |
| Water with 25% syrup | 1087 | 2.63 | 0.073 |
| Water with soap | 998 | 1.0 | 0.039 |
| 95% Ethanol | 800 | 1.2 | 0.023 |

mean liquid level and of the wave height was recorded. The void fraction was found directly as a ratio of cross section occupied by air to total area of channel. The properties of various liquids are shown in Table 1.

## The Tests With Air and Water

The results of the tests with air and water are taken from previous work by Kordyban (1977a, 1978). They were conducted according to the procedures described in the previous section and are used here for comparison with results of tests with other fluids.

While much information is available on the wave growth under the action of wind, the conditions in a conduit of limited cross section are significantly different. The mechanism of producing the initial disturbance on smooth liquid surface is probably identical on open bodies of water and closed channels, but as the waves grow, the negative pressure at the crest is substantially higher in the latter case.

In order to determine some relationships for wave growth under conditions more closely related to slug formation, Kordyban (1978) has studied the growth of water waves in a channel described here.

Some conclusions which may be drawn from this work are:

1. As the waves proceed down the channel, they grow not only in height, but also increase in length and retain a height to length ratio of approximately 0.1.
2. The growth is exponential until the ratio of water depth to wave length reaches about 0.6. At that point, probably due to increased losses at the bottom, the growth rate falls off and, at a depth to wave length ratio of 0.28, the growth ceases, so that an equilibrium wave length, independent of gas velocity is reached. This is not expected to continue indefinitely, because at very high gas velocities the regular structure of the waves is broken up with much turbulence and spray. Figure 4 shows the exponential growth in the region where it is independent of liquid depth.

In the work described by Kordyban (1977) the transition to slug flow for air and water in the rectangular channel described above was studied. During these tests the height of the highest waves just prior to the transition to slug flow was measured. These values are used here to determine whether Eq. (9) agrees with experimental data.

When the values of wave heights were inserted into Eq. (9), $J^*$ thus calculated was plotted as a function of the void fraction $\alpha$ in Fig. 5 where the results correlate fairly cleanly by a single curve. Superimposing this curve upon the data for the transition to slug flow in Fig. 6, it is seen to form an upper bound to the data. This is reasonable, because it is not the measured waves, but rather the next higher ones which became unstable and formed the slugs. In Fig. 6 the values of $J^*$ were calculated using the measured values of air flow rate.

## Wave Growth for Water With Surface Tension Reduced by a Surface-Active Agent

To test the dependence of slug formation on wave height, it was decided to perform experiments with fluids which possess properties substantially different from those for water. The

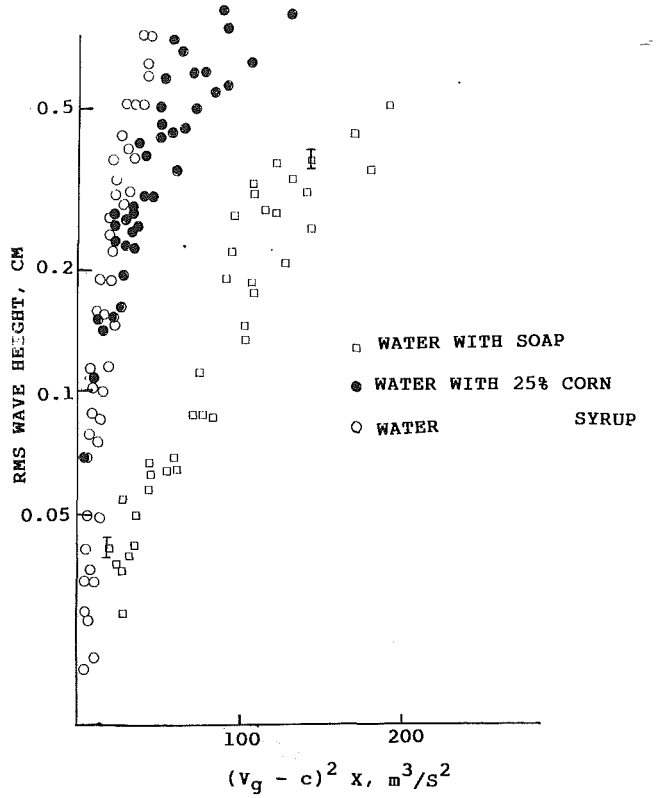


**Fig. 4 RMS wave height as a function of air velocity and fetch for various liquids in the exponential part of wave growth [uncertainty estimate, wave height less than 5 percent $(V_g - c)^2$ X less than 2 percent]. Uncertainty estimates as shown by bars apply to all points in the proportion shown.**

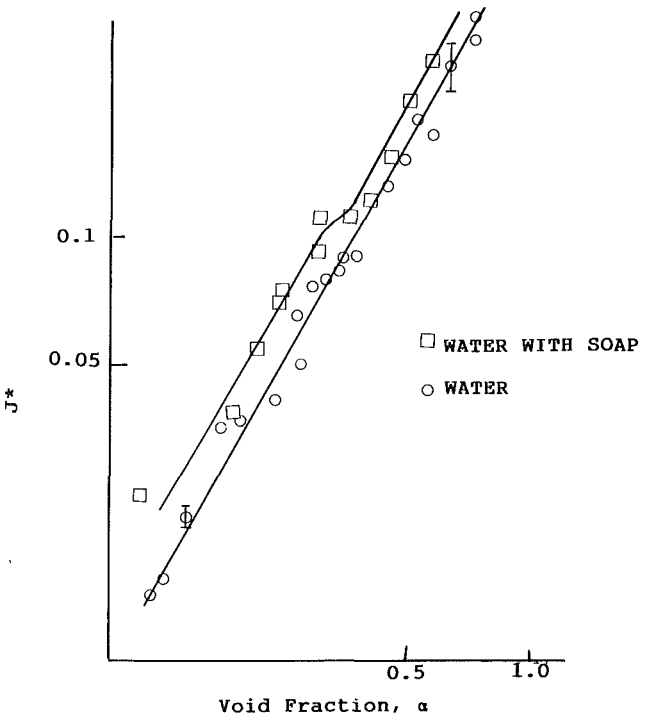


**Fig. 5 $J^*$ calculated from Eq. (9) based on maximum wave height for water and water with soap. [Uncertainty estimate, $J^*$ less than 15 percent, $\alpha$ less than 4 percent.] Uncertainty estimates as shown by bars apply to all points in the proportion shown.**

**Table 2 Results of measurements for various fluids at the transition to slug flow**

A. Air and water with soap

| Superficial air velocity m/s | Mean liquid level cm | Superficial air velocity m/s | Distance from crest to top of channel cm |
|---|---|---|---|
| 1.26 | 8.10 | 1.20 | 0.952 |
| 1.74 | 7.62 | 1.64 | 1.28 |
| 2.21 | 7.30 | 1.90 | 2.54 |
| 2.38 | 6.99 | 2.21 | 1.59 |
| 2.41 | 7.08 | 2.26 | 1.27 |
| 2.71 | 6.66 | 2.51 | 1.90 |
| 2.92 | 6.51 | 2.59 | 1.90 |
| 3.08 | 6.40 | 2.93 | 2.54 |
| 3.25 | 5.87 | 3.33 | 2.22 |
| 3.50 | 6.03 | 4.00 | 2.54 |
| 3.59 | 5.87 | 4.69 | 2.54 |
| 3.90 | 5.24 | 5.46 | 3.17 |
| 3.93 | 4.93 | 5.98 | 3.81 |
| 4.47 | 4.60 | 6.81 | 3.81 |
| 4.47 | 5.08 | 7.42 | 4.44 |
| 4.95 | 4.29 | | |
| 5.06 | 4.36 | | |
| 5.97 | 3.81 | | |
| 6.39 | 3.81 | | |
| 6.99 | 3.49 | | |

B. Air and water with 25% syrup

| Superficial air velocity m/s | Mean liquid level cm | Distance from crest to top of channel cm |
|---|---|---|
| 1.89 | 7.24 | 2.10 |
| 1.93 | 6.91 | 1.63 |
| 2.35 | 6.48 | 2.97 |
| 2.51 | 6.30 | 1.63 |
| 2.87 | 5.59 | 3.86 |
| 3.18 | 5.28 | 2.03 |
| 3.69 | 4.83 | 4.19 |
| 3.94 | 4.32 | 3.86 |
| 3.94 | 4.52 | 1.75 |

C. Air and 95% ethanol

| Superficial air velocity m/s | Mean liquid level cm | Distance from crest to top of channel cm |
|---|---|---|
| 2.29 | 6.35 | 2.53 |
| 2.79 | 5.72 | 2.79 |
| 2.82 | 5.84 | 2.53 |
| 3.20 | 5.33 | 3.17 |
| 3.24 | 5.33 | 3.04 |
| 3.39 | 5.72 | 2.85 |
| 3.62 | 4.83 | 3.55 |
| 2.73 | 4.70 | 3.81 |
| 2.94 | 5.08 | 3.81 |
| 4.02 | 4.45 | 3.94 |
| 4.07 | 4.45 | 3.94 |
| 4.42 | 4.45 | 4.44 |
| 4.55 | 4.45 | 4.37 |
| 5.47 | 3.81 | 5.39 |
| 5.49 | 3.81 | 5.24 |
| 6.24 | 3.81 | 5.07 |
| 6.45 | 3.18 | 5.88 |

theory accounts for the density and the two properties of significance appear to be surface tension and viscosity. Since hydrocarbon liquids, such as crude oil or kerosene, have both a lower surface tension and a higher viscosity than water, a somewhat different approach was taken to separate the effects of these two properties.

In order to determine the effect of lower surface tension, the tests were conducted in the same equipment and under similar conditions as those for water, except that sufficient liquid soap was added to water to reduce the surface tension to 0.039N/m. The viscosity of the mixture was checked and found to be within 5 percent of that of water.

The results of these tests are shown in Table 2 and in Figs. 4, 5, and 6 where an easy comparison with those of air and water can be made. Figure 4 shows the growth of waves. It will be noted that the growth, at least initially, is exponential, but the rate of growth is much lower than that for water and

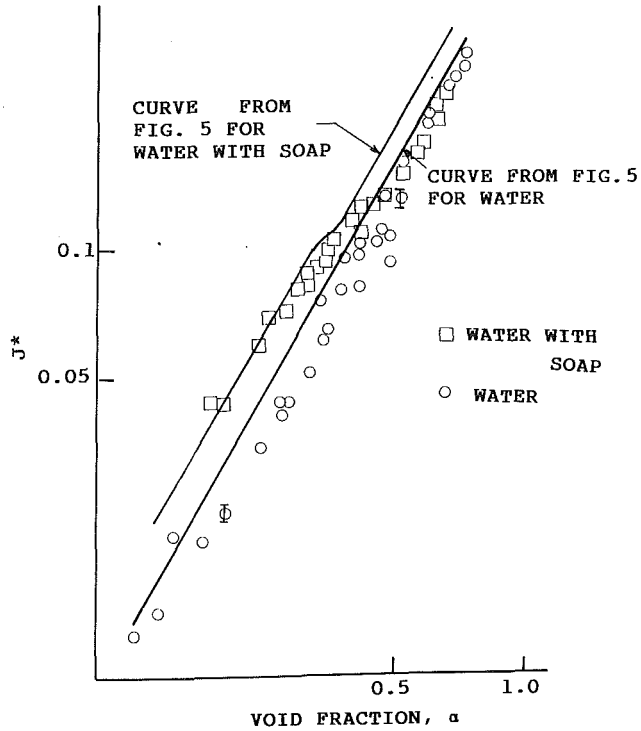


**Fig. 6 Transition to slug flow for water and water with soap. [Uncertainty estimate, $J^*$ less than 3 percent, $\alpha$ less than 4 percent]. Uncertainty estimates as shown by bars apply to all points in the proportion shown.**

this was initially attributed to the reduced surface tension. Further study uncovered that the damping of capillary waves by surface active agents has been studied previously and considerable literature is available on this subject, e.g., Levich (1962). While originally some investigators considered the lower surface tension itself to be responsible for the damping, because the gas could not "grab" the liquids as easily, modern theories propose the existence of a surface tension gradient on the wavy surface.

It can be shown mathematically that such gradient produces wave damping. The effect is most prominent in capillary waves, but, although our waves reach up to 10 cm in length, they are still affected by the surface tension gradient.

Figure 5 shows $J^*$ calculated from Eq. (9) using the value of the highest waves as a function of the void fraction $\alpha$. When the mean curve from Fig. 5 was plotted in Fig. 6, it still forms an upper bound to the data for the transition to slug flow, indicating the validity of Eq. (9).

Another interesting fact can be observed in Fig. 6. While at lower values of the void fraction $\alpha$ there is significant difference between the transition to slug flow for pure water and water and soap, at a value of $\alpha$ about 0.5 the two sets of data become almost coincident. While this deserves a further study, a possible explanation may lie in the fact that, at higher values of $\alpha$, the liquid level is low and thus equilibrium waves are attained faster. For these waves the rate of growth is of no consequence.

## Tests on Water With Increased Viscosity

After experimenting with several mixtures it was decided that the addition of corn syrup presented the best alternative since the viscosity of the liquid could be changed readily without affecting the surface tension. For these tests, a 25 percent addition (by volume) of corn syrup was found to increase the viscosity of the mixture to 2.63 cp at room temperature, while the surface tension remained equal to that of water within the accuracy of our tensiomat.

It should be noted that maintaining accurately proper surface

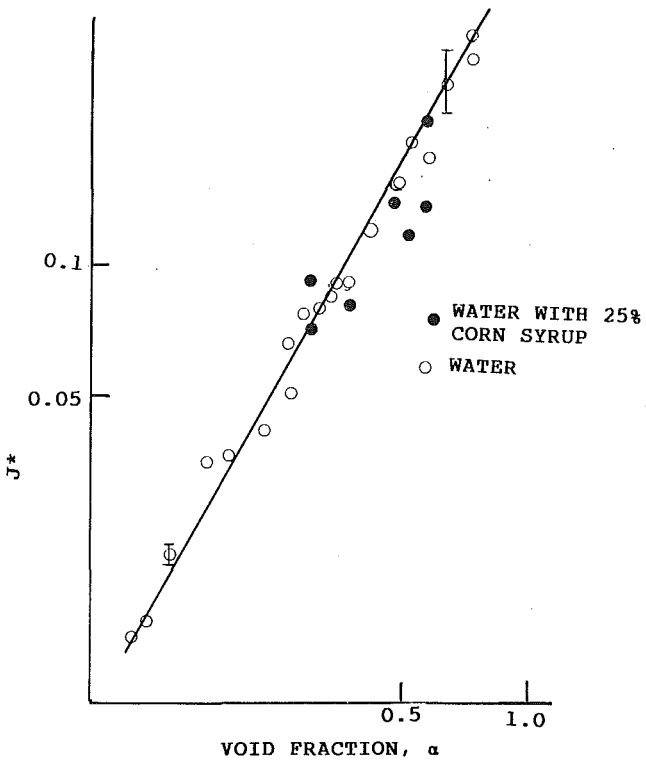


Fig. 7 $J^*$ calculated from Eq. (9) based on measured maximum wave height for water and 25 percent syrup [uncertainty, see caption in Fig. 5]

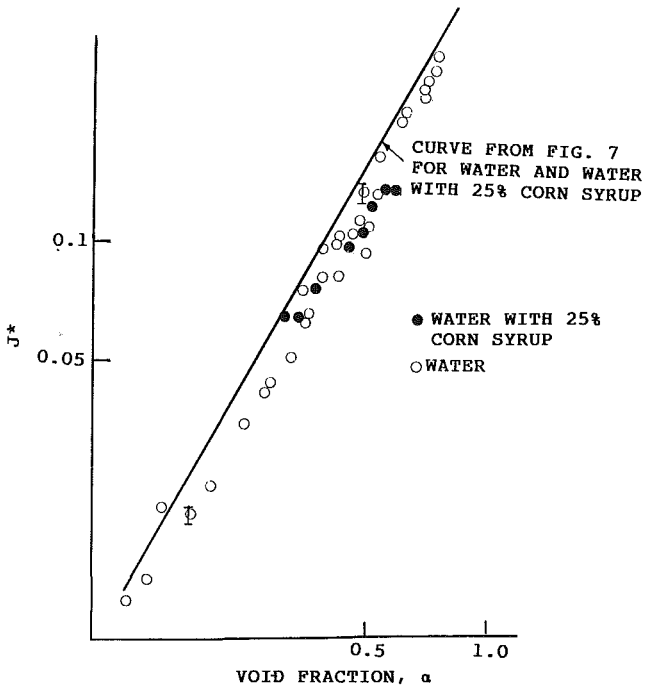


Fig. 8 Transition to slug flow for water and water with syrup [uncertainty, see caption in Fig. 6]

tension is not an easy task, since the contamination affects it to a considerable degree. Furthermore, the syrup-water mixture promotes the growth of microorganisms, which tend to foul the test setup. Therefore, we attempted to conduct the tests rapidly, usually in the course of one day. The addition of syrup to water also tends to increase the electrical conductivity, which is of concern, since the conductivity is used to measure the liquid level. It was found, however, that for the 25 percent addition of syrup the conductivity was still sufficiently low, so that it did not require any major adjustments in our instrumentation.

The tests conducted with water-corn syrup mixture were identical to those for water with soap and the results are shown in Figs. 4, 7, and 8.

It will be noted in Fig. 4 that the wave growth is practically the same as that of pure water, but there is some decrease at the high end. This seems to confirm the supposition that the deviation from the exponential growth is due to friction losses at the bottom of the channel. Higher viscosity would increase such losses.

The curve of $J^*$ calculated from Eq. (9) using the values of the highest waves, as shown in Fig. 4, is identical to that from pure water, as are the data for the transition to slug flow in Fig. 8. Thus the data indicate that there is no effect of increased viscosity on the formation of slugs. It should be noted, however, that our range of viscosities is quite narrow.

This is to be expected. Levich (1962) shows that the viscosity terms may be omitted in wave equations if

$$\frac{\omega\lambda^2}{\nu} \gg 1 \tag{10}$$

But, for deep water waves,

$$C = \frac{\omega}{k}$$

and

$$C = \sqrt{\frac{\sigma k}{\rho_l} + \frac{g}{k}}$$

then Eq. (10) becomes

$$\frac{k\sqrt{\frac{\sigma k}{\rho_l} + g/k} \cdot \left(\frac{2\pi}{k}\right)^2}{\nu} \gg 1 \tag{11}$$

Since we are dealing with the waves of 5 cm and longer, the left-hand member of Eq. (5) is $9.27 \times 10^4$ for water and $3.52 \times 10^3$ for water-syrup mixture, so that this condition is well satisfied.

For highly viscous fluids, the effect of viscosity would probably be to retard the formation of slugs.

## Tests With 95% Ethanol

Having realized that the introduction of surface active agents introduces considerable complications, it was decided to conduct tests with a liquid which has naturally lower surface tension and 95 percent ethanol was selected for this purpose. Kerosene was also considered, but since it is not electrically conductive, its use would have required a considerable redesign of our liquid level measuring system.

Again, the same series of tests was conducted and the results are shown in Figs. 9, 10, and 11. The wave growth here was much more rapid and, by the time the first measuring station was reached, the waves were already past their exponential growth and, therefore, in Fig. 9 the comparison is made with water where the wave growth is reduced by the friction at the bottom. It will be noted that, although initially the waves on ethanol are substantially higher, their equilibrium values are not much different from those on water.

This, in fact, is noted in Fig. 10 where the highest waves for ethanol are practically the same as for water and the transition to slugs in Fig. 11 does not differ from that for water. Thus, the tests seem to indicate that even a substantial reduction in surface tension has no effect on transition to slug flow.

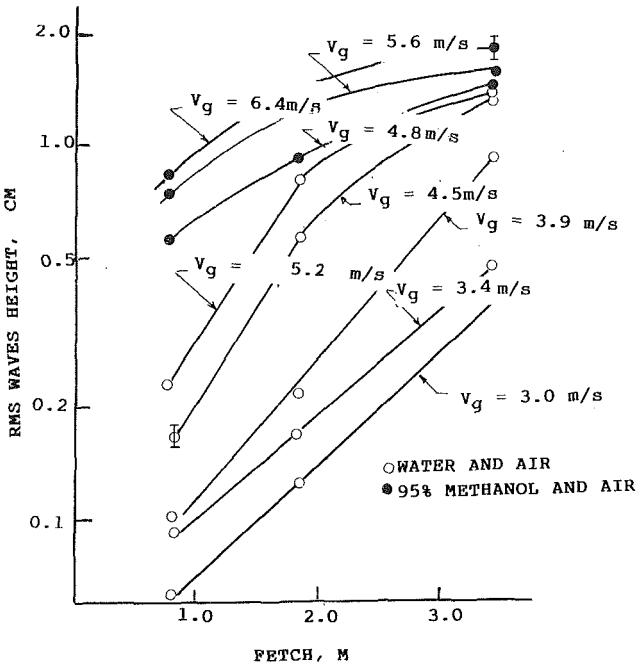


Fig. 9 RMS wave height as a function of air velocity and fetch for water and 95 percent ethanol [uncertainty, wave height less than 5 percent, velocity less than 3 percent, fetch less than 1 percent]. Uncertainty estimates as shown by bars apply to all points in the proportion shown.

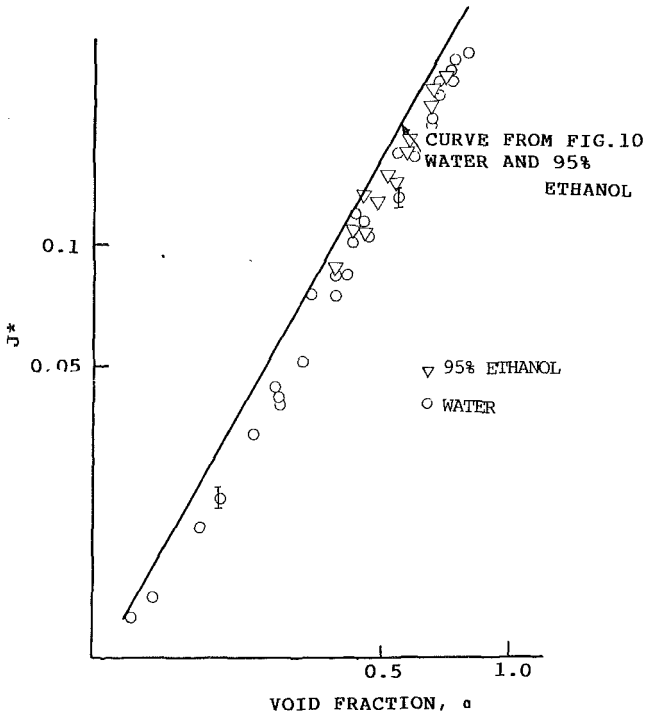


Fig. 11 Transition to slug flow for water and 95 percent ethanol [uncertainty, see caption, Fig. 6]

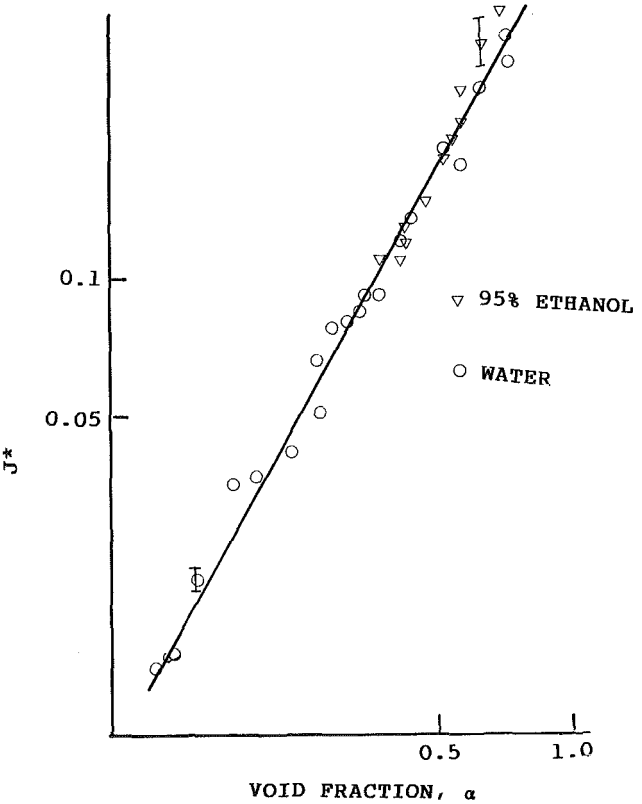


Fig. 10 $J^*$ calculated from Eq. (9) based on measured maximum wave height for water and 95 percent ethanol, [uncertainty, see caption Fig. 5]

## Uncertainty Estimates

The following estimates are based on maximum uncertainty.

The primary quantities measured in this work are liquid level, gas flow rate, and distance from the wave crest to the top of the channel for the transition to slug flow tests. For the wave growth tests, the liquid level, wave height, and the gas flow rate were measured.

The superficial gas velocity was determined from the flow rate by dividing it by the total channel cross section. Since the cross-sectional area is found with negligible uncertainty, the maximum uncertainty for the superficial gas velocity is the same as for the flow rate. It is estimated to be.

3 percent at $J=2$ m/s

1 percent at $J=6$ m/s

The liquid level measured by electrical conductivity gages is judged to be accurate within $\pm 1$ mm. Thus the uncertainty in determining the void fraction $\alpha$ is

2 percent at $\alpha=0.2$

4 percent at $\alpha=0.7$

the uncertainty in the measurement of the distance from the wave crest is estimated to be

10 percent at $h_c=1$ cm

2.5 percent at $h_c=4$ cm

The wave height uncertainty is estimated to be $\pm 5$ percent.

The derived quantities are nondimensionless superficial gas velocity $J^*$ both as found from $J$ and as calculated from Eq. (9) and the actual gas velocity.

Since

$$J^* = J\sqrt{\frac{\rho_g}{\rho_l - \rho_g}\frac{1}{gH}}$$

and the quantities under the radical can be determined with negligible uncertainty, then the uncertainty in $J^*$ is

3 percent at $J^*=0.07$

1 percent at $J^*=0.20$

$J^*$ as calculated from Eq. (9) is

$$J^* = 0.861\left(\alpha - \frac{2}{3}\frac{h}{H}\right)^{3/2} = 0.861(h_c)^{3/2}$$

and its uncertainty is estimated to be

15 percent at $J^* = 0.02$

5 percent at $J^* = 0.20$

the actual gas velocity is found by dividing the flow rate by actual gas flow cross sectional area. The uncertainty is estimated to be

2 percent at $V = 3$ m/s

3 percent at $V = 6$ m/s

## Discussion of Results

The main purpose of this work was to show that the formation of the slugs is related to the growth of liquid waves and, within the scope of the data obtained, this has been demonstrated. The advantage of this hypothesis as compared to others described here lies in the fact that it opens up the possibility of taking into account the effect of various properties and thus may explain the difference between the transition to slug flow for water and other liquids.

While a logical explanation is offered in this work for the appearance of slugs, it does not present a practical method for predicting the transition to slug flow. Rather, it points the way to the complete solution of this problem, namely, by the study of the laws of wave growth under the influence of a gas flowing parallel to the liquid surface.

The literature abounds in the reports on work conducted to investigate the growth of waves. Most of those, however, were carried out with the purpose to uncover the mechanism by which the wind raises waves on open bodies of water and thus are not entirely applicable to the case of two-phase flow. There are two main differences between these cases:

1. The two-phase flow conduits are usually long and relatively small in cross section. As the waves grow in length, they must eventually become shallow-water waves.
2. The pressure variation in the gas over the wavy liquid surface is significantly affected by the proximity of the upper wall.

As far as we discovered, not much is known about the wave growth under such conditions. Some work on two-phase flow waves has been performed in the study of liquid films. Such waves, however, are very small and again out of range applicable to this investigation.

The use of various liquids in this work also permits making some general conclusions. Neither moderate increase in viscosity nor a substantial decrease in surface tension appear to have any effect on the transition to slug flow. In this, the results of this study tend to support the previous hypotheses, which ignored the effects of these properties.

The observation that the use of surface active agents suppresses the formation of slugs over a certain gas velocity range and thus produces a disagreement with the previous hypotheses is, it is felt, a significant contribution of this work. It should be noted that this is accomplished through the damping of the waves, thus tending to confirm further the main proposition of this work, namely, that the formation of the slugs is related to the wave growth.

It should be noted that Weisman et al. (1979) have also studied the transition to slug flow for air and water to which surface active agents were added. Contrary to our results, they found no effect of this addition on the transition to slug flow. While there is no reason to doubt the validity of their results, we are quite certain of our findings, since the retardation of the slug formation was clearly visible, even to unaided eye. This, in our opinion, points to the need for further study of this phenomenon, particularly, since there are many practical situations in which the retardation of slug formation is desirable and the use of surface active agents may be possible.

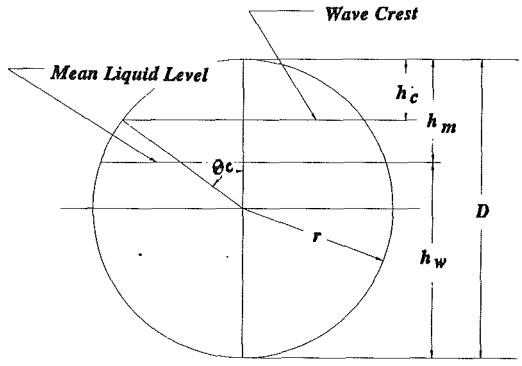


Fig. 12 Geometry of pipe flow

Unresolved remains the question why in the work of Wu et al. (1987) there is a delay in the transition to slug for hydrocarbon fluids at high pressure. Based on this work one might expect a reduced wave growth under these conditions, but the cause for this is unknown at this time.

The experimental portion of this work was carried out in rectangular channel, while most of the flows in practice occur in tubes of circular cross section. Assuming that the onset of wave instability, is a local phenomenon, the mechanism of this instability should be the same for rectangular channel and round tubes. The studies of transition to slug flow in tubes of circular section have been performed by a number of investigators, but the results of Lin and Hanratty (1987) are most suitable for comparison with our data.

To accomplish this comparison we turn to basic equation for wave instability, namely, Eq. (4).

Referring to Fig. 12, we have, by continuity,

$$V_c r^2\left[\theta_c - \frac{1}{2}\sin 2\theta_c\right] = U_{GS}\cdot\pi r^2$$

$$V_c = U_{GS}\frac{\pi}{\theta_c - \frac{1}{2}\sin 2\theta_c}$$

also

$$h_c = (1-\cos\theta_c)r$$

substituting this in Eq. (4)

$$\frac{1.35U_{GS}}{gr}\cdot\frac{\pi^2}{(1-\cos\theta_c)\left(\theta_c - \frac{1}{2}\sin 2\theta_c\right)^2}\cdot\frac{\rho_g}{\rho_l - \rho_g} = 1$$

or

$$\frac{U_{GS}}{\sqrt{gD}} = \frac{\theta_c - \frac{1}{2}\sin 2\theta_c}{\pi}\left(\frac{1-\cos\theta_c}{2x1.35}\cdot\frac{\rho_l}{\rho_l - \rho_g}\right)^{1/2}$$

$\theta_c$ may be determined if the average level and the wave height are known

$$h_c = H - h_w - h = (1-\cos\theta_c)r$$

and

$$\theta_c = \cos^{-1}\left[1 - \frac{H - h_w - h}{r}\right] \tag{12}$$

The other coordinate in Fig. 13 is the ratio of the mean liquid level to the diameter and we shall interpret it as $h_w/H$, or $1 - \alpha$.

Figure 13 contains the data of Lin and Hanratty; we also

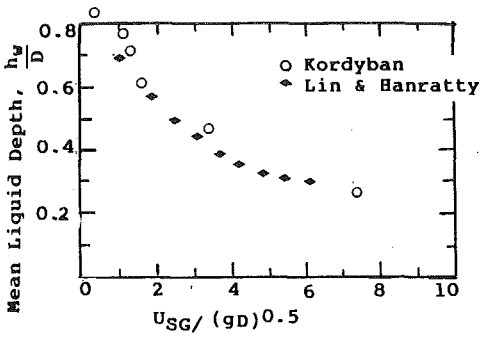


**Fig. 13 Comparison of transition to slug flow for air and water. Data of Kordyban (1977a) for rectangular channel and of Lin and Hanratty (1987) for circular pipe.**

plotted a few of the points from our data for air and water. As may be seen from this figure, there is a fair agreement between the two sets of data, so that the basic mechanism appears to hold for both geometries.

Another point important to note is that, while in our experiments there was no mean motion of water, Lin and Hanratty worked with flowing water. Thus the mean liquid velocity also appears not to have any effect on the transition to slug flow.

## Conclusions

1. The results of work described in this paper indicate that the transition to slug flow is tied to the growth of interfacial waves and can be predicted, if such growth is understood.
2. Neither a moderate increase in viscosity of the liquid nor substantial decrease in surface tension have an effect on the transition to slug flow.
3. The addition of a surface active agent reduces the wave growth and thus retards the transition to slug flow. This appears to be due not to the reduction of surface tension, but rather due to the presence of surface tension gradient.

## References

Ahmed, R., and Banerjee, S., 1985, "Finite Amplitude Waves in Stratified Two-Phase: Transition to Slug Flow," *AIChE Journal*, Vol. 11, p. 1480.

Baker, O., 1954, "Design of Pipeline for Simultaneous Flow of Oil and Gas," *The Oil and Gas Journal*, July 26.

Kordyban, E., and Ranov, T., 1970, "Mechanism of Slug Formation in Horizontal Two-Phase Flow," ASME *Journal of Basic Engineering*, Vol. 92, pp. 857–864.

Kordyban, E., 1977a, "The Transition to Slug Flow in the Presence of Large Waves," *International Journal Multi-Phase Flow*, pp. 603–607.

Kordyban, E., 1977b, "Some Characteristics of Waves Approaching Kelvin-Helmholtz Instability," ASME JOURNAL OF FLUIDS ENGINEERING, Vol. 99.

Kordyban, E., 1978, "Growth of Interfacial Waves in Closed Horizontal Channels," ASME Paper 78WA/FE-8, Presented at ASME Winter Annual Meeting, San Francisco, CA.

Kordyban, E., 1985, "Some Details of Developing Slugs in Horizontal Two-Phase Flow," *AIChE Journal*, Vol. 31, p. 82.

Kordyban, E., 1990, "The Effect of Waves on the Transition to Slug Flow," *Cavitation and Polyphase Forum*, ASME Publication.

Levich, V. G., 1962, *Physicochemical Hydrodynamics*, Prentice-Hall.

Lin, P. Y., and Hanratty, T. J., 1987, "Detection of Slug Flow from Pressure Measurements," *International Journal of Multiphase Flow*, Vol. 13, pp. 13–21.

Taitel, Y., and Dukler, A. E., 1976, "A Model for Predicting Flow Regime Transitions in Horizontal and Near Horizontal Gas Liquid Flow," *AIChE Journal*, Vol. 22, p. 47.

Weisman, J., Ducan, D., Gibson, J., and Crawford, J., 1979, "Effects of Fluid Properties and Pipe Diameters on Two-Phase Flow Patterns in Horizontal Lines," *International Journal of Multiphase Flow*, Vol. 437, p. 5.

Wallis, G. B., and Dobson, J. E., 1973, "The Onset of Slugging in Horizontal Stratified Air-Water Flow," *International Journal of Multiphase Flow*, Vol. 1, pp. 173–193.

Wu, H. L., Pots, B. F. M., Hollenberg, J. F., and Meerthoff, R., 1987, "Flow Pattern Transition in Two-Phase Gas Condensate Flows in 8 in. Horizontal Pipe," *Proc. 3rd Intern. Conf. on Multiphase Flow*, Haque, Netherlands, 18–20 May 1987, pp. 13–21.

**M. T. Rubel**
Exploration and Production Technology Department, Texaco Inc., Bellaire, Texas

**B. D. Timmerman**

**H. M. Soliman**
Mem. ASME

**G. E. Sims**

Department of Mechanical and Industrial Engineering, University of Manitoba, Winnipeg, Manitoba, Canada

**M. A. Ebadian**
Fellow ASME
Department of Mechanical Engineering, Florida International University, Miami, FL 33199

# Phase Distribution of High-Pressure Steam-Water Flow at Large-Diameter Tee Junctions

## (Data Bank Contribution*)

*Experimental data are presented for the phase distribution of high pressure (2.75 to 5.5 MPa) steam-water mixtures at horizontal, equal-sided dividing tee junctions of two different sizes (49.3 and 97.3 mm i.d.). These data correspond to wide ranges of inlet qualities, inlet superficial vapor velocities, and extraction rates. Influences of the independent parameters on the phase-distribution phenomenon are presented and discussed. Comparisons between the present data and existing models have shown that the applicability of some models can be extended to the present test conditions.*

## 1 Introduction

Branching junctions are common features of the piping networks used for single-phase and two-phase flow distribution systems. These networks are essential components of many facilities in the oil and gas, power, and process industries. Examples of these facilities include the surface steam-distribution systems for thermal-enhanced oil recovery (EOR) operations, conventional steam power plants, and boiling-water and pressurized-water nuclear reactors. Knowledge of the pressure drop and phase distribution at branching junctions is important since these parameters can have significant effects on the operation and efficiency of all components downstream from the junction.

The relevance of this problem to many industrial applications has motivated significant research, most of which appeared in the literature during the past ten years (e.g., Saba and Lahey, 1984; Seeger et al., 1986; Shoham et al., 1987; Ballyk et al., 1988; Rubel et al., 1988; Hwang et al., 1988; Azzopardi et al., 1988; Hart et al., 1991; Buell et al., 1993). As well, the current state of the art has been described in four recent reviews by Azzopardi (1986), Lahey (1986), Muller and Reimann (1991), and Azzopardi and Hervieu (1992). These reviews have concluded that the problem of phase distribution at branching junctions has not as yet been solved; i.e., no model is currently available with general applicability to all operating conditions. This is mainly due to the large number of variables on which phase distribution depends, such as junction geometry, fluid properties, inlet mass flow rate and quality, inlet flow regime, and mass split at the junction.

In view of the above, and due to the lack of well-established similarity laws in the area of two-phase flow, it is necessary to generate experimental data relevant to a wide range of field applications and to determine which of the existing models can predict these data with acceptable accuracy. For several industries, such as the oil and gas industry, piping networks are used for distributing high-pressure, steam-water flow through large-size branching junctions. The vast majority of the previously published data corresponds to low-pressure, air-water flow through small-size junctions. The only available data for steam-water, to the authors' best knowledge, have been reported in the following studies:

(i) Seeger et al. (1986) reported data for a horizontal, equal-sided (50-mm i.d.) tee junction covering the pressure range of 2.5–10 MPa and inlet regimes of annular and slug flow.

(ii) Rubel et al. (1988) reported data for a horizontal, equal-sided (37.6-mm i.d.) tee junction covering the pressure range of 0.12–0.21 MPa and inlet regimes of stratified, wavy, and semiannular flow.

* Data have been deposited to the JFE Data Bank. To access the file for this paper, see instructions on p. 664 of this issue.

Contributed by the Fluids Engineering Division for publication in the JOURNAL OF FLUIDS ENGINEERING. Manuscript received by the Fluid Engineering Division April 1, 1993; revised manuscript received February 16, 1994. Associate Technical Editor: R. Arndt.

(iii) Ballyk et al. (1988) reported data for a horizontal junction with an inlet pipe size of 25.65 mm and branch sizes of 25.65 and 12.3 mm. The data cover the pressure range of 0.11–0.21 MPa with an inlet regime of annular flow.

The need for further steam-water data, particularly with large-size junctions, appears obvious in view of the rather narrow data base currently available.

## 2 Test Facility and Procedure

The experimental program was conducted at Texaco's Steamflow Research Facility, located at the Exploration and Production Technology Department in Bellaire, Texas. The facility was designed and constructed to accommodate a wide variety of experimental investigations of steam-water flow through horizontal, vertical, and inclined pipe test sections. The following description highlights the components of the test facility that are most relevant to the present investigation.

**2.1 Flow Loop.** A simplified schematic of the test facility is shown in Fig. 1. A positive displacement feed-water pump transferred chemically treated city water from the generator feed drum to a natural-gas-fired steam generator. The resultant wet steam, generated at a quality of 50 to 80 percent, was directed into an inlet separator. The flow rate of the saturated vapor discharging from the separator was measured by either one of two orifice plates and then directed to the mixer. Measurements of the static pressure were made upstream of the orifice plates and the mixer on the vapor side. Liquid flow into the mixer was circulated by a high-speed centrifugal pump from a supply stored in the flash drum. This liquid flow rate was measured by either one of two orifice plates and the pressure and temperature of this stream were measured before entering the mixer. Knowing the mass flow rate and state properties of both streams (liquid and saturated vapor) entering the mixer, it was possible to determine the effluent mass flow rate, $W_1$, and quality, $x_1$, directed toward the test section (tee junction).

The steam-water mixture emerging from the mixer was passed through a straight adiabatic length of 13.6 m in order to ensure fully developed conditions before entering the test section. Two tee junctions were tested, both horizontal and equal-sided, with inside diameters of 49.3 and 97.3 mm. Therefore, the development length amounted to about 275 pipe diameters for the smaller test section and about 140 pipe diameters for the larger test section.

The incoming flow (stream 1) was split into two streams at the junction; one continuing in the same direction (stream 2 in the run-side of the junction) while the other was diverted at a right angle to the inlet direction (stream 3 in the branch-side of the junction). Each of the two streams leaving the test section was directed to its respective separator, downstream of which measurements of vapor and liquid flow rates were made via appropriate orifice plates. These measurements provided individual values for the vapor and liquid flow rates in the run, $W_{G2}$ and $W_{L2}$, respectively, and the vapor and liquid flow rates in the branch, $W_{G3}$ and $W_{L3}$, respectively. From these measurements, the run and branch total flow rates, $W_2$ and $W_3$, and qualities, $x_2$ and $x_3$, could be easily determined. Control valves downstream from the separators on the vapor

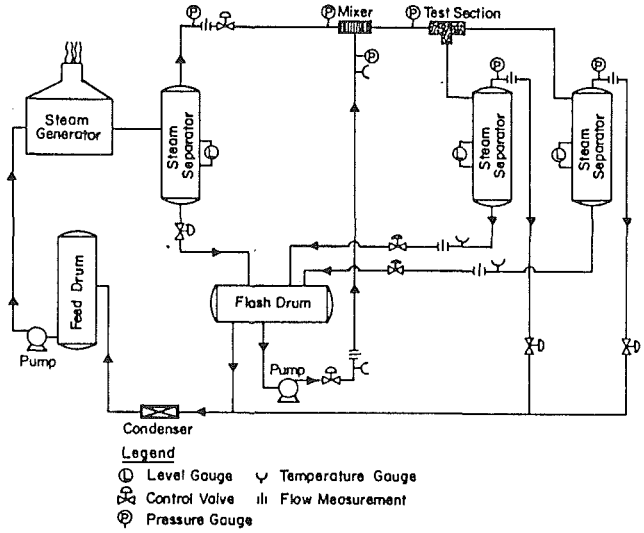


Fig. 1 Experimental test facility

side were used in adjusting the flow split ($W_2/W_3$) to the desired value. The liquid streams from the separators were flashed into the flash drum while the vapor streams were combined, condensed, and returned to the generator feed drum.

The entire facility was insulated with calcium silicate and covered with 1.6-mm thick corrugated aluminum skin to minimize heat losses to the surroundings. The insulation thickness used was 64 mm on all piping with a nominal diameter above 25.4 mm, 25 mm on all piping with nominal diameters of 25.4 mm or lower, and between 64 and 114 mm on all vessels.

**2.2 Instrumentation and Data Acquisition.** The facility was instrumented with 17 flow, 13 pressure, 14 temperature, and 6 level measurements. All orifice-plate flow elements were equipped with differential pressure transmitters. Pressure measurements were made with gauge-pressure transmitters, while temperature measurements were made using J-type thermocouples or 100-ohm platinum-resistance type (RTD) temperature transmitters. Level measurements in the different vessels were monitored with differential pressure transmitters. All measuring devices were calibrated before testing began.

All input and output signals throughout the facility were monitored or controlled by a data-acquisition and control system with a UNIX host computer (HP 9000 model 380). After the desired test conditions were programmed into the host computer, the facility was allowed to run until steady-state conditions were reached, requiring 20 to 40 minutes for each test run. The test-section pressures, temperatures, flow rates, and qualities were monitored continuously over 6-second intervals to ensure that steady state had been reached before any data were recorded. Data-reduction software was developed to calculate the average values of all steady-state signals, the standard deviation of the critical instrument signals, the overall system mass and heat balances, and the specific parameters used later in the analysis of the phase-distribution phenomenon. Mass balances were performed on an overall-flow basis by comparing $W_1$ with $(W_2 + W_3)$ and on a vapor-flow basis

## Nomenclature

$D$ = pipe diameter
$G$ = mass flux $= W/(\pi D^2/4)$
$J_G$ = superficial gas velocity $= W_G/(\pi \rho_G D^2/4)$
$J_L$ = superficial liquid velocity $= W_L/(\pi \rho_L D^2/4)$
$P$ = pressure
$W$ = mass flow rate
$x$ = quality $= W_G/W$
$\rho$ = density

**Subscripts**

1, 2, 3 = inlet, run, or branch
$G$ = gas phase
$L$ = liquid phase

Table 1 Range of operating conditions for each of the three data sets

| Data set no. | $D_1$ (mm) | $P_1$ (nominal) (MPa) | $J_{G1}$ (nominal) (m/s) | $J_{L1}$ (nominal) (m/s) | $x_1$ (nominal) | $W_3/W_1$ (nominal) |
|---|---|---|---|---|---|---|
| 1 | 49.3 | 2.75 | 14.9 | 0.06–0.96 | 0.2–0.8 | 0.13–0.75 |
| | | 2.75 | 23.9 | 0.10–1.47 | 0.2–0.8 | 0.11–0.74 |
| | | 2.75 | 32.6 | 0.14–1.90 | 0.2–0.8 | 0.11–0.75 |
| 2 | 49.3 | 2.75 | 25.9 | 0.12–1.61 | 0.2–0.8 | 0.10–0.77 |
| | | 4.12 | 14.6 | 0.11–1.64 | 0.2–0.8 | 0.13–0.80 |
| | | 4.12 | 17.6 | 0.12–1.66 | 0.2–0.8 | 0.13–0.78 |
| | | 4.12 | 20.5 | 0.13–0.84 | 0.4–0.8 | 0.12–0.78 |
| | | 5.50 | 12.9 | 0.12–1.60 | 0.2–0.8 | 0.14–0.79 |
| 3 | 97.3 | 2.75 | 7.1 | 0.03–0.45 | 0.2–0.8 | 0.13–0.85 |
| | | 4.12 | 4.7 | 0.03–0.46 | 0.2–0.8 | 0.12–0.75 |
| | | 5.50 | 3.4 | 0.03–0.45 | 0.2–0.8 | 0.13–0.84 |

by comparing $W_{G1}$ with $(W_{G2}+W_{G3})$. These mass balances were within ±5 percent for the vast majority of data points.

**2.3 Range of Test Conditions.** The independent parameters covered in this investigation were the tee-junction diameter, $D_1$, inlet pressure, $P_1$, the inlet vapor flow rate, $W_{G1}$, the inlet quality, $x_1$, and the extraction rate $(W_3/W_1)$. For each combination of these independent variables, the phase distribution at the junction is characterized by the dependent variable $(x_3/x_1)$. With fixed values of $D_1$, $P_1$, and $W_{G1}$, the inlet quality was varied over the range of $0.2<x_1<0.8$, and for each $x_1$, different extraction rates were tested covering the range of $0.1<(W_3/W_1)<0.9$.

A total of 327 test runs were performed in this investigation. These tests were classified into three data sets, as shown in Table 1. Data Set No. 1 explores the influences of $W_{G1}$ and $x_1$ for a fixed $P_1$, while Data Set Nos. 2 and 3 were intended to assess the influences of $P_1$ and $D_1$, respectively. A complete tabulation of all experimental data can be obtained either from the recent report by Timmerman et al. (1993), or the JFE Data Bank.

An important parameter affecting the phase distribution at branching junctions is the inlet flow regime (Azzopardi and Whalley, 1982). In view of the present conditions of high pressure and temperature, no attempt was made to visualize the flow regimes at the tee-junction inlet. Instead, it was decided to rely on predictions from some of the existing flow-regime maps. Among the most widely used maps are the empirical map by Mandhane et al. (1974) and the analytical map by Taitel and Dukler (1976). The inlet conditions corresponding to the different test groups in Data Set No. 3 were plotted on these maps and the results are shown in Figs. 2 and 3. The flow-regime boundaries in both maps were determined for a pipe diameter of 97.3 mm and fluid properties corresponding to a saturated steam-water mixture at 4.12 MPa, which is the mean pressure for Data Set No. 3. Significant deviations can be seen between the predictions of the two maps with Mandhane et al. (1974) predicting stratified and slug flow, and Taitel and Dukler (1976) predicting wavy and annular flow. Deviations between the two maps were also noted for Data Set Nos. 1 and 2. Therefore, the conclusion is that the inlet flow regimes are not known with certainty and this fact will be taken into consideration when comparing the present data with flow-regime-specific models.

**2.4 Experimental Uncertainty.** All variables used in presenting the phase-distribution data are based upon single-phase vapor and/or single-phase liquid flow-rate measurements. The procedure outlined by Miller (1983) was used in determining the uncertainty limits for the inlet and outlet single-phase flow-rate measurements using the specific sensitivity coefficients in the appropriate orifice-plate equation. Once the individual single-phase flow uncertainties were calculated, the experimental uncertainty in other variables, such as $W_3/W_1$ and $x_3/x_1$, were determined using the propagation of errors technique as outlined by Bevington (1969).

The experimental uncertainty in all single-phase flow-rate measurements were found to be within ±2 percent. For $J_G$, $J_L$, $x_1$, $x_2$, and $x_3$, the uncertainty was within ±3.5 percent. The extraction rate, $W_3/W_1$, had uncertainties within ±4 percent while $x_3/x_1$ had uncertainties within ±5 percent.

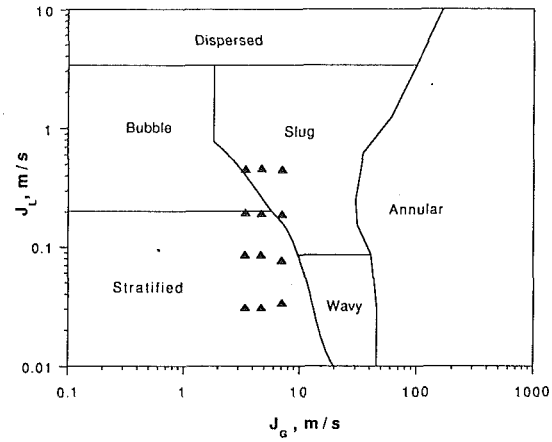


Fig. 2 Prediction of inlet flow regimes for Data Set No. 3 using the map of Mandhane et al. (1974)

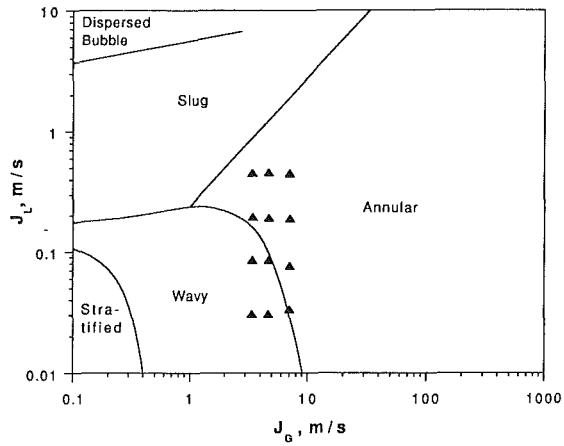


Fig. 3 Prediction of inlet flow regimes for Data Set No. 3 using the map of Taitel and Dukler (1976)

## 3 Experimental Results and Discussion

An attempt was made to compare the present experimental results with other data available in the literature. Such a comparison will be meaningful only if the values of $D_1$, $P_1$, $J_{L1}$, and $J_{G1}$ are matched reasonably well between the two sets of data. The only possible match for the values of $D_1$ and $P_1$ used in Data Set Nos. 1 and 2 can be made with the data of Seeger et al. (1986). However, it was not possible to find a reasonable match of $J_{L1}$ and $J_{G1}$ between the two groups of data. Data Set No. 3 corresponds to a value of $D_1$ for which no results exist in the literature. While direct comparison between data is not possible, it is reassuring that the present data is in good agreement with the empirical correlation of Seeger et al. (which was based on operating conditions closest to the present ones), as shown later.

In presenting the current results, the magnitude of phase redistribution due to the junction is illustrated by plotting $(x_3/x_1)$ versus $(W_3/W_1)$. Two special cases are included in each

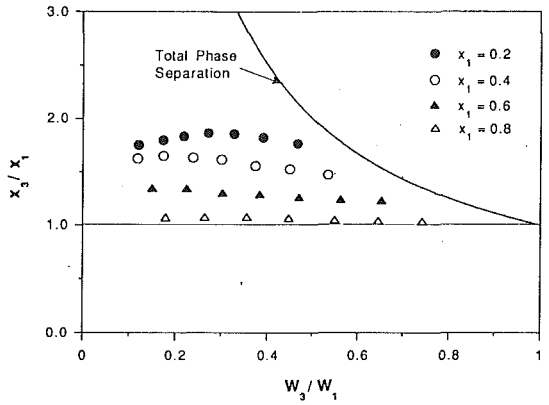


Fig. 4 Effect of inlet quality for Data Set No. 1 when $J_{G1} = 23.9$ m/s and $P_1 = 2.75$ MPa

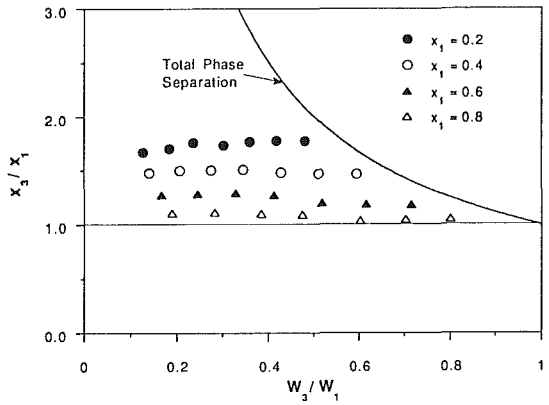


Fig. 5 Effect of inlet quality for Data Set No. 2 when $J_{G1} = 14.6$ m/s and $P_1 = 4.12$ MPa

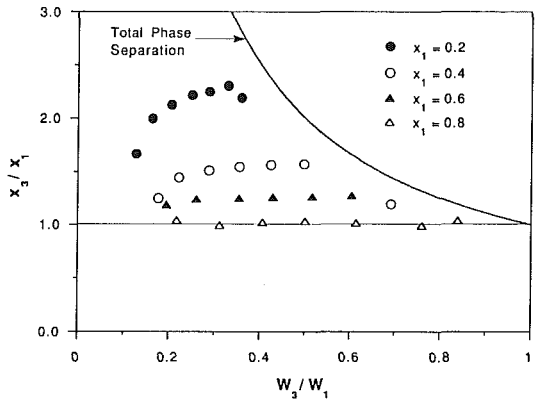


Fig. 6 Effect of inlet quality for Data Set No. 3 when $J_{G1} = 3.4$ m/s and $P_1 = 5.5$ MPa

figure; the case of even phase distribution given by $x_3/x_1 = 1$ and the case of total phase separation, where all incoming vapor is extracted through the branch, resulting in $x_3/x_1 = 1/(W_3/W_1)$. In the following discussion, an attempt is made to isolate the effect of each independent variable in order to illustrate the prevailing trends from this experiment.

**3.1 Effect of Inlet Quality.** Figures 4 to 6 show a representative sample from Data Set Nos. 1, 2, and 3, respectively. The data in each figure correspond to fixed values of $D_1$, $P_1$, and $J_{G1}$, while $x_1$ is varied from 20 to 80 percent. Significant phase redistribution can be seen from these results with $(x_3/x_1)$ generally greater than 1. The degree of uneven phase distribution is particularly evident for extraction rates, $W_3/W_1 < 0.5$, which is the most likely operating conditions for an equal-sided tee junction. In a pipe network involving several junctions, this phenomenon will result in a severe maldistribution of phases.

The consistent trend in all data, as exemplified by Figs. 4-6, is that $(x_3/x_1)$ increases as $x_1$ decreases with fixed $D_1$, $P_1$, and $J_{G1}$. This trend is consistent with previous experiments (e.g., Azzopardi et al., 1988; Ballyk et al., 1988; Rubel et al., 1988). An increase in $(x_3/x_1)$ indicates decreased preference for the liquid to exit through the branch. A possible explanation of this trend is that the mass flow rate of the liquid, and consequently the average axial momentum of this phase, increase at the junction inlet as $x_1$ decreases, thus resulting in a decrease in the probability of the liquid to enter the branch.

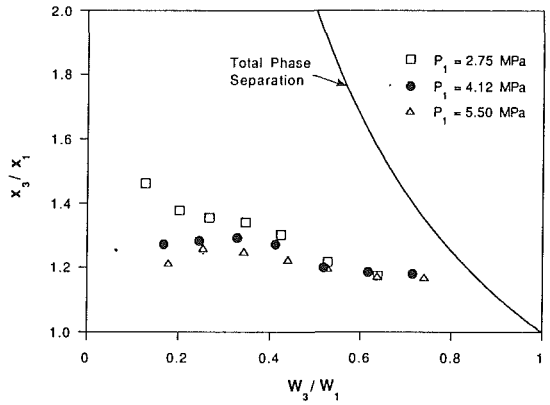


Fig. 7 Effect of inlet pressure when $D_1 = 49.3$ mm, $J_{G1} = 12.9$–$14.9$ m/s, and $J_{L1} = 0.27$–$0.36$ m/s

**3.2 Effect of Inlet Pressure.** Figure 7 shows data corresponding to three different pressures ranging from 2.75 MPa to 5.5 MPa. This segment of data corresponds to the same diameter, $D_1 = 49.3$ mm, and nearly the same superficial vapor velocity, $J_{G1} = 12.9$–$14.9$ m/s, and superficial liquid velocity, $J_{L1} = 0.27$–$0.36$ m/s. In general, the uneven phase distribution due to the junction is seen to decrease as the pressure increases. An increase in pressure results in an increase in vapor density and consequently, an increase in vapor momentum, which decreases the tendency for the vapor to exit through the branch. In the limit, as the critical pressure is approached, the data should approach the condition of even phase distribution. While the data in Fig. 7 obey the expected trend, the effects are small due to the narrow range of pressure tested. A similar trend was reported by Seeger et al. (1986) corresponding to air-water data covering the pressure range of $0.4 < P_1 < 5$ MPa.

**3.3 Effect of Inlet Mass Flux.** This effect was isolated by considering data corresponding to the same $D_1$, $P_1$, and $x_1$, while $G_1$ was varied, as shown in Figs. 8 and 9. The data in each figure correspond to the same proportion of vapor and liquid mass flow rates; however, the superficial velocity of both phases increases as $G_1$ increases. Therefore, it is difficult to predict the corresponding trend in the values of $x_3/x_1$ from simple axial-momentum considerations. The picture is further complicated by the possibility of flow-regime transitions within each of the data segments shown in Figs. 8 and 9.

In previous experiments, Saba and Lahey (1984) noted that the $G_1$-effect was insignificant; however, their data were close to the total-phase-separation condition. Ballyk et al. (1988) and Rubel et al. (1988) reported that while $G_1$ appeared to have some influence, the magnitude of this influence was much smaller than the $x_1$-effect.

The present data, as shown in Figs. 8 and 9, suggest that

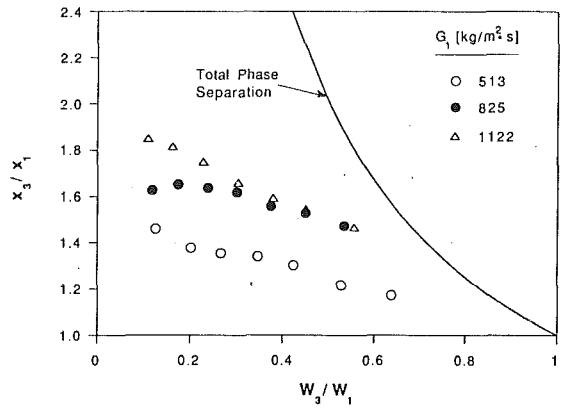


Fig. 8 Effect of inlet mass flux when $D_1 = 49.3$ mm, $P_1 = 2.75$ MPa, and $x_1 = 0.4$

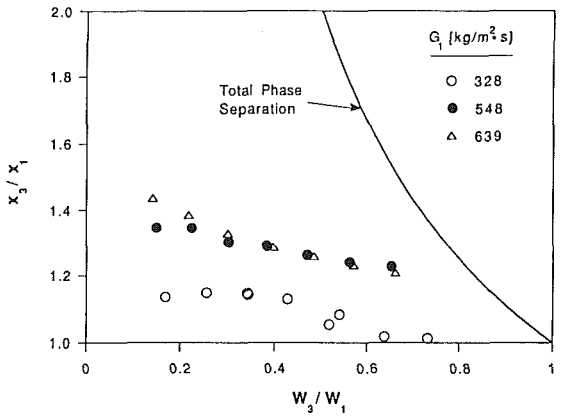


Fig. 9 Effect of inlet mass flux when $D_1 = 49.3$ mm, $P_1 = 2.57$ MPa, and $x_1 = 0.6$

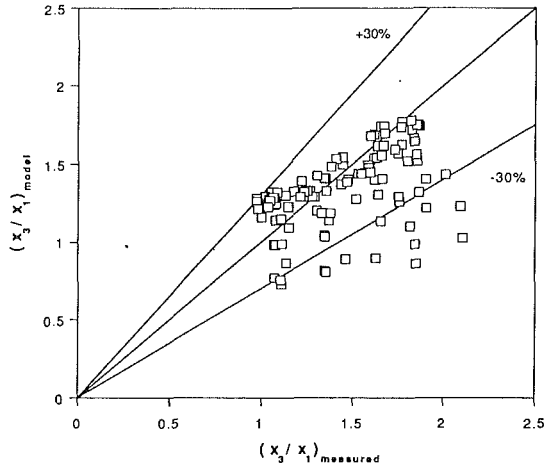


Fig. 10 Comparison between Data Set No. 1 and the correlation of Seeger et al. (1986)

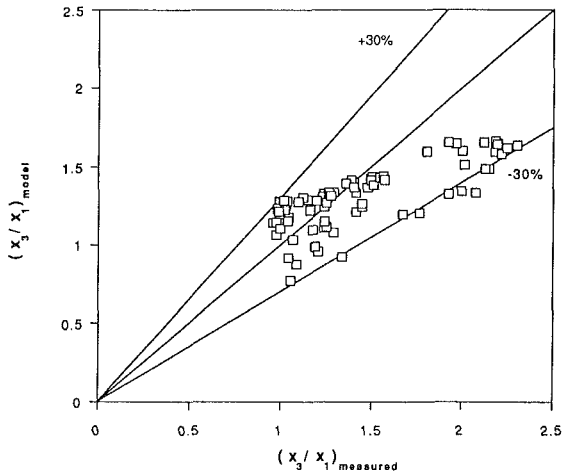


Fig. 11 Comparison between Data Set No. 3 and the correlation of Seeger et al. (1986)

for the present operating conditions, more uneven distribution occurs as $G_1$ increases. This trend is consistent with the predictions from the empirical correlation of Seeger et al. (1986).

## 4 Comparison with Models

The present results represent a significant addition to the available data base in terms of the range of independent parameters tested. Data Set Nos. 1 and 2 correspond to values of $D_1$ and $P_1$ similar to those used by Seeger et al. (1986); however, the present ranges of $J_{G1}$, $J_{L1}$, and $x_1$ are much wider. Data Set No. 3 corresponds to a previously untested value of $D_1$, which is closer to pipe sizes encountered in industrial applications. Therefore, it is very important to test the extendibility of existing models to the present test conditions as a step towards developing generalized predictive models.

Six phase-distribution models were selected for this comparison. A summary of these comparisons is given here, while a more detailed presentation can be found in the report by Timmerman et al. (1993).

**4.1 Seeger et al. (1986).** An empirical correlation was developed by Seeger et al. (1986) based on their own data. For horizontal tee junctions, the correlation is not flow-regime specific, except for data in the dispersed bubble regions (not expected in the present experiment), where one coefficient in the correlation assumes a different value. The comparison between this correlation and Data Set Nos. 1 and 3 is shown in Figs. 10 and 11, respectively. In general, this correlation can be seen to be in very good agreement with the present data. Quantitatively, 87 percent of Data Set No. 1, 93 percent of Data Set No. 2, and 92 percent of Data Set No. 3 were predicted to within ±30 percent. Overall, 99 percent of all data were predicted by the correlation with an accuracy of ±50 percent. This is a remarkable agreement in view of the simplicity of the correlation and the fact that the present test conditions are significantly different from those on which the correlation was based.

**4.2 Hwang et al. (1988).** An analytical model was formulated by Hwang et al. (1988) using phenomenological considerations. The model assumes that the vapor and liquid entering the branch come from different regions of the inlet pipe and that these regions are bounded by respective dividing streamlines. The form of these dividing streamlines was determined from a mechanistic approach. Therefore, the prediction of this model depends on the distribution of phases in the inlet pipe; i.e., the inlet flow regime.

Since the inlet flow regimes are not known with certainty in the present data, as discussed earlier, the comparison between this model and each of the data sets was done twice using the assumptions of annular and wavy flow. A sample of these comparisons is shown in Fig. 12 for Data Set No. 1 assuming annular flow and in Fig. 13 for Data Set No. 3 assuming wavy flow. In general, this model produced better predictions with the assumption of wavy flow for all data sets. For Data Set No. 3, where annular flow is least likely to occur, the proportion of data predicted with ±30 percent improved from 54

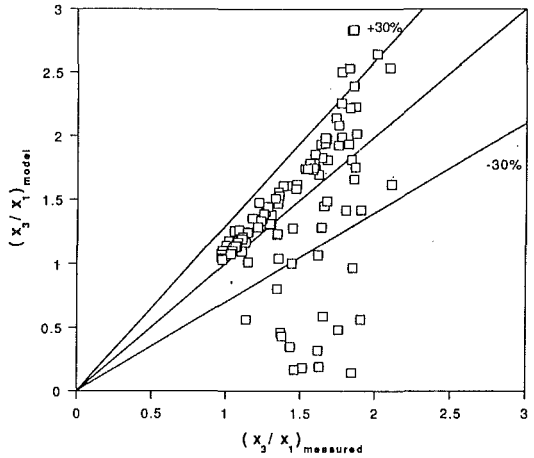


Fig. 12 Comparison between Data Set No. 1 and the model of Hwang et al. (1988), assuming annular flow

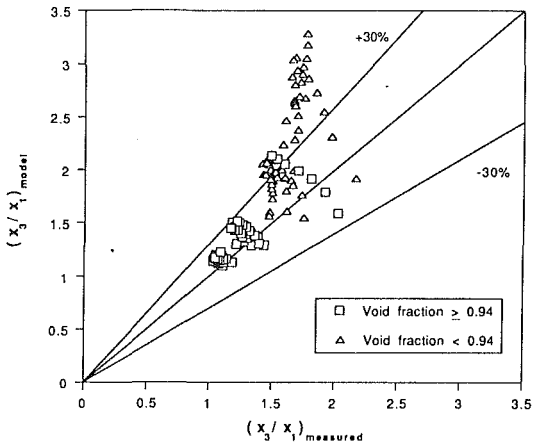


Fig. 14 Comparison between Data Set No. 2 and the model of Hart et al. (1991)

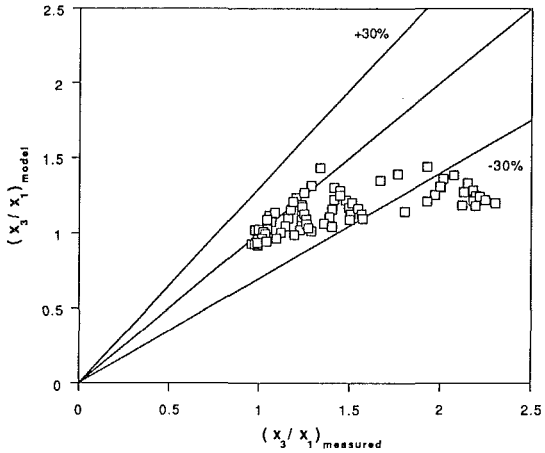


Fig. 13 Comparison between Data Set No. 3 and the model of Hwang et al. (1988), assuming wavy flow

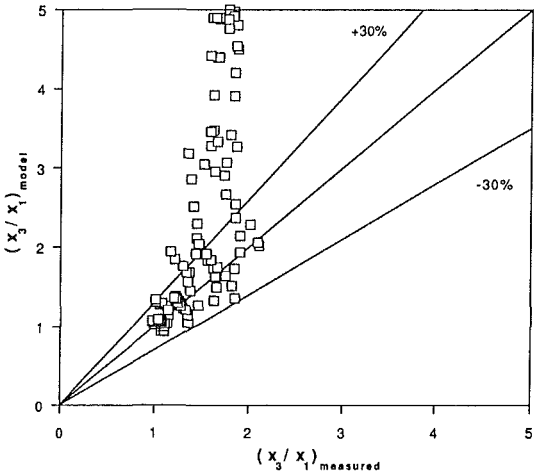


Fig. 15 Comparison between Data Set No. 1 and the model of Shoham et al. (1987), assuming annular flow

percent for annular flow to 78 percent for wavy flow. Overall, the model predicted 80 percent of data (from all three sets) assuming annular flow and 100 percent of data assuming wavy flow to within ±50 percent.

**4.3 Hart et al. (1991).** Hart et al. (1991) derived an analytical model by applying a mechanical energy balance on both the gas and liquid phases for inlet-to-run and inlet-to-branch streamlines. They then used the criterion that the run-to-branch pressure difference is the same for both phases in developing the necessary relations for predicting the phase distribution. The resulting model is independent of the inlet flow regime; however, its application is restricted to inlet void fractions greater than 0.94.

The comparison between this model and the present data produced excellent agreement when the inlet-void-fraction restriction was applied. A sample of the results is shown in Fig. 14 for Data Set No. 2, where 97 percent of the data points (with inlet void fraction >0.94) are predicted within ±30 percent. Figure 14 shows that large deviations can occur when the model restriction is not observed. Using the 192 data points which satisfied the model restriction (out of a total of 327), it was found that this model predicted 89 percent of the data within ±30 percent and 98 percent of the data within ±50 percent.

**4.4 Shoham et al. (1987).** The analytical model by Shoham et al. (1987) uses ideas similar to those adopted by Hwang et al. (1988) in terms of the separate dividing streamlines for the gas and liquid phases. However, the two models differ in the approach used in determining the equations of the two streamlines.

The comparison between the present data and the model of Shoham et al. (1987) did not result in the same level of accuracy obtained in the above comparisons. The assumption of annular flow produced better agreements than the assumption of wavy flow, even for Data Set No. 3, where annular flow is least expected. Figure 15 shows the comparison with Data Set No. 1 assuming annular flow. For this segment of data, 62 percent of the points are within ±30 percent and only 68 percent of the points are within ±50 percent indicating that large disagreement can occur. A closer examination of this model revealed that good accuracy can be obtained against the present data for high inlet qualities ($x_1 > 0.6$), while most of the data with $x_1 < 0.4$ were severely over-predicted (Timmerman et al., 1993).

**4.5 Other Comparisons.** A phenomenological model was developed by Azzopardi and Whalley (1982) for the inlet flow regime of annular flow. The model assumes that the gas and liquid extracted through the branch come from the same region of the pipe; i.e., the same dividing streamline for both phases. Later, Azzopardi (1988) added a modification to account for liquid film stoppage in the run-side of the junction when a high proportion of the inlet gas is extracted through the branch.

In general, the comparison with Data Set Nos. 1 and 2,

where inlet conditions provide the highest probability for annular flow among the present data, did not produce good results. Within the interval of ±50 percent, it was possible to predict 59 percent of Data Set No. 1 and 44 percent of Data Set No. 2 using the model of Azzopardi and Whalley (1982). Slight improvements (up to 60 percent for Data Set No. 1 and 49 percent for Data Set No. 2) resulted from the modification of Azzopardi (1988). Consistently, it was found that the accuracy of both models improves with an increase in $(W_3/W_1)$ and/or $x_1$ (Timmerman et al., 1993). In a recent publication, Buell et al. (1993) reported excellent agreement between these models and their data of annular flow for air-water mixtures at 0.15 MPa. It may be possible that the restriction of coincident dividing streamlines is not suitable for fluid properties corresponding to the high-pressure conditions encountered in the present experiment.

## 5 Concluding Remarks

New experimental data are reported on the redistribution of phases at horizontal tee junctions using steam-water mixtures. These data cover ranges of $0.2<x_1<0.8$, $0.1<(W_3/W_1)<0.9$, $2.75<P_1<5.5$ MPa, $3.4<J_{G1}<32.6$ m/s, and $D_1=49.3$ and 97.3 mm. The present test conditions can be considered a significant extension of the existing data base.

Influences of the independent parameters on the phase-distribution phenomenon were considered separately. For the present test conditions, it is shown that an increase in phase separation (i.e., an increase in $x_3/x_1$) results from a decrease in $x_1$, a decrease in $P_1$, or an increase in $G_1$. Some of these trends were explained by consideration of the relative axial momentum of the phases.

Comparisons were made between the present experimental data and the predictions of available mechanistic and empirical models. These comparisons were conducted in a detailed manner in order to determine the range of operating conditions under which each model is capable of good agreement with the data. For the range of operating conditions covered in this investigation, the model of Seeger et al. (1986) gave good predictions throughout the range, the model of Hwang et al. (1988) gave good predictions, particularly with the assumption of wavy flow at the junction inlet, and the model of Hart et al. (1991) gave good predictions when the model's restriction on void fraction was observed.

## JFE Data Bank Contribution

The experimental data generated in this investigation have been deposited in the JFE Data Bank. The data are listed in three groups, each corresponding to one of the data sets of Table 1.


## Acknowledgment

The financial assistance provided by the Natural Sciences and Engineering Research Council of Canada is gratefully acknowledged.


## References


Azzopardi, B. J., 1986, "Two-Phase Flow in Junctions," *Encyclopedia of Fluid Mechanics*, Vol. 3, Chap. 25, Gulf Publishing, New York.

Azzopardi, B. J., 1988, "An Additional Mechanism in the Flow Split of High Quality Gas-Liquid Flows at a T Junction," UK Atomic Energy Authority, Report AERE-R-13058.

Azzopardi, B. J., and Hervieu, E., 1992, "Phase Separation at T- Junctions," Presented at the Third International Workshop on Two-Phase Flow, London, U.K.

Azzopardi, B. J., Wagstaff, D., Patrick, L., Memory, S. B., and Dowling, J., 1988, "The Split of Two-Phase Flow at a Horizontal T—Annular and Stratified Flow," UK Atomic Energy Authority, Report AERE-R-13059.

Azzopardi, B. J., and Whalley, P. B., 1982, "The Effect of Flow Patterns on Two-Phase Flow in a T Junction," *International Journal of Multiphase Flow*, Vol. 8, pp. 491–507.

Ballyk, J. D., Shoukri, M., and Chan, A. M. C., 1988, "Steam-Water Annular Flow in a Horizontal Dividing T-Junction," *International Journal of Multiphase Flow*, Vol. 14, pp. 265–285.

Bevington, P. R., 1969, *Data Reduction and Error Analysis for the Physical Sciences*, McGraw-Hill, New York.

Buell, J. R., Soliman, H. M., and Sims, G. E., 1993, "Two-Phase Pressure Drop and Phase Distribution at a Horizontal Tee Junction," Gas-Liquid Flows 1993, FED-Vol. 165, pp. 25–37, ASME FED Summer Meeting, Washington, D.C.

Hart, J., Hamersma, P. J., and Fortuin, J. M. H., 1991, "Phase Distribution During Gas-Liquid Flow Through Horizontal Dividing Junctions," *Nuclear Engineering and Design*, Vol. 126, pp. 293–312.

Hwang, S. T., Soliman, H. M., and Lahey, R. T., 1988, "Phase Separation in Dividing Two-Phase Flows," *International Journal of Multiphase Flow*, Vol. 14, pp. 439–458.

Lahey, R. T., 1986, "Current Understanding of Phase Separation Mechanisms in Branching Conduits," *Nuclear Engineering and Design*, Vol. 95, pp. 145–161.

Mandhane, J. M., Gregory, G. A., and Aziz, K., 1974, "A Flow Pattern Map for Gas-Liquid Flow in Horizontal Pipes," *International Journal of Multiphase Flow*, Vol. 1, pp. 537–553.

Miller, R. W., 1983, Flow Measurement Engineering Handbook, McGraw-Hill, New York.

Muller, U., and Reimann, J., 1991, "Redistribution of Two-Phase Flow in Branching Conduits: A Survey," Presented at the International Conference on Multiphase Flows, Tsukuba, Japan.

Rubel, M. T., Soliman, H. M., and Sims, G. E., 1988, "Phase Distribution During Steam-Water Flow in a Horizontal Tee Junction," *International Journal of Multiphase Flow*, Vol. 14, pp. 425–438.

Saba, N., and Lahey, R. T., 1984, "The Analysis of Phase Separation Phenomena in Branching Conduits," *International Journal of Multiphase Flow*, Vol. 10, pp. 1–20.

Seeger, W., Reimann, J., and Muller, U., 1986, "Two-Phase Flow in a T-Junction with a Horizontal Inlet—Part I: Phase Separation," *International Journal of Multiphase Flow*, Vol. 12, pp. 575–585.

Shoham, O., Brill, J. P., and Taitel, Y., 1987, "Two-Phase Flow Splitting in a Tee Junction—Experiment and Modeling," *Chemical Engineering Science*, Vol. 42, pp. 2667–2676.

Taitel, Y., and Dukler, A. E., 1976, "A Model for Predicting Flow Regime Transitions in Horizontal and Near Horizontal Gas-Liquid Flow," *AIChE Journal*, Vol. 22, pp. 47–55.

Timmerman, B. D., Rubel, M. T., Soliman, H. M., and Sims, G. E., 1993, "Evaluation of Available Models to Predict Phase Distribution of Wet Steam Through Branch Tee Junctions," Exploration and Production Technology Department, Texaco Inc., Report No. 92-264.

# Thermal Choking Due to Nonequilibrium Condensation

**Abhijit Guha**
Whittle Laboratory,
University of Cambridge,
Madingley Road, Cambridge CB3 0DY, U.K.

*A theory of thermal choking due to nonequilibrium condensation in a nozzle is presented. An explicit equation for the critical quantity of heat in condensing flow has been derived. The equation is of general validity and applies to vapor-droplet flow with or without a carrier gas. It has been usually assumed in the literature that the classical gas dynamics result for the critical quantity of heat applies in condensing flow as well. The classical result is, however, obtained by considering external heat addition to an ideal gas in a constant area duct. In this paper it is shown that the area variation across the condensation zone (although small) and the depletion in the mass of vapor as a result of condensation have profound effects on the critical quantity of heat. The present equation (derived from an integral, control-volume approach) agrees very well with results from full time-marching solution of the nonequilibrium, differential gas dynamic equations. The classical gas dynamics result, on the other hand, seriously underpredicts the critical heat for condensing flow in nozzles (by a factor of three in the example calculation presented).*

## 1 Introduction

It is well known that heat addition causes a reduction in Mach number in supersonic flow and an increase in Mach number in subsonic flow. In other words, heat addition to a flowing fluid drives the Mach number towards unity. Therefore, at a particular flow Mach number, the fluid can absorb a maximum quantity of heat before the local Mach number equals unity and the flow becomes thermally choked. It can be easily shown from classical gas dynamics that this critical quantity of heat, $q^*_{\text{classical}}$, for simple heat addition (external heat addition without any change in flow cross-sectional area) to an ideal gas is given by (Shapiro, 1953, equation 7.14)

$$\frac{q^*_{\text{classical}}}{c_p T_{01}} = \frac{[M_1^2 - 1]^2}{2(\gamma+1)M_1^2\left[1 + \frac{\gamma-1}{2} M_1^2\right]} \tag{1}$$

where $c_p$ is the isobaric specific heat of the ideal gas, $M_1$ is the Mach number at which the heat addition begins, $T_{01}$ is the stagnation temperature before heat addition, and $\gamma$ is the isentropic index (ratio of the two specific heats).

In many practical situations, the energy is supplied internally. For example, when a dry, superheated vapor is expanded rapidly through a convergent-divergent nozzle, liquid droplets do not form as soon as the vapor reaches the saturation temperature. The vapor goes out of thermodynamic equilibrium and attains considerable subcooling, $\Delta T$, (i.e., the vapor temperature, $T$, falls below the local saturation value, $T_s$) due to continued expansion. The rate of formation of liquid nuclei is very strongly dependent on the subcooling. Thus when the subcooling becomes appreciable (usually in the divergent part of the nozzle where the flow velocity is supersonic), a very large number of very small nuclei form over a relatively short time. These nuclei grow by exchanging heat and mass with the surrounding, subcooled vapor. The resulting release of latent heat is conducted back to the vapor and the vapor temperature quickly rises to the local saturation value (i.e., the subcooling decreases to almost zero). This rapid reversion to equilibrium is generally termed condensation shock and has been the topic of an extremely large number of studies. (The term condensation shock is, in general, a misnomer. Although heat addition in a supersonic flow results in an increase in pressure, the rise is gradual and the Mach number at the end of the condensation zone, in general, remains above unity.)

Similar to the case of external heat addition, the Mach number decreases in the condensation zone (the flow being supersonic). Therefore, for particular combinations of nozzle geometry, supply conditions and the working fluid, the liberation of latent heat could be such that the minimum Mach number becomes unity and the flow is thermally choked. (A numerical computation of this limiting case of thermal choking due to nonequilibrium condensation is later shown in Fig. 4.) If the inlet total temperature, $T_{01}$, is reduced any further, keeping the inlet total pressure, $p_{01}$, fixed, continuous variation of the flow variables is no longer possible and an aerodynamic shock wave appears inside the condensation zone (Barschdorff and Fillipov, 1970; Guha and Young, 1991).

It is often stated (Wegener and Mack, 1958; Pouring, 1965; Wegener, 1969; Wegener and Cagliostro, 1973; Skillings et al., 1987) that supercritical condensation with an inbuilt frozen shock wave occurs when $q > q^*_{\text{classical}}$, where $q^*_{\text{classical}}$ is given by Eq. (1). It has been argued by Guha (1994) that Eq. (1) is not appropriate for a condensing flow primarily for two reasons: (i) In case of a condensation shock, the energy is added

Contributed by the Fluids Engineering Division for publication in the JOURNAL OF FLUIDS ENGINEERING. Manuscript received by the Fluids Engineering Division June 29, 1993; revised manuscript received February 15, 1994. Associate Technical Editor: R. Arndt.

as a result of condensation of a part of the fluid itself. Therefore, the mass flow rate of the condensable vapor changes as the vapor is continually transformed into the liquid phase. Equation (1), which is derived for external heat addition to an ideal gas, does not take into account this mass depletion. (ii) The droplets formed through homogeneous nucleation grow at a *finite rate* by exchanging mass and energy with the surrounding vapor. Therefore, the energy addition due to condensation is not instantaneous and takes place over a short but finite zone. Since condensation shock normally occurs in the diverging section (with dry vapor at inlet), this means the flow area increases between the upstream and downstream of the condensation zone. Equation (1), on the other hand, is derived by assumed heat addition in a constant area duct.

The purpose of the present paper is to derive an expression for the critical amount of heat taking proper account of the above two effects. This would then show the level of errors incurred as a result of the approximations in Eq. (1), which is referred extensively in the context of nonequilibrium condensation. Here we adopt an integral, control volume approach; conditions of choking from differential equations of motion may be found in Guha (1994) and Young (1984). All numerical results presented in this paper are obtained for pure steam, but the analysis is valid for other vapor-droplet mixtures with or without an inert carrier gas.

## 2 Thermal Choking Considering External Heat Addition With Area Variation

In order to appreciate the effects of area variation and mass depletion on the critical quantity of heat separately, the effects of area variation only are considered in this section. We, therefore, consider external heat addition to an *ideal gas* in a diverging flow section. We denote the pressure, density, velocity, temperature, sound speed, flow area and the rate of heat addition per unit mass by $p$, $\rho$, $V$, $T$, $a$, $A$, and $q$, respectively. The subscripts 1 and 2 respectively denote the upstream and downstream sections of the control volume within which the heat $q$ is added. We can then write the continuity, momentum and the energy equation across the control volume as,

Continuity

$$\rho_1 V_1 A_1 = \rho_2 V_2 A_2 \equiv \dot{m} \tag{2}$$

Momentum

$$p_1 A_1 - p_2 A_2 + 0.5\,(p_1 + p_2)\,(A_2 - A_1) = \dot{m}\,(V_2 - V_1) \tag{3}$$

Energy

$$a_1^2\left[\frac{1}{\gamma - 1} + \frac{\mathrm{M}_1^2}{2}\right] + q = a_2^2\left[\frac{1}{\gamma - 1} + \frac{\mathrm{M}_2^2}{2}\right] \tag{4}$$

Equation of state

$$p = \rho R T \tag{5}$$

where $R$ is the specific gas constant. While writing the momentum conservation Eq. (3), the general term $\int A dp$ is expressed as $\int d(Ap) - \int p dA$, and the axial component of the pressure force on the nozzle wall ($\int p dA$) has been approximated by assuming a linear variation of pressure. It is advantageous to employ this approximation in an integral theory. The accuracy of this method has been compared shortly with an exact formulation for an isentropic flow, and later with an accurate time-marching solution of a condensation shock. Both comparisons show that this is a valid approximation for the present problem.

Combining (2) and (5), we obtain

$$p = \frac{\dot{m}}{A\gamma \mathrm{M}^2}\, V \tag{6}$$

Substitute (6) in (3) to give

$$V_2\left[\gamma + \frac{\overline{A}}{A_2}\frac{1}{\mathrm{M}_2^2}\right] = V_1\left[\gamma + \frac{\overline{A}}{A_1}\frac{1}{\mathrm{M}_1^2}\right] \tag{7}$$

where,

$$\overline{A} = 0.5(A_1 + A_2) \tag{8}$$

From (4) and (7),

$$\frac{\dfrac{1}{\mathrm{M}_2^2}\left[\dfrac{1}{\gamma - 1} + \dfrac{\mathrm{M}_2^2}{2}\right]}{\left[\gamma + \dfrac{\overline{A}}{A_2}\dfrac{1}{\mathrm{M}_2^2}\right]^2} = \frac{\dfrac{1}{\mathrm{M}_1^2}\left\{\left[\dfrac{1}{\gamma - 1} + \dfrac{\mathrm{M}_1^2}{2}\right] + \dfrac{q}{a_1^2}\right\}}{\left[\gamma + \dfrac{\overline{A}}{A_1}\dfrac{1}{\mathrm{M}_1^2}\right]^2} \tag{9}$$

Now we are in a position to assess the accuracy of Eq. (3). Assuming the face of the control volume with subscript 1 to coincide with the geometric throat (with area $A^*$) where the Mach number is unity, we can write the variation of local isentropic Mach number as a function of local flow area by setting $q = 0$ in (9). The result is,

$$\left[2\gamma + 1 + \frac{A}{A^*}\right]^2 \mathrm{M}^2\left[\frac{1}{\gamma - 1} + \frac{\mathrm{M}^2}{2}\right] = \left[\frac{1}{\gamma - 1} + \frac{1}{2}\right]\left[2\gamma \mathrm{M}^2 + 1 + \frac{A^*}{A}\right]^2 \tag{10}$$

## Nomenclature

$A$ = flow cross-sectional area
$a$ = speed of sound in gas, or vapor phase
$A^*$ = area at geometric throat of nozzle
$c_p$ = isobaric specific heat of gas, or vapor phase
$\bar{e}$ = specific internal energy of vapor-droplet mixture
$\gamma$ = isentropic exponent of gas or vapor phase
$\bar{h}$ = specific enthalpy of vapor-droplet mixture
$h_{fg}$ = specific enthalpy of evaporation
$h_l$ = specific enthalpy of liquid phase
$h_v$ = specific enthalpy of vapor phase
M = Mach number (frozen value)
$\dot{m}$ = mass flow rate of gas, or vapor phase
$\dot{m}_{\text{total}}$ = combined mass flow rate of vapor plus liquid phase
$p$ = pressure
$p_0$ = stagnation pressure
$q$ = rate of heat addition per unit mass
$q^*$ = critical heat ($q^* \equiv y^* h_{fg}$ in condensing flow)
$\rho$ = density of gas, or vapor phase
$\bar{\rho}$ = density of vapor-droplet mixture
$T$ = temperature of gas, or vapor phase
$T_s$ = saturation temperature
$\Delta T$ = subcooling ($\Delta T = T_s - T$)
$T_0$ = stagnation temperature
$V$ = velocity
$y$ = wetness fraction
$y^*$ = critical amount of condensation

**Subscripts**

1 = upstream of control volume (beginning of condensation zone)
2 = downstream of control volume (point of thermal choking)

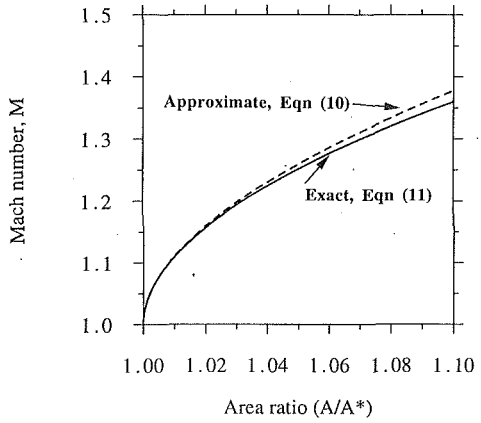


**Fig. 1 Comparison of approximate and exact solutions for isentropic flow**

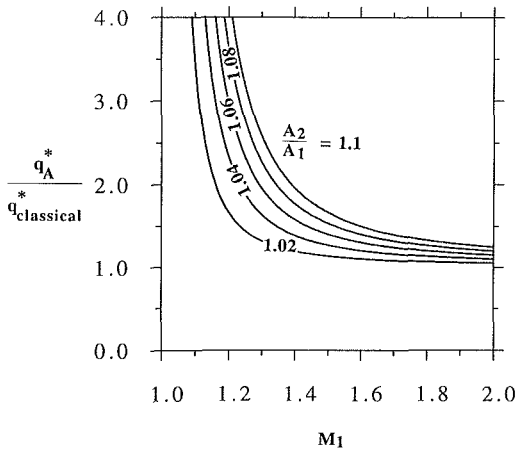


**Fig. 2 Effects of area ratio across the zone of heat addition on the critical amount of heat**

The exact variation for isentropic flow is given in classical gas dynamics (Shapiro, 1953)

$$\left[\frac{A}{A^*}\right]^2=\frac{1}{M^2}\left[\frac{2}{\gamma+1}\left(1+\frac{\gamma-1}{2}M^2\right)\right]^{\frac{\gamma+1}{\gamma-1}} \tag{11}$$

Figure 1 shows the comparison of the approximate result from the present theory, Eq. (10), with the exact solution, Eq. (11). It may be seen that for area ratios of the order of 1.1, the present theory gives acceptable solution. [The area ratio across the condensation zone of the practical example shown later (Section 4) is 1.028. The prediction of Eq. (10) is then little different from the exact solution (11).]

The critical quantity of heat needed to choke the flow thermally may be determined by substituting $M_2 = 1$ in (9). We denote this critical amount of heat by $q_A^*$, to distinguish this from the classical prediction $q^*_{classical}$ of Eq. (1).

$$\frac{q_A^*}{c_pT_{01}}=\frac{\gamma+1}{2\left(\gamma+\frac{\overline{A}}{A_2}\right)^2}\frac{\left[\gamma M_1^2+\frac{\overline{A}}{A_1}\right]^2}{M_1^2\left[1+\frac{\gamma-1}{2}M_1^2\right]}-1 \tag{12}$$

where $\overline{A}$ is given by (8). *Equation (12) reduces to equation (1) if* $A_1 = A_2$. Figure 2 plots the ratio $q_A^*/q^*_{classical}$ for different values of the area ratio $A_2/A_1$. It may be seen that, at low supersonic Mach numbers, even a small increase in area may increase the critical heat many times that predicted by the classical Eq. (1).

## 3 Thermal Choking Considering Condensation With Area Variation and Mass Depletion of the Vapor

In this section, we discuss the case of condensing flow. First, consider a mixture of vapor and liquid phase of the same chemical species. The mass of the vapor is continually depleted as a result of condensation. The vapor phase is assumed to obey the perfect gas law. Assuming no velocity slip between the vapor and the liquid phase, the momentum equation may be written from (3) as,

$$(p_1-p_2)\overline{A}=\dot{m}_{total}(V_2-V_1) \tag{13}$$

where $\dot{m}_{total}$ denotes the *combined* mass flow rate of the vapor and the liquid phase, and is a constant. Assuming that the vapor is dry at Section 1, the energy equation across the condensation zone may be written as (Guha, 1992a),

$$a_1^2\left[\frac{1}{\gamma-1}+\frac{M_1^2}{2}\right]+y_2h_{fg}=a_2^2\left[\frac{1}{\gamma-1}+\frac{M_2^2}{2}\right] \tag{14}$$

where $y_2$ is the wetness fraction at Section 2 and $h_{fg}$ is the specific enthalpy of evaporation. a and M in Eq. (14) are the frozen speed of sound and the frozen Mach number respectively. $a^2 = \gamma RT$, where $\gamma$ is the isentropic exponent of the vapor phase alone and $R$ is the specific gas constant of the vapor phase. (For a discussion on sound speeds in vapor-droplet mixtures see Guha 1992b, Guha 1992a.) The mass flow rate of the vapor alone, $\dot{m}$, at Sections 1 and 2 are related by,

$$\dot{m}_1=\frac{\dot{m}_2}{1-y_2}=\dot{m}_{total} \tag{15}$$

Substitution of (6) and (15) in (13) results in

$$V_2\left[\gamma+\frac{\overline{A}}{A_2}(1-y_2)\frac{1}{M_2^2}\right]=V_1\left[\gamma+\frac{\overline{A}}{A_1}\frac{1}{M_1^2}\right] \tag{16}$$

Combining (14) and (16),

$$\frac{\frac{1}{M_2^2}\left[\frac{1}{\gamma-1}+\frac{M_2^2}{2}\right]}{\left[\gamma+\frac{\overline{A}}{A_2}(1-y_2)\frac{1}{M_2^2}\right]^2}=\frac{\frac{1}{M_1^2}\left\{\left[\frac{1}{\gamma-1}+\frac{M_1^2}{2}\right]+\frac{y_2h_{fg}}{a_1^2}\right\}}{\left[\gamma+\frac{\overline{A}}{A_1}\frac{1}{M_1^2}\right]^2} \tag{17}$$

Compare Eq. (7) with (16) and (9) with (17) to see the effects of mass depletion. The condition of thermal choking is obtained when the local frozen Mach number is unity (Guha, 1994). Therefore, substituting $M_2 = 1$ in (17),

$$\left(1+\frac{y_2^*h_{fg}}{c_pT_{01}}\right)\left[\gamma+\frac{\overline{A}}{A_2}(1-y_2^*)\right]^2=\frac{\gamma+1}{2}\frac{\left[\gamma M_1^2+\frac{\overline{A}}{A_1}\right]^2}{M_1^2\left[1+\frac{\gamma-1}{2}M_1^2\right]} \tag{18}$$

where $y_2^*$ is the critical amount of condensation and $\overline{A}$ is given by (8). Although the flow is overall adiabatic, we define the critical quantity of heat (for comparisons with previous cases) as

$$q^*_{integral}\equiv y_2^*h_{fg} \tag{19}$$

Equation (18) can be solved as a cubic equation in $y_2^*$ (or $q^*_{integral}$). However, the solution is greatly simplified if the squared term in the LHS of (18) is approximated considering $y_2^*$ is a small quantity.

$$\left[\gamma+\frac{\overline{A}}{A_2}(1-y_2^*)\right]^2\approx\left[\gamma+\frac{\overline{A}}{A_2}\right]^2\left[1-\frac{2y_2^*}{\gamma A_2/\overline{A}+1}\right]$$

When this approximation is substituted in (18), (18) becomes a simple quadratic equation.

Figure 3 plots the results of three models: $q^*_{classical}$ given by (1) which deals with external heat addition to an ideal gas in

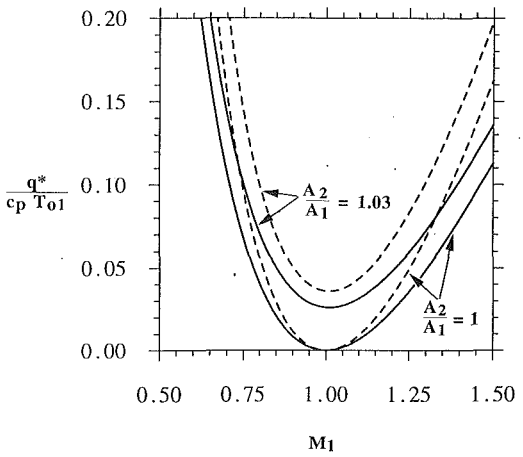


**Fig. 3 Effects of area ratio across the condensation zone and the depletion in vapor mass flow rate on the critical amount of condensation [— Eq. (12), · · · · Eq. (19)]**

a constant area duct, $q_A^*$ given by (12) which deals with external heat addition with area variation, and $q^*_{\text{integral}}$ given by (19) which takes into account of the area variation as well as of depletion in the mass of vapor due to condensation. The dotted lines in Fig. 3 represent Eq. (19) while the solid lines are the plots of Eq. (12). Note that the solid line corresponding to unity area ratio ($A_2/A_1 = 1$) is nothing but the classical solution, Eq. (1). Figure 3 shows clearly that the effects of mass depletion and (even a small) area variation are quite dramatic, especially when the Mach number is close to unity. Equation (1) is a very poor approximation then, and Eq. (19) must be used for determining the critical quantity of heat in non-equilibrium, condensing flow.

Figure 3 shows that Eq. (18) is valid in supersonic as well as in subsonic flow. The same equation can be used for $A_2/A_1 < 1$, i.e., in a converging flow section. In this respect, (18) is quite a versatile equation.

Equation (18) is as well valid if an inert, carrier gas is present. $\gamma$ and $a$ then represent the *frozen* values of the isentropic exponent and the speed of sound respectively in the mixture of the inert gas and the condensable vapor. They are calculated as weighted-averages of the respective values of the components (Guha, 1994). Assume that $\omega_g$ represents the mass fraction of the inert gas, and $\omega_{l2}$ is the mass fraction of the liquid phase at the downstream section. (As before, the vapor at the upstream section is assumed dry.) The corresponding quantities for $c_p$, $\gamma$, $y$, and M in Eq. (18) may then be calculated by starting from the conservation equations for a gas-vapor-droplet flow (Eqs. (28)–(32) in Guha, 1994) and then following exactly the same procedures presented in this section. The results (with some minor approximations) are:

$$c_p = \omega_g c_{pg} + (1-\omega_g)c_{pv}$$

$$R = \omega_g R_g + (1-\omega_g)R_v$$

$$\gamma = \frac{c_p}{c_p - R}$$

$$\mathrm{M} = V/a = V/\sqrt{\gamma RT}$$

$$y_2 = \omega_{l2}$$

The subscripts $g$ and $v$ refer to the respective properties of the inert gas and condensable vapor, respectively.

It should be realized that with finite transition thickness, pressure rise and area change, the boundary layer displacement thickness will change. Therefore, any reference to area such as in Eq. (18) should be interpreted as the effective flow area of the nozzle.

## 4 Time-Marching Solution of Condensation Zone

The equations presented in the previous section rest on an integral, control-volume analysis. We assess its accuracy by comparing the prediction of (19) with a full-blown time-marching solution of the governing differential equations for non-equilibrium condensation. Details of the time-marching calculation procedure may be found in Guha and Young (1991). Here we mention the salient points only. Assuming that there is *no velocity slip* between the vapor and the liquid droplets (which is usually an acceptable approximation as homogeneous nucleation normally produces very small, sub-micron size droplets), the gas dynamic equations for inviscid adiabatic unsteady two-phase vapor-droplet flow becomes:

Continuity

$$\frac{\partial \bar{\rho}}{\partial t} + \nabla \cdot (\bar{\rho}\mathbf{V}) = 0 \tag{20}$$

Momentum

$$\frac{\partial \mathbf{V}}{\partial t} + (\mathbf{V}\cdot\nabla)\mathbf{V} + \frac{\nabla p}{\bar{\rho}} = 0 \tag{21}$$

Energy

$$\frac{\partial}{\partial t}\left[\bar{\rho}\left(\bar{e} + \frac{V^2}{2}\right)\right] + \nabla \cdot \left[\bar{\rho}\mathbf{V}\left(\bar{h} + \frac{V^2}{2}\right)\right] = 0 \tag{22}$$

where the vector quantity $\mathbf{V}$ is the common velocity of the two phases, and $\bar{\rho}$, $\bar{h}$, and $\bar{e}$ are, respectively, the density, the specific enthalpy and the specific internal energy of the *mixture*.

The mixture density, $\bar{\rho}$, is connected to the vapor density, $\rho$, (neglecting the volume of the liquid phase and assuming no carrier gas is present) via

$$\bar{\rho} = \rho/(1-y) \tag{23}$$

and the mixture specific enthalpy is:

$$\bar{h} = (1-y)h_v + yh_l \tag{24}$$

where $h_v$ and $h_l$ are the specific enthalpies of the vapor and the liquid phase, respectively.

Equations (20)–(22) are identical to those describing the adiabatic flow of an inviscid single phase fluid and are valid for unsteady, three-dimensional flow. The differences from an equilibrium calculation are apparent, however, when it is recalled that the wetness fraction $y$ in Eqs. (23) and (24) is not necessarily the equilibrium value and that $h_v$ and $h_l$ in Eq. (24) are evaluated at the respective phase temperatures which are not necessarily equal to the local saturation value $T_s$. In order to close the set of equations for nonequilibrium condensation, one needs a nucleation rate equation specifying the rate of production of new droplets and a droplet growth law specifying the rate of condensation on existing droplets (providing the nonequilibrium value of $y$ to be used in (23) and (24)). Both the rates of nucleation and droplet growth depend on the local subcooling, and have been described by Guha and Young (1991).

One of the most effective methods of calculation is to write a computational "black-box" which contains the nucleation and droplet growth equations, and the energy equation in its thermodynamic form. (The equation $d\bar{h} - dp/\bar{\rho}_e = 0$, derivable from (20)–(22), does not necessarily imply zero entropy increase in multi-phase flow.) Together they furnish the full set of equations that describe completely the formation and growth of liquid droplets in a fluid particle (from a Lagrangian viewpoint) if the pressure-time variation is specified. The pressure-time variation is obtained by time marching solutions of the conservation equations such as Denton's method (Denton, 1983), extensively used for single-phase calculations in turbomachinery blade rows. In this respect, the thermodynamic aspects of phase-change can be completely divorced from fluid dynamical considerations so that the use of the black-box is

**Table 1 Comparison of Integral Predictions with Exact Solution**

| Equation (1) External heat addition to ideal gas in constant area duct | Equation (12) External heat addition to ideal gas in duct of varying area | Equation (19) Condensational heat release with area variation and mass depletion of vapor | Exact solution Time-marching solution of nonequilibrium gas dynamic equations |
|---|---|---|---|
| $q^*_{\text{classical}}/c_pT_{01}$ | $q^*_A/c_pT_{01}$ | $q^*_{\text{integral}}/c_pT_{01}$ | $q^*_{\text{actual}}/c_pT_{01}$ |
| 0.01978 | 0.0423 | 0.0574 | 0.0587 |

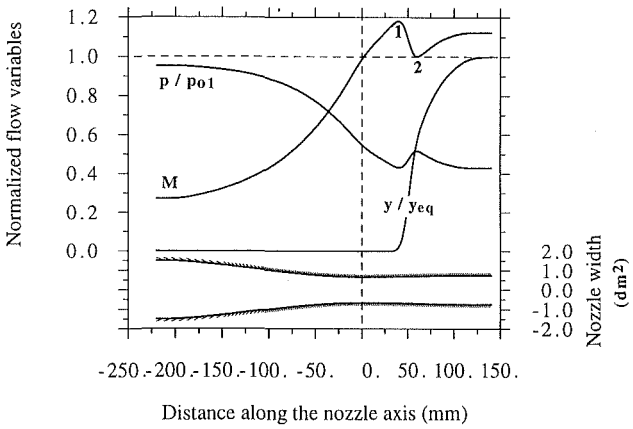


**Fig. 4 Time-marching solution of a limiting condensation shock in a quasi-one-dimensional convergent-divergent nozzle. (Continuous variation of flow variables leading to thermal choking at point 2.)**

effectively independent of any particular CFD application. Thus established single-phase CFD codes can, rather easily, be modified to deal with non-equilibrium two-phase flow with the above-mentioned modular approach. (The flexibility of this scheme may be appreciated from Guha and Young, 1994 where the same black-box has been grafted into a streamline curvature calculation procedure.)

The development of the computational routines within the black-box represents a comparatively major undertaking and has been fully described by Guha and Young (1991). The routines are sufficiently general and robust to deal with any type of nucleating or wet steam flow and (in contrast to many procedures reported in the literature) full details of the droplet size spectrum following nucleation are retained in the calculations. The last aspect is essential for accurate modelling of the nucleation zone. Successive nucleations after the primary are dealt with as a matter of course should the expansion be sufficiently rapid to generate the high levels of subcooling required. The computational scheme has been validated against measurements of steady (both sub and supercritical) and unsteady condensation shock waves (Guha and Young, 1991). Here, we present one calculation corresponding to thermal choking.

Figure 4 shows the nozzle employed for calculation. The working fluid is steam and the upstream total pressure, $p_{01}$, is 35140 N/sq m. Keeping the total pressure fixed, the total temperature, $T_{01}$, was varied until the condition of thermal choking is obtained. This is found to occur at $T_{01} = 356.3$ K. The frozen Mach number profile, M, shows that initially steam expands like a dry gas and attains M = 1 at the throat of the nozzle. Continued expansion to supersonic velocity ultimately generates sufficient subcooling for appreciable nucleation rate. The large number of small nuclei grow very fast, and the resulting release of latent heat erodes the subcooling and reduces the frozen Mach number. The point of maximum frozen Mach number constitutes the point 1 for the integral analysis described in Sections 2 and 3. Numerical calculations show that the Mach number at point 1, $M_1$, is 1.182.

The released heat is conducted back to the vapor and the frozen Mach number decreases. The inlet stagnation conditions are chosen such that, as the Mach number just reaches unity, the effect of area variation assumes dominance over that of heat addition. The flow, therefore, expands subsequently to supersonic velocity. This is the limiting condition for obtaining a continuous variation in all flow properties. Note that two sonic points exist in the flow field: one at the geometric throat and the second at the point of thermal choking. The point of thermal choking (M = 1) constitutes the point 2 in the integral analysis of the previous sections 2 and 3. Numerical calculations show that $y_2 = 0.0172$, and the area ratio between Sections 1 and 2 is $A_2/A_1 = 1.0284$. We refer the critical amount of heat from this direct numerical solution of the nozzle flow by $q^*_{\text{actual}}$. We may now construct Table 1 to compare the results of different integral analyses with the exact solution $q^*_{\text{actual}}$.

## 5 Conclusions

A theory of thermal choking due to nonequilibrium condensation in a nozzle is presented. The theory is based on a simple control volume approach. (A differential theory of thermal choking is discussed by Guha 1994.) It applies to vapor-droplet flow with or without a carrier gas. The expression for critical heat (or condensation) derived is valid for either supersonic or subsonic flow, and for heat release either in the diverging or in the converging part of a nozzle.

Table 1 shows that the present theory, Eq. (19), is in very close agreement with the full numerical solution of the differential equations of motion (giving the detailed structure of a condensation shock wave leading to thermal choking). The usually quoted Eq. (1) underestimates the critical heat by a factor of three in the example calculation presented. The variation of area across the condensation zone (although small) and the depletion in vapor mass as a result of condensation cannot be neglected in determining the critical heat in condensing nozzle flow.

## Acknowledgments

The author is grateful to Gonville & Caius College, Cambridge, for electing him as a Research Fellow.

## References

Barschdorff, D., and Fillipov, G. A., 1970, "Analysis of Certain Special Operating Modes of Laval Nozzles with Local Heat Supply," *Heat Transfer—Soviet Research*, Vol. 2, No. 5, pp. 76–87.

Denton, J. D., 1983, "An Improved Time-Marching Method for Turbomachinery Flow Calculation," ASME *Journal of Engineering for Power*, Vol. 105, pp. 514–524.

Guha, A., 1992a, "Jump Conditions Across Normal Shock Waves in Pure Vapor-Droplet Flows," *Journal of Fluid Mechanics*, Vol. 241, pp. 349–369.

Guha, A., 1992b, "The Physics of Relaxation Processes and of Stationary and Non-stationary Shock Waves in Vapor-droplet Flows," *Transport Phenomena in Heat and Mass Transfer*, Elsevier, ISTP IV, J. Reizes, ed., pp. 1404–1417.

Guha, A., 1994, "A Unified Theory of Aerodynamic and Condensation Shock Waves in Vapor-droplet Flows With or Without a Carrier Gas," to appear in *Physics Fluids*, Vol. 6, No. 5, pp. 1893–1913.

Guha, A., and Young, J. B., 1994, "The Effects of Flow Unsteadiness on the Homogeneous Nucleation of Water Droplets in Steam Turbines," to appear in *Philosophical Transactions of the Royal Society*, Series A.

Guha, A., and Young, J. B., 1991, "Time-Marching Prediction of Unsteady Condensation Phenomena Due to Supercritical Heat Addition," *Proc. Conf.*

*Turbomachinery: Latest Developments in a Changing Scene*, London, IMechE Paper C423/057, pp. 167–177.

Pouring, A. A., 1965, "Thermal Choking and Condensation in Nozzles," *Physics Fluids*, Vol. 8, No. 10, pp. 1802–1810.

Shapiro, A. H., 1953, *The Dynamics and Thermodynamics of Compressible Fluid Flow*, Vol. I, Chapter 7, The Ronald Press Company, NY.

Skillings, S. A., Walters, P. T., and Moore, M. J., 1987, "A Study of Supercritical Heat Addition as a Potential Loss Mechanism in Condensing Steam Turbines," IMechE Conf., Cambridge, England, Paper C259/87, pp. 125–134.

Wegener, P. P., 1969, "Gas Dynamics of Expansion Flows with Condensation, and Homogeneous Nucleation of Water Vapor," *Nonequilibrium Flows*, Part I, Wegener, ed., Chap. 4, Marcel Dekker.

Wegener, P. P., and Mack, L. M., 1958, "Condensation in Supersonic and Hypersonic Wind Tunnels," *Advances in Applied Mechanics*, Vol. 5, pp. 307–447.

Wegener, P. P., and Cagliostro, D. J., 1973, "Periodic Nozzle Flow with Heat Addition," *Combustion Science and Technology*, Vol. 6, pp. 269–277.

Young, J. B., 1984, "Critical Conditions and the Choking Mass Flow Rate in Nonequilibrium Wet Steam Flows," ASME JOURNAL OF FLUIDS ENGINEERING, Vol. 106, pp. 452–458.

# An Experimental Investigation of Throughflow Velocities in Two-Dimensional Fluidized Bed Bubbles: Laser Doppler Anemometer Measurements

**M. Gautam**
Department of Mechanical and Aerospace Engineering, West Virginia University, Morgantown, WV 26506

**J. T. Jurewicz**
Graduate Studies and Research, Florida Atlantic University, Boca Raton, FL 33431

**S. R. Kale**
Department of Mechanical Engineering, Indian Institute of Technology, New Delhi

*Detailed nonintrusive measurements have been made to determine the throughflow velocity in isolated fluidized bed bubbles. In air-fluidized beds, the throughflow component has been rather neglected and measurements of the visible bubble flow alone have, therefore, failed to clarify the overall distribution of gas flow between the phases. A single component fiber optic laser Doppler anemometer was used to map the fluid flow through a bubble rising in a two-dimensional bed. The bed was fluidized at a superficial velocity slightly higher than incipient. The conditioned sampling technique developed to characterize the periodic nature of the bubble phase flow revealed that the throughflow velocity in two-dimensional beds increases linearly with increasing distance from the distributor, thereby enhancing the convective component in the interphase mass transfer process. Bubble growth was accounted for and the end-effects were minimized. Dependence of the bubble throughflow on the elongation of the bubble was observed thus confirming the theoretical analysis of some previous investigators. However, experimental evidence presented in this paper showed that the existing models fail to accurately predict the convective component in the bubble phase of two-dimensional fluidized beds.*

## Introduction

Despite its wide industrial usage, the state-of-the-art design technology for fluidized bed reactors is still at a rudimentary stage (Cheremisinoff, 1986). One of the largest concerns in the commercial use of fluidized beds is scale-up which can in large part be attributed to the absence of an experimentally verified hydrodynamic theory that can describe the complicated transient gas and solids motion in a fluidized bed.

Flow of gas through a bubble is described as a combination of diffusional and convective processes (Sit and Grace, 1981). The work presented in this paper is aimed at understanding the aspects of bed hydrodynamics, especially the fluid flow field inside bubbles, which play a crucial role in promoting gas-solids contacting. A major handicap of the experimental work on distribution of gas between the two phases has been the inability to measure the throughflow in the bubbles and the emulsion phase. The throughflow component of gas, also known as the "invisible" flow, is defined as the component of fluid flow in a bubble, relative to the bubble, across a plane normal to the vertical axis of the bubble. The more easily accessible "visible" flow component has been investigated by several researchers (Grace and Clift, 1985). In the absence of relevant data on the throughflow velocities, there are no generally accepted models for interphase mass transfer despite decades of research on the complex gas-solids motion in fluidized beds (Grace, 1981)

This paper describes the work carried out to study the hydrodynamics inside single isolated fluidized bubbles and provides conclusive evidence on the throughflow velocity, $U_{th}$, (the invisible component) in the bubble phase and raises some interesting questions on some of the observations. As a first step, the uniformity of shape and size of the injected bubbles was established, using an image processor, in order to account for bubble growth. The velocity measurements inside the bubbles were made non-intrusively using a single channel fiber optic laser Doppler anemometer in combination with a unique conditioned sampling technique.

## Background

Lack of experimental data regarding the convective (invisible) component accounts for the continuing popularity of the two-phase theory despite the fact that it deals only with the visible bubble flow in most cases (Grace, 1981). Little, if any, literature exists on the specific problem being addressed-measurement of fluid flow field inside bubbles in fluidized beds.

Contributed by the Fluids Engineering Division for publication in the JOURNAL OF FLUIDS ENGINEERING. Manuscript received by Fluids Engineering Division May 10, 1993; revised manuscript received November 19, 1993. Associated Technical Editor: M. Reeks.

Davidson and Harrison (1963) showed that the magnitude of the throughflow velocity is twice the minimum fluidization velocity, $2U_{mf}$, in a two-dimensional bed. Lockett et al. (1967) considered a single isolated bubble in an infinitely wide bed and showed that the throughflow velocity is constant and equal to $2U_{mf}$. The maximum throughflow was predicted to be $4U_{mf}$ and using models by Murray (1965) they showed that the throughflow velocity varies from $0.5U_{mf}$ at the base of the bubble to $1.5U_{mf}$ at the nose.

Lockett et al. (1967) considered a single isolated bubble in an infinitely wide bed and using the theory given by Davidson and Harrison (1963) showed that the average gas velocity relative to the bubble, across any plane through the bubble normal to the vertical axis is constant. This throughflow velocity was given as $2U_{mf}$ for a two-dimensional bubble and $3U_{mf}$ for a three-dimensional bubble.

Grace and Harrison (1969) estimated throughflow velocity variations as bubbles change shape from circular to an elliptical void. Based on the assumptions of Davidson and Harrison (1966), with the exception of replacing the circular-cylindrical void with an elliptical-cylindrical void, the mean throughflow velocity through the void, relative to the void was directly related to the major and minor axes of the bubbles. For a circular void (when the two axes are equal to each other) the throughflow velocity was given as $2U_{mf}$, similar to Lockett et al. (1967).

Leung and Sandford (1969) derived the equations for the throughflow velocity in a fluidized bed bubble without the restrictive assumption of constant voidage outside the bubble. Jackson's (1963) analysis was simplified to give an approximate equation describing the fluid velocities, and the mean throughflow velocity was calculated by assuming that voidage is constant along the surface of the bubble. Using the values of voidage of the particulate phase as calculated by Stewart (1965), based on Jackson's theory, the mean bubble throughflow velocity was calculated as $1.6U_{mf}$ while using the voidage measurements of Lockett and Harrison (1967) the throughflow velocity was $1.9U_{mf}$. Leung et al. (1970) extended their earlier work (Leung and Sanford, 1969) by using Jackson's more complete equation for $U_r$, the radial component of gas velocity, and allowing voidage variation along the surface of the bubble. The values of the mean throughflow velocities in three-dimensional bed were presented. Lockett et al. (1967) reported the experimental work of Judd (1965) who gave a value for the maximum fluid flow through the two-dimensional bubble of $5.1U_{mf}$ which has been the highest ever reported in the literature.

McGrath and Streatfield (1971) determined the throughflow velocity in a bubble in a large particle fluidized bed system ($d_p > 200$ $\mu$m). The throughflow velocity was shown to remain fairly constant as the excess gas velocity was increased. Their assumption of eruption diameter as a good estimate of bubble diameter in the bed has large uncertainties associated with it as it is very difficult to relate the size of surface eruptions to conditions inside the bed. Garcia et al. (1973) presented only an order of magnitude estimate of the throughflow velocities primarily due to the limitations of their tracer particle technique.

LDA based diagnostics have been employed by several investigators to probe fluidized beds (Patrose and Caram, 1982; Ishida and Hatano, 1984; Levy and Lockwood, 1983; Kale and Eaton, 1985; Hamdullahpur and Mackay, 1986). However, no investigations into the bubble throughflow component using any non-instrusive techniques have been reported. Gautam et al. (1987) and Yianneskis (1987) have reviewed the developments in optical and unobtrusive techniques based on laser Doppler anemometry that permit measurement of velocities and/or particle sizes.

## Experimental Equipment

A two-dimensional fluidized bed vessel, 1.9 cm × 28.0 cm in cross-section and 92.0 cm high, was designed and fabricated for this investigation. The side walls were constructed from clear acrylic sheets (Plexiglas) and the large faces were 6.4 mm thick clear plate glass. Glass plates have the advantage over Plexiglas in that they do not get scratched by the bed material thus providing a good optical quality which is crucial for laser anemometry. The glass walls provided unrestricted optical access to the bed from both sides. Fluidizing air was supplied through a pressure regulator and a rotameter to the plenum (28.0 cm × 4.4 cm × 6.35 cm) which was also constructed from Plexiglas and glued at the edges to form an air tight chamber. A 0.3 cm thick porous distributor plate made of sintered stainless steel with a 5 $\mu$m porosity was sandwiched between the plenum and the vessel. Pressure taps were installed at various locations in one of the side walls to monitor the pressure drop across the bed. The entire upper assembly was bolted to the plenum with 0.16 cm thick neoprene gaskets between the two. The entire vessel along with the pressure gauges, rotameters and the plumbing systems was mounted on a steel structure.

Air was supplied, to the system, by a compressor through two parallel streams and a set of filters and dryers insured that the air was clean and dry. A custom built nozzle, 0.3 cm in diameter, was used for injecting pulses of air vertically upwards into the bed to form single isolated bubbles. The nozzle was centrally located, 1.75 cm above the distributor, on the front face of the bed. A 30 $\mu$m stainless steel screen was fitted on the nozzle opening to prevent bed material from clogging the nozzle. Compressed air was injected through a nozzle into the bed via a computer controlled fast acting solenoid valve. The valve cycles and opening times could be varied from 1/60th second to any duration.

The bed material comprised of spheroidal glass beads and contained less than 15 percent irregularly shaped particles. For the experiments, two types of test material were used: (i) glass beads in the size range of 297 $\mu$m $-$420 $\mu$m in diameter with a mean diameter of 350 $\mu$m, and (ii) glass beads in the range of 420 $\mu$m $-$590 $\mu$m with a mean diameter of 500 $\mu$m.

A low cost unit (Gautam et al., 1991) consisting of an infrared light-emitting diode and a phototransistor permitted detection of a rising bubble. The presence and quality of a "satisfactory" bubble, bridging the emittor-detector assembly, was established using a predetermined discriminator level. The emitter and the transistor were mounted opposite each other on the outside of the two face walls. The pre-conditioned photocell output was used to trigger the LDA to take data.

**Laser Doppler Anemometer.** Pointwise velocity measurements in the bed were made using a single component fiber optic laser Doppler anemometer (FOLDA) system manufactured by DANTEC Electronics. The nonintrusive technique was specially well suited for probing inside single isolated two-dimensional bubbles which span the bed thickness enabling

## Nomenclature

$d_p$ = particle diameter
$D_b$ = bubble width
$D_B$ = bed width
$H_b$ = bubble height
$H_B$ = bed height
$U_b$ = bubble rise velocity
$U_{mf}$ = minimum fluidization velocity
$U_0$ = superficial velocity
$U_{th}$ = throughflow velocity
$\alpha$ = bubble rise velocity/interstial velocity

measurements in forward scatter. The light source was a 15 mW He-Ne laser (wavelength 632.8 nm). The fiber optic LDA was configured in the forward scatter mode using an additional set of conventional receiving optics. The fringe model, the common descriptive model for the LDV technique, adopted in this work involved two intersecting coherent, monochromatic laser beams which formed a fringe pattern at their point of intersection.

A counter processor and frequency shifter along with a Bragg cell (acousto-optical cell) were used. The LDA system was interfaced with a dedicated PDP-11 laboratory computer which was used to acquire and analyze the data. The operation of the LDA was triggered by a conditioned sampling circuitry. The LDA optics and the laser were mounted on a combination of a $X$-$Y$ traversing table and a three-axis mechanism (for the optic probe). The accuracy of positioning the probe volume on the center plane of the two face plates was within $+/-0.02$ cm.

In this investigation very small quantities (approx. 4.0 mg) of titanium dioxide ($TiO_2$) powder, 0.5 $\mu$m to 2.0 $\mu$m, were used to seed the flow. The bed behavior was not affected by the small quantities (0.01 percent by weight of bed) of the seeding material. Titanium dixoide and alumina powders mixed with larger beads in a fluidized bed feeder have been successfully used by several investigators (Kale and Eaton, 1985; Jurewicz et al., 1975; Durst, Melling and Whitelaw, 1981) without any reports of the expected problems regarding smaller particles agglomerating on the glass beads such as to remove all of them from the flow. A long stemmed (0.09 cm inside diameter) stainless steel nozzle was inserted through the side port and the seeding material was injected through this nozzle, using a fluidized bed feeder, at a location above the bubble injector. The nozzle was the only outlet available to the flow from the fluidized bed and this feature prevented potential blockage of the nozzle.

The data acquisition system (Gautam et al., 1991) for this investigation was controlled by a dedicated PDP-11 microcomputer and the software written in FORTRAN and MACRO assembly language. The program sequentially operated the stepper motor driver for the traversing mechanism, activated and controlled the solenoid valve for bubble injection, accepted signal from the bubble detector, triggered that data acquisition via the LDA system and reduced the raw data. The PDP-11 micro was able to accept data at a maximum rate of 10 kHz while the LDA Counter Processor was providing the data at a rate of 1 MHz. In the absence of a Direct Memory Access (DMA) link, data recording at a rate fast enough so as not to affect the operation of the whole experiment was not possible. The data was stored in arrays, in the memory, during the bed operation and processed at the end of each run. A custom built master interface serviced all the systems on the fluidized bed facility during the flow field measurements with the LDA and also during the process of recording bubble images for image analysis.

**Image Processing System.** In order to acquire reliable velocity data on the throughflow in bubbles it was imperative to establish the consistency in the shape and size of bubbles. Stroboscopic photography and image processing techniques were adopted because they are very well suited for acquiring information on the physical properties of bubbles in two-dimensional beds. A General Electric PN2304 Optomation-II Vision System was used for determining the physical properties of the bubbles and also for determining the rise velocites of these bubbles.

## Experimental Procedures

**LDA Velocity Measurements.** Minimizing the "knifing" or the "raining down" of the particles from the roof of the bubble was critical for successful LDA measurements of fluid velocity inside the bubble. The design of the experiments enabled generation of single isolated bubbles with a minimum amount of particles raining down along the face walls—a characteristic typical of two-dimensional bubbles. Since these particles did not fall through the measuring volume, they are not likely to have any affect on LDA measurements. The severe restrictions on bubble shape, size and quality dictated by this study limited the operating region of the bed within which the bubble throughflow could be probed.

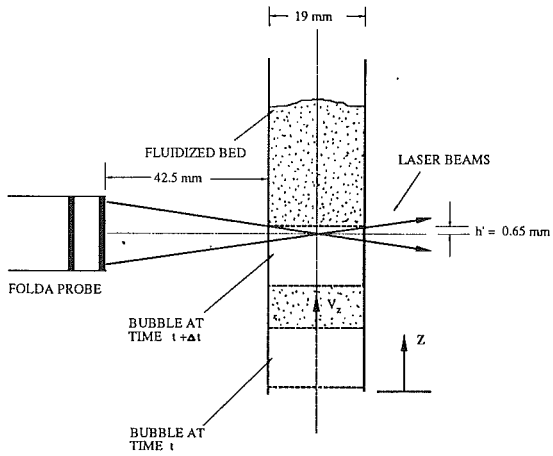


**Fig. 1 Ray diagram showing the inaccessible regions of the bubble**

The velocity measurements in the back scatter mode were rendered unreliable due to the poor signal-to-noise ratio. The receiving optics were placed at an angle of 30 degrees off the central axis in the forward scatter to avoid reflections from the glass faces. All measurements were made along the center plane between the two face plates of the fluidized bed. One of the limitations of this study was the theoretical length (along the vertical direction) of the bubble that could be probed. Figure 1 shows the location of the rising bubble at the instant when both beams can pass clear through the bed unobstructed by the bed material. However, the distance below the roof of the bubble which could not be probed was calculated to be equal to 0.65 mm. Given the inherent instability of the roof surface, this distance was negligible in a typical bubble. Similarly, measurements could be made 0.65 mm above the floor of the bubble.

A dead time of 60 clockticks (one second) between two air pulses was enough to get the bed to stable conditions prior to injection of the next bubble. The periodic nature of the flow demanded a unique conditioned sampling technique (Gautam et al., 1989, 1991) to characterize the flow through the bubble. Data was acquired for the duration of the bubble passage past the probe. With the bubble passage time (determined prior to running the experiments) known and the time history of each data point relative to bubble top also known, the bubble passage time was divided into 25 equal "time intervals" or "time bins" (Gautam et al., 1991). The interval corresponded to a section of the bubble along the height. Typically, 80,000 bubbles were probed in each run until each bin had acquired at least 1000 data points. The data in each bin were ensembled averaged and the value was assigned to the midpoint of the time bin. The standard deviation and ninety-five percent confidence interval, based on Student-t distribution, were also calculated. Anywhere from 8 to 10 runs were required for each location because of the low data rate, typically less than 10 Hz.

Amplitude discrimination was employed to discriminate signals originating from larger bed material and the seeding material. Hence, the bed material selected had a mean diameter greater than 300 $\mu$m thus, rendering signal discrimination tract-

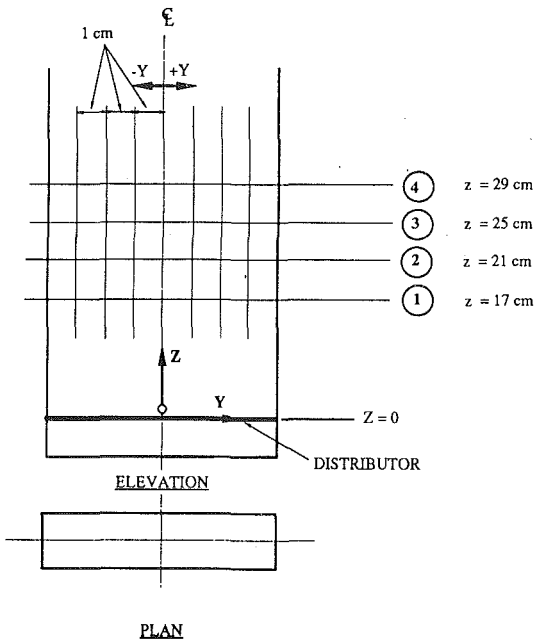


Fig. 2 Test matrix

able. Bed material with a mean particle diameter larger than 650 $\mu$m, did not allow injection of consistently stable bubbles, a condition that was imperative for this study. The threshold settings on the counter processor were set to discard signals from larger particles (larger d.c. component). The threshold settings were determined prior to running the experiments by measuring flow through a two inch diameter clear Plexiglas pipe individually using first, particles larger than 300 $\mu$m, and then with the seeding material, $TiO_2$ particles which had diameters ranging from 0.2 $\mu$m to 2 $\mu$m. Signals from the 300 $\mu$m particles were observed on an oscilloscope and the threshold was reduced until no signals were validated by the processor. The same threshold setting provided a satisfactory data rate for the flow seeded with $TiO_2$ particles. One difficulty encountered with the above approach lay in the inability to accurately distinguish between the signals from small particles passing through the center of the measuring volume and the signals of large particles crossing near the edges of the measuring volume. Since laser beams have Gaussian light intensities both signals may have similar pedestals. This inability to separate large and small particle signals is referred to as trajectory ambiguity.

Vertical or streamwise velocity component measurements of the gas flow were obtained at the vertical centerplane (broadface) of the fluidized bed at a total of nine locations (at 17.0 cm, 21.0 cm and 25.0 cm above the distributor) for each of the two bed heights, 36 cm and 33 cm. The test program is figuratively shown in Fig. 2. Figure 3 shows the fluid velocities in a rising bubble in the laboratory rest frame where $U_b$ is the bubble rise velocity and $U_{th}$ is the throughflow velocity. Therefore, absolute velocity of fluid across a plane normal to the vertical axis of the bubble is a summation of the bubble rise velocity and the bubble throughflow velocity.

The procedure used to calculate measurement uncertainties is based on that given by Kline and McClintock (1953). The uncertainty in the LDA measurements is similar to the uncertainty in the fringe spacing which was estimated at 0.25 percent corresponding to similar uncertainty in the velocity measurements. Uncertainty in the measurements of the superficial gas velocity flowing through the fluidized bed was calculated as 0.89 percent. This is a function of the distributor area measurement whose uncertainty was estimated as 2.64 percent. Details of the uncertainty analysis are presented by Gautam (1989).

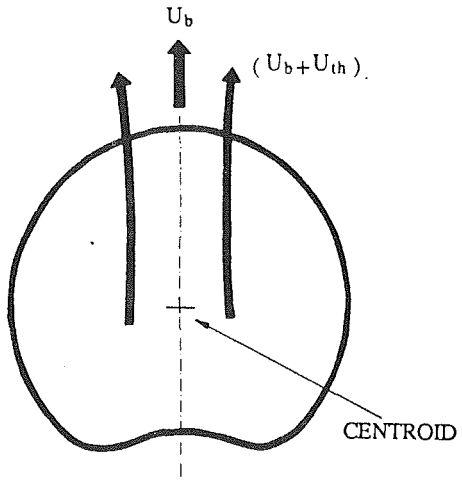


Fig. 3 A single rising bubble in the laboratory rest frame

**Physical Properties of the Bubbles.** Bubbles were videotaped with back illumination provided by the computer controlled strobe operating in tandem with the solenoid valve. The transparent two-dimensional vessel facilitated the study of the physical properties of bubbles, such as bubble centroids, bubble height and diameter through the centroid, and bubble area amongst others. The design of experiments enabled production of isolated bubbles with a minimum amount of particles raining down from the unstable roof of the bubble. Stability of the bubble which was of prime importance demanded the use of rather large bubbles. Simultaneously, in order to minimize the end effects, the region of the bed within which the bubbles could be probed was limited to 17 cm above the distributor and 8 cm below the free surface of the static bed. The superficial velocities were slightly higher than the minimum fluidization velocities. The upstream pressure in the bubble injecting air stream was kept constant. Each run consisted of recording 100 bubbles which were injected into the bed at a rate equal to that used for velocity measurements with the LDA. To obtain the physical properties of the bubbles the strobe was fired once when the bubble reached the required height in the bed. To determine the bubble rise velocity the strobe was fired six times at a rate of 15 Hz. This cycle of events was repeated every second. The images were recorded on a videotape and analyzed frame by frame to obtain the physical properties and velocity of the bubbles.

## Results and Discussion

**Physical Properties of the Bubbles.** Image analysis gave the $y$- and $z$-coordinates of the bubble centroid based on the coordinate system of the PN2304 Optomation-II vision system. The location of the origin of the coordinate system with respect to the bubble injection nozzle was not the same in every case but for a particular run it was maintained constant. The coordinates of bubble centroids are referred to as the $y$-centroid and the $z$-centroid. Figure 4 shows the consistency of locating the $y$- and $z$-centroids of consecutively injected bubbles at a height of 17.0 cm above the distributor plate in a 36 cm high bed with 350 $\mu$m particles. Similar consistency was achieved in the 33 cm high bed with 350 $\mu$m particles and in the 500 $\mu$m particle beds. The runs were made at constant superficial gas velocities such that ratios $U_0/U_{mf}$ were equal to 1.05 and 1.13 for the 500 $\mu$m and 350 $\mu$m particle beds, respectively. Values of $U_{mf}$ in each case were determined experimentally from pressure drop-velocity plots. A smooth line has been fit to the data using a spline routine. The data was found to lie within the 95 percent confidence control limits on individual predicted values. Similar data obtained at heights of 21 cm

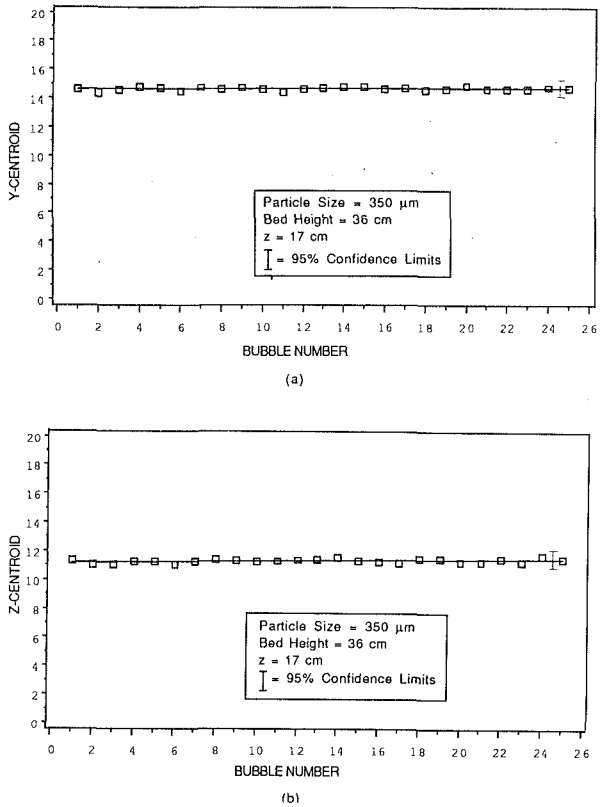


**Fig. 4 Location of (*a*) the *y*-centroid and (*b*) the *z*-centroid of the bubble ($z$ = 17 cm; $H_B$ = 36 cm; $d_p$ = 350 $\mu$m)**

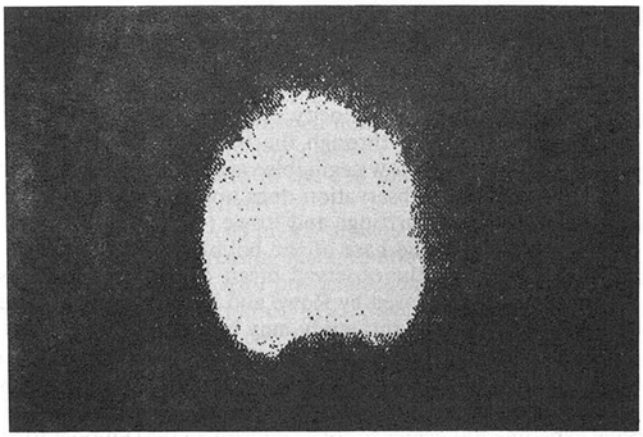

**Fig. 5 Digitized image of typical two-dimensional bubble ($z$ = 25 cm; $H_B$ = 36 cm; $d_p$ = 500 $\mu$m)**

and 25 cm above the distributor qualified the bubble generation technique by establishing the uniformity of the cyclic process of bubble injection, bubble detection, measurements of the throughflow velocity and then injection again. Uniformity in widths and heights of the bubbles was established when negligible variations were observed in the data (within the 95 percent control limit) from over 30 consecutively injected bubbles.

Image analysis results support the findings of Grace and Clift (1974) who have discussed in detail the problems associated with measuring the translation of bubble voids and have shown that even with centroids remaining fixed, the bubble shapes (diameter and height) can change significantly. A careful selection of such variables as, injection pressure, valve cycle timings, superficial gas velocity and bed heights helped minimize the variations in bubble shape and size in single isolated

**Table 1 Variation of bubble aspect ratio with distance above the distributor for different bed heights ($d_p$ = 350 $\mu$m)**

| Distance above the distributor (cm) | Aspect Ratio ($H_b/D_b$) | |
|---|---|---|
| | $H_B$ = 33 cm | $H_B$ = 36 cm |
| 17 | 0.85 | 0.815 |
| 21 | 0.93 | 0.96 |
| 25 | 0.97 | 0.98 |

bubbles (in the absence of coalescence). Figure 5 shows a digitized image of a typical two-dimensional bubble. The data on bubble centroids indicated a remarkable level of consistency in locating consecutively injected bubbles at specific $z$-location at a given time, thereby, establishing that the motion of the single isolated bubbles was almost vertical. Additionally, the consistency with which the $z$-centroid data fell within $+/-5$ percent of the specified $z$-location qualified the bubble generation setup. Table 1 compares the aspect ratios as a function of distance above the distributor for the 350 $\mu$m particle size bed. It may be noted that the bubble shape continues to become more elliptical as it travels up the bed. Therefore, description of a bubble on the basis of just one diameter, either the horizontal or the vertical or an equivalent diameter as has been done by most researchers in the past, is rather incomplete. This observed trend has direct implications on the throughflow velocity in the bubble which increases as the bubble becomes more elongated in the vertical direction.

Results from image analysis established the uniformity of shape and size of consecutively injected bubbles in the bed, hence, lending credence to the fluid velocity measurements with the LDA.

**Velocity Measurements.** The axial velocity component of the fluid flowing through the bubble is considered positive in the vertical direction, that is, along the positive $z$-axis (see Fig. 2). Velocity data are presented as a function of normalized bubble height where the nose of the bubble corresponds to the origin of the abscissa and the floor of the bubble corresponds to a maximum value of 1. The velocity data have been fitted with a smooth line using a spline routine that minimizes a linear combination of the sum of the squares of the residuals of fit and the integral of the square of the second derivative. The data have been acquired at a constant superficial velocity of 24.8 cm/s ($U_0/U_{mf}$ = 1.05) for the 500 $\mu$m diameter particles and at 14.2 cm/s ($U_0/U_{mf}$ = 1.13) for the 350 $\mu$m diameter particles. During the bed qualification runs, superficial gas velocity was varied between the minimum fluidization velocity ($U_0/U_{mf}$ = 1) and 27.4 cm/s ($U_0/U_{mf}$) = 1.16). For gas velocities below 23.0 cm/s and above 26.1 cm/s the shape and quality of the injected bubbles was unacceptable from the standpoint of making LDA measurements. Moreover, no effect on the throughflow was observed within the operational range of the superficial velocity where excess gas velocity varied from 0 cm/s to 2.5 cm/s. Positioning of the LDA measuring volume was dictated by the height above which the axial momentum flux of the injected bubble air (analogous to an isolated jet) was equal to the momentum flux of the emulsion phase. Using a modified pitot-tube probe, it was found that the momentum flux of the injected volume of air decreased with height and dissipated completely into the bed at $z$ = 17 cm. At this point the bed was considered dynamically homogeneous.

Figure 6 shows the profiles of the axial velocity component at $z$ = 17.0 cm, 21.0 cm and 25.0 cm, along the centerline, in a bed of 500 $\mu$m diameter particles and a depth of 36 cm. The throughflow velocity is seen to be fairly constant all along the height of the bubble. The scatter in the velocity data near the top of the bubble is a consequence of higher concentration of larger bed particles near the roof of the bubble. It was

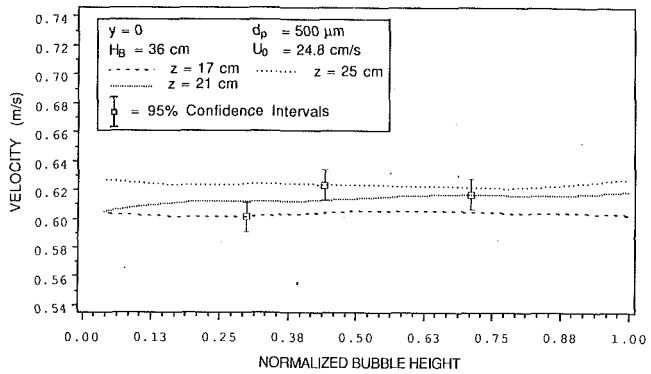


Fig. 6 Axial velocity profiles ($y = 0$, $H_B = 36$ cm; $d_p = 500$ $\mu$m)

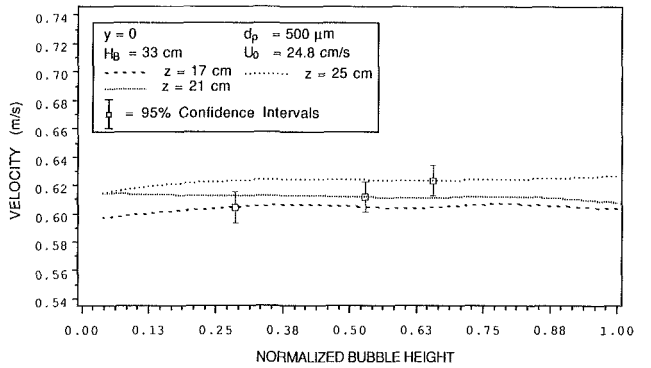


Fig. 7 Axial velocity profiles ($y = 0$, $H_B = 33$ cm; $d_p = 500$ $\mu$m)

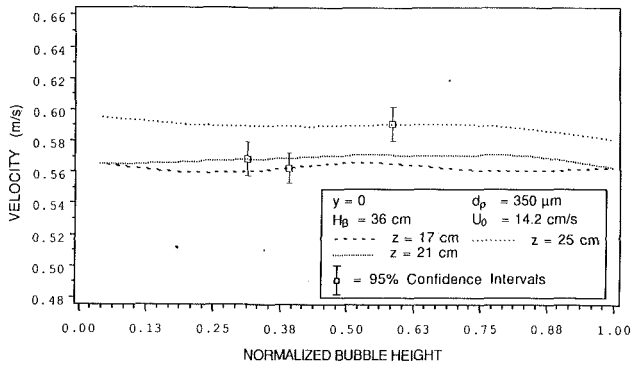


Fig. 8 Axial velocity profiles ($y = 0$, $H_B = 36$ cm; $d_p = 350$ $\mu$m)

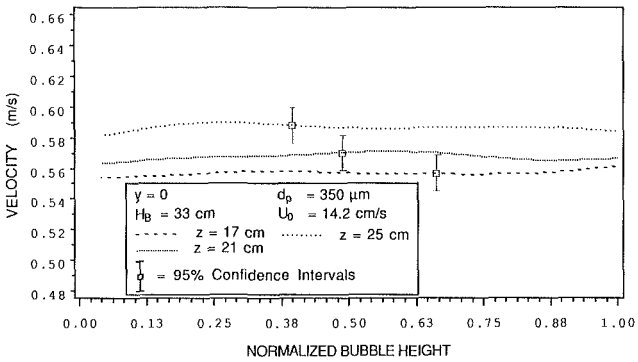


Fig. 9 Axial velocity profiles ($y = 0$, $H_B = 33$ cm; $d_p = 350$ $\mu$m)

observed that individual particles fell from the roof of the bubble even though the roof was stable against a total collapse. The axial component was observed to increase as the bubble travelled upward through the bed. Similar profiles of the axial velocity component were observed at stations removed from the centerline, that is, at $y = -1$ and $y = -2$. The mean velocities were found to be constant at each $z$-location. Profiles in Fig. 7 show that the axial velocity component increases along the centerline in a 33 cm deep bed with 500 $\mu$m mean diameter particles at $z = 17$ cm, 21 cm and 25 cm. The magnitude of the velocity at, for example, $z = 17$ cm in the 33 cm bed agrees well with the mean velocity value along the centerline at $z = 17$ cm in the 36 cm deep bed. A three percent increase over a distance of 8 cm in the 33 cm bed agreed well with the increase observed in the 36 cm bed. Within the range of experimental uncertainties, the profiles across the width of the bubble are in agreement with each other. The trends at $y = -1$ and $y = -2$ were in general agreement with those along the centerline.

Figures 8 and 9 show the velocity profiles of the axial component in a bed of 350 $\mu$m diameter particles. Bed heights of 36 cm and 33 cm were investigated with all other conditions similar to those for the 500 $\mu$m diameter particles. The minimum fluidization velocity was 12.5 cm/s and the bed was operated at a superficial velocity of 14.2 cm/s. The bubble rise velocity, as determined from the image processor, was 37.8 cm/s. The variation in each profile, for the 350 $\mu$m diameter particle bed, was more pronounced than that in the 500 $\mu$m bed but this was probably due to a poorer signal to noise ratio. The bubbles were observed to be less stable than in the 500 $\mu$m particle case. Velocities at each point along the vertical length of the bubble are fairly constant. The increase in the velocity with increasing distance from the distributor is consistent with the findings in the 500 $\mu$m diameter particle bed. Axial velocity profiles at $y = -1$ and at $y = -2$ showed similar trends. The increase in the velocity from $z = 17$ cm to $z = 25$ cm was 5 percent. Unlike in the 500 $\mu$m sized particle bed the increase in velocity from $z = 21$ cm to $z = 25$ cm is greater that from $z = 17$ cm to $z = 21$ cm.

Even though the axial velocity components increase as the bubble travels upward through the bed, at a specified $z$-location, the velocities show negligible variation along the height of the bubble. This observation does not agree with the theoretical analysis of Partridge and Rowe (1966) who predicted a $U_{th}$ of 0.5 $U_{mf}$ at the base of the bubble and 1.5$U_{mf}$ at the nose. Additionally, the observed mean $U_{th}$ was significantly higher than $U_{mf}$ proposed by Rowe and Partridge (1966). The bubble investigated in this study may be classified as "slow" bubbles. While the hydrodynamic models proposed in the past do no more than indicate a qualitative trend of the fluid flow pattern, axial velocity components measured in this study provide experimental evidence for Davidson's (1961) model for a slow bubble. Using voidage fraction of 0.48 at the nose of the bubble, the value of $\alpha$ equal to 0.561 was obtained and this is close to Davidson's ratio of 0.587. An absence of a recirculation zone within a slow bubble was confirmed.

The study has shown that the flow through a bubble has a dominant streamwise component which is constant along the height of the bubble. Figures 10 and 11 show the axial velocity profiles at $y = -1$ and $y = -2$ locations for a bed height of 36 cm and bed material with $d_p = 500$ $\mu$m. Combining the velocity measurements at different $y$-locations for a given distance above the distributor revealed that the velocity profiles may be uniform across the bubble cross-section. Axial velocity profiles for the 36 cm and 33 cm deep beds with both 350 $\mu$m and 500 $\mu$m diameter bed particles showed similar trends at $y = -1$ and $y = -2$ locations. As the excess gas velocity is increased, there is a definite increase in the size of the injected bubble at the expense of the dense phase but the throughflow component remained generally constant.

An increase in the throughflow velocity with bubble aspect

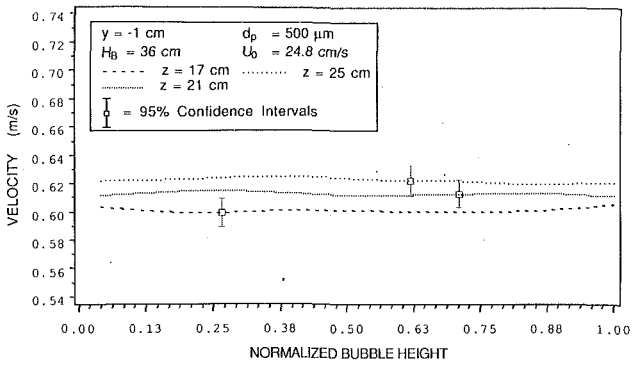


Fig. 10 Axial velocity profiles ($y = -1$, $H_B = 36$, $d_p = 500$ μm)

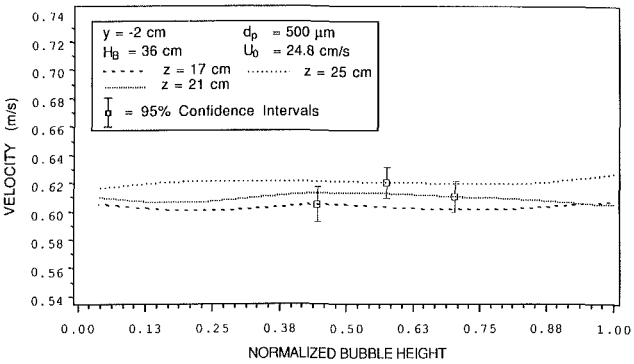


Fig. 11 Axial velocity profiles ($y = -2$, $H_B = 36$ cm, $d_p = 500$ μm)

ratio (ratio of bubble height to bubble width) provides evidence for and supports the model proposed by Grace and Harrison (1969) who had analyzed an elliptical-cylindrical void and equated the major and minor axes to the mean throughflow velocity. They also presented cine photography results that showed that elongated bubbles ($a > b$) were observed much more frequently than flattened bubbles ($a < b$). Tables 2 and 3 show the variation of throughflow velocity as a function of the bubble aspect ratio in the 350 μm and 500 μm diameter particle beds, respectively.

Throughflow velocity in two-dimensional bubbles was found to increase with increasing distance above the distributor. For sake of comparison with published analytical work, $U_{th}$ may be written as a function of $U_{mf}$. It was found that $U_{th}$ varies from $1.38U_{mf}$ ($z = 17$ cm) to $1.46U_{mf}$ ($z = 25$ cm) in the 500 μm bed and from $1.43U_{mf}$ ($z = 17$ cm) to $1.7\ U_{mf}$ ($z = 25$ cm) in the 350 μm bed. Values of $1.6U_{mf}$ to $1.9U_{mf}$ suggested by Leung and Sandford (1969) come very close to the findings of this study. A predicted value of $1.5U_{mf}$ by Murray (1965) at the nose of the bubble is in fair agreement with the present experimental findings.

An interesting observation was the higher value of $U_{th}$ in the 350 μm bed compared to that in the 500 μm bed. An explanation for this observation is open to the research community. It should be mentioned that throughflow velocities may be higher in freely bubbling beds where the interacting bubbles have a tendency to elongate in the vertical direction. The likelihood of the three-dimensional effect in the 1.9 cm thick two-dimensional bed affecting $U_{th}$ can not be neglected.

## Conclusions

Laser Doppler anemometry was successfully applied to non-intrusively measure the throughflow component in single isolated bubbles in a two-dimensional fluidized bed. The bubble throughflow velocity in two-dimensional beds appears to increase with increasing distance from the distributor, thereby, enhancing the convective component in the interphase mass transfer process. At a given height above the distributor, the throughflow in the bubble is constant along the height of the bubble, that is, there is no significant variation from the floor to the roof of the bubble. Further, at a given height above the distributor, the fluid velocity is uniform across the width of the bubble. Two-dimensional fluidized bubbles elongate in the vertical direction as they travel upward in the bed. Velocity profiles suggest a dependence of the bubble throughflow velocity on elongation of the bubble thus confirming the theoretical analysis of Grace and Harrison (1969). Throughflow velocity was observed to be independent of the excess gas flow within the operational range of the superficial velocity. No gas recirculation zones were observed inside individually injected "slow" bubbles in the two-dimensional bed.

The new experimental findings provide researchers with values of throughflow or convective component other than the untested estimates, based on the two-phase theory of fluidization, in the various interphase mass transfer models.

**Table 2 Variation of bubble throughflow velocity with bubble aspect ratio ($d_p = 350$ μm)**

| Aspect ratio ($H_b/D_b$) | Velocity. ($U_{th}/U_{mf}$) $H_B = 33$ cm | $H_B = 36$ cm |
|---|---|---|
| 0.815 | – | 1.7 |
| 0.85 | 1.43 | – |
| 0.93 | 1.52 | – |
| 0.96 | – | 1.56 |
| 0.97 | 1.69 | – |
| 0.98 | – | 1.98 |

**Table 3 Variation of bubble throughflow velocity with bubble aspect ratio ($d_p = 500$ μm)**

| Aspect ratio ($H_b/D_b$) | Velocity ($U_{th}/U_{mf}$) $H_B = 33$ cm | $H_B = 36$ cm |
|---|---|---|
| 1.06 | – | 1.38 |
| 1.07 | – | 1.41 |
| 1.085 | 1.38 | – |
| 1.09 | – | 1.45 |
| 1.10 | 1.41 | – |
| 1.12 | 1.46 | – |

## Acknowledgments

The authors wish to thank the Energy and Water Research Center, West Virginia University and the NSF/Industry/University Cooperative Research Program for providing the funds for the research. The authors also thank Dr. Joseph Mei, Morgantown Energy Technology Center, U.S.D.O.E. and Prof. John R. Grace for their invaluable comments during the course of the research.

## References

Cheremisinoff, N. P., 1986, "Review of Experimental Methods for Studying the Hydrodynamics of Gas Solid Fluidized Beds," *Industrial and Engineering Chemistry, Process Design Development*, Vol. 25, pop. 329–351.

Davidson, J. F., 1961, "Symposium on Fluidization-Discussion," *Transactions of the Institution of Chemical Engineers*, Vol. 39, pp. 230–232.

Davidson, J. F., and Harrison, D., 1963, *Fluidized Particles*, Cambridge Univ. Press.

Durst, F., Melling, A., Whitelaw, J. H., 1981, *Principles and Practice of Laser Doppler Anemometry*, Academic Press.

Garcia, A., Grace, J. R., Clift, R., 1973, "Behaviour of Gas Bubbles in Fluidized Beds," *AIChE Journal*, Vol. 19, No. 2, pp. 369–370.

Gautam, M., 1989, "An Experimental Study of Hydrodynamics Inside Two-Dimensional Fluidized Bed Bubbles," Ph.D. Dissertation, Department of Mechanical and Aerospace Engineering, West Virginia University, Morgantown, WV.

Gautam, M., Bocanegra, L., Jurewicz, J. T., and Morris, G. J., 1987, "Review of LDV Measurements in Gas-Solid Flows," *International Symposium on Multiphase Flows*, C. T. Crowe, and Z. Q. Fan eds., Hangzhou, China.

Gautam, M., Jurewicz, J. T., and Palmer, G. M., 1989, "LDA Measurements in Fluid Flow Field Inside Two-Dimensional Fluidized Bed Bubbles," *III International Symposium on Gas Solid Flows*, ASME Spring Meeting, July 9-12, 1989, San Diego, CA.

Gautam, M., Jurewicz, J. T., and Palmer, G. M., 1991, "Conditioned Sampled Velocity Measurements in Two-Dimensional Fluidized Bed Bubbles," IV International Conference on Laser Anemometry-Advances and Applications, Cleveland, Aug. 5-9, 1991.

Grace, J. R., 1981, "Fluidized Bed Reactor Modelling—An Overview," Americal Chemical Society Symposium Series, No. 168, Chemical Reactors, ed. Fogler, H. Scott.

Grace, J. R., and Clift, R., 1974, "On the Two-Phase Theory of Fludiziation," *Chemical Engineering Science*, Vol. 29, pp. 327-334.

Grace, J. R., and Clift, R., 1985, *Fluidization*, Davidson, J. F., Clift, R., and Harrison, D., eds., Chapter 3, Academic Press.

Grace, J. R., and Harrison, D., 1969, "Behaviour of Freely Bubbling Fluidized Beds," *Chemical Engineering Science*, Vol. 24, pp. 497-508.

Hamdullahpur, F., and Mackay, G. D. M., 1986, "Two Phase Flow Behaviour in the Freeboard of a Gas Fluidized Bed," *AIChE Journal*, Vol. 32, No. 12, pp. 2047-2055.

Ishida, M., and Hatano, H., 1984, "The Behaviour of Gas and Solid Particles in a Gas-Solid Fluidizied Bed Detected by Optical Fiber Probes," Proceedings of the IV International Symposium on Fluidization, Engineering Foundation, pp. 61-68.

Jackson, R., 1963, "The Mechanics of Fluidized Beds, Part II," *Transactions of the Institution of Chemical Engineers*, Vol. 41, pp. 22-28.

Judd, M. R., 1965, Ph.d. dissertation, University of Cape Town (Reported by Lockett et al., 1967).

Jurewicz, J. T., Stock, D. E., Crowe, C. T., and Eschbach, J. E., 1975, "Measurements of Both Gas and Particle Velocities in Turbulent Two-Phase Flows," *Proceedings of the Fourth Symposium of Turbulence in Liquids*, Rolla, MO.

Kale, S. R., and Eaton, J. K., 1985, "An Experimental Investigation of Gas-Particle Flows through Diffusers in the Freeboard Region of Fluidized Beds," *International Journal of Multiphase Flow*, Vol. 11, No. 5, pp. 659-674.

Kline, S. J., and McClintock, F. A., 1953, "Describing Uncertainties in Single-Sample Experiments," *Mechanical Engineering*, pp. 3-8.

Leung, L. S., and Sandford, I. C., 1969, "On the Percolation of Fluid Through Bubbles in Fluidized Beds," *Chemical Engineering Science*, Vol. 24, p. 1391.

Leung, L. S., Sandford, I. C., and Mak, F. K., 1970, "Effect of Voidage Variation on Throughflow in Bubbles in a Fluidized Bed," *Chemical Engineering Science*, Vol. 25, p. 220.

Levy, Y., and Lockwood, F. C., 1983, "Laser Doppler Measurements of Flow in Freeboard of a Fluidized Bed," *AIChE Journal*, Vol. 29, No. 6, pp. 889-895.

Lockett, M. J., and Harrison, D., 1967, "On the Two-Phase Theory of Fluidization," *Chemical Engineering Science*, Vol. 22, pp. 1059-1066.

Lockett, M. J., Davidson, J. F., and Harrison, D., 1967, "On the Two-Phase Theory of Fluidization," *Chemical Engineering Science*, Vol. 22, pp. 1059-1066.

McGrath, L., and Streatfield, R. E., 1971, "Bubbling in Shallow Gas-Fluidized Beds of Large Particles," *Transactions of the Institution of Chemical Engineers*, Vol. 49, pp. 70-79.

Murray, J. D., 1965, "On the Mathematics of Fluidization; Part I, Fundamental Equations and Wave Propagation," *Journal of Fluid Mechanics*, Vol. 21, p. 465.

Partridge, B. A., and Rowe, P. N., 1966, "Analysis of Gas Flow in a Bubbling Fluidized Bed when Cloud Formation Occurs," *Transactions of the Institution of Chemical Engineers*, Vol. 44, pp. 348-349.

Patrose, B., and Caram, H. S., 1982, "Optical Fiber Probe Transit Anemometer for Particle Velocity Measurements in Fluidized Beds," *AIChE Journal*, Vol. 28, No. 4, pp. 604-609, 1982.

Sit, S. P., and Grace, J. R., 1981, "Effect of Bubble Interaction on Interphase Mass Transfer in Gas Fluidized Beds," *Chemical Engineering Science*, Vol. 36, pp. 327-335.

Stewart, P. S. B., 1965, Ph.D. thesis, Univ. of Cambridge (reported by Leung and Sandford, 1970).

Yianneskis, M., 1987, "Velocity, Particle Sizing and Concentration Measurement Techniques for Multiphase Flow," *Powder Technology*, Vol. 49, pp. 261-269.

**Yongliang Chen**
Graduate Research Assistant.

**Stephen D. Heister**
Assistant Professor.

School of Aeronautics and Astronautics,
Purdue University,
W. Lafayette, IN 47907

# A Numerical Treatment for Attached Cavitation

*A new numerical treatment has been developed for the prediction of the flowfield resulting from an attached cavitation region. The cavitation model has been implemented in a viscous calculation which is an improvement over previous inviscid results. The model requires no apriori knowledge of the wall detachment point or bubble length and comparisons with experimental data indicate good predictions of these quantities for a variety of different body shapes and cavitation numbers. Furthermore, wall pressure distributions are also predicted quite accurately using this method. While the treatment has been applied to an axisymmetric calculation, the approach should be applicable to two-dimensional flows.*

## Introduction

Attached cavitated regions occur in a variety of different situations. Marine applications involving attached "bubbles" on propellers and underwater vehicles are obvious examples; but devices such as high speed pumps and high pressure injectors are also subject to this phenomenon. The transient nature involving the creation and collapse of these regions is often implicated in local damage to surfaces of devices which exhibit cavitation. In addition, the presence of a cavitated region can have a large effect on surface pressure distribution as well as the massflow capability of internal flow devices operating in this environment.

For these reasons, substantial efforts have been undertaken to develop capabilities to predict the extent of cavitation for various types of geometries and flow situations. While the advancements of computational fluid dynamics (CFD) techniques have provided a nearly routine treatment of single phase flows, there are still great difficulties in predicting flow-fields (either steady or unsteady) involving regions of vapor. Since even the fundamental mechanisms of the inception of these areas are not well understood (Rood, 1991), and since the presence of cavitation bubbles is usually accompanied by turbulent two-phase regions with complex behavior, numericists have had to resort to approximations to characterize this flowfield. Therefore, numerical treatment of cavitated flowfields has not matured to the extent of the more easily treated single-phase flows.

A schematic description of the general features of an external flow with attached cavitation is shown in Fig. 1. The forebody of the cavity is generally well defined and reasonably steady provided that the freestream flow doesn't oscillate appreciably with time. In the aft portion of the bubble, instability of the surface due to local increases in liquid pressure leads to the formation of small bubbles which are formed in a "wake region." The wake region is characterized by two-phase, unsteady processes involving both the formation and collapse of bubbles. At some point downstream, the freestream pressure has increased to the point where all bubbles have collapsed, thus signaling the end of the wake region and the cavitation event.

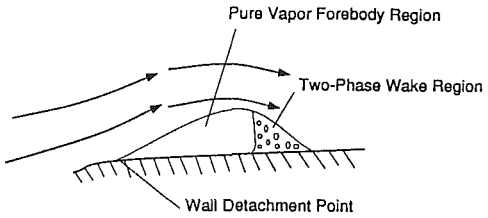


**Fig. 1 Flow field near an attached cavitation bubble**

The modeling of cavitated flows of this nature has taken two distinctly different approaches. One approach (hereafter referred to as an "interface tracking" scheme) seeks a solution in the liquid domain along with a description of the boundary of the cavitated surface. To treat the two-phase wake region, a wake model is required since there is no attempt to define the interface of smaller bubbles lying in this area. Most of the recent efforts (Plesset and Chapman, 1971; Mitchell and Hammitt, 1973; Prosperetti, 1982; Stern and Vorus, 1983; Blake et al., 1986; Stern, 1989, Deshpande, et. al., 1992) using the interface tracking approach have neglected liquid viscosity. Surface-tension forces are usually neglected, even though they may be important in the early growth phase after inception.

Recently, interface tracking solutions using boundary element methods have been used to treat attached cavitation by time-dependent tracing of the bubble boundary, or by using an iterative process to force a constant pressure boundary for a steady solution. (Furness and Hutton, 1975; Lemonnier and Rowe, 1988; Ingber and Hailey, 1991). The time-dependent solution by interface tracking methods is obscured by the fact that there is no well-defined interface in the wake region which can dominate the unsteady feature of the cavitation problem.

The other distinct class of numerical methods makes no

Contributed by the Fluids Engineering Division for publication in the JOURNAL OF FLUIDS ENGINEERING. Manuscript received by the Fluids Engineering Division March 4, 1993; revised manuscript received February 4, 1994. Associate Technical Editor: T. T. Huang.

attempt to track an interface, but instead treats the flow as two-phase with a pseudo-density which varies between liquid and vapor extremes. These two-phase models have the advantage that no special wake treatment is required, but have the disadvantage in that the interface of gas and liquid is not determined and must be inferred from density values in neighboring cells. Generally, these methods (Delannoy and Kueny, 1991; Kubota et al, 1989; Purvis, 1992) treat the fluid as compressible which requires an additional relation between the pseudo-density and other flow variables (such as the pressure). The reason that at present these methods are far from giving an accurate prediction (Dupont and Avellan, 1991) may be caused by the difficulties in defining this relationship.

Unfortunately, there are limited axisymmetric experimental data for use in direct comparison with numerical predictions of an attached cavitation. Many researchers have focused on the flow detachment point, unsteady phenomena and viscous effects for the inception (Kubota et al., 1989; Franc and Michel, 1985). Very few researchers have measured wall pressures and the extent of fully cavitated and wake regions. One notable exception here is the work of Rouse and McNown, (1948); who measured bubble profiles and wall pressure distributions for axisymmetric headforms. We shall make use of these data in comparing the results of our calculations.

In this work, we will consider the attached cavitation flowfield on an axisymmetric body. We will employ an interface tracking scheme capable of defining an average (steady) bubble location and size for a given wake model. This treatment is general and could also be applied to two-dimensional flows. The treatment is implemented in a numerical scheme which includes viscous effects, thus increasing the capability as referenced to other interface tracking approaches. After a brief discussion of the flow solver, a description of the cavitation model will be presented. Finally, flow solutions are compared with experimental data of Rouse and McNown (1948), for a variety of axisymmetric bodies.

## Description of Numerical Model

**Incompressible, Viscous Flow Solver.** The major problem in developing a solver for the incompressible Navier-Stokes equations lies in the solutions of the continuity equation to a high degree of accuracy (generally machine accuracy is preferred). Even a small mass error can lead to dramatic changes in pressure which can cause instabilities or gross error in velocities. Today, several methods have successfully overcome this difficulty. The stream function and vorticity method (Burggraf, 1966), artificial compressibility method (Soh and Goodrich, 1988), and various pressure-based approaches have been employed successfully in viscous incompressible flows. For this work, we choose a popular pressure-based scheme known as the Marker-And-Cell method (Peyret and Taylor, 1986).

The present model neglects turbulent fluctuations in seeking an average "steady" solution for the flowfield. Since many of these flows are characterized by strong accelerations in the region of the detachment point, turbulence effects will be most pronounced in the wake region (and points downstream of the wake). For this reason, we don't expect a drastically different behavior in the bubble forebody even if turbulence were considered. Since we are modeling the region where turbulence effects are most pronounced, and since we are aware of no turbulence model capable of treating these two-phase effects, the present approach is justified.

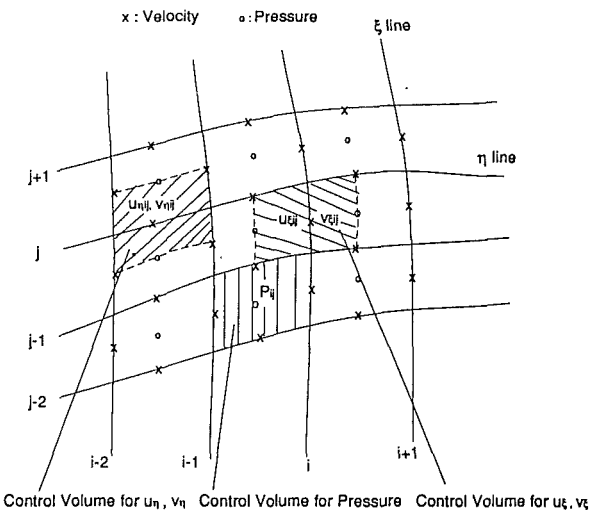


**Fig. 2 Typical mesh cells for marker-and cell formulation**

Under these assumptions, the dimensionless Navier-Stokes equations are:

$$\frac{\partial(rv)}{\partial r}+\frac{\partial(ru)}{\partial z}=0 \tag{1}$$

$$\frac{\partial(rv)}{\partial t}+\frac{\partial(rv^2)}{\partial r}+\frac{\partial(rvu)}{\partial z}=-r\frac{\partial p}{\partial r}+\frac{1}{\mathrm{Re}}\left(r\frac{\partial}{\partial r}\left[\frac{1}{r}\frac{\partial}{\partial r}(rv)\right]+\frac{\partial^2(rv)}{\partial z^2}\right) \tag{2}$$

$$\frac{\partial(ru)}{\partial t}+\frac{\partial}{\partial r}(rvu)+\frac{\partial(ru^2)}{\partial z}=-r\frac{\partial p}{\partial z}+\frac{1}{\mathrm{Re}}\left(\frac{\partial}{\partial r}\left(r\frac{\partial u}{\partial r}\right)+\frac{\partial^2(ru)}{\partial z^2}\right) \tag{3}$$

In performing the nondimensionalization, we have chosen the diameter of the body, the freestream velocity, and the fluid density as dimensions. The discrete equations are derived for the finite volume method in a body-fitted mesh. Central differencing is used for the viscous terms, while the hybrid scheme (Patankar, 1980) is used for convective terms to insure stability at high Reynolds numbers.

The control volumes for velocities and pressure are shown in Fig. 2. The continuity equation is derived for the cell encircled by grid lines with $P_{ij}$ at the center. The discrete equations for the velocities laid on the constant $\xi$ line ($u_\xi$, $v_\xi$) and the velocities laid on the constant $\eta$ line ($u_\eta$, $v_\eta$), are different as indicated by the mesh stars shown in Fig. 2. The convection terms and the viscous terms are calculated in a similar fashion, i.e., using the values at the closest points to the control faces.

## Nomenclature

$K$ = cavitation number
$P$ = pressure
$r$ = radial coordinate
$s$ = local mesh spacing
$S$ = distance from the body's leading edge
$u$ = axial velocity
$v$ = radial velocity
$z$ = axial coordinate
Re = Reynolds number
$\alpha$, $\beta$ = angles defined in Fig. 3
$\xi$ = streamwise index (see Fig. 2)
$\eta$ = transverse index (see Fig. 2)

The momentum equations require pressures on the control surfaces which enclose the points where velocities are given. In order to obtain pressures at locations where no pressure point is given, we use an average of the four neighboring pressure values.

Substituting the velocities into the continuity equation, gives an equation for pressure which is solved by the Successive Line Over-Relaxation method (SLOR). The solution procedure involves a calculation of pressure given an initial guess of the velocity field. This pressure prediction can then be used to update the velocity field for the subsequent iteration.

**Cavitation Treatment.** A simple, well-tested cavitation treatment, which is efficient for axisymmetric and two-dimensional flow problems has been developed. We have three basic assumptions for the cavitation bubble:

1. The bubble boundary is a free surface
2. The pressure inside the bubble is the vapor pressure
3. The rear part of the bubble can be approximated by a wake model

The reader should be aware of the ramifications of such assumptions in describing cavitated flows of this type. The work of Arakeri (1975) reveals a small region (typically a few percent of the body diameter) just upstream of the inception point which can support pressures lower than the local vapor pressure. The actual inception pressure will lie somewhere between this limit determined in relatively "clean flow" experimental conditions, and the actual vapor pressure in the liquid. The availability of nucleation sites from either trapped gas bubbles or particles will determine the actual cavitation inception pressure. For engineering calculations, our second assumption above is generally employed although our model is not restricted by this assumption and will perform well for other cavitation inception criteria.

Numerically, the problem is in enforcing the constant pressure condition. As mentioned before, our approach is to adjust the cavity shape according to the pressure distribution. Dupont and Avellan (1991) have used a similar idea to modify the potential solution and have shown that the modified solution is superior to the initial potential one. At first, a solution is obtained by assuming no cavitation. At locations where the pressure is below vapor pressure, we apply the cavitation model. The boundary of the cavity is permitted to move according to the pressure difference between the local and the vapor pressures.

Unlike the potential model using boundary element methods, it is difficult to use a traditional perturbation method to connect the bubble shape with the pressure. Instead, we take advantage of the situation by noting that the flow passes around a corner. We know that increasing the angle of the corner will increase the pressure behind the corner node, while decreasing the angle will have the opposite effect. For the cavitation model, we look at every computational node as a corner as shown in Fig. 3. Since the pressure at a given location will be effected mostly by the change in $\alpha$ at the adjacent upstream point, we choose the updating scheme:

$$\alpha_i^{n+1} = \alpha_i^n + C(P_v - P_{i+1}) \tag{4}$$

Here, $i$ is the grid point under consideration, $n$ is the iteration number, and $C$ is a small empirical constant. At the next time step, we move the bubble boundary according to the new angles. In the current formulation, points are moved in the radial direction only, and the new location, $r_i^{n+1}$, can be expressed in terms of the movement of the previous points:

$$r_i^{n+1} = r_{i-1}^{n+1} - (z_i - z_{i-1}) \times ctg(\alpha_{i-1}^{n+1} - \beta_{i-1}^{n+1}) \tag{5}$$

where the angle $\beta_{i-1}$ is shown in Fig. 3. After the entire bubble boundary is updated, the rear portion of the bubble is modified by the wake model.

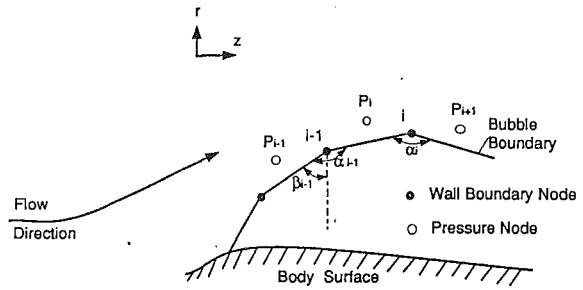


**Fig. 3 Treatment of the cavitation boundary**

After regriding the computational domain and using the previous time step solution as an approximate flow field for the new domain, we perform another subiteration to determine the approximate changes in pressure surrounding the bubble. From the new pressure distribution, the bubble shape can then be readjusted. This process is repeated until the pressure on the forebody of the bubble is close to the vapor pressure to the desired criterion and the solution of the flow field is convergent. An advantage of this approach is that it is relatively independent of the flow solver and it is unnecessary to use the detachment point or bubble length as an input as in potential models.

An important problem here is to choose a suitable constant $C$ and the number of subiterations to estimate the new flowfield about the bubble. Even though it is unnecessary to get a convergent flow field for every bubble shape (it is expensive), we should carry out enough iterations to make the flow field close to convergent. Because of the strong iteraction between the bubble shape and the flow field, we find it is better to choose a very small $C$ value so that few subiterations are required after the change of bubble boundary.

It should be noted that this procedure is permissible only because we are seeking a steady solution to the problem. The accuracy of intermediate solutions is of no consequence so long as the time stepping procedure itself is convergent. For instance, converged solutions are independent of the choice of $C$ so long as the value chosen is small enough to make subiterations stable. This situation is analogous to the application of an implicit solver which may take large timesteps and generate a host of nonphysical solutions in the course of iterations to a steady-state result.

**Treatment of Wake Region.** The interface tracking methods are largely based on free-streamline theory from which the constant pressure and free surface conditions on the cavity become natural assumptions. While there is a well-defined interface between the liquid and vapor on the forebody and center of the attached cavity, this interface *does not* exist within the wake region which is characterized by a disperse field of ever-shrinking bubbles. The formation of the wake has been attributed to a re-entrant jet at the end of the cavity (Furness and Hutton, 1975; Uhlman, 1987; Delannoy and Kueny, 1990) caused by the local increase in pressure along the wall. This jet serves as a mechanism to destabilize the local surface, thus creating the bubble field observed experimentally. The axial extent of the wake depends on the rate of increase of the external pressure (as determined by the body shape) as well as Reynolds number and local turbulence levels.

In the wake region, all interface tracking schemes must apply a "wake model" to provide closure of the bubble boundary to the local surface. Physically, the wake model is required since the local wall pressure is not equal to the fluid vapor pressure in this two-phase region dominated by the collapse of bubbles generated in the forebody of the surface. Since the dynamics of the collapse of this complex, turbulent bubble field are not well understood, there is no attempt to include

them within the solution algorithm. Most authors (e.g., Brennen, 1969) agree that the choice of the wake model, within limits, has little influence to the forebody of the cavity and our calculations support this assertion. Therefore, the interface tracking methods may predict the overall behavior of cavitating flows fairly well in spite of the trouble in modeling the wake region.

Generally, there are two kinds of cavitation closure models. One relies on a prescribed pressure (or velocity in potential models, Kinnas and Fine, 1993), and the other assumes an aft-body geometry (Ingber and Hailey, 1991). It should be noted here that both of these methods are more or less arbitrary. In this work, no explicit wake model is required since we could impose the constant pressure criteria $p = p_v$ over the entire length of the bubble (with the exception of the last point). This treatment would be similar to Uhlman (1987) and Deshpande et al. (1992). The one problem with this approach is that the entire pressure recovery occurs over the last segment of the cavity which leads to a large pressure "spike" at the cavity termination point. Physically, the presence of the re-entrant jet moderates the pressure rise within the wake leading to a smooth pressure distribution in this region.

In order to reflect the physics of this process, we have chosen a wake model which will simulate a streamline on which the pressure is no longer constant. When the bubble height is below half of its maximum value, we presume a streamline which is simply a circular arc tangent to the local cavity and the wall of the body. On this circular arc, $\partial \mathbf{V}/\partial n = 0$ since we presume the arc is a streamline and no mass can cross this boundary. Since the arc is not the interface between liquid and gas, we need to modify the zero shear stress boundary condition in this region. The model allows the viscosity to increase linearly as a function of the distance from the wall such that the full liquid viscosity is realized at the arc termination point. This approach permits a modeling of the physics relevant to the reentrant jet which contributes to the flowfield in this region.

**Boundary Conditions and Mesh Generation.** The boundary conditions at the centerline are standard axisymmetric conditions, i.e., $v = \partial u/\partial r = \partial p/\partial r = 0$. At the solid wall, the physical condition $\mathbf{V} = 0$ is the only boundary condition required since the MAC mesh distribution places no pressure points at the boundary. For the far field, the boundary condition is $\mathbf{V} = \mathbf{U}_\infty$. Finally, along the cavitation surface, we enforce conditions such that the normal velocity and the gradient of the tangential velocity both vanish.

For outflow boundary conditions, we assume the downstream boundary is far away from the region of interest, so it has minor influence to the cavitation calculation. The pressure is far field pressure and the boundary layer near the wall is well developed so that we can use first order extrapolation of all velocity components. In this work, we have chosen an algebraic method for grid generation due to its computational efficiency. Exponential stretching is used in high gradient regions. A typical mesh is shown for a hemispheric headform in Fig. 4.

## Results and Discussion

The current algorithm was tested on the flows across three kinds of headforms: conic, ogival and hemispheric heads. Rouse and McNown (1948) indicated that for high Re, there is negligible Re influence due to turbulence which supports our earlier assertion that turbulence will not have a drastic effect on bubble forebody shapes. The wake model is employed in the region where turbulent effects are most important. All calculations assume $\mathrm{Re} = 1.36 \times 10^5$, consistent with the value quoted by Rouse and McNown (1948).

The strong influence of cavitation on the body pressure distribution is highlighted in Fig. 5 for $K = 0.4$ and $K \geq 1.4$

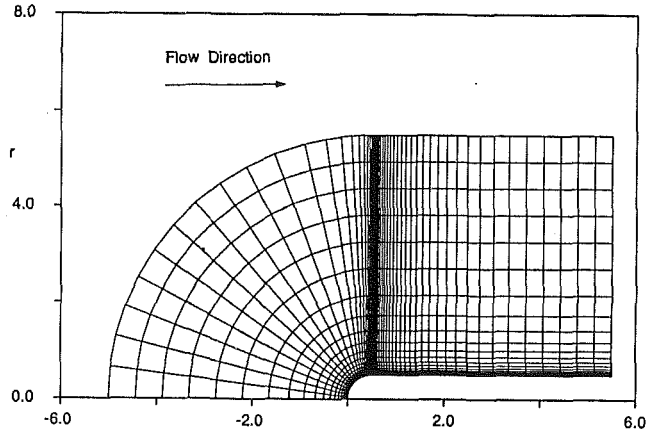


Fig. 4 Typical computation mesh (hemispherical headform)

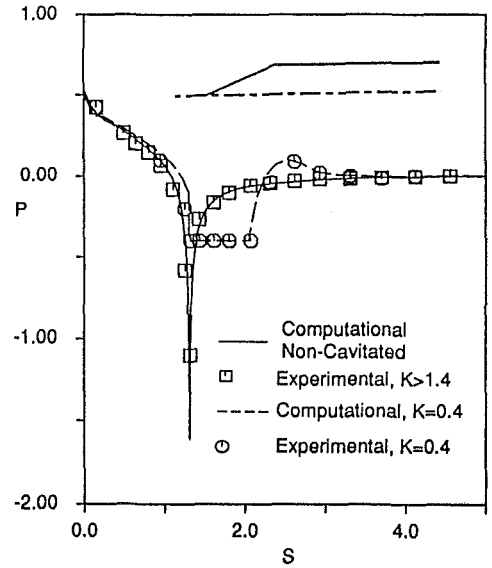


Fig. 5 The influence of the cavitation on wall pressure distribution

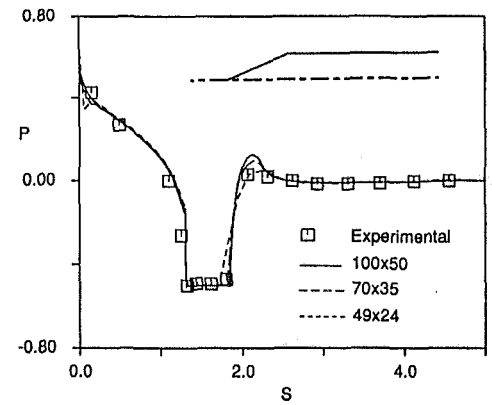


Fig. 6 Convergence test: bubble shapes for $K = 0.5$, conic headform

(approximately non-cavitated case) for the conic head. Here $K = (P_\infty - P_v)/(P_0 - P_\infty)$, where $P_0$ is the total pressure, $P_v$ is the vapor pressure, and $P_\infty$ is the freestream pressure. It is obvious that the cavitation changes the pressure distribution dramatically and the current cavitation model gives a good prediction as compared with the experimental results of Rouse and McNown (1948).

Convergence of the scheme was verified on the conic head-

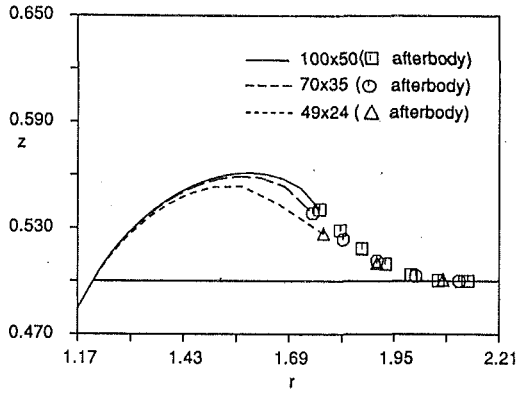


Fig. 7 Convergence test: pressure distributions for $K = 0.5$, conic headform

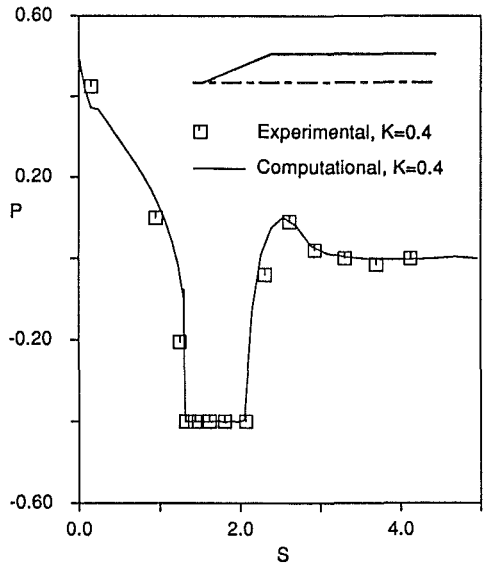


Fig. 8 Pressure distribution for conic headform

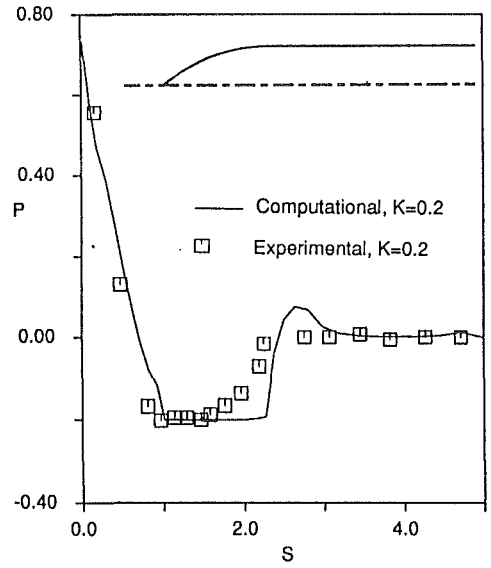


Fig. 9 Pressure distribution for ogival headform

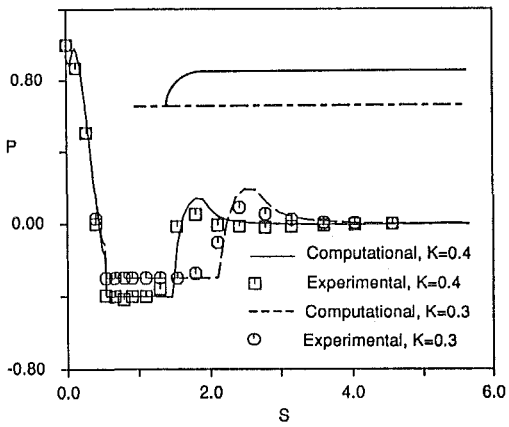


Fig. 10 Pressure distribution for hemispheric headform

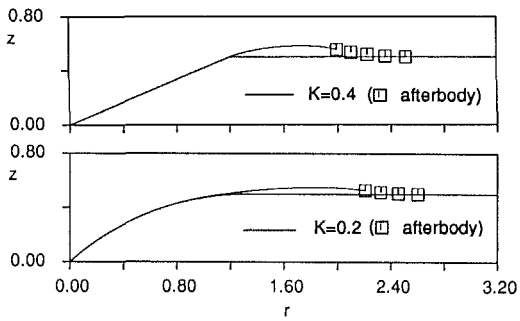


Fig. 11 Bubble shapes for conic and ogival headforms

form for cavitation number $K = 0.5$. Calculations were performed on three meshes: $100 \times 50$, $75 \times 35$, and $49 \times 24$. The wall pressure distribution and predicted bubble shapes are shown in Fig. 6 and Fig. 7, respectively. Note that the region with the symbols in Fig. 7 is the area in which the wake model is applied. The use of a wake model which intercepts the body surface at a low angle permits a smooth pressure distribution near the attachment point (near $S = 2$ in Fig. 6). This result contrasts the relatively large pressure "spikes" obtained in calculations of Deshpande et. al. (1992), in which the bubble intercepts the body at a relatively high angle. The results in Figs. 6 and 7 demonstrate convergence of the numerical scheme as well as the cavitation model.

There were some difficulties in comparing bubble shapes of the model with the experiments of Rouse and McNown (1948). Digitization of their data, the coarseness of bubble pocket measurements, and the evidence of non-axisymmetric bubble shapes all obscured the experimental results. For this reason, only the wall pressure distributions (which are strongly influenced by bubble shapes) are compared with the experimental data. Figure 8 shows good agreement between the computed pressure distribution and the experimental results for $K = 0.4$ for the conical headform. The calculated solution predicts the overall extent of the bubble forebody (minimum pressure region in Fig. 8) as well as the pressure recovery within the wake.

For a sharp edged body, the detachment point is simply at the corner. It is more challenging to predict the detachment point for a smooth body. To test if the model in this case, we performed calculations on an ogival head for $K = 0.2$ and a hemispheric head for $K = 0.4$ and $K = 0.3$. Figures 9 and 10 show the pressure comparison for the ogival head and the hemispheric head respectively. Results in these figures indicate the detachment point (leading edge of the minimum in pressure) is accurately predicted for cavitation on these smooth surfaces which tends to validate the assumed inception criteria ($p = p_v$) for flowfields of this nature. The extent of the fully cavitated region (bubble forebody) is slightly overpredicted in these cases.

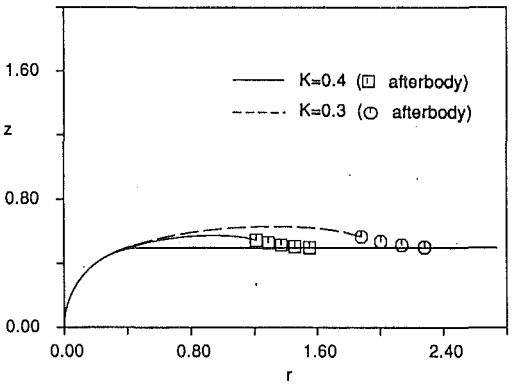


**Fig. 12 Bubble shapes for hemispheric headform**

Errors in the pressure distribution (and hence the bubble shape) are confined to the termination region of the cavity where the wake model is employed.

The computational bubble shapes are shown in Figs. 11 and 12. Once again, wake regions are denoted with symbols in these figures. While it is difficult to make exact comparisons, computed bubble shapes agree with those in Rouse and McNown (1948) except in portions of the wake as indicated in the surface pressure comparisons in Figs. 9 and 10.

## Conclusion

A new numerical treatment has been developed for the prediction of the flowfield resulting from an attached cavitation region. While the treatment has been applied to an axisymmetric calculation in this case, it is quite generic in nature and should also work well for 2-D flows. While the method has been applied using a flow solver consistent with the Marker and Cell formulation, the cavitation model could also be used with other numerical approaches. The cavitation model has been implemented in a viscous calculation which is an improvement over previous inviscid results. Furthermore, the model accurately predicts the wall detachment point even for smooth bodies. Results indicate that wall detachment point, bubble forebody, and wall pressure distributions compare well with experimental data for a variety of different geometries.

## References

Arakeri, V. H., 1975, "Viscous Effects on the Position of Cavitation Separation from Smooth Bodies," *Journal of Fluid Mechanics*, Vol. 68, No. 4, pp. 779–799.

Blake, J. R., and Gibson, D. C., 1987, "Cavitation Bubbles near Boundaries," Ann. Rev. Fluid Mech., Vol. 19, pp. 99–123.

Blake, J. R., Taib, B. B., and Doherty, G., 1986, "Transient Cavities Near Boundaries, Part 1: Rigid Boundary," *Journal of Fluid Mechanics*, Vol. 170, pp. 479–497.

Brennen, C., 1969, "A Numerical Solution of Axisymmetric Cavity Flows," *Journal Fluid Mechanics*, Vol. 37, pp. 671–688.

Burggraf, O. R., 1966, "Analytical and Numerical Studies of the Structure of Steady Separated Flows," *Journal of Fluid Mechanics*, Vol. 24, pp. 113–151.

Delannoy, Y., and Kueny, J. L., 1990, "Two Phase Flow Approach in Unsteady Cavitation Modeling," *Cavitation and Multiphase Flow Forum*, ASME, FED-Vol. 98.

Deshpande, M., Feng, J., and Merkle, C. L., 1992, "Nonlinear Euler Analysis of 2-D Cavity Flow," FED-Vol. 135, *Cavitation and Multiphase Flow Forum*, ASME.

Dupont, Ph., and Avellan, F., 1991, "Numerical Computation of a Leading Edge Cavity," FED-Vol. 116, *Cavitation '91*, ASME.

Franc, J. P. and Michel, J. M., 1985, "Attached Cavitation and the Boundary Layer: Experimental Investigation and Numerical Treatment," *Journal of Fluid Mechanics*, Vol. 154, pp. 63–90.

Furness, R. A., and Hutton, S. P., 1975, "Experimental and Theoretical Studies of Two-Dimensional Fixed-Type Cavities," ASME JOURNAL OF FLUIDS ENGINEERING, pp. 515–522, Dec.

Ingber, M. S., and Hailey, C. E., "A Numerical Approach for Modeling Cavitating Flows," Computational Modeling of Free and Moving Boundary Problems, Proceedings of the First International Conference, held on July 2–4, Southampton, United Kingdom.

Kinnas, S. A., and Fine, N. E., 1993, "A Numerical Nonlinear Analysis of the Flow around Two- and Three-Dimensional Partially Cavitating Hydrofoils," *Journal of Fluid Mechanics*, Vol. 254, pp. 151–181.

Kubota, A. H., H. Kato, and Yamaguchi, H., 1989, "Finite Difference Analysis of Unsteady Cavitation on a Two-Dimensional Hydrofoil," *Proceedings of the 5th Int. Conf. Numerical Ship Hydrodynamics*, Sept. Hiroshima, Japan.

Kubota A., Kato, H., Yamaguchi, H., and Maeda, M., 1989, "Unsteady Structure Measurement of Cloud Cavitation on a Foil Section Using Conditional Sampling Technique," ASME JOURNAL OF FLUIDS ENGINEERING, Vol. 111, pp. 204–210.

Lemonnier, H., and Rowe, A., 1988, "Another Approach in Modelling Cavitating Flows," *Journal of Fluid Mechanics*, Vol. 195, pp. 557–580.

Mitchell, T. M., and Hammitt, F. H., 1973, "Asymmetric Cavitation Bubble Collapse," ASME JOURNAL OF FLUIDS ENGINEERING, Vol. 95, pp. 29–37.

Patankar, S. V., 1980, *Numerical Heat Transfer and Fluid Flow*, McGraw-Hill.

Peyret, R., and T. D. Taylor, 1986, *Computational Methods for Fluid Flow*, Springer-Verlag.

Plesset, M. S., and Chapman, R. B., 1971, "Collapse of an Initially Spherical Vapor Cavity in the Neighbourhood of a Solid Boundary," *Journal of Fluid Mechanics*, Vol. 47, pp. 283–290.

Prosperetti, A., 1982 "Bubble Dynamics: A Review and Some Recent Results," *Appl. Sci. Res.*, Vol. 38, pp. 145–164.

Purvis, D. F., 1992, "Development of a Submodel to Account for the Influence of Cavitation on the Mass Flowrate Through a Plain Orifice," Master thesis, Purdue University.

Rood, E. P., 1991, "Mechanism of Cavitation Inception," 1991, ASME JOURNAL OF FLUIDS ENGINEERING, Vol. 113, No. 2, June, pp. 163–175.

Rouse, H., and McNown, J. S., 1948, "Cavitation and Pressure Distribution. Head forms at Zero Angle of Yaw," State University of Iowa, Engrg. Bull., No. 32.

Soh, W. Y., and Goodrich, J. W., 1988, "Unsteady Solution of Incompressible Navier-Stokes Equations," J. Computational Physics, Vol. 79, pp. 113–134.

Stern, F., 1989, "Comparison of Computational and Experimental Unsteady Cavitation on a Pitching Foil," ASME JOURNAL OF FLUIDS ENGINEERING, pp. 290, Sept.

Uhlman, J. S. Jr., 1987, "The Surface Singularity Method Applied to Partially Cavitating Hydrofoils," *Journal of Ship Research*, Vol. 31, No. 2, June, pp. 107–124.

**R. Zheng**[1]
Postdoctoral Research Fellow.

**N. Phan-Thien**
Professor.

**V. Ilic**
Associate Lecturer.
Mem. ASME

Department of Mechanical
and Mechatronic Engineering,
The University of Sydney,
NSW 2006, Australia

# Falling Needle Rheometry for General Viscoelastic Fluids

*This paper reports theoretical and numerical studies on a flow of a general viscoelastic fluid past a needle placed at the centerline of a cylindrical tube, supplemented by a comparative experimental study. It is shown that the drag per unit length on the needle, which is assumed to be infinitely long, depends on the fluid viscosity only, whatever the first and second normal stress differences may be. This general theory is then specified to obtain solutions for the power-law and the Phan-Thien-Tanner fluids. The power-law fluid results provide a general technique for obtaining flow curves of non-Newtonian fluids from the measured drag forces on falling needles. This is achieved by using* KU/R *as the effective shear rate, where* U *is the terminal velocity of the needle,* R *is the radius of the tube, and* K *is a function of the power-law index* n *and the system geometry* a/R (*where* a *is the radius of the needle*). *The effect of the aspect ratio of the needle on the drag force is investigated numerically using a boundary element method for the flow of Phan-Thien-Tanner fluid. Experimentally, a flow curve was obtained for a kerosene solution of PIB (3.39 percent by weight), using falling needles of aspect ratio greater than 40 in a circular cylinder. The result compared well with Carri-Med 50 CS rheometer data.*

## 1 Introduction

The flow past a rigid particle has been a subject of many theoretical, numerical, and experimental studies. A comprehensive review of research of particle motions in a Newtonian fluid at low Reynolds number (Stokes flow) can be found in Happel and Brenner (1986). Non-Newtonian effects have also received considerable attention in recent years (see Walters and Tanner, 1992 for a review). Much of the work on non-Newtonian effects has been concerned with the flow past a sphere placed in the centerline of a cylindrical tube. This problem is of importance mainly because it forms the theoretical basis of an experimental method known as the falling ball rheometry, where the measurement of the terminal velocity of the falling sphere can be used to infer the viscosity of the fluid tested (see, for example, Powell et al., 1989; Butcher and Irvine, 1990; Phan-Thien et al. 1991a), and that the flow provides a bench-mark problem for the testing of numerical methods in viscoelastic flow calculations (see, for example, Crochet, 1988; Lunsmann et al. 1989; Zheng, et al., 1990; Jin et al., 1991; Phan-Thien et al., 1991b).

However, with regard to viscosity measurements, the falling ball data must be interpreted with caution when applied to viscoelastic fluids. Since the flow around the sphere is non-viscometric in nature, i.e., it is a mixture of shear and elongational flows, the analysis depends on the constitutive model adopted for the fluid, and it is difficult to define *a-priori* an effective shear rate for the flow. Furthermore, not only the viscosity but also the elasticity of the fluid can significantly influence the drag force on the sphere. A simple example is the Maxwell fluid where the viscosity of the fluid is constant but the drag coefficient decreases with increasing elasticity.

It would therefore be useful to redesign the falling object to promote a dominant shear flow, and yet retain the simplicity of the method. A device that seems to achieve these two aims is the falling needle viscometer, as described by Park et al. (1988, 1990), where a slender object replaces the sphere. For the device to work as a viscometer, two problems must be resolved satisfactorily. First, how is the viscosity calculated from a force (or velocity) measurement on the needle, and secondly, what is the shear rate at which this viscosity is measured. The second problem is irrelevant to Newtonian fluids, where the viscosity is independent of shear rate. For non-Newtonian fluids, we must determine the shear rate at which the viscosity is determined, as the drag force depends on the shear stresses along the needle and the tube wall. The corresponding shear rate at which the viscosity is calculated (from the drag force) is, therefore, neither the shear rate along the needle nor the shear rate at the tube wall, but some effective value.

Solutions for the falling needle in a Newtonian fluid have been obtained by Lohrenz et al. (1960) and Cox (1970), among others. Analyses using the power-law fluid model were given by Ashare et al. (1965) and Park and Irvine (1988). Leal (1975) obtained a perturbation solution for a second-order fluid. These analyses are valid in the asymptotic sense, that is, the length of the needle assumed to be large compared to its radius. A finite element analysis for a finite-length needle in the Maxwell and the PTT fluids was given by Phan-Thien et al. (1993). They reported numerical results for two aspect ratios, $L/a$ = 40 and $L/a$ = 100 ($L/a \gg 1$, where $L$ and $a$ is the length

[1]Moldflow Pty. Ltd., 259-261 Colchester Rd., Kilsyth, VIC 3137, Australia.
Contributed by the Fluids Engineering Division for publication in the JOURNAL OF FLUIDS ENGINEERING. Manuscript received by the Fluids Engineering Division May 5, 1993; revised manuscript received October 25, 1993. Associate Technical Editor: J. A. C. Humphrey.

and the radius of the needle, respectively); for these cases, the drag force per unit length does not vary much with the change in aspect ratio. Experimentally, the effect of the aspect ratio has been examined by Park and Irvine (1988) and more recently by Cho et al. (1992).

The motivation of the present paper is to generalize the previous analysis to the "simple fluid," which is completely general and covers almost all the existing constitutive equations for fluids with or without memory (the reader is referred to Tanner, 1988 for a review of most popular constitutive equations), and to describe an alternative procedure with which the viscosity of general viscoelastic fluids can be measured from the terminal velocity of falling needles. The problem of measuring viscosities of viscoelastic fluids has received extensive investigations and has resulted in a series of commercial viscometers, most of which are based on the Poiseuille flow or cylindrical Couette flow, and require measurement of either the pressure drop or the torque. They are more complex in structure and more expensive in production costs than a falling needle equipment. Another potential advantage of the falling needle is its applicability to determine the viscosity of suspensions, where the motion of the needle will not significantly disturb the microstructure of the tested fluids. We shall also show that the proposed procedure, expressed in terms of the effective shear rate, are more succinct and simpler than that described by Park and Irvine (1988). Both analytical and numerical methods are used in this work. Some experimental data are also reported.

## 2 Theoretical Analysis

We now begin with the motion of a needle in a general viscoelastic fluid. Although we will later consider specific constitutive equations (i.e., the power-law and the PTT fluids), the general theory can be developed without need for such specialization. In a viscometric flow, it is well known that there are three material functions for a simple fluid: the first normal stress difference $N_1$, the second normal stress difference $N_2$, and the shear stress function $\tau$ (Coleman et al., 1966). The viscosity $\eta = \eta(\dot\gamma)$ is defined through

$$\tau(\dot\gamma)=\eta(\dot\gamma)\dot\gamma. \tag{1}$$

Knowing the viscometric behavior of the fluid does not allow us to deduce nonviscometric properties, or even the anisotropy of the material, but there is a variety of practical problems that depend only on the viscometric functions and therefore measuring these functions is a major concern in rheometry (Barnes et al., 1989).

The flow field generated by the falling needle is in fact a complex flow including both shearing and elongational flow components. However, if the needle is slender ($L/a \gg 1$), as is the case here, the flow around the needle may be taken to be annular and due to a combination of drag and pressure. Viewed this way, the flow may be considered nearly viscometric.

Using cylindrical coordinate system for the formulation of this problem, the flow field is then described by

$$u_r=0,\ u_\theta=0,\ u_z=u_z(r), \tag{2}$$

and the shear rate is given by $\dot\gamma = du_z/dr$. We assume that the needle is stationary, the container wall is moving with a constant velocity $U$. The fluid inertia terms will not appear in the govern equations since $\mathbf{u}\cdot\nabla\mathbf{u} = \mathbf{0}$. Thus, from the momentum equations, it can be deduced that the pressure gradient $\partial P/\partial z$ must be a constant, and we denote $P_L = \partial P/\partial z$. Then, a simple integration of the momentum equations yields

$$\tau_{rz}=\frac{1}{2}P_L\left(r-\frac{C}{r}\right)=\eta(\dot\gamma)\dot\gamma, \tag{3}$$

where $C$ is a constant.

To determine the constants $P_L$ and $C$, we need to consider the continuity equation and the boundary conditions. By an integration by parts of the continuity equation and the boundary conditions we find (note that we have assumed a stationary needle and a moving wall),

$$\int_a^R r^2\dot\gamma dr=0, \text{ and } \int_a^R \dot\gamma dr=U. \tag{4}$$

In principle, from the three Eqs. (3) and (4), $P_L$, $C$, and $\dot\gamma(r)$ can be obtained and hence the velocity field can be determined. Furthermore, the drag force on the needle can be obtained from a global balance of momentum,

$$D=2\pi RL\tau_{rz}|_{r=R}-\pi R^2LP_L=-\pi CP_LL. \tag{5}$$

Note that the contribution to the drag force from the pressure drop is quite significant.

It is noteworthy from the above results that the velocity field and the drag force depend on the viscosity function $\eta$ only, whatever the two normal stress functions $N_1$ and $N_2$ may be. This conclusion is important, as it implies that the method of using falling needle data to evaluate the viscosity function of the tested liquid is valid for any non-Newtonian fluids with or without elasticity. In reality, the aspect ratio of the needle will be finite, and the fluid elasticity will affect the drag force, but this comes in as high order terms in the aspect ratio of the needle. However, this is not true for a falling sphere in an elastic liquid; therefore the falling sphere method is not quite suitable for general viscometric applications.

As special cases of the simple fluid, two constitutive models will be considered next. They are the power-law and the Phan-Thien-Tanner models. A solution for the falling needle applied to a power-law fluid has been reported by Park and Irvine (1988), but our results, expressed in terms of the effective shear rate, are interpreted differently. For these models, the governing equations (Eqs. (3-4)) are nonlinear. Here we employ an optimization technique to solve these equations. In fact, the original problem is easily shown to be equivalent to the following optimization problem:

Given an objective function

$$f=\left(\int_a^R r^2\dot\gamma dr\right)^2+\left(\int_a^R \dot\gamma dr-U\right)^2, \tag{6}$$

where $\dot\gamma$ satisfies

$$\eta(\dot\gamma)\dot\gamma=\frac{1}{2}P_L\left(r-\frac{C}{r}\right), \tag{7}$$

find the values of $P_L$ and $C$ that minimize $f$.

## 3 Results for the Power-Law and the PTT Fluids

**3.1 Power-Law Fluid.** For a power-law fluid, the viscosity-shear rate relationship is given by

$$\eta(\dot\gamma)=m|\dot\gamma|^{n-1}, \tag{8}$$

where $m$ is a measure of the consistency of the fluid, the higher $m$ the more "viscous" the fluid; $n$ is a measure of the degree of non-Newtonian behavior ($n < 1$), and the greater the departure from unity the more pronounced are the non-Newtonian properties of the fluid.

It can be shown that the drag force on the needle, $D$, for a power-law fluid is given by (Phan-Thien et al., 1992),

$$\frac{D}{D_0}=\frac{m}{\eta_0}\left(K\frac{U}{R}\right)^{n-1}, \tag{9}$$

where $D_0$ is the Newtonian value for the same needle at the same terminal velocity,

$$D_0=\frac{2\pi\eta_0UL(R^2+a^2)}{R^2-a^2-(R^2+a^2)\ln\dfrac{R}{a}}. \tag{10}$$

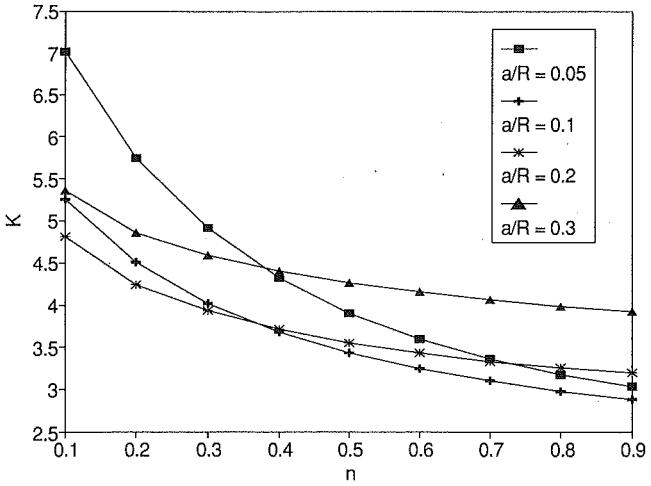


Fig. 1 The shift factor $K$ as a function of $n$ for $a/R$ = 0.05, 0.1, 0.2, 0.3

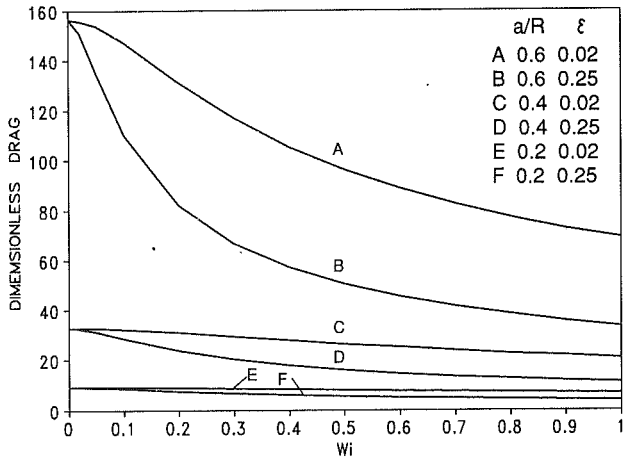


Fig. 2 The dimensionless drag, $D/(\eta_0 UL)$, as a function of the Weissenberg numbers, for the PTT fluid: $\epsilon$ = 0.02, 0.25; $a/R$ = 0.2, 0.4, 0.6

In Eq. (9), $K$ is a function of both the power-law index $n$ and the geometry $a/R$, and is available from the solution of the momentum and continuity equations. Figure 1 shows $K$ versus $n$ at four different $a/R$ values. Some tabulated data were given by Phan-Thien et al. (1993) and a simple regression suggests that

$$\log K = b_0 - b_1 \log n, \tag{11}$$

where

$$b_0 = 0.45790 + 3.2305\left(\frac{a}{R} - 0.1\right)^2,$$

$$\text{and } b_1 = 0.070437\left(\frac{a}{R}\right)^{-0.585},$$

with an average error of less than 1.8 percent for $0.1 \le n \le 0.9$ and $0.05 \le a/R \le 0.3$.

Comparing Eq. (9) to Eq. (8), it is clearly seen that the curve $\eta_0 D/D_0$ versus $KU/R$ must coincide with the flow curve $\eta$ versus $\dot{\gamma}$. Therefore, the flow curve can be constructed from the measured drag force on the needle, provided that $KU/R$ is used as the effective shear rate. Note that $D_0/\eta_0$ is a function of the geometry and the terminal velocity of the needle, and can be calculated using Eq. (10), and therefore finding the zero-shear-rate viscosity $\eta_0$ is not required.

In summary, the steps involved in determining the viscosity by the falling needle method are:

- For the set of terminal velocity observed, the power-law index can be determined from the plot of $\eta_0 D/D_0$ versus $U/R$. Note that $D_0/\eta_0$ can be obtained directly from (10) without the need to measure either $D_0$ or $\eta_0$; the drag force on the needle ($D$) is simply its weight minus its buoyancy force.
- The constant $K$ can then be evaluated from the regression formula (11), provided that the parameters are within the ranges considered.
- The flow curve can now be constructed by plotting $\eta_0 D/D_0$ against $KU/R$.

This method can be extended to generate a general flow curve by considering "local" power-law indices (for fluids that are not necessarily power-law). That is, if the whole curve of $\eta_0 D/D_0$ versus $U/R$ is not a straight line in the log-log coordinate system, we can divide the whole region into several sub-regions so that within each sub-region the curve can be regarded to be a straight line and a local power-law index can be obtained from the slope. Then the flow curve can be constructed by the same procedures as mentioned above, except we now use different $K$ values in different sub-regions.

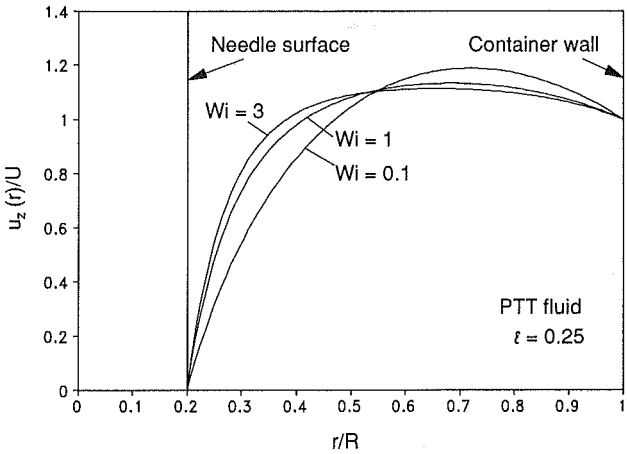


Fig. 3 The velocity profiles between the needle surface and the container wall ($a/R$ = 0.2), for the PTT fluid: $\epsilon$ = 0.25, $Wi$ = 0.1, 1.3

**3.2 Phan-Thien-Tanner Fluid.** We consider next the viscoelastic fluids modelled by the generic differential constitutive equation:

$$G\tau + \lambda\left(\frac{\partial \tau}{\partial t} + \mathbf{u}\cdot\nabla\tau - \nabla\mathbf{u}^T\cdot\tau - \tau\cdot\nabla\mathbf{u}\right) = 2\eta_m\mathbf{D}, \tag{12}$$

where $\mathbf{D} = 1/2(\nabla u + \nabla u^T)$ is the rate of deformation, and $\lambda$, $\eta_m$ are the relaxation time and the molecular-contributed viscosity, respectively, which are allowed to be functions of the generalized shear rate $\dot{\gamma} = \sqrt{2tr(\mathbf{D}\cdot\mathbf{D})}$. Finally, $G$ in (12) is a scalar function of $tr\tau$. With different $G$'s Eq. (12) covers a variety of constitutive models. If $G = 1 + \epsilon\lambda tr\tau/\eta_0$, then the model of Eq. (12) is a particular case of the Phan-Thien-Tanner fluid (Phan-Thien and Tanner, 1977), in which $\eta_0$ is the zero-shear viscosity and $\epsilon$ is a model parameter. When $\epsilon = 0$ and $\eta_m = \eta_0$, Eq. (12) reduces to the well-known upper-convected Maxwell fluid.

In the uni-directional flow between the needle surface and the tube wall, the stress components $\tau_{rr}$ and $\tau_{\theta\theta}$ are zero and the remaining equation for $\tau_{rz}$ and $\tau_{zz}$ are

$$G\tau_{zz} - 2\lambda\dot{\gamma}\tau_{rz} = 0, \text{ and } G\tau_{rz} = \eta_m\dot{\gamma}. \tag{13}$$

Here the generalized shear rate reduces to $\dot{\gamma} = du/dr$. These equations are easily rearranged in terms of $G$ to obtain

$$G^3 - G^2 - 2\epsilon\lambda^2\dot{\gamma}^2\frac{\eta_m(\dot{\gamma})}{\eta_0} = 0. \tag{14}$$

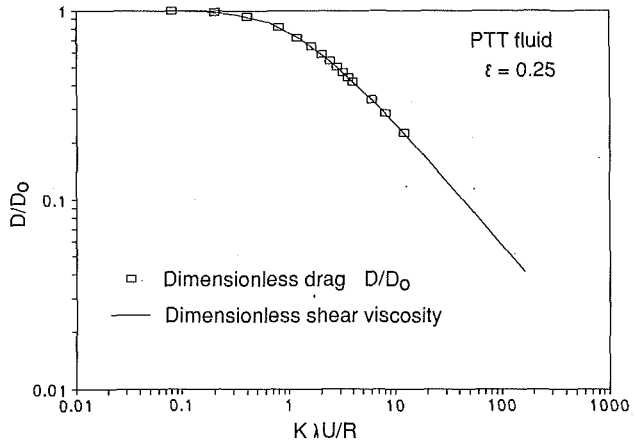


Fig. 4 The drag ratio $D/D_0$ as a function of $K\lambda U/R$ (□), compared with the true viscosity (normalized with respect to zero-shear-rate viscosity) curve of the PTT model ($\epsilon = 0.25$)

Fig. 5 Boundary element mesh, $L/a = 20$ and $a/R = 0.2$

For given $\epsilon$, $\lambda$ and $\eta_0$, Eq. (14) defines $G$ as a function of $\dot{\gamma}$, and hence the viscosity function is given by

$$\eta(\dot{\gamma}) = \frac{\eta_m(\dot{\gamma})}{G(\dot{\gamma})}. \tag{15}$$

As an example, we now consider the PTT model with two different $\epsilon$ values, $\epsilon = 0.02$ and $\epsilon = 0.25$. The former corresponds to a polymer solution and the latter to a polymer melt (Larson, 1988)) and $\eta_m = \eta_0$. We define the Weissenberg number as $\mathrm{Wi} \equiv \lambda U/R$.

Figure 2 shows the dimensionless drag given by $D/(\eta_0 UL)$ as a function of the Weissenberg number at three different diameter ratios, $a/R = 0.2$, 0.4, and 0.6. The drag reduction is due to the shear thinning behavior of the PTT model. The results in Fig. 2 show that the larger $a/R$ is, the quicker is the decrease of the dimensionless drag force with increasing Weissenberg number.

Figure 3 shows the calculated velocity profiles for different Weissenberg numbers. At low *Wi* numbers the velocity field is nearly Newtonian. At higher Weissenberg number, the velocity profile is blunter. It seems likely that at very high *Wi* numbers there exists a thin boundary layer next to the surface of needle, and the flow outside this thin boundary layer is effectively a plug flow.

Equation (14) gives $\eta/\eta_0 \to (2\epsilon)^{1/3}(\lambda\dot{\gamma})^{-2/3}$ at high value of $\lambda\dot{\gamma}$, indicating that the PTT model has a power-law region with $n = 1/3$. This suggests a simple approximate method for constructing a flow curve from the drag measurements, using the shift factor $K$ obtaining from the power-law calculations (Fig. 1 or Eq. (11)). In Fig. 4, we plot the drag ratio $D/D_0$ versus $K\lambda U/R$ where $K \approx 4$ from Fig. 1 for $n = 0.3$ and $a/R = 0.2$. Superimposing on these data are the dimensionless steady shear viscosity curve ($\eta/\eta_0$, where $\eta_0$ is the zero-shear-rate viscosity), in solid lines, for the PTT model. The plot of $D/D_0$ versus $K\lambda U/R$ is visually indistinguishable from the true flow curve of the fluid.

## 4 The Boundary Element Solution

The above solutions are obtained in the asymptotic sense, which do not allow inclusion of the needle aspect ratio effect. We now turn to a full numerical solution for the PTT fluid past a finite-length needle, using a boundary element method. The same method has been described elsewhere (Zheng et al., 1990) for the solution of viscoelastic flows past a sphere, and we shall not repeat the details here.

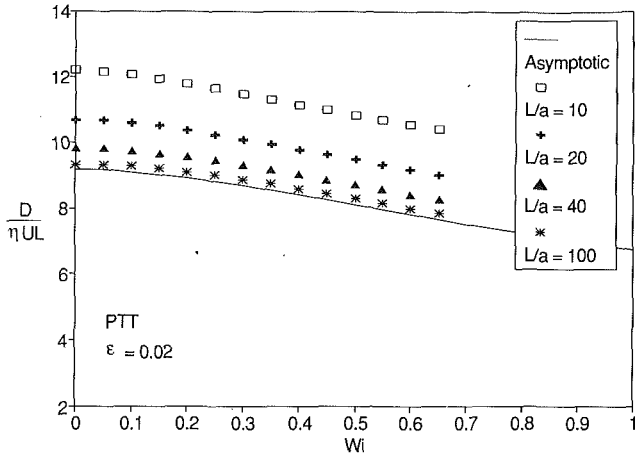


Fig. 6(*a*)

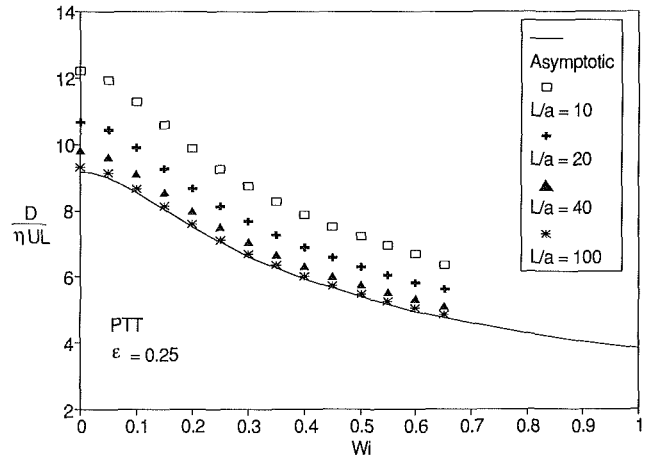


Fig. 6(*b*)

Fig. 6 The dimensionless drag, $D/(\eta_0 UL)$, as a function of the Weissenberg numbers, for the PTT fluid: (*a*) $\epsilon = 0.02$, (*b*) $\epsilon = 0.25$. The symbols are numerical results and the solid lines are the asymptotic solutions. The geometries are: $a/R = 0.2$, $L/a = 10$, 20, 40, 100.

The flow domain of interest is the region between the cylindrical container of radius $R$ and the needle that is represented by a cylinder of radius $a$ and length $L$. Calculations were made for a fixed $a/R = 0.2$, and for $L/a$ values varying from 10 to 100. A typical mesh used is shown in Fig. 5 for the case of $L/a = 20$; the total length of the domain is $5L$. Sufficiently fine elements are required near the needle surface to capture thin velocity and stress boundary layers. On the top boundary (the tube wall) the conditions $u_z = U$ and $u_r = 0$ are imposed; no-slip conditions ($u_z = u_r = 0$) are imposed on the needle surface; along the centerline the radial velocity and the shear stress are zero; at the inlet and outlet boundaries, far away from the needle, the flow is uniform: $u_z = U$ and $u_r = 0$. We had convergent difficulties in calculations after $Wi = 0.65$.

The results of the dimensionless drag force versus the Weissenberg number at four different aspect ratios are given in Figs. 6(*a*) and (*b*), for $\epsilon = 0.02$ and $\epsilon = 0.25$, respectively. The dimensionless drag forces at the smaller aspect ratios are greater than the ones at the larger aspect ratios. As the aspect ratio increases, the dimensionless drag force approaches the asymptotic value.

Figure 7 shows that the dependence of the dimensionless drag force on $a/L$ value is approximately linear. This suggests

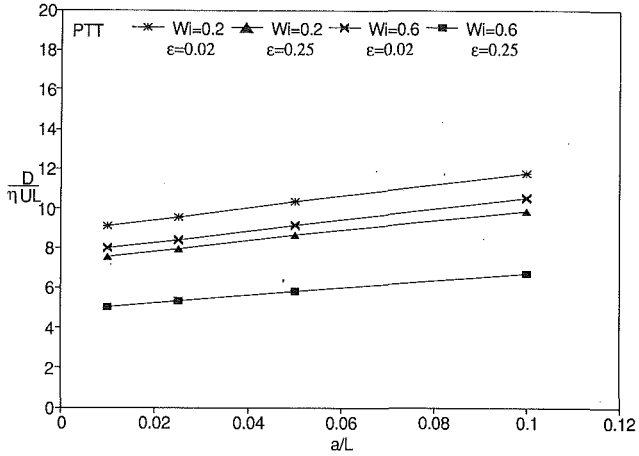


**Fig. 7 The dimensionless drag $D/(\eta_0 UL)$ of the PTT fluid as a function of the aspect ratio**

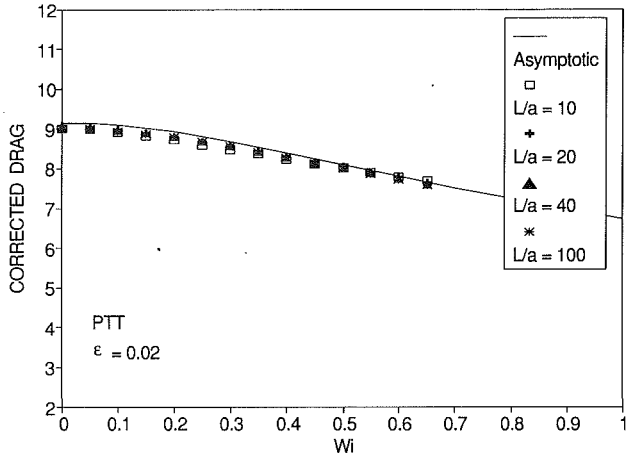


**Fig. 8(*a*)**

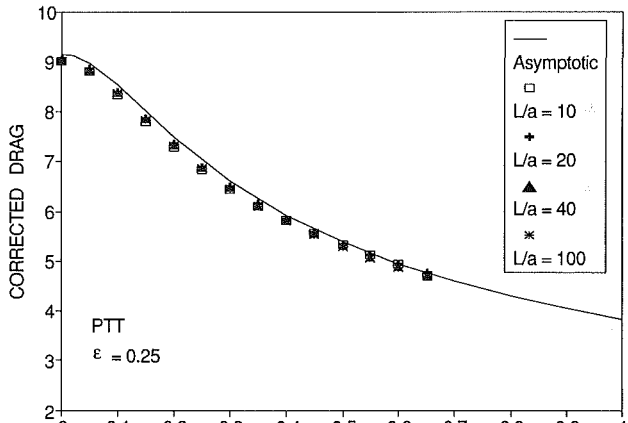


**Fig. 8(*b*)**

**Fig. 8 Same as Fig. 6, except the dimensionless drag forces have been corrected using Eq. (35)**

that the aspect ratio effect on the drag may be corrected by an expression as follows:

$$D^*_\infty = \frac{D^*}{1+e(a/L)}; \tag{16}$$

where $D^*_\infty$ is the dimensionless drag force for $L/a = \infty$, $D^* \equiv D/(\eta_0 UL)$ is the dimensionless drag force in the finite aspect ratio case. The $e$ value can be found by regression. The regression results show that $e$ varies very slowly with $Wi$ and $\epsilon$, so it is reasonable to take a single average value of $e$ for all the cases here. The average value is found to be $e \approx 3.56$. Using this value to correct the data in Fig. 6(*a*) and (*b*), we obtain the corrected dimensionless drag force versus the Weissenberg number as shown in Fig. 8(*a*) and (*b*). Equation (16) indicates that the correction for the dimensionless drag force due to the effect of the finite aspect ratio is $O(a/L)$. Thus when the aspect ratio increases to a certain value (say, $L/a > 40$), the effect of the aspect ratio on the drag force becomes negligible.

## 5 Experiment

**5.1 Experimental Setup.** A 3.39 percent kerosene solution of polyisobutylene (PIB) of 0.82 g/cm$^3$ density was used in a 50.44 mm diameter precision bore glass cylinder 400 mm long at 21.2°C. It was capped with a 30 mm deep aluminum lid having a hole at its center to ensure that the falling particle is released at the cylinder axis. The hole was just large enough for the unwetted needle to fall freely through it when dropped. To accommodate different diameters, an appropriate size sleeve insert was used with each needle. The measuring tank was aligned with the vertical using a spirit level.

For tests reported here, two types of needles were used. A thin-walled stainless steel hypodermic tube 2.015 mm diameter was sealed with hemispherical ends. Similar tubes with squared ends showed no end effects for the given aspect ratio. One plug was glued in place, while the other was removable, with an average overall aspect ratio of 73. The second type of needle was made from glass tube 1.52 mm diameter and 73.56 mm long (thus $L/a \approx 97$), the downstream end of which was sealed and rounded.

The start and finish lines were marked on the glass tank and their separation measured. A video camera (Panasonic WV-BL200) with a Computar TV zoom lens M6Z 1212, 12.5–75 mm focal length, $f = 1.2$, mounted on a Manfrotto 055 tripod with a movie head, was focused at each line. Both video signals were combined with an American Dynamics 1470A video splitter and recorded on a Panasonic NV-FS100A video cassette recorder with time/date information. The latter signal was generated by a National time/date generator WJ-810, with time given to two hundredths of a second.

The commercial viscometer Carri-Med 50 CS was used with the number 4 cone to automatically generate shear stress versus shear strain data and calculate the apparent viscosity using the proprietary software supplied with the instrument.

The density was determined from weighing a known volume of the test liquid on a Sartorius analytic mass balance A200S capable of measuring mass to within 0.0001 g.

The whole laboratory was kept at a constant temperature, and during the test, the liquid temperature did not exceed 0.5°C above the initially measured value, using a mercury-in-glass thermometer with the minimum resolution of 0.1°C.

**5.2 Experimental Method and Accuracy.** The video recording system was switched on and the selected needle was filled with mercury and weighed on the analytical mass balance. The needle was then inserted in the hole provided in the tank lid and held while the record button on the VCR was activated. The needle was then dropped into the test liquid, and its passage across the marker lines recorded. After stopping the VCR record function, the needle was retrieved, cleaned, top end opened and some mercury removed. The above procedure was then repeated until the needle was empty. In the case of the glass needle, the top end was sealed with bees wax.

The needle transit time between the markers was then obtained from the VCR playback and its terminal velocity calculated by dividing the separation between the markers with this time interval.

The calculated terminal velocity is estimated to be within

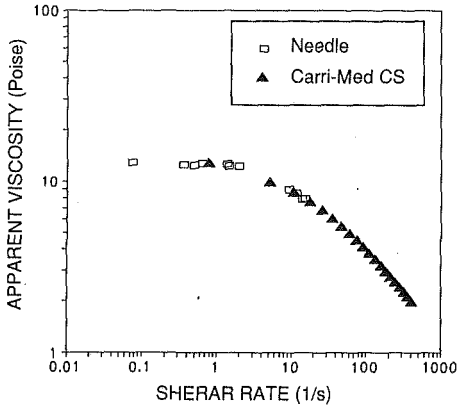


**Fig. 9 Apparent viscosity variation with shear rate from experimental data with falling needles and a Carri-Med CS Rheometer**

about ±1.2%, while the viscosity measurement on the Carri-Med CS 50 was known to within about 2 percent.

**5.3 Results.** The terminal velocities were obtained for a number of needles. The drag force $D$ on each needle was found by subtracting the buoyancy force from the weight of the needle. The Newtonian values of $D_0/\eta_0$ corresponding to the different terminal velocities $U$ were calculated from Eq. (10) without the need of the zero-shear-rate viscosity of the fluid. Thus $\eta_0 D/D_0$ as a function of $U/R$ was obtained. For the geometries used, there is no correction needed for the aspect ratio effect.

The results are shown in Fig. 9. The power-law theory was used to construct the flow curve and it is seen that the agreement is good. The results also compare well with the flow curve measured with the Carri-Med 50 CS rheometer. However, owing to the inherent limitations of this type of apparatus it was not possible to obtain experimental data at high shear rates.

We observed in the experiment that the needle kept falling vertically along the centerline. Indeed, with a small cavity provided at the center of the container bottom, the needle was seen to drop straight into this cavity.

## 6 Conclusion

In summary, we have presented an asymptotic analysis for the simple fluid past a needle placed at the centerline of a cylindrical tube. It was shown theoretically that the drag force on the needle depends on the fluid viscosity only; the fluid elasticity has no effect on the drag asymptotically. The falling needle can therefore be utilized as a simple and accurate viscometer for general viscoelastic fluid. Solutions for the power-law and the Phan-Thien-Tanner models were reported as the special cases for the simple fluid. A boundary element method has also been used to solve the full equations for the PTT model, which involves taking the aspect ratio effect into consideration. Numerical results confirm that the drag per unit length on a long needle ($L/a > 40$) in a container can be approximated by the asymptotic solution. This study is also supplemented with an experimental investigation. A flow curve was obtained experimentally based on the theoretical results of the relationship between the drag and the viscosity, for a kerosene solution of PIB (3.39 percent by weight). The experimental results were confirmed by an independent viscosity measurement with a Carri-Med CS Rheometer.

On the basis of above, we also see the potential usefulness of the falling needle viscometer for determining the viscosity of suspensions, where it is vital not to disturb the microstructure of the tested fluid.

## Acknowledgments

This research was funded by an Australian Research Council Grant, Australian Research Council Australian Post-doctoral Research Fellowship and a University of Sydney Special Projects Grant. All these supports are gratefully acknowledged. The authors are also grateful to Prof. R. I. Tanner for useful comments on this work.

## References

Ashare, E., Bird, R. B., and Lescarboura, J. A., 1965, "Falling Cylinder Viscometer for Non-Newtonian Fluids," *American Institute of Chemical Engineers Journal*, Vol. 11, pp. 910–916.

Barnes, H. A., Hutton, J. F., and Walters, K., 1989, *An Introduction to Rheology*, Elsevier, Amsterdam.

Butcher, T. H., and Irvine, T. F. Jr., 1990, "Use of the Falling Ball Viscometer to Obtain Flow Curves for Inelastic, Non-Newtonian Fluids," *Journal of Non-Newtonian Fluid Mechanics*, Vol. 36, pp. 51–70.

Cho, K., Cho, Y. I., and Park, N. A., 1992, "Hydrodynamics of Vertically Falling Thin Cylinder in Non-Newtonian Fluids," *Journal of Non-Newtonian Fluid Mechanics*, Vol. 45, pp. 105–145.

Coleman, B. D., Markovitz, H., and Noll, W., 1966, *Viscometric Flows of Non-Newtonian Fluids: Theory and Experiment*, Springer-Verlag, New York.

Cox, R. G., 1970, "The Motion of Long Slender Bodies in a Viscous Fluid. Part 1. General Theory," *Journal of Fluid Mechanics*, Vol. 44, pp. 791–810.

Crochet, M. J., 1988, "Numerical Simulation of Highly Viscoelastic Flows," *10th International Congress on Rheology*, Sydney, Vol. 1, pp. 19–24.

Happel, J., and Brenner, H., 1986, *Low Reynolds Number Hydrodynamics*, Martinus Nijhoff, Boston.

Jin, H., Phan-Thien, N., and Tanner, R. I., 1991, "A Finite Element Analysis of the Flow Past a Sphere in a Cylindrical Tube," *Computational Mechanics*, Vol. 8, pp. 409–422.

Larson, R. G., 1988, *Constitutive Equations for Polymer Melts and Solutions*, Butterworths, Boston.

Leal, L. G., 1975, "The Slow Motion of a Slender Rod-Like Particles in a Second-order Fluid," *Journal of Fluid Mechanics*, Vol. 69, pp. 305–337.

Lohrenz, J., Swift, G. W., and Kurata, F., 1960, "An Experimentally Verified Theoretical Study of Falling Cylinder Viscometer," *American Institute of Chemical Engineers Journal*, Vol. 6, pp. 547–560.

Lunsmann, W. J., Brown, R. A., and Armstrong, R. C., 1989, *6th Workshop on Numerical Methods in Non-Newtonian Flows*, Denmark.

Park, N. A., Cho, Y. I., and Irvine, T. F. Jr., 1990, "Steady Shear Viscosity Measurements of Viscoelastic Fluids with the Falling Needle Viscometer," *Journal of Non-Newtonian Fluid Mechanics*, Vol. 34, pp. 351–357.

Park, N. A., Irvine, T. F. Jr., 1988, "Measurements of Rheological Fluid Properties with the Falling Needle Viscometer," *Review in Scientific Instrumentation*, Vol. 59, pp. 2051–2058.

Phan-Thien, N., and Tanner, R. I., 1977, "A New Constitutive Equation Derived from Network Theory," *Journal of Non-Newtonian Fluid Mechanics*, Vol. 2, pp. 353–365.

Phan-Thien, N., Zheng, R., and Graham, A. L., 1991a, "The Flow of Model Suspension Fluid Past a Sphere," *Journal of Statistical Physics*, Vol. 62, pp. 1173–1195.

Phan-Thien, N., Zheng, R., and Tanner, R. I., 1991b, "Flow Along the Centerline Behind a Sphere in Uniform Stream," *Journal of Non-Newtonian Fluid Mechanics*, Vol. 41, pp. 151–170.

Phan-Thien, N., Jin, H., and Zheng, R., 1993, "On the Flow Past a Needle in a Cylindrical Tube," *Journal of Non-Newtonian Fluid Mechanics*, Vol. 47, pp. 137–155.

Powell, R. L., Mondy, L. A., Stoker, G. G., Milliken, W. J., and Graham, A. L., 1989, "Development of a Falling Ball Rheometer with Applications to Opaque Systems: Measurements of the Rheology of Suspensions of Rods," *Journal of Rheology*, Vol. 33, pp. 1173–1188.

Tanner, R. I., 1988, *Engineering Rheology*, Revised Edition, Oxford University Press, London.

Walters, K., and Tanner, R. I., 1992, "The Motion of a Sphere through an Elastic Fluid," *Transport Processes in Bubbles, Drops and Particles*, R. P. Chhabra and D. De Kee, eds., Hemisphere Publication, pp. 73–86.

Zheng, R., Phan-Thien, N., and Tanner, R. I., 1990, "On the Flow Past a Sphere in a Cylindrical Tube: Limiting Weissenberg Number," *Journal of Non-Newtonian Fluid Mechanics*, Vol. 36, pp. 27–49.

# Rankine-Hugoniot Relations for Lennard-Jones Liquids

**Akira Satoh**
Department of Mechanical Engineering,
Faculty of Engineering,
Chiba University,
1-33, Yayoi-cho, Inage-ku,
Chiba 263, Japan

*The purpose of the present study is to clarify the Rankine-Hugoniot relations for Lennard-Jones liquids. First, Monte Carlo simulations are conducted to evaluate the state quantities such as the pressures, the internal energies, and the sound velocities. These computed values are used to obtain the approximate expressions for the state quantities by the method of least squares. The Rankine-Hugoniot relations are then clarified numerically as a function of the shock Mach number by solving the basic equations together with those approximate expressions. For liquid shock waves, not only the pressure but also the temperature increases much larger than those for an ideal gas. The results obtained here enable us to conduct more efficient molecular dynamics simulations such as simulating shock fronts alone for the investigation of the internal structures of liquid shock waves.*

## 1 Introduction

The internal structures of shock waves in gases have been actively studied by applying Monte Carlo direct simulation methods to the Boltzmann equation (Bird, 1970; Nanbu and Watanabe, 1984; Boyd, 1990; Erwin et al., 1991) instead of classical approaches to the Navier-Stokes equation (for example, Schwartz and Hornig, 1963). This is contrast to the case of liquid shock waves, the internal structures of which have not been extensively studied. One of the reasons seems to be that the application of liquid shock waves in engineering fields was not clear. However, liquid shock waves have been recently applied in the medical engineering field (for example, Takayama, 1987), and consequently shock structures in liquids and solids are the important subjects to be clarified.

The Monte Carlo direct simulation method (Bird, 1976) cannot be applied to liquid problems because it is a solution to the Boltzmann equation. Molecular dynamics methods are highly useful for investigation of liquid and solid problems from a microscopic point of view, so they have been widely used so far along with variants of the Monte Carlo technique. There are some studies on liquid shock waves by molecular dynamics methods. Tsai and Trevino (1981) and Holian and his coworkers (1980, 1988) discussed the internal structures of normal shock waves in Lennard-Jones liquids (corresponding to liquid argon) for weak and very strong shock waves, respectively. Since molecular dynamics simulations of generating shock waves in liquid systems are very computationally expensive, those studies were carried out only for a few cases of shock Mach numbers. If the Rankine-Hugoniot relations for a liquid of interest are known, we can develop more efficient simulations including simulations of shock fronts alone.

The purpose of the present study is to clarify the Rankine-Hugoniot relations for Lennard-Jones liquids. First, Monte Carlo simulations are conducted to evaluate the pressures, the internal energies and the sound velocities for various sets of densities and temperatures. Then the Rankine-Hugoniot relations are clarified as functions of the shock Mach number by numerically solving the basic equations together with the approximate expressions obtained by the method of least squares.

## 2 Evaluation of State Quantities by Monte Carlo Simulations

**2.1 State Quantities.** There are a number of previous experimental studies of the state quantities of argon (Streett and Staveley, 1969; Crawford and Daniels, 1969; Morris and Wylie, 1980; Ten Seldam and Biswas, 1991). However, those data were obtained at temperatures below the ambient temperature, so measurements over a wide range of temperatures are desirable for fully evaluating the Rankine-Hugoniot relations. In computer simulations, Lennard-Jones fluids are widely used and it is pointed out that they are satisfactory approximate model systems for liquid argon (McDonald and Singer, 1969). Hence we deal with Lennard-Jones liquids in the present study.

In Monte Carlo (MC) methods, state quantities such as pressures and internal energies are obtained by taking the ensemble average of the corresponding quantities at the microscopic level (Allen and Tildesley, 1987). We briefly summarize the ensemble-averaged forms of thermodynamic quantities of interest.

Consider the canonical ensemble with a number of molecules, $N$, temperature, $T$, and volume, $V$. If the internal virial of the system is denoted by $\mathcal{W}$, the pressure, $p$, is written in the following form from the virial theorem:

$$p = nKT + \langle \mathcal{W} \rangle / V, \tag{1}$$

in which $n$ is the number density of molecules, $k$ is Boltzmann's constant, $\langle * \rangle$ means the ensemble average, and $\mathcal{W}$ is as follows:

Contributed by the Fluids Engineering Division for publication in the JOURNAL OF FLUIDS ENGINEERING. Manuscript received by the Fluids Engineering Division June 15, 1992; revised manuscript received November 1, 1993. Associate Technical Editor: R. W. Metcalfe.

$$\mathfrak{W} = -\frac{1}{3}\sum_i \sum_{j(>i)} w(r_{ij}) \tag{2}$$

$$w(r_{ij}) = r_{ij}\frac{dv(r_{ij})}{dr_{ij}} \tag{3}$$

where $r_{ij}$ is the distance between molecules $i$ and $j$, and $v$ is the Lennard-Jones 12-6 potential written as

$$v(r_{ij}) = 4\epsilon\{(\sigma/r_{ij})^{12} - (\sigma/r_{ij})^6\}. \tag{4}$$

In the above equation, $\epsilon$ and $\sigma$ are constants and, for argon, $\epsilon/k = 119.8$ [$K$] and $\sigma = 3.405 \times 10^{-10}$ [m].

The internal energy per unit mass, $e$, is obtained by taking the ensemble average of the sum of the potential and kinetic energies of the system. Namely,

$$e = \frac{3kT}{2m} + \frac{1}{mN} <\mathfrak{V}>, \tag{5}$$

in which $m$ is the mass of molecules and $\mathfrak{V}$ is as follows:

$$\mathfrak{V} = \sum_i \sum_{j(>i)} v(r_{ij}). \tag{6}$$

The sound velocity, $a$, is defined in terms of the adiabatic compressibility, $\beta_s$, and the density, $\rho$, as

$$a = \left(\frac{\partial p}{\partial \rho}\right)_s = \left(\frac{1}{\rho\,\beta_s}\right)^{1/2}. \tag{7}$$

$\beta_s$ is related to the isothermal compressibility, $\beta_T$, from the Maxwell relations:

$$\beta_s = 1/\left(\frac{1}{\beta_T} + \frac{T}{cv\,\rho}\,\gamma_v{}^2\right), \tag{8}$$

where $c_v$ is the constant-volume specific heat and $\gamma_v$ is the thermal pressure coefficient ($\gamma_v = (\partial p/\partial T)_v$). The quantities $c_v$, $\gamma_v$, and $\beta_T$ are related to the fluctuations of the potential energy, the internal virial, etc.:

$$c_v = \frac{3k}{2m} + \frac{1}{kT^2Nm} \langle (\delta\mathfrak{V})^2\rangle \tag{9}$$

$$\gamma_v = nk + \frac{1}{VkT^2} \langle \delta\mathfrak{V}\delta\mathfrak{W}\rangle \tag{10}$$

$$\beta_T = V/\{NkT + \langle\mathfrak{W}\rangle - \langle(\delta\mathfrak{W})^2\rangle/(kT) + \langle\Psi\rangle\} \tag{11}$$

The unspecified symbols in the above equations are as follows:

$$\Psi = \frac{1}{9}\sum_i \sum_{j(>i)} r_{ij}\frac{dw(r_{ij})}{dr_{ij}} \tag{12}$$

$$\langle(\delta\mathfrak{V})^2\rangle = \langle\mathfrak{V}^2\rangle - (\langle\mathfrak{V}\rangle)^2 \tag{13}$$

$$\langle(\delta\mathfrak{W})^2\rangle = \langle\mathfrak{W}^2\rangle - (\langle\mathfrak{W}\rangle)^2 \tag{14}$$

$$\langle\delta\mathfrak{V}\delta\mathfrak{W}\rangle = \langle\mathfrak{V}\mathfrak{W}\rangle - \langle\mathfrak{V}\rangle\langle\mathfrak{W}\rangle \tag{15}$$

**2.2 Nondimensional Forms.** For Lennard-Jones systems, it is very convenient for each quantity to be normalized by representative values made up of $\epsilon$, $\sigma$, and $m$. So the following representative values are used: the length is $\sigma$, the temperature is $\epsilon/k$, the number density is $1/\sigma^3$, the density is $m/\sigma^3$, the pressure is $\epsilon/\sigma^3$, the energy is $\epsilon$, the velocity is $(\epsilon/m)^{1/2}$, the specific heat is $k/m$, the compressibility is $\sigma^3/\epsilon$, etc. From this point on, the normalized quantities are described by the superscript $^*$. The above-mentioned equations are written in the nondimensional forms:

$$p^* = n^*T^* + \frac{n^*}{N}\langle\mathfrak{W}^*\rangle \tag{16}$$

$$e^* = \frac{3T^*}{2} + \frac{1}{N}\langle\mathfrak{V}^*\rangle \tag{17}$$

$$a^* = \left(\frac{1}{\rho^*\beta_s{}^*}\right)^{1/2}, \tag{18}$$

where

$$\mathfrak{W}^* = -\frac{1}{3}\sum_i \sum_{j(>i)} w^*(r_{ij}{}^*) \tag{19}$$

$$\mathfrak{V}^* = \sum_i \sum_{j(>i)} v^*(r_{ij}{}^*) \tag{20}$$

$$v^*(r_{ij}{}^*) = 4\{1/r_{ij}{}^{*12} - 1/r_{ij}{}^{*6}\} \tag{21}$$

$$w^*(r_{ij}{}^*) = 24\{-2/r_{ij}{}^{*12} + 1/r_{ij}{}^{*6}\} \tag{22}$$

$$\beta_s{}^* = 1/\left(\frac{1}{\beta_T{}^*} + \frac{T^*}{c_v{}^*\rho^*}\,\gamma_v{}^{*2}\right) \tag{23}$$

$$c_v{}^* = \frac{3}{2} + \frac{1}{T^{*2}N}\langle(\delta\mathfrak{V}^*)^2\rangle \tag{24}$$

$$\gamma_v{}^* = n^* + \frac{n^*}{T^{*2}N} <\delta\mathfrak{V}^*\delta\mathfrak{W}^*> \tag{25}$$

$$\beta_T{}^* = 1/[n^*\{T^* + \langle\mathfrak{W}^*\rangle/N - <(\delta\mathfrak{W}^*)^2>/(NT^*) + \langle\Psi^*\rangle/N\}]. \tag{26}$$

**2.3 Some Techniques for Simulations.** The MC algorithm we use here is the ordinary Metropolis algorithm. This algorithm is explained in detail in many books (for example, Allen and Tildesley, 1987), so we do not describe it here.

Since the Lennard-Jones potential is a short-range potential, a cut-off radius, $r_c$, is usually used; the interactions between molecules are neglected at center-to-center distance greater than the cut-off radius. The present paper also adopts this cut-off radius. If a sufficiently large value of $r_c$ cannot be taken in simulations, the computed values such as pressures and energies have to be corrected. Consider the potential energy, for example. The potential energy,

## Nomenclature

$a$ = sound velocity
$c_v$ = constant-volume specific heat
$e$ = internal energy per unit mass
$k$ = Boltzmann's constant
$m$ = mass of molecule
$M$ = Mach number
$n$ = number density of molecules
$N$ = number of molecules
$p$ = pressure
$r_c$ = cut-off radius for computation
$r_{ij}$ = distance between molecules $i$ and $j$
$T$ = temperature
$u$ = velocity
$v$ = Lennard-Jones potential
$V$ = volume of system
$\mathfrak{V}$ = potential energy
$\mathfrak{W}$ = internal virial
$\beta_s$ = adiabatic compressibility
$\beta_T$ = isothermal compressibility
$\gamma_v$ = thermal pressure coefficient
$\epsilon$, $\sigma$ = constants of Lennard-Jones potential
$\rho$ = density
$\langle\rangle$ = ensemble average

**Subscripts**

$^*$ = nondimensional quantity
1 = upstream quantity
2 = downstream quantity

$\langle \nabla^* \rangle$, is obtained as the sum of the computed value from simulations with cut-off radius, $\langle \nabla_c^* \rangle$, and correction term, $\langle \nabla_{LRC}^* \rangle$. The correction term, $\langle \nabla_{LRC}^* \rangle$, is analytically obtainable using the potential energy expressed in terms of the radial distribution function, $g(r^*)$. By regarding $g(r^*)$ as unity at distance over $r_c^*$, we get

$$\langle \nabla_{LRC}^* \rangle = 2\pi n^* N \int_{rc^*}^{\infty} v^*(r^*) r^{*2} dr^* = 8\pi n^* N \left\{ \frac{1}{9 r_c^{*9}} - \frac{1}{3 r_c^{*3}} \right\}. \quad (27)$$

Similarly,

$$\langle \mathcal{W}_{LRC}^* \rangle = -\frac{2\pi n^* N}{3} \int_{rc^*}^{\infty} w^*(r^*) r^{*2} dr^* = 16\pi n^* N \left\{ \frac{2}{9 r_c^{*9}} - \frac{1}{3 r_c^{*3}} \right\}. \quad (28)$$

$$\langle \Psi_{LRC}^* \rangle = \frac{2\pi n^* N}{9} \int_{rc^*}^{\infty} r^* \frac{dw^*(r^*)}{dr^*} \cdot r^{*2} dr^* = 32\pi n^* N \left\{ \frac{4}{9 r_c^{*9}} - \frac{1}{3 r_c^{*3}} \right\}. \quad (29)$$

We make such corrections in the present work. Finally, it is noted that the fluctuations have the following relations:

$$\langle (\nabla c^* + \langle \nabla_{LRC}^* \rangle)^2 \rangle - (\langle \nabla c^* \rangle + \langle \nabla_{LRC} \rangle^*)^2 = \langle \nabla c^{*2} \rangle - (\langle \nabla c^* \rangle)^2. \quad (30)$$

The fluctuations of the other quantities have similar relations.

**2.4 Results.** All simulations have been carried out up to 10,000 MC steps. The statistical averages of state quantities have been taken during 1000 ~ 10000 MC steps; the data of the first 1000 MC steps are eliminated because of the need to remove the influence of initial condition.

Table 1 shows the influence of the number of molecules, $N$, and the cut-off radius, $r_c^*$, on the state quantities for $\rho^* = 1.0$ and $T^* = 5.0$. For the case of $N = 500$, the values of $r_c^*$ do not have significant effect on the pressures, energies, and sound velocities; the errors in ($p^*$, $e^*$, $a^*$) from the data for $r_c^* = 3.5$ are at most (0.16, 0.17, 0.23 percent). The pressures and the energies for $N = 500$ agree with those for $N = 256$ within statistical errors; the errors in ($p^*$, $e^*$, $a^*$) from the data for $N = 500$ and $r_c^* = 3.5$ are (0.12, 0.18, 0.61 percent). These features are also obtained for $\rho^* = 0.7$ and $T^* = 1.2$. It is expected from the above considerations that the results for $N = 500$ and $r_c^* = 3.5$ have a sufficient accuracy, so the following results are all obtained under these conditions.

Table 2 shows the results of the state quantities for various sets of $\rho^*$ and $T^*$. Numerical accuracy is also indicated for typical cases; the errors in ($p^*$, $e^*$, $a^*$) and ($c_v^*$, $\gamma_v^*$, $\beta_T^*$) are obtained by comparing the average values over 9000 MC steps with those over (8000, 7000, 6000, 5000) and (8000, 7000) MC steps, respectively. The comparison between the present and Ree's results (Ree, 1980) is shown in Table 3; Ree's expressions are the least-squares curves of simulation data for $0.05 \le \rho^* \le 0.96$ and $0.76 \le T^* \le 2.698$. It is seen that Ree's values are slightly different from the present data in the region of small densities.

Figure 1 shows the computer-simulation points on the phase diagram of Lennard-Jones fluids. The solid line is the trajectory of Rankine-Hugoniot relations which are described in the following sections. The simulation points scatter around this curve, so there is no inconsistency in using the least-squares curves of the computed data to evaluate the Rankine-Hugoniot relations.

Finally, we show the approximate expressions of the state quantities by the least-squares methods. The results obtained by the present simulations are approximated in the following forms (Ree, 1980):

$$p^* = n^* T^* \{ 1 + \sum_{i=1}^{4} B_i x^i + B_{10} x^{10} - \sum_{i=1}^{5} i C_i x^i / T^{*1/2} + \sum_{i=1}^{5} D_i x^i / T^* \} \quad (31)$$

**Table 1 Influence of number of molecules, $N$, and cut-off radius, $r_c$, on state quantities**

$\rho^* = 1.0$, $T^* = 5.0$

| N | $r_c^*$ | $p^*$ | $e^*$ | $a^*$ | $c_v^*$ | $\gamma_v^*$ | $\beta_T^*$ |
|---|---|---|---|---|---|---|---|
| 500 | 3.5 | 32.247 | 5.3377 | 13.06 | 2.340 | 5.002 | 0.008550 |
| 500 | 3.0 | 32.230 | 5.3322 | 13.08 | 2.312 | 4.877 | 0.008358 |
| 500 | 2.5 | 32.195 | 5.3287 | 13.09 | 2.304 | 4.830 | 0.008279 |
| 500 | 2.0 | 32.213 | 5.3296 | 13.08 | 2.306 | 4.851 | 0.008332 |
| 256 | 3.0 | 32.209 | 5.3282 | 13.14 | 2.275 | 4.689 | 0.008048 |

**Table 2 Results of state quantities by Monte Carlo simulations. Numerical accuracy: (*a*): (0.8, 0.04, 1.2, 0.1, 0.3, 4.8) percent for ($p^*$, $e^*$, $a^*$, $c_v^*$, $\gamma_v^*$, $\beta_T^*$); (*b*): (1.2, 0.09, 2.3, 1.3, 2.7, 8.8); (*c*): (0.3, 0.05, 1.2, 0.2, 0.08, 2.0); (*d*): (0.3, 0.1, 0.8, 1.2, 3.1, 7.6); (*e*): (0.1, 0.3, 0.4, 1.2, 2.7, 3.4); (*f*): (0.07, 0.1, 0.7, 0.3, 0.5, 0.5); (*g*): (0.04, 0.04, 0.2, 0.4, 1.1, 1.0); (*h*): (0.1, 0.08, 0.05, 0.3, 0.8, 0.6); (*i*): (0.04, 0.03, 0.06, 0.1, 0.2, 0.1).**

| | $\rho^*$ | $T^*$ | $p^*$ | $e^*$ | $a^*$ | $c_v^*$ | $\gamma_v^*$ | $\beta_T^*$ |
|---|---|---|---|---|---|---|---|---|
| | 0.65 | 1.2 | 0.3310 | -2.6348 | 3.731 | 2.075 | 2.714 | 0.4677 |
| (a) | 0.65 | 1.3 | 0.5883 | -2.4299 | 4.173 | 2.015 | 2.451 | 0.1867 |
| | 0.65 | 1.4 | 0.8497 | -2.2270 | 4.292 | 2.003 | 2.432 | 0.1781 |
| | 0.7 | 1.2 | 0.6564 | -2.9609 | 4.487 | 2.127 | 3.143 | 0.1630 |
| (b) | 0.7 | 1.3 | 0.9734 | -2.7467 | 4.642 | 2.123 | 3.167 | 0.1585 |
| | 0.7 | 1.4 | 1.2838 | -2.5387 | 4.848 | 2.097 | 3.076 | 0.1346 |
| | 0.75 | 1.2 | 1.1929 | -3.2699 | 5.239 | 2.221 | 3.789 | 0.09767 |
| (c) | 0.75 | 1.4 | 1.9288 | -2.8323 | 5.628 | 2.159 | 3.502 | 0.07606 |
| | 0.75 | 1.7 | 2.9853 | -2.1844 | 5.950 | 2.143 | 3.423 | 0.07066 |
| | 0.8 | 1.4 | 2.8384 | -3.1007 | 6.278 | 2.295 | 4.334 | 0.05814 |
| (d) | 0.8 | 1.7 | 4.1140 | -2.4170 | 6.662 | 2.313 | 4.334 | 0.05481 |
| | 0.8 | 2.0 | 5.2874 | -1.7536 | 7.047 | 2.239 | 3.978 | 0.04534 |
| | 0.9 | 2.0 | 9.0868 | -2.0299 | 8.616 | 2.495 | 5.577 | 0.02557 |
| (e) | 0.9 | 2.5 | 11.590 | -0.8369 | 9.277 | 2.329 | 4.713 | 0.01962 |
| | 0.9 | 3.0 | 13.965 | 0.3328 | 9.742 | 2.305 | 4.549 | 0.01803 |
| | 1.0 | 3.0 | 21.553 | 0.5399 | 11.54 | 2.507 | 5.945 | 0.01099 |
| (f) | 1.0 | 5.0 | 32.247 | 5.3377 | 13.06 | 2.340 | 5.002 | 0.008550 |
| | 1.0 | 7.0 | 41.500 | 9.8698 | 14.25 | 2.202 | 4.294 | 0.006919 |
| | 1.1 | 4.0 | 39.554 | 3.7488 | 14.42 | 2.514 | 6.379 | 0.005891 |
| (g) | 1.1 | 8.0 | 63.386 | 13.542 | 16.82 | 2.314 | 5.211 | 0.004432 |
| | 1.1 | 13.0 | 87.873 | 24.836 | 18.85 | 2.197 | 4.557 | 0.003582 |
| | 1.2 | 8.0 | 86.731 | 15.596 | 19.10 | 2.458 | 6.379 | 0.003053 |
| (h) | 1.2 | 20.0 | 152.83 | 43.248 | 23.30 | 2.209 | 4.959 | 0.002147 |
| | 1.2 | 40.0 | 240.22 | 85.357 | 27.67 | 2.063 | 4.119 | 0.001552 |
| | 1.3 | 20.0 | 197.60 | 47.605 | 26.01 | 2.268 | 5.665 | 0.001511 |
| (i) | 1.3 | 50.0 | 347.50 | 112.35 | 32.21 | 2.064 | 4.438 | 0.001019 |
| | 1.3 | 90.0 | 511.71 | 192.64 | 37.53 | 1.965 | 3.855 | 0.0007648 |

Table 3 Comparison between the present results and Ree's data

(a) present, (b) Ree's expression, (c) discrepancies (%)

| $\rho^*$ | $T^*$ | | $p^*$ | $e^*$ | $a^*$ |
|---|---|---|---|---|---|
| 0.65 | 1.3 | (a) | 0.5883 | -2.4299 | 4.173 |
| | | (b) | 0.5591 | -2.3794 | 4.203 |
| | | (c) | 5.0 | 2.1 | 0.7 |
| 0.7 | 1.3 | (a) | 0.9734 | -2.7467 | 4.642 |
| | | (b) | 0.9605 | -2.7170 | 4.824 |
| | | (c) | 1.3 | 1.1 | 3.9 |
| 0.75 | 1.4 | (a) | 1.9288 | -2.8323 | 5.628 |
| | | (b) | 1.9411 | -2.8195 | 5.654 |
| | | (c) | 0.6 | 0.5 | 0.5 |
| 0.8 | 1.7 | (a) | 4.1140 | -2.4170 | 6.662 |
| | | (b) | 4.1536 | -2.4232 | 6.803 |
| | | (c) | 1.0 | 0.3 | 2.1 |
| 0.9 | 2.5 | (a) | 11.590 | -0.8369 | 9.277 |
| | | (b) | 11.738 | -0.8544 | 9.321 |
| | | (c) | 1.3 | 2.1 | 0.5 |
| 1.0 | 5.0 | (a) | 32.247 | 5.3377 | 13.06 |
| | | (b) | 32.536 | 5.3154 | 13.12 |
| | | (c) | 0.9 | 0.4 | 0.5 |
| 1.1 | 8.0 | (a) | 63.386 | 13.542 | 16.82 |
| | | (b) | 63.907 | 13.545 | 16.85 |
| | | (c) | 0.8 | 0.02 | 0.2 |
| 1.2 | 20.0 | (a) | 152.83 | 43.248 | 23.30 |
| | | (b) | 154.08 | 43.355 | 23.46 |
| | | (c) | 0.8 | 0.2 | 0.7 |
| 1.3 | 50.0 | (a) | 347.50 | 112.35 | 32.21 |
| | | (b) | 349.53 | 112.56 | 32.30 |
| | | (c) | 0.6 | 0.2 | 0.3 |

$$e^* = T^*\left\{\frac{3}{2}+\sum_{i=1}^{4}\frac{B_i}{4}x^i+\frac{B_{10}}{4}x^{10}-\frac{1}{T^{*1/2}}\sum_{i=1}^{5}\left(\frac{i}{4}+\frac{1}{2}\right)C_i x^i + \frac{1}{T^*}\sum_{i=1}^{5}\left(\frac{1}{4}+\frac{1}{i}\right)D_i x^i\right\} \quad (32)$$

$$a^{*2} = \kappa T^*\left\{1+\sum_{i=1}^{4}B_i x^i + B_{10}x^{10} - \sum_{i=1}^{5} iC_i x^i/T^{*1/2} + \sum_{i=1}^{5} D_i x^i/T^*\right\} \quad (33)$$

where $\kappa$ is the specific heat ratio and $x = n^*(1/T^*)^{1/4}$. The constants of each expression which are obtained by the method of least squares are shown in Table 4; the constants for Ree's approximate expressions are also included in column ($d$). The approximate expressions of $p^*$, $e^*$, and $a^{*2}$ have the following errors in the worst case from the computed values: about 0.6 percent for $p^*$, about 0.4 percent for $e^*$, and about 2.6 percent for $a^{*2}$. The approximate expression for $a^{*2}$ is somewhat inferior to the others in accuracy. However, since the average of the errors is about 0.5 percent, so the expression for $a^{*2}$ seems to have a sufficient accuracy.

## 3 Rankine-Hugoniot Relations

**3.1 Basic Equations.** For steady normal shock waves, the relations between the upstream and downstream state quantities are given from the conservation laws of mass, momentum, and energy for both gases and liquids: that is,

$$\rho_1 u_1 = \rho_2 u_2 \quad (34)$$

$$p_1 + \rho_1 u_1^2 = p_2 + \rho_2 u_2^2 \quad (35)$$

$$u_1^2/2 + p_1/\rho_1 + e_1 = u_2^2/2 + p_2/\rho_2 + e_2, \quad (36)$$

where $u$ is the velocity and subscripts 1 and 2 represent the upstream and downstream quantities, respectively.

Eliminating $u_2$ from Eqs. (35) and (36) leads to

$$(\rho_1 u_1)^2 = \rho_2(p_1 - p_2 + \rho_1 u_1^2) \quad (37)$$

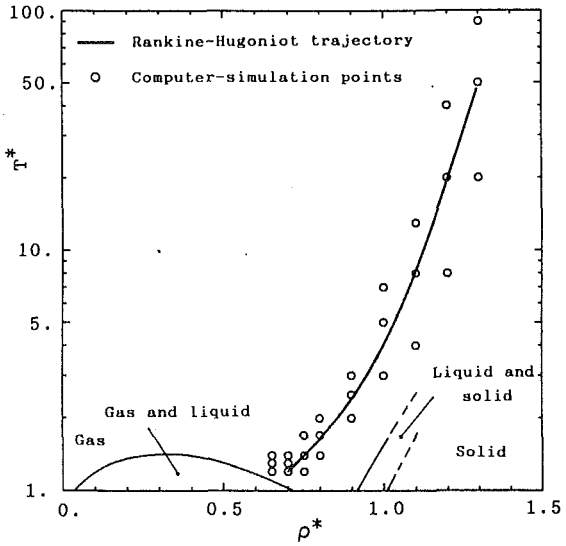


*Fig. 1 Rankine-Hugoniot trajectory and computer-simulation points on phase diagram*

$$\frac{1}{2}u_1^2 + \frac{p_1}{\rho_1} + e_1 = \frac{(p_1+\rho_1 u_1^2)^2 - p_2^2}{2\rho_1^2 u_1^2} + e_2. \quad (38)$$

Since the pressure, $p$, and the internal energy, $e$, are expressed as functions of $\rho$ and $T$ in the preceding section, so the prescription of $u_1$, $\rho_1$, and $T_1$ enables us to evaluate $\rho_2$ and $T_2$ from Eqs. (37) and (38). However, these equations are the simultaneous nonlinear equations, so we cannot solve them analytically. We show the numerical procedure of solving these equations in the following section.

**3.2 Nondimensional Forms.** The above equations are normalized using the representative values shown in Section 2.2, but we do not show the normalized forms here since the transformation is straightforward.

**3.3 Numerical Methods.** The method of successive approximation is usually used to numerically solve simultaneous nonlinear equations such as Eqs. (37) and (38). However, whether or not this method gives converged solutions depends on the computational algorithm employed, so we adopt here a different numerical method which uses quasi-random numbers and has no divergence problems. In addition, it is known that, in numerically solving a multiple integral, the method of using quasi-random numbers is much more efficient than the application of Simpson's rule to a multiple integral. The present method applies this idea to the solution of simultaneous nonlinear equations.

First, we select a sufficiently large area which seems to include the solutions. Second, that area is randomly scanned using quasi-random number (about 500 points in the present study) and we select some points (about 20 points here) which give smaller values of the sum of the absolute residuals of Eqs. (37) and (38). Then a new area which includes all these selected points is defined and the same procedure is repeated until the area becomes sufficiently small, i.e., the solution is obtained. Making such a computational program is straightforward and there are no problems of divergence, so the present method may be a powerful tool for numerically solving more complicated simultaneous nonlinear equations.

**3.4 Results.** Figures 2 to 5 show the Rankine-Hugoniot relations for the upstream condition of $\rho_1^* = 0.7$ and $T_1^* = 1.2$ which corresponds to a liquid state of Lennard-Jones fluids. These results are also compared with those of an ideal gas and the data obtained using the Ree's expressions. The Rankine-Hugoniot trajectory is shown in Fig. 1 for reference.

**Table 4 Values of constants of approximate expressions by the method of least squares**

(a) pressure, (b) energy, (c) square of sound velocity, (d) Ree's expression

| | B1 | B2 | B3 | B4 | B10 |
|---|---|---|---|---|---|
| (a) | -24.025282 | 160.84006 | -282.7695 | 204.5767 | -52.42708 |
| (b) | -39.08913 | 303.4584 | -644.1632 | 482.2779 | -138.0567 |
| (c) | -850.4346 | 5311.687 | -10792.56 | 7417.475 | -1862.315 |
| (d) | 3.629 | 7.2641 | 10.4924 | 11.459 | 2.17619 |

| | C1 | C2 | C3 | C4 | C5 |
|---|---|---|---|---|---|
| (a) | -530.44913 | 1711.6430 | -2718.598 | 2183.567 | -703.4653 |
| (b) | -0.2368550 | 248.9286 | -843.5492 | 1059.927 | -457.2865 |
| (c) | -10174.78 | 37128.30 | -65907.18 | 57283.08 | -19554.85 |
| (d) | 5.3692 | 6.5797 | 6.1745 | -4.2685 | 1.6841 |

| | D1 | D2 | D3 | D4 | D5 |
|---|---|---|---|---|---|
| (a) | -1009.9691 | 6245.3103 | -14488.87 | 14965.43 | -5805.797 |
| (b) | 266.5399 | -2428.503 | 6245.577 | -6311.624 | 2205.504 |
| (c) | -7258.985 | 57814.16 | -163182.0 | 196804.0 | -86430.69 |
| (d) | -3.4921 | 18.6980 | -35.5049 | 31.8151 | -11.1953 |

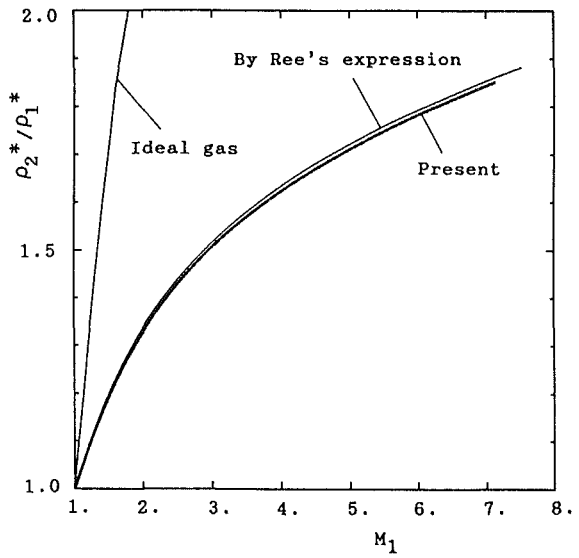


**Fig. 2 Dependence of density ratio on shock Mach number**

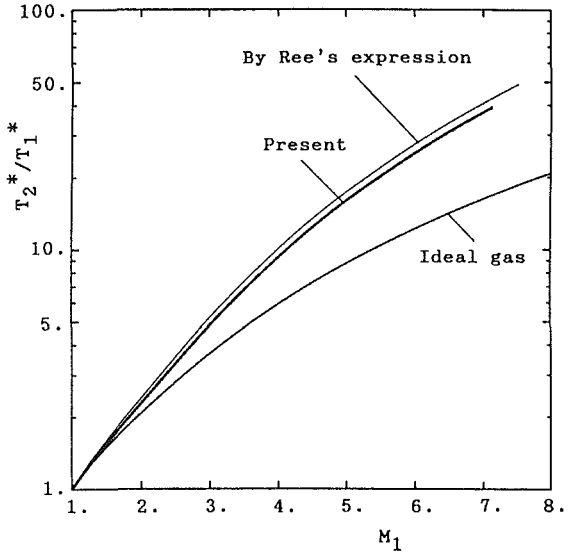


**Fig. 4 Dependence of temperature ratio on shock Mach number**

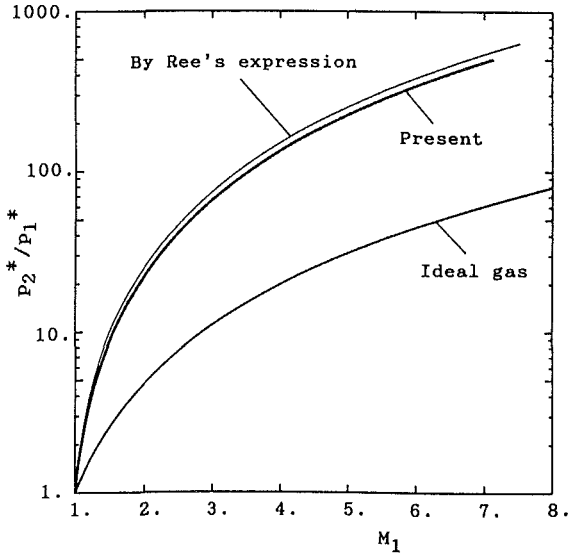


**Fig. 3 Dependence of pressure ratio on shock Mach number**

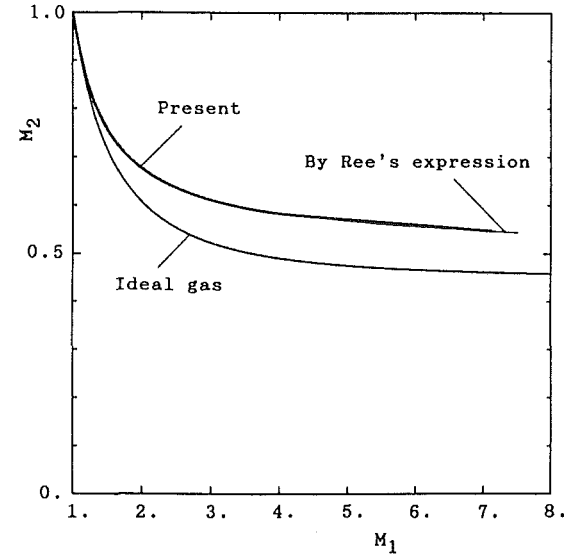


**Fig. 5 Relation between shock Mach number and Mach number behind shock front**

Figure 2 shows the dependence of the density ratio on the shock Mach number. It is reasonable that the increase in density for liquids is not so large as that for gases, since the initial state is a liquid and the molecules are packed closer compared with a gaseous state.

Figure 3 shows the dependence of the pressure ratio on the shock Mach number. As expected, the increase in pressure for the liquid is much greater than that for gases. Equation (1) indicates that the pressure is made up of the kinetic energy

term and the term deriving from interactions between molecules. It is seen from Figs. 3 and 4 that the interaction term is a dominating factor for such large increase in pressure for liquid state.

Figure 4 shows the dependence of the temperature ratio on the shock Mach number. Under the compression process at the shock front, the kinetic energy of the upstream molecules, which have a large mean velocity, is distributed to the thermal velocities to a considerable degree, which leads to a large increase in temperature compared with gases.

Finally, the relation between the upstream and downstream Mach numbers is shown in Fig. 5 for reference. The asymptotic value of the liquid shock wave does not agree with that of the gas.

## 4 Conclusions

Monte Carlo simulations have been carried out to evaluate the state quantities of Lennard-Jones liquids. Then the Rankine-Hugoniot relations were clarified using the least-squares curves of those results by the simulations. As expected, the increase in pressure for liquid shock waves is much greater than that for an ideal gas. The clarification of the Rankine-Hugoniot relations enables us to conduct more efficient molecular dynamics simulations such as simulating shock fronts alone.

## Acknowledgment

This study was partially supported by a Grand-in-Aid for Scientific Research from the Ministry of Education, Science, and Culture of Japan.

## References

Allen, M. P., and Tildesley, D. J., 1987, *Computer Simulation of Liquids*, Clarendon Press, Oxford.

Bird, G. A., 1970, "Aspects of the Structure of Strong Shock Waves," *Physics of Fluids*, Vol. 13, pp. 1172–1177.

Bird, G. A., 1976, *Molecular Gas Dynamics*, Clarendon, Press, Oxford.

Boyd, I. D., 1990, "Rotational-Translational Energy Transfer in Rarefied Nonequilibrium Flows," *Physics of Fluids* A, Vol. 2, pp. 447–452.

Crawford, R. K., and Daniels, W. B., 1969, "Equation-of-State Measurements in Compressed Argon," *Journal of Chemical Physics*, Vol. 50, pp. 3171–3183.

Erwin, D. A., Pham-Van-Diep, G. C., and Muntz, E. P., 1991, "Nonequilibrium Gas Flows. I: A Detailed Validation of Monte Carlo Direct Simulation for Monatomic Gases," *Physics of Fluids A*, Vol. 3, pp. 697–705.

Holian, B. L., Hoover, W. G., Moran, B., and Straub, G. K., 1980, "Shock-Wave Structure via Nonequilibrium Molecular Dynamics and Navier-Stokes Continuum Mechanics," *Physical Review A*, Vol. 22, pp. 2798–2808.

Holian, B. L., 1988, "Modeling Shock-Wave Deformation via Molecular Dynamics," *Physical Review A*, Vol. 37, pp. 2562–2568.

McDonald, I. R., and Singer, K., 1969, "Examination of the Adequacy of the 12-6 Potential for Liquid Argon by Means of Monte Carlo Calculations," *Journal of Chemical Physics*, Vol. 50, pp. 2308–2315.

Morris, E. C., and Wylie, R. G., 1980, "Accurate Method for High Pressure PVT Measurements and Results for Argon for $T = -20$ to $+35$°C and $p$ in the range 200–480 MPa," *Journal of Chemical Physics*, Vol. 73, pp. 1359–1367.

Nanbu, K., and Watanabe, Y., 1984, "Analysis of the Internal Structure of Shock Waves by Means of the Exact Direct-Simulation Method," *Rarefied Gas Dynamics*, (H. Oguchi, ed.,) University of Tokyo Press, Tokyo, pp. 183–190.

Ree, F. H., 1980, "Analytic Representation of Thermodynamic Data for the Lennard-Jones Fluid," *Journal of Chemical Physics*, Vol. 73, pp. 5401–5403.

Schwartz, L. M., and Hornig, D. F., 1963, "Navier-Stokes Calculations of Argon Shock Wave Structure," *Physics of Fluids*, Vol. 6, pp. 1669–1675.

Streett, W. B., and Staveley, L. A. K., 1969, "Experimental Study of the Equation of State of Liquid Argon," *Journal of Chemical Physics*, Vol. 50, pp. 2302–2307.

Takayama, K., 1987, *Shock Waves*, Maruzen, Tokyo (in Japanese).

Ten Seldam, C. A., and Biswas, S. N., 1991, "Determination of the Equation of State and Heat Capacity of Argon at High Pressures from Speed-of-Sound Data," *Journal of Chemical Physics*, Vol. 94, pp. 2130–2135.

Tsai, D. H., and Trevino, S. F., 1981, "Thermal Relaxation in a Dense Liquid Under Shock Compression," *Physical Review A*, Vol. 24, p. 2743–2757.

M. Matovic

S. Oka

Institute for Thermal Engineering
and Energy Research,
Beograd, Yugoslavia

F. Durst

Lehrstuhl für Strömungsmechanik,
Universität Erlangen-Nürnberg,
Erlangen, Germany

# Structure of the Mean Velocity and Turbulence in Premixed Axisymmetric Acetylene Flames

*Laser-Doppler measurements of axial mean velocities and the corresponding rms values of turbulent velocity fluctuations are reported for premixed, axisymmetric, acetylene flames together with the probability density distributions of the turbulent velocity fluctuations. All this information provides an insight into the structure of the flow field. Characteristic zones of the flow field are defined that show common features for all acetylene flames studied by the authors. These features are discussed in the paper and are suggested to characterize, in general, interesting parts of the flames.*

## 1 Introduction

Premixed acetylene flames are widely used in industrial processes such as welding and metal cutting. This has motivated several experimental studies of such flames (Gaydon and Wolfhard, 1960; Fristom and Westenberg, 1965; Oka et al., 1986; Stefanovic et al., 1986) providing both mean velocity and temperature profiles together with photographic records of the overall flame structure. Most experimental investigations have been performed with industrial burners using laser-Doppler anemometry for velocity measurements, with the aim to improve the design of the investigated burners for noise reduction and increased combustion efficiency. Another important aim of most of the studies was the optimization of the flame shape and the control of the flame temperature.

However, there is an evident lack of measurements of the turbulent flow structure in these flames (Kleine, 1974; Moreau, 1980), compared to the large body of data for isothermal jets and mixing layers (Brown and Roshko, 1974; Winant and Browand, 1974; Hussain and Hussain, 1979), and premixed methane and propane flames. Most of our present knowledge on the structure of premixed flames was obtained from measurements carried out in premixed propane or methane flames. Many specific characteristics known of premixed flames resulted from such flames yielding information on the wrinkled flame front structure, length and time scales and the propagation velocity of wrinkles (Yoshida, 1981; Yoshida and Tsuji, 1982). Furthermore, the influence of the volume expansion on turbulence was found from research on methane and propane flames (Pope and Anand, 1982), the gas acceleration in the flame front (Yoshida and Tsuji, 1984), the bimodal velocity pdf of "burned" and "unburned" gas (Shepherd et al., 1982), the interaction of turbulence and combustion (Bray, 1978), and the effect of buoyancy (Jung et al., 1982). The necessity to employ conditional velocity sampling was introduced by Cheng et al. (1984) to further deepen our insight into premixed flames.

In spite of the above-mentioned studies, the available knowledge of premixed, axisymmetric acetylene flames for simple burner configurations such as well shaped nozzles and simple pipes is very limited. These flames are of interest in understanding the interactions of the flame structure with the flow field and this may provide the basis for a generalized treatment of the combustion processes, taking place in the flame. Details of such flames can be used subsequently in treating complex burner configurations as employed in industry.

Looking at the ways combustion processes are treated numerically, it is likely that treatments based on finite volume formulations, that include solutions of transport equations for the thermal energy and chemical species, will be most successful for acetylene flames. Such formulations are available for laminar and turbulent flows (Jones, 1980), but have so far only been employed for laminar and turbulent combusting flows with simpler combustion processes than those encountered in acetylene flames. To help to extent computations in premixed turbulent acetylene flames, the present study includes nozzle and pipe outlets yielding different flame structures. Both the mean flow field components and their correspondent turbulence statistics are measured using laser-Doppler anemometry. The flame characterizing zones are deduced from the measurements that allow the structure of the different acetylene flames to be described in a somewhat uniform manner. These structures are confirmed from photographic studies of the flames.

Section 2 of the paper describes the experimental setup employed. Section 3 presents mean velocity and turbulence intensity profiles along the flame axis, together with velocity histograms providing the basis for the description of the specific flow field characteristics. Conclusions and final remarks

Contributed by the Fluids Engineering Division for publication in the JOURNAL OF FLUIDS ENGINEERING. Manuscript received by the Fluids Engineering Division April 14, 1992; revised manuscript received March 31, 1993. Associate Technical Editor: J. A. C. Humphrey.

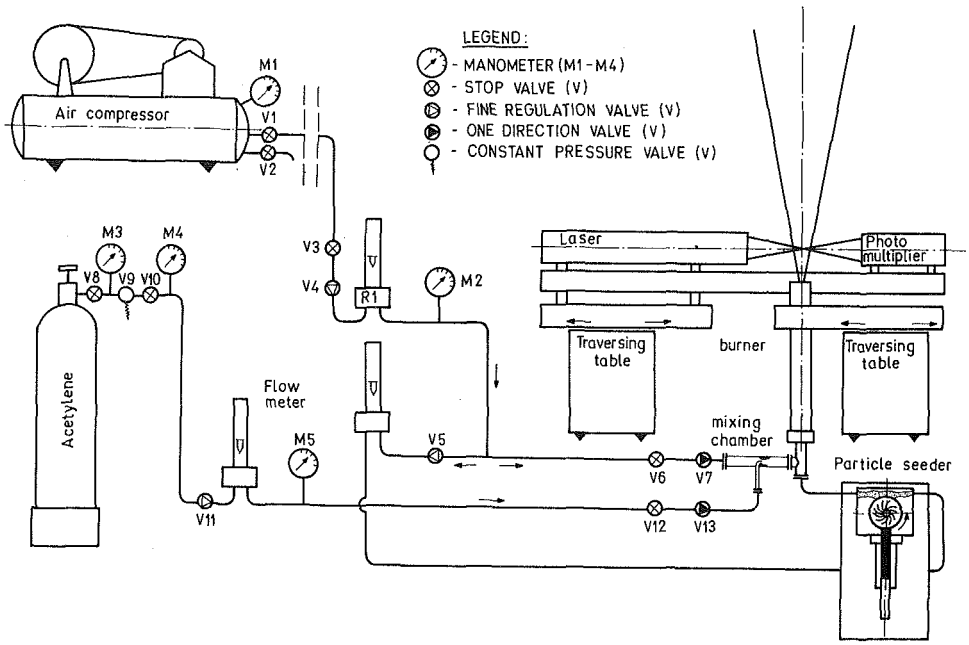


**Fig. 1 Schematic picture of the experimental apparatus**

in Section 4 reveal the division of the premixed acetylene flame flow field in four characteristic zones.

## 2 Experimental Equipment and Flow Conditions

The experimental equipment employed is sketched in Fig. 1. The main parts of the equipment were the burner and the mixing chamber. The entire burner assembly was mounted on a traversing table. Compressed air was supplied from an air compressor and mixed in a mixing chamber with the acetylene gas obtained from a gas bottle. In addition, the supply line also allowed the air to be supplied to a main particle seeder. Various metering devices were available to adjust different gas and air flow conditions. In all of the studies reported here, particles for the LDA-measurements were added after the mixing chamber to the premixed acetylene/air mixture. A separate air line and particle seeder were available for additional particle seeding to the surrounding air. Details of the various components of the entire test rig can be taken from Fig. 1, and even more detailed data on the apparatus and its employment to carry out flow studies can be found in the thesis of Matovic (1988).

Two different burner geometries were employed:

(1) burner No. 1 with a large diameter prechamber with a nozzle at the exit providing a contraction ratio of 20:1. The exit nozzle diameter was 6 mm.
(2) burner No. 2 consisting of a long, constant diameter pipe. The length of this "burner pipe" was 100 D, and the exit (tube) diameter was also 6 mm.

At the exit of the burner No. 1 (with nozzle), a nearly constant velocity across most part of the nozzle mouth (about 80

## Nomenclature

$C_u = (U_m/U_{m,o})(x/D)$ = coefficient of the mean velocity drop along the jet axis (used also for region IV in flames)
$D$ = nozzle diameter
$d_f/2$ = width of the flame front at the half of the flame front region length
$D_f/2$ = width of the outside boundary of the flame at the half of the flame front region length
$D_f$ = width of the outside boundary of the flame at the top of the flame front
$h_{f1}$ = inner length of the flame front in the shape of "brush" (for burner No. 2)
$h_{f2}(h_1)$ = outside length of the flame front in the shape of "brush" (for burner No. 2)
$h_f(h_1)$ = length of the flame front in the shape of cone (for burner No. 1)
$h_{23}$ = boundary between region II and III in the flame
$h_{34}$ = boundary between region III and IV in the flame
$L_1$-$L_5$ = characteristic lengths in flame
$m = 1/C_u$ = flame spreading coefficient
$n = Q_{ac}/Q_a$ = mass flow rates ratio
$Q_{ac}$ = acetylene volume flow rate
$\mathrm{Re}_{av,o} = U_{av,o}D/\nu$ = mean exit Reynolds number
$Q_a$ = air volume flow rate
$U$, $V$ = instantaneous velocities along the $x$ and $y$ direction
$u'$ = turbulence intensity along the $x$ direction
$U_{av,o}$ = averaged mean exit velocity (at the exit of the burner)
$U_{m,o}$ = maximum exit mean velocity (at the exit of the burner)
$U_m$ = maximum mean velocity in the cross section (on the flame axis)
$x$ = coordinate along the flame axis
$y$ = coordinate perpendicular to the flame axis
$\lambda$ = fuel coefficient, acetylene/air ratio (= 1.0 for stoichiometric conditions)
$\nu$ = kinematic viscosity

Table 1 The main flow parameters of the investigated flames

| Lab. | Burner type | $U_{av}$ m/s | $U_{m,o}$ m/s | $(u'/U_m)_o$ | $\lambda$ | $Q_a$ dm$^3$/s | $Q_{ac}$ dm$^3$/s | $n$ | Re |
|---|---|---|---|---|---|---|---|---|---|
| FL1 | No. 1 | 10.57 | 11.15 | 0.031 | 0.8 | 0.3250 | 0.0217 | 1:15 | 4060 |
| FL2 | No. 1 | 10.46 | 11.04 | 0.025 | 1.0 | 0.3167 | 0.0264 | 1:12 | 4020 |
| FL3 | No. 1 | 10.58 | 11.16 | 0.031 | 1.2 | 0.3155 | 0.0315 | 1:10 | 4063 |
| FL4 | No. 2 | 10.62 | 14.65 | 0.051 | 0.8 | 0.3265 | 0.0218 | 1:15 | 4068 |
| FL5 | No. 2 | 10.69 | 14.76 | 0.053 | 1.0 | 0.3236 | 0.0269 | 1:12 | 4124 |
| FL6 | No. 2 | 10.74 | 14.82 | 0.051 | 1.2 | 0.3202 | 0.0320 | 1:10 | 4154 |
| FL7 | No. 2 | 15.00 | 18.66 | 0.057 | 0.8 | 0.4612 | 0.0307 | 1:15 | 5760 |
| FL8 | No. 2 | 14.86 | 18.49 | 0.066 | 1.0 | 0.4500 | 0.0375 | 1:12 | 5786 |
| FL9 | No. 2 | 14.78 | 18.39 | 0.064 | 1.2 | 0.4407 | 0.0441 | 1:10 | 5675 |

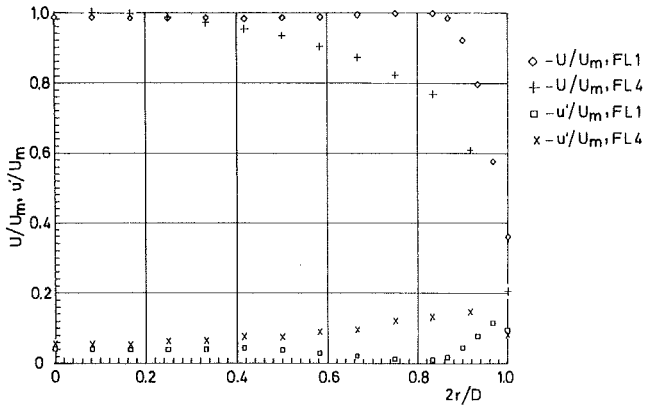


Fig. 2 Mean velocity and turbulence intensity at the exit of the burners used in experiments (burner No. 1—$FL_1$, burner No. 2—$FL_4$)

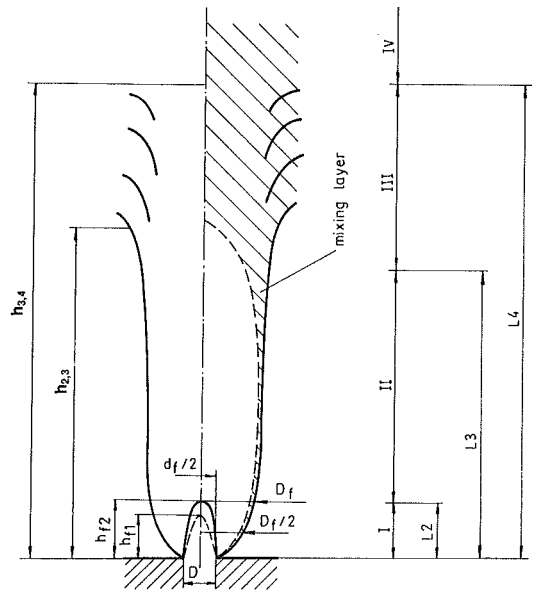


Fig. 3 Schematic picture of the premixed axisymmetric flame flow field

percent of the exit cross section) was obtained. In this region, the turbulence intensity was about 3 percent. At the nozzle wall, a turbulent boundary layer was formed with a maximum turbulence intensity of about 8 percent.

At the exit of the burner No. 2 (long tube), fully developed turbulent velocity profiles were formed with maximum turbulence intensity near the wall of about 14 and 5 percent at the centerline. The velocity and turbulence intensity profiles at the exit cross section of the two burners used (No. 1 and No. 2) are shown in Fig. 2 for the flames FL1 and FL4 (see Table 1). For these two different exit flow conditions of the acetylene/air mixture, quite different shapes of the flame fronts were obtained:

- for burner No. 1, a sharp, bright cone, with a sharp edge and sharp tip was photographically recorded,
- for burner No. 2, a nearly cylindrical "flame brush," with a wide turbulent top was photographically recorded.

Using these two types of burners, various initial measurements of the isothermal jet flow were performed by the authors in order to check if the flow behaved according to results available in the literature (Hinze and Zijnen, 1949; Rajaratram, 1976). Throughout these preliminary measurements, the flow seeding was also adjusted to yield sufficient particles to carry out laser-Doppler measurements. $Al_2O_3$-particles of 2 $\mu$m mean diameter were introduced into the flow. For seeding the main flow, the particle seeder shown in Fig. 1 was used. In order to provide a sufficient particle concentration in the entrained surrounding air, an additional air supply and an additional particle seeder were used. Additional particles were seeded through the small diameter tube with inside diameter 1 mm and with an exit air velocity 0.1 m/s, positioned outside, but near the exit of the burner in the same plane where the velocity profiles were measured along the flame. This velocity was considered small in comparison to the exit velocities, so that its influence on the flames could be considered to be negligible. By using 2 $\mu$m diameter particles and by supplying enough particles both in the acetylene/air mixture and in the surrounding air, mean velocities in most part of the flame cross section were measured with an estimated error of $\sim$1 percent and at the flame periphery with an accuracy of $\sim$5 percent.

Velocity measurements were carried out with a one component laser-Doppler system, consisting of a 15 mW helium-neon laser, a conventional transmission optics, including a beam splitter and a double Bragg cell. Instantaneous velocities in the axial and radial directions were measured at the same point by rotating the LDA-optics by 90 deg. The two parallel beams leaving the Bragg cells were focused by the front lens of the transmission optics yielding the measuring point at the focal distance of 250 mm. Forward scattering was used, with a receiving lens of 150 mm focal length, and a photomultiplier with a pin hole with 0.3 mm in diameter. An angle of 27 deg was chosen between the axis of the transmission optics and the axis of the receiver optics. With this optical arrangement, a measuring control volume of 150 $\mu$m in diameter and 390 $\mu$m in length was produced. The fringe spacing was measured to be 7.8 $\mu$m. All measurements were carried out with a frequency shift of 5 MHz showing a long time stability of $10^{-7}$ Hz. The control volume was positioned in the axial direction with an accuracy of 0.5 mm for $x/D > 10$ and with 0.2 mm for $x/D < 10$. The positioning in the radial direction was with an accuracy of 0.2 mm.

Signals from the photomultiplier were filtered using a band pass filter with a range of 2 to 20 MHz, and were digitized by a transient recorder with a maximum of 1024 point memory and a maximum sampling rate of 10 ns per point. The digitized signals were transmitted to an HP1000 computer where the signal frequency was computed using a software package developed by Matovic and Tropea (1989). At each measuring point, 1000 instantaneous velocity samples were recorded and were employed to compute the local mean velocity and the

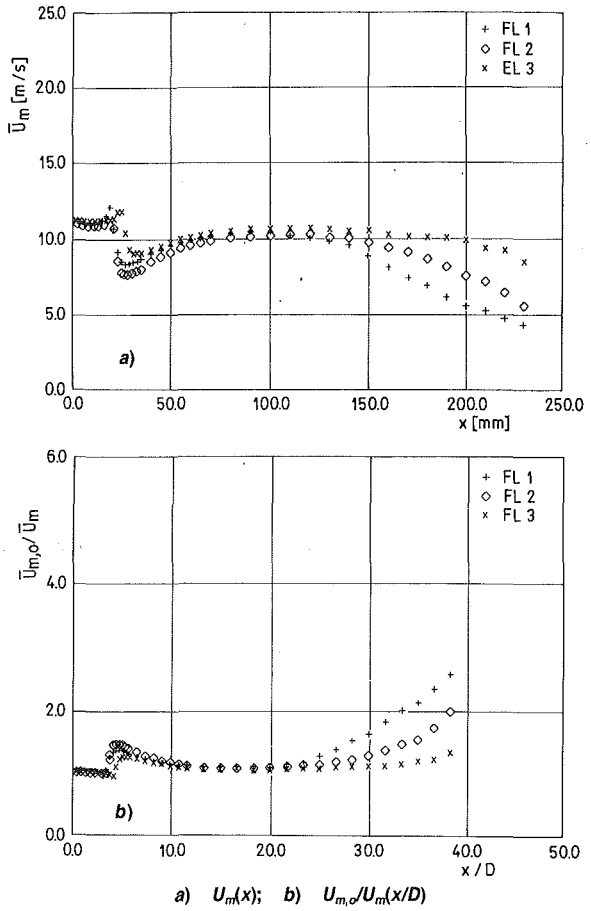


Fig. 4(*a*) Mean velocity along the flame axis, $FL_{1,2,3}$

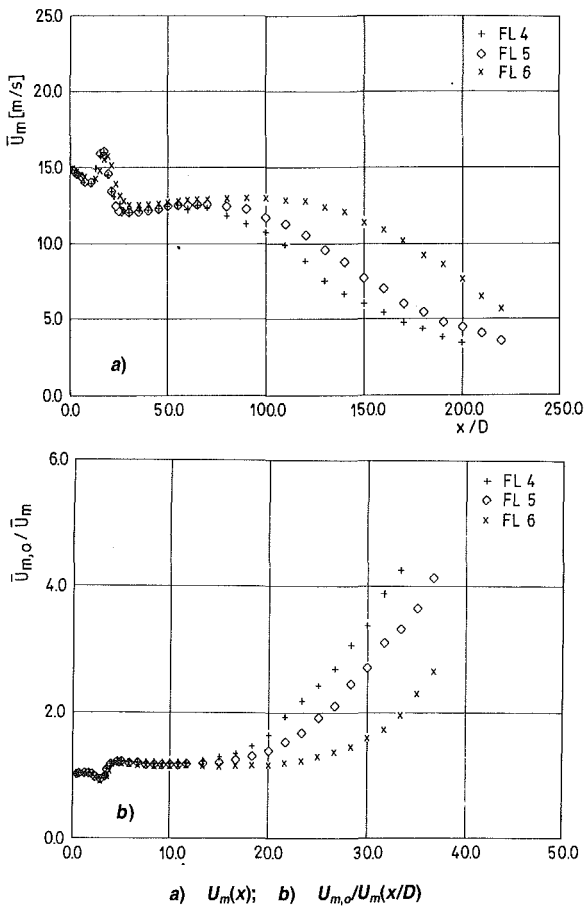


Fig. 4(*b*) Mean velocity along the flame axis, $FL_{4,5,6}$

local turbulence intensity, as well as the corresponding third and fourth order statistical moments. The data were also be processed to yield probability density distributions of the instantaneous velocity fluctuations.

Nine different flames were studied in detail. With burner No. 1, i.e., with the flat velocity distribution at the exit of the nozzle and with a turbulent boundary layer at the nozzle wall, three different acetylene/air ratios for an average exit velocities of about 10.5 m/s were studied. In addition, with burner No. 2, i.e., with the fully developed turbulent flow at the exit of the burner, six flames were studied using two different average exit mean velocities (10.5 m/s and 14.5 m/s) and three acetylene/air ratios. The main parameters of the flames studied are shown in Table 1.

Additional measurements were performed with burner No. 1 but with the exit velocity $U_{m,o} = 18.5$ m/s, in order to make comparisons with the results obtained for flames FL7, FL8, and FL9.

The average nozzle exit velocity, $U_{av}$, calculated using the integral of the mean velocity exit profile and taking the symmetry of the profile into account, was compared for all measurements with the values obtained from the flow rate measurements using rotameters. The agreement of this comparison was $\pm 0.75$ percent. The air flow rate was measured with an accuracy of $\pm 1$ percent, acetylene flow rate with an accuracy of $\pm 0.5$ percent.

## 3 Experimental Results

The experimental equipment and the LDA-System described in Section 2 was employed to yield detailed velocity measurements and from these, characteristic features of the flow field were deduced, Matovic (1988). These revealed that the flow field in acetylene flames can be divided in four characteristic regions, as sketched in Fig. 3.

The mentioned characteristic regions of the flame show the following features:

*Region I:* This region extends from the burner exit to the top of the flame front. This region is characterized by intensive combustion.

*Region II:* Region I is followed by a flame region of constant width with very little change in the axial mean velocity. In this flow region a very small amount of surrounding air seems to be introduced into the flame flow field.

*Region III:* This might be called the jet developing region where an increased entrainment of surrounding air starts after the constant flame width region (Region II), yielding a flow field similar to that of a developing isothermal jet. The entrained air does not, however, reach the axis of the flame where a relatively constant temperature was found.

*Region IV:* Region III is followed by a strongly fluctuating flow region, which one might call the fully developed jet-region. The velocity along the axis is changing like that of an isothermal jet, self similarity of the radial velocity profiles is evident, and the turbulence intensity is much higher than in other parts of the flow.

### 3.1 Axial Mean Flow and Turbulence Intensity Profiles

*3.1.1 Mean Velocity Along Flame Axis.* The subdivision of the combustion region, mentioned in the previous section is reflected by the mean velocity measurements of the authors. Mean velocity measurements along the axis are shown in Figs.

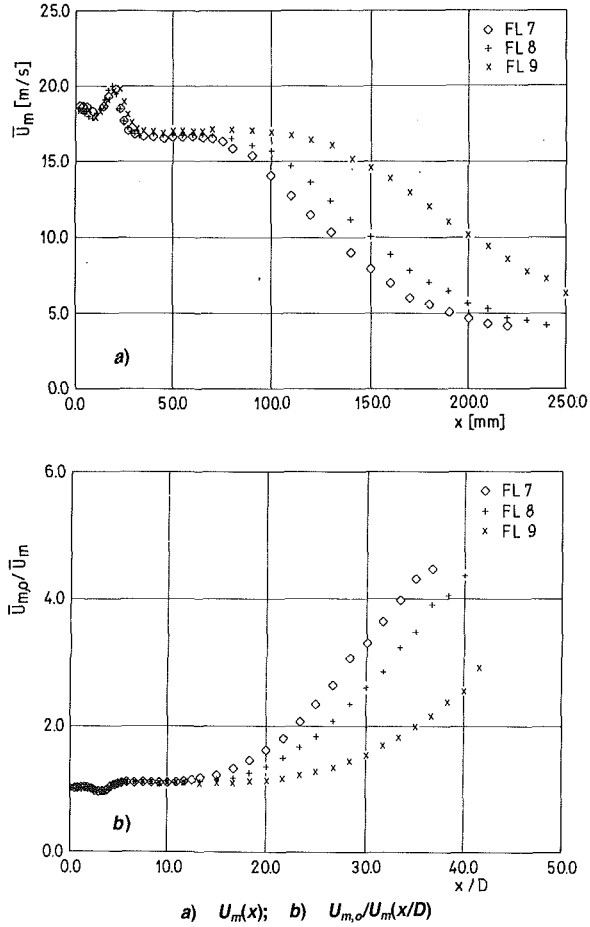


*a)* $U_m(x)$; *b)* $U_{m,o}/U_m(x/D)$

**Fig. 4(*c*) Mean velocity along the flame axis, $FL_{7,\ 8,\ 9}$**

4(*a*) to 4(*c*) for all nine flames of this investigation. It is clearly seen from Figs. 4(*a*) to 4(*c*) that all velocity distributions along the axis show similar features. The axial velocity shows first a slight decrease upstream of the flame front, followed by a relatively sharp velocity increase in the flame front. Thereafter, the velocity drops below the value of the exit velocity to increase thereafter again and to merge into a flame region of relatively constant axial velocity. From thereon, the velocity decreases as known for isothermal jet flows.

Using the above described velocity data, the locations of characteristic points in the flame, $L_1$ to $L_5$ which characterize downstream locations from the burner exit, can be explained as follows:

- $L_1$ location where the velocity starts to increase upstream of the flame front;
- $L_2$ location of the velocity maximum in the flame front;
- $L_3$ location of the velocity minimum downstream of the flame front;
- $L_4$ location of the end of the "velocity plateau" where the velocity starts to decrease gradually
- $L_5$ location where the velocity at the axis decreases to half of the velocity $U_m$ at location $L_4$

The axial extension of regions (I) to (IV) correspond to the locations $L_2$, $L_3$, $L_4$, and $L_5$, respectively. For comparison, at the bottom of Table 2, the corresponding values measured for isothermal jets for which the exit velocities corresponded to flames FL 1-3, (J1) and FL 4-6 (J2) are given. In addition, the flames spreading coefficient ($m = 1/C_u$) in the developed jet region IV, was evaluated employing measurements in the region in which $U_m = f(x)$ has a hyperbolic form.

The radial and axial dimensions of the flame in the characteristic points of regions I to IV were also obtained by authors. Visual observations were performed using a measuring telescope with nonius and utilizing characteristic changes of the flow field and radiation information from the reacting gases and the high-temperature combustion products. The radial and axial dimensions obtained in this manner by "visual time averaging," are given in Table 3.

The following criteria were applied. Transition from zone (I) to zone (II), designated by $-h_{f2}$, is clearly marked by the top of the flame front. The beginning of the region (III) designated by $-h_{23}$, is characterized with the occurrence of small flame protuberances at the edges of the flame. Transition from region (III) to region (IV) designated by $-h_{34}$, is characterized by intensive mixing of combustion products with the surrounding air, which is accompanied by a sudden fall of temperature and radiation intensity. Therefore, it can be considered that the beginning of the region IV will be approximately at the position in which the flame becomes invisible.

Comparing the values given in Table 2 with the values in

**Table 2 Flame (and isothermal jet) parameters obtained on the basis of the axial velocity change**

| Lab. | $L_1$ mm | $L_2$ mm | $L_3$ mm | $L_4$ mm | $L_5$ mm | $L_2$-$L_1$ mm | $L_3$-$L_2$ mm | $L_4$-$L_3$ mm | $L_5$-$L_4$ mm | $m$ | $C_u$ |
|---|---|---|---|---|---|---|---|---|---|---|---|
| FL1 | 15.3 | 18.7 | 26.4 | 140 | 204 | 3.4 | 7.7 | 113.6 | 64 | 0.133 | 7.53 |
| FL2 | 13.9 | 18.7 | 26.4 | 180 | 234 | 4.8 | 7.7 | 153.6 | 54 | — | — |
| FL3 | 20.8 | 25.0 | 30.5 | 209 | 274 | 4.2 | 5.5 | 178.5 | 65 | — | — |
| FL4 | 8.3 | 16.7 | 30.5 | 79 | 141 | 8.4 | 13.8 | 48.5 | 62 | 0.225 | 4.45 |
| FL5 | 8.3 | 16.7 | 30.5 | 100 | 158 | 8.4 | 13.8 | 69.5 | 58 | 0.199 | 5.02 |
| FL6 | 8.3 | 18.7 | 30.0 | 136 | 202 | 10.4 | 11.3 | 106.0 | 66 | 0.199 | 5.02 |
| FL7 | 9.0 | 18.7 | 34.7 | 79 | 138 | 9.7 | 16.0 | 44.3 | 59 | 0.188 | 5.31 |
| FL8 | 9.0 | 18.7 | 34.7 | 105 | 159 | 9.7 | 16.0 | 70.3 | 54 | 0.181 | 5.54 |
| FL9 | 10.4 | 22.2 | 34.7 | 139 | 217 | 11.8 | 12.5 | 104.3 | 78 | 0.165 | 6.07 |
| J1 | — | — | — | — | 42 | — | — | — | — | 0.153 | 6.52 |
| J2 | — | — | — | — | 30 | — | — | — | — | 0.172 | 5.81 |

**Table 3 Visually obtained flame parameters**

| Lab. | $h_{f1}$ mm | $h_{f2}$ mm | $h_{23}$ mm | $h_{34}$ mm | $h_{23}$-$h_{f2}$ mm | $h_{34}$-$h_{23}$ mm | $d_{f/2}$ mm | $D_{f/2}$ mm | $D_f$ mm |
|---|---|---|---|---|---|---|---|---|---|
| FL1 | — | 20.5 | 117 | 210 | 97.5 | 93 | 4.0 | 15.5 | 17.5 |
| FL2 | — | 20.5 | 132 | 250 | 111.5 | 118 | 4.5 | 15.0 | 18.0 |
| FL3 | — | 26.5 | 182 | 290 | 155.5 | 108 | 4.5 | 16.5 | 20.0 |
| FL4 | 10.5 | 20.0 | 69 | 150 | 49.0 | 81 | 5.5 | 15.0 | 17.0 |
| FL5 | 11.0 | 20.0 | 75 | 180 | 55.0 | 105 | 6.0 | 15.5 | 17.5 |
| FL6 | 13.0 | 25.0 | 130 | 230 | 105.0 | 100 | 6.0 | 16.0 | 18.5 |
| FL7 | 12.5 | 21.5 | 73 | 160 | 51.0 | 87 | 5.5 | 15.0 | 16.5 |
| FL8 | 13.0 | 22.0 | 94 | 195 | 72.0 | 101 | 6.0 | 16.0 | 19.0 |
| FL9 | 14.0 | 25.0 | 135 | 260 | 110.0 | 125 | 6.5 | 17.0 | 19.0 |

Table 3 and diagrams in Fig. 4(*a*) to 4(*c*), the general picture of the flame structure, which can be visually observed and which is indicated by the change of the velocity along the axis, can be connected. The inner boundary of the flame front, $h_{f1}$ (obtained visually, only in the flames when a flame front in the form of a "brush" is formed) is placed just a little downstream of the beginning of the region of velocity increase. The flame front top, obtained visually, $h_{f2}$, is placed a little downstream of the velocity maximum. Deceleration of the fluid along the axis downstream the flame front top, is not accompanied by any visually characteristic radiation change. Region (II) ends with the occurrence of "the first flame protuberances" caused in the surrounding air. Further downstream, the decrease of the velocity along the axis takes place ($L_4/h_{23}$ is approximately 1.23 for $FL_{1-3}$, 1.17 for $FL_{4-6}$ and 1.07 for $FL_{7-9}$). The velocity change along the axis acquires the character of the developed isothermal jet at $L_5$, which is a bit earlier than the end of the bright zone of the flame marked with $h_{34}$ ($L_5/h_{34}$ is approximately 0.95 for $FL_{1-3}$ and 0.87 for $FL_{4-9}$). The differences between these values are somewhat greater in flames $FL_{4-9}$ then in the flames $FL_{1-3}$, and vary a little if the flame parameters are significantly changed. It may be concluded that there is a clear and systematic link between the boundaries of the visually observed characteristic flame regions and those obtained from the measured velocity change along the axis.

Comparison of the beginning of the region of developed jet flow ($L_5$ in Table 2) for the flames and for the corresponding isothermal jets (with the same exit flow rate), show that for exit conditions with burner No. 1, the developed flow in the flame occurs approximately at $x/D = 40$. This is about six times later than for the corresponding isothermal jet. For the fully developed turbulent flow at the exit of the burner No. 2, the developed flow region in flames occurs at approximately $x/D = 25$, while in the corresponding isothermal jet (J2), it occurs at $x/D = 5$, i.e., about five times earlier.

*3.1.2 Turbulence Intensity Along the Flame Axis.* Turbulence intensity distributions along the flame axis are shown in Fig. 5 (a: $FL_{1-3}$, b: $FL_{4-6}$, c: $FL_{7-9}$), normalized using the mean velocity at the axis in the cross section where the turbulence fluctuations were measured. Downstream the exit of the burner, the turbulence intensity is approximately constant until the flame front is reached. In the flame front, the first maximum of turbulence intensity occurs at the same point where the mean velocity at the flame axis increases for all flames (Fig. 4). After the decrease of the turbulence intensity, an area of nearly constant value follows, before the turbulence intensity again increases to reach a second maximum. After that maximum, the turbulence intensity decreases again. The first maximum value, for the flames with the average exit velocity about 10.5 m/s ($FL_{1-6}$), is approximately 12 percent and does not differ significantly for both investigated exit conditions at the exit of the burners. For the flames with the exit velocity about 15 m/s ($FL_{7-9}$), the maximum value of turbulence intensity are somewhat smaller, around 10 percent.

It is not probable that high turbulence intensity measured in the flame front is due to the intermittency of the flame front position. In that case, the corresponding velocity histograms have to be bimodal at that point on the flame axis. Figures 11 and 12 show that all velocity histograms at the flame axis for both types of flames are unimodal. Also, turbulence intensity is increased in similar manner for both types of flames, having very different shape of the flame front.

The composition of the premixed gas has very little influence on the turbulence intensity in the region upstream the flame front. That influence can be observed further downstream, and is manifested by the separation of the curves corresponding to different acetylene air ratios. Basic differences occur only in the region of constant flame width (Region II) in which the

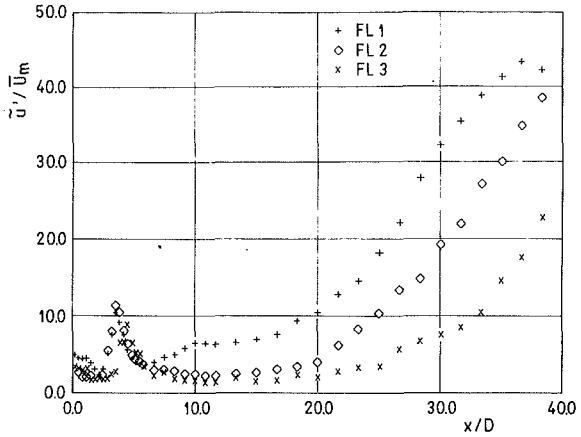


Fig. 5(*a*) $FL_{1, 2, 3}$

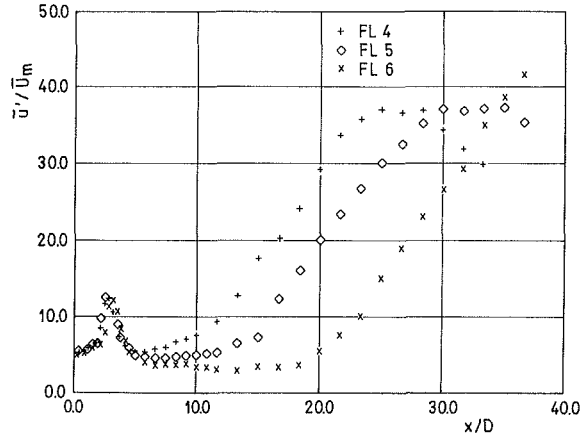


Fig. 5(*b*) $FL_{4, 5, 6}$

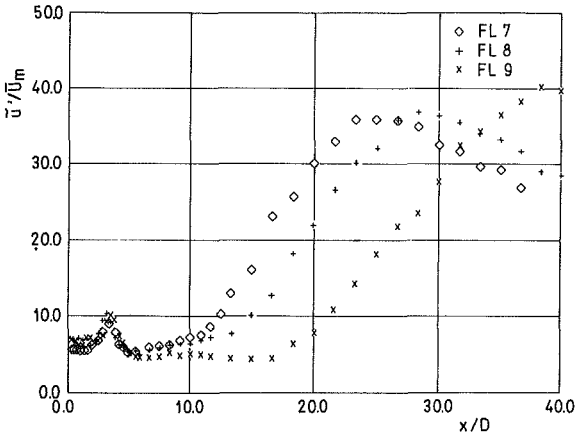


Fig. 5(*c*) $FL_{7, 8, 9}$

**Fig. 5 Turbulence intensity along the flame axis**

acetylene air ratio, i.e. the generated energy in the flame front zone, and flow conditions at the exit of the burners have a controlling role. In all diagrams, one can observe that the turbulence level is the lowest for the flames with highest excess of acetylene ($FL_3$, $FL_6$ and $FL_9$) and it remains constant in the whole region II. In the flames with the stoichiometric ratio for the premixed gases ($FL_2$, $FL_5$ and $FL_8$) the turbulence level is higher and in the flames with fully developed turbulent flow at the exit of the burner, it follows slowly the ascending line. In the flames with excess air ($FL_1$, $FL_4$ and $FL_7$) the turbulence intensities are even higher and is increasing faster. In other words, with the increase of the fuel to air ratio in the mixture, "relaminarisation" after the flame front yields to the smaller turbulence intensity in region II. This is in direct correlation with the length of region II where the mean velocity at the axis

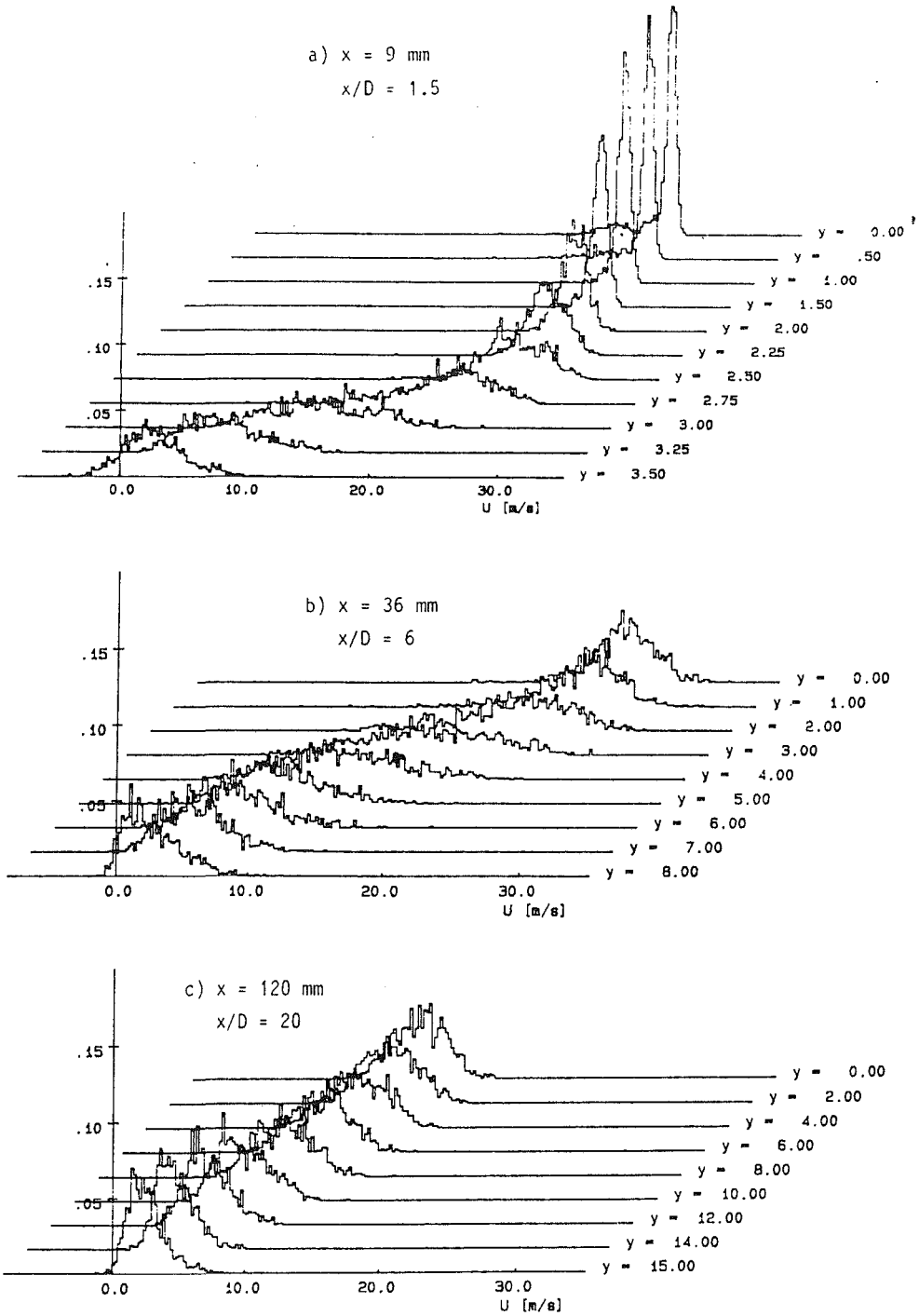


**Fig. 6 Instantaneous velocity histograms at three cross sections of the isothermal jet (J2)**

is constant. A similar region of constant velocity at the axis was observed by Jung et al. (1982), for Reynolds numbers smaller than 3000, and attributed to the bouyancy effect. In this experiment, Reynolds numbers are higher but temperatures are higher as well. As downstream the flame front a sharp increase of gas viscosity occurs as well, the joint effect of "relaminarization" and bouyancy is possible.

In all flames, the position at which the sharp raise of the turbulence level starts again corresponds very well with the beginning of the development zone ($L_4$, Region III), but it is somewhat shifted upstream, about 10 percent toward the burner exit. This is analogous to the behavior in the transition regions in an isothermal jet, where the increase of the turbulence level also starts earlier than the drop of the mean velocity along the axis. Both in the flame and the jet, the increase in turbulence level is shifted for about 6D toward the burner exit. Finally, the gradient of the turbulence level increase in region IV is the same for all flames examined, and it is more than two times smaller than the analogous increase in the corresponding isothermal jets.

At the location of the second maximum, the turbulence intensity reaches values more than 40 percent of the mean velocity for the flames with exit flow conditions as for burner No. 1, and about 38 percent for the flames with exit conditions as for the burner No. 2. This is much larger than the corresponding values in isothermal jets (about 25 percent). If one takes into account the fact that the width of the flow field in this region is also greater, it can be estimated that the total

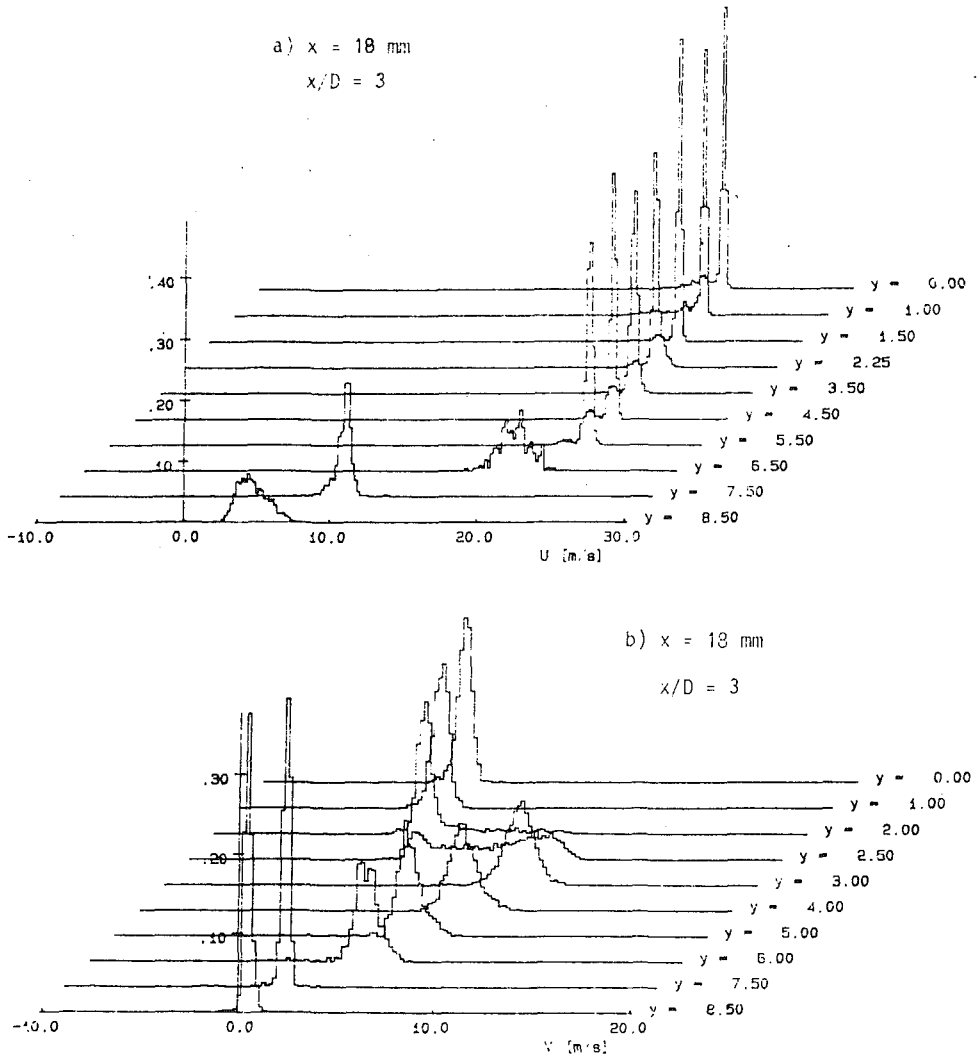


**Fig. 7(*a*, *b*) Instantaneous velocity histograms at the middle of region I, obtained with burner No. 1 ($x/D$ = 3, $U_{m,o}$ = 18.5 m/s) (*a*) velocity *U*-component; (*b*) velocity V-component**

kinetic energy of turbulence contained in this zone is much greater that the one in the corresponding isothermal jet. In contrast to the isothermal jets, in which the turbulence level at the axis has a constant ratio to the local mean velocity, in the flame it decreases further downstream. The present data clearly show that the positions of the second maximum of the turbulence intensities correspond to the location dividing the development region III and the fully developed flow region IV (L5 in Table 2).

**3.2 Velocity Histograms.** An insight into the statistical properties of the instantaneous velocities in free jets and acetylene flames can be obtained from their corresponding histograms (probability density distributions) at various measuring points. Each histogram consists of 240 intervals. To the right of each histogram the coordinate point position is presented. The $y$-values are distances measured from the flame axis in mm. For comparison, the histograms of the instantaneous velocities measured in one of the isothermal jets are presented first. Figures 6(*a–c*) show the histograms of three cross sections, $x/D$ = 1.5, 6 and 20, for jet with exit velocity, $U_{m,o}$ = 18.5 m/s.

In Fig. 6(*a*), the histograms corresponding to the potential core region can be easily distinguished ($y$ = 0.0–1.5 mm). The mixing layer begins at $x$ = 2.0 mm and the point of maximum turbulence intensity is at $y$ = 3.0 mm. In the potential core the histograms are highly asymmetric, skewed to the right (toward larger velocities), while those on the periphery are almost symmetric, or skewed a little to the left (towards smaller velocities). In the downstream cross sections (outside potential core, Fig. 6(*b*) and (*c*)) the histogram asymmetry at points on the axis has disappeared, whereas it has become pronounced at points on the jet boundaries.

Figure 7(*a*) and (*b*) show histograms of the axial and radial velocity components at $x/D$ = 3 in a flame with turbulent boundary layer at the nozzle exit, and Fig. 8(*a*) and (*b*) of $x/d$ = 1.8 in a flame with fully developed turbulent flow at the nozzle exit. These downstream distances are approximately at half the distance of the flame front from the nozzle exit. Note that this distance for the flames $FL_{1-3}$ are approximately two times longer than for the flames $FL_{4-6}$. Significant differences can be observed in the histograms for the flames $FL_{4-6}$ and $FL_{1-3}$ across these planes. In the flames obtained with the burner No. 1, there is no significant change in the shape of U-histograms inside and outside the flame front ($y$ = 2.5 mm). The V-histograms reveal the high acceleration occurring in the flame front through their bimodal nature, which results from the oscillation of the flame front.

The main flame acceleration takes place in the radial direction. At points $y$ = 3, 4 and 5 mm, the V-histograms indicate a sharp increase in turbulence across the flame front simultaneously with a change of their nature, while the U-histograms

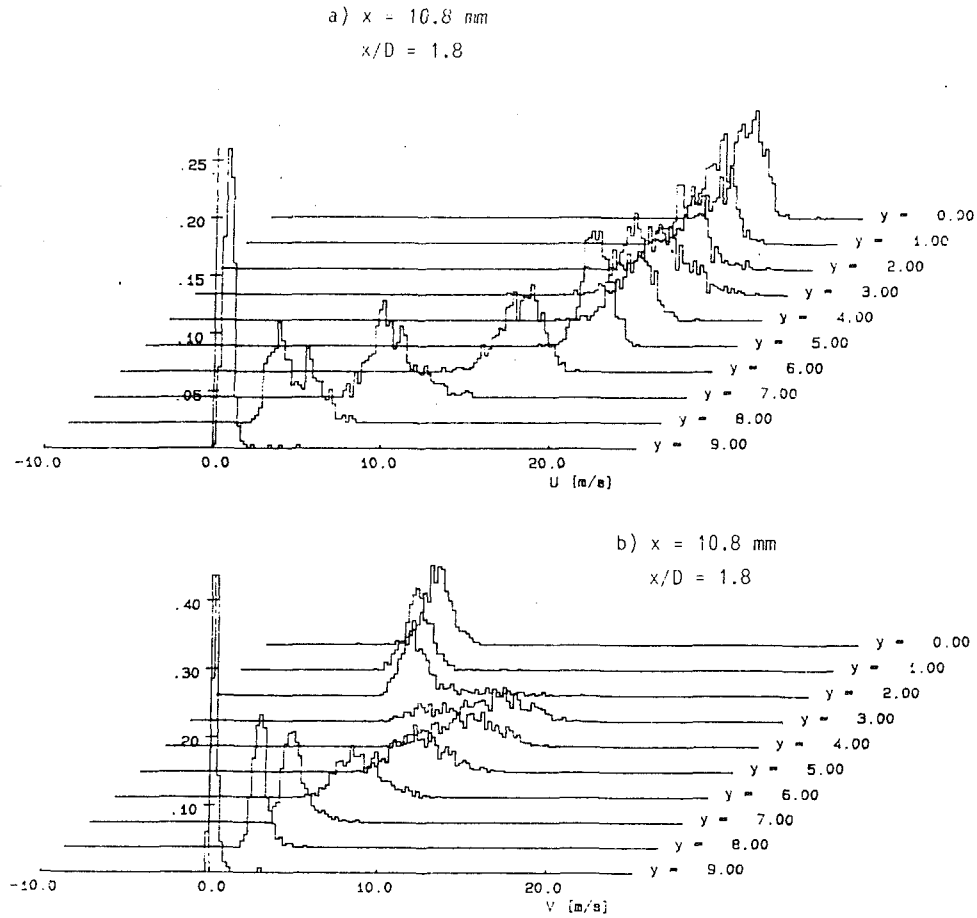


**Fig. 8(*a*, *b*) Instantaneous velocity histograms at the middle of region I, obtained with burner No. 2 ($FL_5$) (*a*) velocity *U*-component; (*b*) velocity V-component**

do not change their nature but show a smooth increase in turbulence intensity. It can be concluded that the flame front, under these conditions, results in highly anisotropical turbulence primarily in the direction perpendicular to the flame front. This anisotropy can easily be seen from the shape of histograms of Fig. 7. The U-histograms are narrower than the V-histograms, and at the same time, the U-mean velocity in the vicinity of the flame front ($y$ = 3 mm) is approximately two times the V-velocity.

In the flames with fully developed turbulent flow at the burner exit (Fig. 8(*a*) and (*b*)), there are no such sudden changes across the flame front, neither in the magnitude nor in the shape of the velocity histograms. The V-histograms in this case are wider in the flame front region but without a sharp change in shape as in flames $FL_{1-3}$. The anisotropic nature of turbulence is also evident. In both types of flames investigated the histograms near the jet axis are skewed to the right towards higher velocities ($FL_{1-3}$ are more pronounced), while outside the flame front are skewed to the left, towards the lower velocities. Also, the mixing layer width is larger in the flames $FL_{4-9}$, where we also observe a gradual transition to lower velocities and to steeper histograms.

A histogram comparison for two flames with different velocity profiles at the burner exit in the region of constant flame width is given in Fig. 9(*a*) and 9(*b*). The histograms of Fig. 9(*a*) correspond to the flame with exit velocity profile obtained with burner No. 1, but with exit velocity $U_{m,o}$ = 18.5 m/s. The histograms of Fig. 9(*b*) correspond to flame $FL_5$, with fully developed turbulent flow at the burner exit and same exit velocity. From Fig. 9(*a*) some specific characteristics of the mixing layer in this region become apparent, noted above in the discussion of mean velocity profiles. There is practically no fluid mixing, but in the mixing layer region only the part of time in which the combustion products pass through the measuring point is altered. At points $y$ = 8 through 11 mm, all velocity histograms are bimodal, with two maxima highly separated and with an area between them of almost zero value which indicates no fluctuating velocities. Comparisons with the corresponding mean velocity profiles in the same flame cross sections show (Matovic, 1988), that the measurements of the mean velocity and turbulence intensity profiles in such highly intermittent flows can cause a false impression of the thickness of the mixing layer.

The given insight into the flow behavior, through the velocity histograms for one cross section in this region, has made it possible to explain the cause of an often observed paradoxon that is the mean velocity at the axis of the flame, in the region of constant flame width does not decrease with downstream distance while the mean velocity profiles across the flame are spreading. It is probably this difference in flow character the reason that the length of the region II in flames with fully developed turbulent flow at burner exit is smaller than that in the corresponding flames of burner No. 1 (see Table 2).

In the downstream cross sections, regions III and IV, the velocity histograms are similar to those in the developed isothermal jet, as observed by comparing Fig. 7(*c*) (jet) and Fig. 10 (flame). There are no observable differences between histograms in these zones, for the two types of flames that have been investigated. It can be concluded that, regarding the nature of the flow, differences between these to types of flames

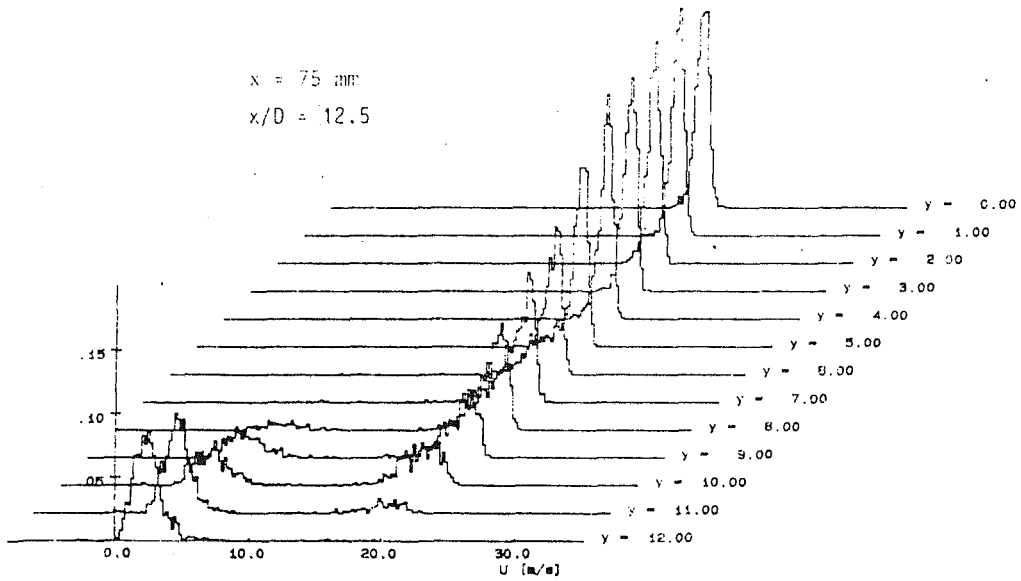


Fig. 9(*a*) Instantaneous velocity histograms in region II, obtained with burner No. 1 ($U_{m,o}$ = 18.5 m/s)

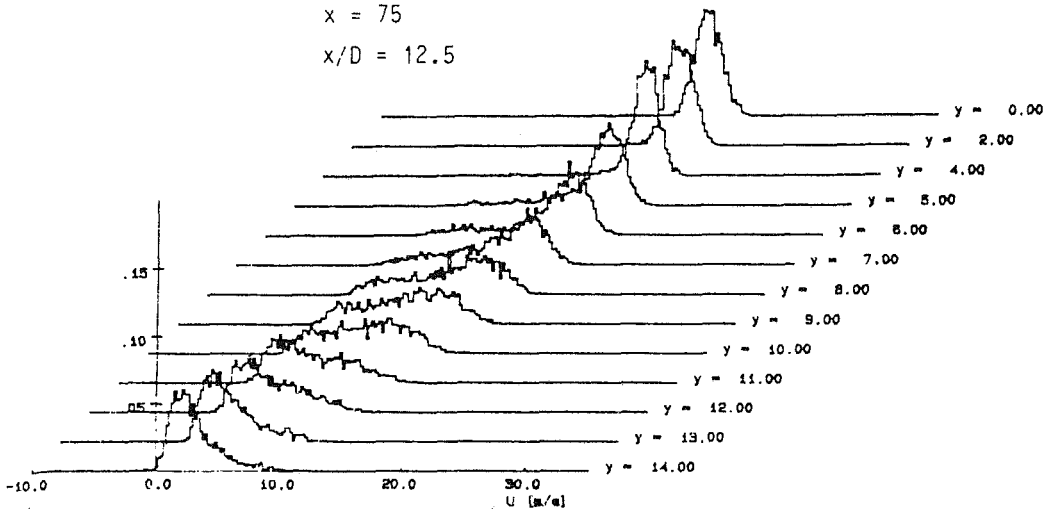


Fig. 9(*b*) Instantaneous velocity histograms in region II, obtained with burner No. 2 ($FL_5$)

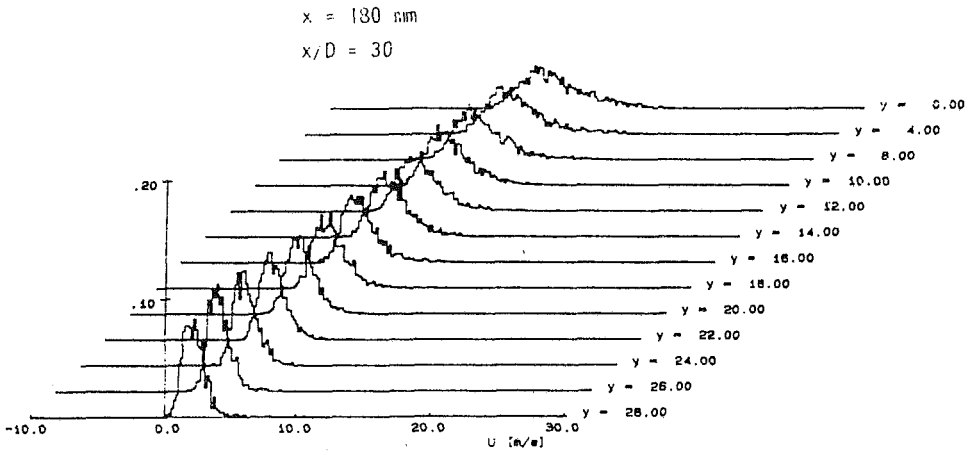


Fig. 10 Instantaneous velocity histograms in region III, obtained with burner No. 2 ($FL_5$)

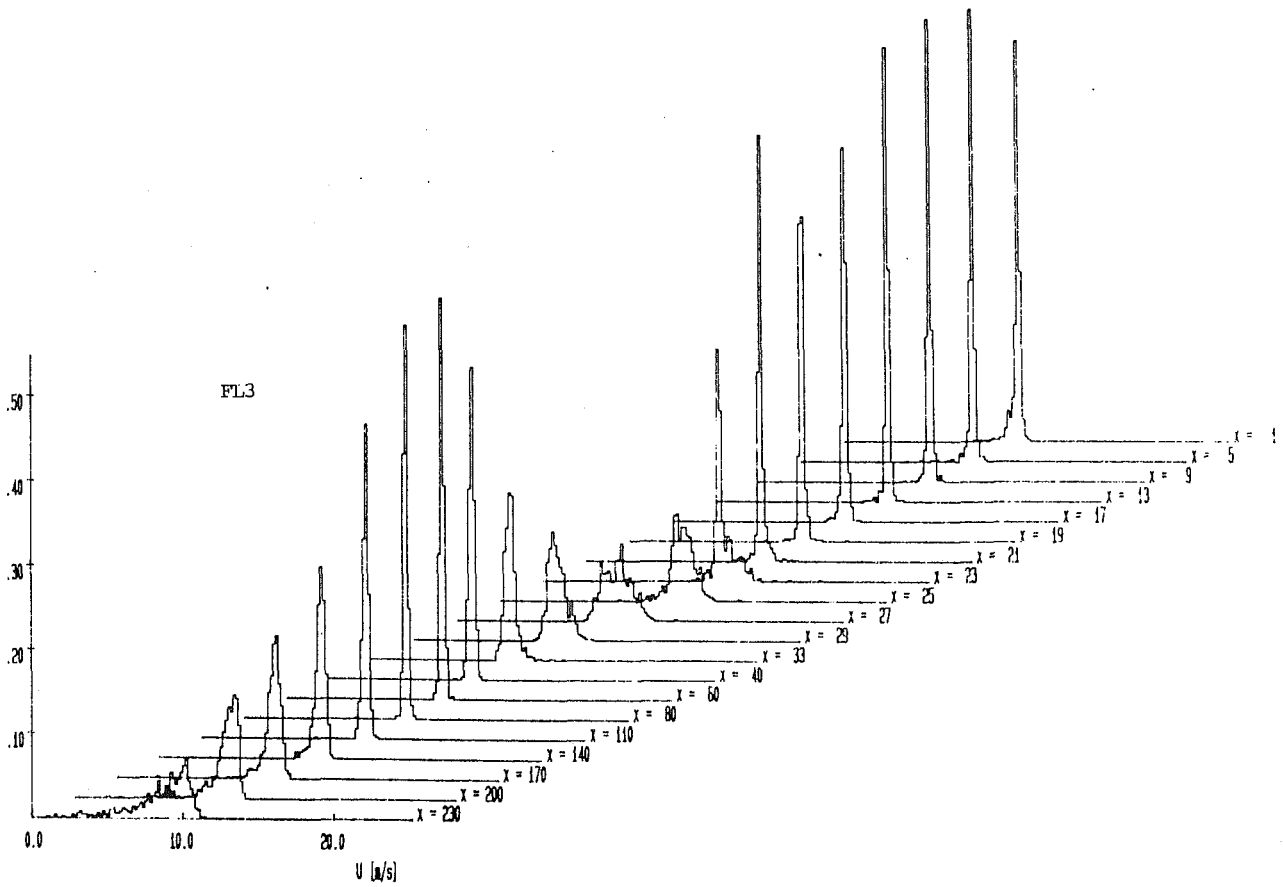


**Fig. 11 Instantaneous velocity histograms along the axis of the flame obtained with burner No. 1 ($FL_3$)**

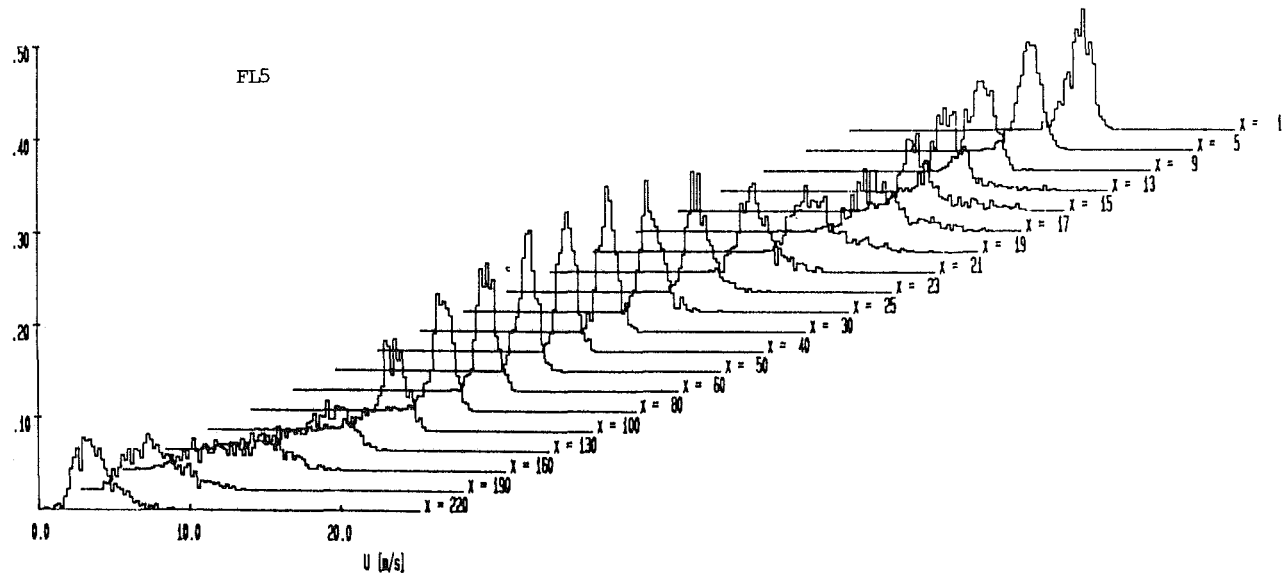


**Fig. 12 Instantaneous velocity histograms along the axis of the flame obtained with burner No. 2 ($FL_5$)**

have disappeared in these regions, although there are differences for fixed distances from the burner exit and also in the spreading rates.

Figures 11 and 12 give the velocity histograms along the axis of flames $FL_3$ and $FL_5$, respectively. These figures clearly show increased levels of turbulence intensity in the flame front which is reduced downstream on it. In region II, reduction of velocity fluctuations occur, the histograms become sharper with their maximum being much larger in flame $FL_3$ than in flame $FL_5$. Also, a large maximum value can be observed after the flame front, i.e., a large reduction of turbulence in the flame with the fuel excess ($FL_{3,\ 6,\ 9}$). In region III where the turbulence fluctuations increase, a drop of the histogram maxima is observed. Comparing the histograms along the jet axis with the information provided in Table 2, we conclude that region III ends of downstream the point where the histograms become the widest. The continuous increase of the histogram maxima marks the beginning of the developed flow region IV.

## 4 Conclusions and Final Remarks

Investigations of the velocity field were conducted in premixed, axisymmetric acetylene/air flames with different velocity profiles at the exit of the burners:

($a$) flat velocity profile in the central part and turbulent boundary layer at the nozzle wall,

($b$) fully developed turbulent velocity profile at the exit of the burner.

Detailed mean velocity measurements were obtained and these measurements along the axis of the flames are reported in the paper. The presented measurements also include the turbulence intensity distribution along the flame axis and embrace also velocity histograms. All this information provided the basis for obtaining an insight into the flow structure of the flames.

Laser-Doppler-Anemometry proved to be a satisfactory method to obtain local, instantaneous velocity measurements in all parts of the flame, although some care had to be taken to provide proper seeding to the flow. A transient recorder based signal processing system yielded the resultant velocity information with high reliability. According to the LDA-velocity information, the flow field of the premixed acetylene/air flame could be divided into four characteristic regions: the region of the flame front (I), the region of constant flame width (II), the developing region (III) and the fully developed jet flow region (IV). Mean velocity and turbulence intensity characteristics of the flow in each of the regions were studied. A good correlation between the various flow regions could be defined on the basis of mean velocity changes along the axis, turbulence intensity variations and the visual characteristics of the flame illumination.

The experimental results for the various flames showed that downstream of the flame front the turbulence level returns to approximately the same level as at the burner exit, and also that over a significant length the flame width remains constant (in region II). Changes of the flame length, which are caused by changes of conditions at the burner exit (exit velocity profiles, and/or different fuel concentrations) are very much linked with the changes of this characteristic flame region.

Considering the spreading of the mean velocity profiles in the flame cross sections in the downstream direction and comparing these with changes of the mean velocity along the axis and with histograms of the instantaneous velocities, a picture of the mixing layer in the region of constant flame width is formed, which is rather different than that for the free mixing layer surrounding an isothermal jet. In the high-temperature flow, possibly due to the very large difference in kinematic viscosities after the flame front and/or bouyancy effects, the disturbances which lead to the spreading of the mixing layer in the isothermal jet and to the entrainment of the surrounding air, seems to lead to the oscillations of the flame as a whole. This is indicated by bimodal velocity histograms in this region of the flow. This results in a constant mean velocity along the axis for this region and a constant turbulence level, and the already mentioned velocity histograms with two maxima at the middle of the mixing layer of the flame.

In addition to providing a general understanding in the flow of acetylene flames, the present paper also gives information of direct use for comparisons with numerical predictions. Numerical predictions must yield the general flow behavior described in this paper and at the same time yield the velocity and turbulence level variations provided here in diagrammatic form.

## Acknowledgments

This work was supported by Scientific Fund of the Republic Serbia, as a part of the research activity in the project E-0801, and also is a part of the joint German-Yugoslav research activity in turbulence research financed in 1980 by the Bundesministerium für Forschung und Technologie. A part of the final work was carried out within a JOULE project of the Commission of the European Communities.

## References

Bray, K. C. N., 1978, "The Interaction between Turbulence and Combustion," *Proceedings of the XVII Symposium (International) on Combustion*, pp. 223–234.

Brown, G. L., and Roshko, A., 1974, "On Density Effects and Large Structure in Turbulent Mixing Layers," *J. Fluid Mech.*, Vol. 64, Part 4, pp. 775–816.

Cheng, R. K., Talbot, L., and Robben, F., 1984, "Conditional Velocity Statistics of Premixed $CH_4$-air and $C_2H_4$-air Turbulent Flames," *Proceedings of the XX Symposium (International) on Combustion*, pp. 453–461.

Fristrom, R. M., and Westenberg, A. A., 1965, *Flame Structure*, McGraw-Hill, N.Y.

Gaydon, A. G., and Wolfhard, H. G., 1960, *Flames and their Structure, Radiation and Temperature*, Chapman & Hall, London.

Hinze, J. Q., Zijnen, B. G., and Van der Hegge, 1949, "Transfer of Heat and Matter in the Turbulent Mixing Zone of an Axially Symmetrical Jet," *Appl. Sci. Res.*, Vol. A1, pp. 435–460.

Hussain, Z. D., and Hussain, A. K. M. F., 1979, "Axisymmetric Mixing Layer: Influence of the Initial and Boundary Conditions," *AIAA*, Vol. 17, No. 1, pp. 48–55.

Jones, W. P., 1980, "Models for Turbulent Flows with Variable Density and Combustion," *Prediction Methods for Turbulent Flows*, W. Kollman, ed., Hemisphere Publ. Corp.

Jung, S. M., Chen, L.-D., and Feath, G. M., 1982, "The Structure of Bouyant Methane and Propane Diffussion Flames," *Proceedings of the XIX Symposium (International) on Combustion*, pp. 349–357.

Kleine, R., 1974, "Anwendung der LDA zur Bestimmung der Turbulenten Flammengeschwindigkeit," Ph.D. thesis, University of Karlsruhe.

Matovic, M., 1988, "Experimental Investigation of the Flow Field of Premixed Turbulent Flame Using LDA," MSc thesis, University of Beograd, Mechanical Engineering Faculty, Yugoslavia (in Serbocroatian).

Matovic, M., and Tropea, C., 1989, "Estimation of LDA Signal Frequency Using the Autocovariance (ACV) Lag Ratio Method," *J. of Phys. E: Scientific Instruments*, Vol. 22, No. 8, pp. 631–637.

Moreau, P., 1980, "Experimental Determination of Probability Density Functions within a Turbulent High Velocity Premixed Flame," O.N.E.R.A. rep. 1980-85.

Oka, S., Radulovic, P., Matovic, M., Pisłar, V., and Stefanovic, P., 1986, "Flow Field Measurements in the Flame of Oxygen-acetylene Burner with LDA," *Transfer Processes in One and Two-Phase Flows*, pp. 112–125, edited by Academy of Sciences USSR, Siberian Branch, Novosibirsk (in Russian).

Pope, S. B., and Anand, M. S., 1984, "Flamelet and Distributed Combustion in Premixed Turbulent Flame," *Proceedings of the XX Symposium (International) on Combustion*, pp. 403–410.

Rajatnaram, N., 1976, *Turbulent Jets*, Elsevier, N.Y.

Shephard, I. G., Moss, J. B., and Bray, K. C. N., 1982, "Turbulent Transport of a Confined Premixed Flame," *Proceedings of the XIX Symposium (International) on Combustion*, pp. 423–432.

Stefanovic, P., Oka, S., and Pavlovic, P., 1986, "Total Pressure Measurement with Flying Pitot Tube," Transfer Processes in One and Two-Phase Flows, pp. 126–139, edited by Academy of Sciences USSR, Siberian Branch, Novosibirsk (in Russian).

Ventura, J. M. P., Yule, A. J., and Chigier, N. A., 1982, "Ionization and Concentration Measurements in the Transitional Region of Partialy Premixed Flames," *Proceedings of the XIX Symposium (International) on Combustion*, pp. 469–476.

Winant, C. D., and Browand, F. K., 1974, "Vortex Pairing, the Mechanism of Turbulent Mixing Layer Growth at Moderate Reynolds Number," *J. Fluid Mech.*, Vol. 64, pp. 237–255.

Yoshida, A., 1981, "An Experimental Study of Wrinkled Laminar Flame," *Proceedings of the XVIII Symposium (International) on Combustion*, pp. 931–940.

Yoshida, A., and Tsuji, H., 1982, "Characteristic Scale of Wrinkles in Turbulent Premixed Flames," *Proceedings of the XIX Symposium (International) on Combustion*, pp. 403–412.

Yoshida, A., and Tsuji, H., 1984, "Mechanism of Flame Wrinkling in Turbulent Premixed Flames," *Proceedings of the XX Symposium (International) on Combustion*, pp. 445–451.

Journal of Fluids Engineering

Technical Briefs

# Flashing Flow Discharge of Initially Subcooled Liquid in Pipes

Joseph C. Leung[1] and William H. Ciolek[2]

## Nomenclature

$C_f$ = liquid specific heat at constant pressure
$D$ = hydraulic diameter of duct
$f$ = fanning friction factor
$G$ = mass velocity or flux
$G^*$ = normalized mass flux
$h$ = specific enthalpy
$h_{fg}$ = latent heat of vaporization
$L$ = duct length
$P$ = pressure, absolute
$T$ = temperature, absolute
$v$ = specific volume
$x$ = quality, vapor mass fraction
$\omega_s$ = correlating parameter, Eq. (5)
$\eta$ = pressure ratio
$\rho$ = fluid density

### Subscripts

$a$ = ambient
$c$ = critical or choked
$f$ = liquid phase
$fg$ = difference between vapor and liquid phase property
$g$ = vapor phase
$o$ = stagnation condition
$r$ = thermodynamic reduced property
$s$ = saturation
$sp$ = single-phase
$st$ = at transition or limiting subcooling
$tp$ = two-phase
1 = pipe inlet (Fig. 1)
2 = pipe exit (Fig. 1)

## Introduction

The release rates of hot fluids stored under pressure during a pipe break or valve failure are a pertinent consideration in source term modeling as part of the environmental health and safety issue. This technical brief presents an analytical treatment for flashing discharge of a hot liquid in a pipe from a high pressure reservoir. Specifically, the liquid is initially subcooled relative to stagnation condition but superheated relative to ambient pressure. The effect of inlet subcooling, pipe length-to-diameter ratio, and physical property groups of the fluid can be readily assessed by the present generalized model. A criterion related to the amount of "limiting" subcooling is found where the discharge rate can be evaluated using a form similar to the incompressible pipe flow formula. Unlike other previously published works (e.g., Pana and Muller, 1978), the present solution yields a smooth transition from saturated inlet to subcooled conditions and reduces exactly to the nozzle flow limit at zero pipe length (Leung and Grolmes, 1988).

## Model Development

Governing steady-state conservation equations for a horizontal turbulent pipe discharge can be written as

$$\text{Mass:} \quad G = \text{constant} \tag{1}$$

$$\text{Momentum:} \quad dP + G^2 dv + 4f\frac{dL}{D}\frac{G^2 v}{2} = 0 \tag{2}$$

$$\text{Energy:} \quad h_o = h + \frac{G^2 v^2}{2} \tag{3}$$

which are equally applicable in the two-phase region when the homogeneous equilibrium model (HEM) is assumed. Admittedly simplistic, this no-slip thermal equilibrium model is used in most engineering calculations (Wallis, 1980). Previous solution methods for the above equations are via either numerical integration (Perry, 1984) or maximization procedure (Wallis, 1969). Detailed thermodynamic properties are hence required in these tedious calculations. Here we seek an analytical solution while employing an approximate equation of state (relating $P$ and $v$) for the saturated two-phase flashing region. Use of such an equation bypasses the necessity of solving the energy equation simultaneously:

$$\frac{v}{v_{fo}} = \omega_s\left(\frac{P_s}{P} - 1\right) + 1 \tag{4}$$

where $\omega_s$, a dimensionless correlating parameter, is given by the same property group as the nozzle case (Leung and Grolmes, 1988),

$$\omega_s = \frac{C_{fo}T_o P_s}{v_{fo}}\left(\frac{v_{fgo}}{h_{fgo}}\right)^2 \tag{5}$$

Here the properties are evaluated at saturation corresponding to the inlet (absolute) temperature $T_o$ with $P_s$ being the corresponding saturation pressure. As before, the assumptions imbedded in Eq. (4) are (*a*) isenthalpic expansion, (*b*) $Pv_{fg} = P_o v_{fgo}$ as in isothermal gas flow with $v_{fg} \approx v_g$, and (*c*) constant properties such as $T = T_o$, $h_{fg} = h_{fgo}$, $C_f = C_{fo}$, and $v_f = v_{fo}$.

[1]Fauske & Associates, Inc., 16W969 West 83rd St., Burr Ridge, IL 60521.
[2]Amoco Corporation, Naperville, IL 60566.

Contributed by the Fluids Engineering Division of THE AMERICAN SOCIETY OF MECHANICAL ENGINEERS. Manuscript received by the Fluids Engineering Division April 26, 1993; revised manuscript received October 7, 1993. Associate Technical Editor: J. A. C. Humphrey.

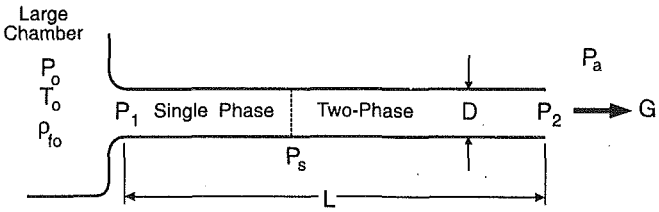


**Fig. 1 Flashing discharge model of an initially subcooled liquid in a pipe**

## Analytical Solutions

Analytical integration of the momentum equation, Eq. (2), can be obtained by considering two distinct regions, the single phase and two-phase regions. Figure 1 illustrates the notation and the flow configuration. Two situations can develop—Case I represents flashing occurring within the constant diameter pipe and Case II denotes flashing occurring prior to the pipe segment, i.e., at the inlet nozzle. (The latter case occurs at low inlet subcooling.) By defining $\eta \equiv P/P_o$, $\eta_s \equiv P_s/P_o$ and $G^* \equiv G/\sqrt{P_o/v_{fo}} = G/\sqrt{P_o\rho_{fo}}$, we can readily integrate the momentum equation, Eq. (2) together with Eq. (4) to yield

Case I: Flashing Within Pipe ($P_1 > P_s$)

$$4f\frac{L}{D}=\frac{2}{G^{*2}}\left[(\eta_1-\eta_s)+\frac{\eta_s-\eta_2}{1-\omega_s}+\frac{\omega_s\eta_s}{(1-\omega_s)^2}\ln\frac{(\eta_s-\eta_2)\omega_s+\eta_2}{\eta_s}\right]-2\ln\left[\frac{(\eta_s-\eta_2)\omega_s+\eta_2}{\eta_2}\right] \quad (6a)$$

Case II: Flashing Within Inlet Nozzle ($P_s > P_1$)

$$4f\frac{L}{D}=\frac{2}{G^{*2}}\left[\frac{\eta_1-\eta_2}{1-\omega_s}+\frac{\omega_s\eta_s}{(1-\omega_s)^2}\ln\frac{(\eta_s-\eta_2)\omega_s+\eta_2}{(\eta_s-\eta_1)\omega_s+\eta_1}\right]-2\ln\left[\frac{(\eta_s-\eta_2)\omega_s+\eta_2}{(\eta_s-\eta_1)\omega_s+\eta_1}\left(\frac{\eta_1}{\eta_2}\right)\right] \quad (6b)$$

Here $f$ denotes an average friction factor over the entire length but for Case I it can be broken down into the single-phase and two-phase components, $4f\,L/D = (4f\,L/D)_{sp} + (4f\,L/D)_{tp}$ where $(4f\,L/D)_{sp} = 2(\eta_1 - \eta_s)/G^{*2}$, i.e., the first term on RHS of Eq. (6*a*). By treating the entrance as a well-rounded frictionless nozzle, the energy equation, Eq. (3), together with the isentropic flow assumption, provides the following relationship between $G$ and $P_1$,

$$G=\left[2\int_{P_1}^{P_o} v\,dP\right]^{0.5}\Big/ v_1 \quad (7)$$

Carrying out the integration, we obtain the following normalized expressions for the two cases:

Case I: (no flashing within inlet nozzle, hence $v = v_{fo}$)

$$G^*=\sqrt{2(1-\eta_1)} \quad (8a)$$

Case II: (flashing within inlet nozzle)

$$G^*=\frac{\left\{2(1-\eta_s)+2\left[\omega_s\eta_s\ln\left(\frac{\eta_s}{\eta_1}\right)-(\omega_s-1)(\eta_s-\eta_1)\right]\right\}^{1/2}}{\omega_s\left(\frac{\eta_s}{\eta_1}-1\right)+1} \quad (8b)$$

Finally, for the condition of exit choking, the following expression provides the relationship between critical mass flux and pipe exit pressure,

$$G_c^*=\frac{\eta_{2c}}{(\omega_s\eta_s)^{0.5}} \quad (9)$$

Thus for each case, we have three equations (Eqs. (6),(8), and (9)) to solve for the three unknowns—$G_c^*$, $\eta_1$, and $\eta_2$. As for the case of unchoked exit, $P_2$ is then equated to the known ambient pressure $P_a$ and only Eqs. (6) and (8) are required to solve for $G^*$ and $\eta_1$ simultaneously.

## Limiting Subcooling

For sufficiently large inlet subcooling, a flow condition can be attained whereby only a single-phase liquid region prevails throughout the entire pipe, and flashing occurs just at the exit end of the pipe (i.e., $P_2 = P_s$). We will denote such a limiting subcooling condition by the pressure ratio $\eta_{st}$; the corresponding inlet subcooling is given by $(T_s - T_o)$ where $T_s$ is the saturation temperature corresponding to the stagnation (vessel) pressure $P_o$. In this situation, Eq. (6*a*) becomes

$$4f\frac{L}{D}=\frac{2}{G^{*2}}(\eta_1-\eta_{st}) \quad (10)$$

Combining Eqs. (8*a*), (9), and (10) and recognizing that $\eta_{2c} = \eta_{st}$, we arrive at a simple criterion for this limiting subcooling condition

$$\eta_{st}=\frac{2\omega_s}{1+4f\frac{L}{D}+2\omega_s} \quad (11)$$

Thus if the inlet subcooling is high such that $\eta_s \le \eta_{st}$, then the critical mass flux is simply given by (combining Eq. (10) with Eq. (8*a*)),

$$G_c^*=\left(\frac{2(1-\eta_s)}{1+4f\frac{L}{D}}\right)^{0.5} \quad (12a)$$

or in dimensional form

$$G_c=\sqrt{\frac{2\rho_{fo}(P_o-P_s)}{1+4f\frac{L}{D}}} \quad (12b)$$

Note that this expression differs from the classical incompressible pipe flow formula in that the pressure drop is not $(P_o - P_a)$ but rather $(P_o - P_s)$ due to the choking condition at exit.

## Comparison With Literature Data

Choked flow water discharge data were obtained by Sozzi and Sutherland (1975) at stagnation pressure of 6.2–6.9 MPa and inlet temperature of 240–280°C. Their pipe discharge data (diameter of 12.7 mm) obtained with a well-rounded inlet nozzle are compared against the present model for three $L/D$'s as shown in Figs. 2 and 3. In the predictions two different values of friction factor, $f = 0.0025$ (typical for single-phase) and $f = 0.005$ (typical for two-phase flow), were employed in an attempt to show the sensitivity to friction factor. Considering the experimental data scatter (of as much as 20 percent), the present model seems to fit the trend quite well for a wide range of inlet subcooling. The vertical bars on these curves denote the onset of the limiting subcooling regime to the left. For the smallest $L/D$ data of 25, the prediction corresponding to a frictionless nozzle ($L/D = 0$) is also shown for comparison in Fig. 2. It should be mentioned that two-phase inlet data ($x_o > 0$) are also included in this comparison and the predictions (dashed curves) are based on a previously published work (Leung and Grolmes, 1987). This previous model for two-phase inlet and the present model for subcooled inlet are found to coincide at the saturated liquid inlet condition ($x_o = 0$) with no discontinuity.

Hendricks and Simoneau (1978) reported discharge data obtained with nitrogen at pressure of 1–10 MPa with large $L/D$.

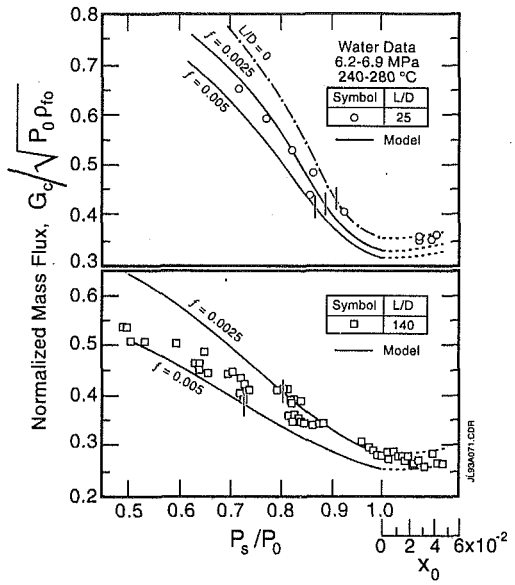


Fig. 2 Prediction of Sozzi and Sutherland's data ($L/D$ = 25, 140)

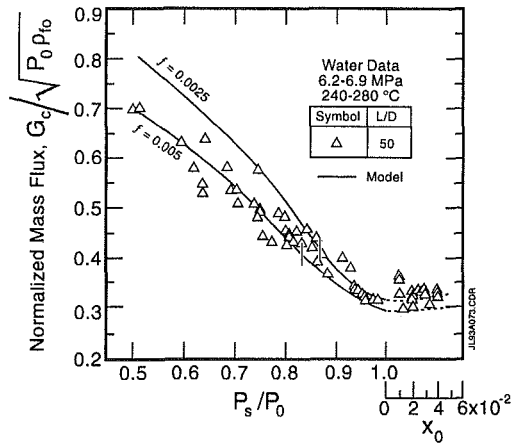


Fig. 3 Prediction of Sozzi and Sutherland's data ($L/D$ = 50)

The ($L/D$ = 16,200) test section was made from 4.8 mm diameter tubing in a 54-turns coil. Only the series obtained at inlet temperatures of 104–111 K corresponding to a reduced temperature $T_r$ of 0.81 was selected in this study. The remaining data at $T_r > 0.96$ were not included because the present model is not applicable near and above the thermodynamic critical point. The mixer chamber temperature was not measured in this series but a good estimate of the inlet temperature was to use the fluid thermocouple measurement at a distance of 75 $L/D$ from the inlet. Since these data span a wide range of inlet subcooling (and therefore the ratio of single-phase length to pipe length varies significantly), we assigned $f = 0.0025$ for the fully developed turbulent single-phase region (Reynolds number $\approx 10^6$) and $f = 0.005$ for the two-phase region (Wallis, 1969). Figure 4 illustrates the good agreement of the present model with the nitrogen data. Also shown are the predictions (dashed curves) if a constant friction factor is used throughout both single-phase and two-phase regions. Due to the long $L/D$, the limiting subcooling occurs at $\eta_{st} = 0.02$ and none of these data exhibited only single-phase (liquid) flow throughout the length of the pipe.

As for the limitation of the present model it should only be used at $T_r$ up to about 0.9 because the imbedded assumptions would not hold near the thermodynamic critical region.

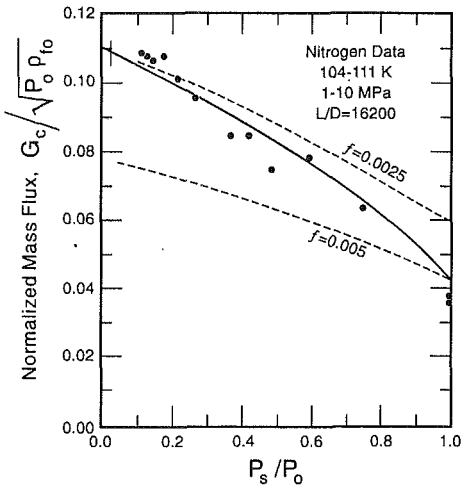


Fig. 4 Prediction of Hendricks and Simoneau's data (— model with $f$ = 0.0025 in single-phase region and $f$ = 0.005 in two-phase region)

## References


Hendricks, R. C., and Simoneau, R. J., 1978, "Two-Phase Choked Flow in Tubes with Very Large L/D," *Advanced Cryogenics Engineering*, Vol. 23, p. 265.

Leung, J. C., and Grolmes, M. A., 1987, "The Discharge of Two-Phase Flashing Flow in a Horizontal Duct," *AIChE J.*, Vol. 33 (3), p. 524.

Leung, J. C., and Grolmes, M. A., 1988, "A Generalized Correlation for Flashing Choked Flow of Initially Subcooled Liquid," *AIChE Journal*, Vol. 34 (4), Apr., p. 688.

Pana, P., and Muller, M., 1978, "Subcooled and Two-Phase Critical Flow States and Comparison with Data," *Nuclear Engineering and Design*, Vol. 45, p. 117.

Perry, R. H., and Greens, D., eds., 1984, *Perry's Chemical Engineers' Handbook*, 6th ed., McGraw-Hill, New York, pp. 5–44.

Sozzi, G. L., and Sutherland, W. A., 1975, "Critical Flow of Saturated and Subcooled Water at High Pressure," General Electric Company Report No. NEDO-13418, July, also ASME *Symp. on Non-Equilibrium Two-Phase Flows*.

Wallis, G. B., 1969, *One-Dimensional Two-Phase Flow*, McGraw-Hill, New York.

Wallis, G. B., 1980, "Critical Two-Phase Flow," *International Journal of Multiphase Flow*, p. 97.


# Preston-Static Tubes for the Measurement of Wall Shear Stress


**Josef Daniel Ackerman,[1,2] Louis Wong,[3] C. Ross Ethier,[1] D. Grant Allen,[3] and Jan K. Spelt[1]**



*We present a Preston tube device that combines both total and static pressure readings for the measurement of wall shear stress. As such, the device facilitates the measurement of wall shear stress under conditions where there is streamline curvature and/or over surfaces on which it is difficult to either*



[1]Research Associate, Graduate Student, Associate Professor, Associate Professor, respectively, Department of Mechanical Engineering, University of Toronto, Toronto, Ontario, Canada M5S 1A4.

[2]Present address: Assistant Professor, Natural Resources and Environmental Studies, University of Northern British Columbia, Prince George, British Columbia, Canada V2N 4Z9.

[3]Department of Chemical Engineering and Applied Chemistry, University of Toronto.



Contributed by the Fluids Engineering Division of THE AMERICAN SOCIETY OF MECHANICAL ENGINEERS. Manuscript received by the Fluids Engineering Division November 29, 1992; revised manuscript received May 2, 1994. Associate Technical Editor: R. L. Panton.

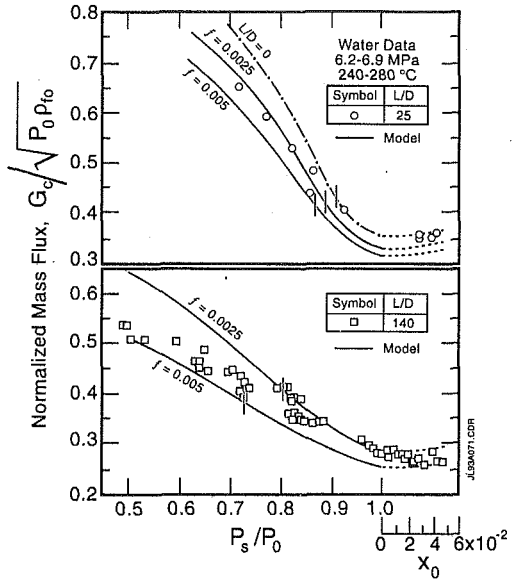


Fig. 2 Prediction of Sozzi and Sutherland's data ($L/D$ = 25, 140)

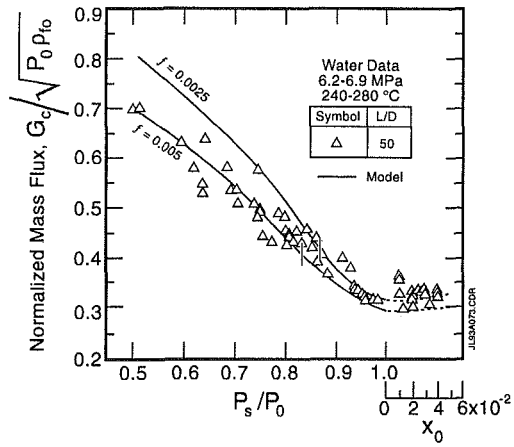


Fig. 3 Prediction of Sozzi and Sutherland's data ($L/D$ = 50)

The ($L/D$ = 16,200) test section was made from 4.8 mm diameter tubing in a 54-turns coil. Only the series obtained at inlet temperatures of 104–111 K corresponding to a reduced temperature $T_r$ of 0.81 was selected in this study. The remaining data at $T_r > 0.96$ were not included because the present model is not applicable near and above the thermodynamic critical point. The mixer chamber temperature was not measured in this series but a good estimate of the inlet temperature was to use the fluid thermocouple measurement at a distance of 75 $L/D$ from the inlet. Since these data span a wide range of inlet subcooling (and therefore the ratio of single-phase length to pipe length varies significantly), we assigned $f = 0.0025$ for the fully developed turbulent single-phase region (Reynolds number $\approx 10^6$) and $f = 0.005$ for the two-phase region (Wallis, 1969). Figure 4 illustrates the good agreement of the present model with the nitrogen data. Also shown are the predictions (dashed curves) if a constant friction factor is used throughout both single-phase and two-phase regions. Due to the long $L/D$, the limiting subcooling occurs at $\eta_{st} = 0.02$ and none of these data exhibited only single-phase (liquid) flow throughout the length of the pipe.

As for the limitation of the present model it should only be used at $T_r$ up to about 0.9 because the imbedded assumptions would not hold near the thermodynamic critical region.

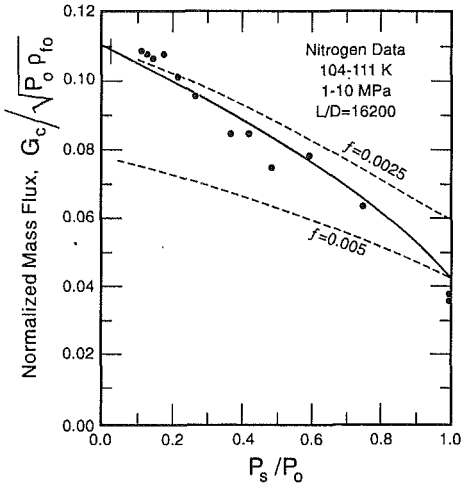


Fig. 4 Prediction of Hendricks and Simoneau's data (— model with $f$ = 0.0025 in single-phase region and $f$ = 0.005 in two-phase region)

## References


Hendricks, R. C., and Simoneau, R. J., 1978, "Two-Phase Choked Flow in Tubes with Very Large L/D," *Advanced Cryogenics Engineering*, Vol. 23, p. 265.

Leung, J. C., and Grolmes, M. A., 1987, "The Discharge of Two-Phase Flashing Flow in a Horizontal Duct," *AIChE J.*, Vol. 33 (3), p. 524.

Leung, J. C., and Grolmes, M. A., 1988, "A Generalized Correlation for Flashing Choked Flow of Initially Subcooled Liquid," *AIChE Journal*, Vol. 34 (4), Apr., p. 688.

Pana, P., and Muller, M., 1978, "Subcooled and Two-Phase Critical Flow States and Comparison with Data," *Nuclear Engineering and Design*, Vol. 45, p. 117.

Perry, R. H., and Greens, D., eds., 1984, *Perry's Chemical Engineers' Handbook*, 6th ed., McGraw-Hill, New York, pp. 5–44.

Sozzi, G. L., and Sutherland, W. A., 1975, "Critical Flow of Saturated and Subcooled Water at High Pressure," General Electric Company Report No. NEDO-13418, July, also ASME *Symp. on Non-Equilibrium Two-Phase Flows*.

Wallis, G. B., 1969, *One-Dimensional Two-Phase Flow*, McGraw-Hill, New York.

Wallis, G. B., 1980, "Critical Two-Phase Flow," *International Journal of Multiphase Flow*, p. 97.


# Preston-Static Tubes for the Measurement of Wall Shear Stress


**Josef Daniel Ackerman,[1,2] Louis Wong,[3] C. Ross Ethier,[1] D. Grant Allen,[3] and Jan K. Spelt[1]**



*We present a Preston tube device that combines both total and static pressure readings for the measurement of wall shear stress. As such, the device facilitates the measurement of wall shear stress under conditions where there is streamline curvature and/or over surfaces on which it is difficult to either*



[1]Research Associate, Graduate Student, Associate Professor, Associate Professor, respectively, Department of Mechanical Engineering, University of Toronto, Toronto, Ontario, Canada M5S 1A4.

[2]Present address: Assistant Professor, Natural Resources and Environmental Studies, University of Northern British Columbia, Prince George, British Columbia, Canada V2N 4Z9.

[3]Department of Chemical Engineering and Applied Chemistry, University of Toronto.



Contributed by the Fluids Engineering Division of THE AMERICAN SOCIETY OF MECHANICAL ENGINEERS. Manuscript received by the Fluids Engineering Division November 29, 1992; revised manuscript received May 2, 1994. Associate Technical Editor: R. L. Panton.

*manufacture an array of static-pressure taps or to position a single tap. Our "Preston-static" device is easily and conveniently constructed from commercially available regular and side-bored syringe needles. The pressure difference between the total pressure measured in the regular syringe needle and the static pressure measured in the side-bored one is used to determine the wall shear stress. Wall shear stresses measured in pipe flow were consistent with independently determined values and values obtained using a conventional Preston tube. These results indicate that Preston-static tubes provide a reliable and convenient method of measuring wall shear stress.*

## Introduction

There are a number of techniques for the measurement of wall shear stress induced by flowing fluid, including force balance methods, velocity gradient methods, mass/liquid transfer methods, hot film methods, and electrochemical film methods (e.g., Winter, 1977; Nitsche et al., 1985). Because of its simplicity and low cost, a Pitot tube resting on solid surface is a popular wall shear stress measuring device within the velocity category above (Preston, 1954). Although "Preston tube" methods have been used extensively (Hollingshead and Rajaratnam, 1980; McAllister et al., 1982; Nitsche et al., 1985; Hirt and Thomann, 1986; Savill, 1989; Taheri and Bragg, 1992), there remains the difficulty of measuring static pressure, which has traditionally been measured using taps located in the wall of the flow chamber (Preston, 1954; Patel, 1965). However, in cases where static pressure is not constant over the area of interest (e.g., due to streamline curvature), surveys of wall shear stress are facilitated if the measurement of static pressure is made without wall taps. One approach is to use multiple Preston tubes joined together, either of different diameter (Rao et al., 1970) or having different chamfer angles (Gupta, 1975). This allows the static pressure to be eliminated from the calculation of wall shear stress, but requires extensive calibration and/or use of "correction factors." Another approach has been to include a static pressure tube within a Preston tube (Bertelrud, 1977). This was possible in Bertelrud's wind tunnel experiments, because a relatively large Preston tube of diameter 3 mm provided adequate spatial resolution. Unfortunately, it is difficult to construct such "tube within a tube" devices for many small-scale applications, especially those in liquid environments. Wall shear stress has, therefore, remained a difficult parameter to measure.

In this report, we describe the development and use of "Preston-static tubes" to measure shear stress. This device was developed to measure wall shear stress around small-scale objects in a flow chamber where static-pressure taps were impractical and the streamlines were curved. It was designed to be inexpensive and easily fabricated from readily available components with no machining needed.

## Apparatus and Experimental Methods

Two Preston tube devices were constructed: a conventional Preston tube, and a "Preston-static tube." In the latter, a 90 deg bevelled-tip syringe needle was fixed to a side-bored one to measure total pressure ($p_{Tot}$) and static (piezometric) pressure ($p_s$), respectively (Fig. 1). The conventional Preston tubes and the total pressure tube of the Preston-static tubes were constructed in two sizes from 20 gauge (20G) and 26G stainless steel syringe needles with point style 5 tip (90 deg bevelled tip; Hamilton Company, Reno, NV). Static pressure was measured using similarly sized round tipped, side-bored needles (point style 3). The nominal location of the side-bored hole in the static pressure needle was approximately 1 mm from the tip. The tip of the static tube was approximately 5 mm downstream

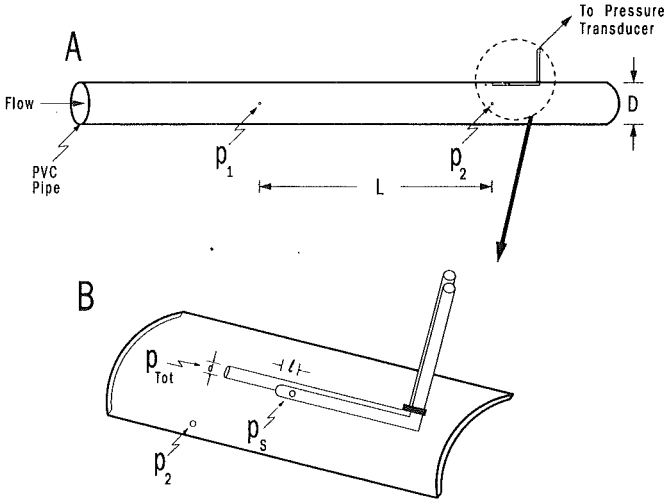


**Fig. 1 Schematic of test apparatus (A) in which Preston-static tubes (B; insert) were used to measure wall shear stress.**

**Legend: Dimensions for 20G and 26G devices as follows:**

| Device size: | 20G | 26G |
|---|---|---|
| Tube outer diameter (d): | $9.09 \cdot 10^{-1}$ mm | $4.62 \cdot 10^{-1}$ mm |
| Tube inner diameter: | $5.58 \cdot 10^{-1}$ mm | $2.54 \cdot 10^{-1}$ mm |
| Side bore hole ($p_s$) diameter: | $5.0 \cdot 10^{-1}$ mm | $1.9 \cdot 10^{-1}$ mm |
| Side bore hole angle to horizontal: | ~80° | ~75° |
| Spacing between tube axes: | $2.5 \cdot 10^{-4}$ mm | $1.1 \cdot 10^{-4}$ mm |
| Distance from $p_{Tot}$ to $p_s$: | 4.5 mm | 5.3 mm |
| Distance from tip to $p_s$ ($l$): | 1.5 mm | 1.0 mm |
| Distance from $p_s$ to exit bend: | 10 mm | 10.9 mm |

of the tip of the Preston tube. Both needles were bent perpendicularly approximately 10 mm downstream of the static hole, where they were connected via flexible tubing to a temperature-compensated differential pressure transducer (Motorola MPX2100GP).

The Preston-static tubes were tested in a 1.54 cm diameter (D) clear PVC pipe, 1.8 m from the entrance. Water at 20–21°C was pumped from a reservoir through the pipe, with flow rate controlled by a downstream throttle valve. Static pressure taps were made in the wall of the pipe at 0.8 m ($p_1$) and 1.8 m ($p_2$) from the entrance, and via a set of valves, could be connected to the differential pressure transducer. In the first set of experiments, a 20G or 26G conventional Preston tube was located either on the upper or lower wall of the pipe to test: 1) whether there were differences between 20G and 26G Preston tubes; 2) whether there were differences in readings between upper and lower walls, due to the obstruction created by the exposed shaft of the Preston tube in the latter case; and 3) to calibrate the Preston tube.

In a second set of experiments, a 20G or 26G Preston-static tube was located on the upper wall only, to determine whether there were differences between the static pressure measured using the wall pressure tap and the static pressure using the static tube.

Experiments were repeated at different flow rates, and flow rate measurements were made using the bucket and stopwatch method each time a set of pressure measurements was taken. For each flow rate, the measured pressure drop between the two wall taps was used to estimate the mean wall shear stress,

$$\tau_W = \frac{p_2 - p_1}{L} \frac{D}{4} \tag{1}$$

where $L$ is the distance between taps 1 and 2.

Preston's (1954) insight into the dynamic similarity of the wall layer, where $\tau_w$, $\rho$ (density) and $\nu$ (kinematic viscosity) are the only independent variables, provides a method for nondimensionalizing the data. The data are thus presented as the nondimensional shear stress

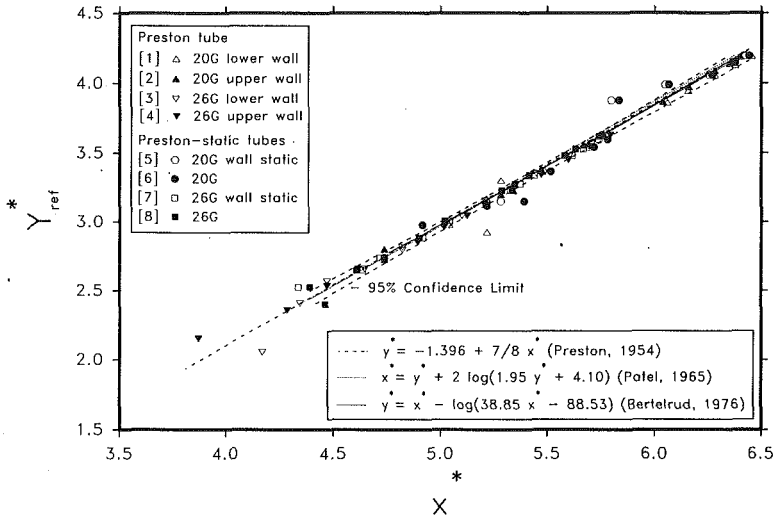


**Fig. 2 Plot of nondimensional shear stress $y^*_{ref} = \log_{10}(\tau_W \cdot d^2/4 \cdot \rho \cdot \nu^2)$ versus nondimensional pressure difference $x^* = \log_{10}(\Delta p \cdot d^2/4 \cdot \rho \cdot \nu^2)$. 95 percent confidence limit for the regression involving data sets [6] and [8] is presented as a dashed line. See Table 1 for linear regression results, including uncertainty estimates. Symbols are measured data, with numbers in square brackets referring to data sets as discussed in text.**

**Table 1 Linear regression of nondimensional shear stress $y^*_{ref} = \log_{10}(\tau_W \cdot d^2/4 \cdot \rho \cdot \nu^2)$ on nondimensional pressure difference $x^* = \log_{10}(\Delta p \cdot d^2/4 \cdot \rho \cdot \nu^2)$.**

| Comparison | No. | $r^2$ | P | Intercept | Slope |
|---|---|---|---|---|---|
| A) Preston tube: | | | | | |
| [1] 20G lower wall | 12 | 0.99 | <0.001 | −1.3 ± 0.2 | 0.85 ± 0.04 |
| [2] 20G upper wall | 13 | 0.99 | <0.001 | −1.36 ± 0.07 | 0.9 ± 0.1 |
| 20G all data | 25 | 0.99 | <0.001 | −1.3 ± 0.1 | 0.86 ± 0.02 |
| [3] 26G lower wall | 12 | 0.99 | <0.001 | −1.5 ± 0.2 | 0.90 ± 0.3 |
| [4] 26G upper wall | 13 | 0.99 | <0.001 | −0.98 ± 0.08 | 0.79 ± 0.02 |
| 26G all data | 25 | 0.99 | <0.001 | −1.2 ± 0.1 | 0.84 ± 0.02 |
| B) Preston-static tubes: | | | | | |
| [5] 20G wall static | 12 | 0.97 | <0.001 | −1.4 ± 0.2 | 0.88 ± 0.04 |
| [6] 20G | 12 | 0.97 | <0.001 | −1.4 ± 0.3 | 0.88 ± 0.05 |
| [7] 26G wall static | 12 | 0.99 | <0.001 | −1.2 ± 0.2 | 0.84 ± 0.03 |
| [8] 26G | 12 | 0.99 | <0.001 | −1.4 ± 0.1 | 0.87 ± 0.03 |

Legend: No.—number of observations; $r^2$—coefficient of determination; $P$—probability value for regression; Intercept and Slope—intercept and slope of linear regression; 20G/26G wall static—refer to shear stress measurements made using wall static taps to measure static pressure at probe location. Data sets in square brackets (e.g., [3]) are plotted in Fig. 2.

$$y^* = \log_{10}\left(\frac{\tau_W \cdot d^2}{4 \cdot \rho \cdot \nu^2}\right) \tag{2}$$

versus the nondimensional pressure difference

$$x^* = \log_{10}\left(\frac{\Delta p \cdot d^2}{4 \cdot \rho \cdot \nu^2}\right) \tag{3}$$

where $\Delta p$ was the difference between total pressure ($p_{Tot}$) and static pressure, measured using the static tube ($p_s$) or the wall tap ($p_2$) depending on the experiment. $x^*$ values ranged from 3.9 to 6.5, corresponding to pipe Reynolds numbers ($Re_D = V \cdot D/\nu$, where $V$ is the velocity) between $1.2 \cdot 10^4$ and $8.8 \cdot 10^4$. The equivalent Reynolds number for the Preston-static tubes (based on the tube diameter, $d$) ranged from $0.71 \cdot 10^3 - 5.2 \cdot 10^3$ for the 20G tubes and $0.36 \cdot 10^3 - 2.6 \cdot 10^3$ for the 26G tubes.

## Results

The data from the different Preston and Preston-static tubes are presented in Fig. 2 (data sets [1]-[4] and [5]-[8], respectively), which plots the dimensionless shear stress ($y^*_{ref}$) based on Eq. (1) versus $x^*$. For the most part, there is a strong linear trend in these data, although there are several points that deviate from this trend. Nonetheless, the data appear to conform well with the empirical relationships determined by Preston (1954), Patel (1965), and Bertelrud (1976). Of these, Preston's (1954) linear relationship

$$y^* = -1.394 + \frac{7}{8}x^* \tag{4}$$

is the simplest and most amenable to statistical analysis. Linear regressions of these data were highly significant ($P < 0.001$), predictive (i.e., $r^2 \geq 0.97$), and the regression equations were within the bounds of Preston's (1954) relationship (Table 1). Figure 2 also shows a 95 percent confidence limit for the regression involving the Preston-static tube data. It is important to note that this confidence limit applies only to data sets [6] and [8], i.e., to data gathered using the static tap of the Preston-static tubes ($p_s$). This confirms that Preston's relationship holds for data gathered using the static pressure tap in the Preston-static tubes.

Analysis of Covariance were used to test for differences in performance among the Preston tubes and Preston-static tubes (i.e., the first and second set of experiments). We specifically wished to test if there were any significant differences in shear stress predictions using the wall static tap versus the static tube. Statistical comparison of data set [5] with [6] and [7] with [8] showed that it was not possible to detect differences among the data sets, i.e., that the shear stress measuring capabilities of the two systems were statistically equivalent (i.e., $P > 0.05$).

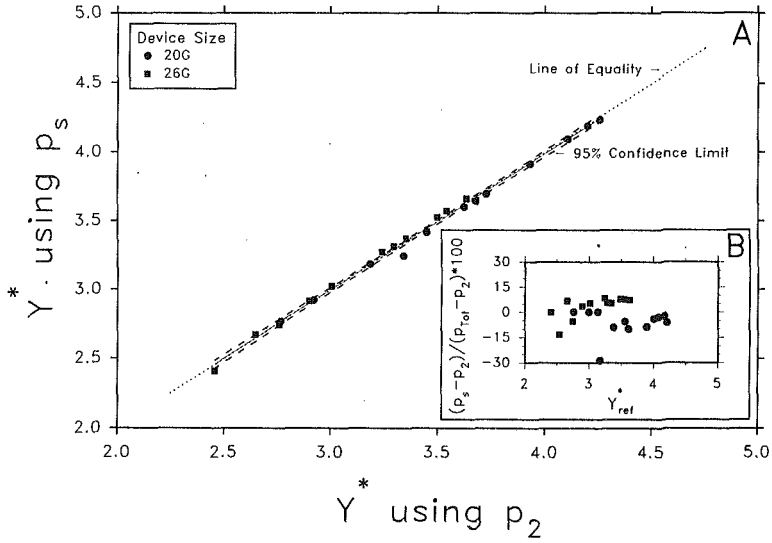


**Fig. 3 (A) Plot of the estimated $y^*$ based on Preston-tube static measurements ($p_s$) versus similar estimates using wall static measurements ($p_2$). Dotted line is the line of equality, solid line is the regression between the $y^*$ estimates, and the dashed line is the 95 percent confidence limit for the regression. (B) Plot of the percentage difference between the static pressure measurement in the Preston-static tubes ($p_s$) and the wall static tap ($p_2$) given by $(p_s - p_2)/(p_{Tot} - p_2) \cdot 100$ versus the nondimensional shear stress ($y^*_{ref}$) measured in the test apparatus.**

It should be noted that differences between 20G and 26G conventional Preston tubes were not detected, nor were differences between shear stresses measured on upper and lower walls.

Since the novel feature of the Preston-static tubes is the use of a static pressure tap on the Preston device, it is necessary to make a direct comparison between the static pressure measured using the Preston-tube static tap ($p_s$) and the static pressure measured using a conventional wall tap ($p_2$). A dimensionless measure of the difference between these two pressure measurements is given by the quantity $(p_s - p_2)/(p_{Tot} - p_2) \cdot 100$, which is plotted in Fig. 3(B) (inset) as a function of $y^*_{ref}$ (based on Eq. (1)). It can be seen that the mean difference is approximately $-1.6$ percent, with some scatter in the data. From a practical perspective, it is necessary to estimate how this small difference affects the estimation of wall shear stress. This can be accomplished by using Preston's relationship (Eq. (4)) to calculate $y^*$ values based on either $p_s$ or $p_2$, and comparing the $y^*$ values thus calculated (Fig. 3(A)). It can be seen that the data is clustered about the line of equality, indicating good agreement in wall shear stresses calculated via traditional and Preston-static approaches.

## Discussion and Conclusions

These results indicate that static pressures measured using Preston-static tubes agree well with static pressures measured using a conventional wall static pressure tap. Further, $y^*$ estimates using Preston-static tube data (i.e., $y^*$ based on $p_s$) agree well with $y^*$ estimates using conventional wall static taps (i.e., $y^*$ based on $p_2$), which in turn agree well with reference $y^*$ measurements ($y^*_{ref}$ based on Eq. (1)). Thus, we conclude that Preston-static tubes can be used to reliably measure wall shear stress. This was due, to some extent, to the design, which conforms to certain criteria. For example, the ratio of inner to outer diameter of the Preston tubes was 0.61 for 20G and 0.55 for 26G, which is reasonably close to the recommended ratio which is $>0.6$ (Bertelrud, 1977).

It is clear that some scatter is present in the above data. This is likely due to the small diameters of the pressure taps, which were easily clogged by particulates in the water. For example, in the case of the two pairs of points above the regression line near $x^* = 6$, it is evident that the dynamic tap (i.e., the Preston tube) was clogged, as the results from the static tube and the static-pressure taps were similar. Consequently, we would recommend using water free of particulates and/or back-flushing the tubes between experiments to dislodge particles.

Another possible cause of scatter, which was experimentally beyond our control, was the nature and location of the side-hole of the static tubes. Microscopic examination of these holes revealed some surface aberrations were present and these may have had some effect. Preston (1954) noted the importance of maintaining a constant ratio of inner to outer diameter and of removing burrs. We did not alter the holes in any way, partly due to the difficulty of working on such a small scale but, also because we wanted to minimize alteration of our device for convenience. The location of the static hole can be addressed through the ratio of $l/d$, which ranged from 1.65 in the 20G static tube to 2.16 in the 26G static tube. Generally, $l/d$ ratios $>2$ are sufficiently far from the local pressure gradient generated by the tube to measure the static pressure (Bertelrud, 1977).

In any case, Fig. 3(A) shows that although scatter is present, there was no systematic difference present in wall shear stress estimates based on $p_s$ or $p_2$. Moreover, the scatter observed in measurements using the Preston-static tubes did not appear to be greater than the scatter observed in measurements using conventional wall taps. This is confirmed by the comparable error estimates in the regression coefficients (Table 1). Further, there are no differences detected in: (1) the measured wall shear stress between 20G and 26G Preston tubes used either on the lower or upper walls of the test apparatus (i.e., comparison of data sets [1] through [4]); (2) the static pressure measured by a static-pressure tap or the static tube of the Preston-static tubes (i.e., comparison of data sets [5] through [8]); and (3) the measured wall shear stress among the conventional Preston tubes and our Preston-static tubes (i.e., comparison of data sets [1] through [8]). Given these results, we conclude that Preston-static tubes provide a simple, convenient, and reasonably accurate method by which to measure wall shear stress.

## Acknowledgments

The logistic and technical support of the following individuals is gratefully acknowledged: Professor H. J. Leutheusser, Miro Kalovsky, Linda Gowman, Paul Zalzal, Doug Barker of J. J. Downs Industrial Plastics, Gerrard Klaus, Cathy Cottrell, John Balkansky, and two anonymous reviewers. Louis Wong was supported by the Environmental Youth Corp Program of the Province of Ontario. This research was supported by funds from Ontario Hydro, the Ontario Ministry of Colleges and Universities through the URIF Program, the International Copper Association, and the Nickel Development Institute.

## References

Bertelrud, A., 1976, "Preston Tube Calibration Accuracy," *AIAA Journal*, Vol. 14, pp. 98–100.

Bertelrud, A., 1977, "Total Head/Static Measurements of Skin Friction and Surface Pressure," *AIAA Journal*, Vol. 15, pp. 436–438.

Gupta, R. P., 1975, "New Device for Skin-Friction Measurement in Three-Dimensional Flows," *AIAA Journal*, Vol. 13, pp. 236–238.

Hirt, F., and Thomann, H., 1986, "Measurement of Wall Shear Stress in Turbulent Boundary Layers Subject to Strong Pressure Gradients," *Journal of Fluid Mechanics*, Vol. 171, pp. 547–562.

Hollingshead, A. B., and Rajaratnam, N., 1980, "A Calibration Chart for the Preston Tube," *Journal of Hydraulic Research*, Vol. 18, pp. 313–326.

McAllister, J. E., Pierce, F. J., and Tennant, M. H., 1982, "Preston Tube Calibration and Direct Force Floating Element Measurement in a Two-Dimensional Turbulent Boundary Layer," *Journal of Fluid Mechanics*, Vol. 104, pp. 156–161.

Nitsche, W., Thünker, R., and Haberland, C., 1985, "A Computational Preston Tube Method," *Turbulent Shear Flows*, Springer-Verlag, Berlin, pp. 261–276.

Patel, V. C., 1965, "Calibration of the Preston Tube and Limitations on its Use in Pressure Gradients," *Journal of Fluid Mechanics*, Vol. 23, pp. 185–208.

Preston, J. H., 1954, "The Determination of Turbulent Skin Friction by Means of Pitot Tubes," *Journal of the Royal Aeronautical Society*, Vol. 58, pp. 109–121.

Rao, G. N. V., Kedravan, N. R., and Mahadevan, R., 1970, "Estimation of Turbulent Boundary Layer Skin Friction by Means of a Dual Pitot Tube," *Journal of the Aeronautical Society of India*, Vol. 22, pp. 269–271.

Savill, A. M., 1989, "The Effect of an Adverse Pressure Gradient on the Drag Reduction Performance of Manipulators," *International Journal of Heat and Fluid Flow*, Vol. 10, pp. 118–124.

Taheri, M., and Bragg, G. M., 1992, "A Study of Particle Resuspension in a Turbulent Flow Using a Preston Tube," *Aerosol Science and Technology*, Vol. 16, pp. 15–20.

Winter, K. G., 1977, "An Outline of the Techniques Available for the Measurement of Skin Friction in Turbulent Boundary Layers," *Progress in Aerospace Sciences*, Vol. 18, pp. 1–57.

# Mechanisms and Directivity of Unsteady Transonic Flow Noise

**A. S. Lyrintzis,[1] J. Lee,[2] and Y. Xue[3]**

## Introduction

In this paper, we report a study of the noise due to unsteady transonic flow around an airfoil. The resulting unsteady shock waves on a blade create shock-related noise that can be studied computationally. We will examine the noise generated by blade-vortex interaction (BVI), an oscillating flap, and a thickening-thinning airfoil (Fig. 1). BVI is the aerodynamic interaction of a rotor blade with the trailing vortex system generated by preceding blades. It usually occurs during helicopter descent, or low speed maneuvers. Interactions generate the most significant noise when the vortex is exactly or nearly parallel to the blade. The flow can be initially modeled by two-dimensional unsteady transonic flow, since BVI is concentrated near the tips and the relative velocity can be assumed constant in this region. An oscillating flap is a typical configuration that is widely employed in the experimental and computational studies of unsteady transonic flow. Tijdeman (1977) used an oscillating flap to experimentally identify three types of unsteady shock motion. The thickening-thinning airfoil is another example used, because for symmetric airfoils, no noise signal is generated due to lift.

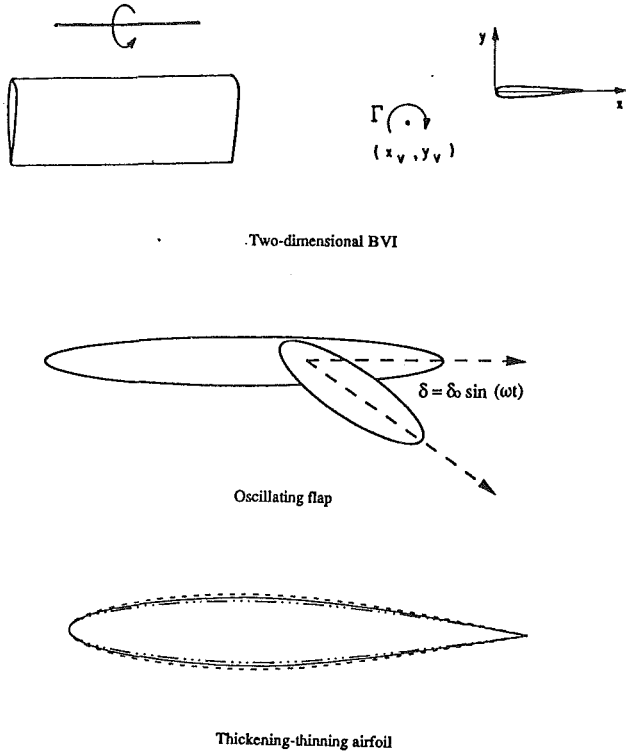


**Fig. 1 Geometry of two-dimensional BVI, oscillating flap, thickening-thinning airfoil**

Unsteady transonic flow problems have been solved numerically in the past. The low frequency approximation of the unsteady two-dimensional Transonic Small Disturbance (TSD) equation was first solved by Ballhaus and Goorjian (1977) and the LTRAN2 code was created. Since then the code has been enhanced and updated. However, the acoustic waves resulting from the unsteady motion have not been adequately studied. Two-dimensional transonic BVI was first studied computationally in the near- and mid-field by George and Chang (1984) who used the high frequency transonic small disturbance equation, including regions of convected vorticity. A comprehensive code, VTRAN2 was developed (George and Lyrintzis, 1988). The code is simple and efficient. In addition, it is able to obtain the main characteristics of transonic BVI, which are the shock motions around airfoils. The code was modified (Lyrintzis and Xue 1991) to include monotone switches (Goorjian et al., 1985) and viscous shock/boundary layer interactions (Guruswamy and Goorjian, 1984). The code was shown to agree well with other, more complex approaches including Euler and thin-layer Navier-Stokes computations.

In the past, both a full-flow-field solution and the acoustic

[1]Associate Professor, School of Aeronautics and Astronautics, Purdue University, West Lafayette, IN 47907-1282. Mem. ASME.

[2]Graduate Research Assistant, Department of Mechanical Engineering, Aeronautical Engineering and Mechanics, Rensselaer Polytechnic Institute, Troy, NY 12180-3590.

[3]Aerospace Engineer, ART Inc., 1685 Plymouth St., Mountain View, CA 94043.

All authors were formerly at Aerospace Engineering and Mechanics, University of Minnesota, Minneapolis, MN 55455-0153.

Contributed by the Fluids Engineering Division of THE AMERICAN SOCIETY OF MECHANICAL ENGINEERS. Manuscript received by the Fluids Engineering Division June 30, 1993; revised manuscript received March 7, 1994. Associate Technical Editor: R. K. Agarwal.

## Acknowledgments

The logistic and technical support of the following individuals is gratefully acknowledged: Professor H. J. Leutheusser, Miro Kalovsky, Linda Gowman, Paul Zalzal, Doug Barker of J. J. Downs Industrial Plastics, Gerrard Klaus, Cathy Cottrell, John Balkansky, and two anonymous reviewers. Louis Wong was supported by the Environmental Youth Corp Program of the Province of Ontario. This research was supported by funds from Ontario Hydro, the Ontario Ministry of Colleges and Universities through the URIF Program, the International Copper Association, and the Nickel Development Institute.

## References

Bertelrud, A., 1976, "Preston Tube Calibration Accuracy," *AIAA Journal*, Vol. 14, pp. 98–100.

Bertelrud, A., 1977, "Total Head/Static Measurements of Skin Friction and Surface Pressure," *AIAA Journal*, Vol. 15, pp. 436–438.

Gupta, R. P., 1975, "New Device for Skin-Friction Measurement in Three-Dimensional Flows," *AIAA Journal*, Vol. 13, pp. 236–238.

Hirt, F., and Thomann, H., 1986, "Measurement of Wall Shear Stress in Turbulent Boundary Layers Subject to Strong Pressure Gradients," *Journal of Fluid Mechanics*, Vol. 171, pp. 547–562.

Hollingshead, A. B., and Rajaratnam, N., 1980, "A Calibration Chart for the Preston Tube," *Journal of Hydraulic Research*, Vol. 18, pp. 313–326.

McAllister, J. E., Pierce, F. J., and Tennant, M. H., 1982, "Preston Tube Calibration and Direct Force Floating Element Measurement in a Two-Dimensional Turbulent Boundary Layer," *Journal of Fluid Mechanics*, Vol. 104, pp. 156–161.

Nitsche, W., Thünker, R., and Haberland, C., 1985, "A Computational Preston Tube Method," *Turbulent Shear Flows*, Springer-Verlag, Berlin, pp. 261–276.

Patel, V. C., 1965, "Calibration of the Preston Tube and Limitations on its Use in Pressure Gradients," *Journal of Fluid Mechanics*, Vol. 23, pp. 185–208.

Preston, J. H., 1954, "The Determination of Turbulent Skin Friction by Means of Pitot Tubes," *Journal of the Royal Aeronautical Society*, Vol. 58, pp. 109–121.

Rao, G. N. V., Kedravan, N. R., and Mahadevan, R., 1970, "Estimation of Turbulent Boundary Layer Skin Friction by Means of a Dual Pitot Tube," *Journal of the Aeronautical Society of India*, Vol. 22, pp. 269–271.

Savill, A. M., 1989, "The Effect of an Adverse Pressure Gradient on the Drag Reduction Performance of Manipulators," *International Journal of Heat and Fluid Flow*, Vol. 10, pp. 118–124.

Taheri, M., and Bragg, G. M., 1992, "A Study of Particle Resuspension in a Turbulent Flow Using a Preston Tube," *Aerosol Science and Technology*, Vol. 16, pp. 15–20.

Winter, K. G., 1977, "An Outline of the Techniques Available for the Measurement of Skin Friction in Turbulent Boundary Layers," *Progress in Aerospace Sciences*, Vol. 18, pp. 1–57.

# Mechanisms and Directivity of Unsteady Transonic Flow Noise

**A. S. Lyrintzis,[1] J. Lee,[2] and Y. Xue[3]**

## Introduction

In this paper, we report a study of the noise due to unsteady transonic flow around an airfoil. The resulting unsteady shock waves on a blade create shock-related noise that can be studied computationally. We will examine the noise generated by blade-vortex interaction (BVI), an oscillating flap, and a thickening-thinning airfoil (Fig. 1). BVI is the aerodynamic interaction of a rotor blade with the trailing vortex system generated by preceding blades. It usually occurs during helicopter descent, or low speed maneuvers. Interactions generate the most significant noise when the vortex is exactly or nearly parallel to the blade. The flow can be initially modeled by two-dimensional unsteady transonic flow, since BVI is concentrated near the tips and the relative velocity can be assumed constant in this region. An oscillating flap is a typical configuration that is widely employed in the experimental and computational studies of unsteady transonic flow. Tijdeman (1977) used an oscillating flap to experimentally identify three types of unsteady shock motion. The thickening-thinning airfoil is another example used, because for symmetric airfoils, no noise signal is generated due to lift.

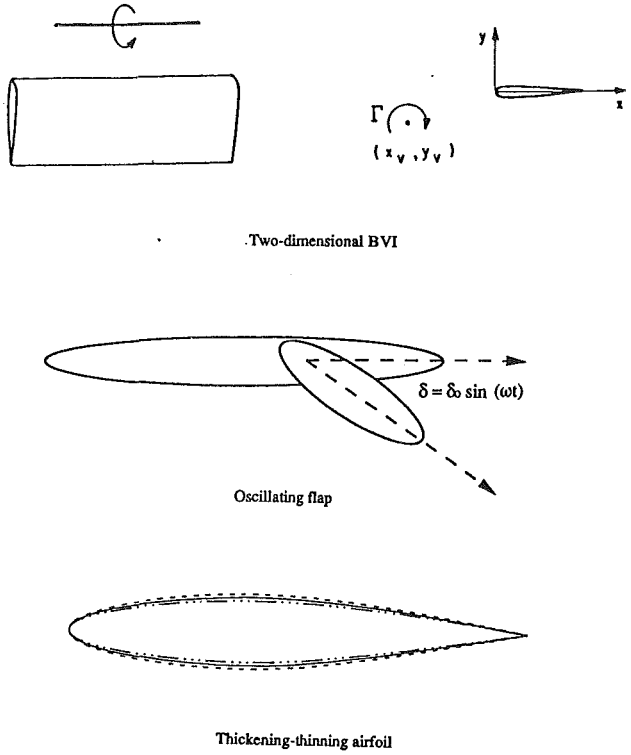


**Fig. 1 Geometry of two-dimensional BVI, oscillating flap, thickening-thinning airfoil**

Unsteady transonic flow problems have been solved numerically in the past. The low frequency approximation of the unsteady two-dimensional Transonic Small Disturbance (TSD) equation was first solved by Ballhaus and Goorjian (1977) and the LTRAN2 code was created. Since then the code has been enhanced and updated. However, the acoustic waves resulting from the unsteady motion have not been adequately studied. Two-dimensional transonic BVI was first studied computationally in the near- and mid-field by George and Chang (1984) who used the high frequency transonic small disturbance equation, including regions of convected vorticity. A comprehensive code, VTRAN2 was developed (George and Lyrintzis, 1988). The code is simple and efficient. In addition, it is able to obtain the main characteristics of transonic BVI, which are the shock motions around airfoils. The code was modified (Lyrintzis and Xue 1991) to include monotone switches (Goorjian et al., 1985) and viscous shock/boundary layer interactions (Guruswamy and Goorjian, 1984). The code was shown to agree well with other, more complex approaches including Euler and thin-layer Navier-Stokes computations.

In the past, both a full-flow-field solution and the acoustic

[1]Associate Professor, School of Aeronautics and Astronautics, Purdue University, West Lafayette, IN 47907-1282. Mem. ASME.

[2]Graduate Research Assistant, Department of Mechanical Engineering, Aeronautical Engineering and Mechanics, Rensselaer Polytechnic Institute, Troy, NY 12180-3590.

[3]Aerospace Engineer, ART Inc., 1685 Plymouth St., Mountain View, CA 94043.

All authors were formerly at Aerospace Engineering and Mechanics, University of Minnesota, Minneapolis, MN 55455-0153.

Contributed by the Fluids Engineering Division of THE AMERICAN SOCIETY OF MECHANICAL ENGINEERS. Manuscript received by the Fluids Engineering Division June 30, 1993; revised manuscript received March 7, 1994. Associate Technical Editor: R. K. Agarwal.

analogy have been used in rotorcraft acoustics. However, a full flow field solution is very expensive, whereas the acoustic analogy has a great difficulty including moving shock waves. Recently, we introduced an innovative approach, i.e., the Kirchhoff method (George and Lyrintzis, 1988 and Lyrintzis and George, 1989), to extend numerically calculated aerodynamic results to the acoustic far-field. The full nonlinear equations are solved in the near-field, usually numerically, and a surface integral of the solution over the control surface gives enough information for the analytical calculation in the far-field. The advantage of the method is that non linear effects (e.g., shock waves) are accounted for. Also, the surface integrals and the first derivatives needed can be easily evaluated from the near-field CFD data. A recent review of the uses of Kirchhoff's method in aeroacoustics is given by Lyrintzis, (1993).

In this paper we will compare the mechanisms and directivity for three unsteady flow cases (i.e., BVI, oscillating flap and thickening-thinning airfoil). It is the first time that various unsteady transonic flow cases are studied together. The reader is also referred in Lyrintzis et al. (1992) which is a more detailed version of this work. While our emphasis is on understanding the physics of unsteady transonic flow noise, it is also expected that the study will lead to ideas for noise reduction. One earlier example based on transonic BVI studies is given by Xue and Lyrintzis (1993).

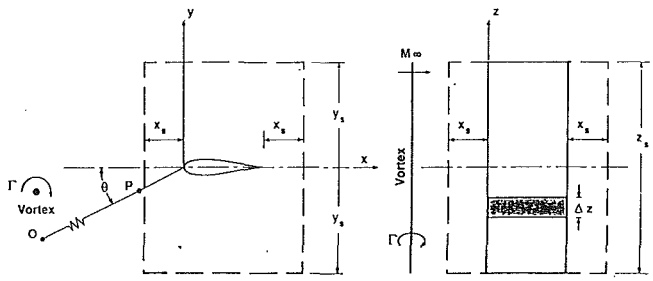


Fig. 2 Kirchhoff's surface for the calculation of the far-field

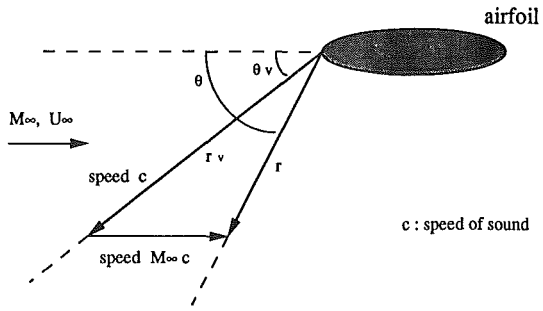


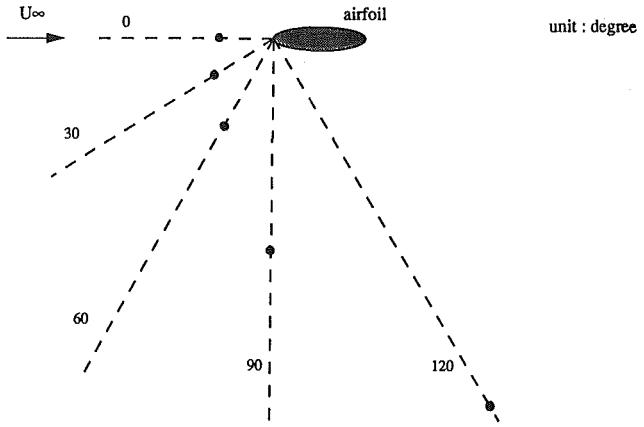


Fig. 3 Propagation speeds for an airfoil-fixed coordinate system

## Results and Discussion

A (229 × 199) mesh is used for the current calculations. The computational mesh points are clustered more densely near and in front of the airfoil and are stretched exponentially from the near airfoil region to about 200 chords from the airfoil in the $x$- and 400 in the $y$-direction. ($x$ and $y$ directions are shown in Fig. 1.) More mesh points are distributed in the $x$-direction in front of the airfoil for a more accurate evaluation of the resulting waves. The code has a high vectorization level and the CPU time for each two-dimensional case on a Cray-2 computer is about 5 minutes for 800 time-marching steps.

Since Kirchhoff's method assumes that linear equations hold outside the control surface $S$, it must be chosen large enough to include the region of nonlinear behavior. However, due to increasing mesh spacing the accuracy of the numerical solution is limited to the region immediately surrounding the moving blade. As a result $S$ cannot be so large as to lose accuracy in the numerical solution for the mid-field. Therefore, a judicious choice of $S$ is required for the effectiveness of the Kirchhoff method. A rectangular box shaped surface (Fig. 2) is used for the calculations. The VTRAN2 code is used to calculate the solutions on the surface $S$. Typical sizes for the Kirchhoff surface are $x_s = 0.25$ and $y_s$ around 2 chords. An optimization study is usually done. Higher Mach numbers yield higher optimum values for $y_s$ (see Lee, 1992) because of the stronger nonlinearities in the larger lateral extent of the flow region, as expected from the scaling laws of transonic flow. A strip theory approximation is used, that is, the two-dimensional VTRAN2 solution is applied on different segments of the blade in a stripwise manner. Blade segments with aspect ratio 4 are used.

Directivity is studied here in an airfoil-fixed coordinate system. The waves travel different distances in different directions (Fig. 3) for a given time. The total velocity is the vector sum of the speed of sound (at some direction) with the free stream. Thus the resulting velocity varies with the direction, and distance $r_v$ is kept constant ($r_v = 50$ chords) in different directions (Fig. 3). The relationship between the angles $\theta$ and $\theta_v$ is also shown in Fig. 3. The observer is fixed with the airfoil.

Tijdeman (1977) showed experimentally, using an oscillating flap, that varying airfoil flow conditions can give three different types of unsteady shock motion:

Type A shock motion, where the shock at the rear of the supersonic region merely moves back and forth with concurrent changes in strength.

Type B shock motion, where the shock moves similarly to type A, but disappears temporarily during the unsteady motion.

Type C shock motion, where the supersonic region disappears, but a shock wave leaves the airfoil and propagates forward to the far-field.

In following only results for the more interesting type C case will be shown due to space limitations.

(*a*) **BVI Results.** BVI directivity is studied here in an airfoil-fixed coordinate system. The unsteadyness is due to the vortex passage. The waves travel different distances in different directions for a given time. The total velocity is the vector sum of the speed of sound (at some direction) with the free stream. Thus the resulting velocity varies with the direction, and distance $r_v$ ($r_v$ is the distance in the vortex coordinate system) is kept constant ($r_v = 50$ chords) in different directions. The observer is fixed with the airfoil. The $C_p(t)$ signal for different

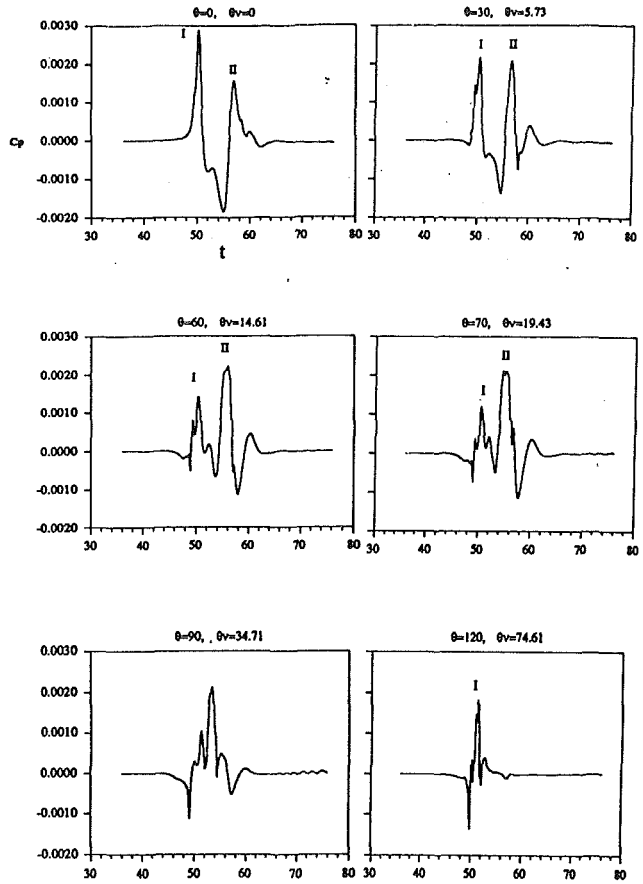


Fig. 4 BVI noise directivity for type C; $r_v$ = 50 chords

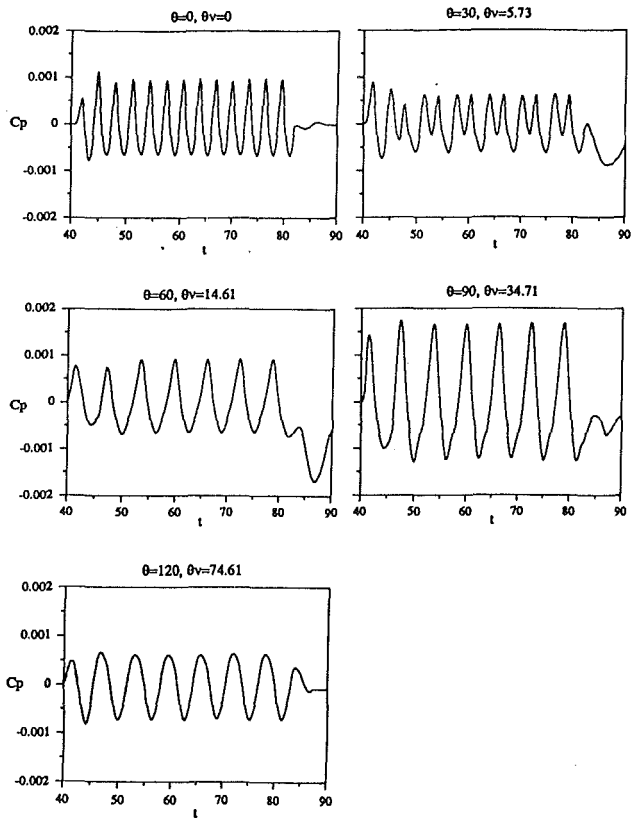


Fig. 5 Oscillating flap noise directivity for type C; $r_v$ = 50 chords

directions is plotted in Fig. 4 for a type C shock motion. Both linear (dipole, e.g., lift coefficient $C_l$, drag coefficient $C_d$) and nonlinear (quadrupole or higher order poles, e.g., shock waves) noise sources are present in this case. The unsteady pressure coefficients $C_p(t)$ shows the existence of two main disturbances in the transonic case for BVI. The first disturbance (I) is believed to be associated with the fluctuating lift coefficient ($C_l$) and the shock strength variations. Disturbance (I) has a forward directivity. The second disturbance (II) is believed to be associated with the movement of the shock wave generated at a later time (i.e., when the vortex is 6–8 chordlengths behind the airfoil) and has a strong downward directivity. Disturbance I can be reduced by weakening the shock formation on the airfoil, and disturbance II can be reduced by stabilizing the shock wave motion on the airfoil. The resulting BVI noise depends heavily on the various BVI parameters i.e., Mach number, vortex strength and miss-distance, airfoil shape. Some ideas for noise reduction can also be developed. For example, the airfoil shape near the leading edge can be modified to create a more stable shock that will reduce the resulting noise. More details for noise reduction can be found in Xue and Lyrintzis (1993).

**(*b*) Oscillating Flap Results.** We use a NACA 64A006 airfoil at Mach number 0.822 which correspond to type C shock wave motion. The flap has a length of 25 percent of the chord (starts at $x/c = 0.75$), the reduced frequency $k$ ($k = c\omega/U_\infty$) of the motion is 0.496 and the amplitude of the flap motion $\delta_0$ is 1.5 deg. These $k$ and $\delta_0$ values correspond to cases reported by Ballhaus and Goorjian (1977).

The $C_l$ variations for the three types of shock motion and the subcritical case yield one disturbance per period (results not shown herein). The inviscid dependence of $C_d$ was also calculated. The frequency is twice the frequency of the oscillation, (i.e., two disturbances per period) because an airfoil's up or down motion has the same effect on $C_d$, (but an opposite effect on $C_l$). Figure 5 shows the $C_p(t)$ signal in different directions for type C for the oscillating flap case in the far-field. We can see that in every cycle there are two main propagating disturbances (I, II) for the transonic cases. The existence of the second disturbance in the mid-field was first detected in the oscillating flap case by Lyrintzis and Xue (1992). The nature of the two disturbances can be explained using the same arguments we have used before for BVI. The first disturbance (I) relates well to the $C_l$ oscillations shown in Fig. 5, whereas there is no disturbance (II) in the $C_l$ signal. The directivity of the noise signal is examined in Fig. 5. By analyzing the plots, we can see that the first disturbance (I) is getting stronger as the direction angle increases from 0 to 90 deg. For the transonic cases the effect of the nonlinear noise in the first disturbance is weaker than the BVI case. In the oscillating flap case the first disturbance remains higher in the downward direction, whereas in the BVI case the nonlinear shock noise dominates the directivity of disturbance I. The second disturbance (II) seems to have a strong forward directivity, as expected.

A parametric study shows that the disturbance amplitude decreases as the reduced frequency $k$ increases. Also an increase in the amplitude of the flap motion increases the resulting disturbance with the results being very sensitive to small changes in the amplitude of the oscillation angle. We also studied the effect of an abrupt step change in the angle $\delta$ of the oscillating flap for the type C case. The resulting time derivatives of $C_l$ for this case are higher compared to the sinusoidal oscillating flap case. Thus the resulting noise level is much higher and the signal has a larger high frequency content.

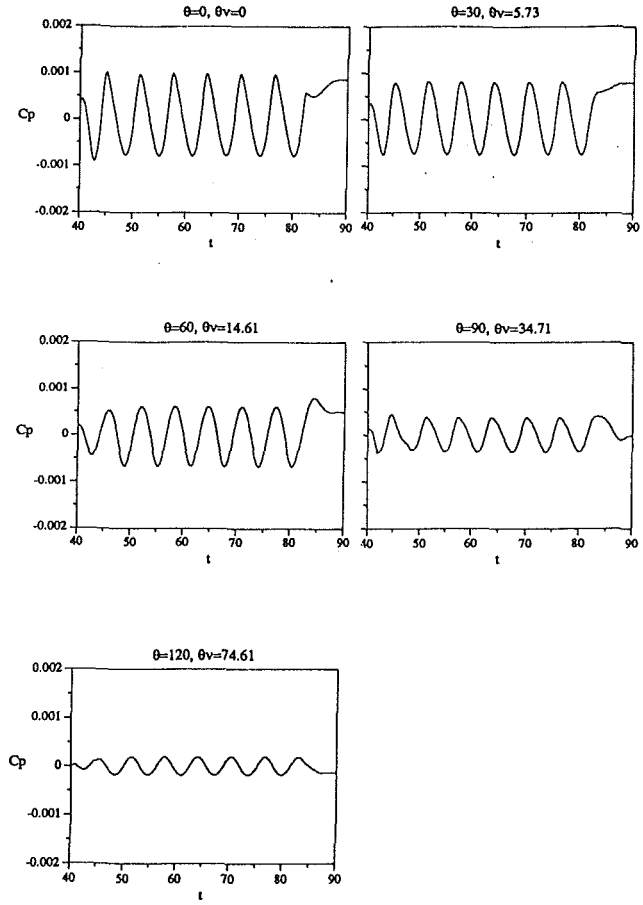


Fig. 6 Thickening-thinning airfoil noise directivity for type C; $r_v$ = 50 chords

(*c*) **Thickening-Thinning Airfoil.** The last case we examined is the thickening-thinning airfoil. The reason this case was chosen is because no lift is generated for a symmetric airfoil at zero angle of attack. We again use a NACA 64A006 airfoil at Mach number 0.833 which corresponds to shock wave motion of type C. The reduced frequency $k$ of the motion is the same as in the oscillating flap case. The total thickness variation is 10 percent (+5 percent for thickening, −5 percent for thinning). The thickening and thinning process is enforced by changing sinusoidally the slope of the airfoil surface.

The $C_d(t)$ signal for this case shows one peak per period of motion, whereas in the oscillating flap case we found two. The corresponding signal directivity for type C motion is shown in Fig. 6. It should be noted that the effect of monopole sources should be taken into account for this case. In all cases we only have one disturbance per cycle that has a forward directivity. Even in transonic cases only one disturbance is observed, whereas two disturbances are found in BVI and the oscillating flap cases. Finally, a parametric study showed that a higher $k$ leads to higher noise signal in this case.

## Concluding Remarks

The mechanisms and directivity of two-dimensional unsteady transonic flow noise have been investigated. Three cases were studied: Blade-Vortex interaction (BVI), an oscillating flap and a thickening-thinning airfoil. An existing numerical finite difference code VTRAN2 was used. The two-dimensional unsteady transonic small disturbance equation was solved numerically using ADI techniques with monotone switches, including viscous effects due to shock-boundary interactions and the cloud-in-cell method for the simulation of the vortex. The Kirchhoff method was used to extend the numerically calculated two-dimensional near-field aerodynamic results to the three-dimensional linear acoustic far-field.

The unsteady pressure coefficients $C_p(t)$ showed the existence of two main disturbances in the transonic case for BVI and an oscillating flap. The first disturbance (I) is believed to be associated with the fluctuating lift coefficient ($C_l$) and the shock strength variations. Depending on the effect of the nonlinear content disturbance (I) can have a forward (BVI) or a downward directivity (oscillating flap). The second disturbance (II) is believed to be associated with the movement of the shock wave generated at a later time (e.g., in BVI when the vortex is 6–8 chordlengths behind the airfoil) and has a strong downward directivity. For BVI, the maximum radiation occurs at an angle $\theta$ between 60 and 90 deg below the horizonal for an airfoil-fixed coordinate system and depends on both disturbances I and II. In the case of a thickening-thinning airfoil there is no $C_l$ signal and only one disturbance is detected. We believe that the above results contribute to the development of a unified theory of unsteady transonic flow noise and could eventually lead to effective noise reduction techniques.

## Acknowledgments

The calculations were performed at the computational facilities of Minnesota Supercomputer Insititute (MSI). This research was supported by a Grant-in-aid of Research from the Graduate School of University of Minnesota.

## References

Ballhaus, W. F., and Goorjian, P. M., 1977, "Implicit Finite-Difference Computations of Unsteady Transonic Flows about Airfoil," *AIAA Journal*, Vol. 15, No. 12, pp. 1728–1735.

George, A. R., and Chang, S. B., 1984, "Flow Field and Acoustics of Two-dimensional Transonic Blade-Vortex Interactions," AIAA Paper 84-2309, AIAA 9th Aeroacoustics Conference, Williamsburg, VA, Oct. 15–17.

George, A. R., and Lyrintzis, A. S., 1988, "Acoustics of Transonic Blade-Vortex Interactions," *AIAA Journal*, Vol. 26, No. 7, pp. 769–776.

Goorjian, P. M., Meagher, M. E., and Van Buskirk, R. D., 1985, "Monotone Switches in Implicit Algorithms for Potential Equations Applied to Transonic Flows," *AIAA Journal*, Vol. 23, No. 4, pp. 492–498.

Guruswamy, P., and Goorjian, P. M., 1984, "Effects of Viscosity on Transonic Aerodynamic and Aeroelastic Characteristics of Oscillating Airfoils," *AIAA Journal*, Vol. 21, No. 9, pp. 700–707.

Lee, J., 1992, "Acoustics of Unsteady Transonic Flow," Master of Science Thesis, Aerospace Engineering and Mechanics, University of Minnesota, Minneapolis, MN.

Lyrintzis, A. S., and George, A. R., 1989, "Far-Field Noise of Transonic Blade-Vortex Interactions," *American Helicopter Society Journal*, Vol. 34, No. 3, pp. 30–39.

Lyrintzis, A. S., and Xue, Y., 1991, "A Study of the Noise Mechanisms of Transonic Blade-Vortex Interactions," *AIAA Journal*, Vol. 29, No. 10, pp. 1562–1572.

Lyrintzis, A. S., Lee, J., and Xue, Y., 1992, "Mechanisms and Directivity of Unsteady Transonic Flow Noise," presented at the International Symposium on Flow Induced Vibration and Noise III, Vol. 3: *Flow-Structure and Flow-Sound Interactions*, Farabee, T. M., Paidoussis, M. P., eds., ASME Winter Annual Meeting, Anaheim, CA, Nov., pp. 85–113.

Lyrintzis, A. S., and Xue, Y., 1992, "Acoustics of Transonic Flow Around an Oscillating Flap," ASME JOURNAL OF FLUIDS ENGINEERING, Vol. 114, No. 2, June, pp. 240–245.

Lyrintzis, A. S., 1993, "The Use of Kirchhoff's Method in Computational Aeroacoustics," *Computational Aero- and Hydro-Acoustics*, FED Vol. 147, Mankbadi, R., R., Lyrintzis, A. S., Baysal, O., Povinelli, L. A, and Hussaini, M. Y., eds., ASME Fluids Engineering Conference, Washington, DC, June, pp. 53–61; also ASME JOURNAL OF FLUIDS ENGINEERING (in press).

Tijdeman, H., 1977, "Investigations of the Transonic Flow Around Oscillating Airfoils," NLR TR 77090-U, NLR The Netherlands.

Xue, Y., and Lyrintzis, A. S., 1993, "Transonic Blade-Vortex Interactions: Noise Reduction Techniques," *AIAA Journal of Aircraft*, Vol. 30, No. 3, May-June, pp. 408–411.

# The Effects of Weak Interaction and Reynolds Number on Boundary Layer Scalars With Tandem Turbulent Spots

**M. H. Krane[1] and W. R. Pauley[2]**

## Introduction

The dynamics of the intermittent portion of a boundary layer transition region are determined by the formation, convection, and merging of individual turbulent spots (Schubauer and Klebanoff, 1955). As these localized regions of turbulence convect downstream, they grow by destabilizing the surrounding laminar boundary layer (Gad-el-Hak et al., 1981), causing it to become turbulent at the edges of each spot. The spots grow and merge to form a fully turbulent boundary layer. Many studies have documented the space-time development of single, isolated turbulent spots (Schubauer and Klebanoff, 1955; Wygnanski et al., 1976; Antonia et al., 1981; Wygnanski et al., 1982). It is expected, however, that turbulent spots in a natural transition zone will be influenced by spot interaction and merging. The characteristics of this interaction may dictate the dynamics of the transition region. Elder (1960) found that a side-by-side pair of turbulent spots merged without detectable change to either's growth. Wygnanski (1981) studied turbulent spots generated periodically along a wind tunnel centerline with different spacings and found that sufficiently close spacing produced velocity profiles similar to a fully-turbulent boundary layer. Gutmark and Blackwelder (1987) showed that the turbulence level and the convection velocity of a closely following trailing spot of a tandem pair was attenuated by interaction. The growth of the trailing spot was reduced by the highly stable "calmed region" behind the leading spot. Zilberman et al. (1977) and Wygnanski (1981) demonstrated that key features of spots are quite persistent, showing that portions of the spot structure furthest from the wall retain their identity for a considerable length of time even after the spot has merged with a fully turbulent boundary layer.

Lauchle (1981) applied knowledge of the scalar descriptors of intermittence in the transition region to predict the radiated sound in terms of the time and length scales of the unsteady displacement thickness. Krane and Pauley (1992a) quantified the temporal and spatial scales of the unsteady displacement thickness for a single turbulent spot and used them to determine the level and character of sound produced. It was shown that the large positive and negative peaks in displacement thickness during passage of the spot can result in significant noise production. The behavior of these peaks can be described in terms of scalars such as their convection speeds and their rise and fall times. Wygnanski (1981) showed that a typical transition region exhibits characteristics of weak rather than strong interaction. To reliably extend the predictions based on the isolated spot to a natural transition, therefore, it is necessary to know if the spot descriptors are modified significantly by weak spot interaction. Further, it was desired to assess the universality of the findings by investigating the influence of Reynolds number on the spot descriptors.

Based on the results of Elder (1960), Wygnanski (1981), and Gutmark and Blackwelder (1987) it appears that tandem rather than side-by-side interaction produces the strongest modification to the spots. Therefore, a tandem pair of turbulent spots generated by two small bursts of a jet was investigated at several stages in its development. The time scales of the displacement thickness peaks were determined and non-dimensional characteristic times were calculated. By comparison with isolated single spot data taken under identical conditions, modifications to the descriptors due to weak interaction were determined. In addition, the Reynolds number was halved and a second isolated spot was investigated to determine if this change modified the characteristic times.

## Experimental Apparatus and Data Acquisition

Experiments were performed in the Aerospace Engineering Laminar Flow Water Channel at the Pennsylvania State University. The facility has a well-documented Blasius profile and a freestream turbulence intensity of less than 0.3 percent. Full details are available in Krane and Pauley (1992b). Unsteady velocity profiles were measured using a TSI single-component LDV system operating in forward-scatter mode. A TSI Model 1980 Counter Processor, equipped with a Model 1988 Analog-Out Module, provided a voltage time series which was proportional to the Doppler frequency of the most recently validated Doppler burst. This technique provided a random sample-and-hold representation of the velocity time series which automatically corrects for velocity biasing errors. The output was sampled at 250 Hz. All results are reported in an $x$, $y$, $z$ coordinate system, where the $x$ origin is at the test plate leading edge, $y$ at the plate surface, and $z$ on the centerline. Ensemble-averaged profiles, which were scaled on the local laminar boundary layer height $\delta_L$ between the wall and a height of $4\delta_L$, were computed from velocity time series. Fifty spot samples were taken at each location which were initiated by a weak impulsive jet issued from a 0.5 mm hole located at $x = 53$ cm. The jet pulse was generated by a computer-controlled peristaltic pump.

## Results and Discussion

A single isolated turbulent spot was first investigated to serve as a baseline in determining the effects of spot interaction and Reynolds number. The edge of the spot's region of influence or "envelope" was found using the criteria of Coles and Barker (1975). The first step was to calculate a perturbation velocity defined as $u_p(x, y, t) = (u(x, y, t) - u_L(x, y))/U_\infty$ where $u_L$ is the local laminar velocity before the arrival of the spot. These velocity time series were low-pass filtered by averaging $u_p$ at each time step with the neighboring $\pm 15$ time steps; this is a convolution of the signal with a square pulse of unit amplitude and 0.124 s duration. The leading and trailing edges of the spot were identified as the first point (moving forward or backward, respectively) where both a level and a slope criteria were met: $|u_p| > 0.02$ and $|du_p/dt| > 3.0(du_p/dt)_{\max}$ where $(du_p/dt)_{\max}$ is the maximum slope of $u_p$ in the initial, laminar portion of the time series. By rescaling the spot outline using the similarity transformations developed by Cantwell et al. (1978): $\eta = y/\delta_T$ and $\xi = x - x_0/U_\infty(t - t_0)$ where $\delta_T = 0.37(\nu/U_\infty)^{1/5}(x - 0.3933\text{m})^{4/5}$ (see Van Atta and Helland, 1980; Itsweire and Van Atta, 1983) we see in Fig. 1 that similarity is achieved for the last three stations ($x = 113$ cm, 133 cm, and 153 cm). These results agree with Schubauer and Klebanoff (1955) and Wygnanski et al. (1976).

To characterize the intermittent signature of the turbulent spot, the unsteady boundary layer displacement thickness was calculated by integrating the following expression using the trapezoid rule: $\delta^*(x, t) = \int_0^H (1 - u(x, y, t)/U_\infty)dy$. The upper integration limit $H$ was chosen to be large enough to capture

[1]Postdoctoral Fellow, Laboratoire de Mecanique des Fluides et d'Acoustique, URA CNRS 263, Ecole Centrale de Lyon, France.

[2]Assistant Professor, Department of Aerospace Engineering, The Pennsylvania State University, University Park, PA 16802. Mem. ASME.

Contributed by the Fluids Engineering Division of the THE AMERICAN SOCIETY OF MECHANICAL ENGINEERS. Manuscript received by the Fluids Engineering Division February 25, 1993; revised manuscript received October 27, 1993. Associate Technical Editor: M. Gharib.

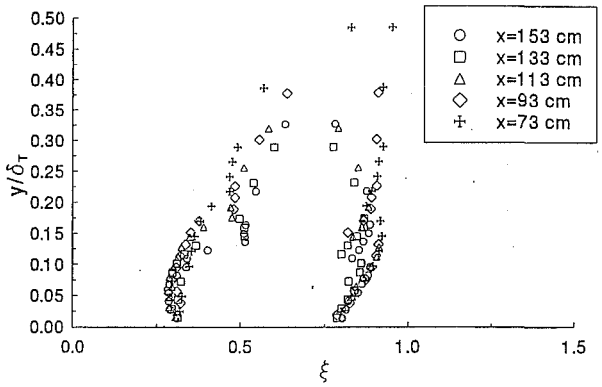


Fig. 1 Turbulent spot envelope in similarity coordinates on centerline, $U_\infty$ = 40.6 m/s

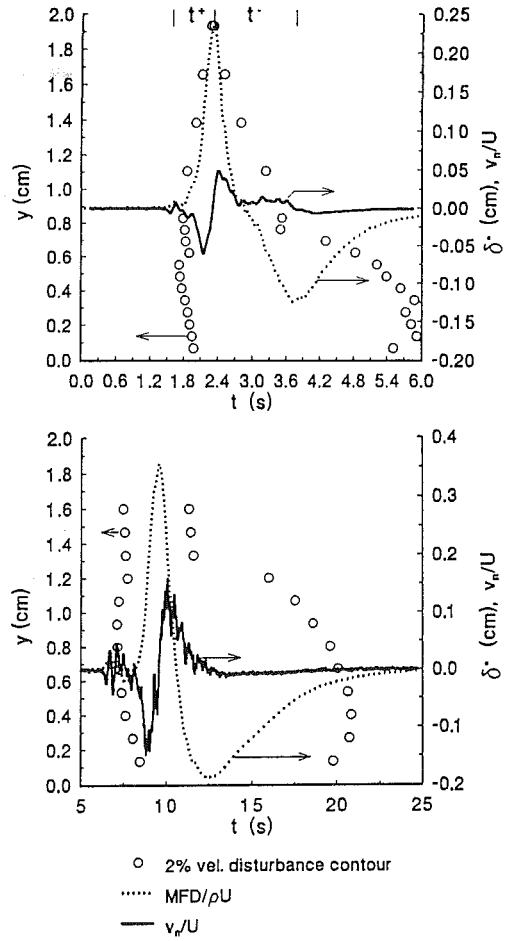


Figs. 2(*a*, *b*) Spot envelope denoted by 2 percent perturbation velocity, displacement thickness, and wall-normal velocity time series on the centerline for a single spot with (*a*) $x$ = 113 cm, $U_\infty$ = 40.6 cm/s, and (*b*) $x$ = 175 cm, $U_\infty$ = 19 cm/s

the spot envelope during its entire passage. The displacement thickness time trace, shown with its corresponding envelope in Fig. 2(*a*) is concordant with results of Wygnanski et al. (1976) and Antonia et al. (1981). The wall-normal velocity at the outer edge of the boundary layer $v_n$ (Fig. 2(*a*)), which represents the displacement effect imposed on the far field due to the spot passage, was calculated using the displacement thickness history by employing the relationship

$$\frac{v_n(x, t)}{U_\infty} = \frac{\partial}{\partial x}\delta^*(x, t) \approx -\frac{1}{U_\infty}\frac{\partial}{\partial t}\delta^*(x, t)$$

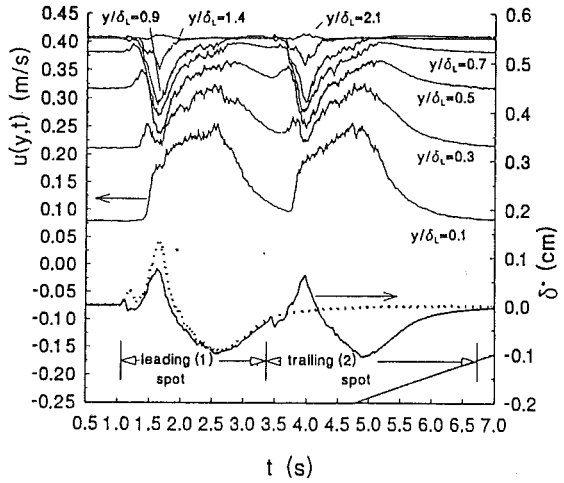


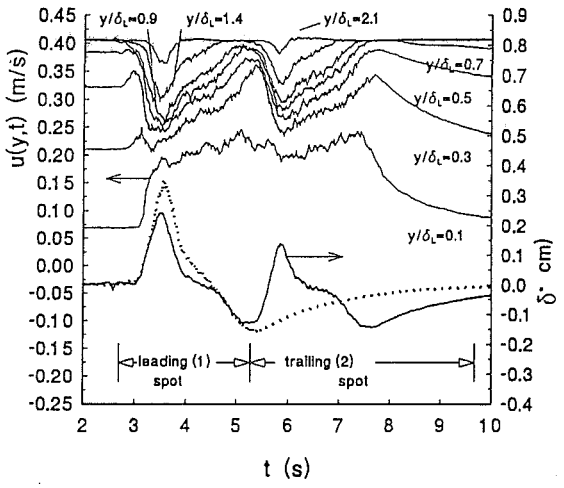


Figs. 3(*a*, *b*) Time traces of velocity at several heights above wall along with resulting displacement thickness at (*a*) $x$ = 93 cm and (*b*) $x$ = 153 cm (corresponding isolated spot profile shown for comparison)

(Van Atta et al., 1982; Lighthill, 1958). This expression is valid only on the centerline where $w$ = 0 (Wygnanski et al., 1976). Note that the spatial derivative has been replaced with a temporal derivative using Taylor's hypothesis. The displacement thickness peak corresponds to the maximum spot height; the minimum peak corresponds to the trailing edge. As the spot passes, the normal velocity undergoes a rapid, negative fluctuation followed by a positive peak, which is first sharp then more gradual. A slow return of the displacement thickness to the initial state represents the "calmed region" first identified by Schubauer and Klebanoff (1955).

To determine if the spot signature was Reynolds number dependent a second spot was measured at $x$ = 175 cm with a velocity of $U_\infty$ = 19 cm/s. Figure 2(*b*) shows the displacement thickness, the 2 percent perturbation velocity contour, and the normal velocity for this case. The overall shape of both displacement thickness and normal velocity are similar to the high velocity case. The only significant difference between the high speed case (Fig. 2(*a*)) and the low speed case (Fig. 2(*b*)), which does not scale as expected, is the sharper decay from the maximum to minimum displacement thickness. This difference is important in describing the noise generation and is reflected in the fall time of the spot discussed below.

Figures 3(*a*, *b*) show the relationship between the unsteady velocity field and the displacement thickness at $x$ = 93 cm and $x$ = 153 cm for a weakly interacting tandem spot pair. These comparisons show how the presence of the first spot affects the development of the second. At $x$ = 93 cm the two spots

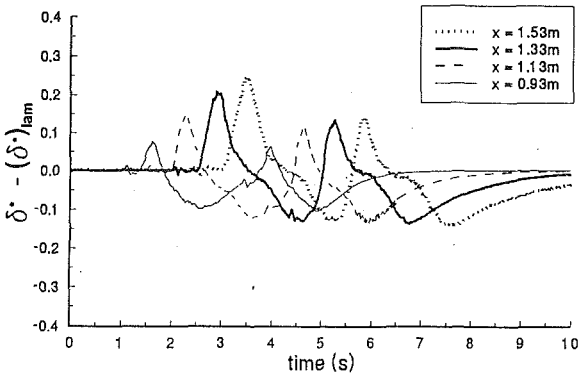


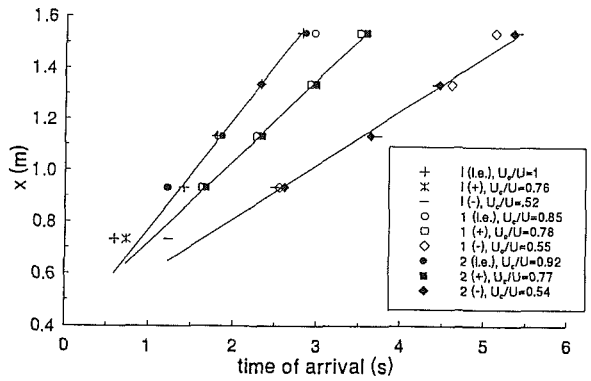


**Fig. 4(*a*, *b*) Development of interacting spot descriptors (*a*) time traces of displacement thickness for $x$ = 0.93, 1.13, 1.33, and 1.53 m and (*b*) corresponding celerity diagram showing streamwise positions of leading edge, positive peak and negative peak (Corresponding isolated spot data shown for comparison).**

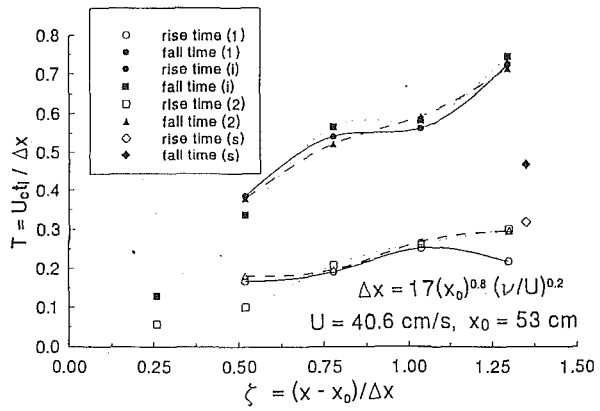


**Fig. 5 Nondimensionalized rise and fall times for interacting spot, isolated spot, and low-Reynolds-number spot**

are distinct, with the leading edge or "overhang" (Schubauer and Klebanoff, 1955) of the trailing spot just beginning to encroach on the calmed region of the leading spot. There is little distortion of the spots due to interaction. At $x$ = 153 cm the overhang of the trailing spot has vanished into the leading spot. Although the spots have partially merged at this point they still have distinct structure: the velocity minima and maxima are still clearly identifiable, as are the corresponding features of the displacement thickness, albeit with some modification in amplitude.

Figure 4(*a*) shows the streamwise evolution in the displacement thickness peaks. At the upstream stations each peak of the pair is similar to that seen for individual spots. The peaks increase with $x$ while the peaks themselves spread apart and become less steep. As the trailing spot catches the leading spot, the trailing spot's peak displacement thickness is attenuated. The second spot leading edge and first spot trailing edge meet at $x$ = 133 cm and merge by $x$ = 153 cm. Using the arrival times of key spot features, celerity diagrams were constructed (Fig. 4(*b*)). The features of the displacement thickness that were located and charted were the leading edge and the maximum and minimum peaks. The leading edge arrival was defined as the moment when the displacement thickness rose 2 percent above the undisturbed mean and the slope reached four times the mean slope found in the undisturbed time series. A linear regression was used to obtain a best-fit straight line through the data for several spot features; the slopes of these lines are the convection velocities. It was found that the convection speeds (Fig. 4(*b*)) are not significantly modified by this weak spot interaction.

The celerity diagrams were used to obtain two characteristic times that describe the spot. The rise time is the period between the leading edge and the maximum peak. The fall time is the period between the maximum and minimum peaks. The importance of a nondimensional characteristic time $T\pm = U_C t^{\pm}/\Delta x$ resulting from these measurements, to transition acoustics, was shown by Lauchle (1981). A transition zone length $\Delta x$ is predicted using the correlation of Josserand and Lauchle (1990): $\Delta x = 17 x_0^{0.8}(\nu/U_\infty)^{0.2}$. For our operating conditions $x_0$ = 53 cm (spot generator location) and the freestream velocity $U_\infty$ = 40.6 m/s, resulting in a transition zone length of $\Delta x$ = 77 cm. Figure 5 shows the nondimensional rise and fall times for the present spots, both isolated and interacting, as they develop in terms of a normalized transition zone streamwise coordinate $\zeta = (x - x_0)/\Delta x$. There is a clear monotonic increase in the magnitude for both rise and fall times. The increase of the rise/fall times is due to the growth of the streamwise extent of the spot. Little modification due to interaction was observed.

Also shown are the rise and fall times for the low-Reynolds-number case. The rise time $T^+$ is the same as for the high-Reynolds-number case while the fall time $T^-$ is considerably lower. Wygnanski et al. (1982) showed that turbulent spot growth rate is sensitive to displacement-thickness Reynolds number based on undisturbed flow displacement thickness at the spot generator location, $\mathrm{Re}_{\delta^*_{gen}}$. For the two cases reported here $\mathrm{Re}_{\delta^*_{gen}}$ was equal to 537 and 797 for $U_\infty$ = 0.19 m/s and $U_\infty$ = 0.41 m/s, respectively. The ratio of trailing edge convection speed to the freestream speed decreased with an increase in $\mathrm{Re}_{\delta^*_{gen}}$. However, the nondimensional convection velocities for the leading edge and spot maximum heights were found to be insensitive to Reynolds numbers. The spot leading edge and maximum height correspond to the leading edge and positive maximum of the displacement thickness, while the spot trailing edge corresponds to the negative displacement thickness peak. Since the rise and fall times are calculated using the convection speeds of these features of the displacement thickness, the nondimensional rise time should be insensitive to $\mathrm{Re}_{\delta^*_{gen}}$ while the nondimensional fall time should decrease with increasing $\mathrm{Re}_{\delta^*_{gen}}$ which is in agreement with the observations presented here.

Gutmark and Blackwelder (1987) showed that below a nondimensional time delay of $T_d$ = 0.65 between the trailing and leading spot generation, the leading edge convection speed of the trailing spot is modified. For the present study $T_d > 0.90$, greater than their critical value. (It should be noted that direct comparison may not be completely valid because of the differences in $\mathrm{Re}_{\delta^*_{gen}}$ between the two studies, 547 for their study and 797 for the present work.) It is clear from Fig. 15 of Gutmark and Blackwelder (1987) that the trailing spot grows in the calmed region of the leading spot for some time without any change in its leading edge celerity. When $\Delta t_d$ is greater than the critical value, as in this study, the trailing spot begins its development outside the calmed region of the leading spot, although the leading edge of the second spot eventually overtakes the calmed region; the celerity of the trailing spot is

modified when formed in the calmed region of another spot but not by entering that region some time after initial formation.

## Conclusions

A comparison was performed between a single turbulent spot, two weakly interacting spots in tandem, and a turbulent spot at one-half the Reynolds number. Key features of both turbulent spots remain individually identifiable during interaction but the leading edge (overhang) of the trailing spot is modified due to merging with the trailing (calmed) region of the leading spot. The initial acceleration in the overhang of the trailing spot disappears once it encroaches significantly on the calmed region of the leading spot. A positive peak in the displacement thickness is still readily identifiable in the trailing spot but its amplitude is diminished. No reduction in amplitude is observed for the negative displacement thickness peak in the trailing spot. This interaction produces no modification to the convection velocities (celerities) of the primary spot features or to characteristic rise and fall times for either spot. This is in spite of the fact that the trailing spot traverses the entire length of the calmed region of the leading spot. Gutmark and Blackwelder (1987) have previously reported modifications for more strongly interacting cases. Comparison with the present results indicates that the trailing spot must form while in the calmed region of the leading spot, not just pass through it, if modification of the celerities is to result. This conforms to a critical non-dimensional delay time advanced by Gutmark and Blackwelder above which trailing spot celerities are not modified. The present data reveal that the non-dimensional rise time is independent of Reynolds number while the nondimensional fall time is proportional, results consistent with Wygnanski et al. (1982).

## Acknowledgments

We gratefully acknowledge the support of the Office of Naval Research Code 1125 OA.

## References

Antonia, R. A., Chambers, A. J., Sokolov, M., and Van Atta, C. W., 1981, "Simultaneous Temperature and Velocity Measurements in the Plane of Symmetry of a Turbulent Spot," *Journal of Fluid Mechanics*, Vol. 108, pp. 317–343.

Cantwell, B., Coles, D., and Dimotakis, P., 1978, "Structure and Entrainment in the Plane of Symmetry of a Turbulent Spot," *Journal of Fluid Mechanics*, Vol. 87, p. 641.

Coles, D., and Barker, S. J., 1975, "Some Remarks on Synthetic Turbulent Boundary Layers," in *Turbulent Mixing in Nonreacting and Reacting Flows*, S. N. B. Murthy, ed., Plenum Press, pp. 285–293.

Elder, J. W., 1962, "An Experimental Investigation of Turbulent Spots and Breakdown to Turbulence," *Journal of Fluid Mechanics*, Vol. 9, pp. 235–246.

Gad-el-Hak, M., Blackwelder, R. R., and Riley, J. J., 1981, "On the Growth of Turbulent Regions in Laminar Boundary Layers," *Journal of Fluid Mechanics*, Vol. 110, pp. 73–95.

Gutmark, E., and Blackwelder, R. F., 1987, "On the Structure of a Turbulent Spot in a Heated Boundary Layer," *Experiments in Fluids*, Vol. 5, pp. 217–229.

Itsweire, E. C., and Van Atta, C. W., 1983, "The Effects of Different Similarity Transformations on Mean Particle Paths in Turbulent Spots," *J. Physique—Letters*, pp. L-917–L-923.

Josserand, M. A., and Lauchle, G. C., 1990, "Modelling the Wavevector-Frequency Spectrum of Boundary-Layer Wall Pressure During Transition on a Flat Plate," *Journal of Vibration and Acoustics*, Vol. 112, pp. 523–534.

Krane, M. H., and Pauley, W. R., 1992a, "Measurements of the Mass Flux Deficit of a Turbulent Spot—Implications for Boundary Layer Transition Noise," *Symposium on Flow-Induced Vibration and Noise*, ASME NCA-Vol. 13 (Vol. 3).

Krane, M. H., and Pauley, W. R., 1992b, "Estimation of the Direct Radiation from Turbulent Spots Using Boundary Layer Velocity Measurements," Applied Research Laboratory Technical Report TR 92-11, Pennsylvania State University, University Park, PA.

Lauchle, G. C., 1981, "Transition Noise—the Role of Fluctuating Displacement Thickness," *Journal of Acoustical Society of America*, Vol. 69, pp. 665–671.

Lighthill, M. J., 1958, "On Displacement Thickness," *Journal of Fluid Mechanics*, Vol. 4, pp. 383–392.

Schubauer, G. B., and Klebanoff, P. S., 1955, "Contributions to the Mechanics of Boundary Layer Transition," NACA TN 3489.

Van Atta, C. W., and Helland, K. N., 1981, "Exploratory Temperature Tagging Measurements of Turbulent Spots in a Heated Boundary Layer," *Journal of Fluid Mechanics*, Vol. 100, pp. 243–255.

Wygnanski, I., Sokolov, M., and Friedmann, D., 1976, "On a Turbulent 'Spot' in a Laminar Boundary Layer," *Journal of Fluid Mechanics*, Vol. 78, pp. 785–819.

Wygnanski, I., 1981, "On the Possible Relationship Between the Transition Process and the Large Coherent Structures in Turbulent Boundary Layers," *Coherent Structures in Modelling Turbulence and Mixing* J. Jimenez, eds., Springer-Verlag, pp. 168–194.

Wygnanski, I., 1991, "On Turbulent Spots," *Symposium on Turbulence*, University of Missouri-Rolla.

Wygnanski, I., Zilberman, M., and Haritonidis, J., 1982, "On the Spreading of a Turbulent Spot in the Absence of a Pressure Gradient," *Journal of Fluid Mechanics*, Vol. 123, p. 69.

Zilberman, M., Wygnanski, I., and Kaplan, R. E., 1977, "Transitional Boundary Layer Spot in a Fully Turbulent Environment," *Physics of Fluids*, Vol. 20, p. S258.